System Development and Studies on Utilization of Concentrated Solar Beam Radiation for Polymer Processing

Lou A. Stoynov, MEng

School of Engineering Systems

Queensland University of Technology

Brisbane, Queensland, Australia

Submitted as a requirement for the degree of Doctor of Philosophy

2004

KEYWORDS

Accelerated Outdoor Ageing, Cassegrainian Concentrator, Solar Radiation, Thermoplastic Joining.

ABSTRACT

Various solar energy technologies are being developed to harness the available environmentally friendly and sustainable solar radiation. New ways of utilizing this "free" power for different energy consuming processes continue to be created. In this thesis, a multi-stage solar energy concentrating system has been developed and its feasibility as a radiation source for polymer processing has been explored. The solar energy concentrator (SEC) facility comprises a modified Cassegrainian configuration combined with auxiliary imaging and non-imaging optics, serving as an alternative energy source for polymer joining, ageing and adhesive curing.

Modeling and improvement of various aspects of the operation and performance of the SEC facility have been implemented. Optical ray tracing models of the Cassegrainian concentrator with various conventional imaging components and non-imaging concentrators have been created to optimize the optical layout and system efficiency. On their basis, combined 3D ray tracing computer models integrated with the mechanical components have been developed to simulate the entire SEC facility and predict the image size, location and orientation. Additionally, the energy transfer, radiation absorption and heat generation and transfer in the irradiated polymer have been modeled in order to study the radiation–polymer interaction.

One novel contribution of this research is the enhancement of the image forming concentrator with non-imaging cone-like concentrators (conical and compound parabolic concentrator (CPC)), utilizing their inherent disadvantage of excessive length. Compared to the refractive type means of transmitting concentrated solar radiation, the truncated cone and CPC concentrators have been found more efficient enhancing further the concentration and widening the utilized spectral range.

The experimental studies have demonstrated that transparent and colored, similar and dissimilar polymers can be successfully joined using the SEC facility. The especially developed through-transmission technique removes the need to use a

special absorbing medium of the radiant energy required by current advanced welding techniques. The tensile strengths of the joints achieved are comparable to those achieved for similar polymers with other advanced plastic joining methods.

The results from the polymer ageing experiments have shown that ultra-accelerated exposure to concentrated sunlight can be performed with the SEC facility without introducing spurious failure mechanisms. Based on the preliminary investigation on adhesive curing utilizing concentrated solar radiation, it has been concluded that with carefully chosen light-curing adhesives solar radiation can be a useful radiation source for adhesive curing.

TABLE OF CONTENTS

LIST OF PUBLICATIONS ..... **xiv**
NOMENCLATURE ..... **xvi**
ABBREVIATIONS ..... **xviii**
STATEMENT OF ORIGINAL AUTHORSHIP ..... **xix**
ACKNOWLEDGMENTS ..... **xx**
CHAPTER 1. INTRODUCTION **1**
1.1 Background **1**
1.2 Outline of present research **3**
1.3 Overview of thesis chapters **4**
CHAPTER 2. THEORY ASPECTS AND REVIEW OF SOLAR RADIATION CONCENTRATION TECHNOLOGY **6**
2.1 Introduction **6**
2.2 Electromagnetic radiation **7**
2.3 Solar radiation **10**
2.3.1 Extraterrestrial solar radiation 11
2.3.2 Terrestrial solar radiation 12
2.3.3 Radiation on a surface 13
2.3.4 Beam solar radiation 14
2.3.5 Direction of beam radiation 14
2.3.6 Visible spectrum 16
2.4 Solar concentrators **16**
2.4.1 Historical aspects of solar focusing devices 16
2.4.2 Optical surfaces used in solar concentrators 18
2.4.3 Concentrating collectors 19
2.4.4 Concentration ratio 22
2.5 Cassegrainian solar concentrator **25**
2.5.1 Background 25
2.5.2 Related work 30
2.6 Relevant non-imaging concentrators **37**
2.6.1 Truncated cone concentrator 37
2.6.2 Compound parabolic concentrator 38
2.6.3 Truncated compound parabolic concentrator 39
2.7 Conclusions **41**
CHAPTER 3. LITERATURE REVIEW OF RELEVANT POLYMER PROCESSING TECHNOLOGIES **42**
3.1 Introduction **42**
3.2 Effects of temperature change on thermoplastics **43**
3.3 Current thermoplastic joining technologies **44**
3.3.1 Background 44
3.3.2 Welding techniques directly using electromagnetism 46
3.3.2.1 Resistance implant 46
3.3.2.2 Induction 46
3.3.2.3 Radio-frequency 47
3.3.2.4 Microwave welding 48
3.3.2.5 Laser 49
3.3.2.6 Infrared welding 51
3.3.2.7 Recent advanced polymer welding techniques 53
3.3.3 Related work 55
3.4 Radiation curing **69**
3.5 Accelerated ageing of polymers **73**
3.5.1 Irradiation 75
3.5.2 Heating 79
3.5.3 Advanced ultra-accelerated ageing 82
3.5.4 Related work 83
3.6 Conclusions **86**

CHAPTER 4. EXPERIMENTAL EQUIPMENT 87
4.1 Introduction 87
4.2 Experimental apparatus 88
4.2.1 Modified Cassegrainian solar concentrator 88
4.2.2 Light transmission 90
4.2.3 Spot monitoring system and motor control 91
4.3 Instrumentation 92
4.3.1 Pyranometer 92
4.3.2 Pyrheliometer 93
4.3.3 IL1400A Radiometer/Photometer 93
4.3.4 SD2000 Miniature Fiber Optic Spectrometer 94
4.3.5 Spectrophotometer 94
4.3.6 Attenuated Total Reflectance Fourier Transform Infrared (ATR/FTIR) Spectrometry 95
4.3.7 Differential Scanning Calorimetry 96
4.3.8 Air Compressor 96
4.3.9 Data logger 96
4.3.10 Computers 98
4.3.11 Optical microscopy 98
4.3.12 Scanning electron microscopy 98
4.3.13 Tensile testing 98
4.3.14 Stress Analysis 100
4.4 Polymer materials 100
4.4.1 ABS 100
4.4.2 PC 101
4.4.3 PMMA 101
4.4.4 Polypropylene 103
4.5 Test specimens 103
CHAPTER 5. EVALUATION OF RELEVANT AMBIENT, SYSTEM AND MATERIAL CHARACTERISTICS 104
5.1 Introduction 104
5.2 Measurement and evaluation of relevant system and ambient meteorological data/parameters 105
5.2.1 Angular size of the sun and available solar radiation 105
5.2.2 Ambient temperature, wind speed and relative humidity 107
5.3 Testing and evaluation of thermal and optical characteristics of the SEC facility 108
5.3.1 Characteristics and amount of re-emitted solar radiation 108
5.3.2 Measured and calculated SEC variables 111
5.3.2.1 Relevant principal Cassegrainian parameters 111
5.3.2.2 Concentration ratios 116
5.4 Radiation characteristics and material properties evaluation 121
5.4.1 Radiation characterization of the assigned polymers 121
5.4.1.1 Spectrophotometric measurements 122
5.4.1.2 Through-transmission solar radiation measurements 126
5.4.2 Other relevant material properties 127
5.4.2.1 Tensile testing of control samples 127
5.4.2.2 Differential scanning calorimetry measurements 129
5.4.3 Experimental outdoor heat generation measurements 131
5.5 Conclusions 134
CHAPTER 6. MODELING 136
6.1 Introduction 136
6.2 Optical ray tracing models 137
6.2.1 Ray tracing model of the Cassegrainian solar energy concentrator 137
6.2.2 Optical ray tracing models of the SEC with conventional imaging optics 138
6.3 Image analysis and optimization 139
6.3.1 Image analysis and evaluation 139
6.3.2 Optimization 144

6.4 Combined three-dimensional computer modeling of the SEC facility systems with ray tracing 147
6.4.1 Computer model of the SEC 148
6.4.2 Combined computer models of the SEC with imaging auxiliary optics 150
6.5 Three-dimensional computer modeling with a non-imaging third stage concentrator 153
6.5.1 Truncated cone concentrator 154
6.5.2 Compound parabolic concentrator 155
6.6 Mathematical modeling of polymer irradiation process 157
6.6.1 Background 158
6.6.2 Summary of the modeling process 163
6.6.2.1 Energy transfer basis of the models 164
6.6.2.2 Description of the models 165
6.6.3 Experimental verification of the models 178
6.7 Empirical modeling of polymer joint strength 181
6.8 Conclusions 182
CHAPTER 7. DEVELOPMENT AND MODIFICATION OF THE SOLAR CONCENTRATOR FACILITY SYSTEMS 184
7.1 Introduction 184
7.2 Design and experimental development of sun-tracking device 185
7.2.1 Background 185
7.2.2 Manual joystick control 186
7.2.3 Electro-optical automatic sun-tracking 187
7.3 Experimental exploration of beam transmitting systems 191
7.3.1 Modification of the light transmission with conventional optics 191
7.3.2 Solar radiation transmission with fiber optic guide 195
7.4 Non-imaging third stage concentrators 198
7.4.1 Solar radiation transmission with truncated cone 198
7.4.2 Solar radiation transmission with CPC 199
7.5 Design and development of other auxiliary systems 201
7.5.1 Positioning and focusing device 201
7.5.2 Clamping devices 203
7.5.3 Experimental cooling system 205
7.5.4 Beam control system 206
7.5.5 Experimental test rig 207
7.6 Conclusions 208
CHAPTER 8. EXPERIMENTAL STUDIES ON POLYMER JOINING 210
8.1 Introduction 210
8.2 Preliminary joining experiments of selected engineering thermoplastics 211
8.2.1 Background 211
8.2.2 Joining of transparent and white thermoplastics 211
8.2.3 Results and discussion 212
8.2.3.1 Joining of thermoplastics without controlling the welding parameters 212
8.2.3.2 Joining of thermoplastics with controlling the exposure duration 213
8.2.3.3 Microscopic examinations 214
8.2.3.4 Comparison with thermoplastic joining using microwave energy 218
8.3 Experimental butt joining of transparent and colored, similar and dissimilar polymers 219
8.3.1 Background 219
8.3.2 Experimental methodology 220
8.3.3 Results and discussion 222
8.3.3.1 Study on identically colored polymer butt joining with imaging auxiliary optics 222
8.3.3.2 Study on identically colored polymer butt joining with non-imaging auxiliary optics 225

8.3.3.3 Study on butt joining of differently colored similar and dissimilar polymers with imaging auxiliary optics....227
8.4 Experimental lap joining of transparent and colored, similar and dissimilar polymers....231
8.4.1 Through-transmission joining technique....232
8.4.2 Results and discussion....233
8.4.2.1 Study on lap joining using auxiliary imaging optics....233
8.4.2.2 Study on lap joining with non-imaging auxiliary optics....235
8.5 Conclusions....237
CHAPTER 9. STUDIES ON ACCELERATED SOLAR RADIATION EXPOSURE AND ADHESIVE CURING OF POLYMERS....239
9.1 Introduction....239
9.2 Irradiation exposure and photoelastic stress analysis....240
9.3 Natural accelerated ageing of transparent and colored polymers....244
9.3.1 Background....244
9.3.2 Experimental methodology....245
9.3.3 Results and discussion....247
9.4 Curing of adhesives for thermoplastic bonding utilizing concentrated insolation....252
9.4.1 Feasibility study on curing of common epoxy adhesives....252
9.4.2 Curing of UV/visible light adhesives for thermoplastic bonding utilizing concentrated insolation....253
9.4.2.1 Experimental procedure....254
9.4.2.2 Results and discussion....255
9.5 Conclusions....258
CHAPTER 10. CONCLUSIONS AND SCOPE FOR FUTURE WORK....260
10.1 Summary of the research outcomes....260
10.2 Some advantages and limitations of the developed system....265
10.3 Original research contributions....266
10.4 Scope for future work....267
APPENDICES
1 OVERALL AIMS AND OBJECTIVES....1-1
2 SPECTRAL RANGES OF ELECTROMAGNETIC RADIATION....2-1
3 CLASSIFICATION OF POLYMERS....3-1
4 SEC LOCATION AND PROTECTIVE SHED....4-1
5A DETERMINISTIC MODEL FOR CALCULATION OF THE VARIABLE PARAMETERS OF SEC FACILITY....5A-1
5B UV MEASUREMENT RESULTS....5B-1
5C OTHER SPECTRAL MEASUREMENT RESULTS....5C-1
5D CALCULATION OF AVERAGE UTILIZED SOLAR ABSORPTANCE....5D-1
5E PHOTOGRAPHS OF EXPOSED SPECIMENS AT FOCUS....5E-1
5F TEMPERATURE VARIATION DURING EXPOSURE....5F-1
6A ALGORITHMS WRITTEN FOR THE RAY TRACING MODELS....6A-1
6B RAY TRACING AND IMAGE ANALYSIS IN OSLO....6B-1
6C CALCULATED PARAMETERS OF VARIOUS CPCs....6C-1
6D EXPERIMENTAL DATA USED IN EMPIRICAL MODEL....6D-1
7A MODIFICATION DESIGN DIAGRAMS....7A-1
7B SOME 3D DESIGNS WITH THE SEC....7B-1
8 EXPERIMENTAL THERMOPLASTIC JOINING RESULTS....8-1
9 EXPERIMENTAL RESULTS FROM STUDIES ON POLYMER AGEING....9-1
GLOSSARY....G-1
REFERENCES....R-1

LIST OF FIGURES

Figure 2.1: The spectrum of electromagnetic radiation (ICNIRP 1992) 9
Figure 2.2: Spectral distribution of extraterrestrial solar radiation 11
Figure 2.3: Solar irradiance and typical application ranges 12
Figure 2.4: Zenith angle, slope, surface azimuth angle and solar azimuth angle for a tilted surface (Stoynov 1997) 15
Figure 2.5: Spherical mirror line focus Figure 2.6: Parabolic mirror point focus....17
Figure 2.7: Common conic sections....18
Figure 2.8: Relative shapes of conic surfaces in two dimensions....19
Figure 2.9: Most commonly used types of collector configurations....20
Figure 2.10: Most commonly used types of paraboloidal concentrators 21
Figure 2.11: Solar radiation transfer through aperture A_a to absorber A_{abs}....22
Figure 2.12: Theoretical thermodynamic concentration limit for a single dish for various angular source size 23
Figure 2.13: Maximum geometric concentration for one- and two-stage systems (Welford and Winston 1989:197)....24
Figure 2.14: Pictorial of Cassegrainian solar concentrator 26
Figure 2.15: Some important characteristics in a Cassegrainian configuration....27
Figure 2.16: Solar collector systems (Mauk et al. 1979) 30
Figure 2.17: Cassegrainian system geometry (Mauk et al. 1979)....31
Figure 2.18: Off-axis Cassegrainian concentration system (Roman et al. 1995)....34
Figure 2.19: Comparison between classic Cassegrain design and complementary Cassegrain concentrator (Feuermann et al. 1999) 34
Figure 2.20: Schematic diagram of a parabolic concentrator coupled to an optical fiber bundle (Yugami et al. 1999)....35
Figure 2.21: Full-spectrum collector/receiver (Dye et al. 2003)....36
Figure 2.22: Schematic diagram of a truncated cone concentrator....37
Figure 2.23: Construction of the CPC profile from the edge-ray principle (adapted from Welford and Winston 1989) 39
Figure 2.24: Truncated CPC profile expressed in polar coordinates (adapted from Welford and Winston 1989) 40
Figure 3.1: Altering of thermoplastic characteristics with temperature change (adapted from (Tlusty 2000)) 43
Figure 3.2: Thermoplastic joining techniques....45
Figure 3.3: Resistance implant welding set-up 46
Figure 3.4: Induction welding of circular parts....47
Figure 3.5: Radio-frequency welding set-up....48
Figure 3.6: System for microwave welding with (a) susceptible material and (b) without auxiliary welding material....49
Figure 3.7: Laser welding system (adapted from www.joiningtech.com)....49
Figure 3.8: Infrared welding process 51
Figure 3.9: Typical spectral distribution of output from a quartz-halogen lamp compared to the solar radiation spectrum (adapted from Grimm 1996) 52

Figure 3.10: Through-transmission laser welding 53
Figure 3.11: Clear PMMA lap joint made with ClearWeld absorber at the interface 54
Figure 3.12: Heating behaviour without and with filter (Grimm 1996) 56
Figure 3.13: Transmission vs. color of ABS sheets (Grimm and Yeh 1998) 57
Figure 3.14: Thermoplastic films joined with CO_2 laser with the aid of transparent heat sink (Kurosaki et al. 2003) 63
Figure 3.15: Weld performance vs. power density for PMMA and PC 64
Figure 3.16: Influence of wavelength on absorption of IR radiation for green, red, blue, natural and yellow colored PA (Kagan et al. 2001) 66
Figure 3.17: Perceived colors in human vision (Kagan et al. 2001a) 67
Figure 3.18: Absorption spectrum of PP (Bonten and Tuchert 2000) 68
Figure 3.19: Surface and volumetric absorption of plastics (Bonten and Tuchert 2000) 69
Figure 3.20: Conventional and volumetric heating 70
Figure 3.21: Energy absorbed for cure by UV (left) and UV/visible (right) structural adhesives (Bachmann 1995) 73
Figure 3.22: Effect of weathering on light transmission of glazing plastics (Blaga 2002) 74
Figure 3.23: Schematic of optical system for Fresnel reflecting concentrator accelerated weathering machine (ASTM-G90 1999) 76
Figure 3.24: EMMAQUA and ACUVEX Fresnel concentrator weathering devices 77
Figure 3.25: Xenon arc lamp output vs. solar radiation spectrum (Crase and Scott 2002) ... 78
Figure 3.26: Schematic diagrams of black standard sensor (left) and two types of black panel sensors (right) (adapted from Boxhammer et al. 1993) 82
Figure 3.27: Thermal degradation steps for PMMA (Nising et al. 2003) 84
Figure 4.1: Originally proposed system with data acquisition 88
Figure 4.2: Primary and secondary mirrors 89
Figure 4.3: Initial arrangement of the solar concentrator 89
Figure 4.4: Initial schematic opto-mechanical layout of the SEC 90
Figure 4.5: Joystick power supply 91
Figure 4.6: DC motor power supply 92
Figure 4.7: (a) Pyranometer Kipp & Zonen CM 6, (b) Pyrheliometer Kipp & Zonen CH 1 and (c) Radiation indicator/integrator CC20 93
Figure 4.8: IL1400A radiometer 93
Figure 4.9: (a) Miniature fiber optic spectrometer and (b) Cary 100 UV/VIS spectrophotometer 94
Figure 4.10: FTIR spectrometer Thermo Nicolet Nexus 95
Figure 4.11: Differential scanning calorimeters TA Q10 (left) and TA Q100 (right) 96
Figure 4.12: Data Taker 500 data logger 97
Figure 4.13: JXA-840A scanning electron microscope 98
Figure 4.14: Tensile specimen used for stress analysis 99
Figure 4.15: Hounsfield tensile machine 99
Figure 4.16: Modular transmission polariscope system 060 series 100
Figure 5.1: Intensity of direct insolation and ambient temperature during a clear day 106
Figure 5.2: Typical spectral distribution at the primary accepting aperture 106

Figure 5.3: Typical diurnal direct total and UV solar radiation on a clear day.....107
Figure 5.4: UVA and UVR comparison.....107
Figure 5.5: Typical spectral distribution of the primary re-emitted radiation.....109
Figure 5.6: Typical beam broadband and UV insolation power at the primary mirror.....109
Figure 5.7: UVA typically incident and transmitted through the system 110
Figure 5.8: UVB typically incident and transmitted through the system.....110
Figure 5.9: UVR typically incident and transmitted through the system.....111
Figure 5.10: SEC section with overall parameters.....112
Figure 5.11: Layout of the Cassegrainian telescope with variable parameters.....113
Figure 5.12: Geometrical derivation of angle ϕ expression 115
Figure 5.13: Cassegrainian concentration ratios for various final image diameters 117
Figure 5.14: Geometric concentration and target area change with image diameter.....117
Figure 5.15: Possible power densities at various beam insolation intensities.....118
Figure 5.16: Range of power densities at 800 and 1000 W/m² and area concentrations 118
Figure 5.17: Variation of the Cassegrainian concentration and angle at the final focus with primary rim radius change.....119
Figure 5.18: Variation of the angle at the final focus and CPC concentration with primary rim radius change 119
Figure 5.19: Variation of Cassegrainian and CPC concentration ratios with collection angle change and primary rim ring radius change.....120
Figure 5.20: Variation of the angle at final focus and combined concentration with primary ring radius change.....121
Figure 5.21: Total reflectance spectra of all samples.....123
Figure 5.22: UV and VIS light transmittance through 3.2 mm PMMA and 2.85 mm PC....124
Figure 5.23: Computed average solar weighted absorptances of all specimens 125
Figure 5.24: Crazes in notched transparent PMMA bar (adapted from (Menges 1973)) 127
Figure 5.25: Stress–strain curves for the assigned polymers 127
Figure 5.26: Ruptured surface of parent ABS, PC and PMMA material before welding.....128
Figure 5.27: PMMA and PC samples used for DSC.....130
Figure 5.28: Glass transition of ABS.....130
Figure 5.29: Glass transition of PC.....131
Figure 5.30: Glass transition of green PMMA.....131
Figure 5.31: Design drawing and pictures of holder with all irradiated specimens.....132
Figure 5.32: Square test specimens and holding devices.....132
Figure 5.33: Exposed red, green and violet specimens.....133
Figure 5.34: Temperature variation during exposure for green and yellow PMMA at the focus 134
Figure 5.35: Temperature variations for all specimens.....134
Figure 6.1: Rendered image of the Cassegrainian concentrator with magnifying unit and two doublet lenses 138
Figure 6.2: Ray trace model of the Cassegrainian concentrator 140
Figure 6.3: Ray intercept curves analysis for the SEC 140
Figure 6.4: Spot and PSF analysis of the SEC.....142

Figure 6.5: Wavefront report with wavefront reference point for minimized RMS on image surface and for best focus 143
Figure 6.6: Generated GENII error function 144
Figure 6.7: Iteration cycles during optimization 145
Figure 6.8: Ray trace analysis after optimization 145
Figure 6.9: Wavefront and PSF analysis after optimization 146
Figure 6.10: Energy analysis before and after optimization 146
Figure 6.11: Modeling of the formation of the Cassegrainian focus of the SEC with rays and cones 149
Figure 6.12: Optical model with magnifying unit and three doublet lenses in ZEMAX (left) and a combined computer model in AutoCad (right) 151
Figure 6.13: Optical model with magnifying unit and two doublet lenses in OSLO (left) and combined computer model in AutoCad (right) 152
Figure 6.14: Model of the SEC with one auxiliary lens 153
Figure 6.15: The SEC complemented with truncated cone concentrator 154
Figure 6.16: Design and location of the first CPC 155
Figure 6.17: Sectional and perspective views of the first CPC with extreme cone rings 156
Figure 6.18: Perspective sectional views of the SEC and second CPC 157
Figure 6.19: Schematic diagram of butt joining of transparent polymers 159
Figure 6.20: Concentrated light cone from last optical component and exposed volume 160
Figure 6.21: Lap joining process 161
Figure 6.22: Attenuation of a radiation beam through an absorbing material 162
Figure 6.23: Temperature variation vs irradiation time for transparent PMMA 169
Figure 6.24: Geometry of the through-transmission model 171
Figure 6.25: Predicted node temperature change with irradiation time 174
Figure 6.26: 3D surface representation of the temperature variation vs time 175
Figure 6.27: Predicted thermocouple response with exposure duration 178
Figure 6.28: Predicted and experimental temperature variation with time for the irradiated transparent PMMA 179
Figure 6.29: Predicted and experimental temperature variation with time for through-transmission joining of transparent and black PMMA 179
Figure 6.30: Location of thermocouple during through-transmission joining 180
Figure 6.31: Comparison between irradiated polymer and thermocouple models 180
Figure 6.32: Predicted vs measured tensile strength 182
Figure 7.1: First acquisition system with CCD 187
Figure 7.2: Sun-tracking sensors with day-night detector 188
Figure 7.3: Sun-tracking sensor with pipe separation 188
Figure 7.4: Sun-tracking sensor with a cross septum 189
Figure 7.5: Sun-tracking sensor with a cross-septum on a two-plate adjustable base 189
Figure 7.6: Design drawing and a photograph of the relocated tracking sensor 190
Figure 7.7: Power supply and automatic control unit 190
Figure 7.8: Cross sectional view of the modified SEC 192
Figure 7.9: First modification of the trunnion box 193

Figure 7.10: Second stage modification of the SEC 194
Figure 7.11: Solar radiation transmission with a fiber optic guide 197
Figure 7.12: Design drawings of the light cone 199
Figure 7.13: Overall view of the SEC with the truncated cone concentrator 199
Figure 7.14: Design drawings of the first CPC 200
Figure 7.15: Design drawings of the second CPC (left) and relative locations of both CPCs 200
Figure 7.16: Short truncated cone 201
Figure 7.17: Design configuration of the focusing device including the last focusing doublet lens, metric stage and butt clamping device 202
Figure 7.18: Front and back perspective views of the modified single axis metric stage 203
Figure 7.19: A perspective view of the butt joint clamping device 203
Figure 7.20: Lap joining clamping device 204
Figure 7.21: Schematic diagram of cooling system 205
Figure 7.22: Cooling system 206
Figure 7.23: Cooling inlet in the provisional third stage concentrator 206
Figure 7.24: Provisional light chopper and experimental mist/smoke maker 207
Figure 7.25: Experimental test rig 208
Figure 8.1: Welded specimens in the preliminary experiments 212
Figure 8.2: ABS specimens with the lowest tensile strength 214
Figure 8.3: ABS specimens with the highest tensile strength 215
Figure 8.4: PC specimens with the lowest tensile strength 216
Figure 8.5: PC specimens with the highest tensile strength 216
Figure 8.6: PMMA specimens with the lowest tensile strength 217
Figure 8.7: PMMA specimens with the highest tensile strength 218
Figure 8.8: Butt joint clamping device mounting 220
Figure 8.9: Identically colored specimens butt joined with imaging optics 222
Figure 8.10: Average deposited solar energy for butt joined specimens using imaging optics 223
Figure 8.11: Method of clamping proposed for butt joining 224
Figure 8.12: Average deposited solar energy for butt joined specimens using non-imaging optics 226
Figure 8.13: Identically colored specimens butt joined with non-imaging optics 226
Figure 8.14: Some butt joined specimens 228
Figure 8.15: SEM images of fractured surface of green PMMA 229
Figure 8.16: SEM images of fractured surface of transparent PMMA 229
Figure 8.17: SEM images of fractured surface of green PMMA 230
Figure 8.18: SEM images of fractured surface of yellow PMMA 230
Figure 8.19: SEM images of fractured surface of blue PMMA 230
Figure 8.20: SEM images of fractured surface of black PMMA 230
Figure 8.21: SEM images of fractured surface of orange PMMA 231
Figure 8.22: SEM images of fractured surface of red PMMA 231
Figure 8.23: Lap joined specimens using imaging optics 233

Figure 8.24: Average deposited solar energy for lap joined specimens using imaging optics 234
Figure 8.25: Lap joined specimens using non-imaging optics 235
Figure 8.26: Average deposited solar energy for lap joined specimens using non-imaging optics 236
Figure 9.1: Photoelastic stress pattern for PSM-1 (left) and transparent PC (right) 241
Figure 9.2: Insolation irradiation exposure location 242
Figure 9.3: Photoelastic stress pattern in transparent PMMA - side and top views 242
Figure 9.4: Photoelastic stress pattern change with irradiation duration build-up 243
Figure 9.5: Specimen mounting – a sectional view and a photograph 246
Figure 9.6: FTIR absorption spectrum of exposed PSM-1 sample 248
Figure 9.7: FTIR absorption spectrum of exposed PSM-1 with observable changes 248
Figure 9.8: FTIR transmission spectra of control and exposed PP samples 249
Figure 9.9: Comparison FTIR absorption spectra of PP with observable changes 249
Figure 9.10: FTIR absorption spectra of white ABS with observable changes 250
Figure 9.11: FTIR absorption spectra of transparent PMMA with observable changes 250
Figure 9.12: FTIR absorption spectra of green PMMA with observable changes 251
Figure 9.13: Test specimens layout and clamping device 253
Figure 9.14: Specimens cured with light sensitive adhesive for 60 seconds 255
Figure 9.15: Specimens cured with light sensitive adhesive for two seconds 256
Figure 9.16: Comparison between tensile strengths of specimens cured for 60 seconds on non-concentrated light and for two seconds on concentrated light 256
Figure 9.17: Cured Ultra Light Weld 3094 (upper left and right) and Ultra Light Weld 4-20418 (bottom left) 257

LIST OF TABLES

Table 2.1: Spectral regions of electromagnetic radiation 9
Table 2.2: Typical black-body temperatures and their corresponding characteristics....10
Table 2.3: Luminous efficacy of global, direct and diffuse radiation (Perez et al. 1990; Lam and Li 1996) 16
Table 3.1: IR laser welding techniques for thermoplastics (Kurosaki et al. 2003)....62
Table 3.2: Typical adhesive cure response to various wavelength combinations 72
Table 3.3: The equivalence of wavelength, energy and bonding 75
Table 4.1: Technical specifications of the mirrors 89
Table 4.2: Visible light transmittance of 3 mm Perspex GS grade (www.perspex.co.uk 2001) 102
Table 5.1: UVA measured data and calculated concentration and power obtainable 110
Table 5.2: UVB measured data and calculated concentration and power obtainable....110
Table 5.3: UVR measured data and calculated concentration and power obtainable....111
Table 5.4: Weighted average solar reflectances of all samples and transmittances of clear samples in the wavelength range of 370-900 nm 125
Table 5.5: Average transmittance data (beam and total) through clear PMMA and PC ...126
Table 5.6: Tensile strength of parent materials (Stoynov et al. 2000)....128
Table 5.7: Average strength of control samples 129
Table 6.1: Description of the variables in the model....166
Table 6.2: Modified and additional variables in the through-transmission model 170
Table 8.1: Average strength of the weld without controlling the welding parameters....212
Table 8.2: Average strength of the weld with exposure duration controlled....213
Table 8.3: Thermoplastic welding utilizing microwave and concentrated solar energy ...219
Table 8.4: Experimental data from butt joining of polymers with identical colors using imaging optics 222
Table 8.5: Tensile loads of identically colored welded specimens using imaging optics .224
Table 8.6: Experimental results from butt joining of polymers with identical colors using non-imaging optics 225
Table 8.7: Experimental results from lap joining using imaging optics....233
Table 8.8: Tensile loads of lap joined specimens using imaging optics....234
Table 8.9: Experimental results from lap joining using non-imaging optics....235
Table 8.10: Tensile loads of lap joined specimens using non-imaging optics....237
Table 9.1: Estimation of typical accelerated annual equivalent exposure....245
Table 9.2: Mean tensile strength of control and exposed samples 251
Table 9.3: Susceptibility wavelengths of most polymers (Leather 1999) 254
Table 9.4: Tensile strength of cured specimens....256

LIST OF PUBLICATIONS

L.A. Stoynov, P. KDV Yarlagadda, W.C. Yen, “A Feasibility Study into Joining of Engineering Thermoplastics Utilizing Concentrated Beam Solar Radiation”, Journal of Renewable Energy, vol. 21, issue 3-4, pp 333-361, 2000.

P. KDV Yarlagadda, L.A. Stoynov, E.T.S. How, “A Preliminary Study on Performance of Adhesive Bonded Joints Cured by Solar Energy Concentration”, International Conference “Shaping the Sustainable Millennium”, Brisbane, ISBN 1 86435 487 9, 5-7 July 2000.

L.A. Stoynov, E.T.S. How, P. KDV Yarlagadda, “Curing of Adhesive Joints Using Solar Radiation” - Poster at the International Conference “Shaping the Sustainable Millennium”, Brisbane, ISBN 1 86435 487 9, 5-7 July 2000.

L.A. Stoynov, P. Yarlagadda, “Joining of Engineering Thermoplastics by Concentrated Beam Insolation - a Feasibility Study”, International Manufacturing Conference in China - IMCC2000 'Innovation and Technology for the New Millennium', Hong Kong, August 2000.

L.A. Stoynov, P. KDV Yarlagadda, “Joining Of Engineering Thermoplastics By Concentrated Beam Insolation - A Feasibility Study” - Poster at the International Manufacturing Conference in China - IMCC2000 'Innovation and Technology for the New Millennium', Hong Kong, August 2000.

P. KDV Yarlagadda, L.A. Stoynov, W.C. Yen, WCK Wong “Joining of Thermoplastics Using a Cassegrainian Solar Energy Concentrator”, Proc. of 5th Pacific Conference on Manufacturing, Detroit, pp. 399-406, September 2000.

L. A. Stoynov, P. Groombridge, P. D. Bigara, A. Oloyede, “A Concept Material and Configurational Basis for the Mass Production of Solar Reflective Panels”, 38th Annual Conference of the Australian and New Zealand Solar Energy Society SOLAR 2000, Brisbane, December 2000.

L.A. Stoynov, “Multipurpose Portable Solar Electric Generator” - Poster at 38th Annual Conference of the Australian and New Zealand Solar Energy Society SOLAR 2000, Brisbane, December 2000.

Annual Conference of the Australian and New Zealand Solar Energy Society - SOLAR 2000 “From Fossils to Photons” (ISBN 0958619212): The author has been a member of the technical review committee and a co-editor of the proceedings.

P. KDV Yarlagadda, L.A. Stoynov, I.S. Kim, “An Investigation into the Performance of Solar Cured Adhesive Bonded Joins”, Journal of Materials Processing Technology, vol. 113, issues 1-3, pp 160-166, 2001.

E. Siores, L.A. Stoynov, P. KDV Yarlagadda, “Thermoplastic Joining using Solar Energy Concentrator”, Journal of Polymer Engineering, vol. 22, issue 1, pp 1-25, 2002.

L.A. Stoynov, P. KDV Yarlagadda, “Development and Modification of a Cassegrainian Solar Concentrator for Utilization of Solar Thermal Power”, International Solar Energy Conference ISEC 2003, Hawaii USA, 15-18 March 2003.

L.A. Stoynov, P. KDV Yarlagadda, “Joining of Engineering Thermoplastics by Concentrated Beam Insolation - a Feasibility Study”, Journal of Materials Processing Technology, vol. 138, issues 1-3, pp 67-74, 2003.

I.S. Kim, P. KDV Yarlagadda, L.A. Stoynov, “Prediction of Tensile Stress in Welding Using Solar Energy Concentration System”, Advances in Materials and Processing Technologies (AMPT) 2003 Conference, Dublin, Ireland, 2003.

I.S. Kim, P. KDV Yarlagadda, L.A. Stoynov, “A Study on an Intelligent System to Predict the Tensile Stress in Welding Using Solar Energy Concentration”, Journal of Materials Processing Technology, vol. 153-154, pp 649-653, 2004.

The author had published more than 14 papers before commencement of this research and holds 13 patents in the area of solar and alternative energy utilization, in particular heating, air conditioning, development and testing of solar collectors, and solar cooling with zeolite.

NOMENCLATURE

A	area [m^2]
A_0	amplitude of sine wave
Å	Angström (1Å=10^{-10} m)
C_R	average flux concentration ratio
c_0	velocity of light in vacuum [m s^{-1}]
c_p	specific heat [J kg^{-1} K^{-1}]
c_1	curvature of primary mirror [mm]
c_2	curvature of secondary mirror [mm]
D_{tot}	total solar radiation received on surface [W m^{-2}]
D_{dir}	direct beam radiation [W m^{-2}]
D_{diff}	diffuse (or sky) radiation [W m^{-2}]
D_p	diameter of primary mirror [mm]
D_s	diameter of secondary mirror [mm]
E	total energy [kJ]
E_c	energy consumed [kJ]
F	Fourier's number
F/#	F/number
f	effective focal length [mm]
f_p	focal length of primary mirror [mm]
f_s	focal length of secondary mirror [mm]
G	global irradiance or solar flux density [W m^{-2}]
G_b	beam irradiance [W m^{-2}]
G_d	diffuse irradiance [W m^{-2}]
G_λ	solar spectral irradiance averaged over a small bandwidth centered at λ [W m^{-2} μm^{-1}]
H	global irradiation [J m^{-2}]
H_b	beam irradiation [J m^{-2}]
H_d	diffuse irradiation [J m^{-2}]
h_c	convection heat transfer coefficient [W m^{-2} K^{-1}]
h	Planck's constant = 6.6256 x 10^{-34} Js
I_s	intensity of available direct solar radiation [W m^{-2}]
k	thermal conductivity [W m^{-1} K^{-1}]

m	mass [kg]
m’	mass flow rate [kg s^{-1}]
n	index of refraction
q	heat flow rate [W]
Q	total quantity of heat transferred [J]
Q_{abs}	total quantity of heat absorbed [J]
R_p	radius of primary mirror [mm]
R_s	radius of secondary mirror [mm]
q’’	heat flux per unit area [W m^{-2}]
q’’’	heat flux per unit volume [W m^{-3}]
t	time [s]
T	temperature [°C] or [K]
T_g	glass transition temperature [°C]
T_m	melting temperature [°C]
U	overall heat transfer coefficient [W m^{-2} K^{-1}]
V	volume [m^3]
Z	sagitta [mm]
α^s	absorptance of solar radiation
α	thermal diffusivity [m^2 s^{-1}]
ε	emittance
ϕ	rim angle [°]
λ	wavelength [m], [wavenumber]
η_p	reflectivity of primary mirror
η_s	reflectivity of secondary mirror
ν	frequency [s^{-1}]
θ_{sun}	half solar rim angle (solid angle) [°]
ρ	density [kg m^{-3}]
ρ^s	reflectance of solar radiation
σ	Stefan-Boltzmann constant = 5.6697 x 10^{-8} W m^{-2} K^{-4}
σ_t	tensile strength [N m^{-2}]
τ	welding duration [s]
τ^s	transmittance of solar radiation

Superscripts . (over dot) quantity per unit time

ABBREVIATIONS

ABS – acrylonitrile-butadiene-styrene

ASTM - American Society for Testing and Materials Standards

ATR – attenuated total reflectance

CCD – charge-coupled device

CPC – compound parabolic concentrator

DSC – differential scanning calorimetry

GRP – glass-fiber reinforced polyester

FTIR – Fourier transform infrared

HDPE – high density polyethylene

IR – infrared

LDPE – low density polyethylene

Nd-YAG – neodymium-doped yttrium-aluminium garnet

NIR – near infrared

PE – polyethylene

PEEK – polyetheretherketone

PEI – polyetherimide

PMMA – polymethyl methacrylate

PP – polypropylene

PTFE – polytetrafluoroethylene

PVC – polyvinyl chloride

PVDF – polyvinylidene fluoride

RF – radio frequency

RMS – root-mean-square

SEC – solar energy concentrator

TTIR – through-transmission infrared

TTLW – through-transmission laser welding

UV – ultraviolet

VIS – visible

STATEMENT OF ORIGINAL AUTHORSHIP

The work contained in this thesis has not been previously submitted for a degree or diploma at any other higher education institution. To the best of my knowledge and belief, the thesis contains no material previously published or written by another person except where due reference is made.

Signed: ……

Date: ……

ACKNOWLEDGMENTS

As with most interdisciplinary PhD research works, the preparation of this thesis was not possible without the assistance of others. I would like to take this opportunity to express my deepest gratitude to them.

I must thank my supervisory team, Prof. Prasad Yarlagadda and Prof. John Bell, for their support and encouragement.

My sincere thanks go to Mr Mark Hayne for his invaluable technical assistance with all electronic and electrical work and making the automatics work properly.

I would also like to extend my gratitude to Mr Alf Small, Mr Terry Beach, Mr Wayne Moore, Mr Jonathan James, Mr Vivian Ashton, Mr David McIntosh, Mr David Allen, and Mr Neil Munro for their assistance in building the necessary hardware used in the experimental work.

I wish to gratefully acknowledge the help of many people in the laboratory work, especially: Dr Ian Cowling – for lending me the IL1400A Radiometer/Photometer and ZEMAX software and for the useful discussions, Dr Thorn Bostrom – for the assistance with the SEM imaging, Dr Llew Rintoul – for the assistance with the FTIR spectroscopy analysis, Dr Greg Cash – for the DSC measurements, Mr Pat Stevens and Ms Katherine McNamara – for the assistance with the spectrophotometric measurements.

I would also like to express my appreciation for the useful discussions on: optics and solar energy – to Adj. Prof. Ian Edmonds, materials – to Dr Tuquabo Tesfamichael, and polymers – to Prof. Graeme George.

I am particularly grateful to Prof. Ellias Siores for initiating the solar energy collimator project and Dr Michael Waterworth for the initial design of the optical system.

Last, but not least I would like to thank everyone who has shared, in different times and places, this adventure with me. You know who you are!

CHAPTER 1.
INTRODUCTION

1.1 Background

Solar radiation has served as an energy source since the beginning of life and, the living creatures illuminated by the terrestrially available sunlight have been using it in many different ways. A variety of solar energy technologies are being developed to harness the available solar radiation but its utilization is still an expanding field of human endeavour. Researchers continue to discover new ways to utilize this "free delivered" power and apply it to different energy consuming processes.

Beam solar radiation that intercepts the earth is fairly uniform with a broader spectral range and relatively low intensity compared to other modern sources of electromagnetic radiation. Therefore, when high temperatures are desired, concentration of the incident solar radiation becomes necessary. Solar concentration technologies have made considerable progress over the years and recent achievements have contributed to further increasing the recognition of solar power as a potentially viable source of renewable energy.

Radiation processing of materials using ionizing electromagnetic energy has had practical application for many years. Modern plastics in particular, because of their versatile properties are gradually becoming prevalent and rapidly displacing conventional materials in numerous engineering applications. Moreover, radiation processing of polymers with ionizing radiation has demonstrated to effectively improve various polymer end-use properties. On the other hand, most conventional and modern polymer processing technologies either use or are based on effects utilizing different types of non-ionizing electromagnetic radiation.

Thermoplastics are being increasingly used in a wide variety of applications where they are often joined together, applying various technologies available in the current manufacturing environment. Adhesive bonding technology has shown high potential in certain areas of structural and mechanical engineering. The application of radiation-curable adhesives in manufacturing industry has demonstrated that it can rapidly increase productivity imparting less pollution in the process. The research progress in degradable polymers, including biodegradable and photodegradable

plastics, has led to the decreasing of their detrimental effect and has increased the need for reliable weathering tests.

The various technologies used in those three polymer-processing fields however, require artificial sources and mechanisms for generation of electromagnetic radiation regardless of its type. On the other hand, the radiation, emitted by the biggest source of broadband electromagnetic radiation, is greatly underutilized.

Although there has been a great deal of research on solar energy utilization in a number of industries, it has not been widely studied for the purposes of polymer processing. Most of the traditionally used polymer processing methods such as joining, ageing and adhesive curing are relatively well established but some no longer meet the requirements of the modern industries using plastics. Furthermore, the advanced development of radiative non-contact heating sources have prompted more sophisticated polymer processing technologies in which the most costly technology serves the most inexpensive material.

Recently developed advanced joining techniques require additional energy absorbing materials such as special dyes and pigments which potentially pose problems related to pigment toxicity and waste management, having negative environmental impact (Jones et al. 2000; Woosman and Sallavanti 2003). Such additives could also initiate or promote further polymer photodegradation. A new technology is needed to address these problems without the necessity of any additional substance.

The degradation of polymers in artificial laboratory conditions has been investigated extensively. However, little research on accelerated ageing of polymers exposed to natural outdoor environment and particularly concentrated solar radiation, has been found in the published literature. Facilities for ultra accelerated natural sunlight exposure testing of materials to predict their service time are needed.

The well-recognized UV curing method of light sensitive adhesives is not always acceptable in all applications because it requires UV exposure and transmission of UV light through the material. In addition, many translucent and colored polymers and other UV blocked materials, even transparent PC could not be cured with UV sources (Bachmann 1995). Because there is limited data on the effect of visible light and no information on using concentrated sunlight for adhesive curing, there is a need in the field for further research into utilization of visible solar radiation.

1.2 Outline of present research

In attempt to address the above identified problems, an alternative energy system has been developed and explored in this research. The lack of information about the useful interaction between concentrated solar radiation and a polymer has also prompted this research. The overall aims of this thesis are to develop an alternative system and technique for utilization of solar radiation for polymer processing, and use them to study and contribute towards better understanding of the radiation – polymer interaction.

The main objectives include:

- meteorological evaluation, optical modeling and development of a solar concentrator capable of continuously measuring, tracking, concentrating and focusing solar radiation, and transmitting it to the work-piece;
- characteristics evaluation, modeling and improvement of various aspects of the operation and performance of the energy system and the polymer irradiation process;
- experimental studies on joining of clear and colored, similar and dissimilar polymers and feasibility studies on polymer ageing and adhesive curing utilizing the developed solar concentrator system.

A detailed description of the research aims and objectives is given in Appendix 1.

The solar energy concentrator (SEC) facility comprises a modified two-mirror Cassegrainian configuration combined with auxiliary imaging and non-imaging optics. The concentrator technology utilizes beam solar radiation, predominantly in the visible and near UV range of the spectrum, to produce the necessary radiant energy required for joining and other irradiation processing of engineering thermoplastics.

The use of various types of Cassegrainian concentrators for different but predominantly theoretical applications has been reported by many researchers in the literature (see Chapter 2, Section 2.5.2). However, no similar three-stage concentrator comprising Cassegrainian configuration utilizing solar radiation for the studied applications has been found. Therefore, in this research a new, alternative irradiation system has been developed and three possible applications have been experimentally studied.

1.3 Overview of thesis chapters

Because this research involves multidisciplinary studies, to reflect the state-of-the-art in several areas pertinent to the research, a substantial amount of published literature has been critically reviewed and summarized in the first two chapters. The researched areas included mainly thermal utilization of solar radiation, in particular focusing and non-imaging solar concentrators and their applications, and polymer processing, especially polymer joining, ageing and radiation curing. The next chapter describes the experimental apparatus, instrumentation and materials used in most of the experimental work performed in this research.

Chapter 5 describes the evaluation tests of the optical and thermal characteristics and capabilities of the SEC facility, as well as the relevant material properties of the thermoplastics used. These evaluation tests have been necessary for the modeling and experimental studies. Because this research involves outdoor utilization of natural solar radiation, this chapter also presents typical variation and limits of ambient parameters and system capabilities in the particular environment. The laboratory assessment of the radiation characteristics and other material properties of the polymers, complemented with outdoor measurements have been a basis for gaining an insight into the radiation-material interaction. An important part of this chapter is the geometrical modeling of the light rays by the especially derived mathematical equations describing the optical path of any ray arriving at the focus after reflection from the clear apertures of the primary and secondary mirrors.

Chapter 6 summarizes the modeling work performed during the development, modification and experimental testing of the SEC facility. Three-dimensional optical ray tracing models of the Cassegrainian solar concentrator as well as the auxiliary imaging and non-imaging optics are presented. They are followed by combined 3D ray tracing computer models integrated with the mechanical components and developed to simulate the whole SEC facility and predict the image size, location and orientation. Emphasis is also given to evaluation and optimization of the image at the Cassegrainian focus. Mathematical modeling of the energy transfer, radiation absorption and heat generation and transfer in the irradiated polymer has been implemented to facilitate the study of the radiation–material interaction. The mathematical models developed to predict the temperature variation and duration for attaining the glass transition state of the irradiated polymer and to simulate the

temperature distribution during through-transmission polymer joining are described. Their experimental verification follows. A simple linear statistical model created in an attempt to predict the most probable joint strength for particular ambient parameters is also presented.

A major part of this research was focused on the development and continuous modification of the SEC facility systems during the course of the research. Chapter 7 describes the development and implementation of a sun-tracking and controlling system for acquisition of the solar image, as well as the significant modifications to the originally proposed beam transmission optical path via auxiliary optics. The design of non-imaging third stage concentrators for solar radiation transmission is discussed along with the design and development of innovative auxiliary systems for the implementation of the concentrated solar flux utilization process.

Chapter 8 discusses the experimental studies performed to determine the weldability of identically and differently colored, similar and dissimilar polymers in butt and lap joint configurations using concentrated solar radiation. Particular attention is given to studying the effect of color (chromatic and achromatic) on the radiation-material interaction. A new insolation utilization system using a third stage non-imaging concentrator to serve as an alternative radiation source for polymer joining is presented. A new through-transmission irradiation technique explored for polymer joining without the need for any additional absorbing substance is also discussed.

Chapter 9 summarizes the experimental studies on two other applications of the developed SEC facility. They include ultra accelerated natural weathering tests to study the polymer ageing process and radiation curing of adhesive-bonded thermoplastic joints. A study on irradiation exposure and photoelastic stress analysis initiated to assess the effect of concentrated solar radiation on the properties of thermosetting and thermoplastic polymers is also presented.

The thesis concludes with a summary of the outcomes of the research, discussion on advantages and limitations of the developed system and outline of future work.

CHAPTER 2.
THEORY ASPECTS AND REVIEW OF SOLAR RADIATION CONCENTRATION TECHNOLOGY

2.1 Introduction

Extensive research is being dedicated to making solar radiation applications more efficient and introducing the utilization of solar energy into new technologies. Solar concentration technologies have made considerable progress and can be applied not only to generate cost-effective electricity, but also to provide the energy needs in other applications for industry in general. Some relevant data and theory aspects of beam solar radiation concentration are discussed briefly in this chapter.

Central objectives of this research are to study the interaction of solar radiation with polymers and perform experimental joining, adhesive curing and ageing of clear and colored polymers. In order to achieve these objectives the initially designed experimental SEC facility has been continuously modified during the research. Since in this research an imaging Cassegrainian type concentrator with either auxiliary refracting or reflecting parabolic third stage re-concentration has been used, relevant theory aspects as well as related work are included in this chapter. Because of lack of information describing identical or similar systems using concentrated solar radiation for the researched applications, comparable current and alternative technologies used for such applications have been reviewed. Different forms of the known electromagnetic radiation are artificially generated and utilized in most of the technologies discussed in the following Chapter 3. Because of this, for comparison the electromagnetic radiation and its spectrum with particular emphasis on solar radiation are briefly discussed in this chapter.

It begins with a brief review of electromagnetic radiation theory. The following sections give an overview of solar radiation because of its importance and relevance to this research and include a review of relevant solar radiation data, solar radiation concentration principles and devices. Some pertinent theoretical aspects of solar radiation concentration technology and related research are also incorporated in this chapter. The chapter concludes with some Cassegrainian concentrator theory aspects and a related literature review.

2.2 Electromagnetic radiation

Also referred to as radiant energy or sometimes light, by definition electromagnetic radiation is a form of energy (of waves and particles) produced by an acceleration of electric charges/fields. Therefore, the term 'double nature of the electromagnetic radiation' is sometimes used.

In 1864 it was postulated by James Clerk Maxwell that accelerated charges or changing electric currents give rise to electric and magnetic fields, which has become the theoretical foundation of electromagnetic waves. His theory is used to explain optical properties like the color of different wavelengths and their diffraction interference, polarization, etc. Corresponding to certain wavelengths in vacuum, the light waves with different frequencies have different colors. The existence of such waves was demonstrated experimentally by Heinrich Hertz in 1887. Considered linear in space, the electromagnetic waves can be reflected or refracted at a constant speed, which in vacuum is:

$$c_0 = \nu\lambda \approx 3 \times 10^8 \text{ ms}^{-1} \qquad (2.1)$$

In another words, the electromagnetic waves are oscillating electric and magnetic fields travelling together through space at the speed of light. In the ordinary optics it is believed that these electric and magnetic fields are mutually perpendicular and both perpendicular to the main path of light propagation. As the wave propagates, if the light beam is linearly polarized, the electric and magnetic fields could have fixed orientation changing only its magnitude. The magnitude E of the electric field along the path of propagation of the light beam can be written as (Malacara and Malacara 1994):

$$E = Ae^{i(ks-\omega t)} = Ae^{i(\phi-\omega t)} \qquad (2.2)$$

where A is the amplitude of the wave, i is the angle of incidence of the light beam, k is the wave number, defined by $k=2\pi/\lambda$, s is the distance traveled along the light path, ω is the angular frequency, defined by $\omega=2\pi\nu$, ϕ is the phase difference between the point being considered and the origin, and $\phi-\omega t$ is the instantaneous phase, assuming that it is zero at the origin for $t=0$.

The wavefront in the light beam analyzed in this thesis is a surface in space for which all points have the same instantaneous phase ϕ. The distance between two such consecutive wavefronts is then the wavelength.

On the other hand, the quantum theory, in particular corpuscular description of electromagnetic radiation is more convenient for mathematical interpretation of other electromagnetic radiation properties such as black-body radiation. A black-body is a perfect absorber of radiation in general i.e. all incident radiation on such body will be absorbed regardless of its wavelength. This absence or negligible reflectance of radiation is the reason for the name given to a black-body. The wavelength distribution of radiation emitted by a black-body is described by Planck's law (Duffie and Beckman 1991):

$$E_{\lambda b} = \frac{2\pi hc_0^2}{\lambda^5 (e^{\frac{hc_0}{\lambda k_0 T}} - 1)} \qquad (2.3)$$

where k_0 is Boltzmann's constant (1.380622×10^{-23} J/K). The groups $2\pi hc_0^2$ and hc_0 / k_0 are often called Planck's first and second radiation constants and given the symbols C_1 and C_2 respectively. Recommended values are $C_1 = 3.7405 \times 10^{-16}$ m^2W and $C_2 = 0.0143879$ mK. According to Planck's law all heated objects emit a characteristic spectrum of electromagnetic radiation.

In 1900 it was proposed by Max Planck, in conjunction with the quantum theory, that the propagation of electromagnetic radiation could be considered as a collection of discrete packets of energy, called photons or quanta, whose magnitude depends on their frequency (Cengel 2003):

$$E = h\nu \qquad (2.4)$$

Depending on its energy, a photon could behave more like a wave or more like a particle. When used in its broadest sense the term electromagnetic radiation includes different types of radiation that resemble white light and can be characterized by their frequency and wavelength. The frequency ν is the number of field oscillations that occur each second, usually given in Hertz or cycles/second. The wavelength λ is the distance in space between two maxima and minima in a wave observed at the same time, usually given in units of length.

The term electromagnetic radiation is a broad term and theoretically, the range of possible wavelengths or frequencies is considered limitless. In reality, the known spectral range of electromagnetic radiation is divided into regions according to their properties and frequency, as shown in Figure 2.1.

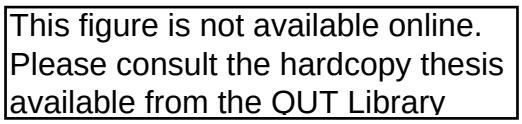

Figure 2.1: The spectrum of electromagnetic radiation (ICNIRP 1992)

In general, the most utilized part of the electromagnetic spectrum covers a very broad range from extremely short wavelengths, less than a billionth of a meter (X-rays) to relatively long, more than a meter (radio waves). Most regions of the electromagnetic radiation are typically used in different industries, the boundaries between those regions are not well defined and may vary depending on the user. (In this work most data is adapted from ASTM-G113 1994, SAA-HB9 1994 and AS/NZS2243.5 2004.) The central region associated with wavelengths between 200 nm and 3000 nm is sometimes called optical radiation because a conventional optical material can be used to alter the direction of propagation and focus the radiant energy. Covering a considerable part of this region, solar radiation is considered as optical radiation. The divisions of the electromagnetic spectrum and their limits in more detail are shown on Table 2.1.

Table 2.1: Spectral regions of electromagnetic radiation

Radiation type		Wavelength range
Cosmic rays		< 0.01 Å
Gamma rays		0.01 – 1 Å
X-rays		1 – 100 Å
Ultraviolet	Extreme UV (vacuum) (UV-C) Far UV (UV-B) Near UV (UV-A black light)	1 to 10 – 190 (10 – 280) nm (200 – 280) nm 190 – 300 (280 – 315) nm 300 – 400 (315 – 400) nm
Visible Light		0.38 – 0.78 μm
Infrared	Near IR (IR-A) Middle IR (IR-B) Far IR (IR-C)	0.78 – 3.0 (0.78 – 1.4) μm 3.0 – 30 (1.4 – 3.0) μm 30 –1000 (3.0 – 1000) μm
Hertzian waves	Microwave Radio & TV	1 – 1000 mm 0.1 – 1000 m

In this research, as in most terrestrial solar energy applications only the electromagnetic radiation in the region of (0.2-1000) μm approximately is considered. It is called thermal radiation and is emitted by all substances by the virtue of their temperature. Being an ideal concept, by definition the black-body must absorb and emit the maximum amount of radiation. When the wavelength corresponding to the maximum intensity of black-body radiation is of interest,

Wien's displacement law can be derived by differentiating Planck's distribution law and equating to zero:

$$\lambda_{max} T = 2897.8 \ \mu mK \qquad (2.5)$$

When the total energy emitted by a black-body is of interest, the Stefan-Boltzmann's law can be derived by integrating Planck's law over all wavelengths:

$$E_b = \int_0^\infty E_{b\lambda} d\lambda = \sigma T^4 \qquad (2.6)$$

Typical black-body temperatures necessary to give a peak for emitted radiation in various regions of the spectrum are given in Table 2.2.

Table 2.2: Typical black-body temperatures and their corresponding characteristics

Region	Wavelength [cm]	Energy [eV]	Black-body Temperature [K]
Radio	> 10	$< 10^{-5}$	< 0.03
Microwave	10 – 0.01	10^{-5} – 0.01	0.03 – 30
Infrared	0.01 – 7 x 10^{-5}	0.01 – 2	30 – 4100
Visible	7 x 10^{-5} – 4 x 10^{-5}	2 – 3	4100 – 7300
Ultraviolet	4 x 10^{-5} – 10^{-7}	3 – 10^3	7300 – 3 x 10^6
X-Rays	10^{-7} – 10^{-9}	10^3 – 10^5	3 x 10^6 – 3 x 10^8
Gamma Rays	< 10^{-9}	> 10^5	> 3 x 10^8

The utilized spectral regions of the non-ionizing electromagnetic radiation and their corresponding typical applications are presented in Appendix 2.

2.3 Solar radiation

Although today most types of electromagnetic radiation can be created artificially, the most common type electromagnetic radiation, solar radiation, exists naturally emitted by the sun. In the sun, every second 657 million tons of hydrogen convert into 653 million tons of helium. During this conversion process every two atoms of hydrogen join together and make one atom of helium, emitting one photon of light (Wagner 1991). This is why the stars are shining and the sun emits in all directions as much energy as earth receives from it in 100 years. The sun generates radiation energy at the rate of 3.827 x 10^{20} MW by the conversion of mass directly to energy according to Einstein's equation (Wagner 1991):

$$E = mc_0^2 \qquad (2.7)$$

Even though only about one two-billionth of this energy is intercepted by the earth, the energy that strikes the earth's atmosphere in the form of sunlight each year represents the equivalent of nearly 1,000 trillion barrels of oil, sufficient to fuel the global economy thousands of times over (Solar'95 1995).

2.3.1 Extraterrestrial solar radiation

Emitted in all directions, the radiation generated by the sun arrives on the earth in about 8.3 minutes on average (8.17167 at perihelion and 8.45 at aphelion assuming the sun-earth distance as 147.09 x 10^6 km at perihelion and 152.1 x 10^6 km at aphelion). The term radiation flux is used to define the energy passing through an imaginary plane per unit area per unit time in all directions. Radiation intensity is used to define the energy passing through an imaginary plane with unit area per unit time and per unit solid angle with central direction perpendicular to the imaginary plane. The intensity of the extraterrestrial radiation normal to the sun's rays beyond the earth's atmosphere at the mean earth-sun distance of 149,638,420±80 km is referred to as the solar constant. The World Radiation Center has adopted a value of 1367 W/m^2 with an uncertainty of 1% (Kreith and Kreider 1987). The ASTM Committee E21 has recommended 1321.7 W/m^2 at aphelion and 1412.5 W/m^2 at perihelion (ASTM-E490 2000a). In 1800 W. Herschel confirmed that solar radiation includes IR and in 1801 J. W. Ritter noted that it also includes UV.

The extraterrestrial irradiance received on earth is a function of date and apparent time. The standard extraterrestrial solar spectral irradiance is given in Figure 2.2.

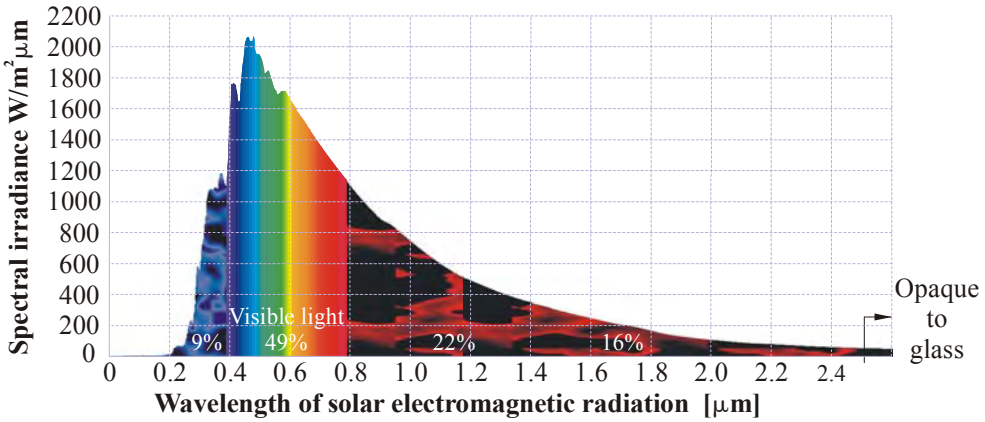

Figure 2.2: Spectral distribution of extraterrestrial solar radiation

Since the distance between the sun and the earth varies during the year, the intensity of the extraterrestrial solar radiation reaching the earth also varies with it. Its maximum is around December 21 when the earth is nearest to the sun, and its minimum is around June 21 when it is furthest from the sun. For engineering purposes many designers prefer the figures given by the ASHRAE as 1398.5 W/m^2 for the former and 1309.9 W/m^2 for the latter (ASHRAE Handbook 1977).

2.3.2 Terrestrial solar radiation

While the intensity of the incoming extraterrestrial solar irradiation is nearly constant outside the earth's atmosphere, the amount and spectral distribution of the incident solar radiation, or insolation, on earth's surface is variable. At any point on earth it is intermittent and varies with changing atmospheric conditions such as clouds and dust, and the shifting position of the earth relative to the sun. Some of the early measured data of the arriving form of the solar spectrum was recorded by Samuel Langley over a period of years, beginning in 1880 (Langley 1883). Typical solar irradiance distribution and the corresponding application ranges are shown in Figure 2.3 (Kreith and Kreider 1987).

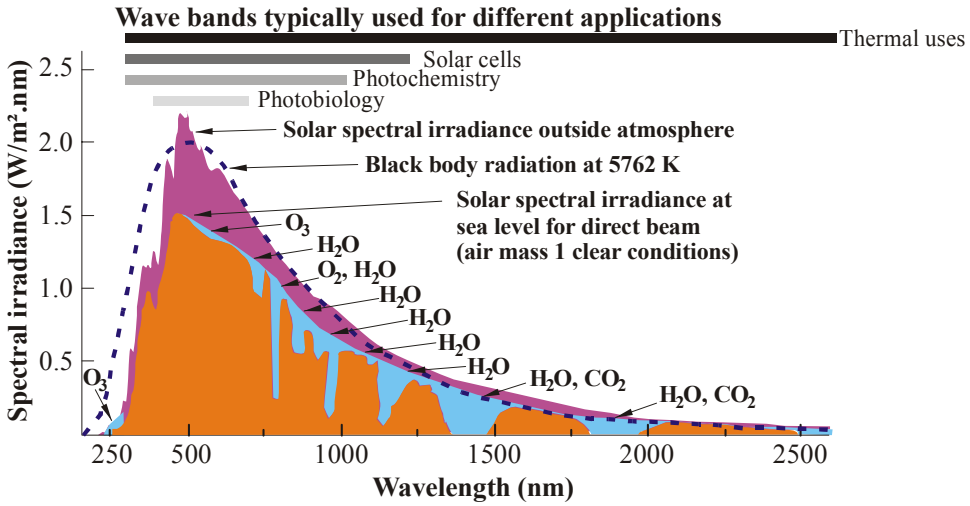

Figure 2.3: Solar irradiance and typical application ranges

Although it is variable, the amount of solar energy falling on one square meter terrestrial flat-leveled surface over the duration of sunshine in a clear day could be 5 kWh on average. For example, in Australia there are four global radiation zones in which the intensity of the daily mean global radiation ranges from less than 4 kWh to more than 6 kWh (AS1745.1 1989). Over the duration of the mean solar day, this corresponds to an average of around (0.16–0.24) kW/m². When compared to other modern energy sources, the terrestrially available insolation is considered as a low power density energy source. Thus, advanced utilization of solar energy is needed and especially when high temperatures are desired, concentration of solar radiation becomes necessary. In practice, for engineering purposes (1) solar energy systems use collectors over a relatively large area or (2) solar energy is utilized by means of concentrating collectors. While in the former case it is necessary to increase the area

on which solar radiation is captured, in the latter case the temperature gained can be increased by decreasing the area from which heat losses occur. The experimental SEC facility used in this research as an energy source for polymer processing is designed to utilize electromagnetic solar radiation in the range of ~0.38 to ~1.2 μm.

2.3.3 Radiation on a surface

The earth receives a vast amount of energy from the sun in the form of solar radiation and all life depends on it. Theoretically the incident total solar radiation (D_{tot}) received on a surface is represented as a sum of the direct or beam radiation (D_{dir}), sky (or diffuse) radiation (D_{diff}) and ground reflected radiation (D_g).

$$D_{tot} = D_{dir} + D_{diff} + D_g \tag{2.8}$$

During the initial experiments of this research the intensity of the total and diffuse insolation components available on the primary mirror surface were measured with a pyranometer and the UV amount, in particular, with a radiometer. As most concentrating collectors utilize beam radiation only, in most experiments the intensity of the direct or beam component was measured with a first class normal incidence pyrheliometer and the incident energy calculated with an integrator.

When solar radiation strikes a surface, typically it is absorbed, reflected and transmitted in different proportions. In accordance with the first law of thermodynamics, the sum of the absorbed, reflected and transmitted radiation energy is equal to the incident radiation:

$$G_{abs} + G_{ref} + G_{tr} = G \tag{2.9}$$

where G is the radiation energy incident on the surface, and G_{abs}, G_{ref} and G_{tr} are the absorbed, reflected and transmitted portions of it, respectively. Generally, the following terms for absorptance, reflectance and transmittance may be defined as:

$$\alpha^s = \frac{G_{abs}}{G} \qquad \rho^s = \frac{G_{ref}}{G} \qquad \tau^s = \frac{G_{tr}}{G} \tag{2.10}$$

Thus, the law of conservation of energy for light on a surface is usually written as:

$$\alpha^s + \rho^s + \tau^s = 1 \tag{2.11}$$

The average absorptance, reflectance and transmittance of a surface can be defined as (adapted from Cengel 2003):

$$\alpha^s = \frac{\int_0^\infty \alpha_\lambda^s G_\lambda d\lambda}{\int_0^\infty G_\lambda d\lambda}; \qquad \rho^s = \frac{\int_0^\infty \rho_\lambda^s G_\lambda d\lambda}{\int_0^\infty G_\lambda d\lambda}; \qquad \tau^s = \frac{\int_0^\infty \tau_\lambda^s G_\lambda d\lambda}{\int_0^\infty G_\lambda d\lambda} \tag{2.12}$$

where G_λ is the spectral irradiance incident on the surface.

According to Kirchhoff's law, if a body has a constant temperature, its emission is identical to its absorption:

$$\varepsilon = \alpha \qquad (2.13)$$

This does not only apply for the radiation as a whole, but for radiation at every wavelength as well (Bonten and Tuchert 2000). However, for any surface, in general, the magnitude of the intensity reflected in a particular direction is a function of the spatial distribution and the wavelength of the incident radiation.

Typically, any concentrating solar collector, including the one used in this research, requires a surface of high specular (mirror-like) reflectance of radiation from the solar spectrum. On the other hand, high efficiency utilization requires low reflectance of radiation in the solar spectrum. It should be noted that if material surfaces have or spread the light intensity equal to a constant, they are called Lambertian or, in more common terminology, diffuse surfaces. Thus the specimen surface in this research, although polished, is considered non-entirely specular.

2.3.4 Beam solar radiation

The component of solar radiation incoming directly from the sun without being scattered by the atmosphere, referred to as direct or beam radiation, has been used in this research. The rate at which this radiant energy is incident on a flat surface is referred to as solar irradiance. On a tilted plane D_{dir} is given by:

$$D_{dir} = D_N \cos(\theta) \qquad (2.14)$$

where D_N is the radiation normal to solar beam and θ is the incident angle of solar beam on a tilted plane.

2.3.5 Direction of beam radiation

The geometric relationships between a plane of any particular orientation relative to the earth at any time (whether that plane is fixed or moving relative to the earth) and the incoming beam solar radiation, that is, the position of the sun relative to that plane, can be described in terms of several angles (Duffie and Beckman 1991). These angles and the relationships between them are as follows:

ϕ **Latitude**, the angular location north or south of the equator, north positive; $-90° \le \phi \le 90°$.

δ **Declination**, the angular position of the sun at solar noon with respect to

the plane of the equator, north positive; - 23.45°≤ δ ≤23.45°.

β **Slope**, the angle between the plane surface in question and the horizontal; 0° ≤ β ≤ 180° (β > 90° means that the surface has a downward facing component).

γ **Surface azimuth angle**, the deviation of the projection on a horizontal plane of the normal to the surface from the local meridian, with zero due south, east negative, west positive; -180° ≤ γ ≤ 180°.

ω **Hour angle**, the angular displacement of the sun east or west of the local meridian due to rotation of the earth on its axis at 15° per hour, morning negative, afternoon positive.

θ **Angle of incidence**, the angle between the beam radiation on a surface and the normal to that surface.

The declination reaches its maximum value, +23°45′, on June 21-22 (the summer solstice in the northern hemisphere, the winter solstice in the southern hemisphere). The minimum value, -23°45′, is reached on December 21-22. Zenith angle, slope, and surface azimuth angle are shown in Figure 2.4.

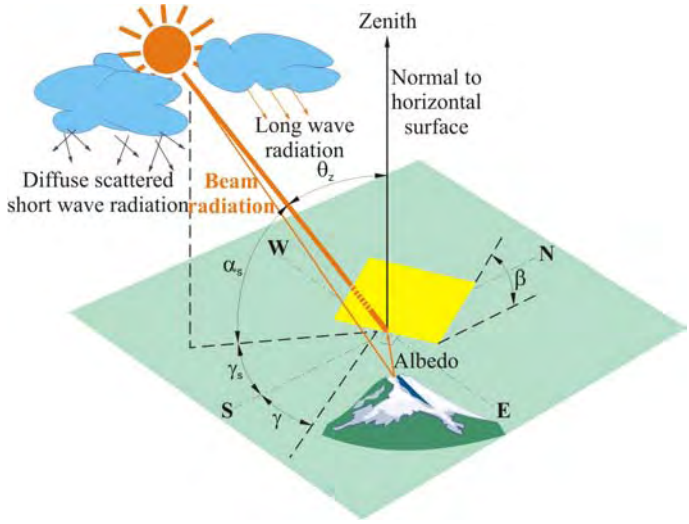

Figure 2.4: Zenith angle, slope, surface azimuth angle and solar azimuth angle for a tilted surface (Stoynov 1997)

The declination, δ, can be found from the equation of Cooper (Duffie and Beckman 1991):

$$\delta = 23.45 \sin(360 \frac{284 + n}{365}) \qquad (2.15)$$

where *n* is the day of the year; 1 ≤ *n* ≤ 365.

The equation relating the angle of incidence of the beam radiation, θ, and the other angles that could be used as an alternative computer controlled tracking is:

$$\cos\theta = \sin\delta \sin\phi \cos\beta - \sin\delta \cos\phi \sin\beta \cos\gamma + \cos\delta \cos\phi \cos\beta \cos\omega + \\ + \cos\delta \sin\phi \sin\beta \cos\gamma \cos\omega + \cos\delta \sin\beta \sin\gamma \sin\omega \quad (2.16)$$

2.3.6 Visible spectrum

The visible portion of the solar spectrum lies in the wavelength band 0.38 μm to 0.78 μm. The human eye is, however, not equally sensitive throughout the band. Luminous efficacy of solar radiation ξ is the amount of visible radiation per unit of total radiation expressed in lumens per watt.

$$\xi = \frac{\int_{0.4}^{0.7} E_\lambda I_\lambda d\lambda}{\int_{0}^{\infty} I_\lambda d\lambda} \quad (2.17)$$

where I_λ is the intensity of solar irradiance (W/m²/μm) and E_λ is the sensitivity of the normal adapted human eye (lm/W).

Luminous efficacy varies with the condition of the atmosphere including cloud cover and type, water vapour and dust. Perez et al. have suggested comprehensive models for predicting the luminous efficacy from the three basic components of global, direct and diffuse radiation (Perez et al. 1990). For average sky conditions for two latitudes (above and below 60 degrees), the luminous efficacy of global, direct and diffuse radiation is given in Table 2.3.

Table 2.3: Luminous efficacy of global, direct and diffuse radiation (Perez et al. 1990; Lam and Li 1996)

Radiation Component	Luminous Efficacy [lumens/watt]		
	Overcast conditions and/or high solar zenith angles >60°	Average value	Clear sky conditions and/or low solar zenith angles<60°
Global	100	118	125
Direct	60	100	108
Diffuse	115	130	160

2.4 Solar concentrators

2.4.1 Historical aspects of solar focusing devices

Being the most important energy source for almost every living biological being, sunlight has been utilized since the beginning of time. There are a number of different ways of using solar radiation that had been utilized by nature even before

humans discovered them. But probably some of the most ancient and mature ways are those that are based on optical and thermal processes utilizing the "free" energy.

It is well known that in the Fourth Century BC Theophrastus reported a number of plane mirrors made of polished copper or silver held in a proper position to focus on the same point which could set fire at that point. By the Third Century BC the Ancient Greeks were capable of building spherical mirrors and producing a similar effect with them instead of using a large number of people holding flat mirrors. During that time they were building parabolic mirrors which were more efficient.

One of the first formal geometric proofs of the different focal properties of spherical and parabolic concave mirrors was given in the Second Century by Diocles, a Greek mathematician. They are shown in Figure 2.5 and Figure 2.6 (Kreider and Kreith 1981).

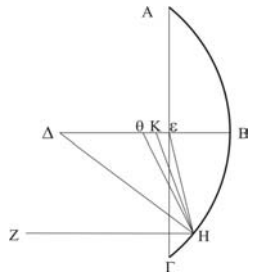

Figure 2.5: Spherical mirror line focus

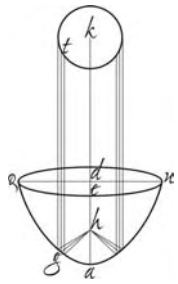

Figure 2.6: Parabolic mirror point focus

Diocles referred to these mirrors as "burning mirrors" and actually the story of Archimedes burning the fleet at Syracuse in 212 BC by using solar reflectors, has existed as a legend for many years since the event. At that time the Ancient Greeks were able to explore the different optical and thermal properties of the burning mirrors acknowledging that when the sunlight is reflected to a single point the intensity is greater than when the rays are reflected to a straight line. A legend existed about Leonardo DaVinci's secret construction of a giant concave mirror with solar boiler that was left unfinished after his death in 1519. Another legendary parabolic "burning mirror" was created with 168 individual mirrors by Comte de Buffon in 1747 and was used to set a pile of tarred planks afire from 195 feet away.

Throughout history there have been a number of great designs and methods used for the construction of spherical and parabolic concave reflectors or a combination of such including new types. The ancient idea to reflect the sun rays incident on a bigger area focusing them on a smaller target has been used in construction of solar furnaces. Since the invention of the lens in the 16th Century another type, the

refracting concentrator, has emerged and is still an expanding endeavour. Among the most significant achievements are: the so-called Fisheye lens (a form of spherical gradient first described by Maxwell in 1854); the Luneburg lens (Luneburg proposed in 1964 the simplest ideal concentrator with maximum theoretical concentration for acceptance angles up to $\pi/2$); the Fresnel lens (one of the most developed optical systems). Linear Fresnel lenses offer the advantage of relatively easy manufacturing in both small and large widths and lengths (Kaplan 1985).

Although it has been well known for centuries that the paraboloid can focus rays parallel to the axis to a point focus making it the ideal shape for a solar reflector, other shapes have also been explored. One of the earliest non-imaging solar collectors in the form of a truncated cone reflector focusing the light uniformly along the axis of the cone, called an "axicon" in modern times, was designed by Mouchot in 1875. The principles of non-imaging optical concentration describing the use of a wedge-shaped optical concentrator was explored by Mendenhall in 1911 (Mendenhall 1911).

2.4.2 Optical surfaces used in solar concentrators

Many different surface types have been explored as reflecting and useful optical surfaces. Most optical components typically use spherical, paraboloidal etc. surfaces that are the surfaces of revolution of so-called conic sections or just conics. These conics, as prompted by their generic name, are the two-dimensional figures resulting from a plane intersecting a cone at various angles (see Figure 2.7).

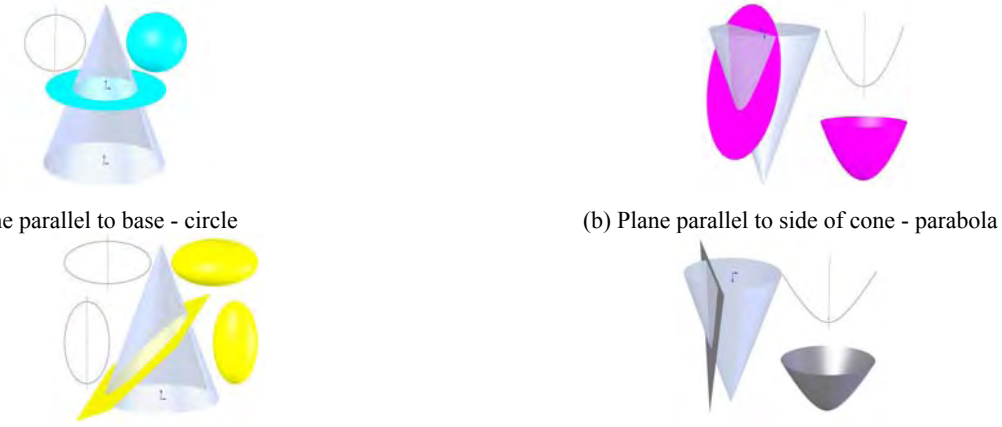

(a) Plane parallel to base - circle

(b) Plane parallel to side of cone - parabola

(c) Plane on angle less than parallel to the side – ellipse

(d) Plane perpendicular to base - hyperbola

Figure 2.7: Common conic sections

The conic equation as given by (Malacara and Malacara 1994) is:

$$Z = \frac{cS^2}{1+\sqrt{1-(1+K)c^2S^2}} \qquad (2.18)$$

where Z is the sagitta i.e. the vertical depth of the curve of a spherical mirror, K is the conic constant, c is the surface base curvature, and S is the semi aperture (radial height on the surface). The relative shapes of these surfaces are illustrated in Figure 2.8.

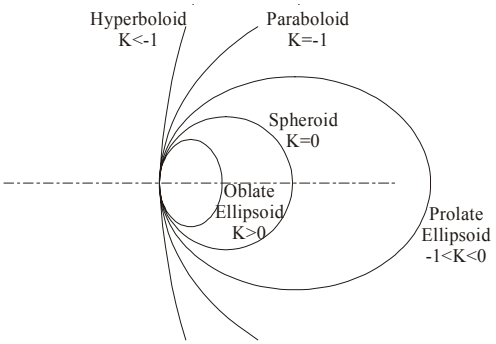

Note: In some of the software used in this thesis, (e.g. OSLO) the term Oblate Spheroid is used instead of Oblate Ellipsoid, and the Prolate Ellipsoid is called Ellipsoid.

Figure 2.8: Relative shapes of conic surfaces in two dimensions

The design of systems consisting of two reflecting surfaces is complicated by the necessity to choose the types of surfaces and by the determination of their parameters. These parameters include the ratio of the diameters of the system entrance and exit pupils, the distance between the vertices of the reflecting surfaces, the system exit angle, the relationship between the exit angle and the slight aperture of the principal reflector.

2.4.3 Concentrating collectors

While in nature solar energy conversion is based on direct conversion of photons, in solar energy concentration technology the efficiency is greatly dependent on the concentrator capabilities. In this research a concentrating collector has been used as a radiative energy source for materials processing.

Since the Ancient Greeks many novel solar concentrator types have been designed, developed and tested but in general they all use reflectors or refractors. Concentrating collectors use mirrored surfaces to concentrate solar radiation on an absorber sometimes called a receiver. The mirrored surface focuses sunlight collected over a large area onto a smaller absorber area to achieve high temperatures. Some designs concentrate solar energy onto a focal point, while others concentrate the sun's rays along a thin line called a focal line. The receiver is located at the focal point or along the focal line. Concentrators could use reflectors or refractors that can

be cylindrical, surfaces of revolution, continuous or segmented. Receivers can be convex, flat, or concave and can be covered or uncovered.

Concentrators are generally classified in three groups: (1) non-imaging with low concentration ratio, (2) linear imaging with intermediate concentration ratios, and (3) special designs (including combined) having high and ultra-high concentration ratios. Both imaging and non-imaging types usually use cylindrical reflectors to focus the sunlight on a "line" or circular reflectors to focus on a "point". The term solar furnace is associated with concentrating collectors at the highest range of concentration achieved with the highest precision of optics, used for studying properties of materials at high temperatures (Stoynov 1997).

There are many different types of collector configurations in use as shown in Figure 2.9, but in general concentrators with receivers much smaller than the aperture are effective only on beam radiation (Duffie and Beckman 1991).

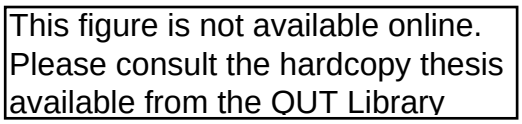

Figure 2.9: Most commonly used types of collector configurations

Concentrators are classified by some researchers into two general categories: non-imaging and image-forming or imaging (Welford and Winston 1989; Duffie and Beckman 1991). Most, if not all, non-imaging concentrators do not form visually coherent images of the sun on the absorber but instead focus the radiation from all parts of the solar disk onto all parts of the clear aperture of the absorber. The concentration ratios of linear non-imaging concentrators are generally low (below 10). By contrast, imaging concentrators form images of the sun which are of a relatively low quality by ordinary optical standards. In this research an imaging, point focusing solar concentrator in conjunction with auxiliary doublet focusing lenses or non-imaging optics are used.

There is ongoing research in creating highly concentrated solar energy, or solar flux, using various concentrating devices and techniques. To attain high efficiency

and temperature performance, solar collectors require concentrators both with high concentration ratios and small absorbers on which the image of the sun is constantly focused. The most common concentrators with high concentration ratios are: parabolic dish reflectors, hemispherical bowl reflectors, central receiver systems and parabolic trough reflectors/concentrators.

The most common reflective imaging concentrator geometry is the paraboloidal usually employing the technique of specular reflections. Paraboloid is the ideal shape for the reflecting surface of a solar concentrator because it can concentrate the broad solar radiation coming directly from the sun to the concentrator's focal point. However, this would be valid only for meridional, parallel to the optical axis rays from a point source, and any slightly off-axis beam of rays will sustain aberration called coma (rays from oblique beam meet farther from the axis).

In practice, it is still often easier to fabricate multiple spherically shaped surfaces that also concentrate solar radiation. The focusing capability of spherically shaped mirrors approaches that of a paraboloid-shaped mirror when the region of concentration is many mirror diameters away from the reflecting surface (i.e. the mirror is only slightly curved). It is believed that spherical aberration becomes negligible only when the focal length is large compared with the aperture ($f/D > 10$). Parabolic dish reflectors focus the incident radiation in front of them. However, this can be an inconvenient place to put an absorber as the heat transfer fluid needs to be fed to and from it. In an exposed position heat loss is greater and where the absorber is not the center of rotation flexible feed lines are required. The most commonly used types of parabolic concentrators are shown in Figure 2.10.

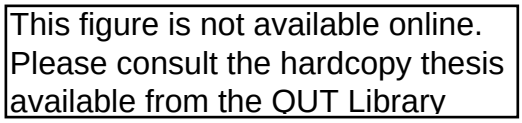

Figure 2.10: Most commonly used types of paraboloidal concentrators

To increase absorptance and reduce convective losses from the absorbing surface, a parabolic dish/cavity receiver configuration is often used. Harris and Lenz

have analyzed the energy loss mechanisms of such a system. Results of the study have indicated that a thermal efficiency between 0.6 and 0.7 is achievable with state-of-the-art concentrator technology operated in the temperature range of 550°–990°C (Harris and Lenz 1986). Elliptical and parabolic non-imaging concentrators have been studied by several researchers (Lumsdaine and Cherng 1976; Gurnee 1977; Friedman et al. 1993). They argued that the parabolic target would achieve a slightly higher absolute value for maximum concentration than the elliptical cylinder would at its maximum concentration.

2.4.4 Concentration ratio

In the process of solar radiation concentration usually the incoming uniform stream of solar radiation is redirected to a smaller area. Since the concentrator is used to increase the power density of solar radiation, one of the most important properties of the concentrator is the maximum concentration it can achieve.

Because the intensity of the insolation is variable with time, a flux concentration ratio is defined as the ratio of the average energy flux on the receiver to that on the clear aperture. As the flux over the exposed surface of the receiver may vary substantially, a local flux concentration ratio is defined as the ratio of the flux at any point on the receiver to that incident on the clear aperture. However, the most commonly used concentration ratio is the area concentration ratio, defined as the ratio of the aperture area to the receiver area (Duffie and Beckman 1991). Since the flux concentration ratio, as well as the local concentration ratio, usually vary across the receiver, in this work the area concentration ratio is used, expressed as:

$$C = \frac{A_a}{A_{abs}} \tag{2.19}$$

where A_a is area of the clear aperture of the concentrator normal to a line from the center of the source, and A_{abs} is the absorber area (see Figure 2.11).

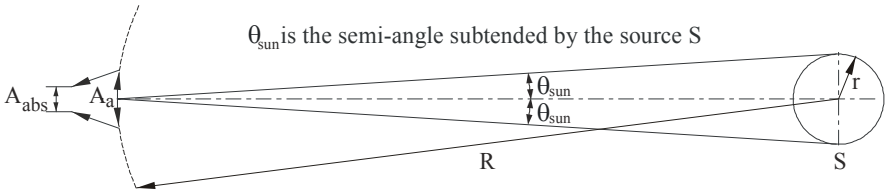

Figure 2.11: Solar radiation transfer through aperture A_a to absorber A_{abs}

Based on the second law of thermodynamics where there cannot be any net heat transfer between two bodies of equal temperatures, Rabl has developed the following

equation for the concentration ratio of circular concentrator (Rabl 1976):

$$C = \frac{A_a}{A_{abs}} = \frac{R^2}{r^2} E_{abs \to S} = \frac{E_{abs \to S}}{\sin^2 \theta_{sun}} \tag{2.20}$$

where $E_{abs \to S}$ is an exchange factor as defined by (Sparrow and Cess 1970).

Since the maximum value of $E_{abs \to S}$ is unity, the maximum concentration ratio for a circular concentrator (sometimes called 3D concentrator) is:

$$C_{circular,max} = \frac{1}{\sin^2 \theta_{sun}} \tag{2.21}$$

and for a linear concentrator (called also 2D concentrator) is:

$$C_{linear,max} = \frac{1}{\sin \theta_{sun}} \tag{2.22}$$

The concentrators that reach the theoretical thermodynamic limit are sometimes called ideal concentrators. Because the distance between the sun and earth is variable, θ_{sun} and respectively the maximum concentration possibly achievable on the earth would also vary with it throughout the year. Thus, a concentrator could achieve the theoretical maximum concentration at aphelion when the earth is farthest from the sun, which would be 47756.32 for a circular concentrator and 218.53 for a linear concentrator if $\theta_{sun}=\arcsin[(1.392 \times 10^6)/(152.1 \times 10^6)]=0.26218553°$ is assumed.

In addition, it is easy to see from Equation 2.21 that any increase of the angular size of the source will lead to a decrease of the achievable maximum theoretical concentration even when an ideal single concentrator is used. An illustration of this is shown in Figure 2.12 where the maximum theoretical concentration is calculated for angular size of the source in the range of 0.25 to 0.272 degrees.

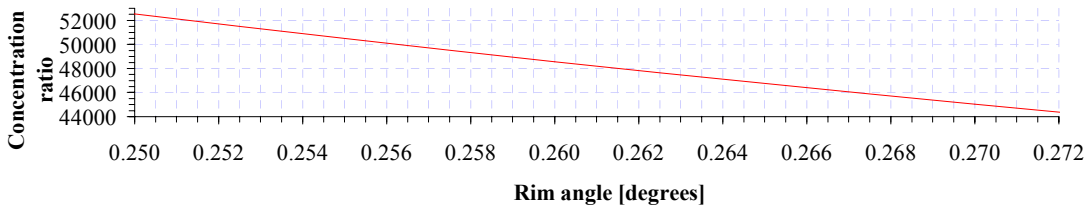

Figure 2.12: Theoretical thermodynamic concentration limit for a single dish for various angular source size

However, most imaging systems including Fresnel and parabolic concentrators fall short of this limit by a factor of 4 or more (Welford and Winston 1989; Smestad et al. 1990) (see Figure 2.13).

Figure 2.13: Maximum geometric concentration for one- and two-stage systems (Welford and Winston 1989:197)

The concentration factor for the primary alone (neglecting the shadow) can be calculated by (Welford and Winston 1989):

$$C_{primary} \approx \frac{\cos^2 \phi \sin^2 \phi}{\sin^2 \theta_{sun}} \tag{2.23}$$

If a refracting secondary is used to match the primary and enhance the concentration, its concentration ratio can be expressed by:

$$C_{secondary} \approx \frac{n^2}{\sin^2 \phi} \tag{2.24}$$

where *n* is the index of refraction of the medium surrounding the absorber.

The overall net geometric concentration of such a two-stage concentrator using a refractive secondary is therefore a product of the concentration of each stage

$$C \approx \frac{\cos^2 \phi \sin^2 \phi}{\sin^2 \theta_{sun}} \times \frac{n^2}{\sin^2 \phi} \approx \frac{n^2 \cos^2 \phi}{\sin^2 \theta_{sun}} \tag{2.25}$$

and it could be considerably higher than the theoretical thermodynamic limit in air for the first stage. The comparison between the maximum geometric concentration of one- and two-stage systems as a function of the primary focal ratio is illustrated in Figure 2.13.

In an actual solar concentrating system the portion of the traced incident rays that leave through the exit aperture determine another type of concentration ratio, called an optical concentration ratio. Also, all losses caused by optical, manufacturing and subjective errors could be taken into account with this concentration ratio.

Concentrators can have concentration ratios from low values less than unity to

high values in the order of 10^5 (Duffie and Beckman 1991). Increasing ratios mean increasing temperatures at which energy can be delivered and increasing requirements for precision in optical quality and positioning of an optical system. Although the thermodynamic limit of concentration with a single ideal device is on average 45,000, very high solar flux systems (up to 100,000 times concentration) have been developed (Winston et al. 1992). Such very high flux has a potential in a number of high technology applications including materials processing. Initial evaluations indicate that very high solar flux has significant economic advantages over electric arcs or lasers in very high temperature material processing. Typically, for melting of most metals, power densities approaching 10 W/mm^2 are required.

O'Gallagher and Winston have developed a performance model for evaluating benefits associated with the addition of a non-imaging secondary concentrator to a conventional paraboloidal solar dish (O'Gallagher and Winston 1988). The comparative optimisations have shown that the efficiency of a two-stage concentrator is always greater than that of a single stage if all other design parameters are the same. In a previous paper the authors discussed the design of a simple trumpet secondary whose hyperbolic shape was derived from the theory of the geometrical vector flux (O'Gallagher and Winston 1986). At the gross geometrical ratio of 4800:1 used, they reported an increase of the intercepted energy by 30% with the addition of a trumpet. In another words, the trumpet increased the geometric concentration ratio from 2200:1 for the primary to nearly 4800:1 with an efficiency greater than 96%.

2.5 Cassegrainian solar concentrator

2.5.1 Background

When more than one concentrating device/stage are used in the concentration, a great number of combinations become possible. Many two-stage solar concentrators involving large primary and small secondary mirrors in a variety of geometric shapes have been studied and reported. The particular type imaging solar concentrator used in this research is based on a modified Cassegrainian optical system named after N. Cassegrain, an astronomer of the 17th Century. In 1672 he designed a reflecting two-mirror telescope comprising a large concave paraboloidal primary mirror and a small convex hyperboloidal secondary mirror. The major advantage of the

Cassegrainian configuration was not fully appreciated until a century later when it was found by Jesse Ramsden, an English optician, that this design decreases the image blurring (spherical aberration). The pictorial presentation of a typical Cassegrainian is shown in Figure 2.14 (Mauk et al. 1979).

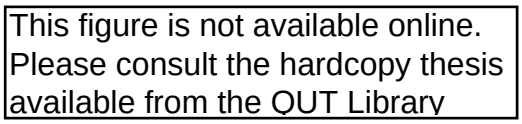

Figure 2.14: Pictorial of Cassegrainian solar concentrator

In general, the Cassegrainian arrangement produces a low concentration at its lower focus and in most cases the final image lies behind the primary mirror. However, although its overall telescope length is relatively short, it also produces a narrow view angle and a large effective focal length (due to magnification by the hyperboloidal mirror). This reduces optical aberrations, and allows a higher overall maximum concentration by a secondary concentrator installed at the lower focus. In a typical Cassegrainian telescope the spherical aberration is corrected separately on each of the mirrors.

If the acceptance surface of the primary mirror is a paraboloid, its eccentricity would be equal to one and its conic constant would be -1 (see Figure 2.8). However, the effective focal length of the Cassegrainian system is determined primarily by the choice of eccentricity of the hyperboloid.

In practice, since the classical Cassegrainian telescope has been invented, a number of variations have been developed and some explored as imaging concentrators in the field of solar energy. Some examples recognized as a type of Cassegrainian or similar configurations are as follows:

(a) The Schmidt-Cassegrainian telescope has a concave spherical surface on its primary mirror;

(b) The Pressmann-Camichel variant of the Cassegrainian also uses a concave spherical primary mirror;

(c) The Dall-Kirkham variant uses an ellipsoidal primary mirror and a spherical surface on its convex secondary mirror;

(d) All surfaces on the Maksutov telescope are spherical; and

(e) The Ritchey-Chrétien telescope has a modified parabolic primary mirror and a modified hyperbolic secondary mirror.

In general, the construction of the hyperbolic secondary mirror in the Cassegrainian is a complex task. A useful optical surface could have many different shapes, but the most popular is the spherical. Most telescopes used in astronomy are two-mirror telescopes, and the Cassegrainian is the most common one. It has been known for years that at low field angles normal incident aplanatic telescope designs have better performance than the ones corrected for a spherical aberration. This could be the main reason why in the past 50 years most astronomical telescopes have been of the Ritchey-Chrétien design rather than of the classical Cassegrainian one.

The focus of the paraboloid in the Cassegrainian coincides with the upper focus of the hyperboloid (see Figure 2.15). The image is formed behind the primary mirror with the light passing through the hole in its center. The cone of light reflected from the primary mirror is cut off at the same point before it reaches the focal plane and is replaced by another, but longer cone. The length of the new cone divided by the part cut from the original one, equals the amplification, or increase in magnification, of the system.

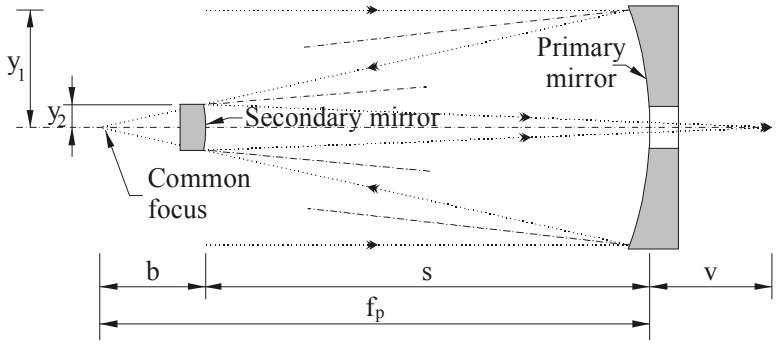

Figure 2.15: Some important characteristics in a Cassegrainian configuration

Since various Cassegrainian configurations exist due to variation in the shape of the mirror surfaces, a number of formulas are used for their design. In this work first order analysis of a two-mirror telescope has been used in conjunction with aspects of corresponding non-imaging optics.

Assuming that the curvatures c_1 and c_2 of the mirrors are inverse of the radii of curvature R_p and R_s and using the first order theory, the correlation between the focal lengths of the primary and secondary mirrors, f_p and f_s respectively, and their curvatures can be defined as:

$$c_1 = \frac{1}{R_p} = -2f_p \tag{2.26}$$

and

$$c_2 = \frac{1}{R_s} = 2f_s \tag{2.27}$$

In the most widely used sign convention it is assumed that the light travels from left to right and the radius of curvature is positive if the center of the curvature is to the right of the surface vertex. Thus, f_p is positive and f_s negative since both radii of curvature R_p and R_s are negative. As in most two-mirror telescopes, the primary mirror forms an image which is used by the secondary as an object to form a magnified image at the secondary focus. The magnification of the secondary mirror, m_s, can be expressed by:

$$m_s = \frac{f}{f_p} = \frac{s+v}{b} = \frac{s+v}{f_p - s} \tag{2.28}$$

where f is the effective focal length of the Cassegrainian, s is the separation between the mirrors and v is the distance from the vertex of the primary mirror to the focus of the secondary mirror.

The classical Cassegrainian optical system has been popular in astronomy because it allows a large system focal length to be achieved in a relatively compact design. Although this can be a great asset for astronomy, when used in solar radiation concentration, the relatively long effective length of the Cassegrainian configuration becomes a drawback.

The focal ratio or F/number, one of the most important properties of any optical system, especially when dealing with image forming instruments with the object at infinity, is determined by the following:

$$F_{/\#} = \frac{1}{2n \sin \theta_{image}} \tag{2.29}$$

where n is the index of refraction of the surrounding medium and θ_{image} is half the angle of the cone of electromagnetic radiation, or half the angle subtended by the converging rays at the image. For small angles only a paraxial approximation is often used:

$$F_{/\#} = \frac{f}{D} \tag{2.30}$$

where D is the clear aperture diameter.

The size of the absorber area for a certain concentration $(D/d)^2$ can be determined by the image diameter *d* as follows:

$$d = 2f \sin \theta_{sun} \tag{2.31}$$

Other expressions for some fundamental properties used in the first order analysis of most two-mirror telescopes and in this work include:

$$\frac{y_1}{y_2} = \frac{f}{s+v} = \frac{f_p - Z_p}{f_p - s - Z_s} = \frac{f_p - Z_p}{b - Z_s} = \frac{D_p}{D_s} \tag{2.32}$$

where $y_1 = D_p/2$ is the height of the meridional ray on the primary mirror, $y_2 = D_s/2$ is the height of the meridional ray on the secondary mirror (half the diameter of the reflected conic light beam), Z_p is the sagitta of the primary mirror, and Z_s is the sagitta of the secondary mirror. From Equation 2.28 the separation between the mirrors can be expressed as:

$$s = \frac{f - v}{1 + f/f_p} = \frac{m_s f_p - v}{1 + m_s} \tag{2.33}$$

and, after substituting in Equation 2.32:

$$\frac{y_1}{y_2} = \frac{f_p + f}{f_p + v} \tag{2.34}$$

Using the analogy with the thin lens formula for the secondary mirror:

$$\frac{1}{f_s} = \frac{1}{s+v} - \frac{1}{b} = \frac{1}{s+v} - \frac{1}{f_p - s} \tag{2.35}$$

and, after substituting in Equation 2.34, the height of ray y_2 is:

$$y_2 = y_1 \left(\frac{f_p + v}{f_p + f} \right) = \frac{D_p}{2} \left(\frac{f_p + v}{f_p + f} \right) \tag{2.36}$$

From Equations 2.32 and 2.35, the focal length of the secondary mirror is:

$$\frac{1}{f_s} = \frac{y_1}{y_2} \left(\frac{1}{f} - \frac{1}{f_p} \right) \tag{2.37}$$

From Equation 2.34, the focal length of the secondary mirror can be defined as:

$$f_s = \frac{f}{f_p} \left(\frac{f_p + v}{1 - (f/f_p)^2} \right) = f_p \frac{m_s \left(1 + \frac{v}{f_p} \right)}{1 - m_s} \tag{2.38}$$

By using these equations it is possible to calculate the optimum concentrator parameters and corresponding dimensions, depending on the application and the energy flow through the concentrator.

2.5.2 Related work

The use of different types of Cassegrainian systems for different applications has been reported by many researchers. Some applications that have been studied include chemical reactor use (Mauk et al. 1979), photovoltaic conversion enhancement (Kaplow and Frank 1976), melting of aluminium oxide (Alimov and Alavutdinov 1979), solar thermal electricity generation systems (Scishido et al. 1989; Kribus et al. 1998; Kribus 2002), solar surgery (Feuermann and Gordon 1998), and terrestrial solar pumped iodine gas laser (Terry et al. 1996). However, no similar Cassegrainian configuration for the applications explored in this research has been reported.

Using graphical methods, Novikov et al. calculated energy concentration and distribution on and off the focal plane for a Cassegrainian system (Novikov and al. 1966). The results were compared with the calculations for a parabolic secondary and the ratios of primary to secondary mirror diameters were in the range of 2 to 3.43 in both cases. The authors reported that the ratio of mirror diameters was the most important parameter and the highest energy concentration was achieved by the classical Cassegrainian system. This finding may be of interest, however the choice of suitable parameters could make the difference in concentration insignificant.

Kaplow and Frank investigated a tracking Cassegrainian with 610 mm diameter paraboloid for enhancing photovoltaic conversion, but instead of hyperbolic secondary, they used plano-convex glass lenses with reflective coatings (Kaplow and Frank 1976).

An extensive study of Cassegrainian solar concentrators was performed by Mauk et al. (Mauk et al. 1979). The authors presented an illustrative example of a Cassegrainian solar collection system designed for chemical reactor use. They considered and compared three possible configurations: (1) a simple parabolic collector, (2) a parabolic collector with heliostat, and (3) a Cassegrainian system (see Figure 2.16).

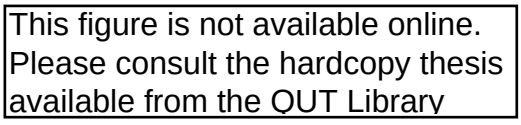

Figure 2.16: Solar collector systems (Mauk et al. 1979)

The geometry of the analyzed Cassegrainian system is shown in Figure 2.17.

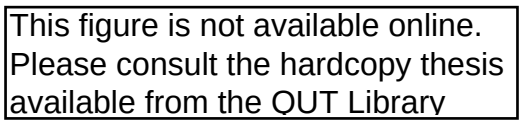

Figure 2.17: Cassegrainian system geometry (Mauk et al. 1979)

In their work, to calculate the average flux concentration ratio the following formula was used:

$$C_R = \frac{\rho_p \rho_s}{A_a} \frac{\pi}{4} (D_p^2 - D_s^2) \tag{2.39}$$

The possible total solar power through the effective aperture was estimated by:

$$Q = G_b C_R A_a \tag{2.40}$$

where G_b is the beam irradiance or solar flux parallel to the center line of the primary mirror. Then the re-radiated power through the aperture was calculated by:

$$Q_{RR} = A_a \sigma T_c^4 \tag{2.41}$$

where Q_{RR} is the re-radiated power through the focal spot and T_c is the furnace cavity temperature.

The authors concluded that the Cassegrainian solar system appeared to present the best compromise, having a small angle of approach without a large separation, and with a smaller, less expensive second reflecting surface. It also used a primary mirror with a relatively small F/number.

Umarov et al. developed a nomographic technique for predicting mirror parameters, without regard to energy, considering on-axis configurations and a Cassegrainian system with perfect surfaces (Umarov et al. 1973). They derived several equations to determine the geometric parameters of the hyperboloidal counter-reflector of a two-mirror system. The authors concluded that the eccentricity of the hyperboloid would never be greater than three, otherwise the flux concentration region would lie between the mirrors.

This finding was confirmed by a subsequent study in which a computational method for a coaxial system consisting of a paraboloid of revolution and a hyperboloidal counter-reflector was developed (Kirgizbaev and Zakhidov 1974).

The mathematical analysis of the parameters of the Cassegrainian reflecting surfaces and the effect of their precision on the energy distribution in the system showed that the paraboloid precision had a greater effect on the energy distribution than that of the hyperboloid. Acknowledging the significance of the mathematical work, it could be argued that this finding is obvious since the image formed by the paraboloid is used as an object by the hyperboloid.

Using a similar computational method Zakhidov and Vainer developed a computer model for calculation of the precision, energy and temperature parameters of a Cassegrainian system with mirrors of different precision (Zakhidov and Vainer 1975). The authors argued that since the accuracy of the concentrator was entirely dependent on the paraboloid, the errors of the paraboloid could not be corrected by the hyperboloid. Despite the significance of the developed model as being one of the earliest computer models, its usefulness could be disputed again as the findings of the study appear obvious.

The optical and energy characteristics of Cassegrainian arrangements were also studied and experimentally evaluated by several researchers (Umarov et al. 1976; Alimov and Alavutdinov 1979; Vainer and Zakhidov 1981). Umarov et al. investigated several two-mirror systems, consisting of a parabolic primary and an auxiliary convex paraboloidal mirror, and capable of concentrating solar radiation at points outside the installation (Umarov et al. 1976; Vainer and Zakhidov 1981). By using a system of this kind, they achieved solar energy concentrations in the order of 2000 and a peak intensity of 4 MW/m² in a focal spot 0.042 m in diameter. The authors also experimentally measured the focal plane intensity distribution for a Cassegrainian system with a paraboloidal mirror of diameter 1.5 m and a convex hyperbolic reflector of diameter 0.53 m. The solar power produced by the system for an incident radiation of 784 W/m² on a focal spot with a diameter of 0.025 m was 970 W with an average solar concentration of 3000. Interestingly, in both cases the experimental intensity distribution plots did not confirm the typical theoretical distribution plots.

Alimov and Alavutdinov studied a two-stage tracking Cassegrainian solar concentrator to melt aluminium oxide (Alimov and Alavutdinov 1979). They reported a maximum flux density of 2300 W/cm² achieved with a principal paraboloidal diameter of 20 m and a power of 150 kW, employing plane or hyperboloidal counter-reflectors. It was concluded that such a system could be used

for various energy and high temperature applications.

Vainer and Zakhidov investigated a two-mirror Cassegrainian system with a paraboloid aperture angle of 74° and a back-reflector relative diameter of 0.35 m, for various values of inter-focus separation (Vainer and Zakhidov 1981). These types of systems are interesting from a practical viewpoint since the working zone of the furnace is situated behind the concentrator. This permits such units to be employed for the processing of products and structures with large overall dimensions. It was established that an increase in the separation causes the irradiance to fall with improved uniformity of distribution. The authors also investigated a large Cassegrainian system furnace with a main mirror 54 m in diameter and a back reflector 19 m in diameter. They established that the accuracy requirements for the second mirror were significantly lower than for the primary. This confirmed the findings of previous studies (Umarov et al. 1973; Kirgizbaev and Zakhidov 1974).

The influence of the receiver plane displacement and secondary reflection on the radiation distribution in the focal spot of a Cassegrainian system was studied by Vainer (Vainer 1983). The theoretically investigated system consisted of a paraboloidal mirror with a diameter 960 mm and a focal length 366 mm, and a hyperboloidal mirror with a diameter of 0.4 of the paraboloidal diameter. It was found that a shift in the receiver plane led to spreading of the spot and the appearance of a central gap, and a shift in the secondary reflector caused similar effect. Investigation of the combined influence of the shifts of the receiver and the secondary reflector showed that a partial compensation of the two forms of adjustment was possible. Cobble et al. analyzed the variation of the ideal theoretical concentration of a Cassegrainian solar furnace for various eccentricities and vertex to focus distances (Cobble et al. 1978). They showed some results for paraboloid with a radius of 42 feet and a focal length of 25 feet, but no application was discussed.

Roman et al. conducted a study on coupling an off-axis Cassegrainian concentrator with a compound parabolic concentrator (CPC) for more efficient concentration of solar radiation (Roman et al. 1995). The Cassegrainian system with short focal length f/D=0.5 included a 7 m-diameter parabolic primary reflector, a hyperbolic secondary reflector and a non-imaging concentrator located on the polar axis of the primary. However, the authors considered an off-axis reflective system as an alternative to the traditional system and suggested its use for applications involving short focal length primary mirrors, or when the experimental equipment

needed to be located outside the primary aperture. A schematic of the off-axis system is shown in Figure 2.18.

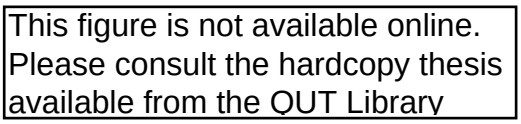

Figure 2.18: Off-axis Cassegrainian concentration system (Roman et al. 1995)

Potential applications that were suggested include solar laser pumping and detoxification/distillation hybrid systems.

The common Cassegrainian optical arrangement typically has been used in telescopes and alone has a relatively limited use as a concentrator of solar radiation. Despite this, some researchers (Feuermann et al. 1999) claimed they could attain a high flux concentration using purely an imaging two-stage solar concentrator which is a type of Cassegrainian called complementary Cassegrainian concentrator. This concentrator had the conventional paraboloidal dish as a primary reflector but instead of the upper branch, as in the classical arrangement, the lower branch of the hyperbola was used as a secondary (see Figure 2.19).

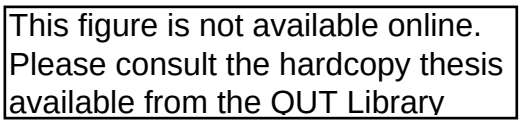

Figure 2.19: Comparison between classic Cassegrain design and complementary Cassegrain concentrator (Feuermann et al. 1999)

The use of a CPC for concentration of fiber transmitted solar energy was

reported by Yugami et al. (Yugami et al. 1999). The incident solar radiation, initially concentrated by a Cassegrainian configuration onto a fiber optic bundle, was re-concentrated by a CPC placed at the other end of the fiber bundle. The experimental system is shown in Figure 2.20.

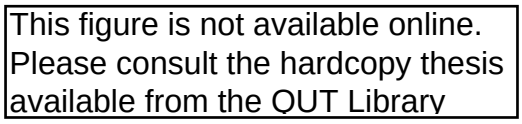

Figure 2.20: Schematic diagram of a parabolic concentrator coupled to an optical fiber bundle (Yugami et al. 1999)

The authors calculated the rim angle of the parabolic concentrator, θ_r by the following expression:

$$\theta_r = \cos^{-1}\left(\frac{16 - n_c^2}{16 + n_c^2}\right) \qquad (2.42)$$

where n_c is the ratio of the diameter to the focal length of the parabolic concentrator. The diameter of the primary mirror used was 1560 mm and its focal length 650 mm, thus the value calculated for n_c was 2.4 and respectively, the rim angle was 62°.

Unlike their system, in the initially proposed idea in this research to transfer the concentrated solar energy to the test material via fiber optic bundle, the rim angle of the SEC is only approximately 6°.

Since the acceptance angle of the optical fiber used was only 24°, the authors acknowledged that not all concentrated solar radiation could be fed into the optical fiber, thus the losses of concentrated light were significant. Instead, a smaller parabolic mirror could have been used with a relatively narrow rim angle coinciding with the calculated acceptance angle of the fiber optic bundle. Therefore, the wasting of a considerable portion of the already captured solar power concentrated by the parabolic mirror could have been decreased significantly, as well as minimizing the need for cooling.

No information was provided about the effective focal length of the concentrator

or the size and focal length of the hyperbolic mirror, except that it magnifies the sun's image three times. As a result, the maximum local flux concentration after the reflection from the hyperbolic mirror was decreased. However, the authors reported that a concentration ratio of 36,000 and a 6 mm diameter of the sun's image were achieved, although no information was given on how they were obtained.

It should be noted that, using similar configuration to the one initially proposed in this research, Yugami et al. acknowledged that there was a significant difference between the dish rim angle and the acceptance angle of the fiber optic bundle. Also, the shadow from the secondary should have appeared in the image which would inevitably lead to drastically reduced power transmitted through the fibers in the center of the bundle. This was one of the major reasons that in this research a CPC was used at the principal Cassegrainian focus.

A unique utilization of a major part of the solar spectrum was reported by Dye et al. (Dye et al. 2003). A modified Cassegrainian system coupled to a non-imaging device was designed with the purpose of splitting the infrared and visible energy for two different end uses. It was proposed to use the infrared energy for electrical power generation and the visible light for day lighting.

The prototype primary mirror, reported previously by Wood, was a ground glass parabolic dish with a diameter of 1.18 m and a focal length of 0.42 m (Wood 2002). The secondary mirror had a surface area of 69.4 cm^2 and had been designed with multiple planar segments with a spectrally selective cold mirror coating to reflect the visible light and allow the IR energy to pass through (Tekelioglu and Wood 2003). In this way, the visible part of the solar spectrum was separated from the infrared and concentrated for day light transmittance via polymer light fiber optics to hybrid luminaries or photobioreactors. The infrared component of the concentrated radiation by the primary mirror and transmitted through the secondary mirror was intended to be directed onto a thermal photovoltaic array (see Figure 2.21).

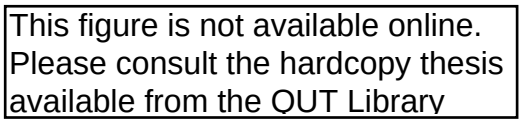

Figure 2.21: Full-spectrum collector/receiver (Dye et al. 2003)

Since a highly concentrated flux may cause a problem, a hollow internal reflecting non-imaging device to de-focus and distribute the flux on the PV array was investigated by the authors. This Cassegrainian collector/receiver configuration was experimentally explored as a source of a hybrid lighting system in a commercial building (Muhs et al. 2003). Although for different applications, this study investigated a solar energy system comprising components similar to those documented in this research.

Most of the studies reported in the literature and reviewed in this chapter have been predominantly theoretical or investigated only the correlation between the different parameters of the Cassegrainian configurations. In contrast, in this research not only has an alternative energy source been developed but three possible applications have been experimentally studied as well.

2.6 Relevant non-imaging concentrators

2.6.1 Truncated cone concentrator

Compared to image forming concentrators, the light cone or truncated cone concentrator is a relatively simple concentrator. Although considered by some researchers as a primitive form of non-imaging concentrator, it has been used for many years. The major drawback of the light cone is that, irrespective of its dimensions, it is possible for an input ray at a particular angle to be returned back after a few or many reflections, as illustrated in Figure 2.22.

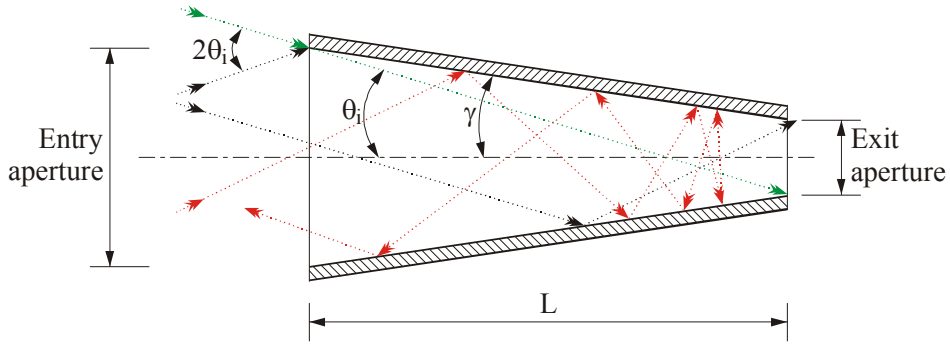

Figure 2.22: Schematic diagram of a truncated cone concentrator

Moreover, it is believed that each time a photon is absorbed and re-emitted, a fraction of $(1 - \cos\theta_c)$ is lost, where θ_c is the critical angle of the concentrator, $\theta_c = \sin^{-1}(1/n)$ (Smestad et al. 1990). Another disadvantage is that a longer length of the cone is required to achieve higher concentration. However, those limitations

become less critical when such type concentrator is used in conjunction with an imaging concentrator, since its extreme input angle could be designed to coincide with the rim angle of the concentrator.

2.6.2 Compound parabolic concentrator

In order to enhance the concentration capability of a single concentrator, different types of second stage concentrators have been studied. In particular, for a typical concave paraboloidal mirror several second-stage concentrators have been explored analytically or experimentally. These include non-imaging compound parabolic concentrators (CPC), compound elliptical concentrators and flow-line concentrators or "trumpet" concentrators. Ultra high concentration of solar radiation has been reported with a non-imaging CPC as a second stage to a paraboloidal mirror - 84,000 (Winston et al. 1992) and 102,000 (Winston et al. 1991). In general, two basic design principles are used in the development of the non-imaging concentrators – the "maximum slope" or "extreme ray" principle and the principle of geometric vector flux.

A description of CPCs in various contexts appeared in the literature in the mid 1960s (Baranov 1965; Baranov and Melnikov 1966; Hinterberger and Winston 1966a; Hinterberger and Winston 1966b). One of the earliest applications of a CPC as a type non-imaging concentrator was for detection and collection of Čerenkov radiation by photomultipliers. The concept of the CPC was further explored by (Malifaud 1971; Rabl 1976; Mills and Giutronich 1978; Rabl et al. 1979; Collares-Pereira et al. 1991).

CPC, as an example of the optically ideal class concentrators, consists of two different parabolas as prompted by its name (Rabl 1976).

The basic dimensions of the ordinary CPC are typically obtained using the equation of the parabola with origin at its focus. When Cartesian coordinates are used, it is expressed as follows:

$$z = \frac{y^2}{4f} \tag{2.43}$$

where f is the focal length i.e. the distance from the focus of the parabola to its vertex. However, for simplicity the equation of the parabola in polar coordinates (r, φ) is used (see Figure 2.24):

$$r = \frac{2f}{1-\cos\varphi} = \frac{f}{\sin^2 \frac{1}{2}\varphi} \tag{2.44}$$

The shape of the CPC is determined by the diameter of the exit aperture *d* and the extreme collecting angle θ_i (see Figure 2.23). The focal length of the parabola is:

$$f = \frac{d}{2}(1+\sin\theta_i) \tag{2.45}$$

and the overall length, *L* of the parabola is:

$$L = \frac{d}{2}(1+\sin\theta_i)\frac{\cos\theta_i}{\sin^2\theta_i} = \frac{d}{2}\frac{(1+\sin\theta_i)}{\tan\theta_i \sin\theta_i} \tag{2.46}$$

The radius of the entry aperture, *D/2* is:

$$\frac{D}{2} = \frac{d}{2\sin\theta_i} \Rightarrow D = \frac{d}{\sin\theta_i} \Rightarrow R = \frac{r}{\sin\theta_i} \tag{2.47}$$

From Equations 2.46 and 2.47 the overall length of the parabola is:

$$L = \frac{D+d}{2}\cot\theta_i \Rightarrow L = (R+r)\cot\theta_i \tag{2.48}$$

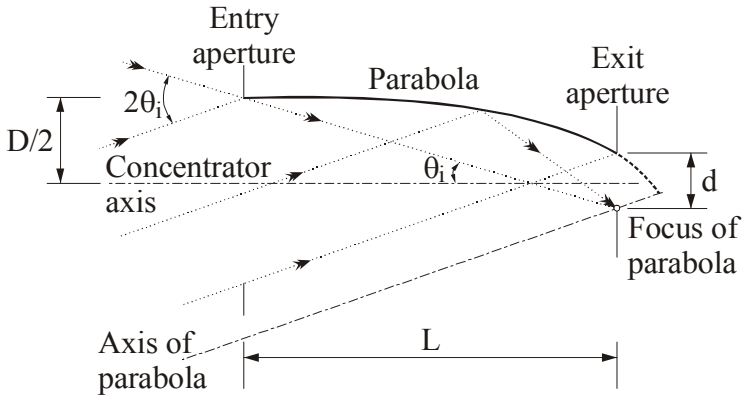

Figure 2.23: Construction of the CPC profile from the edge-ray principle (adapted from Welford and Winston 1989)

In general, when a second stage reflector or refractor is introduced, gains in concentration are offset by a reduction in efficiency. However, some of the best and well-recognized secondary reflector designs developed thus far are non-imaging e.g. compound parabolic concentrators (Welford and Winston 1989) and trumpet concentrators (O'Gallagher and Winston 1986).

2.6.3 Truncated compound parabolic concentrator

It is believed that both 2D and 3D typical CPCs, compared to other concentrators with relatively smaller concentration ratios, have the disadvantage of being very long

relative to the diameter of the collecting aperture. The length, as given by Equation 2.46, is approximately equal to the diameter of the collecting aperture divided by the full collecting angle (Welford and Winston 1989):

$$L = \frac{2R}{2\theta_i} \tag{2.49}$$

It is possible to achieve a considerable reduction in length by truncating or removing part of the entry aperture, causing only a little decrease in concentration. If a polar coordinate system (r,φ) is used, as shown in Figure 2.24, the length of the truncated parabola can be determined by the following (Welford and Winston 1989):

$$\frac{L_T}{R_T} = \frac{(1+\sin\theta_i)\cos(\varphi_T-\theta_i)}{\sin(\varphi_T-\theta_i)(1+\sin\theta_i)-\sin^2\frac{1}{2}\varphi_T} \tag{2.50}$$

The relation between surface area of a reflector and aperture area can be expressed for 2D truncated CPC as (Welford and Winston 1989):

$$\frac{-f}{R_T}\left\{\frac{\cos\frac{1}{2}\varphi}{\sin^2\frac{1}{2}\varphi}+\ln\cot\frac{1}{4}\varphi\right\}\Bigg|_{\varphi_T}^{\theta_i+\pi/2} \tag{2.51}$$

and for 3D truncated CPC as:

$$\frac{2f}{R_T^2}\int_{\varphi_T}^{\theta_i+\pi/2}\left\{\frac{f\sin(\varphi-\theta_i)}{\sin^5\frac{1}{2}\varphi}-\frac{r}{\sin^3\frac{1}{2}\varphi}\right\}d\varphi \tag{2.52}$$

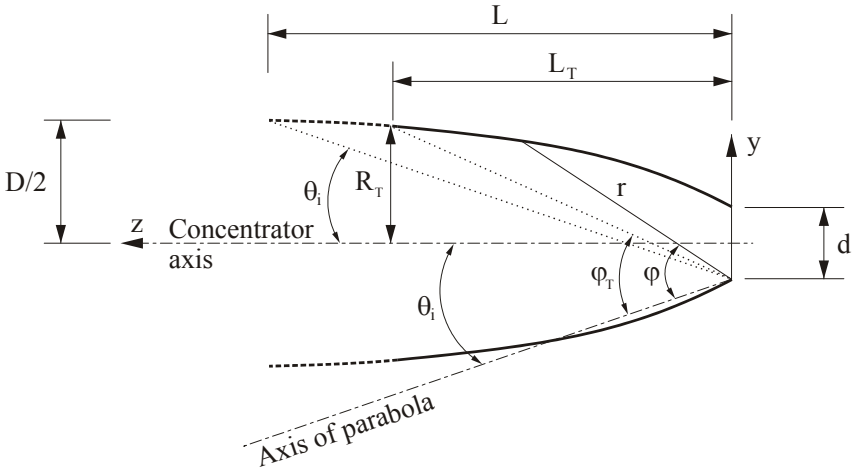

Figure 2.24: Truncated CPC profile expressed in polar coordinates (adapted from Welford and Winston 1989)

In this research, a truncated cone concentrator as well as a CPC have been designed as light transmitting and concentrating devices, enhancing the concentration ratio of the system. They are discussed in Chapters 6 and 7.

2.7 Conclusions

Most of the known forms of electromagnetic radiation are utilized in various technologies and require artificial sources and mechanisms for their generation. Nuclear reactions within the sun are the biggest source generating a full spectrum of electromagnetic radiation and relatively broad band insolation is available even at the earth's surface. This solar energy has been utilized in a number of industries, but it has not been widely studied for the purposes of polymer processing.

The utilization of concentrated solar radiation on its own generally comprises two major areas – optical engineering and radiation energy transfer. In this extensive review of information sources (including patent literature) it has been found that there are many types of solar energy concentrators associated with different applications from a very small to a very large scale. However, no three-stage concentrator comprising a Cassegrainian configuration similar to the one explored in this research for polymer processing, has been found.

The most comparable prior research conducted was a solar energy system comprising components similar to those used in this research but proposed for different applications such as electrical power generation and day lighting (Dye et al. 2003). The only modified Cassegrainian configuration used in a three-stage solar concentrator system has been reported by Roman et al. (Roman et al. 1995). However, the proposed configuration is an off-axis system, no experimental data has been presented and the suggested potential applications are different to the applications explored in this research. Because of this, the development of a reliable experimental facility, as well as a demonstration of feasible applications, are needed.

The theoretical review of electromagnetic radiation and solar concentration principles summarized in this chapter has been necessary for the concentrator development as well as for studying and a proper understanding of the radiation-material interaction. However, most modern polymer processing technologies that are pertinent to this research use artificial sources and their review is presented in the following chapter.

CHAPTER 3.
LITERATURE REVIEW OF RELEVANT POLYMER PROCESSING TECHNOLOGIES

3.1 Introduction

Being continuously improved, polymers and their composites have been rapidly displacing conventional materials in numerous engineering applications in mass production. The emerging need to produce more complex parts from plastics has increased the need for joining, in particular of thermoplastics. Such thermoplastics, including the most common acrylic polymer – PMMA, can be repeatedly softened and melted on heating and hardened on cooling with insignificant property changes and without considerable degradation. There are many techniques used for joining of plastic materials, but most of them involve either fusion welding, mainly used for thermoplastics, or adhesive joining. In both of these, however, the process of joining or curing usually requires, at some stage, electromagnetic radiation application or generation of heat. There are numerous mechanisms developed to generate the heat necessary for the materials processing used, and especially the joining technology, but they typically require artificial energy sources.

On the other hand, even non-professionals know from experience that sunlight can damage plastic materials. There has been extensive research into why sunlight has been detrimental for plastics since their creation. As a result, the properties of most modern plastics, especially those used in outdoor applications, have been constantly improved and their outdoor lifetime significantly extended. Inevitably, because of this, the potential use of solar radiation as an energy source for processing those polymers becomes more feasible. However, as documented in the previous chapter, in this age of plastics the use of concentrated solar energy in the process of joining plastic materials has not been particularly studied. All current process heat generating technologies use relatively sophisticated and expensive systems for artificially generated electromagnetic radiation. In materials processing solar energy can serve as an alternative heat generating source and trigger thermally induced structural modifications.

This chapter reviews polymer processing technologies and related theory and research, relevant to the studied applications. It begins with an overview of current

and alternative thermoplastic joining technologies, in particular welding techniques directly using electromagnetism. The next sections review some current curing and ageing methods and technologies based on or using electromagnetic radiation.

3.2 Effects of temperature change on thermoplastics

Different structural changes occur within amorphous, semicrystalline and highly crystalline polymers with temperature variation, but generally for most polymers the alteration of some typical characteristics with temperature change can be summarized in three stages, as shown in Figure 3.1.

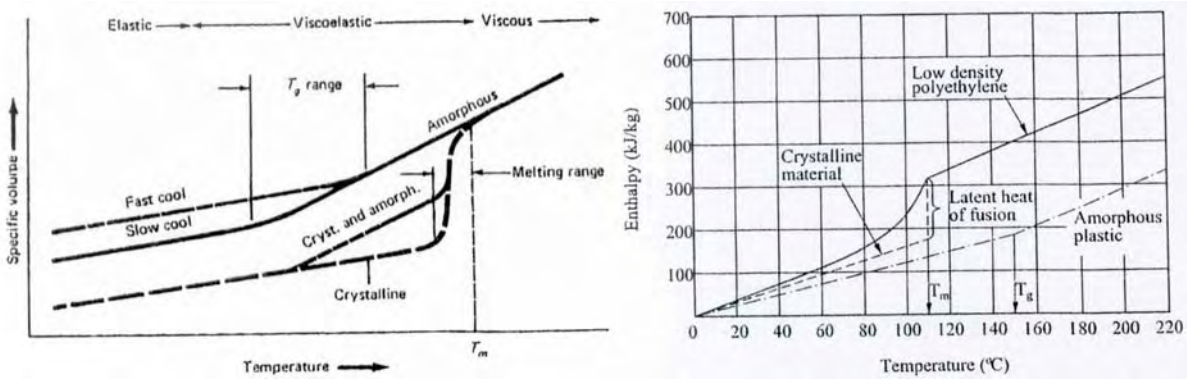

Figure 3.1: Altering of thermoplastic characteristics with temperature change (adapted from (Tlusty 2000))

Typically most polymers are stiff elastic below their glass-transmission temperature (T_g). Some are rather brittle, others can have rather high ductility with short term modulus of elasticity in the range of 500-3500 MPa on average. When the temperature of amorphous thermoplastics is gradually rising, they pass through a phase in which they change from rigid or glassy to a soft and pliable state. Similar to the solidification of a liquid to a glassy state, this glass transition generally occurs over a relatively narrow temperature region. Most thermoplastic properties such as brittleness, hardness, specific heat and thermal expansibility, undergo rapid changes in this region. This phenomenon is also called a second order or a rubbery transition. It is believed that when the temperature of a thermoplastic is rising, an uncoiling of the molecular bonds of the large chain molecules causes softening of the material. Usually the glass transition is associated with segmental motions of the polymer backbone chain or accompanied by the largest change in properties.

The approximate mid-point of the temperature range over which the glass transition takes place is called the glass transition temperature (ASTM-D883 2000). In practice, the glass transition temperature is determined by observing if a

significant change takes place in a particular property of the material while measuring the temperature at which this occurs. Moreover, depending on the chosen specific property and method to test it, the glass transition temperature can vary considerably (AS1886 1991). For example, if a thermoplastic is heated at a higher rate, the material could exhibit a glass transition temperature in the upper range. The observed glass transition temperature can therefore be considered only an estimate. The results obtained from the loss peak, observed in dynamic mechanical tests or from dialatometric data, are typically reliable estimates (ASTM-D883 2000).

When welding amorphous thermoplastics, their temperature needs to be above the glass transition temperature, since a flow state is a necessary prerequisite for welding to occur. In this research, especially in the polymer joining studies, it has been important to ensure that the specimen temperature has been maintained above its glass transition temperature. The observation of the glass transition temperature, as a distinctive process parameter, has been a useful tool during the welding process.

3.3 Current thermoplastic joining technologies

3.3.1 Background

Polymers can be classified in two main groups, thermoplastics and thermosets. Thermoplastics can be repeatedly softened and melted on heating and hardened on cooling without considerable degradation. Therefore, thermoplastic parts can be easily joined or formed by various manufacturing processes (Vijay 1989). Thermosets, on the other hand, will not melt and flow and thus cannot be welded. Thermoplastics can be divided into two categories as well – amorphous, which are characterized by a random molecular arrangement in the bulk polymer, and crystalline, which have an orderly molecular structure. Crystalline polymers typically have sharp and clearly defined melting points, whereas amorphous thermoplastics soften over a wide range of temperatures. A general classification of polymers is shown in Appendix 3.

Joining of plastic materials and their composites can be broadly divided into mechanical fastening and bonding. Bonding can be further classified into adhesive bonding, solvent bonding, and welding (Vijay 1989). For any plastic welding technology, there is a need to heat and melt the polymers at the joint surfaces to create weld inter-phase formation. Based on the method used to introduce heat to the joint, the techniques available to industry for welding of thermoplastics are often

divided into three distinct groups according to the means by which heat is generated and applied (Beevers 1991; Wise 1999; Hartley and Sallavanti 2002). These are: (1) *mechanical movement* – mechanical energy is converted to heat through intermolecular friction; (2) *external conventional source* – externally generated heat is transferred to the surfaces through conduction or convection; and (3) *electrical and electromagnetic effects* – heat is generated by electromagnetic energy absorption.

While many of the conventional plastics joining technologies have been used for years, some modern welding technologies are in fairly early stages of development. Most of the currently used conventional, modern and still-under-development thermoplastic joining techniques, categorized according to their heating mechanism are shown in Figure 3.2.

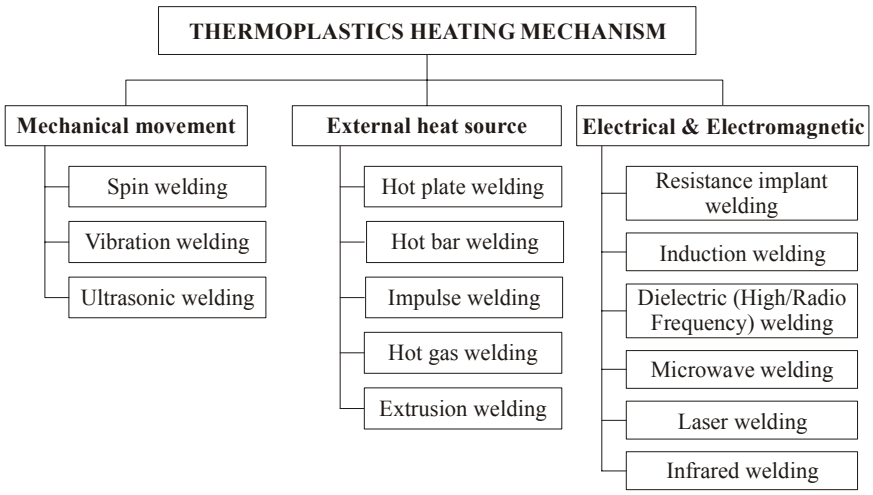

Figure 3.2: Thermoplastic joining techniques

Nearly all conventional and modern plastics joining technologies either are based on electrical and electromagnetic effects or directly use different types of non-ionizing electromagnetic radiation. As a consequence, most modern plastic joining technologies require an artificial source of electromagnetic radiation. For example, dielectric and induction heating rely on a radio frequency generator to supply the necessary electromagnetic energy with wavelengths from 2.5 to 150 m (2–120 MHz).

Microwave heating uses electromagnetic radiation with a lower wavelength range than the radio range and requires magnetron for generating the microwave energy. Infrared heating uses high-intensity quartz heating lamps, producing electromagnetic radiation with wavelengths on average one micron (from 0.76×10^{-6} to 10×10^{-6} m). In this research the utilization of non-ionizing electromagnetic radiation with shorter wavelengths has been explored for heating of polymers.

A central objective of this research is to study the feasibility of utilization of

concentrated solar radiation, a relatively broadband type of electromagnetic radiation, for polymer processing. In particular, the suitability of concentrated beam solar radiation for generating the heat required for welding or curing of various polymers has been targeted. Because of this, in the literature review summarized below, only the joining techniques based on electromagnetism or directly using electromagnetic radiation, including laser, to generate heat are included.

3.3.2 Welding techniques directly using electromagnetism

3.3.2.1 Resistance implant

Resistance implant welding is based on the principle of trapping an electrically conductive implant, usually a high electrical resistance wire, at the joint interface and applying a high electric current (up to 150A) to cause resistance heating. As the implant is heated, the surrounding plastic melts and flows together, forming a weld. The principle of resistance implant welding is illustrated in Figure 3.3.

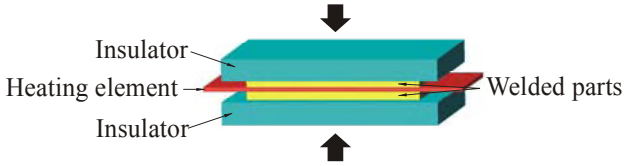

Figure 3.3: Resistance implant welding set-up

Although the process is very economical and easy to implement, the implant remains embedded in the welded material which could adversely affect the quality of the joint (Stokes 1989). Resistance welding is a useful method for welding dissimilar or difficult to weld materials such as thermoplastics, thermoplastic composites, thermosets and metals in various combinations.

A widely used modification of resistance implant welding is the electrofusion technique for joining small diameter (less than 180 mm) pipes by using specially designed couplers with heating elements on the inside diameter (Taylor and Watson 1988; Wise 1999). Although expensive, this process is very efficient for confined spaces due to the simplicity and portability of the equipment.

3.3.2.2 Induction

In induction welding, as in resistance implant welding, an electrically conducting implant is used at the joint interface. However, in this process a work coil connected to a high frequency power supply is placed in close proximity to the joint. As a high frequency electric current passes through the work coil, a dynamic electromagnetic

field (2–30 MHz) is generated whose flux interacts with the implant. Eddy currents are induced in the implant, producing heat within the conductive material due to the Joule-Lenz effect. The heat is transferred to the surrounding thermoplastic parts which melt and soften. When a pressure is applied to the joint, a weld is formed (Wise 1999). Induction welding is very fast, weld times may be a few seconds. Applications include sealing plastic coated metallic caps to plastic bottles.

In order to boost the heating, metal implants in the form of foils, screens or powders are used. Although they increase heating rates, they also act as contaminants, introduce shear stress concentrations and can result in poor bond between the metal and matrix (Beevers 1991). Induction welding by eddy current heating is most efficient when the thermoplastic components are of a circular symmetrical shape (illustrated in Figure 3.4). Long thin linear joints are difficult to achieve with this technique because complete circuits are needed in order to allow eddy currents to flow in the implant.

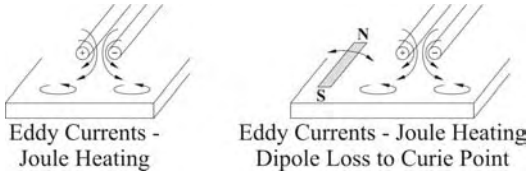

Figure 3.4: Induction welding of circular parts

A new form of induction welding, however, allows long linear welds to be produced in only a few seconds. In this process, the implant is a composite of thermoplastic with a particulate ferromagnetic filler, usually based on iron. It is trapped between the two components to be welded and excited by the dynamic magnetic field generated by a work coil placed near the implant. The heating is generated by hysteresis loss in the ferromagnetic material. Applications include welding of automotive and domestic appliance components.

3.3.2.3 Radio-frequency

Radio-frequency, also called dielectric or high frequency welding, uses high frequency (13 to 120 MHz) electromagnetic field, generating dielectric heating of the thermoplastic directly. The thermoplastic parts to be joined are placed under pressure between two electrodes which transmit the current to the joint interface, resulting in melting and forming a weld after cooling. The principle of radio-frequency welding is illustrated in Figure 3.5.

Figure 3.5: Radio-frequency welding set-up

Radio-frequency welding is mainly used in packaging and sealing applications and is especially suitable for the medical industry because no solvents or adhesives are present in the joint, thus minimizing the likelihood of contamination (Handbook of Plastics Joining 1997). The process is fast, highly energy efficient and can be easily automated, but the cost of the equipment is relatively high. Also, not all materials can be dielectrically welded because heat can be generated only in certain thermoplastics when exposed to a rapidly alternating electric field. The most widely used materials in radio-frequency welding are PVC, polyurethanes, nylons, cellulose acetate, and some ABS resins. The technique is not generally used for rigid materials with high melt points. Thermoplastics that cannot be welded with this technique include PC, PP, PE and PTFE (Wise 1999).

3.3.2.4 Microwave welding

The microwave heating effect was discovered in 1946 by Dr Percy Spencer, and implementation of microwave heating in the field of polymer welding is still in the research and development stage. Sometimes called millimetre waves, microwaves occupy the part of the electromagnetic spectrum with typical frequencies between 0.3 and 300 GHz, i.e. wavelengths between 1 and 1000 mm respectively. However, the two most common frequencies used are 915 MHz and 2.45 GHz, the latter being very efficient in terms of energy conversion. The heat necessary for microwave welding is generated directly inside the material itself by an alternating electromagnetic field.

Most thermoplastics do not experience a temperature rise when subjected to microwaves. However, by inserting a microwave susceptible implant at the joint, local heating takes place (Wu and Benatar 1995). If the joint is irradiated by microwave radiation and pressure is applied simultaneously, melting of the surrounding plastic occurs and a weld is formed (Figure 3.6a). Materials that contain polar groups as part of their molecular structure or are electrically conductive, are among the implants that are suitable for microwave joining of thermoplastics (metals, carbon or a wide range of conducting polymers). Auxiliary welding

material is not needed when the materials to be joined can be directly heated by the microwave radiation (Figure 3.6b).

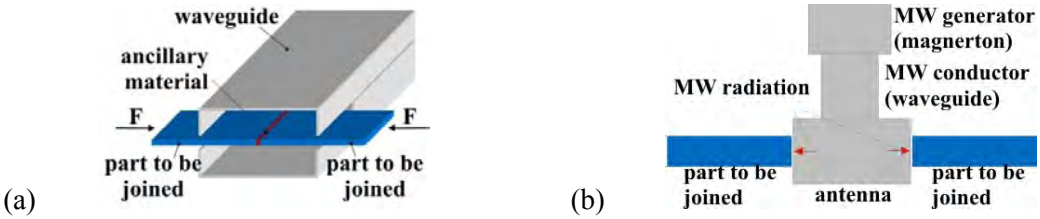

Figure 3.6: System for microwave welding with (a) susceptible material and (b) without auxiliary welding material

Microwave welding offers several advantages over the other methods of welding. The main advantage is that the microwave welding technique is capable of irradiating the entire component volumetrically when needed. Other benefits include relatively shorter weld times, continuous processing of welds and non-contact processing. The higher frequency leads to faster heating than in radio-frequency welding. However, if the heating rate and power level are not controlled, the polymers containing polar molecular groups can heat up rapidly, exhibiting runway heating, thus causing material degradation.

3.3.2.5 Laser

The Light Amplification by Stimulated Emission of Radiation (laser) was discovered in the 1960s and the laser thermoplastic welding was first demonstrated in the 1970s. The laser welding technique requires generation of an intense laser beam, usually in the infrared or visible areas of the electromagnetic spectrum, and focusing it onto the material. During this process the absorbed laser energy is converted to thermal energy which causes melting of the plastics in the joint region. The molten surfaces form a weld after cooling and solidifying under pressure (Jones and Taylor 1994). The laser welding process is illustrated in Figure 3.7.

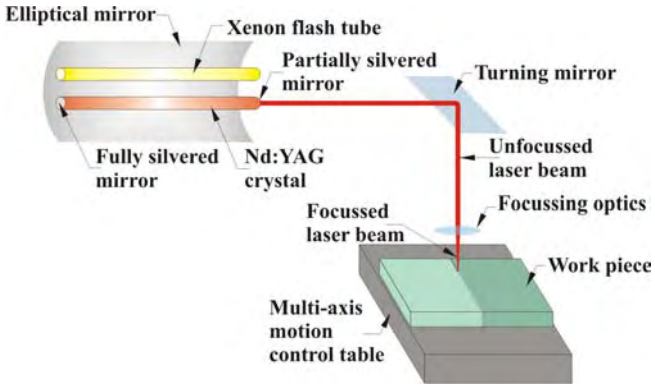

Figure 3.7: Laser welding system (adapted from www.joiningtech.com)

The most commonly used types of lasers – carbon dioxide (CO_2) and solid-state Neodymium-Doped Yttrium-Aluminium Garnet (Nd-YAG) are well established material processing tools at present. CO_2 lasers emit radiation at wavelengths 9.2–10.8 μm with the strongest emission at 10.6 μm and the power ranges from 30 W to 40 kW. The laser beam is reflected by mirrors and transmitted through air. CO_2 laser energy is rapidly absorbed by plastics, resulting in quick but limited in depth joints. However, most thermoplastics absorb strongly at 10.6 μm, which limits the CO_2 laser only to applications involving thin films (less than 20 μm). The strongest emission of radiation from Nd-YAG lasers is at 1.064 μm wavelength. The beam is transmitted through a fiber optic transmitting system and the power ranges from 30 W to 4 kW. CO_2 lasers typically operate in pulsed mode, whereas Nd-YAG lasers can be used either in pulsed or continuous wave modes (Kagan et al. 2000).

High power diode lasers are relatively new and more efficient materials processing tools. They are similar to Nd-YAG lasers, but the laser beam is focused onto a rectangular spot which, while advantageous for some applications, limits the minimum spot size and maximum power density available. Typical diode lasers emit at wavelengths 808 ± 10 nm, 830 ± 10 nm and 940 ± 10 nm. An advantage of the direct diode transmission welding is very high strength welds and seals, sometimes even in excess of parent material strength. Although the application of diode lasers is limited due to their inferior laser beam quality compared to that of the CO_2 and Nd:YAG lasers, their usage in welding of thermoplastics is rapidly growing.

Laser welding offers numerous advantages over the traditional joining techniques. The heat-affected zone is significantly smaller than that in the other welding techniques and is limited to the joint region only, thus no contamination of the bulk material by particles occurs. This method is particularly suitable for joining of plastic components that are too sensitive to other joining processes such as spin vibration and hot plate welding. Disadvantages include high equipment costs and need for ventilation systems to remove hazardous shielding gases and particulate materials resulting from vaporization of polymer degradation (Ou et al. 1992). Another disadvantage is the low level of efficiency, e.g. a diode laser has an efficiency of 30%, CO_2 laser – 10% and Nd:YAG – 3% (Kagan and Punho 2000).

The application of lasers in materials processing, especially for welding of metals and ceramics and for marking, cutting and drilling polymers, is still growing.

Although lasers have had limited use in the joining of plastics due to their inherent properties, advances in materials processing are overcoming many of these limitations.

3.3.2.6 Infrared welding

Infrared welding involves the heating of the joint surfaces of the thermoplastic parts to the melting temperature using focused infrared electromagnetic radiation at a wavelength range of 1–15 μm. The parts are held at a pre-determined distance (up to 20 mm) from the heat source and are heated to the melting temperature of the thermoplastic. When the molten layer reaches a specified thickness, the heat source is removed and the parts are brought together under pressure until the joint cools and solidifies (Potente et al. 1991; Chen and Benatar 1995). The infrared welding process is illustrated in Figure 3.8.

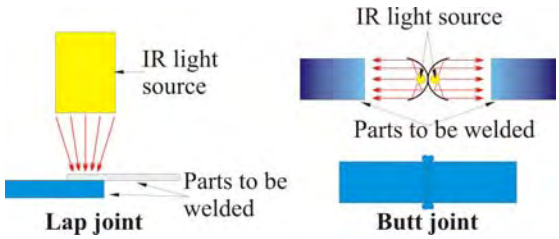

Figure 3.8: Infrared welding process

The infrared heat sources include radiant heaters or lamps such as quartz-halogen, tungsten, nickel-chromium or ceramic coated heating elements.

Unlike IR lasers which emit radiation in only a particular wavelength and one direction, IR lamps emit radiation within the whole IR range and in all directions. The infrared lamps can be short wave (0.78–1.4 μm), medium wave (1.4–3.0 μm) and long wave (3.0–1000 μm) lamps. Short-wave IR radiation (short-wave lamp, Nd:YAG lasers) causes volumetric absorption i.e. high optical penetration depth in the irradiated material (Bonten and Tuchert 2000). Therefore, when a source of short-wave IR radiation is used, the processing parameters are dependent on the type of material being irradiated. Medium and long-wave IR radiation (medium- and long-wave IR lamps and CO_2 laser) does not have such an effect on the working material and can be used unrestrictedly.

Although the output of a quartz-halogen IR lamp can extend over a range of wavelengths, its maximum output can be determined by Wien's displacement law (Equation 2.5). Typically, the quartz-halogen lamps emit maximum radiation in the near-infrared part of the spectrum. As can be seen from Figure 3.9, the IR lamps also emit visible light along with a small amount of UV.

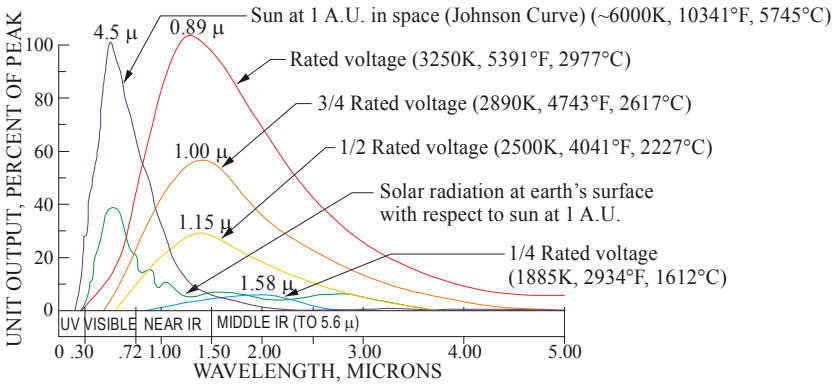

Figure 3.9: Typical spectral distribution of output from a quartz-halogen lamp compared to the solar radiation spectrum (adapted from Grimm 1996)

The near-infrared part of the spectrum is not as useful as the mid-range frequencies and therefore very little is known about it. This has been one of the motives behind this research, to specifically utilize the broad range (including near-infrared) natural solar radiation for polymer processing.

Infrared welding can be used to join virtually all thermoplastics and is particularly suitable for temperature resistant materials because high temperatures up to 3000°C can be reached at short heating times. Infrared welding is a fast, economical and safe method of joining thermoplastics which can be readily automated. The main advantage is the non-contact method of heating that eliminates the possibility of contamination of the joint surface. Infrared welding is similar to hot plate welding but parts can be welded at least 30% faster and the heat intensity at the joint surface is lower. In addition, unlike the stepwise process necessary in hot tool welding, the process in infrared welding can be used for continuous joining. In infrared welding, not only the surface but the material below the surface can be heated (Chen and Benatar 1995), resulting in faster welding and a high quality of weld. Infrared welding offers the potential for stronger joints because a deeper melt zone is created by absorption instantly, rather than by conduction through the polymers (Grimm 1998). On the other hand, compared to hot tool welding, the infrared welding process requires a thicker melt layer due to thermal decomposition at the joint interface (Potente et al. 1991).

Although the use of IR radiation for thermoplastic welding started before the 1970s, this method for joining of plastics is not as well established as the other traditional techniques such as vibration, ultrasonic and hot plate welding. Some of the main reasons are problems related to IR lamp life and heat build-up, complexity of robotics and optics for curved parts, and high cost (Grewell and Nijenhuis 2000).

The main disadvantage of IR lamps is that they are difficult to focus and this is the reason they have not been widely used for thermoplastic welding. At present there exist only butt welding machines for tubes. IR lamps are mainly used in polymer thermoforming and blow molding (Bonten and Tuchert 2000).

3.3.2.7 Recent advanced polymer welding techniques

Through-transmission infrared/laser technique

Nearly all polymers, even those that are very opaque to the visible light, are 'transparent' to infrared radiation in the near IR part of the spectrum. Since most polymers typically contain carbon-hydrogen bonds, they will absorb in the mid IR wavelengths (3.2–3.6 μm), but the radiation in the near-infrared region will directly propagate through them with a relatively little effect. In order to successfully use IR radiation for joining plastics, a sufficient amount must be absorbed at the joint interface generating the heat required for melting. As a solution to this problem, an innovative welding technique called through-transmission welding has been developed. In the initial version of this technique, a carbon black pigment dispersed throughout the bottom substrate has been used to absorb the IR radiation. The IR light beam that propagates through the IR-transparent component is absorbed by the IR-absorbing component generating heat, as illustrated in Figure 3.10.

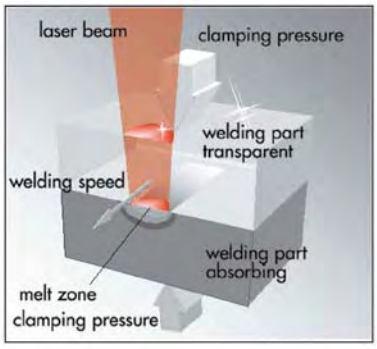

Figure 3.10: Through-transmission laser welding

The heat is exchanged with the non-absorbing polymer through conduction. As a result, both polymers melt and form a weld after cooling. However, this technique is not suitable for welding clear polymers since the carbon black contaminates the material and makes it opaque. Moreover, the use of carbon black imposes limitations in applications where the visual appearance is essential. A further development of the through-transmission welding has been the incorporation of other IR absorbing

pigments, dyes and opaque filters into the bulk material used as a bottom substrate. Among the non-absorbing IR radiation polymers, usually clear polymers like acrylic and sometimes natural opaque polymers such as Teflon that are transparent to IR radiation, are used (Grimm 1996). It is known that in general the IR absorbing pigments offer better heat stability than dyes, but they also cause light scattering which leads to a reduction of light absorption efficiency. Also, pigments may cause other problems such as changes of important mechanical and optical properties of the polymers. The IR dyes, on the other hand, can offer the advantage of minimal visual coloration which is an important requirement in many applications. However, they are relatively unstable and may degrade to color by-products. In laser transmission welding it is critical (Hartley and Sallavanti 2002) that the laser wavelength matches the wavelength at which the material (or the dye) is designed to absorb.

TTIR laser welding is not suitable when both thermoplastics have the same optical characteristics. If the top part has high absorptance, when the incident beam hits its surface, significant thermal degradation occurs at the irradiated surface, while an insufficient amount of heat is transferred to the joint interface. On the other hand, if both parts have low absorptance, welding cannot occur.

A disadvantage of the TTIR welding is the void formation in the center of the weld which occurs often and may lead to weak and unattractive welds. Sometimes the void formation can occur even at the edges of the weld, resulting in loss of hermeticity. The voids form mainly due to non-uniform temperature distribution within the weld zone and out-gassing of volatiles (Caldwell and Grewell 2003).

ClearWeld technique

As already mentioned, most thermoplastics do not absorb near infrared light and a great deal of research has been oriented towards developing unique materials capable of absorbing the near IR radiation sufficiently. In a recent development the transmission laser welding technique enables the joining of completely clear or similarly colored thermoplastics with an almost invisible weld line (Figure 3.11).

Figure 3.11: Clear PMMA lap joint made with ClearWeld absorber at the interface

Patented by TWI and Gentex Corporation, 'ClearWeld®' requires specially developed organic near-infrared absorbing dyes or solutions in a specific proportion applied at the specimen interface. The dyes can also be incorporated into the bulk of the polymer or applied in a thin film inserted between the surfaces of the parts. The almost colorless dyes absorb infrared laser energy efficiently, and convert it to heat without significantly absorbing visible light. The dyes have a peak absorption at 940 nm and are suitable for use with diode or Nd-YAG lasers (McGrath et al. 2001).

Similar to the through-transmission infrared welding, the ClearWeld process is dependent on the transmission efficiency of the IR light through the IR transparent component. Once the absorber used in the ClearWeld process is irradiated with the laser energy, it decomposes and no further heating/welding can be performed. Typically, for the ClearWeld process higher energy densities than the through-transmission infrared/laser welding are required (Woosman and Sallavanti 2003).

3.3.3 Related work

Information on studies similar to those performed in this research could not be sourced in the literature. However, a number of researchers have reported studies on capabilities of other modern polymer joining techniques using the same or similar materials.

Experiments with continuous through-transmission infrared (TTIR) welding of clear acrylic (PMMA) in contact with a black polycarbonate (PC) were reported by Grimm (Grimm 1996; Grimm 1998). The sources of IR radiation were spot a focusing quartz-halogen lamp operating at a filament temperature of 3000°C and a line heating quartz-tungsten lamp with a filament temperature of 2300°C. The samples were T-shaped with a welding surface of 3.1 x 50 mm. The flux densities at the focal length were 140 W/cm² from the spot heater and 111 W/cm² from the line heater. Temperatures were measured by 0.15 mm K-type thermocouples, one of which was placed in the weld zone and in contact with the clear PMMA sample and the surface of the black PC sample. The other was embedded in the PMMA sample at the incident surface. The author noted that the thermocouples were not thoroughly calibrated and the temperature readings were within 10% of the expected values.

A maximum temperature of 220°C was measured during the welding process. Continuous welds were performed under pressure of 21 to 42 kPa. The strongest welds were achieved with the lowest speed of 19 cm/min. A distinctive feature of

the TTIR process is that when welding dissimilar materials, the polymer with the higher melting temperature can be selectively heated by making it the absorbing material. For instance, PC has a higher melting temperature than PMMA, however, since the energy is absorbed by the black PC material and transferred to the clear PMMA material by conduction, PC reaches a higher temperature and lower viscosity than PMMA. In this study the weld zones showed PC enveloping PMMA rather than the other way around, as with hot plate welding. In summary, strong welds with good aesthetics were achieved, but the continuous welding speeds were relatively slow and further improvement in this regard was suggested.

In the same study, trials with different types of quartz filters were also conducted in order to reduce the amount of energy propagating trough the upper transparent PMMA sample. However, since all quartz filters broke under the high thermal stress, the only successful experiments were completed with an ordinary sheet of PMMA. The author argued that the PMMA filter removed from the lamp output exactly those wavelengths that caused overheating of the acrylic sample. When there was no filter, the temperatures at the surface of incidence and the weld line were almost equivalent. However, with the PMMA filter in place, the surface temperature of the clear acrylic was lowered by nearly 100°C. Figure 3.12 shows the heating behaviour at the weld line and surface of incidence without and with PMMA sheet filter. An experiment with flowing air over the weld interface showed that forced cooling can also enhance heating selectivity.

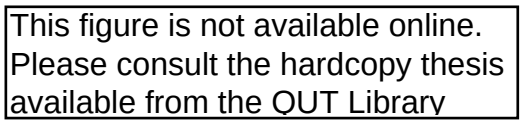

Figure 3.12: Heating behaviour without and with filter (Grimm 1996)

In a subsequent study (Grimm 2002), several other types of filter media such as dibasic esters (DBE) with different thicknesses and cooling by air were examined. The trials were conducted with clear PMMA samples in red, amber, crystal clear and neutral colors welded to opaque PC samples in grey or black colors. The author concluded that 2 mm thick layers of DBE esters could provide a good filter medium

and that the effect of air flow on the joint area was minimal when an effective filter was used. However, the study confirmed the findings of the previous study (Grimm 1996) that an acrylic sheet is the most effective filter medium for selective heating in the process of welding acrylic parts.

Grimm and Yeh published results on the effect of different colors on the absorption behaviour of ABS during through-transmission IR welding (Grimm and Yeh 1998). ABS films of red, orange, yellow, green and blue colors with thicknesses 0.25 mm and 0.5 mm were exposed to radiation emitted by a MR16 quartz-halogen IR lamp a with a filament temperature of 3000°C (see Figure 3.13).

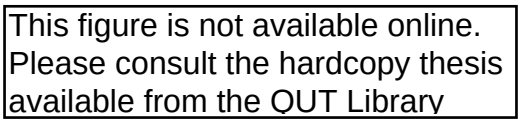

Figure 3.13: Transmission vs. color of ABS sheets (Grimm and Yeh 1998)

The flux density at the focal plane was 140 W/cm^2 with a maximum output around 0.89 μm (see Figure 3.9). Examination of the used quartz-halogen lamp showed a higher flux density at the red end of the spectrum. The amount of energy transmitted through the films was determined by the temperature change measured with a thermocouple fixed under the sample. It is believed that a material exposed on visible light at room temperature and normal pressure may absorb all colors and re-emit the observed color. However, the authors reported that the red specimens absorbed the most IR energy, followed by the yellow, orange and green, and the least amount of energy was absorbed by the blue specimens. In the same study the authors investigated the effect of different carbon black amounts (0.03-0.07%) on infrared absorption in polyethylene (PE) films. The authors concluded that polymers with different colors would be heated differently by the lamp output radiation. They would have different heating times and melting depths depending on the pigment concentration or polymer color. In subsequent studies the same authors showed that in IR welding colored, opaque and transparent materials could be used as absorbing layers given that proper color combinations are chosen.

Some research work was carried out to assess the IR absorption behaviour of 11 commonly used thermoplastics and the suitability of the TTIR technique for their welding (Yeh and Grimm 1998). Unpigmented polymer films with thicknesses of 0.3–1.2 mm including PMMA, PC, ABS, PP, PE, PA-6, HDPE and PVC were exposed to the same type quartz spot heating lamp described in a previous study (Grimm and Yeh 1998). To evaluate the amount of transmitted energy, a thermocouple was embedded in a block of white polymer under the irradiated film. All tested films showed strong transmission in the region around 1 μm due to the relatively weak absorption of this part of the spectrum in most polymers.

The translucent polymers attained temperatures of 200°C to 275°C, showing little transmission in the visible range due to their crystallinity or insoluble phases content (e.g. rubber content in ABS). The polymers with a relatively higher number of C-H bonds, such as PE and PP that are opaque to visible light, absorbed more of the lamp output radiation than the clear polymers did. One of the polymers showing the lowest transmission was ABS due to a scattering of the absorbed lamp output radiation by its rubber particles. Another low transmissive polymer was PVC because of its inorganic content which makes it opaque to all wavelengths of the lamp output radiation.

PE and PP which are opaque to the visible light, were found to be relatively transparent to the lamp output radiation, although not as transparent as the clear polymers because of their higher number of C-H bonds. Clear polymers such as PC, PMMA and PA-6 transmitted most of the lamp output radiation, reaching temperatures up to 300°C for a film thickness of 0.3 mm. The transparent PMMA, PC, and clear PS polymers showed a smaller decrease in temperature under the film with the increase of the film thicknesses compared to the translucent polymers.

In general, although a great number of polymers have been included in this study, most of the findings are logically predictable. They only prove that, as expected all tested unfilled, natural polymer films transmit the majority of the lamp output radiation (including the opaque films, though to a lesser degree). Thus, in order to understand the absorbing mechanism of the radiation spectra used in those polymers, more detailed studies involving the optical and thermal characteristic of each polymer are necessary.

Another study on TTIR welding of colored and transparent polymers has been reported (Grimm et al. 2000). The source of IR radiation was a Soft Beam Optical

Light Heating System which transmitted the light from a xenon lamp through a fiber optic and lens system to the welding interface. The typical focal spot diameter used was 4 to 5 mm and the power delivered was 30 W. The experiments were performed with transparent but colored acrylic samples with sizes of 25 mm x 50 mm and thicknesses of 3.2 mm. Opaque acrylic of the same color was used as the absorbing component rather than applying carbon black.

Studies with similarly colored opaque acrylic T-samples and black T-sections were also carried out. However, unlike previous successful experiments with quartz halogen lamps, the Soft Beam System could not perform this type of welds. Instead, an overheating and distortion of the colored opaque sheets occurred. The Soft Beam System was also used to weld clear acrylic sheets together by using inter-layers of thin (0.25–0.5 mm) opaque, colored acrylic strips. Experiments with applying a solution of black acrylic to the bond surface showed that the prepared ink was capable of absorbing the IR radiation.

Potente et al. analyzed the influence of a carbon black content on the ratio of the melt thickness for unfilled nylon 6 during laser transmission welding (Potente et al. 1998). The authors argued that if the absorbing part contains an insufficient quantity of carbon black, only a small amount of the laser energy would be absorbed in a relatively broad layer of material, causing a shallow temperature profile. By contrast, when the carbon black content is high enough, it will absorb most of the laser energy in a relatively thin absorbing layer and then will be conducted in both parts. The experiments showed that when the absorbing part contained a sufficient amount of carbon black, the thickness of the melt layer was identical in both parts. The authors also presented a mathematical model of the temperature stratification similar to single sided-heat impulse welding.

The development of an infrared assembly method (IRAM) of thermoplastics that had overcome the already mentioned problems with IR lamps has been reported in literature (Grewell 1999). This method operated on the principle of TTIR welding but had the advantage of illuminating the entire welding surface simultaneously. The technology was used to successfully weld PC, Acrylic, PS and ABS thermoplastics. IRAM was also used with special pigments that allowed the polymers to be either transparent or opaque to the NIR laser and at the same time invisible to the human eye. The minimal heating time to melt the interface with a given heat input q_0 was estimated using the general heat equation:

$$\frac{\partial T}{\partial t} = \alpha \frac{\partial^2 T}{\partial x^2} \tag{3.1}$$

and the minimal power required to melt the interface by the equation

$$q_0 = \sqrt{\frac{\pi k^2 T^2}{\alpha t_m}} \tag{3.2}$$

where k = 4.7 x 10-4 cal/s cm °C; α = 1.15 x 10-3 cm^2/s (for PC sample);
t_m = minimum weld time = 4 s; $T_m = T_g$ = 128 C°.

The minimum power required to make a weld in four seconds with a weld thickness of 1 mm was estimated to be q_0 = 1.53 Cal/cm or q_0 = 6.4 J/cm. However, the experimental value was 6 J/cm.

An experimental study to weld 3 to 5 mm thick clear acrylic and carbon black filled PC samples using the TTIR technique was performed by the author. A high-power laser diode with an output of 20 W was used as a source of IR radiation. The peak wavelengths were in the range of 800-900 nm. The results showed that although almost all IR radiation was absorbed by the black sample, both components melted uniformly. Thus, when the clear sample has a lower melting temperature, very uniform melting can be accomplished. In another study where both components were from the same material, it was found that there was slightly more melt in the black sample than the clear one. Although formation of particulate was not observed, flash was produced which remained attached to the weld. When clear PC and PMMA samples were used, it was found that there was a 10% to 27% increase in the minimum power and a 100% increase in the weld time required.

Grewell extended his research to experimentally determine the weldability of Polyketone with the TTIR technique (Grewell and Nijenhuis 2000). For the study, a 45 W lensed bar diode with a wavelength output of 800-900 nm was used to weld 3 to 5 mm thick samples in lap shear configuration. High weld strengths were achieved although weld flash was formed during the welding process. Another drawback that was noted in this and in previous findings, was the formation of moisture-generated bubbles leading to porosity when the cycle times were relatively long. This research confirmed that thermoplastic materials with thicknesses above 8 mm would be difficult to weld using the TTIR technique at wavelengths of 800-900 nm due to surface overheating and high power requirements (more than 45 W/cm).

Studies on the transmission beam welding of polymers with a diode laser showed

that the transparent part transmitted the laser beam with very little energy loss due to the reflection and scattering at the surface (Schulz and Haberstroh 2000). The other component which was filled with carbon black absorbed the laser beam entirely. It was shown that the laser beam could penetrate the pigmented polymer within a few millimetres depending on the pigment concentration. Experiments with carbon black filled ABS and transparent PMMA thermoplastics revealed that the samples containing smaller particles of carbon black (20 nm) had considerably higher weld strengths than the samples containing bigger particles (60 nm). It was found that a low laser absorption of the samples with smaller particles of carbon black caused a higher penetration depth and more homogenous melt, thus better welds. Additional investigations were conducted with welding of components both filled with special colors which showed that it was possible to have a polymer appearing black to the human eye but transparent to the laser beam. However, a disadvantage of the beam transmission method with this type materials was that it was limited by the thickness (maximum 1 mm) of the joining component; special dyes were required for thicker materials.

An experimental study on through-transmission laser welding (TTLW) for PC and HDPE was reported by Rhew et al. They used clear and black PC with 0.5% carbon black, and natural and black HDPE film with 0.5% carbon black (Rhew et al. 2003). Two TTLW systems were used – one with a laser diode bar (50 W) with a lens and another with an additional fiber optic bundle. Standard G1 (AWS) samples 10 mm and 20 mm long for the PC, and Tee-samples 20 mm long and 3.43 mm thick for the HDPE were used. The black film with dimensions 20 x 7 x 0.13 mm was applied at the interface of the natural and unfilled HDPE sample.

The authors reported that stronger welds were achieved when the fiber optic bundle was used because of the reshaping of the beam and more uniform power distribution provided by the fiber optics. It was demonstrated that although the weld strength improved with prolonged exposure, it decreased with further exposure beyond a certain heating duration. One disadvantage of this method is the formation of voids within the center of the weld due to out-gassing from polymer degradation. Also, charring usually occurs at the outer edges of the weld flash, as it was observed in almost all samples in the above-mentioned study. By contrast, in the joint technique performed in the present research, charring in the middle of the weld was not observed because of the Cassegrainian image formation used.

In another research paper Rhew et al. reported a study on laser energy transmittance and reflectance for the same materials and equipment (Rhew et al. 2003a). The transmittance and reflectance for PC and HDPE were measured at angles 0° (only transmittance), 30°, 45°, 60° and 75° and varying thicknesses – 0.37-12.2 mm for PC and 1.58-9.5 mm for HDPE. The authors showed that the thickness had minimal effect on the reflectance from PC and HDPE and the transmittance of the PC samples. Regardless of the thickness of the PC sample, at 0° incident angle the transmittance of the laser beam was ~90%. Being semi-crystalline, HDPE caused higher dispersion of the beam and its transmittance was not only much lower than that of PC, but decreased with increasing thickness. Along with measurement of the optical properties of PC and HDPE, the authors discussed the characterization of the laser diodes and the power intensity distribution. The limitation of the non-uniformity in the power intensity distribution of the laser bar could be partially overcome by using a fiber optics bundle. However, the output of the fiber optics typically has a high divergence in the vertical axis which is of concern during the TTLW process.

An alternative welding procedure for overlapped thermoplastic parts using infrared CO_2 laser as a radiation heat source was reported (Kurosaki et al. 2003). The authors outlined some characteristics of the commonly used types of IR laser welding techniques for overlapped thermoplastics, as shown in Table 3.1.

Table 3.1: IR laser welding techniques for thermoplastics (Kurosaki et al. 2003)

The proposed technique utilized a heat sink which is a solid material transparent to the laser beam and with much higher thermal conductivity than that of the thermoplastic to be welded (see Figure 3.14). The heat sink was placed in contact with the top part of the thermoplastic which was irradiated by a laser beam.

Figure 3.14: Thermoplastic films joined with CO_2 laser with the aid of transparent heat sink (Kurosaki et al. 2003)

Unlike the traditional through-transmission method, the top component has to be an absorber of the particular laser. The purpose of the heat sink was to diffusively absorb the thermal energy from the thermoplastic through the contact surface and thus to prevent surface thermal damage due to excessive raise of temperature.

In contrast to the traditional through-transmission welding, it was not necessary for the bottom part of the thermoplastic to be an absorber of the particular laser, hence the use of pigmentation or dyes was not required. The feasibility of this technique was tested by joining two HDPE films with thicknesses of 300 μm each. While the main advantage of this welding procedure is that there is no need for pigments or dyes, there are some disadvantages such as the requirement for a heat sink, transparent to CO_2 laser, and the fact that there are only a few suitable materials most of which are toxic. Furthermore, this technique is limited to identical kinds of thin thermoplastic parts such as films and tubes.

The development work on the ClearWeld technique was mainly performed with 3 mm thick PMMA plates using NIR absorbing film at the interface. This welding technique was also used for welding nylon based fabrics and thin films (PE, PEEK) where the dye was dissolved in a suitable solvent and painted over the joint area (Jones et al. 2000). Tensile strength similar to that achieved with other traditional joining methods was attained with ClearWeld butt joining of nylon and acrylic specimens. The dyes were hand-painted on the surface of the plaques to be joined (Kagan et al. 2000). In general the transmission laser welding process is applicable to sheet and moulded parts, films and fabrics in a wide range of polymers.

There have been numerous studies on the efficiency of various types of dyes mixed into films as an absorbing medium in lap joint configurations (Jones and

Taylor 1994; Jones 1998; Grimm et al. 2000; Jones et al. 2000). Kagan and Woosman explored the application and efficiency of nearly colorless, laser absorbing dyes in clear-welding of various types of polyamides, including transparent, and one type of acrylic plastic (Kagan and Woosman 2002). Butt joint experiments were performed with T-type nylon 6 and PMMA samples 150 x 38 mm with thicknesses of 4.8 mm in the weld area. The liquid dyes were hand-painted on the surface of one of the specimens prior to the assembly. The clear-welding process was performed with a high-powered diode laser with a wavelength of 940 nm, output power of 150 W and a beam at focus 2 x 2 mm. The clear-welding process was not very efficient in non-optimized processing conditions. In optimized processing conditions however, the achieved tensile strength of the joints was similar to that achieved for nylon by other traditional and laser through-transmission IR techniques.

Hartley and Salavanti discussed the clear welding process for PC, PMMA, nylon and polyester (Hartley and Sallavanti 2002). Lap joints of PMMA and PC samples with thicknesses 3 mm were performed using the clear-welding technique with a 940 nm diode laser. Spectral scans showed a significant decrease in the transmittance of PMMA caused by a high concentration of the absorbing layer. By contrast, a low concentration of the absorbing layer led to less reduction in the transmittance of PC. However, in both cases the application of an absorbing layer was crucial to form a weld. Tensile tests showed the tensile strength dependence on the incident power density became relatively linear after reaching the minimal energy density threshold (see Figure 3.15). It was concluded that the increase of absorption at the specific diode laser wavelength, as well as the high susceptibility of the absorbing dye in the same wavelength, were crucial factors for a good performance in the clear welding process.

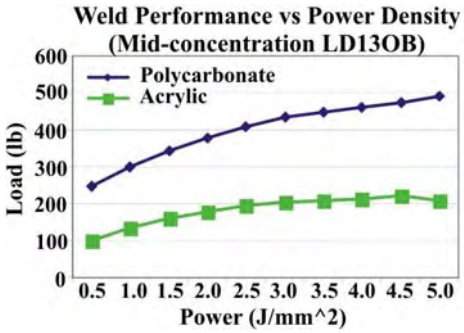

Figure 3.15: Weld performance vs. power density for PMMA and PC

A comprehensive study with a number of different thermoplastics including

PMMA, PC, ABS and PVC was conducted to explore the capabilities and limitations of the clear-welding process (Woosman and Sallavanti 2003). Samples with sizes of 25 x 100 mm were joined using a high-power diode laser at a wavelength of 940±10 nm with maximum output power of 300 W and a beam size 2 x 2 mm. The samples were placed between a 9.5 mm piece of borosilicate glass and an aluminium plate and clamping pressure was applied by air cylinders. After evaluation of the tensile strengths and weld efficiency the authors concluded that Acrylic/PVC and Polystyrene could not be welded due to their low transmission when applying the absorber. After the absorber decomposed, the PTFE samples did not even melt despite the sufficient laser transmission. The thermoplastics with the lowest weld efficiencies (less than 0.5) were Nylon 66, PEI and Acetal due to their high melting temperatures or low transmission. The researchers also observed some burning on the surface of PMMA, PC and ABS due to laser-induced breakdown above a critical energy density. This experimental work demonstrated that clear-welding process could be used to weld a range of thermoplastics but there were some limitations on the thickness and transmission capability of the material.

Typically, apart from the welding process conditions used, the radiation-material characteristics have a great impact on the optimization of the welding process. Studies into the optical characterization of colored and non-colored thermoplastics for TTIR/laser welding have found that additives such as carbon black, fillers and pigments can significantly reduce the light transmission in plastics. Kagan et al. analyzed the properties of colored and non-colored nylon-based plastics and observed that the color of the plastic played an important role in the transmission of laser energy (Kagan et al. 2000). The green and yellow colors reduced the transmission by 75-85%, whereas the transmission of the red specimens was similar to that of the naturally colored specimens. The carbon black pigment reduced the transmission to almost zero, while the levels of transmission in non-carbon black colorants were similar to those of the green and yellow colorants. The authors argued that the decreased transmission at a particular laser wavelength was due to the increased absorption by the colorants and particulate scattering, the latter being more significant. They also explored the relationship between specimen color and thickness (0.8, 1.6, 3.2 and 6.25 mm) and observed different behaviour in the reduction of the laser energy transmission with increasing thickness. For non-colored and red samples the laser energy transmission decreased steadily (from 85%

to 42%), whereas for the yellow, green and white it decreased from 60-40% to 1-3%.

Studies with the same material (nylon 6) were performed in order to assess the efficiency of the laser transmission welding technique for this type of material (Kagan and Punho 2000). Butt joint specimens with rectangular shape (150 x 60 x 3.2 mm) and T-shape (150 x 38 x 3.2 mm) and lap joint samples (150 x 60 x 3.2 mm) were used. A fiber coupled diode laser system with a power range of 20-100 W at a wavelength of 808±10 nm was used to weld natural nylon samples with carbon black filled samples. Compared to some of the traditional welding technologies, relatively good weld strengths were achieved with the butt joint configuration. By contrast, the lap joints did not perform well due to design limitations on the welding of long rectangular plaques and the formation of non-uniform melt pool at the joint interface. The authors concluded that further improvements are needed in order to optimize the processing conditions for colored thermoplastics, particularly related to the effect of colorants and types of pigments on the weld quality.

A study on optical characterization, in particular absorption and transmission, of colored and non-colored polyamides (PA) was performed by (Kagan et al. 2001). They observed that at spectral wavelengths in the NIR range (800-1100 nm) the uncolored PA samples absorbed a maximum 20% of the laser energy (Figure 3.16).

Figure 3.16: Influence of wavelength on absorption of IR radiation for green, red, blue, natural and yellow colored PA (Kagan et al. 2001)

Pigments and dyes such as organic green considerably increased the absorption to more than 90%. The authors argued that the increase of diffuse light scattering would lead to a decrease in transmission of the thermoplastics. Experiments with colored PA specimens (red, yellow, green and white) showed that the yellow had

significantly reduced transmittance due to diffuse light scattering compared to the red and non-colored specimens. The experiments confirmed that except for the green specimen, the transmission of the other specimens only slightly decreased with decreasing the wavelength from 1064 nm to 830 nm. The reduced transmittance of the green specimen was probably due to the intrinsic absorption of the colorant.

In another study the authors reported that they were not able to weld white PA 6 based plastic because of the inability of the laser energy to be focused at the joint interface due to high light scattering (Kagan et al. 2001a). To overcome this, an optimisation of the content and type colorant of white pigments was suggested. In the same study the researchers discussed the advantages and disadvantages of colorants in plastics such as pigments and dyes. Since organic pigments have finer particle sizes, much smaller that the wavelength of visible light (see Figure 3.17) and lower refractive indices, they are recommended as colorants for transparent polymers along with dyes. However, the organic pigments are relatively difficult to disperse and can decrease the absorptance due to decreased light scattering caused by the smaller particle size.

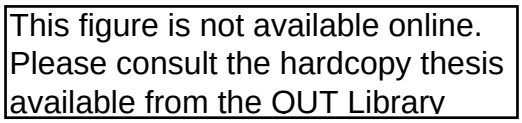

Figure 3.17: Perceived colors in human vision (Kagan et al. 2001a)

The relationship between the optical properties of colored and non-colored polyamides and welding processing parameters was also studied by Grewell et al. (Grewell et al. 2002). TTIR welding experiments were carried out with nylon 6 clear and colored samples with sizes of 150 x 62 mm and 150 x 38 mm with thicknesses 3.2 mm, using a high-power diode laser system IRAM at a wavelength of 810 nm.

Uncolored (natural) nylon 6 samples were welded in a butt configuration to similar specimens using carbon black as an absorbing material. Various colored nylon 6 specimens were also welded to specimens filled with carbon black.

The authors reported that the transparency of the nylon was not affected by the red pigment but significantly affected by the yellow. The white sample did not absorb enough laser energy but rather scattered the incident beam to such an extent that the welding time was significantly increased. The green colored samples, however, absorbed almost all laser energy in the NIR wavelength of 900 nm. For this reason it was suggested by the authors that the green pigment could be used as an absorbent pigment similar to the carbon black.

Bonten and Tuchert analyzed the current most common techniques for welding plastics through heating by radiation (Bonten and Tuchert 2000). Also, they discussed the reaction of thermoplastics on IR radiation, in particular their absorption capabilities. Different thermoplastics will have different absorption and transmission bands depending on the individual absorption bands of their functional groups (an example is given in Figure 3.18).

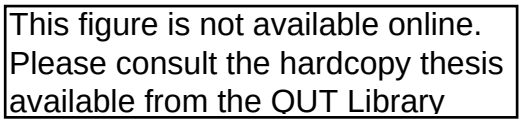

Figure 3.18: Absorption spectrum of PP (Bonten and Tuchert 2000)

Assuming linear mechanism of absorption and using Lambert-Bouguer's law, the authors expressed the intensity decrease as follows:

$$I(x) = I_{(x=0)}e^{-\alpha x} \qquad (3.3)$$

where I is the radiation intensity (W/m^2) and α is the absorption coefficient which is dependent on the color and surface finish. It is inversely proportional to the optical penetration depth, dp i.e. $\alpha = dp^{-1}$. If the plastic has a high absorption coefficient and a low optical penetration depth, most of the incident IR radiation will be absorbed on

the surface and the temperature change with depth increase will be relatively steep. By contrast, if the plastic has a low absorption coefficient and a high optical penetration depth, the incident IR radiation will propagate deeper causing volumetric absorption (see Figure 3.19).

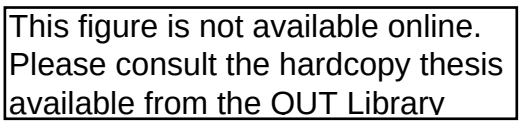

Figure 3.19: Surface and volumetric absorption of plastics (Bonten and Tuchert 2000)

3.4 Radiation curing

Light curing of natural adhesives has been known for more than 3000 years, and rapid curing of synthetic adhesives by radiation became an ecologically sound technology in the 20th Century. The research in radiation curing of cross-linking polymers using photo-initiators sensitive to UV light dates back to the 1950s, and the development of the first UV cured adhesives – to the early 1960s. In the 1980s light curing, being originally developed for ink and thin coatings (250 nm UV range), became popular for other applications such as industrial bonding and sealing. The first widely recognized structural (UV aerobic acrylic) adhesives cured with radiation curing technology were introduced in 1982 (Bachmann 1995). Unlike the UV curing inks and coatings, these adhesives are cured in deeper layers (up to 6 mm).

In radiation curing usually electromagnetic radiation is used to alter the physical change and chemical nature of the material. Essentially electromagnetic radiation intersects with organic substances or its photons interact with the substance on an atomic level to develop cross-linked structures. Most current radiant-cured adhesives are solvent-free adhesives which have an environmental, health and safety advantage and cure relatively quickly. However, they require energy, typically from an irradiation source that can promote photochemical reactions when absorbed within an organic substance. Apart from the high energy electron beam (EB) most of the used energy sources utilize electromagnetic radiation of various spectral ranges including ultraviolet (UV), infrared (IR), microwave and radio frequency (RF).

Adhesive bonding is a widely used method of joining thermoplastics. However, adhesives cured under ambient light usually require long curing times, e.g. several hours to a day, to develop a handling strength and several days to a week for

complete curing (Kwan et al. 1999). In order to shorten the curing times, additional heating may be applied to accelerate the chemical reaction rates. Conventional means of heating include ovens, press heating and induction heating, however, their heating rates are relatively slow and dependent on the geometry and thermal properties of the components to be joined.

In order to further accelerate the heating rate, rapid curing methods have been developed. In such methods heat is generated more efficiently within the material, unlike conventional curing methods where heat is applied externally and transferred to the material predominantly through conduction (see Figure 3.20). The internal heat generation is governed by loss modulus (e.g. ultrasonic heating) or dielectric losses (e.g. microwave and RF heating) (Kwan et al. 1998a).

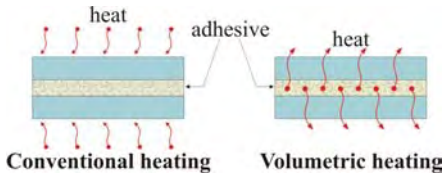

Figure 3.20: Conventional and volumetric heating

The acceleration of the chemical reactions during the curing process at ambient conditions can be achieved by volumetric heating applied to the adhesive system. Research work has been carried out to assess the feasibility of different volumetric heating methods for rapid curing of structural adhesives in metal and plastic joints.

The possibility of using IR heating for rapid curing has been studied by several researchers. Frank argued that IR ovens could attain faster curing times than the conventional ovens (Frank 1985). He claimed that IR heating was a cost-effective process especially in the plastic finishing industry. Zimmerly explored the advantages of using RF heating in drying of adhesives (Zimmerly 1987). He observed that heating and drying times did not depend on the temperature gradient. Jones disputed the advantages and limitations of using RF heating for drying of adhesives (Jones 1991). He claimed that despite the high initial cost, RF heating would be cost-effective in a long-term production process. Malaczynski and Cinpinski discussed the results of their experimental study and computer simulations which found that RF curing could not be used effectively for all adhesive systems because of the possibility of thermal runway (Malaczynski and Cinpinski 1996).

Another method for curing of polymers by incorporating a variable frequency microwave furnace system has been suggested (Lauf et al. 1998). By varying the

frequency of the microwave signal, non-uniformities within the cavity are minimised so that the cure throughout the specimen is more uniform.

Ultrasonic heating has been compared to two types of electromagnetic heating, RF and microwave (Kwan et al. 1998). After evaluation of different processing parameters such as heating pressure, power and time, it has been shown that heating time had the most significant effect on joint strength. RF heating proved to be the most effective way for curing epoxy and urethane adhesives, producing the highest joint strength and reducing the recommended curing time by 50%. It has been found also that ultrasonic heating and microwave heating could be feasible methods for adhesive curing. However, the microwave heating had some limitations related to the equipment such as size of the waveguide, wave pattern and pressure application. It has also been shown that the choice of adhesive plays an important role in the rapid curing process. While the polyurethane adhesive was cured successfully in all rapid curing methods studied, the epoxy adhesive produced arcing and smoking in the RF and microwave heating.

In a subsequent study, two types of volumetric heating using IR and RF were explored for rapid heating and curing of two-part polyurethane adhesive (Kwan et al. 1999). The curing time to achieve the handling strength was reduced from 25 minutes to less than three minutes. It was demonstrated that maximum joint strength could be achieved in 5 minutes. However, the results indicated that in RF heating the conductive polymer, used to enhance rapid heating, significantly reduced the joint strength and increased the curing time of the adhesive. In both RF and IR heating, when the heating time was extended to 130 seconds, yellowing and foaming in the urethane adhesive were observed which led to a reduction of the joint strength.

Two of the most widely used radiation sources to directly or indirectly initiate polymerization are UV and EB (Nunez et al. 1995). When fast curing or special cure considerations are required, UV light is commonly used for polymerization of adhesives or coatings free of solvents. However, the UV lamp effective output of energy decreases gradually, and their cleaning and maintenance can be very costly. Typically, the reflectors used to focus the “black light” energy from the UV lamp lose their reflection properties over time due to various factors such as a high filament temperature or accumulation of a large amount of UV light or ozone.

Also, the depth of cure is limited since the adhesive cures from its initial site of exposure down, normally resulting in a cured top layer within a 2 mm nominal depth.

This firstly cured layer prevents the occurring of any further photo-initiation beneath it. Moreover, the advanced UV curing method is not always suitable since it requires transmission of UV light through the material and UV exposure is not acceptable in all applications. In fact, many of the translucent and colored polymers and other UV blocked materials could not be cured with UV sources (Bachmann 1995).

One way to overcome some of these problems is to use an irradiation source with a longer wavelength i.e. visible light, when possible. The research in curing with visible light dates back to the early 1970s and pure visible light adhesives have been used predominantly in dentistry. Bachmann has reported results from curing of two types of adhesives (UV susceptible and UV-VIS susceptible) with traditional UV only, visible light only and a combination of both (Bachmann 1995). The results are shown in Table 3.2.

Table 3.2: Typical adhesive cure response to various wavelength combinations

Peak wavelength	Long wave UV "Black light"	Visible light	Combined UV and visible light
365 nm	50 mW/cm^2	–	50 mW/cm^2
405 nm	5 mW/cm^2	20 mW/cm^2	20 mW/cm^2
436 nm	–	25 mW/cm^2	25 mW/cm^2
Available energy	55 mW/cm^2	45 mW/cm^2	95 mW/cm^2
Typical cure speed of UV only adhesive	10 sec	–	5 sec
Typical cure speed of UV/visible adhesive	5 sec	20 sec	2 sec

It can be seen that curing with visible light only is much longer than traditional UV curing. Typically the synergistic use of both UV and visible photo-catalysts produces an up to 50% faster cure than formulation absorbing only UV light.

In general, two types of light sensitive materials are predominantly used, aerobic acrylates and epoxies. Special type aerobic acrylic adhesive has been developed to take advantage of the visible light curing capability to cure through (bond or seal) any transparent or translucent polymer. Higher radiation intensity is expected to lead to faster cures, however the irradiation source spectral output, as well as the spectral susceptibility of the adhesive, also have a great impact on the speed and depth of cure. Bachmann has shown the possible additional spectral range that can be gained by using UV/visible adhesives (Bachmann 1995). Figure 3.21 illustrates the spectral output characteristics of a typical UV light source. The shaded area shows the energy absorbed by a UV structural potting resin and a UV/visible adhesive respectively.

Figure 3.21: Energy absorbed for cure by UV (left) and UV/visible (right) structural adhesives (Bachmann 1995)

Since the photon energy is inversely proportional to its wavelength, the shorter the wavelength the higher the energy, and consequently the UV is the most energetic portion of light. Thus, curing with visible light on its own will take a longer time. However, curing with concentrated visible sunlight has not been reported in literature. If concentrated solar radiation is used, by carefully chosen light-curing adhesives and adherends the productivity could be increased and manufacturing pollution significantly reduced.

3.5 Accelerated ageing of polymers

It is well recognised that sunlight, especially the ultraviolet portion of the solar spectrum, can damage plastic materials. Natural weathering could induce photochemical or chemical degradation causing discoloration, surface cracking, embrittlement and other deterioration of the optical and physical properties of thermoplastics. Other changes include a reduction in molecular weight and formation of chemical groups like carbonyl, carboxylic acids and hydroperoxides (Rabek 1995). Most organic polymers are susceptible to absorption of UV radiation. The energy of a photon of UV light is transferred to the molecule resulting in bond scission. This in turn leads to embrittlement, discoloration and chain breaking. Raising the temperature of most polymers in the range of 200-400°C usually causes thermal vibrations of the molecules which results in bond scission. This leads to thermal degradation of the polymer with reduced physical properties.

There are two main types of thermal degradation processes in polymers, i.e. chain depolymerization and side-group reactions. During depolymerization, the polymer chain breaks at some point, leading to reactions in which all products have the same composition but consist of smaller molecules. PMMA can degrade

thermally via this process as illustrated bellow (Stuart 2002):

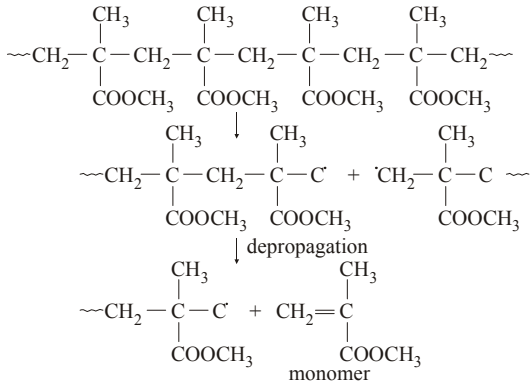

Figure 3.22 demonstrates the detrimental effect of prolonged outdoor exposure on the light transmittance of three common thermoplastics - PMMA, PC and GRP used in glazing (Blaga 2002). After 11 ½ years of exposure to natural weathering the visible light transmission of PMMA was the least affected, it was moderately reduced in PC and significantly reduced in GRP.

This figure is not available online. Please consult the hardcopy thesis available from the OUT Library

Figure 3.22: Effect of weathering on light transmission of glazing plastics (Blaga 2002)

In this research the possibility of using the SEC facility for performing accelerated natural weathering tests to study the polymer ageing process has been explored. Since an application of similar equipment for weathering of polymers has not been found in literature, the current practice for performing outdoor weathering and accelerated testing, and some related work are outlined in the following sections.

Although the accelerated weathering tests may be inaccurate, in some cases due to reciprocity law failure, they can provide reliable information in a considerably short-term period, compared to real-time weathering. Typical short-term radiation exposure of 1-2 years could be achieved in 10-20 days by increasing the intensity of natural sunlight up to 100 times. In this research, depending on the irradiated area, such acceleration rates and even higher have been achieved by the SEC facility.

Plastic manufacturers, as well as manufactures of exterior coatings, paints and finishes periodically require information on the performance and durability of their products in order to predict their service lifetime. However, such data is needed in a much shorter time than it would take to expose materials to weathering effects in natural environment.

Weathering tests are performed for various other reasons including quality control, durability and performance requirements, and development of new materials. There is an increased recognition of the influence of environmental variables on the current techniques available to accelerate the polymer ageing process either in natural outdoor or simulated laboratory conditions. The most important environmental factors that cause weather degradation are irradiation, heating and moisture (Jacques 2000).

3.5.1 Irradiation

Generally, polymer exposure to UV or visible radiation could cause light-induced polymer degradation, or photodegradation, leading to physical and chemical changes. Therefore, the irradiation, particularly with solar radiation, is a critical factor for the weathering of most polymer materials. Consequently, the radiation absorption plays a significant role in the photodegradation process.

In particular, a requirement for the photochemical reaction initiation is the existence of the light absorbing (sometimes called chromophoric) groups, such as carbon double bond (C=C), carbonyl (C=O), etc. in the macromolecule of a polymer or its additives. It can cause discoloration, fading, surface erosion, loss of gloss and other deteriorations. Different chemical bonds in polymers can be broken by different types of radiation with different frequencies carrying different photon energies related to Planck's law (given in Equation 2.4). Typical chemical bonds with their bond energies and the corresponding radiation wavelengths with their photon energies are shown in Table 3.3 (Leather 1999).

Table 3.3: The equivalence of wavelength, energy and bonding

Wavelength [nm]		240		260		280		300	320	340	360	370	400	420	440	460	480	500	520	540	560	580
Photon energy [kcal/mol]								95	89	84	79	75	71	68	65	62	60	57	55	53	51	49
Bond energy [kcal/mol]	166	147	145	111	103	102	102	99		83	80	78		68	65							
Chemical bond	C=O	C=C	C=N	O–H	H–H	CH_3–H	H–Cl	C–H		C–C	C–O	C–Cl		C–N	C–S							

It can be seen that the initiation of polymer degradation is mainly caused by

photons with energies in the UV portion of the solar spectrum. Energy carried by a photon of UV radiation is sufficient to break the double bond in a polymer and initiate polymerization. Since most polymers absorb strongly the higher energies from the photons with shorter wavelengths, their chemical bonds could be easily broken. The energy source in the present research utilizes the available solar radiation and provides concentrated light, predominantly the visible and near UV light of the spectrum. For this reason, in line with the objectives of this research, the possibility of using concentrated visible light to initiate chemical bond breaking with bond energies higher than 71 kcal/mol has been studied.

It has been known for years that the exposure on concentrated solar energy greatly increases the speed of changes in material properties and performance such as the degradation of various plastics, fading of colors, failure of paints and coatings. One of the earliest apparatus for concentrating solar rays on sample materials to be tested for color fading and ageing is disclosed in US Patent No. 2945417 (Caryl and Helmick 1960). However, during the outdoor accelerated tests it has been observed that the temperature of the test samples can vary widely depending on the daylight hour or the season, despite the constant supply of cooling air. Subsequently, the cooling system of the device has been improved by incorporating a temperature sensor to control variable speed motors (Robbins 1989).

Based on these inventions, at present a Fresnel-reflecting concentrator accelerated weathering machine (Figure 3.23) is used to perform standard outdoor accelerated tests utilizing high irradiance levels (ASTM-G90 1999).

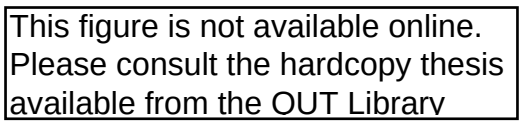

Figure 3.23: Schematic of optical system for Fresnel reflecting concentrator accelerated weathering machine (ASTM-G90 1999)

The direct solar radiation is concentrated onto the specimen surface by a Fresnel

array of 10 highly reflective flat mirrors, 15 x 142 cm each. The mirrors are positioned as tangents to an imaginary parabolic trough in such a way that the sun rays fall on them at near-normal incident angles, as shown on the schematic diagram.

The cooling of the test specimens is provided by a variable-speed fan that blows ambient air over the specimen surface. A nozzle assembly for spraying water onto the exposed specimens may be added to the system. Specimens typically have dimensions of 13 x 7.5 cm and thicknesses of 3 mm. The Fresnel test machine is equipped with a single or dual axis sun-tracking device to keep the target area in focus throughout the day. The sun is continuously tracked by the machine in both azimuth and elevation directions. The machine rotates about horizontal and vertical axes. With this device the amount of the UV component of the available solar radiation can be increased up to 500% and that of the visible and longer wavelength components by at least 800%. This method of exposure is considered more realistic because it uses the natural solar radiation as a source.

The Fresnel concentrator is predominantly used in a desert environment. There are numerous commercial Fresnel-reflecting solar concentration devices such as EMMA (Equatorial Mount with Mirrors for Acceleration) and EMMAQUA (Equatorial Mount with Mirrors for Acceleration with Water). At present EMMAQUA (Figure 3.24 - left) is the most widely used outdoor accelerated weathering test method in the world (AWSG 2003).

Figure 3.24: EMMAQUA and ACUVEX Fresnel concentrator weathering devices

Other similar test devices are Q-Trac (Q-Lab 2002), ACUVEX (AZTEST 2002) (Figure 3.24 - right) and Super-Maq (Jacques 2000). Super-Maq is the largest sun-tracking Fresnel-reflecting solar concentrator in the world. It utilizes the same design as EMMAQUA but is four times larger. Each mirror and the target board measure approximately 61 cm x 6 m. Super-Maq is used for testing complete components, especially in the automotive industry.

Rack exposure is another method of weathering when simple exposure

conditions are needed. With this method a large number of specimens can be exposed simultaneously for a certain period of time in the same orientation. The exposure angle greatly affects the test results as it is closely related to the amount of radiant energy received on the specimen surface. Typical angles of orientation are 90°, 45° and 5° south (for Northern hemisphere) and at latitude and horizontal angles (Jacques 2000). Racks can utilize glass covers or a water spraying system. In addition, greater levels of radiant exposure can be achieved if the rack continuously tracks the sun throughout the day.

From all weather factors, solar radiation, particularly the UV component, is predominantly responsible for the photochemical degradation of materials exposed to natural weathering conditions. Therefore, the nature of the radiation source is the most important component in simulated laboratory conditions. The light sources that are predominantly used in laboratory accelerated testing are xenon arc, carbon arc and fluorescent lamps. Metal halide and mercury lamps are less commonly used. In order for laboratory weathering test to simulate accurately the real-time exposure, it is of paramount importance that the output spectrum of the light source closely simulates the spectral power distribution of solar radiation over the whole range of active wavelengths. From all artificial sources of light, the xenon arc lamp provides the closest match to the solar spectrum when specific filters are used. However, it contains some intense spectral lines in the IR which may lead to excessive heating during accelerated testing. It also extends deeper into the UV portion than the sun does. The output of a xenon arc lamp, compared to the solar radiation spectrum, is shown in Figure 3.25.

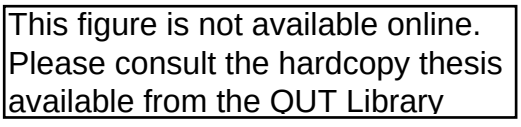

Figure 3.25: Xenon arc lamp output vs. solar radiation spectrum (Crase and Scott 2002)

The advantage of the UV fluorescent lamps is that they achieve greater acceleration at a lower cost. However, since they simulate solar radiation predominantly at the short wavelength end of the UV spectrum, with this method the chance of obtaining erroneous results is increased (Jacques 2000). In general, the presence of wavelengths shorter than 300 nm can lead to accelerated degradation, but it can also result in unrealistic alteration of the mechanism and type of degradation. This is the major reason the use of such an artificial light source cannot be relied upon to predict the service life of materials exposed to terrestrial solar radiation.

It has been reported that a substantial increase of the irradiance level in laboratory conditions has not only led to significant acceleration of the photodegradation but to unnatural chemical degradation as well. It has also been shown that the increase of the irradiance level accelerated the degradation of some of the exposed materials but not all. Furthermore, it has been observed that in most cases the acceleration rate is not proportional to the increase of the irradiance level e.g. doubling the intensity does not necessarily double the rate of degradation (Crewdson 1992; Crewdson and Scott 1994). This can be explained by the so-called "cage effect" in a free radical process. The high concentration of free radicals formed as a result of high irradiance levels leads to recombination of the excess radicals so that the efficiency of the high irradiance exposure is reduced. However, in a similar study with various polymers it has been shown that when intensifying the irradiance by up to a factor of three, there is a good proportionality between the material property changes and the amount of radiant energy (Boxhammer 2001).

3.5.2 Heating

Because of the surface absorption of solar light in polymers, i.e. the surface of polymers can be heated to high temperatures without affecting the bulk, it has been suggested that applications in the areas of polymers should be researched (Clemens 1990). The heating caused by absorbed radiation or direct heat exchange is another critical weathering variable that can lead to material thermo-oxidative degradation and acceleration of other weathering reactions. Temperature rise is a main accelerating technique in many weathering test methods. During weathering the temperature of the exposed specimen could become much higher than the ambient temperature.

Typically solar radiation, mainly in the visible spectral range, has a penetration

depth of 20-50 nm in most metals and other opaque materials (Clemens 1990). In thermoplastic polymers the thin surface layer (usually less than 0.2 mm) becomes most damaged during the ageing process, while the bulk of the material remains virtually unchanged. Since weathering is essentially a surface effect, the specimen surface temperature has a greater impact on the weathering process than the ambient temperature. The surface temperature depends on the radiation characteristics of the material such as absorptance, transmittance and reflectance, along with the material interaction (by conduction, convection and emittance) with solar radiation. The available solar radiation (ISO4892 1994) typically comprises:

- 37.8% non-visible light (or IR) (> 800 nm wavelength) which contributes to heating but does not cause photochemical reactions in polymers;
- 55.4% visible light (400-800 nm wavelength) which also contributes to heating but can initiate photochemical reactions; and
- 6.8% UV radiation (<400 nm wavelength) that does not cause heating but initiates photochemical reactions which lead to polymer degradation.

The availability of each of these components could have a profound contribution to the surface temperature change of the exposed material. Since any material would have specific absorptive, emissive and conductive properties, the final effect on the material heating would be a result of the radiation-material interaction. If radiation transmittance through the material is considered negligible, the absorbed radiation that could cause its heating has been defined by the following equation as a first approximation (Kockott 1996):

$$E_{abs} = \int k_{\lambda}\alpha(\lambda)d\lambda \qquad (3.4)$$

where $\alpha(\lambda)$ is the absorptance and k_{λ} is the thermal conductivity of the material.

During degradation, when an electron is exited, certain molecules undergo bond-dissociation and break into free radicals. The relationship between the released bond-dissociation energy and wavelength of light can be calculated using the following formula:

$$\lambda = \frac{hC}{E} \qquad (3.5)$$

where λ is the wavelength of light, h is Plank's constant, c is the speed of light, and E is the bond-dissociation energy (Summers and Rabinovitch 1999).

Generally, the primary photochemical processes in a material are caused by the

absorbed UV portion of the solar spectrum. Since almost all secondary decomposition processes that occur as a result of primary photochemical change in organic materials are temperature dependent, the speed of the decomposition reaction increases with temperature rise (Boxhammer 1999). As a rule of thumb, the reaction rates double for every 10°C increase in temperature. In many cases this relationship is not linear but material dependent. Initially, there is very little change in material properties, but when a material-specific critical temperature is reached, the reaction rates begin to increase rapidly. In the case of amorphous and semi-crystalline polymers, if the temperature during exposure is approaching the glass-transition temperature, even small differences in temperature can lead to large differences in the weathering results. Discoloration and rapid decrease in the impact resistance of ABS after reaching the glass-transition temperature have been reported (Tiganis et al. 2002). In most polymers, ageing at temperatures below the glass-transition temperature causes physical changes, whereas at temperatures greater than the glass-transition temperature thermo-oxidative degradation predominantly occurs.

The surface temperature measurements are typically taken with T-type thermocouples fixed on black or white panels. Black panel temperature is used to estimate the maximum attainable temperature by an exposed test specimen. White panel temperature is used in addition to the black panel temperature to estimate the temperature of a light colored test specimen.

The most widely used black panel sensor consists of a black coated steel plate and a thermocouple fixed either to the front or back of the panel. There are, however, some limitations to both designs. Depending on the position of the thermocouple, different temperature readings may be obtained. If the thermocouple is mounted at the back of the panel, it does not accurately measure the specimen surface temperature. On the other hand, the temperature measured by the front-mounted thermocouple is affected by the epoxy used for attachment and the radiation heat exchange directly with source.

Different degradation results have been reported when identical black panel temperatures and identical exposure conditions have been maintained by different types of weathering machines. Even when the same equipment has been used, different temperatures have been attained by different types of black panel sensors (Boxhammer et al. 1993). In order to improve the temperature measurement process and obtain more consistent results, a black standard thermometer has been

developed. It is mounted on a thermally insulating plastic material and is used to determine the maximum temperature of a 5 mm thick opaque black polymer. It typically produces higher temperature measurements compared to the black panel sensor. It should be noted, however, that the black panel sensors give only an indication of the material surface temperature and the most accurate results can be obtained by measuring the actual temperature of the specimen itself. Typical black standard and black panel sensors are shown in Figure 3.26.

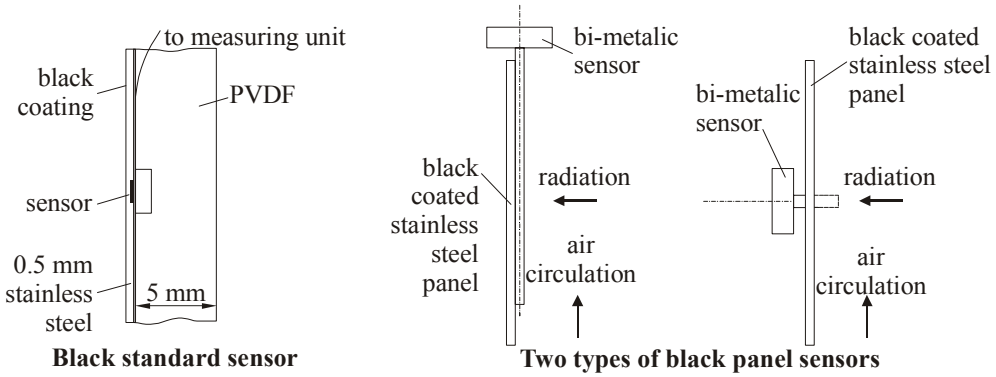

Figure 3.26: Schematic diagrams of black standard sensor (left) and two types of black panel sensors (right) (adapted from Boxhammer et al. 1993)

It has been observed that the surface temperature is greatly affected by the light source of the weathering machine and the light intensity (Fisher 1998). It has been suggested that since differently colored materials attain different surface temperatures, the test data obtained indoors could be unrealistic compared to the outdoor measurement if unsuitable light sources and intensities are used. While the indoor weathering tests have the advantage of precise control and repeatability, they can never accurately duplicate outdoor exposure conditions and therefore can only be used to complement natural exposure tests.

3.5.3 Advanced ultra-accelerated ageing

There is sometimes a need to predict the service lifetime of certain materials (especially those used in insolation concentration) by exposing them to ultra-accelerated natural sunlight and comparing the results with those obtained during normal use conditions. It was reported that a high flux solar furnace (at the National Renewable Energy Laboratory in USA) was used to obtain between 25 and 100 suns concentration for accelerated testing of materials (Jorgensen et al. 1999; Jorgensen et al. 2000). Three different types of commercial 3M materials with PMMA film as base resin and with different UV absorber present in it were explored. A series of experiments were performed using three levels of concentration - 50, 75 and 100

suns at controlled levels of temperature and humidity.

The first experiment used 50 suns concentration at which level one year's equivalent exposure in Colorado would be obtained in 40.2 hours. Accordingly, at a concentration of 75 suns, one year's equivalent exposure would be achieved after 26.8 hours, and at 100 suns – after 20.1 hours. The targeted maximum temperature during the experiments was 70°C. The analysis of the results after the exposure supported the claim that ultra-accelerated natural sunlight exposure of the tested materials did not change failure modes and degradation mechanisms. The research indicated that with this device the degradation caused by one year exposure could be achieved in one to three days with an ultra-accelerated exposure test, using concentrated sunlight at an intensity of 50 to 100 times that of natural sunlight.

3.5.4 Related work

A significant amount of research work has been carried out for years to study the degradation of polymers, particularly PMMA. It is believed that PMMA degrades by end chain scission and gives a very high yield of monomer (Wilkie 1999). It has been demonstrated that the degradation begins at the end chain groups and is by random scission (Kashiwagi et al. 1986).

Caykara and Guven investigated the degradation effect of UV radiation (259 nm) on PMMA and observed changes in mechanical properties, as well as chain and ester side-group breaking (Caykara and Guven 1999). Colom et al. studied the ageing process of PMMA using a xenon arc lamp by irradiating the samples for up to 1570 hours equivalent to 750 days of solar radiation exposure (Colom et al. 2001). The test results indicated the presence of chain breaking or methyl group scission and the lack of groups related to oxidation phenomena. It was also found that with every 1000 hours of artificial ageing the glass transition temperature decreased with approximately 2°C.

The mechanism of thermal degradation of PMMA has been studied by many researchers. It is well recognized that the degradation process represents a radical chain reaction involving initiation, depropagation, transfer and termination reactions (Zhang and Blum 2001). Oxygen presence causes both crosslinking and chain scission. Thermal decomposition of PMMA in the absence of oxygen occurs by radical depolymerazation above temperatures 220-230°C. Below this temperature polymerization is predominant (Baeyens et al. 2002). PMMA is typically degraded

in three steps due to three different initiation mechanisms of degradation, as shown in Figure 3.27. The process of degradation begins at a temperature around 180°C with breaking the weakest head-to-head (H-H) bonds, followed by the unsaturated end group (Nising et al. 2003).

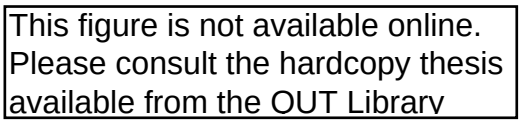

Figure 3.27: Thermal degradation steps for PMMA (Nising et al. 2003)

However, as noted by Kashiwagi et al., there is an additional weight loss during thermal degradation already at about 150°C which is considered to be caused by chain scission of the H-H bonds (Kashiwagi et al. 1986). The majority of the bonds are the head-to-tail bonds which break in the random chain scission at around 350°C (Nising et al. 2003).

Torikai and Hasegawa studied the wavelength sensitivity in photodegradation of PMMA by monochromatic radiation and found that the threshold wavelength of the main chain scission was below 320 nm (Torikai and Hasegawa 1998). Their experiments with adding β-carotene to PMMA resulted in shifting the threshold to around 400 nm which shows that accelerated photodegradation of PMMA can occur under terrestrial sunlight. It was reported that at 254 nm PMMA undergoes extensive random chain scissions which leads to formation of low molecular weight.

At wavelengths higher than 300 nm, the photooxidation of PMMA was found to require very long irradiation times with limited formation of hydroxyl groups and new carbonyl absorptions (Chiantore et al. 2000). Other researchers reported that the carbonyl group absorbs at 215 nm, leading to chain scission and consequent degradation (Lin and Lee 1992). It was found that pure PMMA photodegrades to monomer in high yield at temperatures higher than 130°C at 254 nm (Cowley and Melville 1952).

Generally, PMMA is not susceptible to photodegradation since it has the lowest sensitivity to UV radiation of any plastic. However, PMMA has poor hydrolysis resistance hence it could be easily damaged by moisture. It was reported that after

10 years of outdoor exposure of PMMA in the UK only 4% loss of transmissivity had been observed (ICI 2003). Over a similar period in tropical conditions only slight discoloration was detected. Another study performed with various plastics including PMMA found that after five years of natural weathering PMMA and acrylic paint changed little in color, but more than rigid PVC (Summers and Rabinovitch 1999). The stability of PMMA was also confirmed by an extensive study of six commonly used polymers exposed to both natural and artificial weathering. By measuring the basic physical-mechanical properties of the polymers after exposure it has been proven that PMMA is clearly the superior polymer, as it has been well recognized in industry (Wypych 2003:204).

A study on photodegradation of colored polyethylene (PE) films under UV light found that the yellow pigment promoted the process of photooxidation, whereas a delay in ageing was observed with the green, orange and blue colored films (Mlinac et al. 1976). A comparative study of photoxidation of two polypropylene (PP) films with high and low crystallinity under natural and accelerated conditions was reported. Under accelerated conditions the rate of photooxidation of high and low PP were different, while under natural conditions the formation of functional groups did not differ for high and low PP. Also, the mechanical properties of the high PP failed after 10 days of natural exposure, whereas the low PP retained its physical properties for 21 days (Tidjani 1997).

Observations on correlation between results of natural and artificial tests were presented by Jakubowicz. In his study, accelerated exposure tests of several commercial PVC materials were performed in a Weather-O-Meter accelerated weathering instrument equipped with a xenon arc as a light source, for periods corresponding to up to 12 years of natural exposure. The author claimed that after comparison with the samples exposed on racks under natural conditions, there was no correlation between the results of natural and artificial tests. For example, the impact strength of the materials exposed to natural weather did not change after 12 years of natural ageing, whereas in the artificial ageing the impact strength decreased by 25% after a period equivalent to up to 10 years (Jakubowicz 2001). Studies of ageing PE and PP for a period of 20 years also showed no correlation between artificial exposure and natural weathering (Gugumus 1995).

The poor correlation between the degradation effects in natural and artificial weathering exposure could be contributed to the fact that each material absorbs and

utilizes only a specific portion of the available solar radiation. When artificial sources are used however, the total available radiation and in particular the UV portion may differ considerably from the available solar radiation.

3.6 Conclusions

In general, no similar solar concentrator system used as electromagnetic radiation source for polymer processing has been found.

From the literature review of polymer processing technologies it has been found that electromagnetic radiation is used in both processes of heat generation and accelerated ageing. Many conventional and modern plastics joining technologies either use directly or are based on effects using different types of artificial non-ionizing electromagnetic radiation. However, no other applications of solar radiation for polymer heating or curing have been found, except for polymer ageing, however using Fresnel concentrator. The degradation of polymers and in particular, PMMA, in artificial laboratory conditions has been investigated extensively for many years. On the other hand, the ageing of PMMA exposed to natural outdoor environment and particularly concentrated solar radiation, has not been a widely studied area.

It has also been evident from the reviewed publications, that although advanced techniques such as TTIR and ClearWeld have been recently developed, they still require additional energy absorbing material. The use of special dyes and pigments to facilitate the welding process may present a health risk especially in the food and medical industries. Therefore, there is a need in the field for another method which does not require any additional substance.

Another finding from the review of the literature has shown that a relatively new advanced curing technique utilizing UV and visible light appears to be very promising. It has been the intention of this research to explore the capabilities of the developed SEC facility in the area of curing light sensitive polymers and adhesives with concentrated solar radiation. Based on the preliminary investigation on adhesive curing utilizing concentrated insolation it can be concluded that by carefully chosen light-curing adhesives solar radiation can be a useful radiation source for adhesive curing.

Therefore, experimental studies on heating/welding, curing and ageing of clear and colored, similar and dissimilar polymers could be beneficial for both solar radiation utilization and polymer processing research.

CHAPTER 4.
EXPERIMENTAL EQUIPMENT

4.1 Introduction

As it has been shown in the previous chapters, the use of various types of Cassegrainian systems for different applications has been reported by many researchers in the literature. However, no similar configuration utilizing solar radiation for the applications studied in this research has been found. Therefore, in order to explore the feasibility of the research concept, experimental test rig with the necessary equipment has been set up and preliminary experimental studies on polymer joining have been conducted.

A considerable part of the experimental equipment used, particularly the SEC facility, has been especially designed for the experimental studies of this research. Since many of the SEC systems and their components have been developed, modified and optimized during the course of the research, they are discussed in Chapter 7. Details of the experimental procedures and some auxiliary instrumentation are discussed in Chapters 8 and 9.

This chapter describes the experimental apparatus, instrumentation and materials used in most of the experimental work performed in this research. It begins with a description of the experimental apparatus, used without or with insignificant changes only, and considered an integral part of the experimental equipment at various stages of the research. In particular the modified Cassegrainian type concentrator itself, its support stand and driving motors have not been modified for the duration of the different experimental applications. However, a description of the initial temporary optical arrangement, proposed by the telescope provider instead of transmission via optical fibers, is included in this chapter, although it has been modified and other means of beam transmission have been explored. They are described in Chapter 7.

A brief discussion of the instrumentation used for measuring, monitoring, recording and analysis of the experimental data follows. This chapter concludes with a description of the materials and test specimens used in each experiment.

4.2 Experimental apparatus

4.2.1 Modified Cassegrainian solar concentrator

The solar energy concentrator facility providing the electromagnetic radiation in this research uses a modified two-mirror Cassegrainian configuration supported in an altitude-azimuth mounting. A schematic layout of the original version is shown in Figure 4.1.

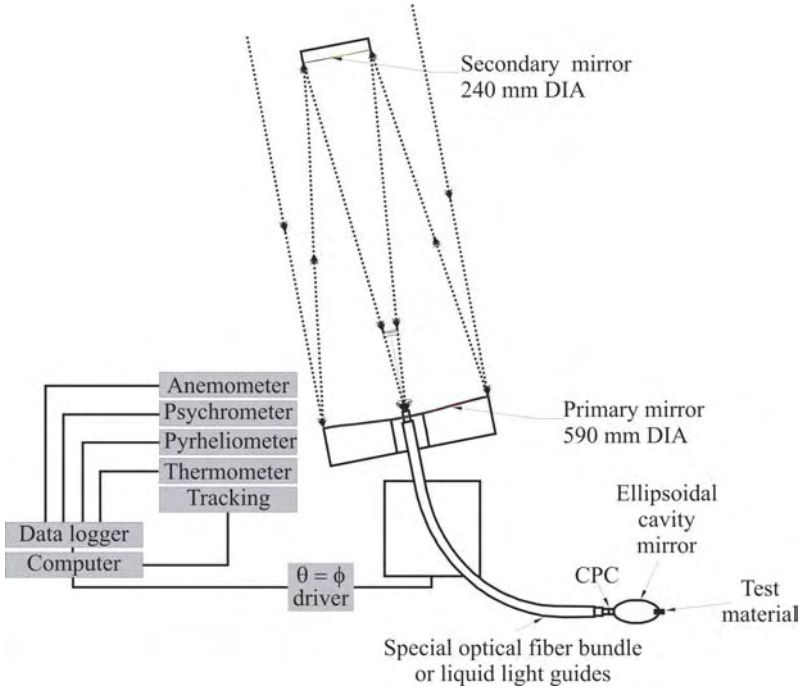

Figure 4.1: Originally proposed system with data acquisition

The initial modified Cassegrainian arrangement has been designed with the intention to employ flexible fiber optic transmission of the concentrated beam of solar radiation. As a consequence, the primary mirror has been constructed with a comparatively large ratio of focal length to aperture diameter, or big F/number, to allow relatively narrow primary rim and reflectance angles. Also, if the focal length of the mirror is large enough compared to its diameter, it is believed that the spherical aberration of such a spherical mirror becomes negligible, thus a spherical mirror could be used instead of paraboloidal.

The primary reflector of the experimental SEC facility is a telescope mirror. The secondary mirror has also been designed to allow quite a narrow re-radiation acceptance angle and with a rather large diameter. The actual technical specifications of both mirrors, as provided by the supplier, are summarized in Table 4.1.

Table 4.1: Technical specifications of the mirrors

Specifications	Primary mirror	Secondary mirror
Radius of curvature	– 4267 mm	– 7433 mm
Overall mirror diameter	600 mm (actual effective aperture 590 mm)	240 mm
Front mirror surface	EPN coated aluminium E5082	Enhanced aluminium coating on E3 glass substrate
Spherical profile accurate to:	±1 wavelength at 546.1 nm in the range of 15–50°C	±1 wavelength at 546.1 nm in the range of 15–50°C
Energy obstruction fraction		0.16
Mirror construction/ mounting	Double sided mirror with special inter-surface structure for minimizing heating effects. Mirror sealed in housing with weatherproof epoxy resin	Glass mounted on flat aluminium base plate attached to secondary mirror supports
Reflection coefficient in (400 – 1200) nm wavelength range	greater than 0.8	greater than 0.8

Some construction details of the mirrors and their supports can be seen in the photographs in Figure 4.2.

Figure 4.2: Primary and secondary mirrors

The solar image diameter at the principle Cassegrainian focus is 25 mm, allowing for aberrations in the mirror system to have negligible effect on the solar image. An overall view of the initial arrangement of the SEC facility is shown in Figure 4.3. The location and protective shed are shown in Appendix 4.

Figure 4.3: Initial arrangement of the solar concentrator

4.2.2 Light transmission

In the initial system design, because of the unavailability of suitable fibers at the time, the fiber guide has been replaced by the provider with common optical components. The original schematic opto-mechanical layout is shown in Figure 4.4.

The magnifying unit is actually an adjustable air-spaced doublet (similar to a Barlow lens) used to adjust the focal length in a telescope. When used for focusing a laser beam, such configuration, regarded as a Galilean type beam expander, typically consists of a negative diverging lens followed by a positive collimating lens which are normally positioned with their points coincident. By placing a combination of these two lenses in the converging light cone re-emitted by a spherical mirror at a distance in front of its focal plane, the spherical aberration of this mirror can be corrected without introducing additional chromatic aberration.

In the case of the SEC, both lenses are mounted in a barrel allowing correction of the separation between them. This ensures that the solar image formed by the secondary mirror is focused onto the next lens of the optical path of the beam transmission (see Chapter 7). Canister and periscopic optical systems of lenses, mirrors, auxiliary and de-magnifying optics and mechanics have been used to project the telescope image reducing further the image diameter (see Figure 4.4).

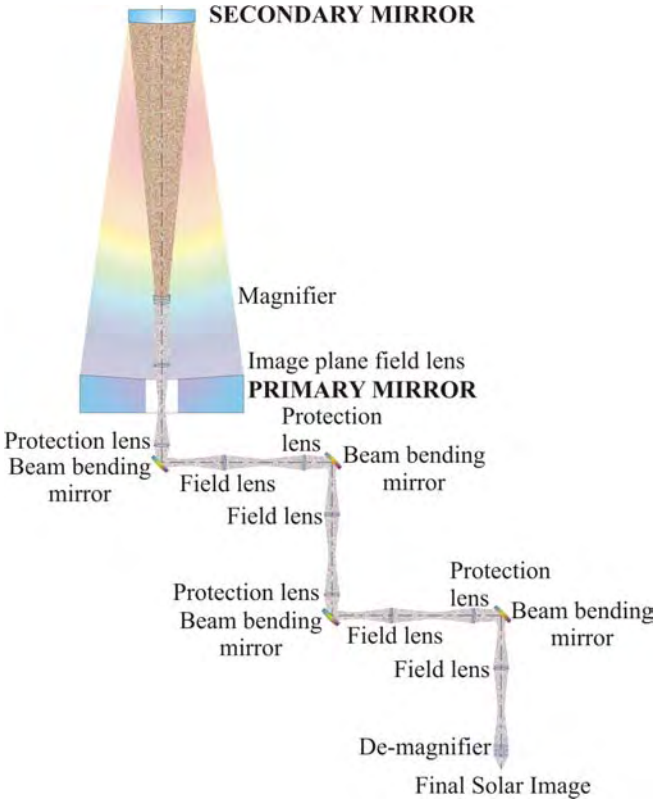

Figure 4.4: Initial schematic opto-mechanical layout of the SEC

The originally proposed optional “hot mirror” and image magnifying unit placed ahead of the periscopic system and auxiliary re-imaging optics have also been explored in the initial version of the SEC system. The “hot mirror” has been used to selectively transmit predominantly visible radiation and reflect infrared radiation. In order to avoid achromatic aberration, all lenses used were achromatic doublets.

4.2.3 Spot monitoring system and motor control

In the original feasibility version of the SEC facility the acquisition of the solar image has been achieved either by line-of-sight or by observation of the secondary mirror filled with light. This initial sun-tracking technique has been used predominantly for the preliminary experimental testing of the SEC facility capabilities. Although considered practicable for the feasibility study, in this indirect controlling technique the sun-tracking and telescope pointing were achieved manually via joystick control and were dependent on the operator skills (Figure 4.3).

The drive system that moves the telescope to track the sun consists of two Baldor DC motors, a switching relay system and a low voltage supply to activate the relays via joystick control. The telescope is powered by single phase 240 volts. The motors which are of low power, maximum 96 watts, drive the telescope axes through worm/wormwheel reduction gearboxes. The gearboxes which are BTS 1:50, 1:5 and 1:2.5 are connected to the telescope axes via timing belts. The relays used for activating the motors are of standard low voltage type and are energized by a 12 volt DC supply via the joystick control, as shown in Figures 4.5 and 4.6.

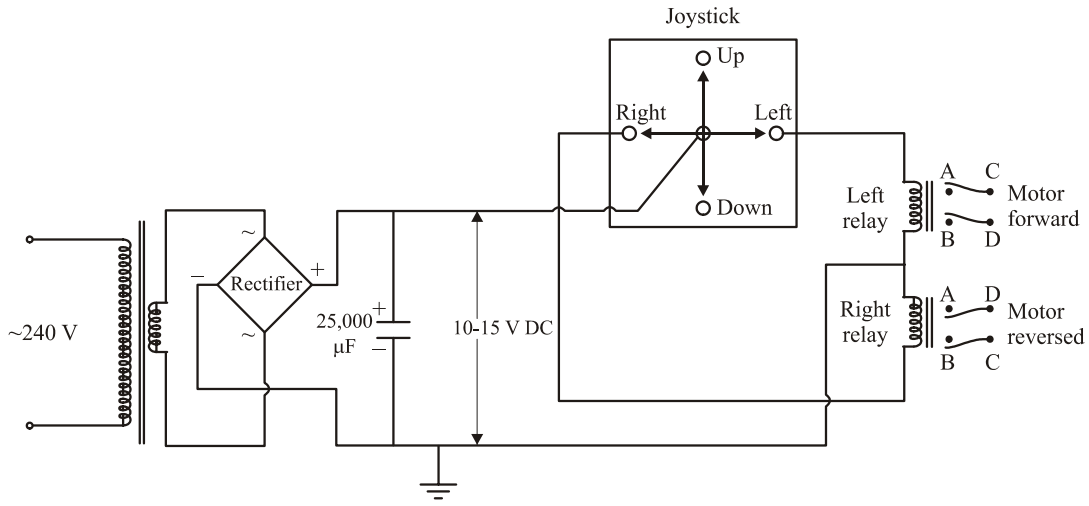

Figure 4.5: Joystick power supply

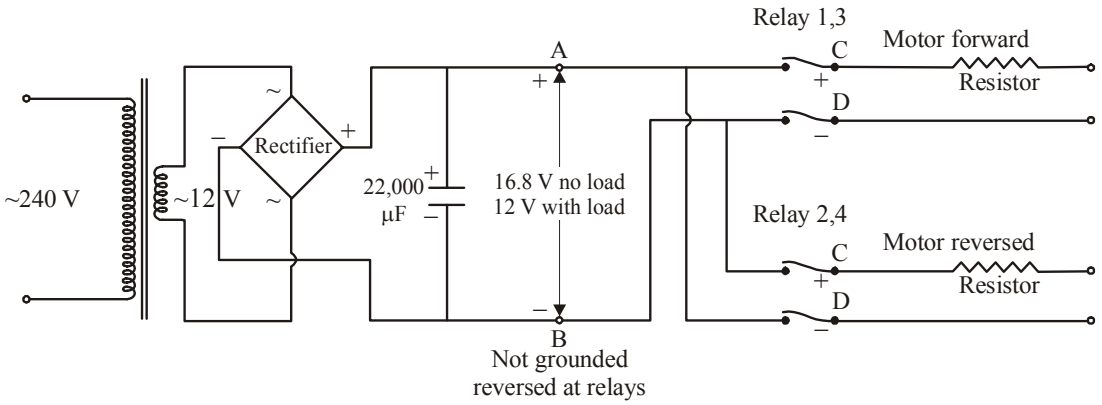

Figure 4.6: DC motor power supply

The telescope is moved in altitude and azimuth using motors and gearboxes activated by joystick control. In the original version the axis speed was 45 degrees per minute for both axes. Details about the altitude-azimuth mounting including axes, bearing assemblies, counterweights, gear boxes, and variable speed motor drives are provided in the Manual for Solar Telescope (Waterworth 1999).

On a later stage, the sun-tracking process has been improved by a specially designed photoelectric sensor and sun-tracking device. Also, an additional lower speed mode has been introduced in order to enhance the telescope movement process. These further developments are discussed in Chapter 7.

4.3 Instrumentation

4.3.1 Pyranometer

In the initial experiments of this study, the intensity of the available solar radiation was measured with an Eppley precision spectral pyranometer - EP16 with a spectral range of 0.300-3.0 μm. Subsequently, for measuring the intensity of beam insolation incident on the primary mirror surface, a pyranometer type Kipp & Zonen CM6 (Figure 4.7a) with a spectral range of 0.305-2.8 μm was used by employing two different techniques. In the first one, an additional collimating tube and integrator were used to filter out the scattered diffuse radiation and to allow only the direct beam radiation to enter the aperture of the sensor. In the second technique, both total and diffuse radiation were measured with the aid of the pyranometer. Measurements of the diffuse radiation were made by shading the sensor of the instrument from the beam radiation. The amount of the direct solar radiation was determined by subtracting the diffuse solar radiation from the total solar radiation.

4.3.2 Pyrheliometer

In subsequent experiments the intensity of the direct beam solar radiation at normal incidence was measured with a Kipp & Zonen CH 1 type normal incidence pyrheliometer (Figure 4.7b). It is an ISO first class pyrheliometer designed to measure the irradiance from the solar disk in a solid angle of 5° with sensitivity 9.83 $\mu m/Wm^{-2}$ in the spectral range 200-4000 nm. A suitable clamping fixture was designed to maintain the aperture plane of the pyrheliometer parallel to the primary mirror plane (pyrheliometer axis parallel to the telescope axis).

To allow continuous collecting of the necessary data and integrating of the measured values, radiation indicator/integrator CC20 (Figure 4.7c) connected to a computer via the standard RS-232 serial port was used.

(a) (b) (c)

Figure 4.7: (a) Pyranometer Kipp & Zonen CM 6, (b) Pyrheliometer Kipp & Zonen CH 1 and (c) Radiation indicator/integrator CC20

The instant value of the measured intensity of direct solar radiation was displayed on the computer screen and the integrated amount of incident solar energy was recorded in a comma separated format for subsequent analysis in a spreadsheet program.

4.3.3 IL1400A Radiometer/Photometer

A portable IL1400A radiometer/photometer was used to evaluate the amount of the intercepted and reflected solar energy with regards to the different UV wavelength ranges. An example of the actual measurement of the intensity of UV at the primary mirror plane is shown in Figure 4.8.

Figure 4.8: IL1400A radiometer

An UVA hazard detector SEL 033/UVA/W was used to measure the amount of UVA radiation in the spectral range of 315 to 390 nm. The amount of UVB radiation in the spectral range of 185 to 310 nm was measured with the aid of an UVB hazard detector SEL 240/TD. Alternatively, an UVR hazard detector SED (SEL) 005/WBS320/TD was used to measure the amount of UVR in the spectral range of 250 to 400 nm. The instrument had been recently calibrated and the calibration coefficients were used in the analysis of the measurement results.

4.3.4 SD2000 Miniature Fiber Optic Spectrometer

Because in this work only direct solar radiation has been utilized, a SD2000 Miniature Fiber Optic Spectrometer was used to measure the solar spectral irradiance available on the aperture of the primary mirror. Also, it was used to measure the spectral distribution of the insolation re-radiated from the secondary mirror.

The SD2000 Dual Channel Miniature Fiber Optic Spectrometer (Figure 4.9a), manufactured by Ocean Optics Inc., is a UV-VIS-Shortwave NIR spectrometer with quartz glass fibers and silicon detector (SONY) coated with UV absorbing material. It has two gratings, '02' for the master (250-800 nm) and '14' for the slave (650-1100 nm) channels. The instrument was used with OOIBase32 operational software for all data acquisition and control, providing real-time interface to the signal processing function. A notebook computer was used to show the real-time spectrum on the screen and store the received data.

4.3.5 Spectrophotometer

To study the solar radiation absorption in clear and colored polymers, transmittance and reflectance measurements of most of the materials used were performed. These measurements were carried out with UV-VIS-NIR Cary 100 (Figure 4.9b) and Cary 5000 spectrophotometers mostly in the range of 200-900 nm.

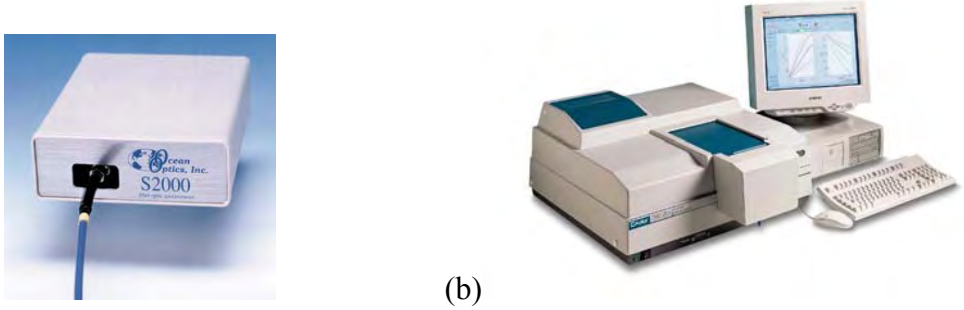

(a) (b)

Figure 4.9: (a) Miniature fiber optic spectrometer and (b) Cary 100 UV/VIS spectrophotometer

Cary 100 and Cary 5000 are double beam, dual chopper spectrophotometers controlled by a computer running WinUV software. Cary 100 was used with a diffuse reflectance accessory (DRA) with a 73 mm diameter integrating sphere. Cary 5000 is a high performance instrument with an internal DRA 2500 (PbS detector for up to 2500 nm). In addition, in order to evaluate the absorptance of the different dyes used, the transmittance through chloroform solutions of the colored and clear materials was measured using a UV-VIS Cary 50 spectrophotometer.

4.3.6 Attenuated Total Reflectance Fourier Transform Infrared (ATR/FTIR) Spectrometry

FTIR spectroscopy is a widely used technique for studying the spatial distribution of polymer photooxidation products, mainly because of its capability to identify alcohols, carbonyls and hydroperoxides. The method is based on the interference of radiation between two beams to generate a signal as a function of the change of pathlength between the two beams. FTIR spectrometers record the interaction of IR radiation with the sample, measuring the frequencies and the intensities at which the sample absorbs the radiation (Griffiths and de Hasseth 1986).

Thermogravimetric analysis coupled to Fourier transform infrared spectroscopy (TGA/FTIR) has been reported as an extremely useful technique for studying polymer degradation, especially for PMMA (Wilkie 1999). In the past, traditionally ATR has not been applied for analysis of plastics because of the difficulty in achieving satisfactory surface contact with the ATR element. However, with the introduction of a single reflection diamond that can withstand a much larger force from plastics, now ATR can be used to accurately analyze polymer materials.

In this work the ATR-FTIR spectra of the polymer specimens aged by accelerated natural exposure to concentrated sunlight were captured using Thermo Nicolet Nexus spectrometer and Continuμm IR microscope (Figure 4.10).

Figure 4.10: FTIR spectrometer Thermo Nicolet Nexus

4.3.7 Differential Scanning Calorimetry

Differential Scanning Calorimetry (DSC) is a technique in which the heat flow difference into a substance and a reference material is measured as a function of temperature while the substance and inert reference material are subjected to a controlled-temperature program (ASTM-E473 2000). The specimen and reference material are subjected to identical temperature regimes in an environment heated or cooled at a controlled rate, while measuring the energy necessary to establish a nearly zero temperature difference between both materials. DSC is typically used to determine melting point and glass transition temperatures of polymers.

The data for the different types of engineering thermoplastics used in the experimental studies in this research were collected with TA Q10 and TA Q100 differential scanning calorimeters with Advanced Tzero^{TM} technology (Figure 4.11).

Figure 4.11: Differential scanning calorimeters TA Q10 (left) and TA Q100 (right)

4.3.8 Air Compressor

A two horse-power air compressor was used for cooling the specimens during the experimental studies. The other components of the provisional cooling system designed and used for the purposes of the different experiments are discussed in Chapter 7.

4.3.9 Data logger

Although most polymers show high emissivity and it is possible to measure their surface temperature with infra-red thermometers quite accurately, they may be partially transparent in the specific wavelengths. This may cause errors, especially near the glass transition temperature range, when the polymer state changes. Furthermore, in butt and especially lap joining of two different polymers having different emissivity this will cause an additional error. For these reasons, in order to avoid such errors, in the initial temperature measurements a thermocouple (used as a

black panel thermometer) was calibrated with an IR thermometer. The non-contact pyrometer used was a modified IR pyrometer type Land Micra Therm 3. In order to continuously monitor and study the variation of working and ambient temperatures in-process sensors such as K and T type thermocouples were installed in appropriate areas. Data Taker 500 series datalogger (Figure 4.12) was used for data acquisition.

Figure 4.12: Data Taker 500 data logger

The ambient temperature sensor was located away from radiation or heat sources in a surrounding air temperature (Stevenson) screen. In the joining experiments one thermocouple was embedded in the joint interface between the two specimens, and another thermocouple was placed on the exposed specimen surface. In the case of lap joining, especially when two transparent specimens were used, an additional thermocouple was positioned on the back side of the specimen. For some particular cases, to avoid charring in the heat affected zone which can significantly influence the temperature readings, air spacing, insulating film and additional coloring of the thermocouple were used. For the ageing experiments, assuming that nearly all photochemical processes are influenced by the surface temperature of the specimen, one thermocouple was positioned on the surface of the specimen being tested.

The data logger was set up to take measurements simultaneously in one-second intervals from all channels used. In order to continuously record the data collected, the data logger was connected to an IBM compatible computer via a communication cable and with the aid of DeLogger Plus software. It is a Windows-based software that allows programming and supervising the Data Taker to display real-time and logged data, store incoming data for future replaying or for a wide range of reporting, and perform real-time data calculations. The real-time data was displayed on the computer screen as it was acquired and simultaneously stored on the computer hard disk. The data taken was selectively formatted by the Data Taker in comma-separated mode and later imported into a spreadsheet program for subsequent analysis and graphic presentation.

4.3.10 Computers

Two computers with the following specifications were used during the experimental work for the acquisition, monitoring, integrating and recording of data:

- IBM work station, Intel Pentium processor 133 MHz, 16 MB RAM, hard disk 10 MB, operating system Windows 95; and
- Toshiba Satellite Pro 4300 Notebook, Intel Pentium 3 processor, 256 MB RAM, hard disk 20 MB, operating system Windows 2000.

4.3.11 Optical microscopy

Optical microscopy was used for the visual examination of the joined specimens and the surface of the aged specimens. An Olympus MJ optical microscope with magnification of up to 100x was used for the examination of selected specimens.

4.3.12 Scanning electron microscopy

The scanning electron microscope (SEM) is a valuable tool in the examination of the composition microstructure and properties of materials (Goldstein et al. 2002). In this research conventional scanning electron microscopy techniques were employed in order to study the microstructure of the ruptured specimens. The model of scanning electron microscope used was JXA-840A (Figure 4.13).

Figure 4.13: JXA-840A scanning electron microscope

In order to obtain a good image, the sample surface must be electrically and thermally conductive and to improve conductivity, the sample is usually coated with carbon or metal. Since polymers are poor conductors, for studying the microstructure of the welded specimens, in this research some specimens were coated with carbon and others with gold.

4.3.13 Tensile testing

Tensile test is the most common method used to analyze plastic welds. The tensile strength achieved is greatly dependent on the type of plastic and welding

procedure used. Before performing each joining or ageing experiment, in order to evaluate the tensile strength of the parent materials, specimens from all polymer types and colors were tested. All transparent specimens were inspected in a polariscope before testing and those that showed residual concentrated strain patterns were rejected.

After completion of each experiment, a selected number of joined or exposed specimens were also subjected to tensile testing. The achieved bonding strengths were calculated by dividing the tensile loads at fracture by the original cross area. An example of a test specimen used in tensile testing is shown in Figure 4.14. In some of the tests the reduced cross sectional area of the test specimens was made equal to the cross section of the specimens used for joining.

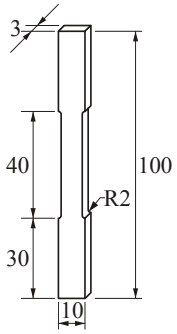

Figure 4.14: Tensile specimen used for stress analysis

The tests were performed using a Hounsfield testing machine H10KM. In general, the standard procedures of the (AS1145.1 2001) for determination of tensile properties of plastics were followed. During testing the sample is mounted by its ends into the grips of the testing machine and is elongated at a constant rate which can be set in the range of 0.005 – 1,000 mm per minute. The speed used for most of the experiments in this research was 5 mm per minute which is recommended for rigid materials in (AS1145.1 2001). An overall view of the tensile testing machine and a close view of one of the grip fixtures holding joined specimens being tested are shown on the photographs in Figure 4.15.

Figure 4.15: Hounsfield tensile machine

4.3.14 Stress Analysis

Photoelastic stress analysis is a useful method for examining the stress distribution in materials. Since most materials are not photoelastic, typically three techniques are used – (1) bonding of specially formulated plastic coating to the test part; (2) using of photoelastic material for two-dimensional model analysis; and (3) using of a specially formulated epoxy plastic for three-dimensional model analysis. Some semicrystalline and oriented polymers display birefringence and Polycarbonate (PC) has been reported in the literature (Anantharaman and Benatar 2003) as a birefringent polymer. Materials, such as glass and acrylic, that become doubly refracting when subjected to mechanical stress, are also considered as photoelastic.

In this research photoelastic material PSM-1, transparent PMMA and PC were visually examined by using 060 Series Modular Transmission Polariscope System (Figure 4.16) after exposure to concentrated solar radiation.

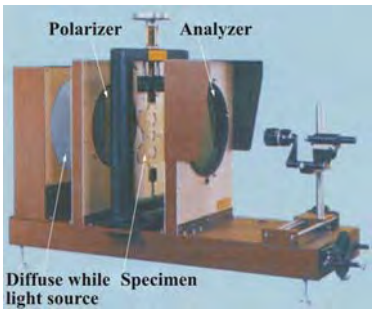

Figure 4.16: Modular transmission polariscope system 060 series

4.4 Polymer materials

The three types of thermoplastics that were chosen for the initial polymer joining experiments and used predominantly in this research were: Acrylonitrile/ Butadiene/Styrene (ABS), Polycarbonate (PC) and Polymethylmethacrylate (PMMA). The ABS material belongs to the copolymer group, while the other two belong to the homopolymer group (Dominghaus 1988). Such materials were selected for their excellent physical properties, wide industrial application and their linear chain polymer structure. Almost all polymers used in this research, except for the Polypropylene film in the ageing experiments, are commercially available.

4.4.1 ABS

ABS terpolymers are elastomeric and thermoplastic composites formed from three different monomers. Typically ABS contains 20% rubber, 25% acrylonitrile

and 55% styrene. Other trade names are ‘Cycolac’ and ‘Lustran’.

Owing to the contributing properties of each component, ABS has very high impact strength, good moulding properties, low softening point, rigidity and strength for structural use. It is used when good dimensional tolerance, surface finish and high impact strength are required (Birley and Scott 1982). ABS has good chemical and restricted weathering resistance but poor solvent resistance. Both glass transition temperatures of ABS are above 100°C and the melting temperature for thermoforming is between 160°C and 180°C (Domininghaus 1988; Gruenwald 1993). Some of the thermal properties of ABS in molten state include: specific heat 2.4 kJ/kgK and thermal conductivity 0.18 W/mK. Typical applications of ABS include auto parts, pipe fittings, waste pipes, computer housings.

4.4.2 PC

Polycarbonate (PC), also known under the trade names ‘Lexan’, ‘Makrolon’ and ‘Merlon’, is one of the strongest, toughest and most preferred engineering thermoplastics. The structural repeat unit of PC is shown below.

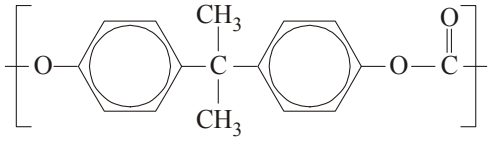

PC belongs to the class of high-performance polymers having characteristics such as low density, high strength, stiffness, hardness and toughness. It is clear and colorless with a highly glossy surface. PC is notable for its high impact resistance. It has relatively good temperature resistance and dimensional stability. Its weldability is only adequate. The limitations of this material are restricted chemical resistance, notch sensitivity and susceptibility to stress cracking. The visible light transmission is in the range of 82% to 89%. The refractive index is 1.59. The glass transition temperature of the material is 150°C and the melting temperature for thermoforming is between 180°C and 210°C. PC is used widely in outdoor applications such as commercial and residential lighting. Other applications include compact disks, glazing, power tool housings and aeronautical engineering.

4.4.3 PMMA

One of the earliest polymers, PMMA, was first discovered in 1870s and commercialized in 1935 as ‘Plexiglas’. PMMA is now the best known and most

widely used type of acrylic thermoplastic. It is also known by the trade names 'Perspex' (a trademark first registered in 1934), 'Lucite', 'Oroglas', 'Acrylplas', 'Acrylite', 'Acrylic glass' or simply 'Acrylic'. PMMA's giant molecule is composed of many joined together monomers of the type shown below (Stuart 2002):

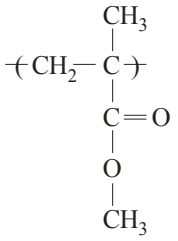

PMMA is naturally transparent and colorless and has a high surface gloss. In its natural form Plexiglas® acrylic sheet has a transparency equal to optical glass with total light transmittance of 92% and insignificant light absorptance in all ordinary thicknesses. Some commercial grades contain UV absorbers (290-350 nm). The visible (400-700 nm) light transmission through clear PMMA is 91% to 93%. Typically it transmits light in the range of 360-1000 nm. A colorless Plexiglas® acrylic sheet transmits most of the near-infrared radiation in the 700-2800 nm region. The average transmittance of visible light (380–780 nm) through colored 3 mm thick Perspex GS grade (essentially transparent) is given in Table 4.2.

Table 4.2: Visible light transmittance of 3 mm Perspex GS grade (www.perspex.co.uk 2001)

This table is not available online. Please consult the hardcopy thesis available from the QUT Library

PMMA is a lightweight material having outstanding weatherability, good chemical resistance, and excellent thermoformability and machinability. It has the highest surface hardness of all common thermoplastics. Its impact resistance is 10 times higher than the glass (Plastic Reference Handbook 2000). The density of PMMA is 1.16–1.20 g/cm^3 and the refractive index is 1.498. Enthalpy of melting is 9.6 kJ mol^{-1} (Krevelen 1976) and thermal conductivity is 0.15 W/mK (0-50°C) or 0.25 W/mK (100°C). The glass transition temperature (T_g) of PMMA is 106°C and the melting temperature (T_m) for thermoforming is between 140°C and 160°C. (According to other sources (Tlusty 2000) T_g is 105°C, T_m is 200°C and the processing temperature T_p is in the range of 180–250°C).

One limitation of PMMA is that it is highly flammable with an ignition temperature of 425°C. It can be produced in all colors. Its outstanding ultraviolet and weather resistance makes it superior to other thermoplastics. The rigidity of

PMMA is due to the steric hindrance resulting from the large side group in the structure (Stuart 2002). Applications of PMMA include aircraft glazing, street furniture, skylights, displays and signs, and automotive rear light housings.

4.4.4 Polypropylene

Polypropylene (PP) is a widely used semicrystalline polymer with the following structural repeat unit:

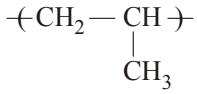

Although PP is a relatively low working temperature material, it has excellent chemical resistance and high dimensional stability, as well as low impact resistance and brittleness at low temperature. PP is mainly used in diverse applications such as bottles, carpets, casings and packaging (Stuart 2002).

4.5 Test specimens

In all polymer joining and ageing experimental tests the specimen sizes used were 40 x 6 mm x sheet thickness. In the case of lap joint the overlapping length was the same as the specimen width – 6 mm. The ABS specimens were cut from a 2.9 mm thick sheet. The PC specimens were cut from a 2.85 mm thick sheet with one side UV-stabilized. The transparent and colored PMMA specimens used in all experiments were cut from sheet materials with the following thicknesses: transparent - 3.2 mm, violet – 2.9 mm, blue – 2.95 mm, green – 2.95 mm, yellow – 2.8 mm, orange – 2.95 mm, red – 3.05 mm, and black – 3.15 mm. For the colored samples used in this research plastic sheets manufactured by Mulford Plastics with standard cast acrylic colors were chosen as follows: violet A-327, blue A-835, green A-348, yellow A-235, orange A-266, red A-128, black A-502.

The test specimens for the curing experiments were with sizes 50 x 10 mm x sheet thickness. For the measurement of absolute transmittance and total reflectance of the colored specimens appropriate specimen sizes (45 x 20 mm x sheet thickness) were used. The specular measurements were performed with bigger specimens, 75 x 75 mm x sheet thickness.

The test specimens used for experimental evaluation of the effects of color on concentrated insolation absorption were cut from the sheet materials specified above with the following sizes: for individual exposure - 42 x 42 mm x sheet thickness and for simultaneous exposure - 40 x 6 mm x sheet thickness.

CHAPTER 5.
EVALUATION OF RELEVANT AMBIENT, SYSTEM AND MATERIAL CHARACTERISTICS

5.1 Introduction

While in the previous chapter most of the equipment, instrumentation and materials are described, in this chapter the studies on relevant SEC facility characteristics and the intrinsic properties of the materials used are summarized. The evaluation tests of the optical and thermal characteristics and capabilities of the SEC facility, as well as the relevant material properties of the thermoplastics used, have been necessary for the modeling and experimental studies. Since this research involved utilization of natural solar radiation in outdoor experiments, it has also been essential to explore the typical variation and limits of the ambient parameters and system capabilities in the particular environment.

For better understanding of the concentrated solar radiation-material interaction in an outdoor environment, the necessary relevant data was collected and analyzed in three different manners. Firstly, the intensity and spectral distribution of solar radiation incident on the accepting apertures (including UV, visible and NIR), which were considered most important, were evaluated in ambient conditions. Secondly, the interactions between the materials and an artificial light with various wavelengths of the utilized range were studied and the relationships between the SEC parameters and variables were determined. Thirdly, the interactions between the concentrated solar radiation and the materials were experimentally studied in ambient conditions.

This chapter begins with a summary of the measured and evaluated typical ambient data such as intensity and duration of the insolation (including UV), ambient temperature, relative humidity and wind speed. Next, the corresponding evaluation tests of the optical and thermal characteristics of the SEC facility are described. The calculated maximum possible concentrations achievable by the SEC with auxiliary imaging optics and a non-imaging third stage concentrator, as well as the maximum idle temperature attained, are also discussed. Typical data on the radiation available at the primary and secondary apertures and at the principal Cassegrainian focus are also presented. In conclusion, the experimentally measured radiation characteristics and other material properties of the thermoplastics used in the research are discussed.

5.2 Measurement and evaluation of relevant system and ambient meteorological data/parameters

5.2.1 Angular size of the sun and available solar radiation

As discussed in Chapter 2, the solar irradiance received on earth is a function of date and apparent time. Since the distance between the sun and the earth varies during the year, the angular size of the sun and intensity of the available solar radiation reaching the earth also vary with it. In most calculations here it is assumed that at perihelion the diameter of the sun is (1.392+0.0181%) x 10^6 km and the earth-sun distance is 147.09 x 10^6 km, respectively at aphelion (1.392–0.0181%) x 10^6 km and 152.1 x 10^6 km. Since the orbital parameters are quoted with a slight variation in different sources, their values are included as variables in the deterministic model discussed in Section 5.3.2. Although considered insignificant, the variation of the angular size of the sun has been also taken into account in the model.

The solar energy concentrator used in this research utilizes primarily the direct visible and near IR ranges of the entire solar spectrum available at a given time. Thus, in order to determine the capabilities and limitations of the SEC facility, the evaluation of the spectral distribution of the typically available incident solar radiation and its intensity has been necessary. Moreover, since different applications have been studied, it has been important to determine the availability of a particular wavelength (or range) at a given time by spectral measurements.

Considered extremely important and a main driver of many physical processes on earth, the available solar irradiance (especially its variation at different terrestrial planes) has been monitored simultaneously and continuously for years. Typically, the intensity and the spectral distribution of the total solar radiation available on a flat terrestrial surface during the course of the day can vary significantly.

For this reason, in the present research a sun-tracking system was used and the beam intensity was constantly recorded, ensuring that the variation is acceptable for the duration of each experiment. The graph in Figure 5.1 illustrates a typical diurnal intensity variation of the direct solar radiation on a clear day. The intensity fluctuation (including tracking error) was less than ± 3% between 10 am and 2 pm. Most experiments were carried out predominantly during that period.

The ageing experiments were conducted for most of the day in clear conditions since they were not critically dependent on the radiation intensity. Moreover, the

radiation exposure was integrated until reaching a preset value calculated prior to the experiments.

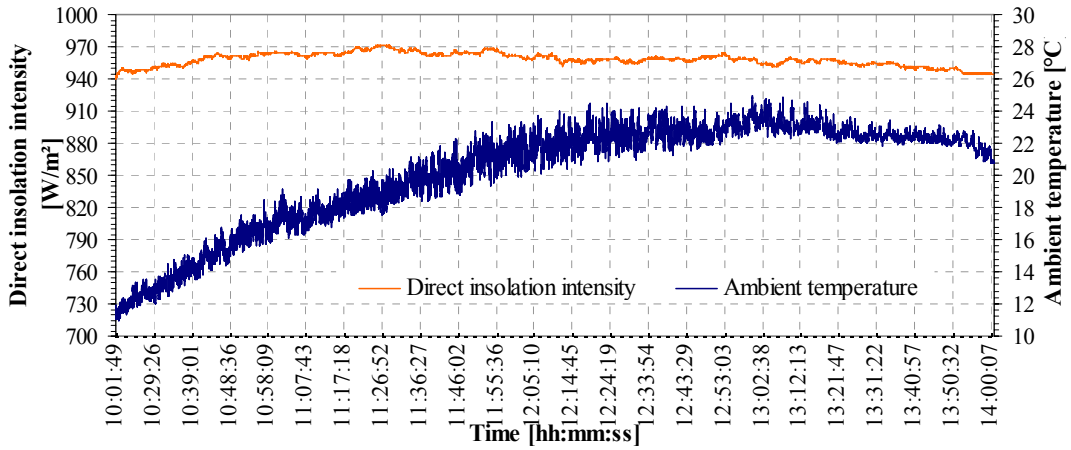

Figure 5.1: Intensity of direct insolation and ambient temperature during a clear day

In order to study its effect on the material–radiation interaction, the spectral distribution of the incident solar radiation available on the accepting aperture, as well as after its reflection from the mirrors were determined, where possible. It was observed that in general the spectral distribution of the incident solar radiation does not deviate significantly from the standard solar spectrum on a clear day. A typical graph representing the spectral distribution of the incident solar radiation measured at the primary accepting aperture on a clear day is shown in Figure 5.2.

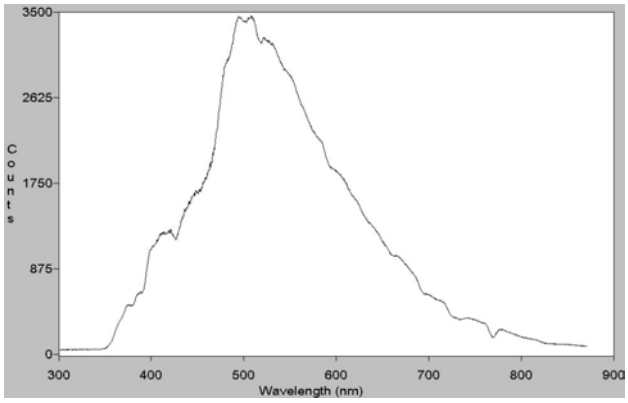

Figure 5.2: Typical spectral distribution at the primary accepting aperture

The measurements of the intensity of the UVA and UVB radiation (and UVR at times) at the primary aperture were taken simultaneously and in the same plane as those of the intensity of total beam radiation. This allowed the comparison of the available UVA, UVB and UVR components with the total radiation available at the same time.

Comparison between the beam solar radiation and its corresponding UV component on a typical clear winter day is given in the graph in Figure 5.3. As can be seen, although the UV component is the most energetic part, it is only about 5% on average compared to the direct global terrestrial solar radiation. The measurement data is given in Appendix 5B.

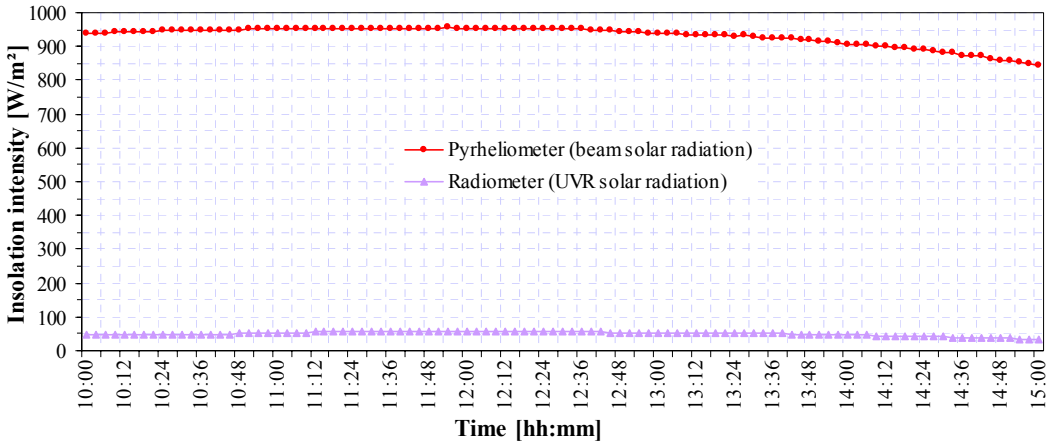

Figure 5.3: Typical diurnal direct total and UV solar radiation on a clear day

Although not much UVB radiation was detected during most experiments, on average the UVR component showed higher values than the UVA, as can be seen in Figure 5.4. The measurement data is given in Appendix 5B.

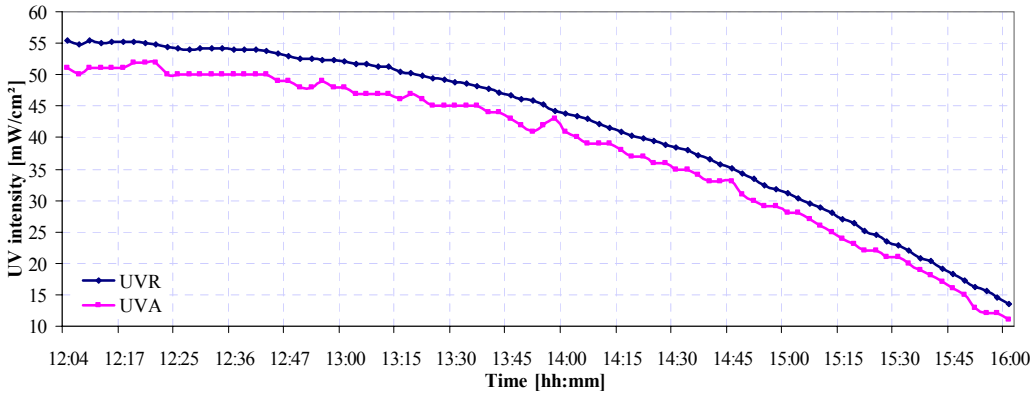

Figure 5.4: UVA and UVR comparison

It can be seen that for the same period, the decrease in UV intensity is much greater than that of the beam component. It should be noted that the data was taken in Brisbane and would vary for other locations.

5.2.2 Ambient temperature, wind speed and relative humidity

The ambient temperature was constantly measured and recorded during all types of experiments in general accordance with the procedure set out in AS2535 (AS2535

1986; Stoynov 1994). On the whole, the recorded ambient temperature was in the range of 18–30°C (see Figure 5.1 for a typical ambient temperature variation on a clear day). Usually the ambient temperature did not change by more than a degree during each experiment. Its variation was greater only during the accelerated ageing experiments since some of these experiments were performed during the course of several days and using air cooling. The data is presented in Chapters 8 and 9.

Any change in wind speed and direction over a test period, if significant enough, is likely to adversely affect the results, producing a greater scattering of the experimental data. Therefore, the wind speed was measured with an anemometer and used for interpretation of the results when necessary. Typically, when testing solar collectors outdoors, there is a requirement for the wind speed not to exceed 2 m/s (Stoynov 1994). During the experimental studies in this research the recorded wind velocity varied between 0 and 4 m/s. It was observed that even wind speed of 1–2 m/s could lead to inconsistent results, thus the experiments with wind speed above 1 m/s were disregarded for the model verification.

The relative humidity, measured with a psychrometer, varied mostly between 22% and 64% since the experiments were conducted during different months of the year and different times of the day. In general, the variation of the relative humidity did not have an observable effect on the results obtained. Exceptions were the curing experiments, where the joining surfaces sometimes formed cavities due to moist air leading to a reduction of the strength achieved.

5.3 Testing and evaluation of thermal and optical characteristics of the SEC facility

5.3.1 Characteristics and amount of re-emitted solar radiation

After evaluation of the spectral distribution of the typically available insolation, further spectral measurements to capture the spectrum of the reflected solar radiation by the primary mirror were performed. Considering that the detector used in the spectrometer has a very limited maximum signal intensity (counts) up to 4100, it was easily saturated even with relatively low concentrated solar radiation from the primary mirror. However, with careful and quick exposure it was possible to capture the spectrum of the reflected radiation by the primary (Figure 5.5).

When compared to the spectrum in Figure 5.2, it can be seen that there is no

significant difference between the spectral distribution of the solar radiation reflected from the primary mirror and that measured at the primary aperture. However, some decrease of the near UV and near IR components has been observed.

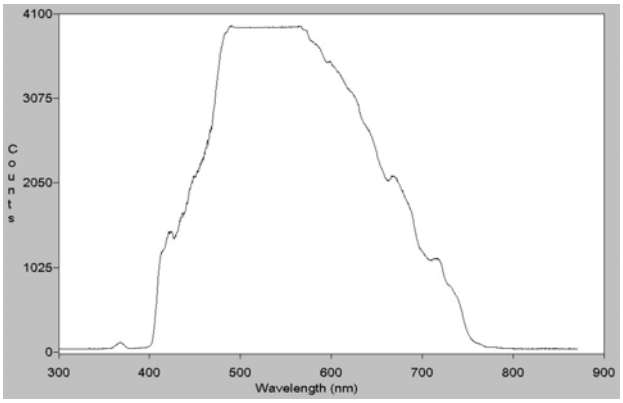

Figure 5.5: Typical spectral distribution of the primary re-emitted radiation

The presence of the UV component has been considered important since an alternative natural accelerated ageing of polymers has been explored. Because of this, an attempt to evaluate the actual amount of UV was initiated. Since the radiation reflected from the primary and secondary is concentrated, it was possible to measure only its UV component with the radiometer described in the previous chapter. These measurements were used to assess the efficiency and optical characteristics of the mirrors. Based on the measured beam insolation typically available at the clear primary accepting aperture (see Figure 5.3), the corresponding power obtainable by the primary during a typical experimental test then could be estimated as shown in Figure 5.6.

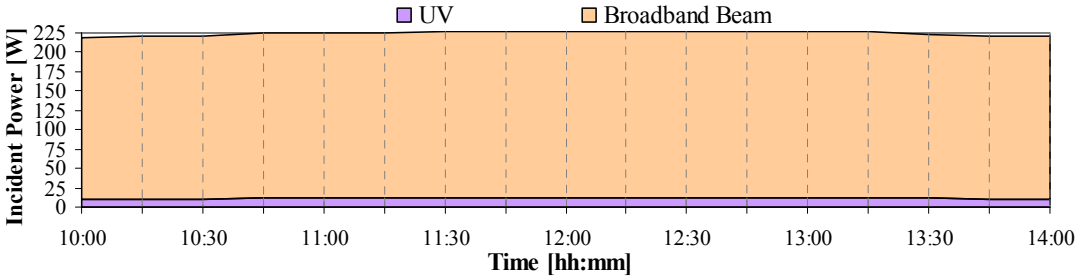

Figure 5.6: Typical beam broadband and UV insolation power at the primary mirror

As can be seen from the graph above, the beam broadband and UV power are relatively constant for the experimental period. This has allowed different types of outdoor experiments to be performed utilizing the available solar radiation. Before attempting such experiments, especially the accelerated ageing, it was important to determine if there is any cut-off or changes of the available spectrum caused by the

coating of the mirrors. Also, it was necessary to evaluate the amount of the UV component incident on the specimen surface.

Thus, in addition to the spectral measurements discussed above, the intensity of the UV component present in the insolation concentrated by the primary mirror at the effective aperture of the secondary mirror and in the principal Cassegrainian focus was also measured. During the experimental measurements it was observed that the UV component decreases from the primary to the secondary but increases at the focus. This variation may be due to the mirror coating and uneven distribution of the UV on the secondary mirror. The results are summarized in the following tables and graphs (Tables 5.1 to 5.3 and Figures 5.7 to 5.9).

Table 5.1: UVA measured data and calculated concentration and power obtainable

Time	UVA at primary [mW/cm²]	UVA at secondary [mW/cm²]	UVA at focus [mW/cm²]	Concentration at 3rd stage compared to secondary	Beam Insolation Intensity [W/m²]	Total Beam [W]	UVA [%]
10:30	1.703	1.268	11.04	8.707	924	210.818	1.843
11:42	1.801	1.391	12.36	8.886	937	213.784	1.922
14:00	1.564	1.165	12.56	10.781	918	209.449	1.704

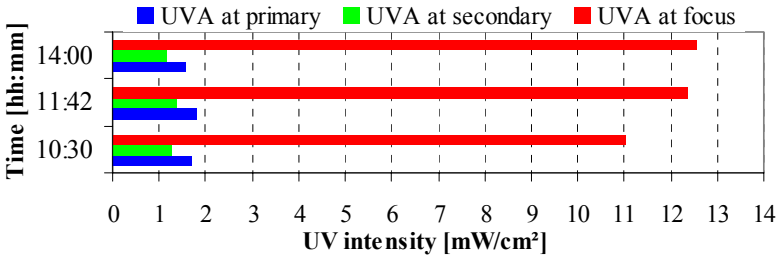

Figure 5.7: UVA typically incident and transmitted through the system

Table 5.2: UVB measured data and calculated concentration and power obtainable

Time	UVB at primary [mW/cm²]	UVB at secondary [mW/cm²]	UVB at focus [mW/cm²]	Concentration at 3rd stage compared to secondary	Beam Insolation Intensity [W/m²]	Total Beam [W]	UVB [%]
10:40	0.1345	0.0723	0.5002	6.918	933	212.872	0.144
11:48	0.1455	0.0777	0.521	6.705	938	214.012	0.155
14:05	0.0963	0.057	0.46	8.070	915	208.765	0.105

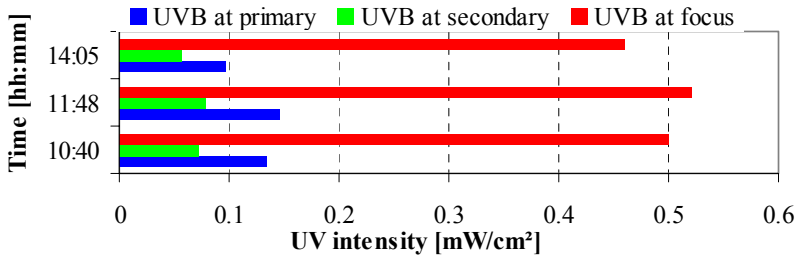

Figure 5.8: UVB typically incident and transmitted through the system

Table 5.3: UVR measured data and calculated concentration and power obtainable

Time	UVR at primary [mW/cm²]	UVR at secondary [mW/cm²]	UVR at focus [mW/cm²]	Concentration at 3rd stage compared to secondary	Beam Insolation Intensity [W/m²]	Total Beam [W]	UVR [%]
10:45	5.47	3.54	29.0	8.192	933	212.872	5.863
11:54	5.72	3.88	29.7	7.655	941	214.697	6.079
14:10	4.64	3.11	25.7	8.264	916	208.993	5.066

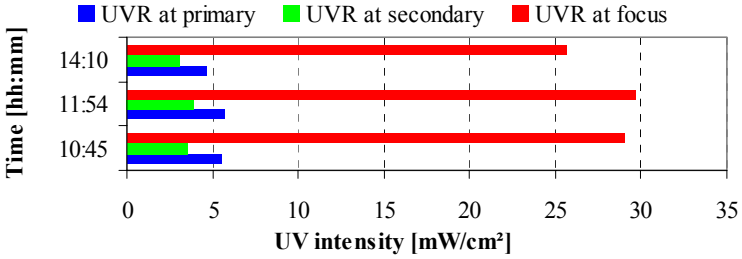

Figure 5.9: UVR typically incident and transmitted through the system

The thermal characteristics and capabilities discussed above represent the typical energy, or the heat obtainable by the SEC, and could be considered annually average daily evaluation. Actual experimental measurements of the temperature at the focus achievable on idle running were also conducted and are discussed in Section 5.4.3.

5.3.2 Measured and calculated SEC variables

5.3.2.1 Relevant principal Cassegrainian parameters

In general the Cassegrainian configuration is considered optically simple with a few degrees of freedom. However, there are numerous parameters that have to be considered carefully in order to ensure its intrinsic aberrations are kept within acceptable limits.

The Cassegrainian system was designed to be coupled to an optical fiber for transmission of concentrated solar radiation and built accordingly. Thus, some of the optical design parameters, as given in the manual provided, are described in the same chapter. However, since the SEC facility had to be modified during the experimental studies, it has been necessary to evaluate all relevant parameters required during its alteration and incorporation of additional systems.

Most principal theoretical aspects of non-imaging and Cassegrainian imaging optics have been discussed in Chapter 2. Following them, in conjunction with the appropriate geometrical and optical principles, the SEC operational parameters have been determined by proper measurements and calculations.

Some of the parameters (e.g. clear or effective aperture of primary and secondary, mirror separation) were directly measured and others were mathematically determined and confirmed geometrically. These parameters were incorporated in a deterministic mathematical model formulated to exactly determine the output variables for any specified input data (see Appendix 5A). The derived equations for this model are discussed below. Most relationships between the principal design variables of the modified Cassegrainian concentrator discussed in this section are geometrically represented in Figure 5.10.

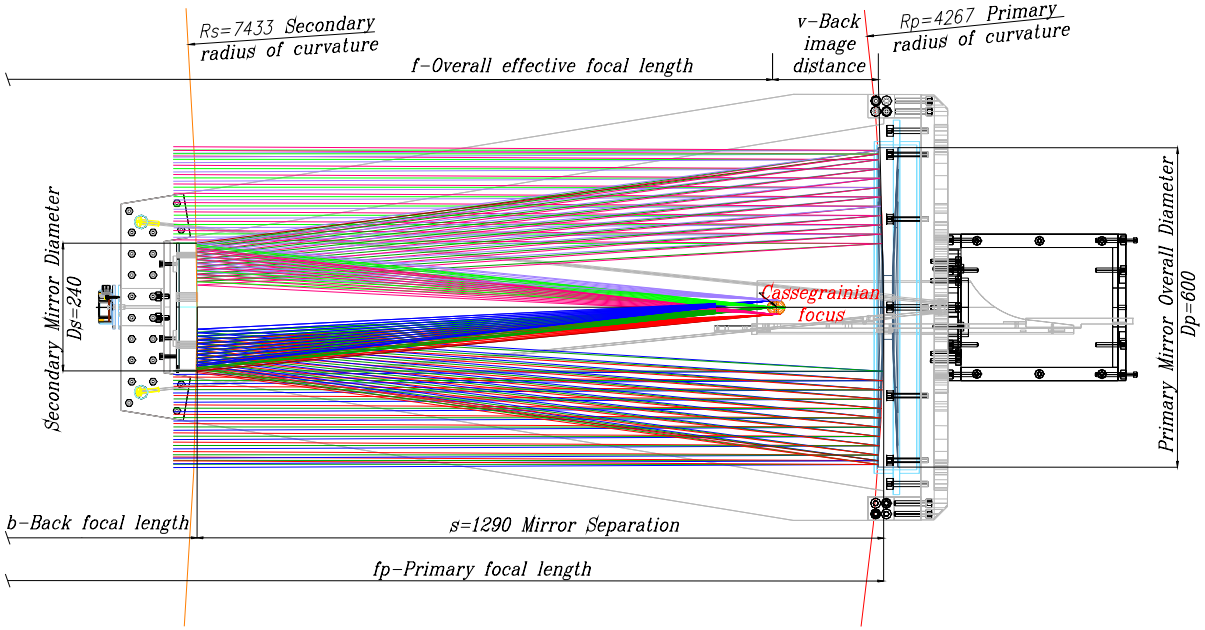

Figure 5.10: SEC section with overall parameters

The process of propagation and concentration of the rays incident on any point of the primary accepting aperture and re-emitted from the secondary mirror and auxiliary optics involves a number of variables. To model and gain a better understanding of this process, the most important variables and constants were identified and the mathematical equations that express the relationships between them were derived. For this purpose, the important parameters as shown in Figure 5.11 were defined and related through a set of formulae discussed below.

The deterministic model was developed with the assumption that in the sectional plane any point on the primary mirror can be defined with X and Y coordinates. The abscissa X_{pc} is defined as the distance from the center of primary curvature along the principal optical axis and can be expressed as:

$$X_{pc} = \sqrt{R_p^{\,2} - Y_p^{\,2}} \tag{5.1}$$

where R_p is the radius of the primary curvature (R_p=4267 mm). Y_p is the ordinate defined as the distance from the principal optical axis and is an input variable.

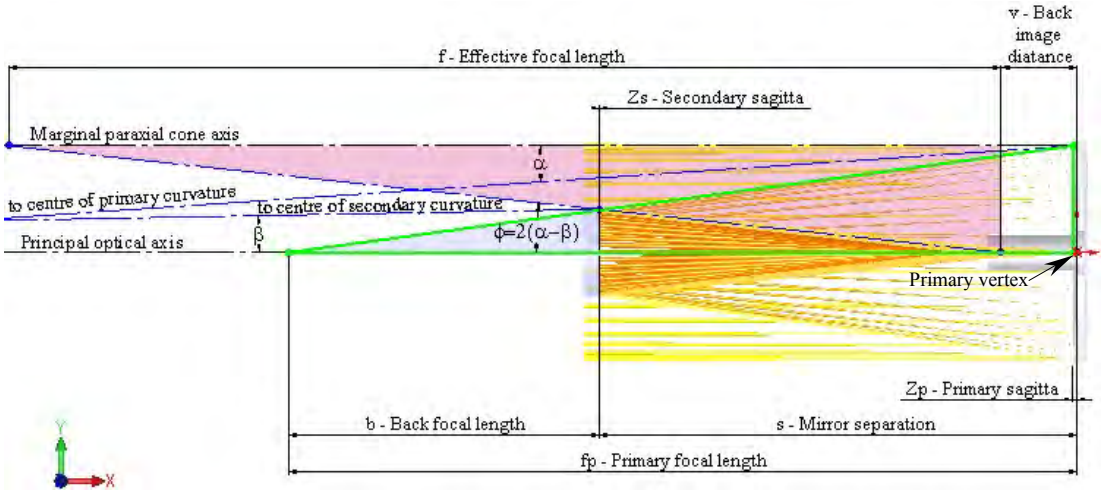

Figure 5.11: Layout of the Cassegrainian telescope with variable parameters

Defined with respect to the primary vertex the abscissa X_{pv} of any point on the primary mirror can be calculated from:

$$X_{pv} = X_{pc} - R_p \tag{5.2}$$

in which case it would be equal to the primary sagitta but with a negative sign.

The angle α between a ray incident on the primary mirror and a line passing through the point of ray's arrival and the center of the primary mirror curvature can be determined by:

$$\alpha = \arcsin\left(\frac{Y_p}{R_p}\right) \tag{5.3}$$

Using this angle, it is easy to see from Figure 5.11 (green outlined triangle) that the ordinate Y_p and the primary focal length f_p can be expressed as:

$$Y_p = (f_p - Z_p)\tan 2\alpha \tag{5.4}$$

and

$$f_p = \frac{Y_p}{\tan 2\alpha} + Z_p \tag{5.5}$$

Also, using the radius of primary curvature, the primary sagitta Z_p at any point where the associated incident ray arrives can be determined by:

$$Z_p = R_p - \sqrt{R_p^{\,2} - Y_p^{\,2}} \tag{5.6}$$

Substituting the primary sagitta Z_p from Equation 5.6 in Equation 5.5 the primary focal length f_p for the associated incident ray can be calculated by the following:

$$f_p = \frac{Y_p}{\tan 2\alpha} + R_p - \sqrt{R_p^{\,2} - Y_p^{\,2}} \tag{5.7}$$

In the deterministic model (Appendix 5A) the point at which a primary reflected ray arrives at the secondary mirror is defined in the sectional plane with its X and Y coordinates. The abscissa X_{sc} is defined as the distance from the center of the secondary curvature along the principal optical axis and can be expressed as:

$$X_{sc} = \sqrt{R_s^{\,2} - Y_s^{\,2}} \tag{5.8}$$

where R_s is the radius of the secondary curvature (R_s=7433 mm), and Y_s is the ordinate of a point at which a ray reflected from the primary mirror arrives at the secondary mirror measured from the principal Cassegrainian optical axis.

The abscissa X_{sv} of any point on the secondary mirror defined with respect to the primary vertex can be calculated from:

$$X_{sv} = X_{sc} - R_s - s \tag{5.9}$$

where s is the separation between the mirrors (s=1290 mm).

Using the radius of secondary curvature, the secondary sagitta Z_s at any point where the associated incident ray arrives can be determined by:

$$Z_s = R_s - \sqrt{R_s^{\,2} - Y_s^{\,2}} \tag{5.10}$$

In order to determine the ordinate Y_s the following equations were derived geometrically. The ordinate Y_s can be expressed from the smaller grey triangle in Figure 5.11 as:

$$\frac{Y_s}{f_p - Z_s - s} = \tan 2\alpha \tag{5.11}$$

or

$$Y_s = (f_p - s - Z_s)\tan 2\alpha \tag{5.12}$$

Substituting α from Equation 5.3, f_p from Equation 5.5, Z_p from Equation 5.6 and Z_s from Equation 5.10 in Equation 5.12, it becomes:

$$\frac{Y_s}{\tan 2(\arcsin\frac{Y_p}{R_p})} - \sqrt{R_s^{\,2} - Y_s^{\,2}} - \frac{Y_p}{\tan 2(\arcsin\frac{Y_p}{R_p})} + \sqrt{R_p^{\,2} - Y_p^{\,2}} - R_p + R_s + s = 0 \tag{5.13}$$

Equation 5.13 was solved for Y_s with the Engineering Equation Solver (EES) software and the same results for Y_s with a precision up to the 6th decimal place (10^{-4} %) were obtained with the SolidWorks software.

The maximum angle β between the principal optical axis and a line passing through the center of the secondary mirror curvature, and the point of ray's arrival at the secondary mirror, can be determined by:

$$\beta = \arcsin\left(\frac{Y_s}{R_s}\right) \tag{5.14}$$

Using this angle, the secondary focal length f_s for the associated incident ray can be calculated by the following:

$$f_s = \frac{Y_s}{\tan\phi} - R_s + \sqrt{R_s^{\,2} - Y_s^{\,2}} \tag{5.15}$$

where ϕ is the angle between the secondary reflected ray and the principal axis. It is easy to prove (see Figure 5.12) that ϕ can be geometrically defined as:

$$\phi = 2(\alpha - \beta) \tag{5.16}$$

The back focal length, b, can be expressed as follows:

$$b = f_p - s - Z_s \tag{5.17}$$

On the other hand, for relatively small angles the effective focal length, f, can be calculated as:

$$f = \frac{Y_p}{\tan\phi} \approx \frac{Y_p}{\sin\phi} \tag{5.18}$$

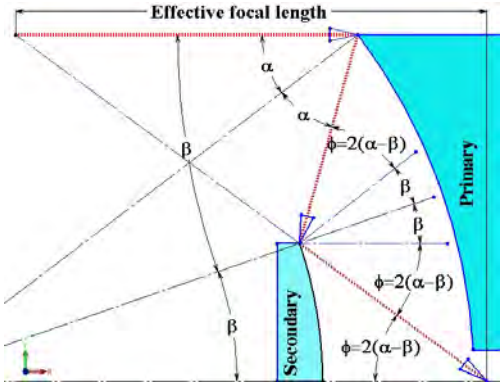

Figure 5.12: Geometrical derivation of angle ϕ expression

Using Equation 2.31 from Chapter 2, the maximum image diameter, d_{max}, can be calculated with the angular size of the sun at perihelion as:

$$d_{max} = 2f \sin \theta_{sun}^{max} \tag{5.19}$$

and the minimum image diameter, d_{min}, can be calculated using the angular size of the sun at aphelion as:

$$d_{min} = 2f \sin \theta_{sun}^{min} \tag{5.20}$$

5.3.2.2 Concentration ratios

The maximum theoretical concentration of the primary mirror alone, C_{pt}, can be calculated using Equation 2.23 from Chapter 2. Using the angular size of the sun at aphelion and neglecting the shading, C_{pt} can be calculated as:

$$C_{pt} = \frac{\cos^2 2\alpha \times \sin^2 2\alpha}{\sin^2 \theta_{sun}^{min}} \tag{5.21}$$

To account for imperfections in the shape of the dish, the beam reflected from it could be considered having an angular width of (θ_{sun}+δ), where δ is the dish dispersion angle. Then for a dish without tracking error, the maximum theoretical concentration C_{ptd} on a flat receiver can be determined by the following (Duffie and Beckman 1991):

$$C_{ptd} = \frac{\cos^2(2\alpha + \theta_{sun} + \delta/2) \times \sin^2 2\alpha}{4\sin^2(\theta_{sun} + \delta/2)} - 1 \tag{5.22}$$

On the other hand, the average area concentration of the primary mirror, C_{pa}, can be defined by the following equation:

$$C_{pa} = \frac{Y_p^{\,2}}{Y_s^{\,2}} \tag{5.23}$$

When using the minimum image diameter defined by Equation 5.20 and its ordinate, the geometric area concentration of the secondary mirror, C_{sg}, can be calculated by:

$$C_{sg} = \frac{Y_s^{\,2}}{(d_{min}/2)^2} \tag{5.24}$$

Then, the geometric area concentration of the SEC at any ray ring, $C_{SEC,a}$, (see Appendix 5A) has been calculated as a combined product by the following:

$$C_{SEC,a} = C_{pa} \times C_{sg} = \frac{Y_p^{\,2}}{(d_{min}/2)^2} \tag{5.25}$$

Using the values for the corresponding angles α and ϕ at any ring of the primary mirror, the theoretical maximum geometric concentration of the SEC, $C_{SEC,t}$, can be defined as:

$$C_{SEC,t} = \frac{\sin^2 \phi}{\cos^2 \phi \times \sin^2 \theta_{sun}^{min}} \tag{5.26}$$

Assuming the efficiency of each mirror to be 80% in the utilized spectral range and using the effective primary, secondary and minimum image aperture areas, the overall geometrical net area concentration of the SEC, $C_{SEC,net}$, can be calculated by:

$$C_{SEC,net} = 0.64 \times \frac{A_p^{eff} - A_s^{eff}}{A_{image}^{eff}} \tag{5.27}$$

The variation of the geometrical net area concentration achievable at the principal Cassegrainian focus for final image diameters in the range of 1 to 50 mm is shown in Figure 5.13.

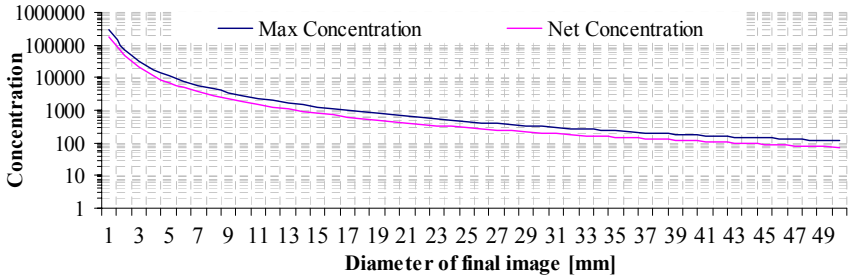

Figure 5.13: Cassegrainian concentration ratios for various final image diameters

When the Cassegrainian concentrator is complemented only with a single doublet lens to focus and further concentrate the beam cone from the secondary, it will also increase further the concentration with minimal losses. If the Cassegrainian concentrator is complemented with five lenses to achieve light transmission over a longer length, they will collimate the beam but also increase the losses.

The considered range of various target areas and possible geometrical area concentrations, achievable for final image diameters in the range of 1 to 50 mm, are shown in Figure 5.14.

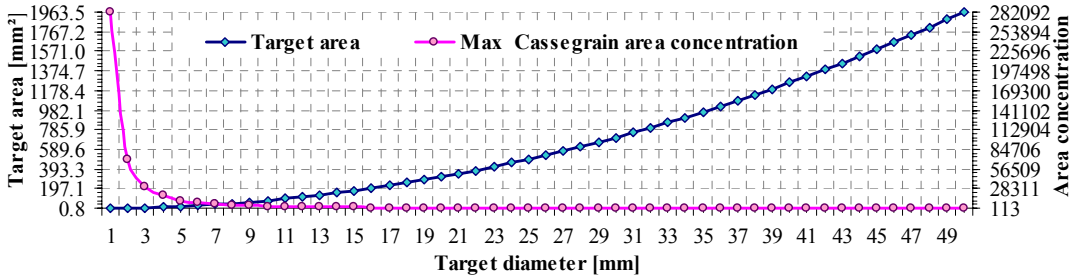

Figure 5.14: Geometric concentration and target area change with image diameter

When one or a succession of five auxiliary doublet lenses are used to enable further decreasing of the final target diameter, the possible power densities at various

beam insolation intensities are presented together in Figure 5.15.

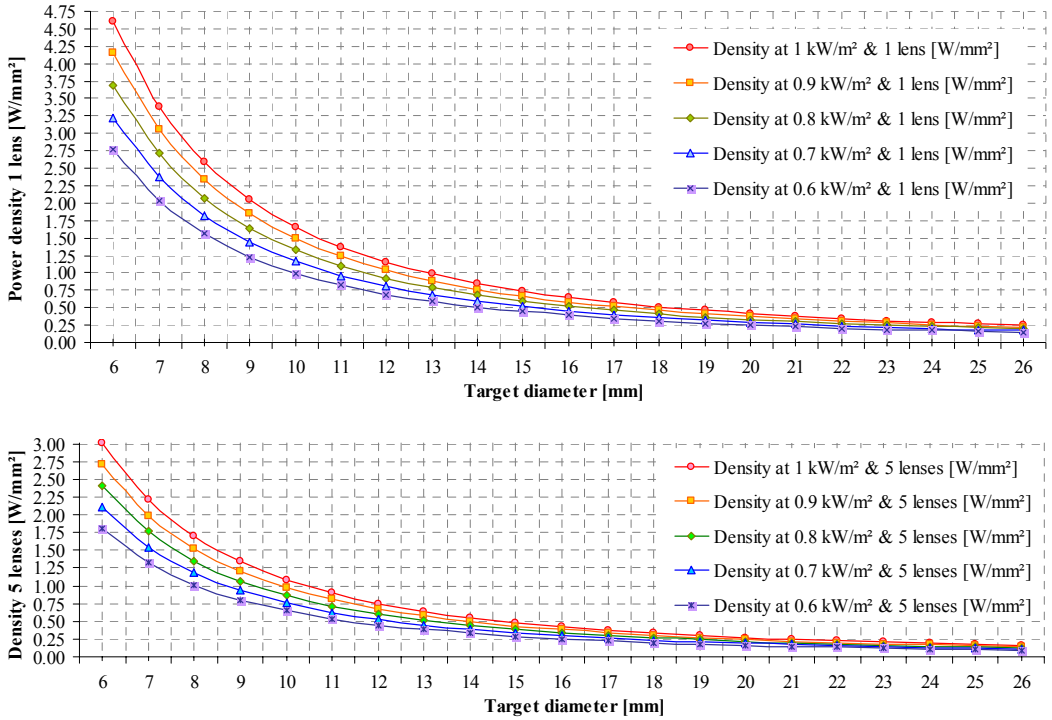

Figure 5.15: Possible power densities at various beam insolation intensities

Considering the typical diurnal beam insolation intensity to be in the range of 0.8–1 kW/m², the range of possible power densities at various area concentrations when one doublet lens and five lenses are used is shown in Figure 5.16.

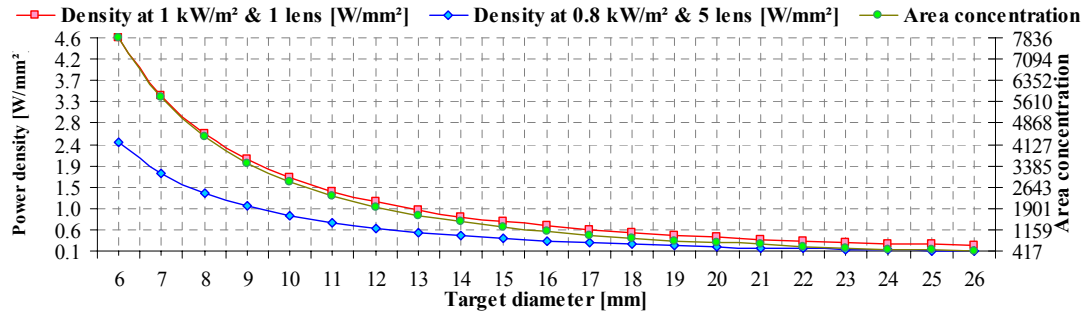

Figure 5.16: Range of power densities at 800 and 1000 W/m² and area concentrations

The angular variation of the secondary rays at the final focus and the corresponding Cassegrainian area concentration with primary rim radius change have been included in the deterministic model in Appendix 5A. The graph in Figure 5.17 illustrates this relationship. With respect to the optical axis, the rim angle could be defined as the maximum possible angle subtended by a ray re-emitted off a point on the widest ring allowed by the clear aperture.

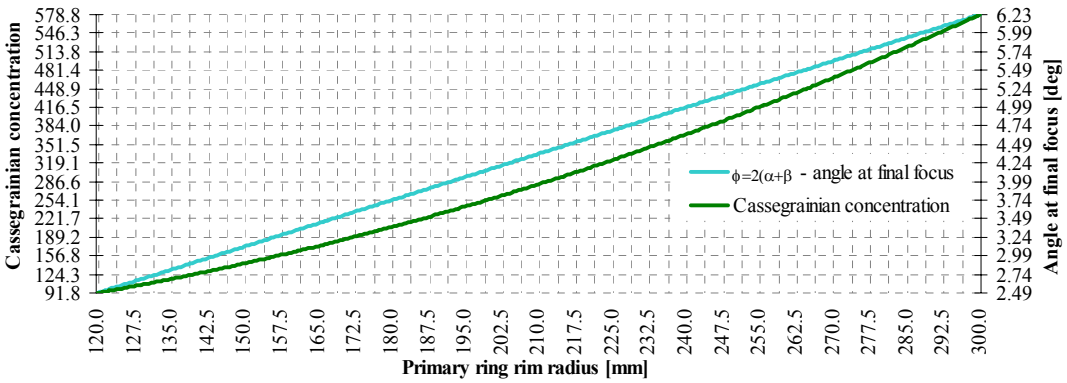

Figure 5.17: Variation of the Cassegrainian concentration and angle at the final focus with primary rim radius change

It can be seen from the graph that the ray angles at the final focal plane vary from 2.49 to 6.23 degrees and the Cassegrainian area concentration increases proportionally with them from about 91.7 to 571.9 respectively.

When the Cassegrainian concentrator is complemented with a CPC used as a type of beam transducer to transmit the beam energy, it will also increase further the concentration. As discussed in Chapter 2, the maximum geometrical concentration of the CPC, $C_{CPC,g}$, is given by:

$$C_{CPC,a} = \left(\frac{D}{d}\right)^2 = C_{CPC,g} = \frac{1}{\sin^2 \phi} \qquad (5.28)$$

The maximum concentration range of the CPC, achievable with the corresponding collection angles of the rays arriving at the final Cassegrainian focus, is also calculated in the deterministic model in Appendix 5A. The graph in Figure 5.18 illustrates this relationship.

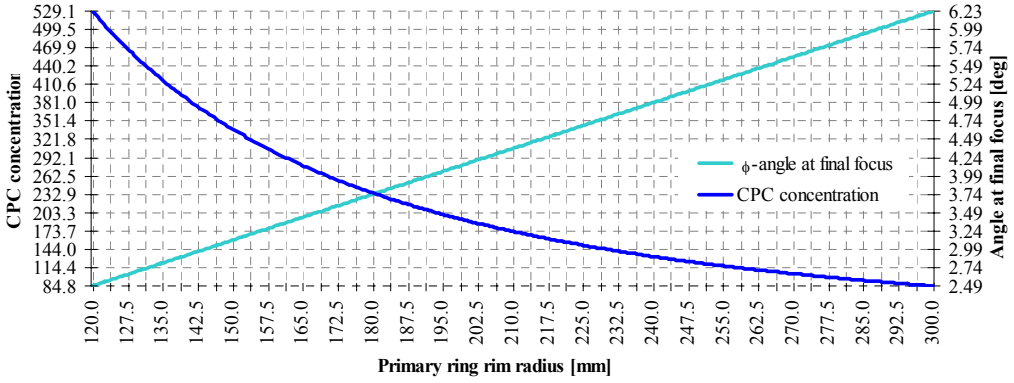

Figure 5.18: Variation of the angle at the final focus and CPC concentration with primary rim radius change

As expected, with the increase of the collection angle, the Cassegrainian concentration also increases and the CPC concentration ratio decreases. Using the

actual collection angle range, the limits of the achievable concentration by the Cassegrainian concentrator and CPC are illustrated in Figure 5.19.

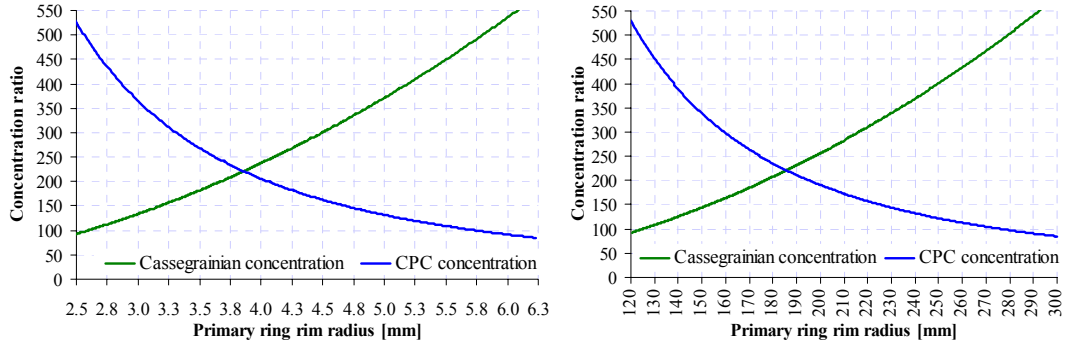

Figure 5.19: Variation of Cassegrainian and CPC concentration ratios with collection angle change and primary rim ring radius change

It should be noted that since the modeling of the SEC complemented with a CPC is discussed also in Chapter 6, Appendix 6C, most of the calculated CPC parameters are described there. The combined theoretical concentration of the SEC and CPC, $C_{comb,t}$ however, can be found by the following equation:

$$C_{comb,t} = C_{SEC,t} \times C_{CPC,g} \tag{5.29}$$

Substituting $C_{SEC,t}$ from Equation 5.26 and $C_{CPC,g}$ from Equation 5.28, Equation 5.29 can be expressed as follows:

$$C_{comb,t} = \frac{1}{\cos^2 \phi \times \sin^2 \theta_{sun}^{min}} \tag{5.30}$$

As it has been shown already that $\phi = 2(\alpha - \beta)$ (Equation 5.16; Figure 5.12), the combined theoretical concentration of the SEC and CPC can be also expressed as:

$$C_{comb,t} = \frac{1}{\cos^2 2(\alpha - \beta) \times \sin^2 \theta_{sun}^{min}} \tag{5.31}$$

Substituting the corresponding angles α, β and θ_{sun} in the above equation, the combined theoretical concentration for each of the calculated ray re-reflecting points on the reflective surface, has been computed. Also, as shown in Appendix 5A, the combined area concentration of the SEC and CPC, $C_{comb,a}$, can be defined as:

$$C_{comb,a} = C_{SEC,a} \times C_{CPC,t} \tag{5.32}$$

Although calculated in different ways, it was found that the theoretical area and geometrical concentration ratios give relatively identical results for the various input collecting angles. The most remarkable result was the finding that the combined concentration of the SEC, when complemented with the CPC, remains relatively constant for any of the selected points on the rim rings, as shown in Figure 5.20.

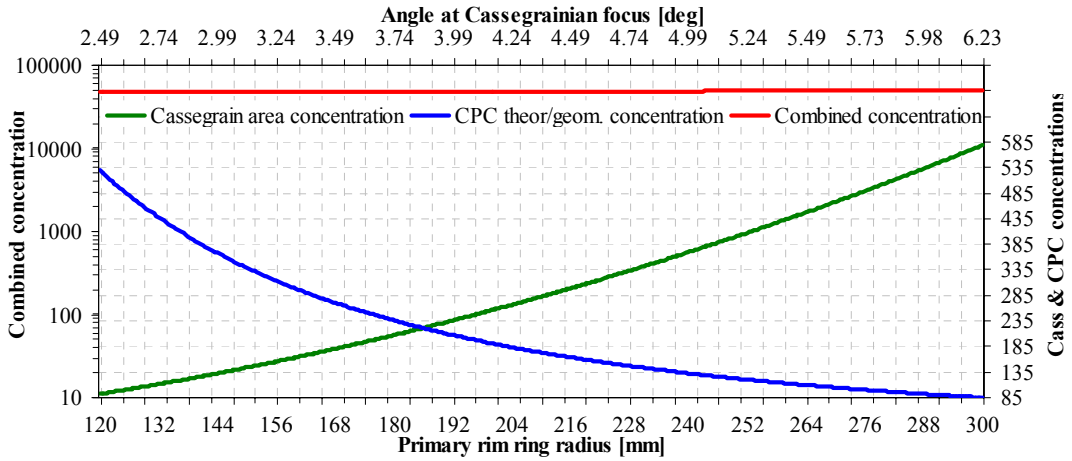

Figure 5.20: Variation of the angle at final focus and combined concentration with primary ring radius change

5.4 Radiation characteristics and material properties evaluation

After evaluation of the ambient and system characteristics discussed previously, it was necessary to assess the radiation characteristics and other properties of the thermoplastics that can affect the heating, joining and ageing processes. In solar energy engineering, the solar absorptance and emittance of the material along with the relevant material properties are typically required for the prediction of the energy gain/loss. In order to compute the solar absorptance, the total monochromatic angular-hemispherical reflectances[1] and absolute transmittances of the materials were measured for the utilized wavelength range. In addition, other relevant material properties such as tensile strength and glass transition temperature were measured and are presented in this section.

5.4.1 Radiation characterization of the assigned polymers

In general, as discussed in Chapter 2, if solar radiation is incident on a real surface it could be absorbed and re-emitted, scattered or transmitted, and reflected if rejected. The terrestrial insolation utilized in this study, although predominantly beam, comprises a relatively wide band of wavelengths. As a consequence, the irradiated polymer specimen will be exposed to various photon energies simultaneously. Also, since imaging and non-imaging auxiliary optics have been used, the concentrated beam, incident on the polymer surface, could have diffuse spatial distribution that may differ from that of the intercepted non-concentrated

[1] When a narrow cone of radiation is incident on a surface and all reflected radiation is accounted for.

insolation. Thus, an assessment of the polymer radiation characteristics has been regarded as essential for better understanding of the solar energy-material interaction.

Two methods are recommended for the measurement of the terrestrial solar energy reflectance and transmittance of sheet materials (ASTM-E424 1993). In the first method (the referee method), a spectrophotometer is used to measure both spectral reflectance and transmittance, and in the second – a pyranometer is used for measurement of the solar transmittance only. However, if in the first method the specimens are limited by the size of the sample port, in the second one a specimen with 0.61 m^2 is required (0.25 m^2 in (ASTM-D1084 1996)). Also, in the first method monochromatic reflectances and transmittances are measured, while in the second only the intensity of the actual transmitted solar energy is measured.

In this work generally both methods were used to determine the polymer solar absorptance in the utilized range, required for the modeling and energy calculations.

5.4.1.1 Spectrophotometric measurements

Initially, the monochromatic angular-hemispherical reflectances for all polymers and the absolute transmittances of the transparent ones were captured with a Cary 100 UV-VIS-NIR spectrophotometer described in the previous chapter. Also, specular reflectance and transmittance measurements for all polymers were conducted at an angle of incidence of 5.5°. The results are shown in Figures 5C.1 and 5C.2 in Appendix 5C. Additionally, the specular reflectance of the transparent PMMA (considered with a smooth surface) was computed using the Fresnel equation (adapted from Duffie and Beckman 1991):

$$\rho_F = \frac{1}{2}\left(\frac{\sin^2(r-i)}{\sin^2(r+i)} + \frac{\tan^2(r-i)}{\tan^2(r+i)}\right) \qquad (5.33)$$

where $r = \sin^{-1}(\sin i / n)$ is the angle of refraction, i is the angle of incidence and n is the refraction index. As it has been shown in Section 5.3.2, since the concentrated light rays are reflected from the secondary mirror on angles from 2.49 to 6.23 degrees, the specular reflectance was calculated at those angles. Because these input angles were relatively small, the computed specular reflectance of the transparent PMMA was found to be 3.975%.

However, it was concluded that rather than using different methods and instrumentation, more precise results could be obtained if the total reflectance and absolute transmittance are measured using one instrument. This was achieved with a

Cary 5000 spectrophotometer described in Chapter 4. Considering the range of the utilized solar radiation, these measurements were performed predominantly in the wavelength range of 200-900 nm. Although the results confirmed the trend observed in the initial measurements, they were considered much more reliable (Figure 5.21).

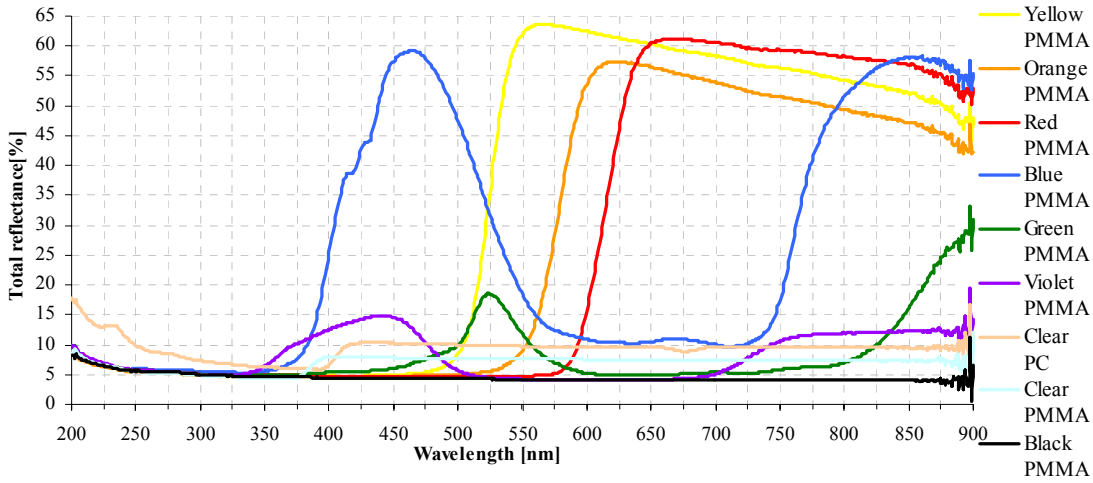

Figure 5.21: Total reflectance spectra of all samples

It can be seen from the graph that when irradiated with UV, VIS and NIR artificial light, the most reflective is the yellow PMMA and the least reflective - the black PMMA. Also, as expected, in general the maximum reflectance for each of the colored samples lies within their corresponding spectral color range. The two transparent samples maintain relatively constant reflectance in the visible light range.

The violet, blue and green show more distinctive maxima than the yellow, orange and red that also cover a relatively wider wavelength range. This may be caused by the dyes and other impurities in combination with the instrument efficiency or light emanating from the illuminated diffuse surface of the integrating sphere. The reflectances of all specimens drop significantly (to ~5-10%) and remain approximately equal in the UV range. An exception is the transparent PC which rises above 15% probably due to the UV coating.

Principally, for transmittance measurements of smooth surfaces exact normal incidence is avoided, as multiple reflections could arise between the last optical component and the sample (Nostrell 2000). However, since clear PMMA and PC were used in most experiments as a transparent component, their transmittances were captured in the above specified wavelength range (see Figure 5.22). Clearly PMMA maintains higher transmittance compared to PC for the whole studied wavelength range (despite the difference in thickness). As can be noticed from the expanded

view on the left, PMMA is more transparent to UV light than PC, especially in the black light region (approximately 370-390 nm).

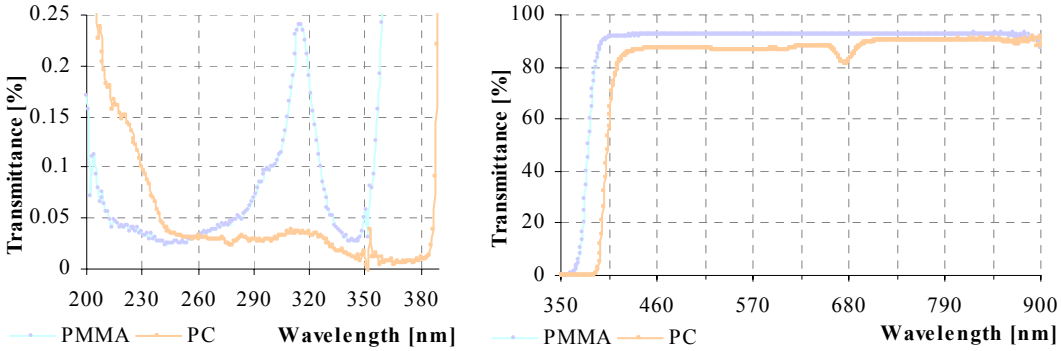

Figure 5.22: UV and VIS light transmittance through 3.2 mm PMMA and 2.85 mm PC

PMMA also has a small peak around 315 nm, whereas the transmittance of PC drops significantly around 385 nm. However, there exists specially formulated Plexiglas – UV-3 that is UV absorbing PMMA material which has been considered for future ageing work. The noise at 350 nm is probably due to the source changeover in the spectrophotometer.

In addition, to evaluate and compare the absorptances of the dyes used, the transmittance and absorbance of chloroform solutions of the colored and clear materials were measured. The spectral profiles of the samples are shown in Figures 5C.3 and 5C.4 in Appendix 5C. It should be noted that it was not feasible to use equal material-chloroform proportion because if a certain proportion was sufficient for some samples, it was not for others (e.g. black and yellow). However, these measurements show that most solutions exhibit increasing absorbance in the UV region and the highest is the clear PC followed by white ABS.

The above results for absorbance, reflectance and transmittance were obtained as a function of wavelength in the explored range. Since the intrinsic nature of solar radiation is such that all wavelengths are impinging simultaneously on the polymer surface, the reflectance and transmittance are typically computed as weighted average values for the utilized solar spectrum. As discussed in Chapter 2, the average absorptance of solar radiation, as defined by Equation 2.12, can be expressed specifically for the studied wavelength range as follows:

$$\alpha^s = \frac{\int_{\lambda_1}^{\lambda_2} \alpha_\lambda^s G_\lambda d\lambda}{\int_{\lambda_1}^{\lambda_2} G_\lambda d\lambda} \qquad (5.34)$$

To perform this integration, the variation of the spectral irradiance with the

wavelength is needed. Since the integrand is usually a relatively complicated function, the integration has to be performed numerically. In practice, by dividing the solar spectrum into a sufficient number of wavelength bands (of equal energy) and assuming that the absorptance remains constant over each band, the function $G_\lambda(\lambda)$ can be expressed as a step function. This simplification allows the transformation of the integration with summation with sufficient accuracy. The solar energy reflected or transmitted is obtained by integrating over a standard solar energy distribution curve by the following equations:

$$\rho^s = \frac{1}{n}\sum_{i=1}^{n}\rho_{\lambda,i}^s \qquad \tau^s = \frac{1}{n}\sum_{i=1}^{n}\tau_{\lambda,i}^s \tag{5.35}$$

where *n* is the number of the wavelength bands into which the solar spectrum has been divided. The computed solar reflectances and transmittances of the materials used in this work for the utilized insolation by the SEC are given in Table 5.4.

Table 5.4: Weighted average solar reflectances of all samples and transmittances of clear samples in the wavelength range of 370-900 nm

Specimen	Solar reflectance %	Solar transmittance %
Black PMMA	2.96	
Green PMMA	5.76	
Violet PMMA	6.30	
Blue PMMA	21.53	
Red PMMA	22.76	
Orange PMMA	23.36	
Yellow PMMA	30.18	
White ABS	59.63	
Clear PC	6.71	84.33
Clear PMMA	5.25	91.04

The average solar weighted absorptances of the studied materials for the spectral range utilized by the SEC were calculated using Equation 2.11 and are given in Figure 5.23. The calculations were based on an Air Mass 1.5 spectrum. An example of detailed calculations for one sample is presented in Appendix 5D.

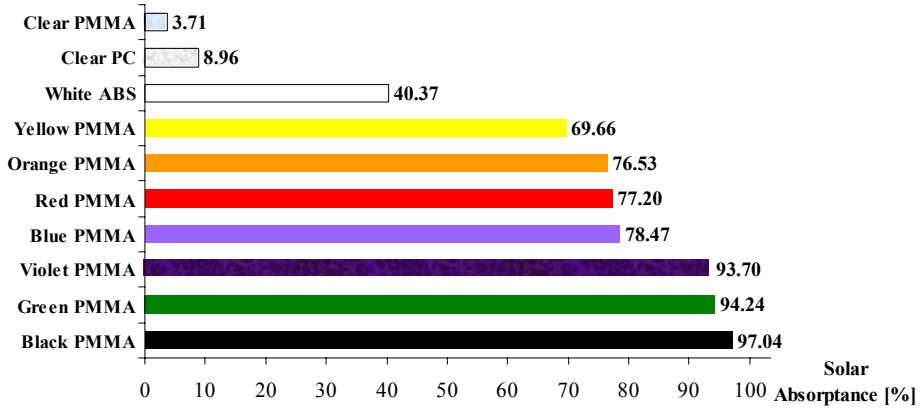

Figure 5.23: Computed average solar weighted absorptances of all specimens

It can be seen that for the wavelength range utilized by the SEC the least absorbing colored material is the yellow (69.66%) and the most absorbing is the green (94.24%).

5.4.1.2 Through-transmission solar radiation measurements

In addition to the spectrophotometric method, measurements of the solar energy transmittance through clear PMMA and PC using pyrheliometer and pyranomer simultaneously were performed. Both instruments were mounted in the primary mirror plane and interfaced to two computers with synchronized timing. The beam and total insolation intensities were recorded continuously for the experiment duration between 11 am and 1 pm. The readings were taken without and with specimens after allowing adequate time for the reading to stabilize.

The transmitted solar radiation through the test specimens was computed as the ratio of the solar flux, measured with the specimen placed between the sensor and the sun, to the insolation intensity, measured by the sensor with no specimen in place. The estimated standard deviation of the average transmittance, S_t, was computed by the following equation:

$$S_t = \pm\sqrt{[\sum_{i=1}^{n}(\tau - \overline{\tau_i})^2]/[(n(n-1)]} \qquad (5.36)$$

where τ is the average transmittance, i is i-th individual measurement and n is the number of the individual measurements made. The results from the transmittance measurements are summarized in Table 5.5.

Table 5.5: Average transmittance data (beam and total) through clear PMMA and PC

	Clear PMMA		Clear PC	
	Beam	**Total**	**Beam**	**Total**
Insolation intensity with no specimen in place [W/m²]	875.750	964.842	875.750	964.842
Insolation intensity with specimen in place [W/m²]	727.176	834.200	701.471	801.500
Directly measured solar transmittance [%]	82.989	86.669	80.146	83.319
Estimated standard deviation [%]	0.0191	0.0343	0.0098	0.0364

It can be seen that the solar transmittances through clear PMMA and PC are lower than those obtained with the spectrophotometric measurements. This may be due to the fact that the used pyrheliometer and pyranomer have broad band sensors sensitive in the spectral range of 0.2 to 4 μm which contributes to the relatively higher transmittance measured without the specimen in place.

5.4.2 Other relevant material properties

5.4.2.1 Tensile testing of control samples

Regardless of the application, welded joints or the surrounding areas in any plastic structure often become potential sites of weakness of the material. This is why it is important that these sites are tested to assure that the welded joints are capable of fulfilling their purpose. This especially is applicable in this research where attempts have been made to develop an alternative plastic welding technique utilizing concentrated direct solar energy, which may also alter the material. Depending on the type of polymers and purpose of the weld, there are many test methods that could be used for testing parent and welded materials.

Most specimen preparation methods for polymer testing involve damage or fracture process that must be understood for image interpretation. Although multiple preparation techniques may be used, they can also impose additional stress as in the following example shown in Figure 5.24.

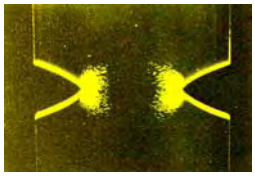

Figure 5.24: Crazes in notched transparent PMMA bar (adapted from (Menges 1973))

As a result, a reduction of mechanical properties of notched specimens from various polymers has been reported. In particular, the tensile strength of PMMA has decreased by 76% (from 76±4 MPa to 18±3 MPa) and that of PC by 7% (from 71±2 MPa to 66±2 MPa) (Liu and Piggott 1998). To avoid obtaining unrealistic results, most specimens used in the experimental studies of this research were unnotched.

Initially, tensile testing of the control samples of the ABS, PC and PMMA materials was performed before the welding process according to (AS1145.1 2001), as discussed in Chapter 4. Some of the obtained results are shown in Figure 5.25.

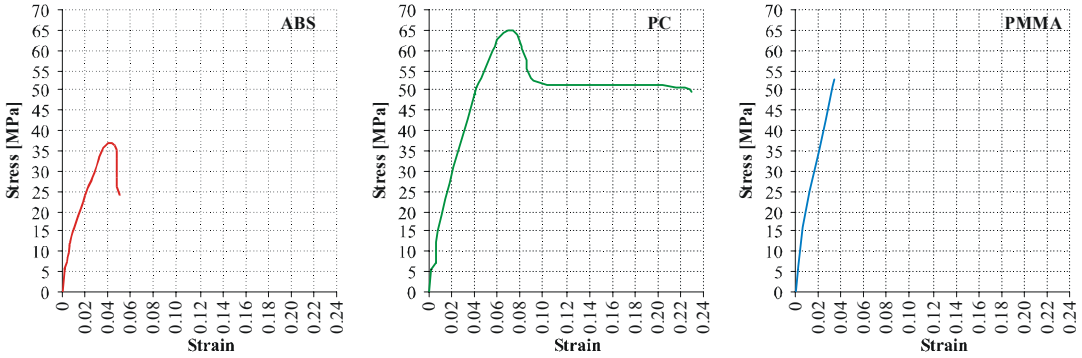

Figure 5.25: Stress–strain curves for the assigned polymers

Among the three thermoplastic materials tested, PC had the highest tensile strength and was the most ductile material, whereas PMMA had a relatively high tensile strength and was the most brittle material. ABS had the lowest tensile strength and was relatively brittle. The average tensile strength of the ABS, PC and PMMA parent materials was determined to be 35.5 MPa, 66.5 MPa and 54.7 MPa respectively (Table 5.6). The absolute and relative elongations of each specimen from the three materials before the welding process are also given in Table 5.6.

Table 5.6: Tensile strength of parent materials (Stoynov et al. 2000)

Material	Specimen	Absolute elongation [mm]	Relative elongation [μm/N]	Average strength of parent material [MPa]
ABS	1	1.90	3.025	35.5
	2	2.25	3.664	
	3	2.70	4.259	
	4	1.62	2.324	
	5	1.74	2.797	
PC	1	9.12	7.782	66.5
	2	10.80	9.310	
	3	9.33	7.057	
	4	8.77	7.165	
	5	8.02	7.232	
PMMA	1	1.32	1.392	54.7
	2	1.97	1.976	
	3	1.14	1.058	
	4	1.09	1.247	
	5	1.21	1.179	

Note: The average tensile strength of the parent materials was obtained by dividing the applied tensile load by the cross sectional area subjected to the test (6 x sheet thickness x 10^{-6} m^2).

Conventional scanning electron microscopy techniques were used to study the microstructure of the ruptured specimens. Figure 5.26 shows the ruptured surfaces of the parent materials under the SEM before the welding process.

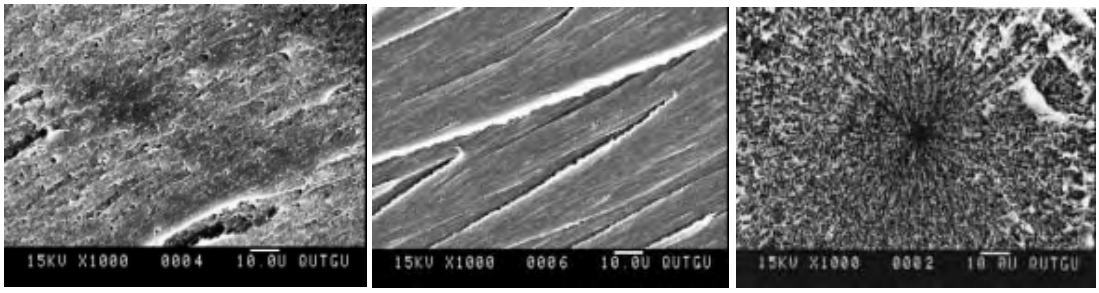

ABS PC PMMA

Figure 5.26: Ruptured surface of parent ABS, PC and PMMA material before welding

Tensile testing of control samples of the transparent (PMMA) and colored (PMMA and ABS) thermoplastics was also performed before the welding process. Three samples of each color were fractured and the results are summarized in Table 5.7. It should also be noted that, although relatively small, the variation in the

dimensions of the control specimens may have affected the test results. In order to decrease this effect, the average tensile strength was calculated per mm^2 and is shown in the last column of the table.

Table 5.7: Average strength of control samples

Specimen	Average load at failure [N]	Tensile strength [N/mm²]			Average tensile strength [N/mm²]
		#1	#2	#3	
Yellow PMMA	1272	69.17	78.57	79.40	75.71
Violet PMMA	1250.67	73.22	72.41	70.00	71.88
Orange PMMA	1248	69.27	68.93	73.33	70.51
Green PMMA	1233.33	68.36	61.02	79.66	69.68
Blue PMMA	1223.67	59.60	74.01	73.79	69.13
Red PMMA	1226	59.67	71.15	70.16	66.99
Black PMMA	1220	61.80	78.41	53.44	64.55
Transparent PMMA	1222	76.46	54.48	60.00	63.65
White ABS	673.73	37.72	37.21	41.23	38.72

Notes: (1) The tensile weld strengths were obtained by dividing the load of failure by the original cross-sectional area of the specimen (6 x sheet thickness x 10^{-6} m^2). (2) 1 N/mm^2=1 MPa.

It can be seen that although the individual tensile peak loads for rupture vary significantly (38%), the average load values obtained for the transparent, black and differently colored PMMA samples do not vary much (4%). This may be due to the testing procedure, in particular the specimen clamping. A consistent trend dependent on color could be established if more precise or simultaneous tests were possible. However, it was found that the black PMMA is more brittle than the standard PMMA.

5.4.2.2 Differential scanning calorimetry measurements

In a heating process thermoplastics can exhibit various thermal reactions amongst which is the glass transition. Also, the molecular mobility and with it the volume, heat capacity and coefficient of expansion increase during this process. One useful tool for characterizing amorphous thermoplastics by determining the glass transition parameters is Differential Scanning Calorimetry (DSC). Since most applications studied in this research involve the raising of polymer temperature, the objective of these measurements was to study the thermal transitions in the polymer.

Because different amorphous polymers were used, it was necessary to examine their glass transition. For this purpose DSC was used to quantify the glass transition temperature range of the polymers by analyzing the heat flow to the specimen resulting from the change in heat capacity. The determination of the transition temperatures of the polymers was performed following in general ASTM-D3418

(ASTM-D3418 1999). Since this test is applicable to polymers in granular form, appropriate specimen sizes were cut accordingly and several runs were performed to ensure repeatability of the results. In the first set of runs TA Q100 calorimeter was used, and in the second – TA Q10 (described in Chapter 4). The DSC thermograms shown below were obtained on heating and the sample amounts used were in the range of 2.2 to 3 mg. Some of the used specimen capsules are shown in Figure 5.27.

Figure 5.27: PMMA and PC samples used for DSC

ABS undergoes two amorphous phases during a temperature change: a rubbery phase caused by butadiene, and a strength-lending styrene acrylonitrile (SAN) copolymer two-component phase. Because of this it has two glass transitions. The thermal curve for the glass transition determination of ABS is shown in Figure 5.28.

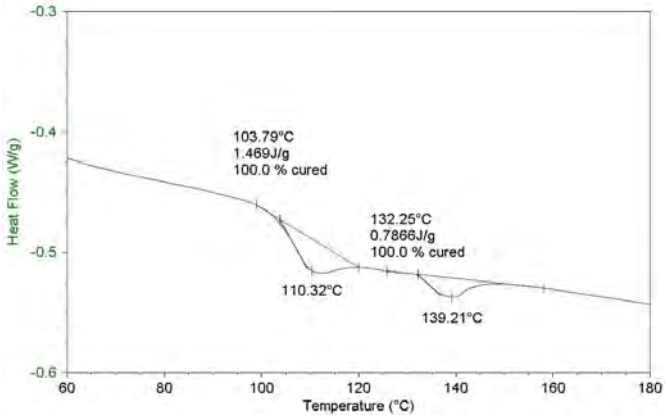

Figure 5.28: Glass transition of ABS

The low glass transition temperature which is due to the butadiene was measured to be around 110°C. The higher glass transition temperature which is due to the SAN phase was measured to be around 139°C. It should be noted that using TA Q100 and relatively larger specimens, the glass transition temperatures obtained were lower – 104°C and 122°C.

The DSC results for PC obtained during the first run were lower than those obtained in the second run (shown in Figure 5.29). The glass transition temperature measured was comparable to that given in the literature – 150°C (see Chapter 4).

In the case of PMMA several runs were performed with black, green and transparent samples. In general, although clear and colored samples were used, the variation of the temperature was insignificant.

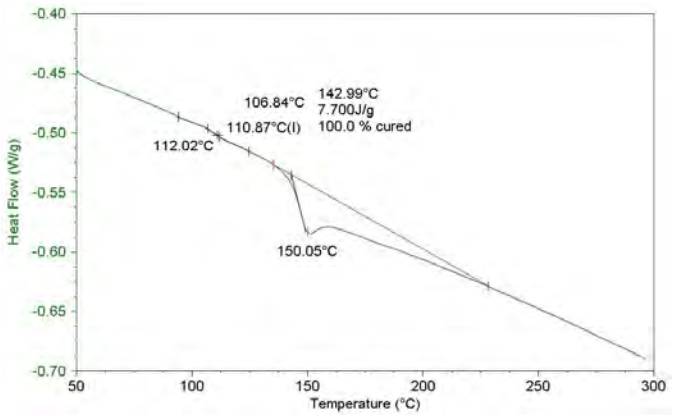

Figure 5.29: Glass transition of PC

Figure 5.30 shows the thermogram with the lowest results obtained with TA Q10 for the green PMMA.

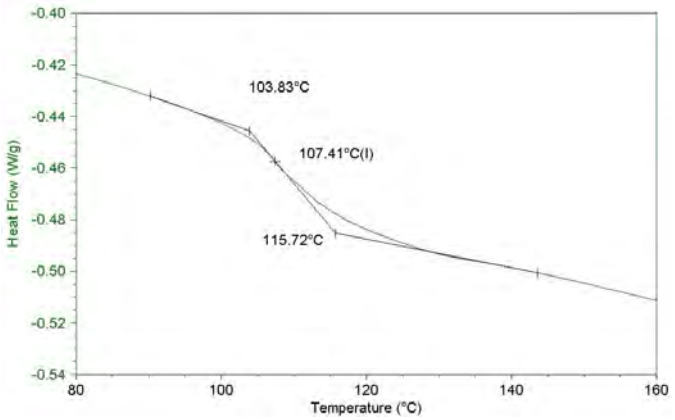

Figure 5.30: Glass transition of green PMMA

In the initial runs using TA Q100 however, relatively higher values for the glass transition temperatures of these samples were obtained – 127.19°C, 126.82°C, 125.54°C, 125.49°C.

5.4.3 Experimental outdoor heat generation measurements

While the laboratory experiments were very useful, especially for comparison purposes, the solar energy transmittance and reflectance were not sufficient to define the rate of heat transfer without studying other factors. The outdoor measurements with the use of the natural solar radiation source in ambient conditions were essential for the evaluation of the SEC capabilities and limits. Also, as can be seen from the through-transmission solar radiation measurements (Table 5.5) the average transmittance through transparent PMMA is lower than that measured over the whole beam insolation range available.

To ensure that input parameters like insolation intensity, ambient temperature

and time of the day are all identical during the testing, a simultaneous exposure of all specimens was performed. Test specimens with dimensions 40 mm x 6 mm x sheet thickness were cut and mounted radially in an appropriate holder. The holder was especially designed to accommodate all specimens, allowing the irradiation of an equal area of each specimen. Figure 5.31 shows the design drawing and photographs of the holder with the irradiated specimens at the Cassegrainian focus.

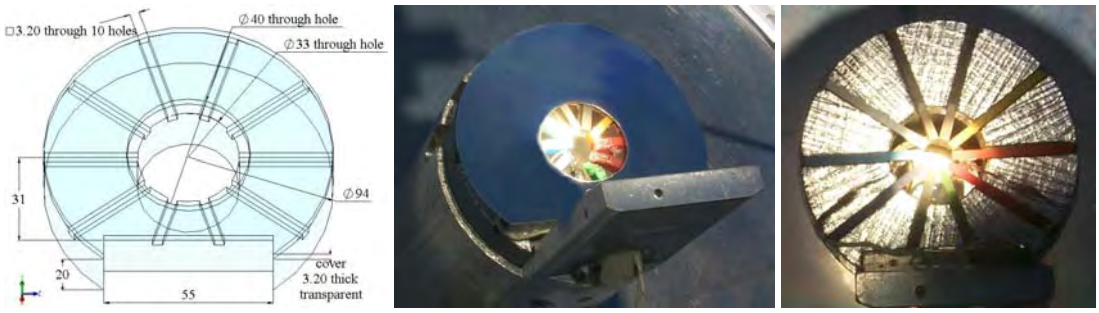

Figure 5.31: Design drawing and pictures of holder with all irradiated specimens

In order to practically assess the capabilities of the SEC to generate heat for polymer processing, appropriate specimens from each of the materials used were exposed to concentrated solar radiation. In these experiments, the solar irradiance, ambient environment and heat generation rate had stabilized to such an extent that quasi-steady state conditions were considered essentially constant. Furthermore because of their short duration, all heat generation experiments were conducted in ambient conditions with a relatively constant intensity of beam insolation and surrounding temperature. The variation of the wind speed during all experiments was insignificant, in the range of 0 to 0.2 m/s. The relative humidity was fairly constant around 45%.

These preliminary experiments were performed at the principal Cassegrainian focus without an additional third stage concentration. The test specimens were with overall dimensions 42 mm x 42 mm x sheet thickness and can be seen on the photograph in Figure 5.32 together with the provisional holding devices.

Figure 5.32: Square test specimens and holding devices

To minimize the error in the temperature measurements caused by different absorptance and emittance of the thermocouple and polymer, initially the thermocouples were masked according to the polymer color. Also, the exposed surface of the thermocouple sensor tip, typically made from more conductive material, is much smaller compared to the polymer specimen and could be easily affected even by a light whiff of air. Thus, the expected average temperature of the irradiated polymer would be less volatile than the temperature registered by the thermocouple, even if its sensor is appropriately coated.

Later, the thermocouples were embedded on the exposed surface prior to each experiment, ensuring that the thermocouple tip is covered with material. In addition, to study the possible errors caused by the polymer acting as an insulator of the unexposed thermocouple back side, another thermocouple was attached under the specimen. Further measurements with a non-contact infrared thermometer have been proposed for future work.

Photographs of the samples were taken during the test runs. Three examples of the exposed specimens placed in the holder are shown in Figure 5.33. Photographs of the reminding exposed specimens are given in Appendix 5E.

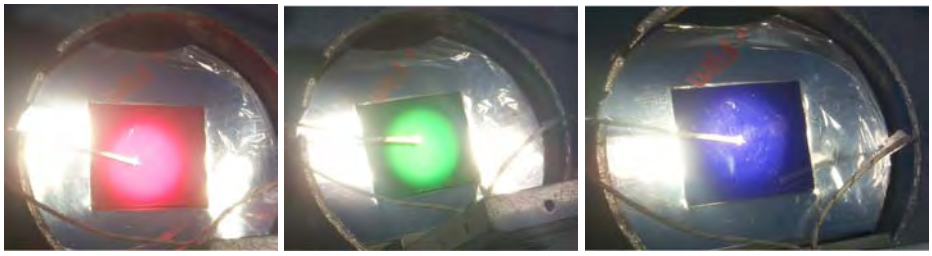

Figure 5.33: Exposed red, green and violet specimens

In the preliminary heat generation experiments, the duration for reaching the melting point of each colored specimen and the temperature change during this period were studied. The plots of the results obtained for each of the exposed specimens and a comparison graph are given in Appendix 5F. The initial experiments confirmed the findings from the spectrophotometric measurements. As expected, among all specimens the thermocouple in front of the black PMMA specimen recorded the fastest response (~11 seconds) in achieving the melting temperature and the thermocouple behind the specimen recorded no change. By contrast, the thermocouple in front of the transparent PMMA recorded the longest duration to reach the polymer melting temperature (more than 60 seconds).

Among the colored specimens, the thermocouple in front of the green PMMA

had the quickest response (~17 seconds) and the thermocouple in front of the yellow PMMA (~29 seconds) had the slowest (see Figure 5.34). The readings of the thermocouples in front and behind all specimens during the first 10 seconds of exposure are given in Figure 5.35 for comparison.

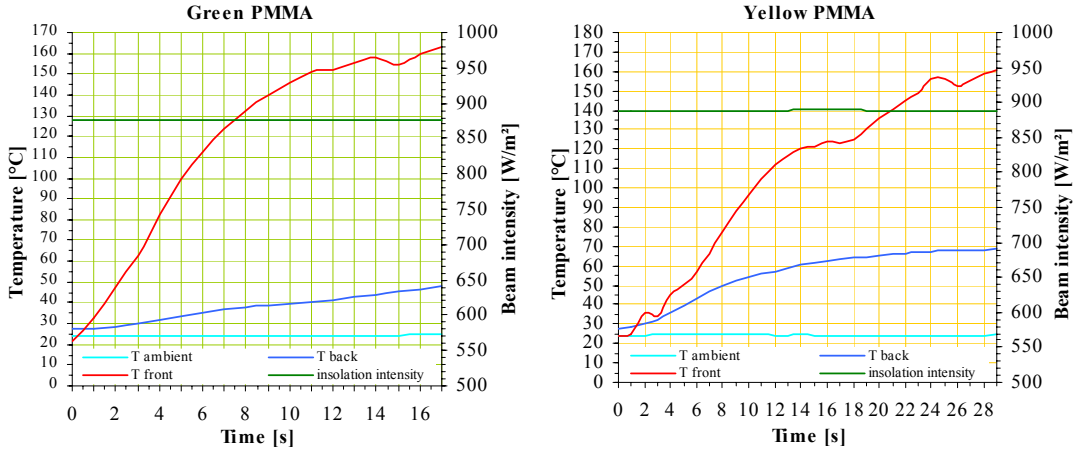

Figure 5.34: Temperature variation during exposure for green and yellow PMMA at the focus

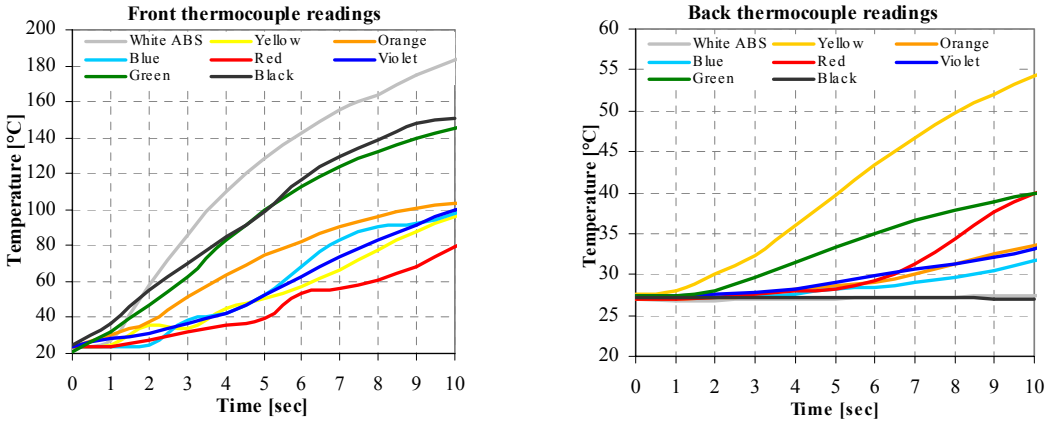

Figure 5.35: Temperature variations for all specimens

The results obtained in this experiment confirmed the previously observed trend that among the colored samples the green PMMA was the fastest to achieve melting temperature and the yellow was the slowest. However, this may be due to the back reflectance from the polymer to the unexposed surface of the thermocouple tip.

5.5 Conclusions

The experimental evaluation of the relevant meteorological data revealed that on a clear day the spectral distribution of incident solar radiation varies insignificantly. Also, the beam insolation intensity varies steadily by only 0.83 W/m^2 (0.1%) per minute on average, and its maximum value, though variable throughout the year, stays between 800 and 1000 W/m^2. Thus, conducting of experiments with an

intensity relatively constant for their duration is possible. Another important outcome from these evaluation measurements was the conformation that a certain amount of the available UV insolation component (as shown in Figures 5.7 to 5.9) is propagating with the insolation re-emitted from the mirrors.

Using this data, the evaluation of the optical and thermal characteristics of the SEC facility has proved that utilizing the available insolation as a source for polymer processing is feasible. The calculations of the variable parameters of the SEC system discussed in this chapter have demonstrated that the output power could be sufficient for the different applications proposed.

One significant finding was that the combined concentration achievable by the SEC when complemented with a CPC remains relatively constant for any of the calculated points on the rim rings. Another important result was that the extreme angle of the cone of concentrated light beam at the Cassegrainian final focus could be expressed using Equation 5.16 i.e. $\phi = 2(\alpha - \beta)$.

It became evident from the measurements that in polymer processing the temperature distribution in the polymer is extremely complex and has a significant effect on the material properties. In addition, the temperature distribution in the bulk of the material is usually non-uniform. Being of transient nature, the temperature changes in the polymer occur on relatively short time scales and their measurement is very complicated. Although typically the energy emitted by a polymer is not evenly distributed in the IR spectrum, the use of a remote temperature IR radiometry during the polymer processing would be more appropriate and is considered for future work.

Furthermore, the laboratory assessment of the radiation characteristics and other material properties, complemented with outdoor measurements, reported in this chapter have been shown to be sufficient for predicting the temperature variation during exposure. Good correlation was found between the results from the spectrophotometric measurements and those obtained during the outdoor heat generation experiments for the transparent and colored thermoplastics. The most absorbing colored material was found to be the green (94.24%) and the least absorbing - the yellow (69.66%).

The evaluation of the outdoor environmental and SEC facility capabilities, radiation material characteristics and the determination of the SEC variables confirm the practicability of the proposed applications. Further modeling of the SEC facility systems and the material irradiation process are described in the following chapter.

CHAPTER 6.
MODELING

6.1 Introduction

The evaluation of the radiation and material characteristics and properties, as well as the capabilities of the SEC facility, discussed in the previous chapter, has been essential for the modeling, systems development and studied applications. This chapter summarizes the modeling work proposed and performed in different stages during the development, modification and experimental testing of the SEC facility with its components and applications. Generally, the modeling has been involved in three principal areas as follows:

- Optical ray tracing and combined 3D modeling (see Sections 6.2 to 6.5)

Most optical imaging problems are typically solved using simple geometrical wavefront or ray models. The optical ray tracing 3D models and analysis of the SEC systems created using Optica with Mathematica, OSLO and ZEMAX software have been necessary for the development, experimental evaluation and modification of the facility. On their basis, combined 3D computer models integrating ray/cone tracing with the mechanical components were developed to simulate the whole SEC facility and predict the image size, location and energy distribution. These models were individually created (using AutoCad and SolidWorks) for the different configurations comprising imaging and non-imaging auxiliary optics.

- Radiation–polymer interaction modeling (see Section 6.6)

To enable the prediction of the heating/joining process, mathematical modeling of the energy transfer, radiation absorption and heat generation and transfer in the irradiated polymer was required. To model the electromagnetic energy transfer, the amount of the absorbed radiation and the overall heat gain and losses in the system, a simple analytical model was developed. Consequently, the propagation and transfer of the absorbed energy/generated heat exchange through the irradiated polymers were modeled. While the first model is intended to predict the temperature variation and duration for attaining the glass transition state of the irradiated polymer, the second model simulates the temperature distribution during through-transmission polymer joining.

- Empirical modeling of the polymer joint strength (see Section 6.7)

Since the initial joining experiments have shown that variable tensile strengths of the joints have been achieved, an attempt to predict the most probable joint strength for particular ambient parameters has been initiated. For this purpose, a simple linear statistical model of the system response was developed in collaboration with the Mokpo National University.

This chapter begins with a description of the 3D optical ray tracing models, followed by analysis, evaluation and optimization of the image at the Cassegrainian focus. Next, the 3D ray tracing computer models integrated with the mechanical components of the SEC, as well as the modeling of a non-imaging third stage concentrator are discussed. Description of the mathematical models of the polymer irradiation process and their experimental verification follows. In conclusion, the modeling of the polymer joint strength is summarized.

6.2 Optical ray tracing models

Since the optical performance of any imaging solar concentrator is often considered to be paramount for the efficient solar energy conversion, a detailed study and modeling of the optical characteristics of the SEC systems was performed.

Although there are numerous software programs for ray tracing in various optical systems, only a few are capable of producing ray traces through a Cassegrainian telescope. Initially, the Optica package, a high-level component-structuring language extension of the Mathematica software, was used for modeling, ray tracing and rendering of the optical systems explored in this research. Later, the OSLO EDU and ZEMAX software were used for image analysis and optimization.

6.2.1 Ray tracing model of the Cassegrainian solar energy concentrator

The initial optical modeling of the SEC was performed, as mentioned above, with Mathematica adapting the capabilities of Optica for ray tracing and especially for design of an astronomical telescope. The starting point for the optical modeling was the building of a three-dimensional model of the Cassegrainian concentrator. It was a prerequisite for the proper ray tracing modeling, design and alignment of the auxiliary conventional imaging as well as the non-imaging optics. The steps of the modeling process and a description of the program code written for defining and analyzing the Cassegrainian concentrator are given in Appendix 6A, Section 6A.1.

6.2.2 Optical ray tracing models of the SEC with conventional imaging optics

In order to model a beam transmitting means via conventional imaging optics, additional ray tracing optical models of the SEC using the available auxiliary doublet lenses were developed. The created optical models of the Cassegrainian concentrator with the auxiliary optical components were also necessary for the development of the 3D models of the SEC facility (see Section 6.4).

Various arrangements were explored for transmitting the concentrated solar energy at the principal Cassegrainian focus to the working site. Initially, a temporary proposed auxiliary periscope optics for transmitting through the body of the concentrator, comprising conventional optics was explored. However, the initial optical path to the application location was relatively long, containing a number of conventional doublet lenses and beam bending mirrors. This led to significant loss of power, additional limitations on spectral range use and relatively complicated operation.

Several optical models were created to facilitate the three different applications of the SEC facility explored. In all of them the final focusing doublet lens had a relatively low F/number or short focal length. During the course of the research, the optical path has been shortened gradually, exploring the feasibility of different locations for the working site. The most suitable arrangement preserving the existing components and used for the joining experimental tests is shown in Figure 6.1. The rest of the modeled arrangements and descriptions of the program codes written are also given in Appendix 6A, Sections 6A.2 to 6A.5.

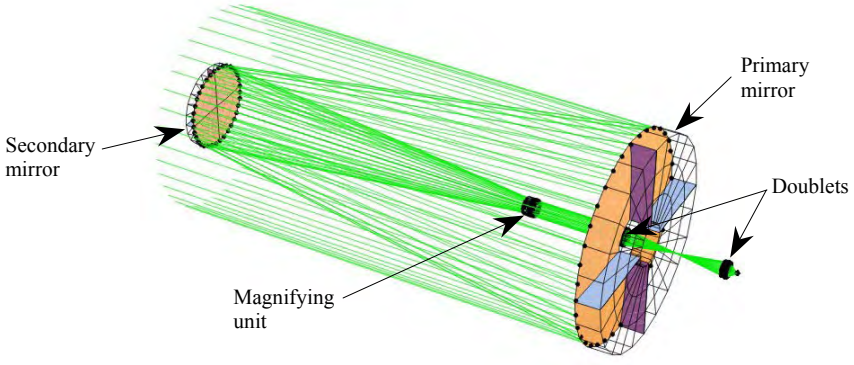

Figure 6.1: Rendered image of the Cassegrainian concentrator with magnifying unit and two doublet lenses

On the basis of these optical models most of the actual optical components of the SEC systems were built, experimentally evaluated and modified continuously during

the research. The modifications of the SEC facility are discussed in Chapter 7 and the experimental studies in Chapters 8 and 9.

6.3 Image analysis and optimization

Generally most optical systems, and especially all imaging systems, are described by a sequential surface optical model which allows detailed analysis and optimization. For a two-mirror telescope typically three sequential surfaces are required – the first one serves as a central obstruction and the other two are primary and secondary mirrors. In this research, however, because of the auxiliary optics required, the SEC facility optical model included up to 14 sequential surfaces. Usually a designer of a Cassegrainian telescope must know the parameters that need to be maintained stable in order to control the variables based on them.

The Cassegrainian arrangement used in this research was designed and built by a third party, thus it was necessary to model its characteristics in order to analyze and evaluate them, as well as to align the auxiliary optics and optimize the system optical performance. The purpose of this section is to describe this process of image analysis and possible optimization by maintaining the overall characteristics of the built components, allowing modeling of the extended source and alignment of the auxiliary optics.

6.3.1 Image analysis and evaluation

Although the initial ray tracing with Optica was useful, further insight of the wavefront and spot characteristics, as well as the point spread function (PSF) at the principal Cassegrainian focal spot was possible with the ray tracing capabilities of OSLO. Adapting the Hubble space telescope feature, the SEC parameters, discussed in the previous chapter, were used to construct and analyze the model in OSLO in a highly interactive mode, as shown in Figure 6B.1 in Appendix 6B.

Ray trace analysis for the SEC model was performed using three wavelengths: 0.39, 0.535 and 0.9 μm. These wavelengths represent the range predominantly utilized by the SEC. The result obtained after performing ray tracing is shown in Figure 6.2. Unlike the modeling with Optica, in this ray tracing, in addition to the central rays from the sun, the extreme rays from the bottom of the sun (represented in blue) were also included. This allowed the angular height of the sun and the height of the solar image to be taken into account.

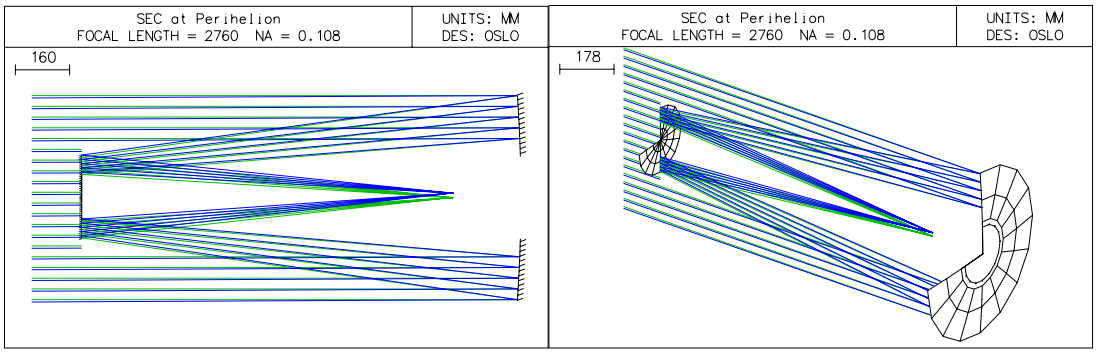

Figure 6.2: Ray trace model of the Cassegrainian concentrator

Using some of the analysis tools of OSLO, an evaluation of the image quality was performed by calculations of ray aberration curves, spot diagrams, wavefront and the point spread function. Figure 6.3 presents the ray trace analysis for the SEC model. In this thesis it has been assumed that during the experimental studies, the source (the sun) is maintained symmetrically around the SEC optical axis since a tracking device has been used. Therefore, even for a reflecting optical system it can be expected that the astigmatism is relatively small. As can be seen in Figure 6.3, the astigmatism for the SEC model is less than 160 μm.

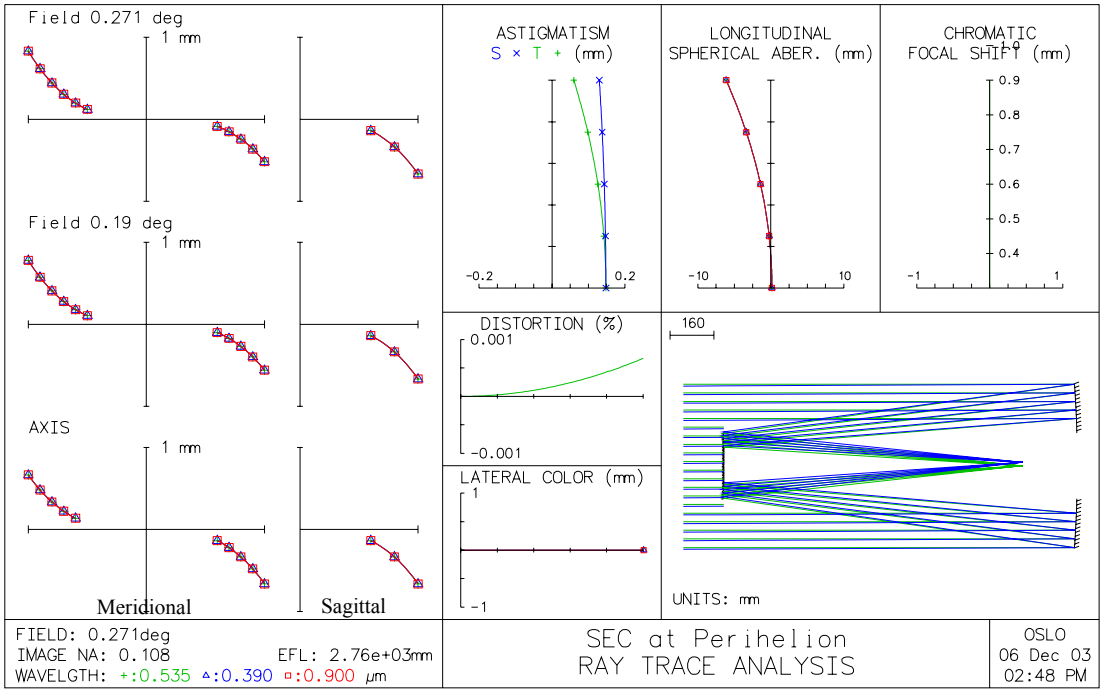

Figure 6.3: Ray intercept curves analysis for the SEC

The ray intercept curves for the three field points shown on the left side are almost identical. The reason for this is that the sagittal cross section of the telescope seen from the object point does not change as rapidly as the meridional section when

the object point is moved off axis. The SEC image is not perfect since a system that forms a perfect geometrical image would have the meridional ray intercept curve as a straight line along the abscissa.

In general, if the incident light is not confined to the paraxial region, some light rays may deviate from the common focal point causing spherical aberration. The longitudinal spherical aberration then can be defined as a distance between the axial intersection of a ray and the principal focal point. Typically, a long focal ratio telescope would be expected to have smaller aberrations than a shorter focal ratio design. It can be seen from Figure 6.3 that although the reflecting surfaces are spherical, the longitudinal spherical aberration in the defined wavelengths for the SEC is not significant.

Also, it can be noted that the longitudinal displacement of the (paraxial) focus as a function of wavelength (i.e. the chromatic focal shift) is zero, which is logical for a reflecting optical system. Perhaps it was not necessary to use several wavelengths since mirrors generally are not a source of chromatic aberration. Similar to an astronomical telescope, such system should have an uniform lateral magnification over the entire field in order to be free of distortion. From the ray trace analysis seen on the graph it is evident that there is very small positive (pincushion) distortion, less than 0.001% at the edge of the field and 0% on axis. Although having a relatively larger field angle compared to astronomical telescopes, the distortion for this system was found to be extremely small.

Even if all components of such an imaging system are considered to be perfect, the resolution achieved by the imaging process will still be limited by diffraction. The diffraction pattern in the final image would affect its quality as well as the concentration efficiency. Because of this, to examine the limits imposed by diffraction, spot diagram analysis was performed. The resultant pattern, representing the intersection points of the rays (traced through the system) with the image surface, is shown in Figure 6.4 (left).

However, since the spot diagram does not entirely represent the distribution of the irradiance at the image surface, the direct integration-based PSF analysis was used to examine the intensity distribution at the image surface. It should be noted that the PSF represents the flux distribution due to diffraction in the image of an ideal point-like source accepted by the optical system at the specified wavelength. The PSF plot is also shown in Figure 6.4.

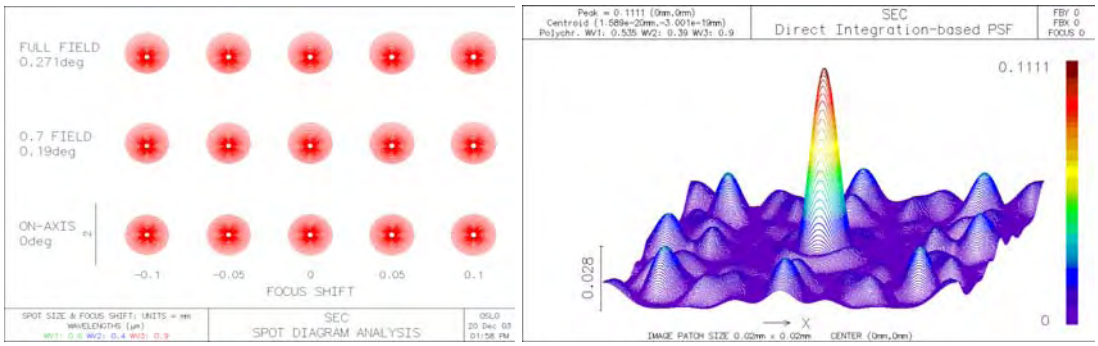

Figure 6.4: Spot and PSF analysis of the SEC

It can be seen that the further the spot is from the axis, the more asymmetrical it becomes relative to its center, which is logical since the extreme rays are at the maximum inclination. However, there is no significant difference in the spot profile on the axis, in the middle and full field. The second plot shows a distinct central peak indicating that the energy density is relatively centralized.

The beam profile becomes more complex in amplitude and phase, as the wavefront propagates towards the image plane, and the wavefront expands over an extended space. Therefore, for the description of the wavefront and image quality, it is critically important to evaluate the phase error in the effective secondary aperture. For this reason, the geometric wavefront formed from the rays in the spot diagram was analyzed.

Theoretically, when a geometrically perfect point source of radiation emits into free space, any pulse would produce a corresponding spherical wavefront centered upon this source. The wavefront aberration or optical path difference (OPD) represents the deviation of the actual wavefront from this reference sphere or the phase error of the wavefront forming an image.

Peak to valley (P-V) error is the maximum wavefront error, however it does not specify the area over which this error is occurring (OSLO Reference Manual 2001). Because the P-V error is calculated from only two data points out of possibly thousands, sometimes an optical system with a large P-V error may in practice perform better than a system having a small P-V error. If the error corresponds to only a very small part of the aperture, even a relatively large wavefront error may have little effect on the optical system performance. This is why the RMS (root-mean-squared) error, which is a statistic calculated from the evaluated data, generally gives a better indication of the optical quality of the system. While the P-V error specifies the difference between the 'highest' and 'lowest' parts of the wavefront, the

RMS error shows how much the 'height' varies across the entire wavefront.

Figure 6.5 shows the wavefront analysis results illustrated as false-color interferograms and sliced-contour representations of the image-space wavefront for each data field point.

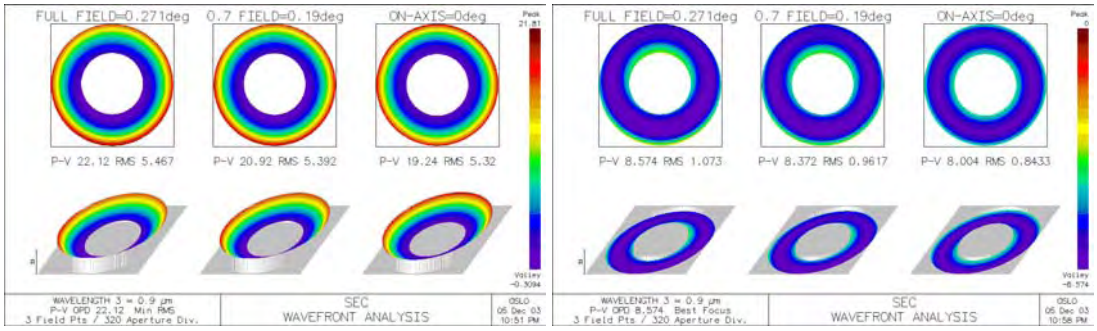

Figure 6.5: Wavefront report with wavefront reference point for minimized RMS on image surface and for best focus

Note: RMS analysis determines the optimal reference sphere center on the image surface after applying the Focus shift feature. The reported RMS OPD is the square root of the wavelength-weighted average of the wavefront variances in each of the defined wavelengths. Best focus analysis determines the optimal reference sphere center on the image surface before applying the Focus shift feature.

It can be seen that again the wavefront profile does not vary significantly on the axis compared to that in the middle and full field. The left diagram shows that the minimum P-V error on axis is 19.24 wavelengths and the RMS error is 5.32 wavelengths. When the wavefront reference point is calculated for the best focus, the wavefront profile, as before, does not vary much across all fields. The P-V error on axis however has been reduced to approximately 8.04 wavelengths, and the RMS error to 0.84 wavelengths, as shown in the right diagram.

Nevertheless, the Cassegrainian concentrator itself is not diffraction limited as expected since the P-V OPD is in excess of one quarter wave (Rayleigh tolerance).

Further assessment of the SEC system optical aberrations was performed and the evaluation report is shown in Figure 6B.2 in Appendix 6B. As can be seen from the report, the third-order (Seidel) and fifth-order image aberrations such as spherical aberration, coma, astigmatism, Petzval curvature, and distortion, are not significant and the system is relatively well corrected.

Based on the above analysis, the image quality of the SEC optical system was considered satisfactory especially for the on-axis performance.

Furthermore, another common measure used to evaluate optical image quality for very high quality imaging systems is the Strehl ratio. The Strehl ratio is the ratio of peak focal intensities in the aberrated and ideal point spread functions (Born and

Wolf 1999). It is expressed as follows:

$$S \equiv e^{-2(2\pi\sigma)^2} \tag{6.1}$$

where σ is the RMS deviation of the wavefront measured in wavelengths. For moderate Strehl ratios (Strehl >~0.2) this parameter is in close proximity to the amount of energy in the core of the PSF.

As a solar concentrator the SEC is not a very high quality imaging system, thus a perfect image is not critical. The initial Strehl ratio of the SEC was computed to be approximately 0.058. Since this is considered a relatively small number, further analysis and optimization of the system were performed.

6.3.2 Optimization

Similar to the expert designer error function used in conventional optics, an acceptable error function was generated for the SEC using its input set parameters. The GENII error function of OSLO was used since it generates a compact error function using multiple items of data from each of the traced rays. The ray data is used in conjunction with classical aberrations to derive a set with 48 operands, of which 31 have a non-zero weight (as shown in Figure 6.6).

*OPERANDS

OP	MODE	WGT	NAME	VALUE	%CNTRB	DEFINITION
O 9	M	1.000000	Fnb diff	-1.4470e-09	0.00	OCM9/OCM8
O 10	M	1.000000	Focus diff	0.798283	0.00	OCM10/OCM4
O 11	M	1.000000	Axial DY	-99.703450	39.12	OCM11/OCM1
O 12	M	1.000000	Axial OPD	72.194113	20.51	OCM12/OCM6
O 13	M	1.000000	Axial DMD	--	--	OCM13/OCM6
O 16	M	1.000000	0.7 Dist	0.000327	0.00	OCM15/OCM14
O 17	M	1.000000	0.7 YFS	0.807850	0.00	OCM17/OCM2
O 18	M	1.000000	0.7 XFS	1.072413	0.00	OCM18/OCM2
O 19	M	1.000000	0.7 Coma	-3.398936	0.05	OCM19/OCM7
O 20	M	1.000000	0.7 DY U	-21.230498	1.77	OCM20/OCM3
O 21	M	1.000000	0.7 OPD U	35.816723	5.05	OCM21/OCM6
O 22	M	1.000000	0.7 DMD U	--	--	OCM22/OCM6
O 23	M	1.000000	0.7 DY L	30.769872	3.73	OCM23/OCM3
O 24	M	1.000000	0.7 OPD L	59.546356	13.95	OCM24/OCM6
O 25	M	1.000000	0.7 DMD L	--	--	OCM25/OCM6
O 26	M	1.000000	0.7 Sag DX	-17.971645	1.27	OCM26/OCM3
O 27	M	1.000000	0.7 Sag DY	3.499078	0.05	OCM27/OCM1
O 28	M	1.000000	.7 Sag OPD	28.908242	3.29	OCM28/OCM6
O 31	M	1.000000	1.0 Dist	0.000667	0.00	OCM30/OCM29
O 32	M	1.000000	1.0 YFS	0.323201	0.00	OCM32/OCM4
O 33	M	1.000000	1.0 XFS	2.103455	0.02	OCM33/OCM1
O 34	M	1.000000	1.0 Coma	-4.855818	0.09	OCM34/OCM7
O 35	M	1.000000	1.0 DY U	-9.080573	0.32	OCM35/OCM5
O 36	M	1.000000	1.0 OPD U	18.223313	1.31	OCM36/OCM6
O 37	M	1.000000	1.0 DMD U	--	--	OCM37/OCM6
O 38	M	1.000000	1.0 DY L	16.601437	1.08	OCM38/OCM5
O 39	M	1.000000	1.0 OPD L	42.044076	6.96	OCM39/OCM6
O 40	M	1.000000	1.0 DMD L	--	--	OCM40/OCM6
O 41	M	1.000000	1.0 Sag DX	-8.350946	0.27	OCM41/OCM5
O 42	M	1.000000	1.0 Sag DY	3.822402	0.06	OCM42/OCM1
O 43	M	1.000000	1 Sag OPD	16.673533	1.09	OCM43/OCM6

MIN RMS ERROR: 28.631202

Figure 6.6: Generated GENII error function

Because the GENII error function is designed to balance aberrations in a focal plane shifted from the paraxial image plane, the image distance was selected to be

the parameter that varies during optimization. The optimization advanced through only 3 cycles as shown in Figure 6.7

```
*ITERATE FULL  10
NBR      DAMPING    MIN ERROR    CON ERROR   PERCENT CHG.
  0   1.0000e-08   28.631202       --
  1   6.1580e-09   16.217781       --         43.356269
  2   6.1580e-09   16.217767       --        8.4706e-05
  3   6.1580e-07   16.217767       --        1.1740e-07
```

Figure 6.7: Iteration cycles during optimization

Ray trace analysis was performed to evaluate the optimized optical system and the result is shown in Figure 6.8.

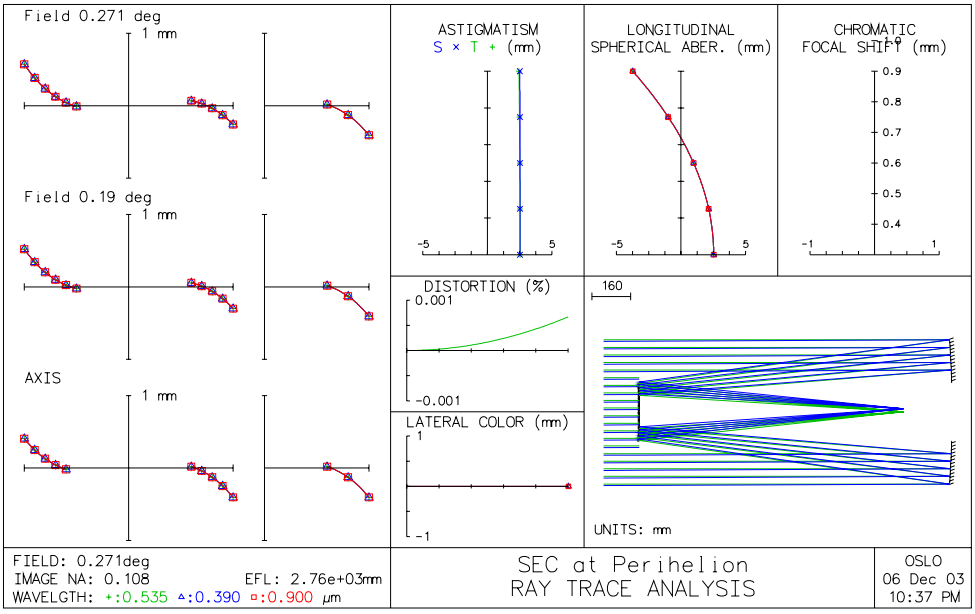

Figure 6.8: Ray trace analysis after optimization

Compared to the ray analysis before optimization (Figure 6.3), the ray intercept curves after optimization (Figure 6.8) show that the transverse aberration has decreased and become more centralized for all fields. The longitudinal spherical aberration has been reduced but at the expense of astigmatic aberrations. In addition, the optimization has led to a change of the location of the image field. It was moved by 2.39 mm towards the secondary mirror.

After the optimization the wavefront P-V and RMS optical path difference on axis (for minimized RMS) have been reduced to approximately 7 and 2 wavelengths respectively (Figure 6.9). However, the OPDs for best focus remained unchanged.

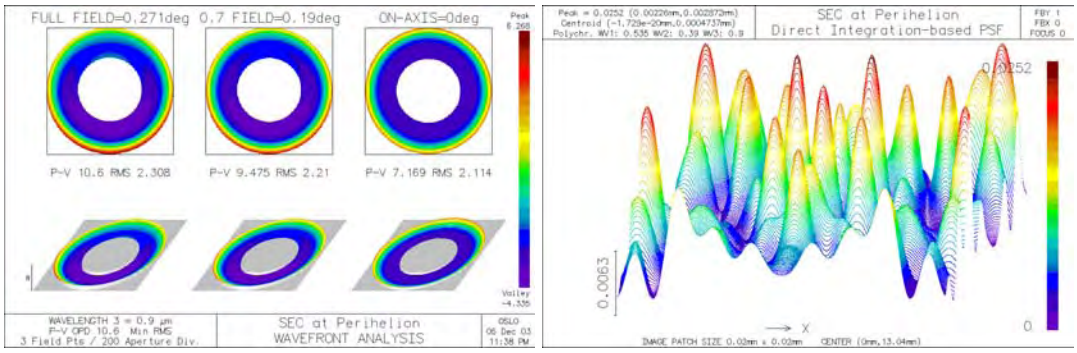

Figure 6.9: Wavefront and PSF analysis after optimization

As can be seen from Figure 6.9, although relatively smaller in value (4.4 times), the variation in the intensity distribution at the image surface obtained from the PSF analysis, appears more spread out.

To evaluate what portion of the total energy incident on the point image is contained within a circle with a given size, a computation of this energy distribution was used. Usually such computation is established on geometric (when spot diagram is used) or diffraction (using the PSF) basis. For this system, the geometric method was employed using the OSLO software.

The radial energy distribution (RED) or encircled energy for a circle of radius '*a*' is computed by the following equation:

$$\mathrm{RED}(a) = \int_0^a \int_0^{2a} \mathrm{PSF}(r',\theta')\, r'\, dr'\, d\theta' \qquad (6.2)$$

where PSF is the point spread function considered as a function of two image plane coordinates, the polar coordinates r' and θ'.

The results before and after optimization are presented in Figure 6.10.

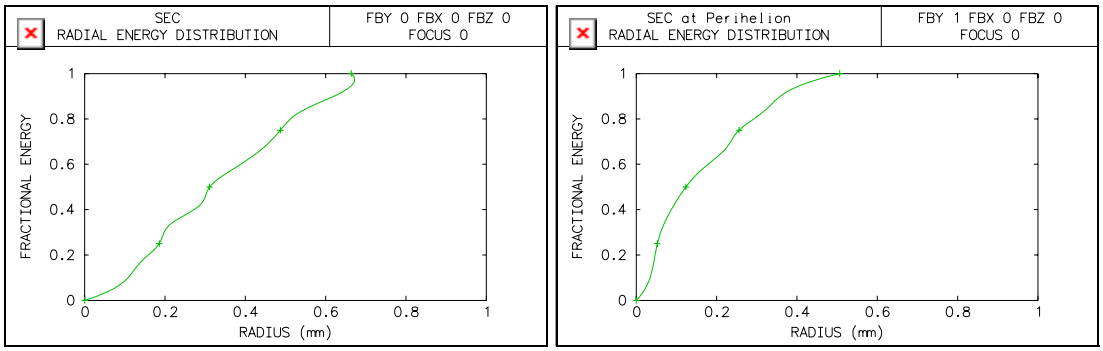

Figure 6.10: Energy analysis before and after optimization

The graph on the left suggests that most of the energy is included within a maximum radius of 0.7 mm. The optimization has led to concentration of the energy

in a relatively smaller radius of 0.5 mm. As there are no flat segments on the curves it could be interpreted that there are no dark rings in the energy pattern i.e. there are no radii with energy disruption for the chosen spot size.

When further and more complex optimization was performed, it was found that the modification of the spherical surfaces could lead to achieving a Strehl ratio of 0.96, considered in optics as very good. The result from this optimization analysis, including the corresponding conic constants, is shown in Figure 6B.3 in Appendix 6B. On the other hand, a wavefront with less variance would have been achievable if a classical Cassegrainian with parabolic primary and hyperbolic secondary mirrors was used, as shown in Figure 6B.4 in Appendix 6B.

From the analysis and optimization it is evident that there exists a potential for further improvement of one or more system characteristics. However, its implementation is beyond the scope of this thesis and has been considered for future work in which Zernike and/or third-order Seidel calculations could be explored. Fourier analysis of the wavefronts could be used to study the diffraction effects and further investigate the image characteristics.

The optical models developed with Optica and OSLO were incorporated on a later stage in more complex and precise three-dimensional AutoCad models of the SEC systems, which are discussed in the following section. The actual detailed three-dimensional layouts including the optical, focusing and other mechanical components used in the polymer processing experiments are also included below.

6.4 Combined three-dimensional computer modeling of the SEC facility systems with ray tracing

Although the optical models, initially developed with Optica using the Mathematica software, have been very useful for the overall ray tracing through the optical components of the SEC facility, they have been based on a point source. This point source approximation of the sun is often assumed so when a perfect paraboloid is used, the incident radiation is focused onto a point. However, due to the finite size of the sun even a perfect paraboloidal mirror cannot concentrate the sun rays exactly into the focus of the parabola. On the other hand, the spherical surface being the most common in optics is assumed as the default since it is most easily produced. Still, the majority of spherical surfaces introduce spherical aberrations.

In addition, as it has been indicated in Chapter 2, the distance between the sun

and the earth is variable throughout the year and the sun image size varies with it. With the exception of the flat mirrors, most reflecting concentrators used in solar energy utilization have reflecting surfaces with variable radius of curvature. The efficiency of the reflector could be also affected by the orientation of the plane, formed by the incident ray and the normal to the surface.

In this research two-axis tracking has been used and only in the initial optical models, described in the previous section have parallel rays from a point source at infinity been traced. For more accurate representation of the finite light source used in this study, more detailed and realistic 3D combined model of the actual ray tracing and SEC facility components has been necessary. This 3D model has been a valuable tool during the process of many modifications required during the research.

6.4.1 Computer model of the SEC

The most common surface used in optics is the spherical refracting surface. Modeled initially with Optica (discussed in Section 6.2), the conventional optical components used for beam transmitting and focusing were modeled in more detail using the AutoCad and SolidWorks software. The underlying premise here is that by using design tools such as AutoCad or SolidWorks, more precise models than those produced with Optica are achievable, allowing inclusion of mechanical components in the model. Geometric modeling was also preferred because of its ability to quickly and interactively change the viewpoint and generate a rendered image.

The use of spherical lenses and doublets is the most studied area in optical engineering. In many ray tracing programs including Optica, paraxial meridional rays are most often traced through spherical refracting lenses. In comparison, the tracing of skew rays is a more complex mathematical task. In this work, since the lenses are used as additional optical components, the ray tracing of the non-parallel skew rays re-reflected by the secondary mirror was performed before the implementation.

Thus, it was necessary firstly to model the Cassegrainian concentrator since the first two stages are the primary and secondary reflectors. To achieve this, combined 3D models of the Cassegrainian and all relevant mechanical components of the SEC facility were created in AutoCad and SolidWorks. Although it has not been the purpose of this research to develop a method for ray tracing, a ray tracing technique based on the “edge-ray principle” has been derived (Section 5.3.2.1) and used here.

Because of the spherical nature of the sun as well as the mirrors, radial symmetry has been considered and a 3D array has been used to illustrate the combined 3D model. In this modeling it is assumed that the image forming rays are incident with equal intensity at each point of the cross sectional plane of the primary clear aperture.

To describe the light cones originating from the sun, incident on any point of the accepting primary aperture, a central ray and two extreme geometrical rays were traced. The rays originating from the specified object coordinates (top, center and bottom of the light source) were iterated to pass through the specified reference surface coordinates. For convenience, all paraxial rays from the center of the sun are shown in green, the extreme rays from the very top of the sun - in red and those from the bottom - in blue (see Figures 5.10, 6.11, 6.13 to 6.15).

In general, using the law of reflection (as shown in Figure 5.10), each ray was traced after its reflection from the primary and then secondary mirrors until its arrival at the principal focus. To achieve this, after defining the point of incidence and finding the normal at that point, the direction of the reflected ray was determined. This process was repeated when it was necessary to take into account reflection from another surface.

The traced rays were considered sufficient for determination of the size and orientation of the image and were drawn with the same color legend for each of the equally distributed points on the primary aperture (see Figure 6.11a). More details can be seen in Figure 7B.1 in Appendix 7B.

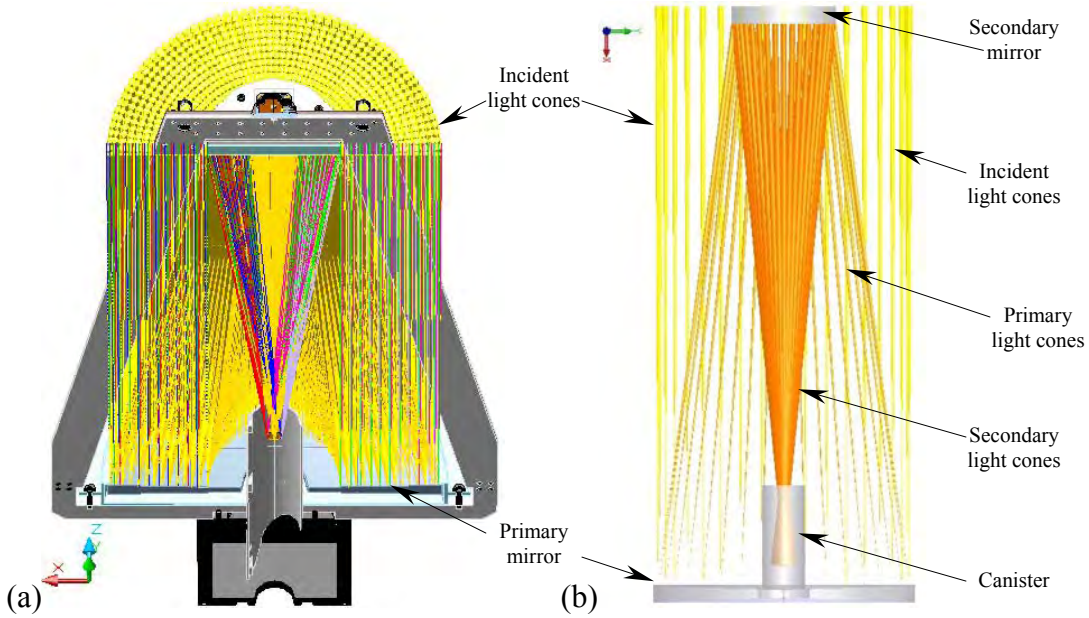

Figure 6.11: Modeling of the formation of the Cassegrainian focus of the SEC with rays and cones

In order to evaluate and visualize the maximum image size of the sun at the principal Cassegrainian focus, the angular size of the sun at perihelion was used. Figure 6.11b illustrates the cones of light arriving at each of the selected points representing the maximum angular width of the sun, used in the calculations in Chapter 5. Note that this figure only illustrates the 3D representation of the final model. Detailed descriptions of the SEC component dimensions and variable parameters used in the modeling are given in Appendix 5A.

By using the color code described above, the model indicated that the image of the sun at the principal Cassegrainian focus is inverted. It was also found that the central rays after the second stage cross the optical axis in a line rather than a point, probably due to spherical aberrations. As mentioned before, the focus of a spherical mirror is imperfect – the rays pass near but not exactly through the focal point. Only when the angle of reflection is small, do the rays converge to a tight focus.

6.4.2 Combined computer models of the SEC with imaging auxiliary optics

In order to validate and experimentally evaluate the optical ray tracing models created in Optica, combined and more detailed 3D models of the configurations, most suitable for the studied applications, were developed. For this purpose, three models of the optical components, integrated with most of the mechanical parts, were created with a scale factor of one and later verified with outdoor experiments.

Combined computer model with magnifying unit and three doublet lenses

The purpose of this 3D combined model was to integrate the optical components into the mechanical ones, fitting them in the necessary holding fixtures at the required positions. It was also used as a detailed drawing for the first modification of the SEC facility described in the following chapter.

The modeling of this arrangement was necessary for the modification aiming at the shortening of the originally proposed optical path by combining new and available components. The intention was to utilize the space under the trunnion box still allowing free access to the working site.

Based on the initial ray tracing model created with Optica and optimized later with ZEMAX, a combined 3D model was created in AutoCad to assist the system alteration. Figure 6.12 shows a schematic sectional and magnified view of the rays from the center of the source and the beam traced through the components.

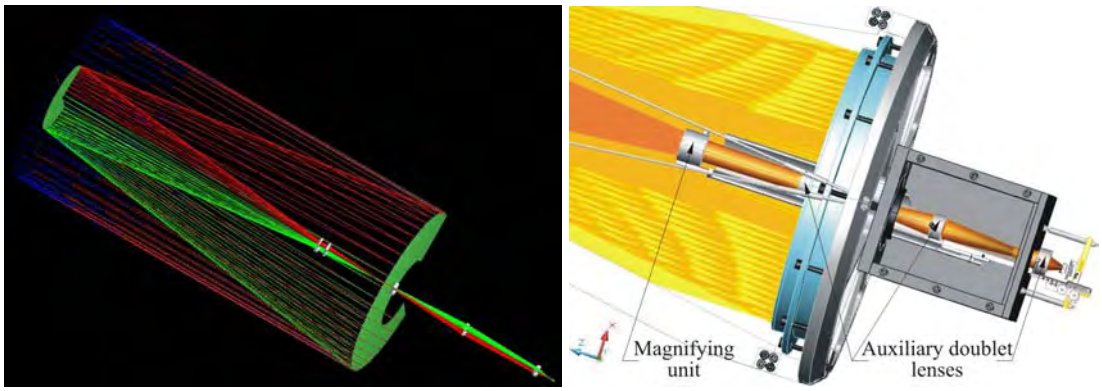

Figure 6.12: Optical model with magnifying unit and three doublet lenses in ZEMAX (left) and a combined computer model in AutoCad (right)

This model was used to establish how the image could be maintained through the optical path and further focused onto the working site. It was a very useful tool in obtaining the necessary optical layout, allowing the complementing of the existing optical components with new doublet lenses. It also ensured that the required focal length and image dimensions were achieved. On the basis of this model, the SEC facility was modified to allow performing the first successful butt and lap joining of clear and colored thermoplastics under the trunnion box.

Combined computer model with magnifying unit and two doublet lenses

To assist the second modification of the SEC facility aiming at further shortening of the optical path, the detailed 3D computer model was modified accordingly. The goal was also to utilize the trunnion box as an enclosed working site. In this arrangement the beam of concentrated solar radiation, re-radiated by the secondary mirror, was expanded by the magnifying unit and then further collimated and focused with only two doublet lenses.

The initial ray tracing models, created with Optica and optimized later with OSLO, were used as a basis for the combined 3D model, designed in AutoCad to facilitate the system modification. Figure 6.13 shows the sectional optical layout and enlarged view of the central and extreme rays originating from the sun and traced through the optical components.

Based on this model, the SEC facility was modified to allow performing successful butt and lap joining of clear and colored thermoplastics inside the trunnion box. This modification is discussed in the next chapter.

The modeling with OSLO has shown that further shortening of the optical path of the beam transmitting system is possible using two doublets without the

magnifying unit. This ray tracing model is presented in Figure 6B.5 in Appendix 6B.

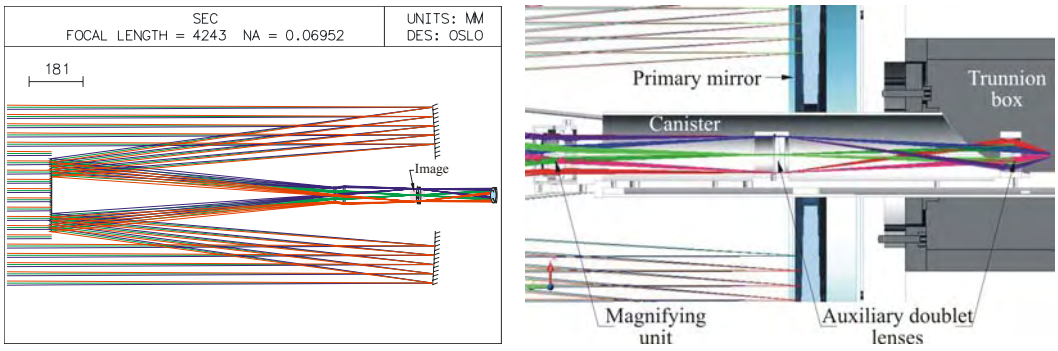

Figure 6.13: Optical model with magnifying unit and two doublet lenses in OSLO (left) and combined computer model in AutoCad (right)

Combined computer model with one auxiliary lens

While the previously described configurations were used for the implementation of the proposed practical applications of the SEC, the aim of this configuration was to model the arrangement for maximum power gain. The intention was to create a model with the shortest optical path, using minimum conventional auxiliary optics, thus predicting the maximum possible energy gain for certain ambient conditions.

To model the most powerful arrangement of the SEC facility, as discussed in Chapter 5 (see Figures 5.15 and 5.16), a single lens with a relatively small F/# was used. The initial ray tracing model was developed with the OSLO software using the SEC complemented with a singlet lens, type JMLCBX10632/000 with a diameter of 60 mm, a focal length of 50.8 mm and a thickness of 23.7 mm (see Figure 6B.6 in Appendix 6B). Using the OSLO analysis, the most suitable place for the lens location was determined by optimizing the image position for a minimum on axis spot size.

The ray tracing has shown that a lens with a relatively short focal length should be used in order to fit the optical path into the available space. Such a lens would increase the concentration further. This arrangement was considered feasible since the model revealed that the lens and working site could be located on the top of the canister pipe. On the basis of this optical model, using an available similar lens mounted in a suitable barrel and fitted into the system components, a combined 3D model was developed. The actual lens used was bi-convex with a 60 mm diameter and a 60 mm focal length. It was allocated, as calculated in OSLO, in front of the principal Cassegrainian focus for further concentration and final focusing.

Figure 6.14 shows a section and an enlarged view of the central and extreme rays traced through the optical components, complemented with the mechanical parts of the SEC facility. This combined computer model was generated in AutoCad with a scale factor of one and, both graphical representations were scaled down proportionally for the illustration.

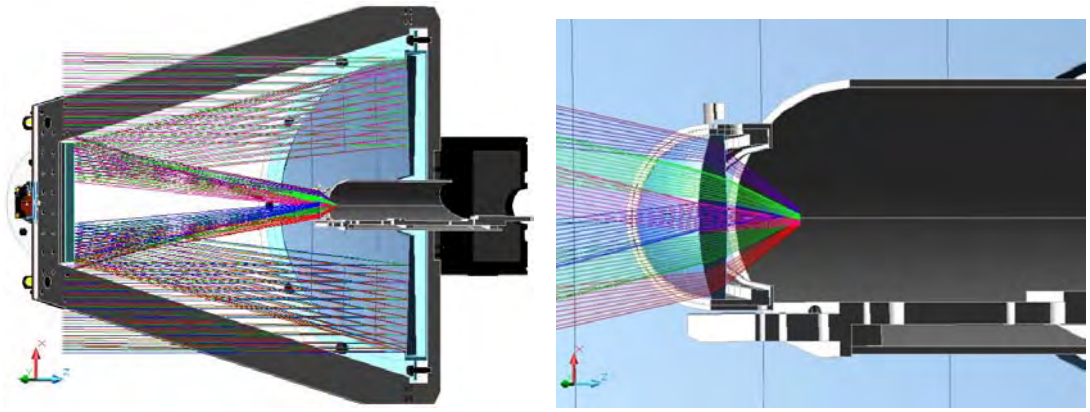

Figure 6.14: Model of the SEC with one auxiliary lens

The possible net power gain using this arrangement was estimated on the basis of the following assumptions: 800 W/m^2 insolation intensity at the primary aperture, 80% reflectance of each mirror and 4% loss at each lens surface. Then the resultant power captured by the system could be about 104 W.

This figure could become 143 W at maximum when the insolation intensity reaches 1100 W/m^2 (which has been measured during some of the outdoor experiments). The above estimated power has been considered to be the maximum net power achievable with the SEC, since in this arrangement the minimum number of auxiliary conventional optics (singlet lens) has been used. In a later stage the model was implemented experimentally with attaining of the highest achievable temperature above 700°C at the final solar image location on idle running.

6.5 Three-dimensional computer modeling with a non-imaging third stage concentrator

The performed spectral measurements of the available terrestrial insolation, as well as the concentrated beam insolation re-emitted from the primary and secondary mirrors, have shown that almost the entire terrestrial solar spectrum is re-emitted with minimal spectral losses. When auxiliary conventional optical components are used, they also increase the losses in power and impose limitations on the spectral range use. In order to decrease the former and minimize the latter, suitable non-

imaging, third stage concentrators were modeled and designed (especially for the purpose of the natural accelerated polymer ageing experiments). Two similar types, light cones and CPCs, were considered and ray tracing was used to predict the ray propagation through the system and the possible losses. The experimental development of these light concentrators is discussed in the next chapter.

6.5.1 Truncated cone concentrator

Initially, the simplest version of a third stage concentrator, a truncated cone, was modeled to accept the rim angle of the extreme concentrated light cone re-emitted from the secondary mirror. The entrance aperture of the third stage was made to coincide with the solar image and, the modeling was used to determine the most suitable position of the cone on the SEC optical axis. The tracing of the central and extreme rays was used to track the light propagation through the internal reflection. Figure 6.15 shows a skewed sectional view of the SEC complemented with a truncated cone concentrator and a closer view of the cone section with the traced rays.

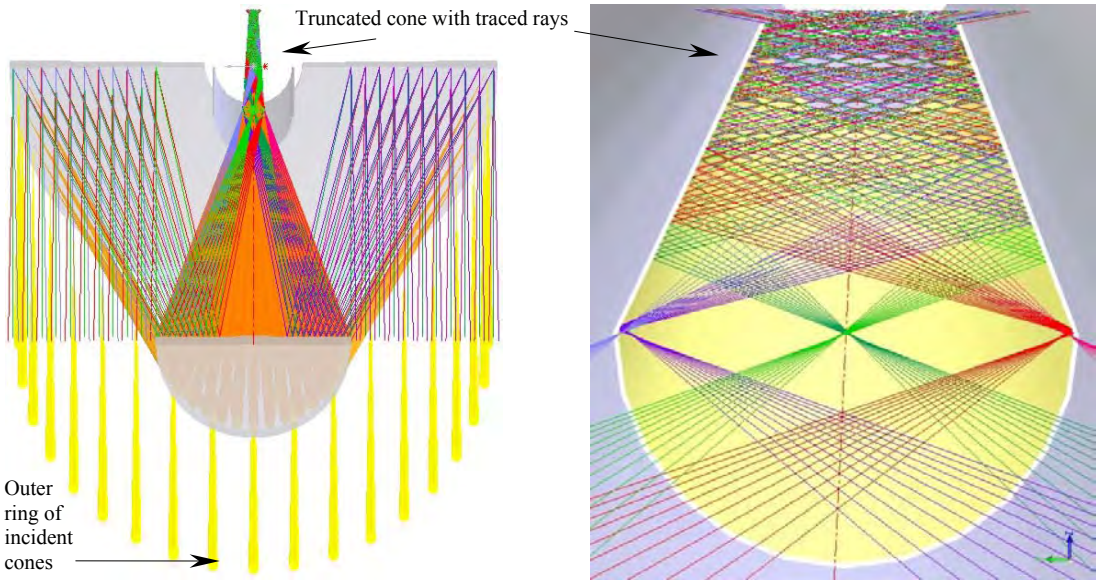

Figure 6.15: The SEC complemented with truncated cone concentrator

In this configuration the non-imaging concentrator is located near the focal plane of the Cassegrainian solar concentrator, having a relatively long focal length. Therefore, the common disadvantage of the longer length of the cone concentrator (as discussed in Chapter 2) has become an advantage when the cone has been used as a beam transmitting means. As can be seen from Figure 6.15, none of the traced rays have been returned back.

6.5.2 Compound parabolic concentrator

Similar to the models of the SEC with conventional imaging optics, an optical ray tracing model with a CPC was created using Optica, in order to determine its optimal position within the concentrator system. A detailed description of the program code written for the modeling of the Cassegrainian concentrator with the third stage non-imaging concentrator is given in Appendix 6A, Section 6A.6.

On the basis of this model, detailed 3D graphical representations of the SEC complemented with two CPCs with different sizes were developed using the SolidWorks software. These CPCs were designed with the maximum acceptance/ collection angle equal to the maximum rim angle of the light cone at perihelion (used as a critical angle for total internal reflection) and with corresponding diameters.

To assist this process, using the theory described in Chapter 2, Section 2.6.2, a deterministic model was created to calculate the CPC parameters such as entrance and exit apertures, length and geometric concentration. The results are given in Appendix 6C. Because it allows modification of the design in an interactive mode, SolidWorks has been very useful for exploring the feasibility of CPCs with different sizes and determining the actual dimensions and tolerances. Two of the explored CPCs have been considered and are discussed here. The first CPC (Figure 6.16) was intended predominantly as a beam transmitting device to transfer the concentrated power below the primary mirror.

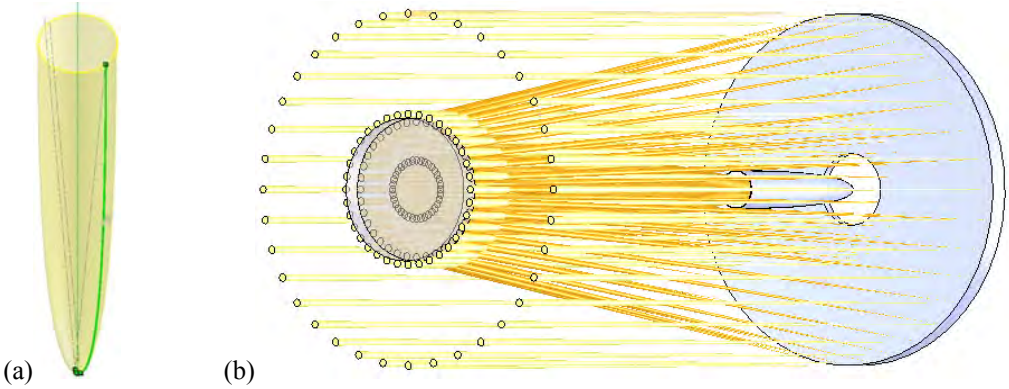

(a) (b)

Figure 6.16: Design and location of the first CPC

As mentioned in Chapter 2, the CPC is usually truncated because of its intrinsic disadvantage of being very long compared to the diameter of the collecting aperture. However, in this research this disadvantage of excessive length was used to overcome the design limitations of the Cassegrainian concentrator. That was achieved by modeling the beam transmitting CPC with a longer length and larger

entry aperture to allow acceptance of the skew rays caused by the tracking device errors and thus reducing the losses. This CPC was proposed for applications such as ageing which could utilize the not-collimated beam leaving the exit aperture.

Designed in 2D, the desired CPC shape is revolved along its central axis to obtain the 3D image, as shown in Figure 6.16a. It should be noted that in Figure 6.16b only two extreme outer and inner cone rings are shown and the secondary mirror is displayed transparent to allow visibility.

Figure 6.17 shows the CPC and light cone array under the secondary mirror. The two extreme light cone rings incident on and reflected from the secondary mirror are shown in Figure 6.17a in a plane perpendicular to the principal optical axis.

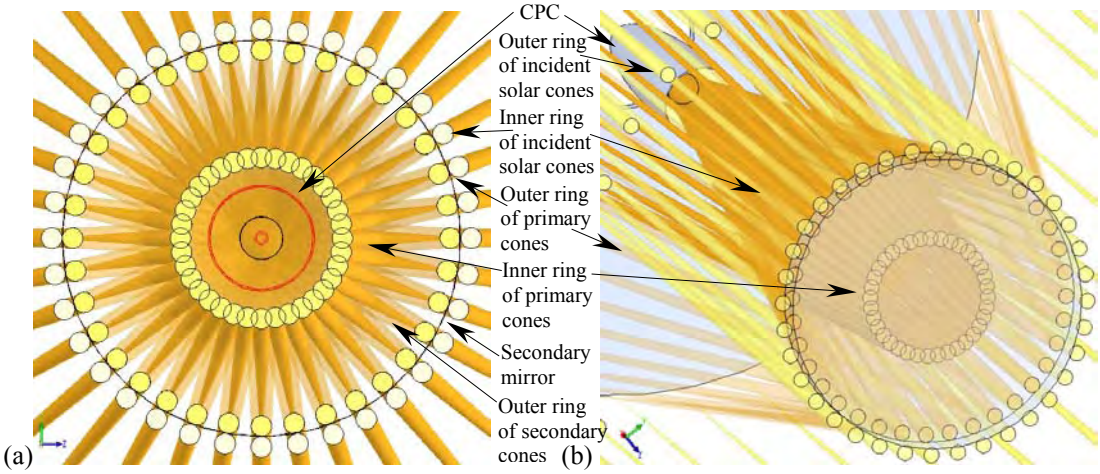

Figure 6.17: Sectional and perspective views of the first CPC with extreme cone rings

This model was created in SolidWorks with a scale factor of one but, for the illustration it was scaled down proportionally. An equal number of light cones in the outer and inner rings were assumed. Thus, compared to the outer, the inner ring of light cones would occupy a smaller area of the secondary mirror. As can be seen on both graphics, the images of the inner ring, unlike the outer ring, are overlapping which would lead to increased energy density in this region compared to the one formed by the outer cones. This finding was confirmed on a later stage during the experimental polymer joining. It has been also an important factor in the CPC design, since the inner cones (rays) form a relatively narrow incident rim angle and would require a CPC with a narrow acceptance angle.

Another disadvantage of the CPC is that it diverges the rays leaving its exit aperture. For this reason the second CPC was modeled with the same concentration ratio as the first one, but with a relatively smaller entry aperture and length, with the

intention to achieve high temperatures at its exit aperture. This CPC was proposed for use in applications such as welding which require more collimated beam and relatively higher temperatures. Sectional views of the SEC configuration and the second CPC with extreme light cones and rays traced through the optical components are shown in Figure 6.18.

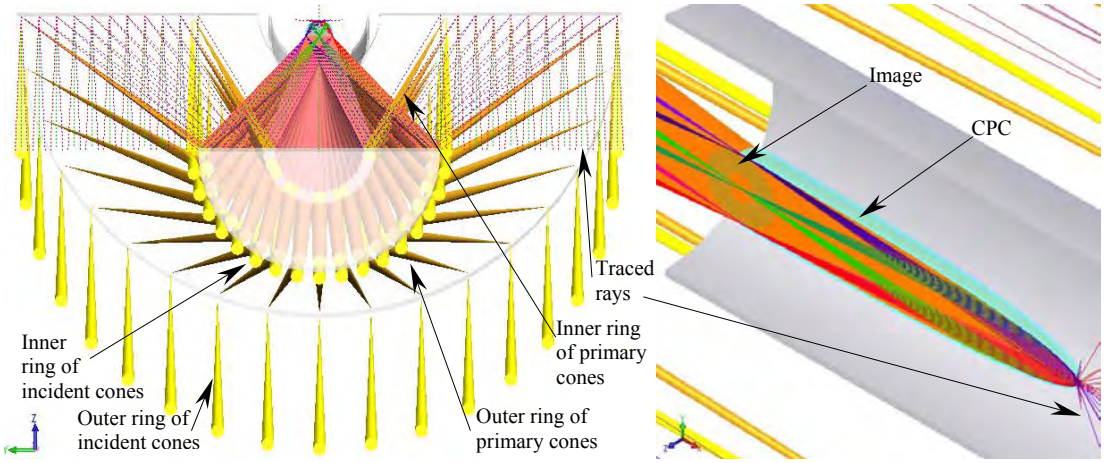

Figure 6.18: Perspective sectional views of the SEC and second CPC

The design parameters and the expected concentration ratios of both CPCs are given in Appendix 6C. As can be seen from the model, both of the discussed above CPCs not only have the same concentration ratios but have been computed with the same collecting angle. However, while the first CPC was proposed for more practical use as a beam transducer having relatively larger dimensions, the second one was intended for the SEC research purposes, requiring more precise tracking.

6.6 Mathematical modeling of polymer irradiation process

While the optical and combined SEC models proved useful in designing and optimizing the used optical components, they could not predict heat flow and heat build-up or the temperature increase as a function of time.

There have been numerous attempts to measure the actual concentration of solar radiation attained at the exit aperture, and the accuracy of this process is still a challenging task. A common problem is that most measuring instruments using sensors can only measure the fraction of the incident energy that falls on the sensor, but the spatial distribution of the concentrated irradiance usually varies across the receiver.

The majority of the proposed devices and methods are specifically designed or developed for a particular type of solar concentrator. In general, they are based on

direct measurement and/or indirect energy conversion calculations. The quite commonly used video camera technique typically requires a Lambertian target (Neumann and Schmitz 1998) and a careful alignment of the camera is crucial. The use of more advanced remote sensing IR pyrometry is complicated since the energy emitted by a polymer is not evenly distributed in the infrared spectrum. This problem is further complicated by the ambient conditions in which the outdoor experimental studies are conducted. Furthermore, typically the present IR thermometers are used for taking the bulk temperature not the polymer surface, and are more suitable for higher temperature targets above 120°C (Bendada et al. 2003).

Therefore, experimentation and additional analysis as provided by thermal heat flow modeling, were required. For this purpose, in this work two heat transfer models were developed and are discussed below. The goal of these models was to enable the prediction of the rates at which electromagnetic radiation is transmitted through the optical components of the SEC facility to the specimen surface, as well as the finally deposited and utilized energy. Also, these models were intended to predict the possible amount of the available radiation energy that could be absorbed by the specimen. The prediction of the energy rates and amount was necessary to determine the temperature distribution in the heat affected zone as a function of time.

6.6.1 Background

Electromagnetic radiation is emitted by all matter at any temperature above absolute zero (0K). The term heat is sometimes used to indicate sensible or latent forms of released or internal energy of a body. However, to avoid any confusion with heat transfer, in modern thermodynamics the internal energy of a body is often referred to as thermal energy. In this work the term electromagnetic energy transfer is preferred until this energy is absorbed and heat is generated, and consequently the produced thermal energy is referred to as heat, and the transfer of the thermal energy – as heat transfer.

The interaction of the uniformly distributed solar radiation incident on a body, as well as the radiation re-emitted from that body, are complex phenomena. They become even more complicated when concentrated radiation is utilized in ambient conditions and the radiation characteristics of the body are dependent on the radiation wavelength and direction. The spectral distribution of the available insolation may be different than that of the radiation re-emitted from any of the

reflectors. Typically the intercepted insolation occupies the shorter wavelength region unlike the re-emitted one, which is in the longer infrared wavelength region. During the radiation–polymer interaction a surface could gain energy by absorbing more or less of the incident radiation and could lose energy by re-emitting a certain amount of the absorbed radiation.

At the same time, the emittance of a real surface is not constant and varies with the temperature of the surface, as well as with the wavelength and direction of the emitted radiation. The surface finish i.e. rough, smooth, polished, also has an effect on the emittance. Thus, the radiation characteristics of the polymers used in this research were evaluated (see Chapter 5) and taken into account in the modeling.

The solar radiation–polymer interaction has been studied and used to explain the particular polymer processing taking place during the explored applications. To describe the initial butt joining of transparent PMMA with concentrated solar radiation, predominantly volumetric absorption has been considered (Figure 6.19).

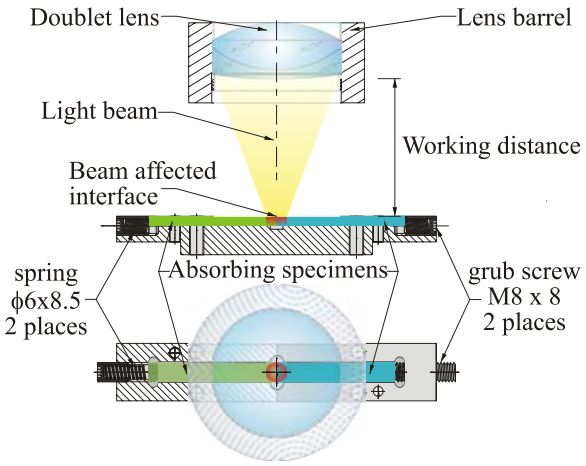

Figure 6.19: Schematic diagram of butt joining of transparent polymers

Although the radiation in general is a volumetric phenomenon, when incident on solids that are opaque particularly to thermal radiation, it is considered a surface phenomenon since the internal radiation does not affect the surface energy equilibrium. Typically, the propagation of uniform solar radiation through a transparent polymer is regarded predominantly as a volumetric phenomenon and the absorption considered insignificant. For example, a clear PMMA can be up to 92% transparent to the visible radiation. If the surface effect is negligible, the light beam could penetrate to considerable depths while interacting with the material, before any significant absorption takes place. The surface effect, in its strict sense, becomes significant only for totally opaque materials where the radiation is absorbed only at

the surface. Even then, the utilized solar radiation incident on the surface is believed to be absorbed within a very thin layer of a few microns from the specimen surface.

Although in this research a radiant type energy source is used, all three modes of heat transfer i.e. radiation, convection and conduction are relevant in the thermoplastic heating process and considered in the modeling. In general, the terrestrial beam solar radiation after two- or three-stage concentration is further focused on the exposed specimen.

Since in this study clear and colored polymers are processed with concentrated insolation, both the volumetric and surface phenomena of the solar radiation interaction with the material have been considered. However, unlike volumetric absorption of the uniform insolation in transparent polymer, the absorption of concentrated solar radiation is believed to be more complicated. Thus, the estimation of the affected volume becomes a challenging task, and in this case it was geometrically determined as shown in Figure 6.20.

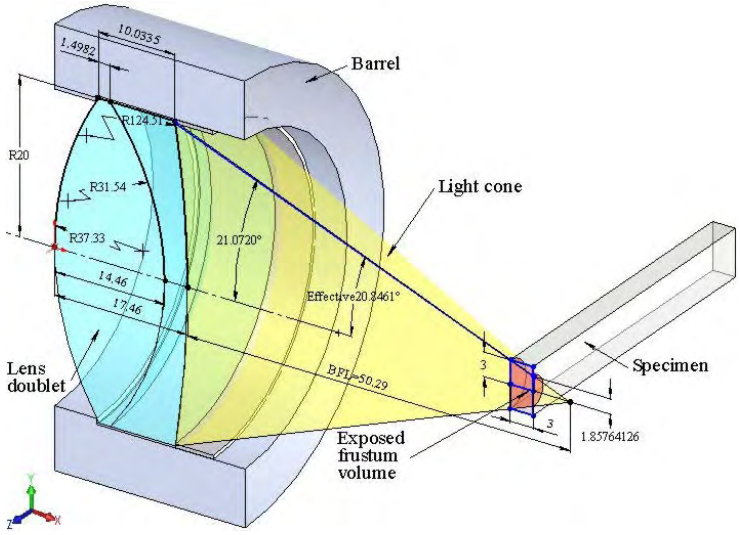

Figure 6.20: Concentrated light cone from last optical component and exposed volume

Although shown as a semi-frustum, the exposed volume of the transparent polymer may be a hyperboloid and further extended by scattering in the surrounding material which is not accounted for in the modeling.

Furthermore, being able to propagate deeper through the bulk of the polymer, the concentrated insolation could be volumetrically absorbed and generate thicker melting zone. The building of energy then is achieved gradually by further absorption of radiation rather than by conduction through the polymer. In the first model, however, the three types of losses are calculated independently and the

corresponding coefficients are set to be adjustable for materials with different conductivity.

In through transmission, when radiation strikes an opaque component after propagating through a transparent one, a certain amount of the radiation energy is re-emitted back towards the joint interface by the opaque component intensifying the heat generation. The transparent component becomes good trapping matter for the rising heat, generated on the opaque (colored) polymer surface, since the polymer has a relatively poor thermal conductivity. In this process the heat conduction in the transparent specimen is a function of the temperature gradient and a relatively small portion of the absorbed energy reaches the surface of the transparent component.

This is the case in lap joining of a transparent over colored polymer, where the concentrated beam is focused on the upper surface of the joint interface of the opaque specimen, after being transmitted through the upper transparent specimen. This process is illustrated in Figure 6.21.

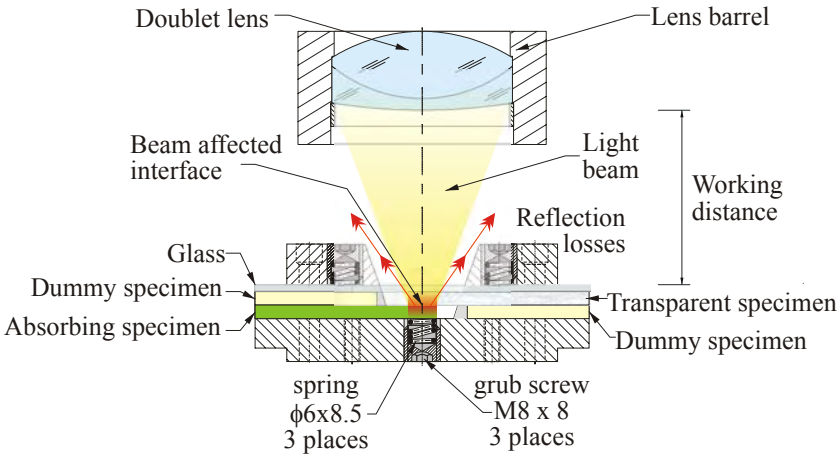

Figure 6.21: Lap joining process

In this process because the beam is relatively narrow and the rays are almost normal to the specimen surface, it is believed that only a relatively small amount of energy (~4%) is rejected. Based on the spectroscopic measurements, it is assumed that another ~4% from the concentrated solar radiation that has propagated through the transparent specimen is also reflected when it strikes the opaque surface of the bottom specimen. If not obstructed, most of the radiation is believed to be transmitted (~92%). In butt joining of transparent specimens, even though only a small portion of the incident solar radiation (~3.7% for PMMA) is absorbed in the exposed volume, it could rise the temperature of this volume to its melting stage.

Most of the polymers used in this research i.e. white, black and colored, are opaque to the utilized concentrated, predominantly visible solar radiation, and for them the radiation absorption/emission is regarded to be a surface phenomenon. However, except for the black and white, they are not entirely opaque to the radiation in the utilized range. It is believed that when concentrated solar radiation, containing predominantly white light with little near IR radiation, is incident on an opaque material it is absorbed on its surface. The surface is then assumed to contain no volume nor mass and thus no energy. Also, even if additional radiation is generated in and emitted by its interior regions, it does not reach the polymer surface. Therefore, the energy content of the surface can be considered constant during this process and the energy balance relation for the surface can be expressed as:

$$\dot{E}_{in} = \dot{E}_{out} \tag{6.3}$$

As discussed above, during its propagation even through a highly transparent polymer such as PMMA, the radiation beam would be attenuated due to absorption. Theoretically, while propagating through a layer of thickness *dx,* the decrease of the monochromatic radiation intensity, imposed by Beer's law, is proportional to the intensity itself and the thickness *dx*. It is expressed as:

$$dI_\lambda(x) = -k_\lambda I_\lambda(x)dx \tag{6.4}$$

where k_λ is the spectral absorption coefficient of the medium in m^{-1} (Figure 6.22).

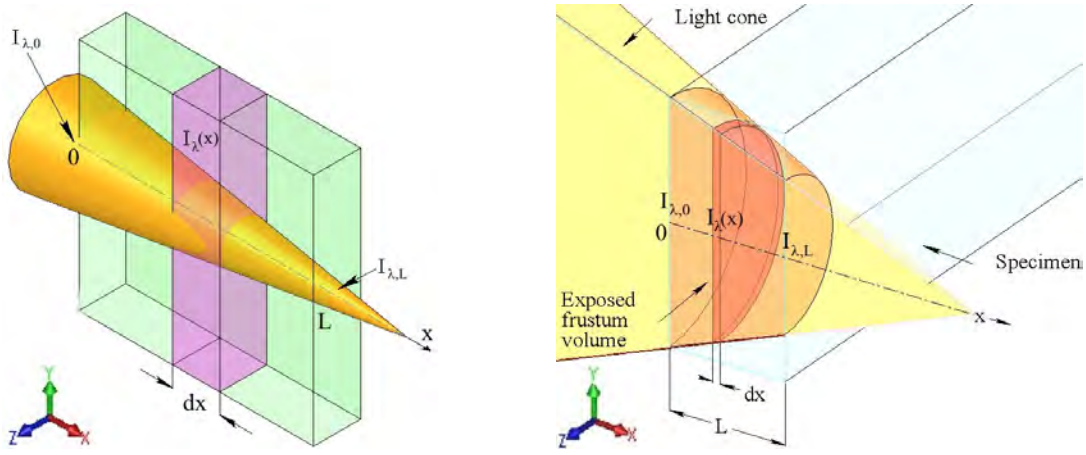

Figure 6.22: Attenuation of a radiation beam through an absorbing material

Assuming for simplicity that Beer's law is valid for concentrated radiation beam and the absorptance of the polymer is independent of *x*, after separating the variables and integrating from *x=0* to *x=L*, Equation 6.4 can be expressed as:

$$\frac{I_{\lambda,L}}{I_{\lambda,0}} = e^{-k_\lambda L} \tag{6.5}$$

Since the spectral transmittance of the polymer material is the ratio of the intensity of radiation leaving the material with thickness L to that entering the material, it can be expressed as:

$$\tau_\lambda = \frac{I_{\lambda,L}}{I_{\lambda,0}} = e^{-k_\lambda L} \tag{6.6}$$

In another words, the radiation intensity decreases exponentially and if the reflection has been accounted for, the absorbed fraction of light can be expressed using Beer's law:

$$\alpha_\lambda = 1 - e^{-k_\lambda L} \tag{6.7}$$

6.6.2 Summary of the modeling process

While there have been numerous analytical and numerical models for laser welding of metals, only a few such models for laser polymer welding have emerged, and none could be sourced for polymer welding with solar radiation.

Heat flow models for laser polymer welding that could be related to some extent with this work have been described by Potente et al. 1998; Grewell 1999; Kennish et al. 2002; and Kurosaki et al. 2003. However, even by using laser in a controlled environment, the modeling of heat flow for welding of plastics is still considered a very complicated problem. This is because the polymer material properties vary with temperature change, especially near their glass transition or melting phase. The limits imposed by this complexity turn the analytical modeling into an extremely difficult task. The complexity is drawn even further in this research where the experimental studies have been conducted outdoors.

To simulate the solar radiation-polymer interaction during the polymer exposure and joining, two simple transient energy transfer models were developed. The first model is an approximate analytical model that predicts the temperature variation and duration for attaining the glass transition state of the irradiated polymer in certain ambient conditions. The second transient model is intended to simulate the temperature distribution during through-transmission polymer joining. Since these models were verified with polymer radiative heating and joining experiments using a thermocouple embedded in an appropriate location, to study the possible radiation effect on the temperature reading, a model of the thermocouple was also developed.

6.6.2.1 Energy transfer basis of the models

The amount of energy arriving or leaving the exposed specimen at any time in the transient process can be generally defined by the transient heat transfer equation:

$$Q(x,y,z,t,T) = \rho C_p \frac{\partial T}{\partial t} - k\left(\frac{\partial^2 T}{\partial x^2} + \frac{\partial^2 T}{\partial y^2} + \frac{\partial^2 T}{\partial z^2}\right) \tag{6.8}$$

where Q is the power generated by the absorbed solar radiation (in W/m^3) as a function of the time and temperature in the coordinate system (x,y,z).

However, the incident light beam has rotational symmetry with direction of travel along the x axis (see Figure 6.22) and the polymers used in this work are heat insulators. Therefore, the heat generation in the y-z plane could be considered identical along the y and z axes, dependent predominantly on the size and shape of the beam at the focus. Consequently, the temperature change along the x axis would depend strongly on the light absorption and attenuation and can be determined from the heat generation/losses in the bulk of the material.

It should be noted that in addition the beam radiation attenuation through 3 mm thick transparent PMMA was experimentally determined, as discussed in Chapter 5 (Table 5.5). The results were used in conjunction with the spectrophotometric measurements for determination of the average solar absorptance for the models.

It was assumed for simplicity that for each time interval Δt the temperature gradient ΔT can be determined from the internal energy change ΔU of the polymer without considering any mass transfer.

$$\Delta U = mC_p\Delta T = E_{in} - E_{out} \tag{6.9}$$

The internal energy can be calculated from the energy balance of the absorbed amount of the deposited energy and the radiation, conduction and convection losses.

The net rate of radiation heat transfer between a surface of emittance ε and area A, at an absolute temperature T, that is enclosed by a much larger surface at absolute temperature T_∞ can be determined by (Cengel 2003):

$$\dot{Q}_{rad} = \varepsilon\sigma A(T^4 - T_\infty^4) \tag{6.10}$$

The conduction losses of the exposed polymer can be calculated using Fourier's law of heat conduction. The heat conduction rate in a medium in a particular direction is proportional to the temperature difference across the medium and the

area normal to the direction of heat transfer but inversely proportional to the distance in that direction. This is expressed in differential form as:

$$\dot{Q}_{cond} = -kA\frac{\partial T}{\partial n} \tag{6.11}$$

where *n* is the direction normal to the surface.

The convection losses can be determined by Newton's law of cooling. The rate of convection heat transfer is proportional to the temperature difference and is expressed as:

$$\dot{Q}_{conv} = hA(T - T_{\infty}) \tag{6.12}$$

It should be noted that T_{∞} in this case is the ambient temperature.

6.6.2.2 Description of the models

In this study the energy transfer problem, as most heat transfer problems in reality, could be considered transient. However, if some steady conditions are presumed in a very short time interval, the process could be analyzed without a significant error. In the development of the models the physical phenomena such as radiation, heat conduction and convective cooling were taken into account. The following assumptions were made:

1. The relevant material properties change with time and temperature in the explored range is assumed negligible and the radiation extinction coefficient in a transparent material is independent of wavelength.
2. Radiation exchange is between a relatively small surface and large surroundings.
3. The spectrum of the incident solar radiation is transmitted through the optical components without significant change and solar radiation is only slightly polarized as it passes through the optical components.
4. As the concentrated light beam produced by the Cassegrainian concentrator is non-Gaussian but donut-shaped, it could be assumed that it is relatively uniformly distributed over the irradiated area.
5. The convection coefficient is assumed independent of time.
6. The trend of predicted temperature change is not affected by variation of the temperature at the edges of the specimen.
7. The initial temperature is equal to the ambient temperature.

It should be noted that although the polymer absorptance and emittance changes with temperature are not explicitly represented, their values used in the models are assumed to be average, but representative values.

A. Irradiated polymer modeling

Since this model has been intended for different SEC configurations, it allows input of different corresponding parameters. The input parameters in this model could be divided into three categories – measured variable ambient and process parameters, known and assumed thermophysical properties, and known and measured system parameters (see Chapters 4 and 5). The illustrative example below includes relevant parameters used in the model for the particular SEC arrangement with a truncated cone concentrator as a provisional third stage (see Table 6.1). The exposed polymer is transparent PMMA.

Table 6.1: Description of the variables in the model

Symbol	Value	Dimension	Description
k	0.15	W/m°C	Thermal conductivity of exposed material
ρ	1190	kg/m^3	Density of exposed material
C_p	1470	J/kgK	Specific heat of exposed material
T_{amb}	26	°C	Ambient temperature
G	937	W/m^2	Intensity of available beam solar radiation
α^s	0.037		Average solar absorptance of exposed material
h	10	$W/m^2°C$	Convection heat transfer coefficient
A_s	0.000565	m^2	Area with external losses
A_a	0.221	m^2	Clear aperture area of primary mirror
A_{af}	0.0000283	m^2	Directly affected area with external losses
A_r	0.0000141	m^2	Area with internal losses
ε	0.94		Emittance of exposed material
σ	$5.67x10^{-8}$	W/m^2K^4	Stefan-Boltzmann constant
L	0.0032	m	Specimen thickness
V	$8.482x10^{-8}$	m^3	Volume of exposed material
m	0.0001	kg	Mass of exposed volume
η_p	0.8		Efficiency of primary mirror
η_s	0.8		Efficiency of secondary mirror
η_a	0.6		Efficiency of auxiliary optics
D_p	0.59	m	Diameter of primary mirror
D_s	0.24	m	Diameter of secondary mirror
d	0.006	m	Diameter of affected area

It should be noted that in the case of a configuration of the SEC with conventional optics, the additional power loss of each lens is assumed to be not less than 8%. Thus, the example presented could be considered equivalent to a configuration with five auxiliary lenses.

Firstly, the net energy deposited at the receiver for each time interval Δt between the time steps i and $i+1$ was computed using the following equation:

$$Q^{i}_{dep} = G\, A_a\, \eta_p\, \eta_s\, \eta_a\, \Delta t \tag{6.13}$$

where A_a is calculated by: $$A_a = \frac{\pi}{4}(D_p{}^2 - D_s{}^2) - O \tag{6.14}$$

and O is the additional spider obscuration from the secondary mirror support, geometrically calculated to be 0.006604 m^2. Thus, the clear aperture area, A_a, was calculated to be 0.221 m^2.

Next, using the calculated with Equation 6.13 Q_{dep}, the energy absorbed by the exposed polymer for each time interval Δt is computed as:

$$Q^{i}_{abs} = \alpha^{s}\, Q^{i}_{dep} \tag{6.15}$$

A fictitious interim temperature, T_n, is then introduced and calculated using the absorbed energy, as determined above, for each time interval Δt assuming no loss:

$$T^{i}_{n} = T_{amb} + \frac{Q^{i}_{dep}}{m\, C_p} \tag{6.16}$$

where m = ρV. The volume, V, is determined by the geometrical shape of the exposed volume depending on the final optical element ($V = \frac{\pi}{4} d^2 L$ if cylinder or $V = \frac{\pi}{3} L \left[\left(\frac{d_{in}}{2} \right)^2 + \left(\frac{d_{out}}{2} \right)^2 + \frac{d_{in}}{2} \frac{d_{out}}{2} \right]$ if frustum).

The actual temperature of the polymer, T, is a result of the balance between the input and output energy of the system. This balance is realized between the heat generated by the absorbed solar radiation and the losses in the system which are function of the same temperature $T < T_n$. The average temperature of the exposed material is necessary in order to calculate the radiation, convection and conduction losses. An iteration technique could be used to achieve this, but it would require reliable experimental temperature measurements.

However, since the temperature distribution in an exposed polymer is an extremely complex one that affects the material properties, the true polymer temperature determination is very difficult, as discussed earlier. Therefore, based on T_n, the thermal loses in this model are calculated using the following calculating temperature, T_{cal}:

$$T_{cal}^{i} = \frac{T_{n}^{i} + T_{cal}^{i-1}}{2} \tag{6.17}$$

It should be noted that the starting T_{cal} is assumed equal to the ambient temperature i.e. $T_{cal}^{0} = T_{amb}$.

Although the evaluation of the thermal capability of the SEC assumes clear outdoor conditions, to predict the performance of the system, it is necessary to assess the radiation exchange losses between the specimen surface and the incoming concentrated radiation flux. To estimate these losses, for each time interval Δt, on the basis of Equation 6.10, the following equation was derived for the model:

$$\begin{aligned} Q_{rad}^{i} = {} & \varepsilon \sigma 2A_{af}[(273.15 + T_{cal}^{i})^{4} - (273.15 + T_{amb})^{4}]\Delta t + \\ & + \varepsilon \sigma 2A_{r}[(273.15 + \frac{T_{cal}^{i} + T_{amb}}{2})^{4} - (273.15 + T_{amb})^{4}]\Delta t \end{aligned} \tag{6.18}$$

As can be seen, absolute temperatures are used with a conversion factor of 273.15. Also, the radiation losses are computed as a composite variable calculated for two different areas, since internal and external radiation losses are assumed. A_{af} is the external area in contact with the surrounding environment considered affected from and having radiation losses. It is assumed to be the area of the focal spot on the specimen and is estimated by:

$$A_{af} = \frac{\pi}{4} d^{2} \tag{6.19}$$

Although believed to be insignificant, the internal radiation losses are computed with the area A_r, assumed to be the internal boundary of the affected volume. Since this boundary (although considered in general hyperboloid) could be affected by various material properties or process characteristics, three shapes – hyperboloid, frustum and cylinder were explored. Because the volume is relatively small, the choice of the shape affects significantly the assumed absorbed energy. A cylindrical volume was used in the case shown here, as it is the average between the three shapes. Accordingly, A_r is estimated using:

$$A_{r} = \pi d L \tag{6.20}$$

The convection losses were assumed equal for the top and bottom surfaces of the specimen. These losses were estimated for each time interval Δt on the basis of Equation 6.12 by the following:

$$Q^{i}_{conv} = h\, 2\, A_{af}\, (T^{i}_{cal} - T_{amb})\Delta t \qquad (6.21)$$

Intended to predict the peak temperature, its variation and the duration for attaining the glass transition state, the model considers conduction losses throughout the specimen thickness. Although the process described before reaching a steady state is transient in nature, a 'rough' estimation of the conduction losses for each time interval Δt can be obtained on the basis of Equation 6.11 by the following:

$$Q^{i}_{cond} = k \frac{A_s}{L} (T^{i}_{cal} - T_{amb})\Delta t \qquad (6.22)$$

Finally, to find the temperature variation in the affected zone as a function of irradiation time, the solution is obtained by applying an energy balance for each time interval Δt using the following equation:

$$Q^{i}_{abs} - Q^{i}_{rad} - Q^{i}_{conv} - Q^{i}_{cond} = m\, C_p (T^{i} - T_{amb}) \qquad (6.23)$$

The temperature can be expressed by rearranging Equation 6.23:

$$T^{i} = T_{amb} + \frac{Q^{i}_{abs} - Q^{i}_{rad} - Q^{i}_{conv} - Q^{i}_{cond}}{m\, C_p} \qquad (6.24)$$

The above equations were solved in an Excel spreadsheet. The graphical representation of the predicted variation of the effective temperature of the irradiated transparent PMMA with time is given in Figure 6.23.

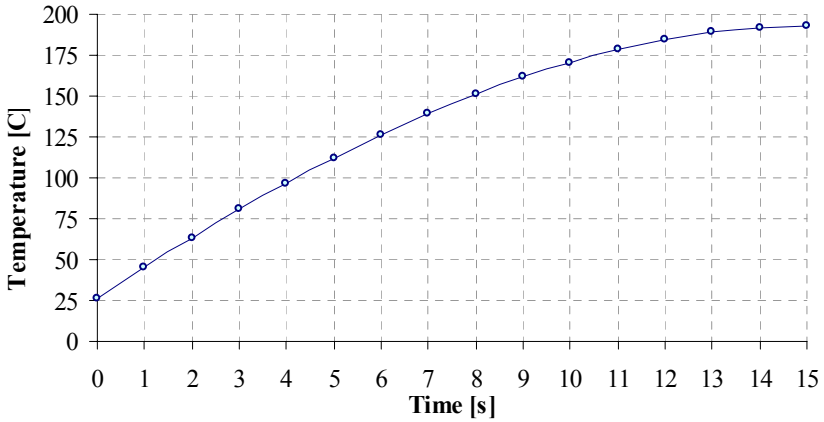

Figure 6.23: Temperature variation vs irradiation time for transparent PMMA

As can be seen, the temperature variation curve is almost linear until the region of glass transition is reached. Although it is believed that this process does not involve latent heat, at this transition the second derivatives of Gibbs free energy are discontinuous and certain physical properties of the material change. Because of this

phenomenon and the associated changes with it, the simulation of the solar radiation–polymer interaction as well as its verification beyond the glass transition temperature becomes complicated and, the assumptions used in this model may not hold.

B. Model of through-transmission polymer joining

As discussed previously in this chapter, the utilization of the concentrated photons from the visible and near-visible solar spectra, explored in this research has been demonstrated with polymer processing applications. To facilitate the study of the solar radiation–polymer interaction, the temperature distribution throughout the exposed region thickness during through-transmission polymer lap-joining was simulated with the following model. Transparent over black PMMA specimens with a typical SEC configuration were used in the illustrative example of this model. Most of the used parameters are as specified in Table 6.1 but some are modified accordingly and additional measured and calculated parameters are included. The modified and new parameters are shown in Table 6.2.

Table 6.2: Modified and additional variables in the through-transmission model

Symbol	Value	Dimension	Description
T_{amb}	24	°C	Ambient temperature
G	800	W/m^2	Intensity of available beam solar radiation
α	$8.57486x10^{-8}$	$W\ m^2/s$	Thermal diffusivity
α_t^s	0.037		Average solar absorptance of transparent PMMA
α_b^s	0.97		Average solar absorptance of black PMMA
A_{tr}	0.00009	m^2	Area of transparent specimen
Δx	0.001	m	Distance between two nodes
Δt	1	s	Time interval
F	0.085748585	dimensionless	Mesh Fourier number
$\dot{q}$	145.92	W/m^2	Solar radiation flux
$\dot{g}_t$	13306428.42	W/m^3	Rate of heat generation in transparent specimen
$\dot{q}_b$	133.7722	W/m^2	Radiation flux transmitted through transparent specimen

As discussed before, since rotational symmetry is assumed, the temperature distribution in y and z axes is predominantly determined by the circular symmetry of the beam and could be predicted by the optical models. Thus, one dimensional transient model was considered sufficient to study this energy transfer problem. The x axis is normal to the exposed specimen surface and the origin is at the middle of the exposed area.

The thickness of the exposed region was discretized in seven volume elements determined by seven equally spaced nodal points. Each internal node is located in

the middle of its associated element assuming that the properties of the node represent the average properties of the element. These nodes are shown in the lap-joint geometry of the model in Figure 6.24. In addition to the discretization in space, discretization in time was done by selecting a suitable time step Δt.

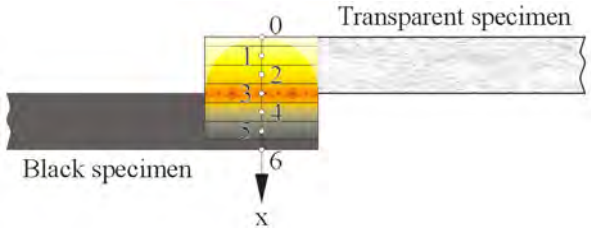

Figure 6.24: Geometry of the through-transmission model

The transient temperature distribution in the exposed region can be determined from the solution of the energy transfer equation derived for this problem:

$$k\frac{\partial^2 T(x,t)}{\partial x^2} + G(x) = \rho C_p \frac{\partial T(x,t)}{\partial t} \qquad (6.25)$$

where t is time variable (s), x – space variable; T – average or bulk temperature (°C); and G – rate of absorption of solar radiation per unit volume at a distance x from the surface (W/m^3).

A numerical formulation of the governing equation 6.25 was obtained using the energy balance approach for each control volume instead of complicated mathematical formulations. This approach was preferred because it is relatively simple and the boundary conditions can be handled with it. The explicit finite difference method, where the time derivative is expressed in forward difference form, was used. The explicit method calculates the following nodal temperature on the basis of the temperature at the previous time step. Although this method imposes stability restrictions on the allowable time step, it was chosen because it provides simpler and more flexible implementation.

The explicit finite difference formulation of Equation 6.25 can be expressed in a general form as:

$$\sum_{\text{allsides}} \dot{Q}^i + \dot{G}^i{}_{\text{element}} = \rho V_{\text{element}} C_p \frac{T_m^{i+1} - T_m^i}{\Delta t} \qquad (6.26)$$

for any node m in the medium and its volume element, where T_m^i and T_m^{i+1} are the temperatures of node m at times $t_i = i\Delta t$ and $t_{i+1} = (i+1)\Delta t$ respectively. $T_m^{i+1} - T_m$

is the temperature change of node *m* during the time interval *Δt* between the time steps *i* and *i+1*.

The model has the following initial and boundary conditions:

1. $T_0^i = T_{amb}$ for i=0 since node 0 is external.

2. The exterior surface is subjected to solar flux and has combined convection and radiation losses.

$$k\frac{\partial^2 T}{\partial x^2} + h(T_{amb} - T_0^i) + \varepsilon\sigma(T_{amb}^4 - T_0^{i4}) + \alpha_t^s \dot{q} = 0 \text{ for } i>0 \qquad (6.27)$$

The explicit finite difference formulation at the upper boundary is obtained by the energy balance equation on the volume element represented by node 0:

$$hA_{af}(T_{amb} - T_0^i) + \varepsilon\sigma A_{af}(T_{amb}^4 - T_0^{i4}) + kA_{af}\frac{T_0^{i+1} - T_0^i}{\Delta x} + \dot{g}_0^i A_{af}\frac{\Delta x}{2} = \\ = \rho A_{af}\frac{\Delta x}{2}C_p\frac{T_0^{i+1} - T_0^i}{\Delta t} \qquad (6.28)$$

where $\dot{g}_0^i$ is the heat generation rate in the corresponding volume (in W/m^3) at node 0 and is estimated by:

$$\dot{g}_0^i = \alpha_t^s \dot{q}\frac{A_a}{A_{af}L} \qquad (6.29)$$

3. Since the two specimens are believed to be in perfect contact and thus having the same temperature at the interface, an interface boundary condition exists. The explicit finite difference formulation at that boundary is obtained by the energy balance equation on the volume element represented by node 3:

$$kA_{af}\frac{T_2^i - T_3^i}{\Delta x} + kA_{af}\frac{T_4^i - T_3^i}{\Delta x} + \dot{g}_m^i A_{af}\frac{\Delta x}{2} + \alpha_b^s A_{af}\dot{q}_b = \rho A_{af}\Delta x C_p\frac{T_3^{i+1} - T_3^i}{\Delta t} \qquad (6.30)$$

In addition to the assumptions specified in the previous section, for nodes 5 and 6 it is assumed that $T_5^i = T_{amb}$ and $T_6^i = T_{amb}$ since it is believed that solar radiation does not propagate to such depth and the internal polymer conduction is negligible.

Instead of the differential equation 6.25, a number of algebraic equations for the unknown temperatures at the selected discrete points in the exposed region were simultaneously solved.

On the basis of Equation 6.26, the transient finite difference formulation for an internal node can be expressed as:

$$kA_{af}\frac{T^i_{m-1}-T^i_m}{\Delta x}+kA_{af}\frac{T^i_{m+1}-T^i_m}{\Delta x}+\dot{g}^{\,i}_m A_{af}\Delta x+\varepsilon\sigma A_{af}(T^4_{amb}-T^{i\,4}_0)= \\ =\rho A_{af}\Delta x C_p\frac{T^{i+1}_m-T^i_m}{\Delta t} \tag{6.31}$$

After cancelling the area A_{af} and multiplying by $\Delta x/k$, Equation 6.31 becomes:

$$T^i_{m-1}-2T^i_m+T^i_{m+1}+\frac{\dot{g}^{\,i}_m\Delta x^2}{k}+\frac{\Delta x\varepsilon\sigma(T^4_{amb}-T^{i\,4}_m)}{k}=\frac{\Delta x^2}{\alpha\Delta t}(T^{i+1}_m-T^i_m) \tag{6.32}$$

where α is the thermal diffusivity of the material defined as $\alpha = k/\rho C_p$.

After introducing a dimensionless mesh Fourier number, F, expressed as

$$F=\frac{\alpha\Delta t}{\Delta x^2} \tag{6.33}$$

Equation 6.32 simplifies to

$$T^i_{m-1}-2T^i_m+T^i_{m+1}+\frac{\dot{g}^{\,i}_m\Delta x^2}{k}+\frac{\Delta x\varepsilon\sigma(T^4_{amb}-T^{i\,4}_m)}{k}=\frac{T^{i+1}_m-T^i_m}{F} \tag{6.34}$$

The unknown temperature T^{i+1}_m can be found by solving Equation 6.34:

$$T^{i+1}_m=F(T^i_{m-1}+T^i_{m+1})+(1-2F)T^i_m+F\frac{\dot{g}^{\,i}_m\Delta x^2}{k}+\frac{\Delta x}{k}\varepsilon\sigma(T^4_{amb}-T^{i\,4}_m) \tag{6.35}$$

It should be noted that absolute temperature is used for calculation of radiation losses.

The selected time step Δt of one second satisfies the stability criterion that the coefficients of all T^i_m in the T^{i+1}_m expressions (primary coefficients) are greater or equal to zero for all nodes m. In Equation 6.35 the coefficient of T^i_m in the T^{i+1}_m expression is 1–2F and the stability criterion can be expressed as $1-2F\geq 0$ or $F=\frac{\alpha\Delta t}{\Delta x^2}\leq\frac{1}{2}$. Thus, the upper limit of the time step in the model is

$$\Delta t\leq\frac{\Delta x^2}{2\alpha}=\frac{(0.001\,\mathrm{m})^2}{2(8.57486\times10^{-8}\,\mathrm{m^2/s})}=5.831\,\mathrm{s} \tag{6.36}$$

The final transient finite difference formulations for each of the selected nodal points were obtained as follows:

$$\text{Node 0 (m = 0)}\quad T_0^{i+1} = (1-2F-2Fh\frac{\Delta x}{k})T_0^i + 2FT_1^i + 2Fh\frac{\Delta x}{k}T_{amb} + \\ + F\dot{g}_0^i\frac{\Delta x^2}{k} + \frac{\Delta x}{k}\varepsilon\sigma(T_{amb}+273.15)^4 - (T_0^i+273.15)^4 \tag{6.37}$$

$$\text{Node 1 (m = 1)}\quad T_1^{i+1} = F(T_0^i + T_2^i) + (1-2F)T_1^i + F\dot{g}_1^i\frac{\Delta x^2}{k} + \\ + \frac{\Delta x}{k}\varepsilon\sigma(T_{amb}+273.15)^4 - (T_1^i+273.15)^4 \tag{6.38}$$

$$\text{Node 2 (m = 2)}\quad T_2^{i+1} = F(T_1^i + T_3^i) + (1-2F)T_2^i + F\dot{g}_2^i\frac{\Delta x^2}{k} + \\ + \frac{\Delta x}{k}\varepsilon\sigma(T_{amb}+273.15)^4 - (T_1^i+273.15)^4 \tag{6.39}$$

$$\text{Node 3 (m = 3)}\quad T_3^{i+1} = F(T_2^i + T_4^i) + (1-2F)T_3^i + 2F\dot{g}_3^i\frac{\Delta x^2}{k} + F\dot{q}_b\frac{\Delta x}{k} \tag{6.40}$$

When a polymer possesses a relatively high absorption coefficient and a low optical penetration depth (as in the case of black PMMA), the greatest portion of solar radiation is absorbed on the surface. Thus, the radiation propagation and generated heat in node 4 are believed to be negligible, and only the conduction is taken in consideration for the temperature calculation.

$$\text{Node 4 (m = 4)}\quad T_4^{i+1} = T(T_3^i + T_5^i) + (1-2F)T_4^i \tag{6.41}$$

The above equations were solved simultaneously in an Excel spreadsheet. The results for the variation of the temperature distribution in each node are given in Figures 6.25 and 6.26.

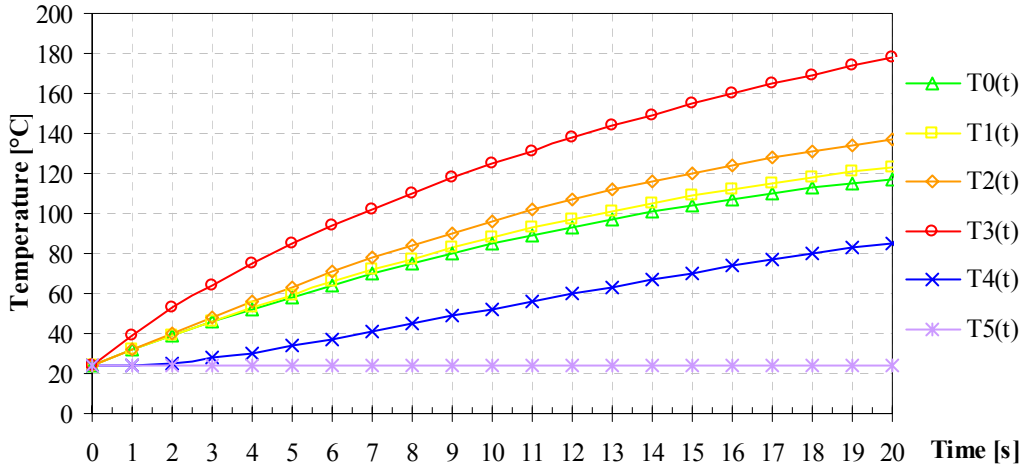

Figure 6.25: Predicted node temperature change with irradiation time

The trend in temperature variation at the selected nodal points shows that, as expected, the highest temperature is achieved at the joint interface. This is logical since the beam solar radiation propagating through the transparent polymer is further absorbed and re-radiated from the black specimen as infrared towards the adjacent bottom surface of the transparent, somehow trapping it. The model also shows that the variation of all temperatures tends to have convex exponential profile except for the temperature at node 4 which is 1 mm under the joint interface in the black specimen.

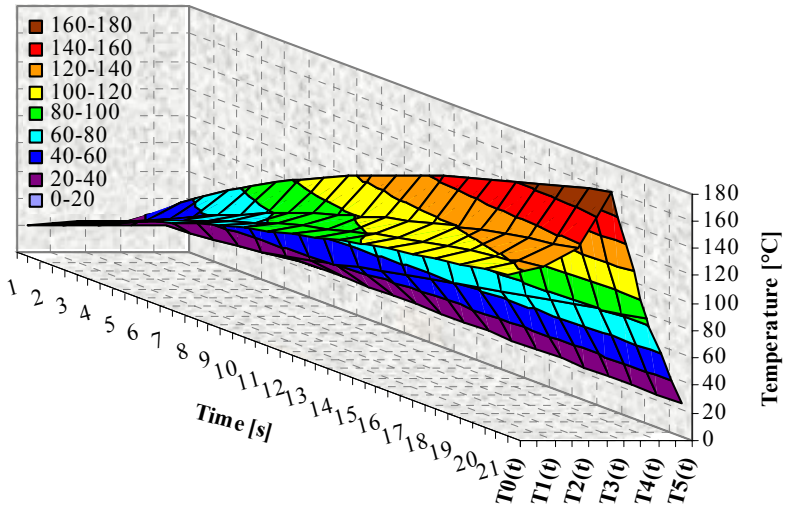

Figure 6.26: 3D surface representation of the temperature variation vs time

The 3D surface representation in Figure 6.26 shows that the temperature rises with the penetration depth increase into the transparent PMMA, but after reaching node 3 at the interface, it drops significantly and the maximum temperature at node 4 is almost half of that of the previous node 3.

C. Model of irradiated thermocouple

During the polymer processing experiments utilizing solar radiation, a thermocouple was used to determine the temperature change of the polymer surface or joint interface. As the thermocouple junction is typically made of two metals, it has different solar absorptance and emittance from those of the polymer, which is a dielectric material. If in metals heat is exchanged primarily by electrons, in non-metallic materials it is primarily by phonons. Also, since any such temperature measuring device would indicate only the temperature of its sensor, any radiation effect associated with it can lead to incorrect readings.

In addition, when the sensor is surrounded by an environment containing surfaces with different temperatures, radiation exchange could take place between the sensor and the surrounding surfaces, as in this case. Because of this, the polymer and thermocouple, being simultaneously exposed at the focal spot of the beam, would interact and the thermocouple would act as an additional heating tool of the polymer surface. The polymer on the other hand becomes a relatively good insulator, trapping the generated heat at the joint interface in the case of polymer joining. While in joining of colored or opaque polymers the possibility of incident radiation heating the embedded thermocouple sensor directly is relatively remote, when transparent polymers are used this becomes a problem.

In order to study and account for the possible radiation effect on the temperature measurement of the polymer, as well as to verify the modeling theory, the temperature change of the thermocouple was modeled.

Based on the first model described in the beginning of this section, the irradiated thermocouple model uses input parameters appropriate for the thermocouple as an absorbing medium. The thermocouple junction is assumed to approximate a 1 mm diameter sphere with a changing surface temperature, proportional to the amount of energy absorbed. The relevant properties of the thermocouple junction in this case are ρ=8500 kg m^{-3}, C_p=320 J kg^{-1} °C^{-1}, k=35 W m^{-1} °C^{-1}, α=0.12, ε=0.6. To ensure the applicability of lumped system analysis in this model, a characteristic length, L_c, is defined as:

$$L_c = \frac{V}{A} \tag{6.42}$$

where V and A are the volume and area of the thermocouple junction respectively.

The Biot number is defined as:

$$Bi = \frac{hL_c}{k} \tag{6.43}$$

The characteristic length of the thermocouple junction used then becomes:

$$L_c = \frac{V}{A} = \frac{\frac{4}{3}\pi\left(\frac{D_j}{2}\right)^3}{4\pi\left(\frac{D_j}{2}\right)^2} = \frac{\frac{\pi}{6}D_j^{\,3}}{\pi D_j^{\,2}} = \frac{D_j}{6} = \frac{0.001}{6} = 1.667\times10^{-4}\,\text{m} \tag{6.44}$$

where D_j is the diameter of the thermocouple junction.

Assuming h = 10 W m^{-2} °C, the Biot number then becomes:

$$Bi = \frac{hL_c}{k} = \frac{10 \times 1.667 \times 10^{-4}}{35} = 4.763 \times 10^{-5} \quad (6.45)$$

which is obviously less than 0.1, thus a lumped system analysis will be applicable, and the error involved in this approximation will be negligible. Therefore, although the temperature of the surroundings may be different and the temperature of the thermocouple varies with time, it does not change much with position at any given time. Although the thermocouple junction is assumed to approximate a lumped system in the model, in the irradiation process the heat transfer is transient. Applying the first law of thermodynamics, the energy balance can be expressed as:

$$E_{in} - E_{out} = \Delta E_{system} \quad (6.46)$$

Since in this research solar radiation is used as an energy source to generate heat in the polymer, the modeling of the energy balance becomes modeling of the generated heat and the prediction of temperature rise with time. Thus, the energy conversion into thermal energy can be considered as a heat generation and the energy balance can be expressed as:

$$Q_{in} - Q_{out} + E_{gen} = \Delta E_{thermal,system} \quad (6.47)$$

where Q_{in}–Q_{out} is the net heat transfer, E_{gen} is the generated heat, and $E_{thermal}$ is the change in the thermal energy of the system.

In the modeling of the heat transfer in the polymer thermocouple system, irradiated with concentrated solar radiation, the three modes of heat transfer – radiation, convection and conduction were again considered. It is assumed that the atmospheric radiation or other input energy sources are negligible and the heat generation is caused only by solar radiation, thus Equation 6.47 can be rewritten as:

$$E_{gen} - Q_{out} = \Delta E_{thermal,system} \quad (6.48)$$

and

$$E_{gen} = E_{abs} = \alpha^{s} Q_{dep} \quad (6.49)$$

where the generated energy is equal to the absorbed solar energy, converted to thermal energy on the surface of the thermocouple junction.

Using the relevant equations (6.13 to 6.24) derived for the first model of the irradiated polymer, an Excel spreadsheet was created for solving the equations. The graphical representation of the predicted temperature variation with time of the irradiated thermocouple is given in Figure 6.27.

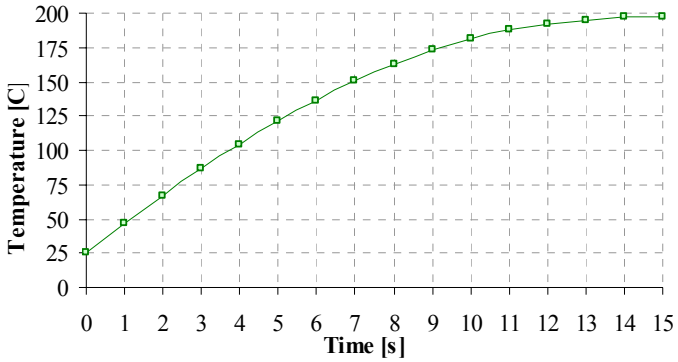

Figure 6.27: Predicted thermocouple response with exposure duration

It can be seen that the thermocouple approaches the maximum temperature exponentially. The shape of the curve is similar to those of the polymer models but reaches relatively higher values at the corresponding time instance (see Figures 6.23 and 6.25).

6.6.3 Experimental verification of the models

In this research, since three different applications of concentrated solar energy utilization have been explored, different experiments were conducted outdoors to evaluate the feasibility of each application. These applications were intended to demonstrate the possibility of concentrated insolation utilization for polymer processing which is one of the central objectives of this research. Accordingly, some of the experiments were also used in the verification of the models described in Section 6.6.2.

The verification of the models was a challenging task because of the complexity of the temperature measurements and the fact that the material properties vary near the glass transition or melting phase. This is one of the reasons for the development of three different models in order to cover the two extreme polymer interactions (transparent and black) and that of the thermocouple for a comparative analysis.

Experimental data from irradiation of transparent PMMA with concentrated solar radiation was used to verify the first model. Since the experiments were performed outdoors, for comparison with the model only a typical representative of the experimental data is shown in Figure 6.28.

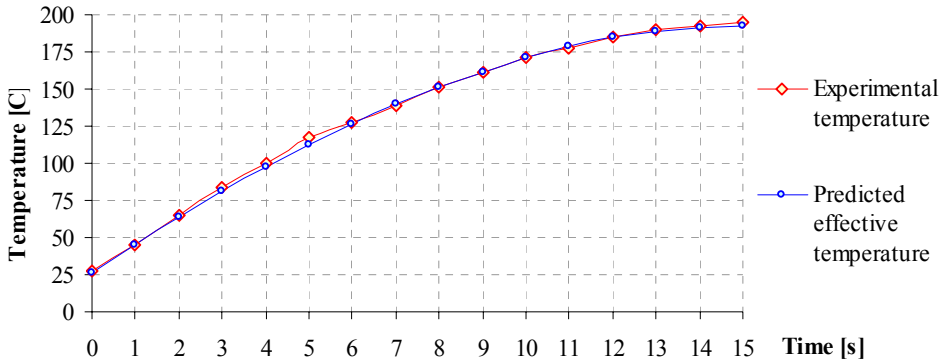

Figure 6.28: Predicted and experimental temperature variation with time for the irradiated transparent PMMA

Figure 6.28 shows a very good agreement between the theoretical and experimental results for the irradiation duration shown. It can be seen that in general, below the glass transition the temperature curve is almost linear and beyond it has a convex exponential profile. However, since the thermocouple and polymer act as a system, the variation in the temperature is governed by the balance of the difference in the absorptance and emittance of the polymer and thermocouple. The curve is not smooth because the size of the exposed area of the thermocouple is 36 times smaller than that of the polymer, thus more sensitive to temperature change. The model can be considered sufficiently accurate below the melting range, which is in this case the object of interest.

Experimental data from through-transmission joining of transparent over opaque polymers (in particular black PMMA) was used for verification of the through-transmission model. Since slight variation of the experimental results was obtained for different times of the year, a typical representative curve was chosen and compared with the model, as shown in Figure 6.29.

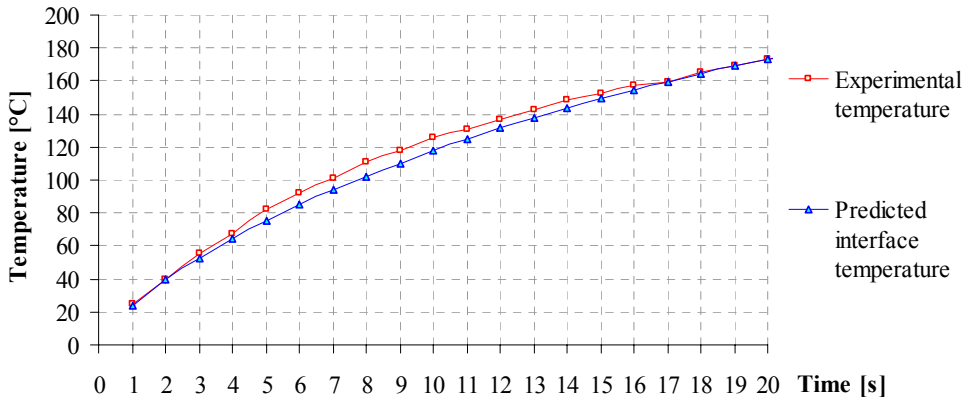

Figure 6.29: Predicted and experimental temperature variation with time for through-transmission joining of transparent and black PMMA

Since the temperature measurements were taken by a thermocouple embedded at the interface joint (node 3) of the two specimens (see Figure 6.30), the experimental results were compared to the temperature predicted by the model at node 3.

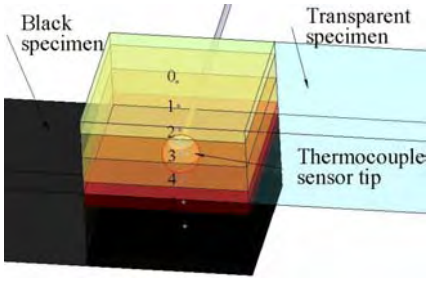

Figure 6.30: Location of thermocouple during through-transmission joining

There is again a relatively good agreement between the predicted and experimental results. The measured temperature is slightly higher than the predicted one in the middle of the exposure duration probably because the thermocouple is not only well insulated, but its lower surface area is exposed on additional IR radiation re-radiated from the black specimen. Nevertheless, this deviation of the predicted result from the experimentally measured data is only within 5.4% on average.

The development of the irradiated thermocouple model has proved very useful, allowing analysis and interpretation of the results obtained from the verification of the first model and comparing them with the predicted thermocouple response. The relevant radiation characteristics and thermal properties of both materials have been invoked in this way to explain the negligible discrepancy. Moreover, it is in line with the argument that the thermocouple would have quicker response than the polymer and would acquire higher temperatures in the irradiation process. It has been determined by the comparison (Figure 6.31) that the predicted temperature of the irradiated polymer is on average 3.8% lower than that of the irradiated thermocouple.

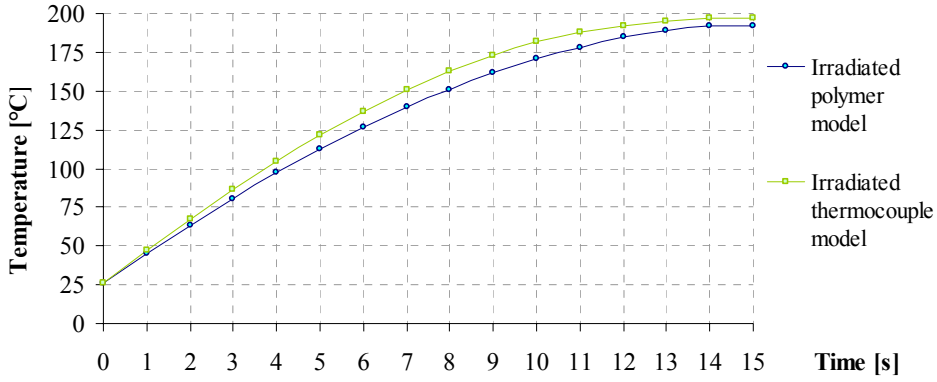

Figure 6.31: Comparison between irradiated polymer and thermocouple models

The results from the experimental verification indicate that the models are sufficiently accurate in predicting the temperature increments and distribution as a function of the exposure time. They enabled the determination of the energy required for the polymer processing, and the process time in different ambient conditions.

6.7 Empirical modeling of polymer joint strength

After the SEC facility has become operational and its optical and thermal characteristics have been evaluated, the typical energy gain from solar radiation and heat loss in the environment have been calculated. On their basis and using the models described above, the energy necessary for the particular polymer processing has also been estimated.

However, it has been determined that the required energy output can be delivered by the facility utilizing different power rates for different time durations. The weld strength of the joined polymers on the other hand is typically dependent on a number of variable factors. To study the effect of power output on the achieved tensile strength of the joint, a simple linear statistical model of the system response was developed. This model attempts to predict the most probable strength of the joint depending on the selected variables.

Since the joining experiments were carried out in ambient conditions and many of the environmental parameters were variable, a representative set of experimental data was selected. The experimental data parameters used are specified in Appendix 6D. Ignoring the possible subjective error, if a linear relationship with equal weight could be assumed between selected process variable parameters and the expected outcome, it could be expressed as:

$$\sigma_t = C_0 + C_1 T + C_2 \tau + C_3 D_{dir} \qquad (6.50)$$

where σ_t is the tensile strength during tensile test of the welded specimen [N m^{-2}]

T is the average process temperature [C°]

τ is the exposure duration [sec]

D_{dir} is the intensity of direct radiation [W m^{-2}]

C_0, C_1, C_2, and C_3 are linear coefficients to be estimated for the model.

Analyses were carried out using a standard statistical software package, SAS. The following equation was derived on the basis of the regression analysis using the

least square method and significance at the 1% level of Fisher's F-ratio.

$$\sigma_t = 233.323 + 10.785T + 5.324\tau + 3.004D_{dir} \qquad (6.51)$$

To evaluate the spread of the values and calculate the accuracy of the created model using the derived equation, the theoretically predicted results were plotted together with the experimental data and are shown in Figure 6.32. The line of best fit using the plotted points was calculated using the regression.

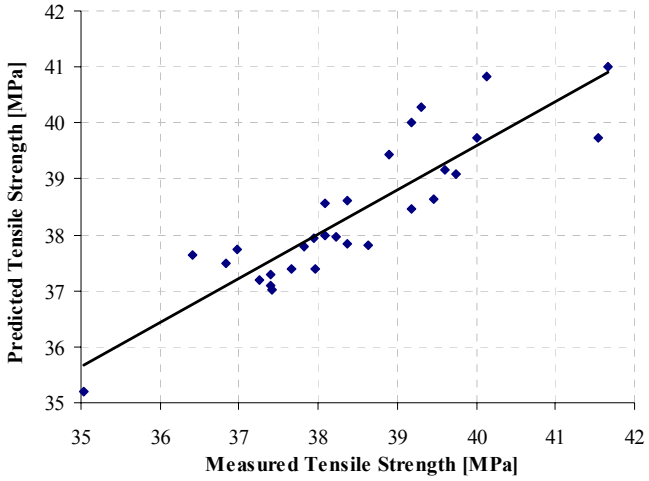

Figure 6.32: Predicted vs measured tensile strength

The standard error of estimate, coefficient of multiple correlation and coefficient of determination for Equation 6.50 were calculated to be 4.462, 0.922 and 0.834 respectively. Because the computed coefficient of multiple regression showed an agreement greater than 70% for the derived equation, a relatively accurate prediction of the tensile strength was considered possible.

6.8 Conclusions

All modeling work performed with the especially developed program codes, adapting professional optical modeling software, as well as the created transient energy and heat transfer models, have proved to be a valuable tool for the development and optimization of the SEC facility. It has been demonstrated how some of the originally developed systems could be improved further.

The initial ray tracing codes especially written as a part of this thesis, using Optica and Mathematica, supported the concept layout of the optical components, revealing that several arrangements are possible depending on the application. Determined by the proposed application, four different principal configurations with conventional imaging refractive optics were considered feasible. In addition, it was

concluded that non-imaging optics such as a truncated light cone and CPC, based on total internal reflection, would be more suitable for ageing and curing experiments. On the other hand, the flexible polymer fiber optic cable could be considered feasible for applications requiring relatively lower concentration and thus was not included in the modeling at that stage.

The modeling and optimization performed with the professional optical software showed that the models developed could be optimized and they were further implemented in the modifications, discussed in the following chapter. The image analysis and evaluation performed with the OSLO software revealed that after initial optimization the image quality of the SEC optical system was satisfactory especially for on-axis performance and the system was relatively well corrected. However, if classical Cassegrainian parabolic primary and hyperbolic secondary mirrors are used, an excellent Strehl ratio of 0.96 could be achieved.

Another finding from the optical modeling was that the possible net power gain would vary with the different configurations and for the most used configuration it would be about 104 W. The maximum net power that the system can deliver is about 143 W and is achievable with one auxiliary lens only.

In addition to the optical models, the more detailed 3D combined computer models developed with AutoCad and SolidWorks proved to be very useful during the process of many modifications required during the research. With these models it was found that since the light cones of the inner rings incoming from the sun and re-radiated from the primary mirror were overlapping on the inner area of the secondary, concentration at that area would be higher.

Used for thermal characterization, the simple mathematical models presented here showed a good agreement with the experimental results. The predicted temperature increments were well within 1.3% of the experimental values for the polymer irradiation model and 5.4% for the through-transmission model. The latter figure may be affected by differences in the material and irradiated surface shape of the exposed polymer and thermocouple tip.

Further refinements of the models may lead to more accurate predictions but the results prove the usefulness of the models. Furthermore, since most experiments were conducted outdoors in variable ambient conditions, the use of all models has saved a great deal of time in the system characterization.

CHAPTER 7.
DEVELOPMENT AND MODIFICATION OF THE SOLAR CONCENTRATOR FACILITY SYSTEMS

7.1 Introduction

On the basis of the 3D optical, ray tracing and combined computer models described in the previous chapter, most of the SEC facility systems have been developed and further modified continuously during the course of the research. Since several aspects of this work, as discussed in Chapters 5 and 6, have been dependent to a great extent on these modifications, they are briefly described in this chapter.

Although not significantly modified, during the development of the SEC facility its principal component, the Cassegrainian concentrator, has been supplemented with several application study systems discussed in this chapter. Intended to serve as an energy source for different applications, the SEC facility has been improved and equipped with especially developed innovative auxiliary systems.

When continuous maintaining of high temperatures is desired, typically a high concentration of the incident solar radiation becomes necessary. Furthermore, especially in this study where a point focusing type solar concentrator is used, sun-tracking is essential. In general, the image formed by even an ideal paraboloid is always imperfect, containing different types of aberrations that are inherent to the concentrator geometry. Moreover, if the telescope is not aligned properly, it will give non-symmetric images, which makes accurate photometry difficult and could lead to even further increasing the unevenness of the concentrated flux distribution.

For these reasons the development and implementation of a sun-tracking and controlling system for acquisition of the solar image were considered crucial for improving the overall performance of the SEC facility. Three different prototype models of sun-tracking devices with appropriate sensors were designed, developed and experimentally tested (Stoynov and Yarlagadda 2003). Some details of this development are described in the beginning of this chapter.

Next, two significant modifications to the original beam transmission optical path via auxiliary optics are discussed. These modifications have been essential for reducing the substantial power losses and the effect of the changing ambient

conditions on the exposure process. The experimental exploration of a fiber optic guide as a beam transmitting system is also included.

The design of non-imaging third stage concentrators for solar radiation transmission is discussed further in the chapter. Firstly, a truncated light cone, experimentally explored as an alternative to the refractive light transmission optics, is depicted. Next, two non-imaging CPC devices, considered as an alternative to conventional optics for beam transmitting and further concentration, are described.

This chapter concludes with a discussion on the design and development of innovative auxiliary systems necessary for the implementation of the concentrated solar flux utilization process. These include a target positioning and focusing device, butt and lap joint clamping devices, specimen cooling and beam control systems.

7.2 Design and experimental development of sun-tracking device

7.2.1 Background

Many solar energy collectors, especially most types solar concentrators and other solar energy devices, typically achieve or realize their greatest efficiency only when their effective acceptance aperture areas are aimed directly at the sun. Only after continuous precise alignment of the effective aperture area, will the output of any type solar concentrator depend almost solely on the intensity of the direct solar radiation, regardless of the energy conversion application. As a consequence, usually the absorbing, reflecting or refracting accepting element of such types of solar energy devices needs to be continuously shifted to follow the movement of the sun for the sunshine duration. Typically solar concentrators require sun-tracking and it is well known that even non-imaging solar concentrators achieve better performance if they have a sun-tracking mechanism. In this work where an imaging concentrator is employed, the continuous sun-tracking has become crucial for maintaining the solar image on target.

Numerous mechanical, photoelectrical and other types alignment systems and tracking devices have been described in the patent literature (Hammens 1980; Russell 1981; Wyland 1981; Carter 1992; Stone and Blackmon 1999; Nyesyn 2001). Also, various designs of sun-tracking and control systems have been suggested and explored (Hession and Bonwick 1984; Zogbi and Laplaze 1984; Lynch and Salameh 1990; Imenes et al. 2002; Beshears et al. 2003).

In general, there are three types of sun-trackers (single or dual axis) – passive,

microprocessor and electro-optically controlled units. Passive systems are the simplest and are typically based on physical effects with fluids or other means of self-tracking mechanism. They do not require any driving motors or electronic control, however, they provide only moderate accuracy tracking. Microprocessor controlled sun-tracking systems are based on mathematical formulas to predict the sun's position and therefore track the sun without the need of sensors. These trackers are highly accurate as they are not dependent on atmospheric variables, but are relatively complex and the most expensive. Electro-optical sun-tracking units are simpler and less expensive than the microprocessor units.

In this research a sensorless (computer controlled) tracking controller which calculates the theoretical position of the sun based on the time of the day was initially considered. The mathematical equations described in Chapter 2, Section 2.3.5, were intended to be used in a computer controlled tracking. However, a less expensive and simpler electro-optical sun-tracking device with a specially designed photoelectric sensor was experimentally developed and used simultaneously with a pinhole telescope with a CCD detector and monitor.

Any Cassegrainian telescope is almost never used without acquisition and guiding units in place. Also, any CPC type non-imaging device, even when used only as a second stage concentrator, will have practical limitations related to the tracking system used. This is because its entry aperture is typically designed to fit the image size, thus any guidance error could cause significant reduction of the concentrator efficiency. Only 0.1° tracking error can cause up to 20% losses of the flux. Furthermore, since in this research a CPC is used as a third stage concentrator, this becomes an even more critical issue.

7.2.2 Manual joystick control

In the initial feasibility version of the SEC facility the acquisition of the solar image was achieved either by line-of-sight or by observation of the secondary mirror filled with light. This simplistic telescope aligning technique was considered reliable at the time and was used predominantly for the preliminary experimental testing of the capabilities of the SEC facility. Although practicable for the feasibility study, in this indirect controlling technique the sun-tracking and telescope pointing were achieved manually with the aid of joystick control and were dependent on the skill of the operator.

The first acquisition system consisted of a small auxiliary telescope (pinhole type sensor), charge-coupled device (CCD) detector and monitor display, as illustrated in Figure 7.1. CCD cameras are being frequently used in measurement systems for the control, testing and analysis of various solar concentrating systems. Although they have many advantages, especially in visualizing the shape and size of the beam spot, they require constant monitoring and manual control which lead to subjective errors.

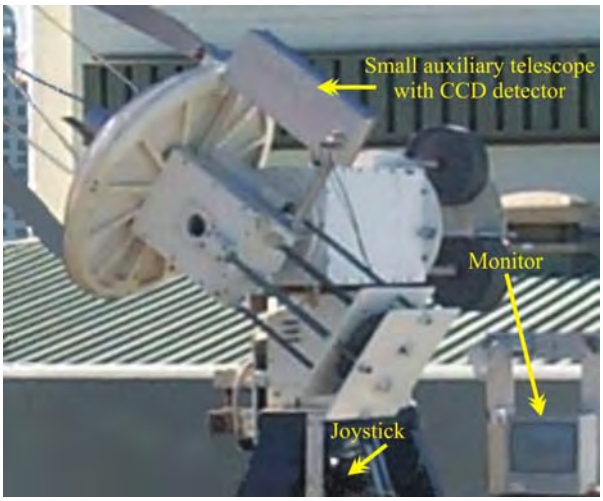

Figure 7.1: First acquisition system with CCD

During the initial tests, this acquisition system was found to be over-sensitive and the precise alignment of the telescope with it and without the aid of a diagnostic instrument became an extremely difficult task. Moreover, this type of sun-tracking system used a manual joystick, i.e. it was still greatly dependent on the manual skills of the operator controlling the joystick, adding a subjective human error.

To overcome this problem, a suitable photoelectric sensor with tracking automatics was developed. Several sensor designs using photoresistors were built and experimentally compared and are discussed below.

7.2.3 Electro-optical automatic sun-tracking

Two major concepts with four types of tracking sensors were explored during the process of the sun-tracker development. All four sensors consist of four concentric and equally spaced photoelectrical detectors working in pairs and located in the first concept each in a separate tube, and in the second, in a cross septum.

Initially two sun-tracking sensors were designed with the intention to enable automatic shifting of the concentrator to point towards the eastern horizon at dawn the next day, in order to avoid the required manual control. To ensure that, an

additional pipe was mounted in the middle, containing a day-night detector, located at the free end of the pipe and adapted to be able to receive sunlight. Those two initial designs are shown in Figure 7.2a and 7.2b. They were proposed for the case when continuous automatic operation of the SEC facility from sunrise to sunset is necessary.

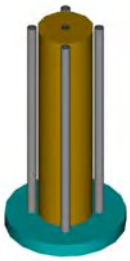

(a) Sensor with day-night detector and pipe separation

(b) Sensor with day-night detector and septum separation

Figure 7.2: Sun-tracking sensors with day-night detector

For the polymer processing experiments conducted in this research, two sun-tracking sensors without a day-night detector were built and experimentally tested. The first sensor, shown in Figure 7.3, was designed with four individual pipes of 60 mm long with a 6 mm internal diameter to accommodate the photoresistors.

(a) Design drawing

(b) Photograph of the sensor built

Figure 7.3: Sun-tracking sensor with pipe separation

The initial experiments showed that the sensor was extremely sensitive for its purpose. Even after shortening the pipe length, it remained extremely sensitive, leading to jerking of the drive mechanism. To overcome this problem, another sensor with a cross septum instead of pipes was designed and developed (see Figure 7.4). The operation with this model was successful and as a result of the testing experiments this last design was considered the most suitable and reliable for the driving system used. The photoelectric sensor, as can be seen from Figure 7.4, comprises four photo-resistors separated with a cross septum (later modified to a rectangular septum) working in pairs.

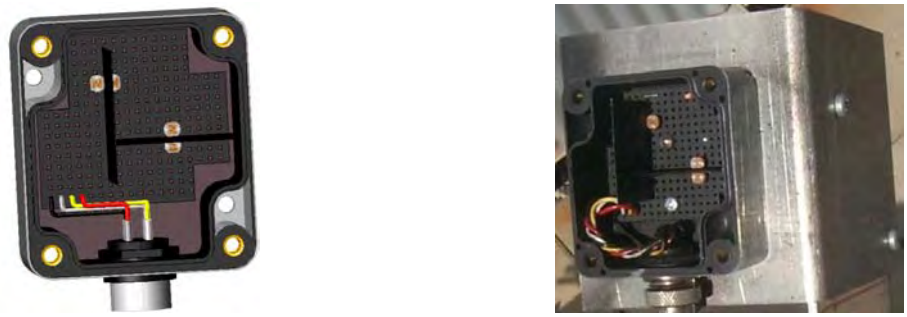

(a) Design drawing *(b) Photograph of the device built*

Figure 7.4: Sun-tracking sensor with a cross septum

In general, this electro-optical tracker, as most electromechanical tracking mechanisms, would activate the necessary motor(s) to move in a direction which equalizes the insolation intensity on the sensors. Each pair of sensors is located in front and behind the septum wall and for proper operation equal insolation exposure should be ensured. When the principal telescope axis is not pointed at the sun, an electrical error signal appears which is then suitably amplified and applied to control the corresponding driving motor until targeting is achieved. The sensor output becomes balanced when this occurs and the output from the differential amplifier becomes zero. In this way the electrical signal causes continuous adjustment of the azimuth and zenith angles, following the sun across the sky and keeping the beam insolation parallel to the principal telescope axis.

Initially the sensor was mounted on an adjustable one-plate base placed asymmetrically on the top side of the primary mirror. To achieve fine alignment, the sensor was mounted on a two-plate adjustable base as shown in Figure 7.5.

(a) Design drawing *(b) A photograph of the built device*

Figure 7.5: Sun-tracking sensor with a cross-septum on a two-plate adjustable base

In a later stage, to further improve the precision of the tracking operation, the sensor was relocated to the top side of the secondary mirror, symmetrically aligned with the principal telescope axis (see Figure 7.6).

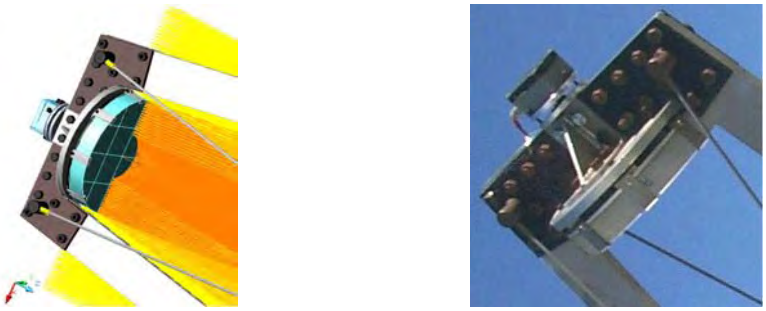

Figure 7.6: Design drawing and a photograph of the relocated tracking sensor

In the original version the axis speed was 45 degrees per minute for both axes. Since the earth's rotation is about 0.25 degrees per minute, when the sun-tracking device was introduced, appropriate resistors in series with the motor supply, in addition to the reduction gearboxes, were used to adjust the necessary speed. The initial experiments showed that the tracking precision could be improved by decreasing the speed further. An additional switch was introduced to allow two-speed operation, fast readjustment (45 degrees per minute) and fine tuning (four degrees per minute) during both automatic and manual modes.

The schematic diagram of the actual electronic tracking system developed is given in Appendix 7A and a photograph of the built sun-tracking system is shown in Figure 7.7.

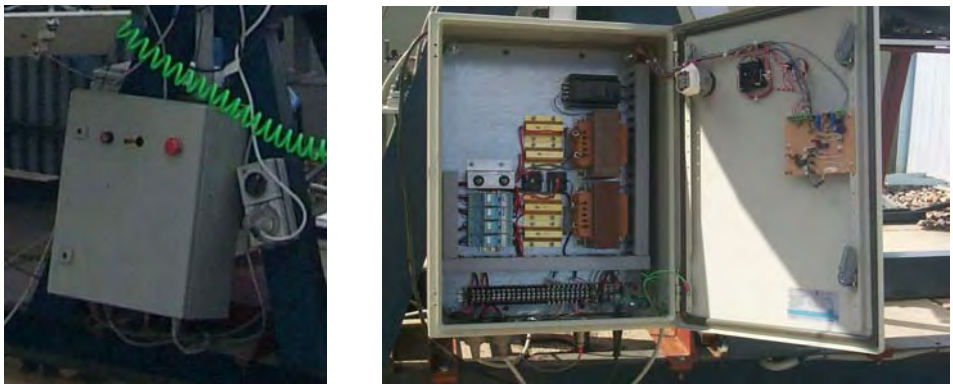

(a) Front view *(b) View from inside*

Figure 7.7: Power supply and automatic control unit

During the development and modification of the described sun-tracking sensors, the originally built automatics to control the telescope movement and power supply including the joystick system were rebuilt. Figure 7.7a shows the front view of the power supply and automatic control unit – the manual/automatic switch on the left, the joystick in the middle and the emergency switch on the right. Figure 7.7b shows

the rebuilt power supply and automatic control unit, and tracking electronics in a standard weather proved case. Driving motors are activated to move the telescope in the necessary direction until the light intensity over each pair is equalized. Controlled by the tracking sensor signal, the driving motors continuously adjust the required azimuth and altitude angles to keep the principal axis of the Cassegrainian concentrator in line with the beam insolation.

7.3 Experimental exploration of beam transmitting systems

7.3.1 Modification of the light transmission with conventional optics

Regardless of the need to directly use or preserve the concentrated solar energy for later utilization in process heat or other energy consumption, with some exceptions, most energy conversion systems typically require energy transmission. However, if the energy transmission in most conventional energy systems as well as alternative ones is well studied and easily realized, the difficulties to achieve this task increase greatly when concentrated broad band electromagnetic radiation is involved.

Although it is well known that the vacuum, compared to any refractive material, is the best transmitting medium for solar radiation, the incorporation of converging refractive components is often used to remedy the disadvantage of excessive lengths. Therefore, the use of conventional optics was initially explored for transmission of the concentrated radiation. Moreover, conventional optical elements were predominantly involved in the polymer joining studies.

As discussed in Chapter 4, in the initial system design because of the unavailability of suitable fibers at the time, the fiber guide was replaced by common optical components. This initial system comprised canister and periscopic optical systems of lenses, mirrors, auxiliary and de-magnifying optics and mechanics.

It has been obvious that the beam transmission optical path via auxiliary optics, originally proposed by the supplier instead of fiber optics, has been considerably long (see Figure 4.4). It has also led to substantial loss of power and additional limitations on the spectral range use.

Furthermore, the secondary mirror causes obstruction of the incident sunlight, leading to forming an umbra shadow by the sun's rays. Any auxiliary imaging component used, such as doublet lens, although compensated for the red and blue difference in wavelength, will keep the shadow of the secondary mirror in the image.

Nevertheless, the use of conventional optics was a starting point for

modifications toward the improvement of the experimental SEC facility systems. Two modifications of the optical path with auxiliary conventional optics were initiated on the basis of the optical ray tracing and the combined 3D computer models, discussed in Chapter 6.

Although the SEC facility has been explored for different applications, in general they all have included exposure of a polymer to concentrated solar radiation. Since the exposure process takes place in outdoor open environment, two locations of the working station were explored. The first location, immediately below the trunnion box, was intended to allow free access to the exposed material and manipulate relatively larger specimens. The second location, inside the trunnion box, was proposed in order to decrease the influence of the changing ambient conditions on the exposure process.

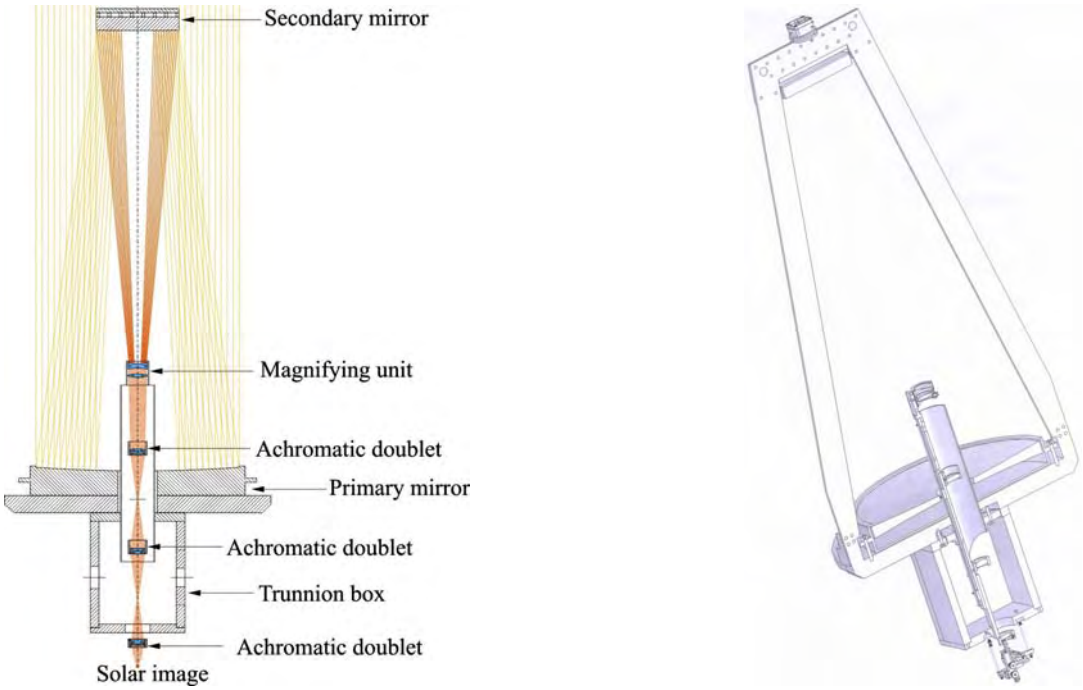

Figure 7.8: Cross sectional view of the modified SEC

The first modification (see Figure 7.8 and Figure 7B.2 in Appendix 7B) of the optical system was considered necessary for reducing the length and number of optical elements in the path, thus decreasing the power losses and spectral range use limitations. For this purpose, the ray tracing model with five lenses (discussed in Chapter 6) was used for the optical arrangement. As can be seen in Figure 7.8, the new optical path consisted of the magnifying unit, two of the doublets from the original configuration and an additional final doublet lens with shorter focal length.

An appropriate barrel to accommodate this third lens (purchased from Edmund Optics) was designed and manufactured from a quality instrument-grade aluminium. It was fixed to the positioning stage to allow very fine focus adjustment. The design drawing of the barrel is given in Appendix 7A.

On the basis of the detailed 3D combined computer model (described in Chapter 6), to ensure relocating of the final image directly under the trunnion box, its bottom plate was appropriately modified. The new arrangement with the modified shortened optical path is illustrated on the overall schematic diagram in Figure 7.8.

The design drawing of the final focus relocation under the trunnion box is illustrated in Figure 7.9a. Photographs of the back plate of the trunnion box before and after the modification are shown in Figure 7.9b and 7.9c respectively. The positioning and focusing device, which is discussed further in the chapter, was appropriately mounted to allow free movement on all three axes and can also be seen on the drawing in Figure 7.9a.

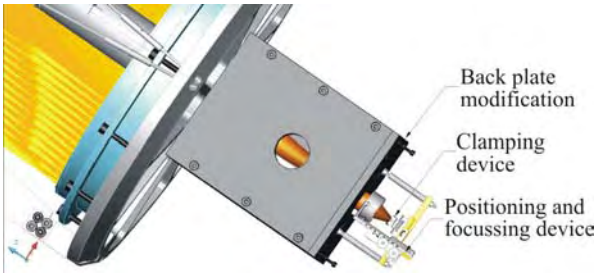

(a) Design drawing of the modified back plate

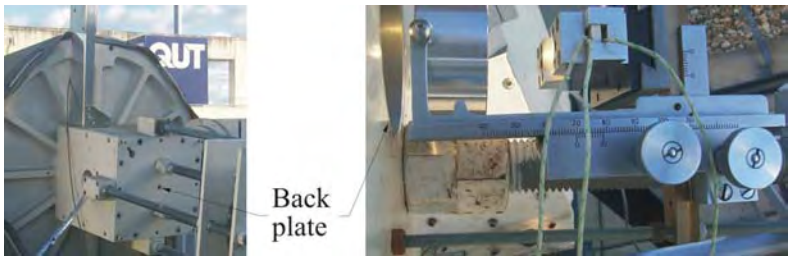

(b) Trunnion box before modification

(c) Working station (focus adjustable and clamping devices) under trunnion box

Figure 7.9: First modification of the trunnion box

Since the number of the auxiliary conventional optical elements was reduced, the spectral and power losses imposed by physics of the optics and the thermodynamics of the thermal system decreased significantly. Although a lens would increase the concentration, it also would contribute to the losses (assumed to be around 8%).

The maximum temperature achieved at the final image spot on idle running was

used as a criterion to evaluate the reduction in power losses. The temperature was measured in ambient conditions similar to those before the modification so that the results could be compared. The range of variation in the intensity of direct solar radiation was between 850 W/m^2 and 900 W/m^2. The ambient temperature was between 25°C and 27°C. The wind speed was in the range of 1-2 m/s.

In these conditions the maximum temperature achieved at the final solar image location on idle running after the modification was 371°C, compared to 155°C measured before the modification with the use of a de-magnifier. This significant increase in the temperature attained was due not only to the reduced number of lenses but also to the removal of all beam bending mirrors. It has also improved the spectral characteristics of the insolation re-radiated by the SEC facility.

The second modification has further shortened the optical path and reduced the number of achromatic doublets used. Based on the ray tracing model with the magnifying unit and two doublets and its corresponding detailed combined 3D computer model (see Figure 7B.3 in Appendix 7B), the canister and outer side plate of the trunnion box were altered in order to relocate the working station inside the trunnion box A design drawing of the modified back plate of the trunnion box and a photograph of the working station inside the trunnion box are shown in Figure 7.10.

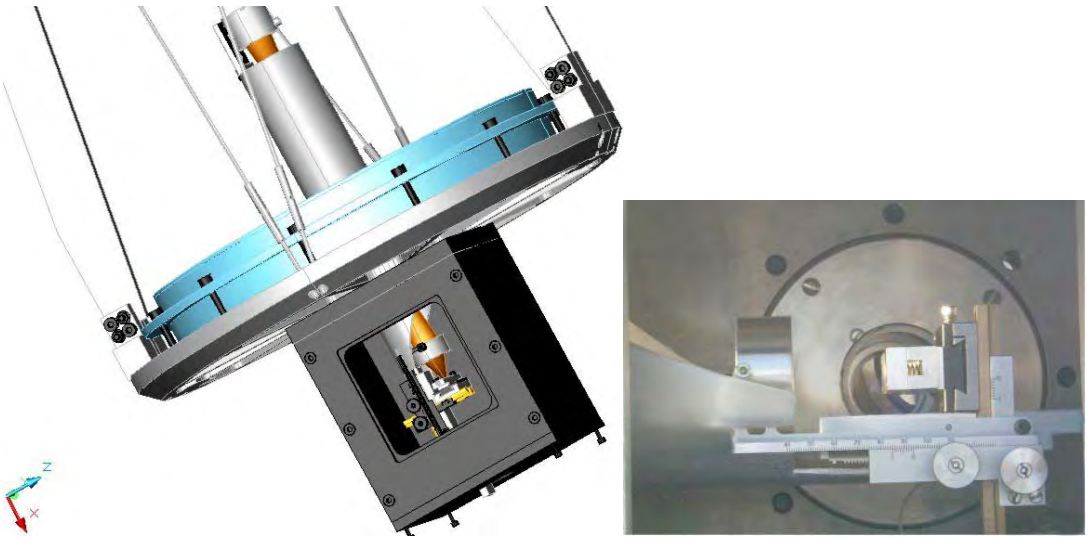

(*a) Design drawing of the modified trunnion box* *(b) Working station inside the trunnion box*

Figure 7.10: Second stage modification of the SEC

As can be seen, both of the modifications discussed above implement two of the models described in the previous chapter. After completion of each modification, experimental tests were performed and considered successful. The experimental

studies are discussed in the following chapter.

Further shortening of the beam transmitting optical path, modeled as a SEC configuration with two doublet lenses and without a magnifying unit, has been considered for future work since further alteration of the canister is required.

The SEC configuration using the shortest beam transmitting optical path, based on the model with one auxiliary doublet lens, was set up for an evaluation test only. With the provisional arrangement holding the doublet lens in the barrel at the required position, a maximum temperature of 742°C was measured on idle running at the focal spot. Since this arrangement requires the work station to be located between the two mirrors, it has not been used for performing feasible polymer processing experiments.

7.3.2 Solar radiation transmission with fiber optic guide

The transmission of concentrated solar energy with optical fibers has been studied by many researchers and numerous advanced achievements have been accomplished. Robieux proposed the use of large parabolic mirrors with rigid light guides to transmit concentrated solar radiation (Robieux 1975). Cariou et al. studied the theoretical ability of the transmission of solar energy by optical fibers (Cariou et al. 1982). They showed that modules in which one fiber is associated with a small parabolic mirror may supply 2W with an efficiency greater than 70%.

Yugami et al. experimentally investigated a Cassegrainian solar concentrator system with a parabolic mirror 1560 mm in diameter, equipped with a 18 mm-diameter bundle of 250 fiber elements of 1 mm diameter each. The authors observed an average energy transmission efficiency of 63%, which is more than 70% of the theoretically calculated value (65.6%) (Yugami et al. 1999). Jaramillo et al. performed a theoretical thermal study of optical fiber transmitting concentrated solar energy (Jaramillo et al. 1999). They found that, in order to efficiently transmit concentrated solar energy, a paraboloidal mirror (21.8 cm in diameter with a focal distance of 51.9 cm) would be the optimal concentration device to couple with a SiO_2 optical fiber (maximum diameter of 5 mm and aperture angle of 12°). They achieved a total efficiency of 85%.

Liang et al. reported experimental solar energy concentration and transmission systems intended for solar pumping of lasers by using flexible light guides consisting of single fiber and bundles of 2, 7 and 19 fibers (Liang et al. 1998). To test the fiber

optic transmission, a 406 mm-diameter telescope mirror (f=4.5) with a primary focus of 15 mm diameter was used. The light was further concentrated by an aspheric lens to a 6 mm-diameter light spot at the input end of a 7 mm-diameter and a 3 m long optical fiber guide. Their remarkably fine work on polishing and joining 19 optical fibers of 1.5 mm-diameter each in a compact fiber-optic bundle resulted in achieving 60% efficiency or 60 W output optical power (2 W/mm^2). On the other hand, for the same purpose of laser pumping, Winston et al. achieved a power density of 50 W/mm^2 in their preferred prototypical embodiment, employing the same diameter primary telescope mirror with a focal ratio of 2.5 and a non-imaging secondary concentrator (Winston et al. 1991).

Feuermann et al. reported transmitting concentrated sunlight from mini-dish concentrators through a 1 mm-diameter optical fiber and measured solar flux levels of 11-12 kilosuns at a remote target (Feuermann et al. 2002). Kribus et al. studied the potential use of optical fibers for solar thermal power generation (Kribus et al. 2000). They concluded that the long distance transport could become feasible only if the cost of 1 mm-diameter solar-compatible fibers drops significantly below $0.2/m. For short distance transport, a fiber distributor for a small central receiver plant was found to be preferable to the mini-dish systems although the specific cost was still high.

Tekelioglu and Wood reported a hybrid solar lighting system to transmit predominantly visible light form a modified Cassegrainian concentrator to a luminaire via a large core polymer fiber optic (Tekelioglu and Wood 2003). The solar concentrator system, described in Chapter 2, Section 2.5.2, also included eight PMMA-core optical fibers, 12 mm in diameter and equally spaced on a 160 mm-diameter circle. An infrared filter in front of the fibers was used to transmit the visible spectrum and reflect the IR component. It was observed, however, that the fiber tip burnt after three hours exposure and the fiber protection case covering the cladding was damaged after bending beyond the critical bending radius.

On the whole, the use of fiber optical guides to transmit concentrated solar energy has been shown to be feasible, but it is also associated with significant power losses and spectral limitations.

In this research the initial Cassegrainian configuration has been developed with the intention to utilize the cone of concentrated solar light propagating through a flexible fiber optic guide. Preliminary feasible experiments with a polymer fiber

optic cable 14 mm in diameter and 1.5 m long were carried out aiming to transmit the gained solar energy (Figure 7.11).

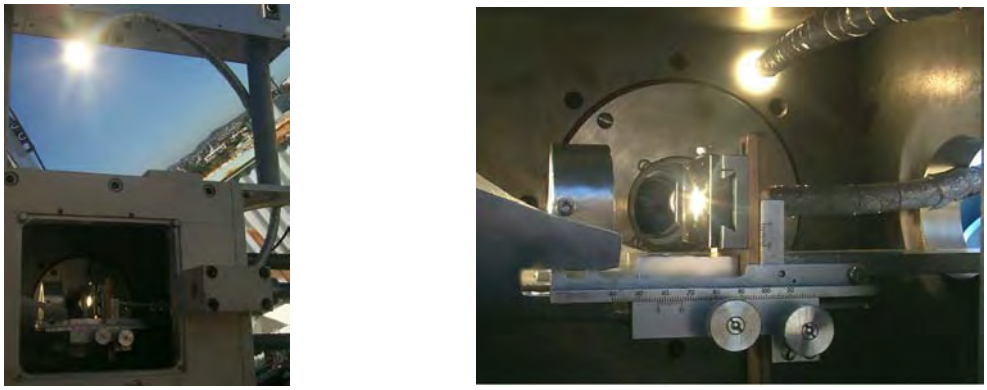

Figure 7.11: Solar radiation transmission with a fiber optic guide

The fiber optic cable had the following optical characteristics – a glass transition temperature of 53.8°C, a spectral range of 370-690 nm, an acceptance angle of 45°, a numerical aperture of 0.65, and an attenuation less than 5.3% per metre.

The experiments showed that without a non-imaging third stage concentrator the concentrated beam of solar photons was very unevenly distributed at the Cassegrainian focus. As a result, the cone of concentrated light generated heat, raising the temperature of the first layer of the core, especially the light accepting surface. This was probably due to the fact that the cladding and the polymer core, although transparent, acted as a good insulator.

These only provisional experiments showed that without forced cooling of the light-accepting surface, the fiber could be easily overheated, quickly reaching the polymer glass transition and subsequently melting temperatures. The readings of one of the embedded control thermocouples showed that its temperature reached the glass transition temperature of this particular fiber in five seconds and the polymer melting temperature in 18 seconds. (The recorded radiation intensity was 868 W/m^2 on average and the ambient temperature was 25°C.) Because of this, the use of a polymer fiber optic with this arrangement has been considered non-feasible for applications requiring relatively higher concentration and temperatures. However, if a "hot mirror" is used to filter the infrared part of the solar spectrum (transmitting up to 700 nm), this particular flexible polymer fiber guide could be practicable for relatively low power densities (under 50 W).

7.4 Non-imaging third stage concentrators

7.4.1 Solar radiation transmission with truncated cone

Although the so-called light cone has been known for many years, it is considered to be far from being an ideal solar concentrator. As mentioned in Chapter 2, a truncated cone with an excessive length would be required to achieve higher concentration. However, since the Cassegrainian concentrator used in this research has been designed with its final focus between the mirrors, the feasibility of such a relatively long cone as a light transmission means to the working site has been studied. In addition, a light cone, compared to a CPC, has been much easier to manufacture.

Initially, a provisional light cone was experimentally explored as an alternative to the refractive light transmission optics. In a typical two-stage concentrator system with a non-imaging secondary, the entrance aperture diameter of the non-imaging stage is designed to coincide with the solar image diameter of the primary. Thus, the design of the explored light cone was imposed by the final angle, formed by the secondary mirror, the beam diameter and the distance between the Cassegrainian focus and working site (similar to the CPC modeling as discussed in Chapter 6). As in most non-imaging cone-like concentrators, the design of the light cone was based on the edge ray principle.

The design followed the model described in Section 6.5.1, but the truncated cone was made deliberately larger in order to reduce the error from the tracking misalignment. Furthermore, the third stage non-imaging concentrator was intended as an alternative means for transmission of concentrated insolation, and achieving of a very high concentration was not required for the studied applications. Therefore, its acceptance angle was made to accommodate the extreme rim angle of the secondary mirror and to fit in the required length, enhancing the concentration.

The truncated cone was made from a double-sided polymer material less than 0.1 mm thick, sandwiching a layer of 3M Silverlux^{TM} high strength, high performance, specular reflective silver mirror-like film. The size of its larger input diameter was determined by the diameter of the beam and the solar image in the principal Cassegrainian focus. The length of the cone was chosen to fit the distance from the principal focus to the working station which for the first modification was 890 mm. For the second modification with relocation of the working site in the trunnion box,

the effective length of the cone was further shortened to 550 mm (Figure 7.12).

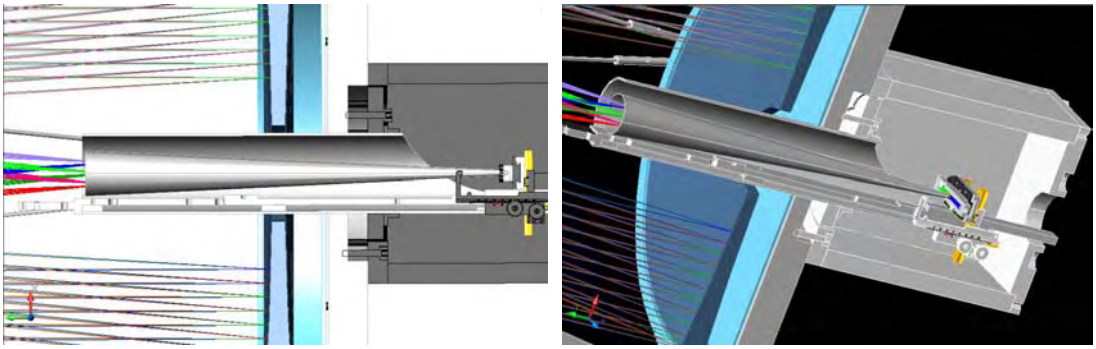

Figure 7.12: Design drawings of the light cone

Design drawings of the truncated light cone are also shown in Appendix 7A. A 3D design with traced rays through the SEC facility is shown in Figure 7B.4 in Appendix 7B and a photograph of the prototype made can be seen in Figure 7.13.

Figure 7.13: Overall view of the SEC with the truncated cone concentrator

Compared to the other means of transmitting concentrated solar radiation, the use of this truncated conic concentrator led to an additional increase of the concentration at its small output end. Since this third stage concentrator was subject to a feasibility study only, a cooling system was not developed at that stage. This resulted in deforming the shape after continuous use. In general, the conic concentrator has been considered potentially feasible for some applications such as ageing, where cooling is used, but for higher temperature applications the cone has to be made from heat resistant material. The truncated cone concentrator used as a beam transmitting device appears more efficient than the explored fiber optical cable, however they both require final focusing.

7.4.2 Solar radiation transmission with CPC

As it has been discussed in Chapter 6, two non-imaging CPC devices were

modeled for use as an alternative to conventional optics for beam transmitting and further concentration. By contrast to the parabola, as these third stage concentrators are non-imaging devices, it was expected that the concentrated flux emanating from their internal surfaces and illuminating the exposed area will be diffuse. Moreover, for the polymer ageing experiments the use of the non-imaging concentrator was necessary to allow the propagation of the UV component of solar radiation, which would be cut if conventional lenses were used instead.

On the basis of the models, two suitable CPCs were designed to serve in different experimental applications. The design drawings are shown in Figures 7.14 and 7.15. The location of both CPCs is shown in Figure 7B.5 in Appendix 7B.

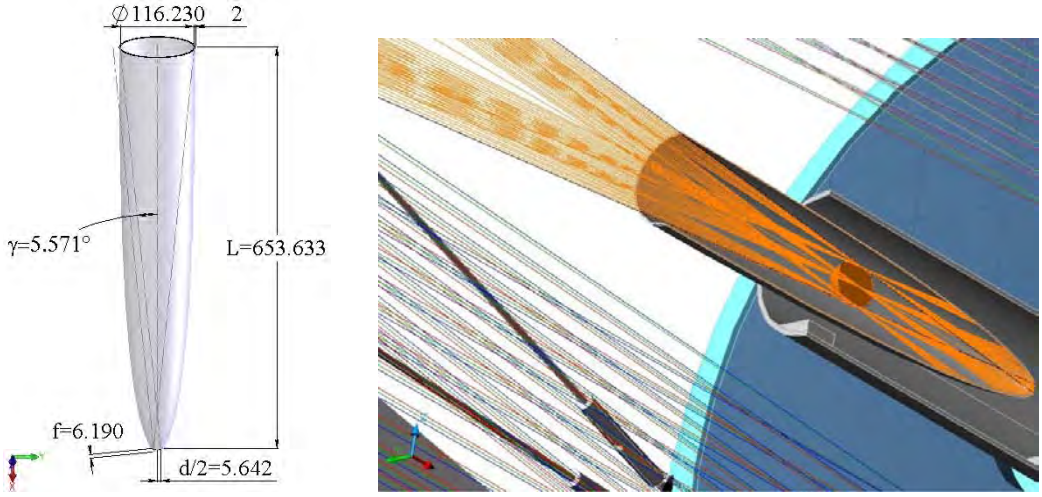

Figure 7.14: Design drawings of the first CPC

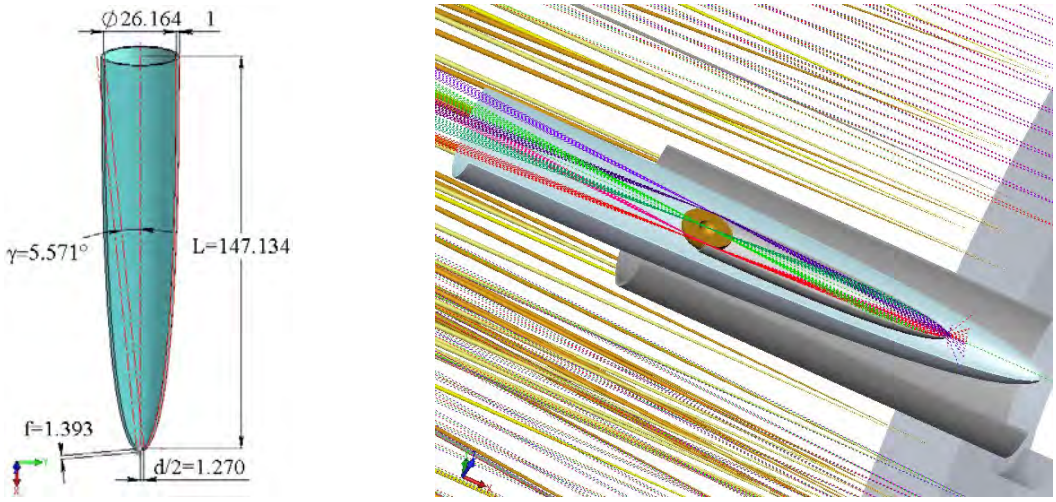

Figure 7.15: Design drawings of the second CPC (left) and relative locations of both CPCs

In the first design, the entrance aperture of the CPC was made two times larger

than the solar image diameter. This was considered an acceptable compromise since this CPC was intended for applications requiring a relatively larger exposed area rather than a higher concentration. Furthermore, by having a larger entrance/exit aperture it would accept rays from even a disaligned beam caused by a tracking error, but at the expense of decreasing third stage concentration.

By contrast, the second CPC was intended to achieve a relatively higher concentration and accordingly more precise sun-tracking would be required. Another issue with this design is the high temperature at the exit aperture, leading to a requirement for a material with higher heat resistance. Thus, although the use of this CPC as a complementary concentrator can offer a good solution, it would not be the ideal solution if the tracking could not ensure the necessary precision.

Since the non-imaging CPCs discussed above could not be manufactured at the time of the experimental studies, the feasibility experiments were carried out with a shorter truncated cone instead. The detailed design drawings are given in Appendix 7A. The truncated cone was manufactured from aluminium and made to fit into the upper end of the canister. It was especially designed to accommodate the specimens inside, and with through holes to allow air cooling for the ageing experiments. A perspective view of the design and a photograph of the truncated cone fitted into the canister pipe are shown in Figure 7.16.

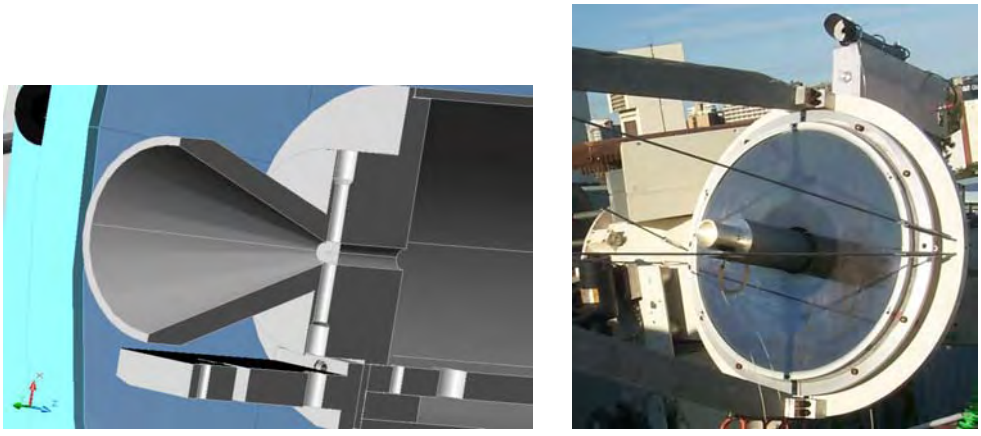

(a) Design drawing *(b) Overall view of the SEC with truncated cone*

Figure 7.16: Short truncated cone

7.5 Design and development of other auxiliary systems

7.5.1 Positioning and focusing device

Along with the sun-tracking and light transmission controlling systems, the development of a beam focusing and specimen positioning device was necessary for

the proper conducting of the experiments. An appropriate X-Y-Z moving mechanism was developed as a means for precise positioning of the specimen, fixed by a clamping device in the required location. It also allowed fine adjustment of the beam focus size over the specimen. It comprises a two axis positioning stage from a microscope and a small metric stage.

In the different applications investigated in this research, alternative approaches for the design of the positioning and focusing device were used, some of which are described here. The principal design configuration used with conventional lenses is illustrated in Figure 7.17a and a photograph of the built device – in Figure 7.17b.

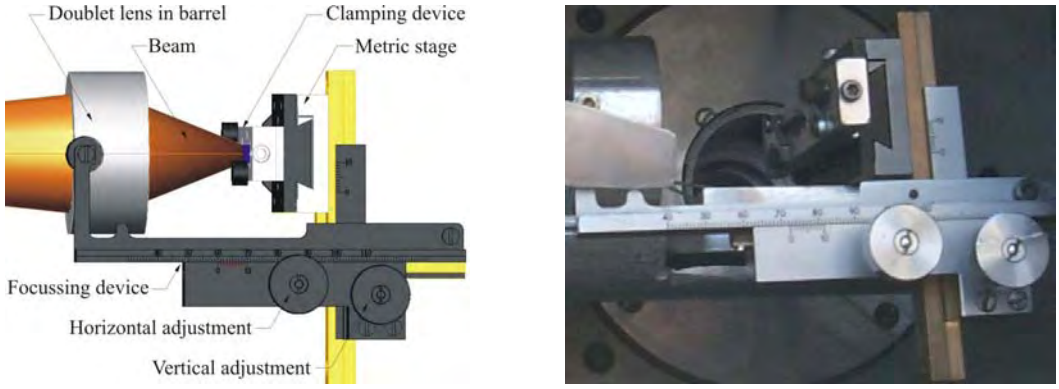

(a) Design drawing *(b) Photograph of the built device*

Figure 7.17: Design configuration of the focusing device including the last focusing doublet lens, metric stage and butt clamping device

The two axis positioning stage was mounted along the telescope in such a way that its horizontal axis movement serves as a focus size adjusting device. The movement along the vertical axis allows for elevation adjustment of the focal beam and its target. The micro-positioning stage utilizes two rack and pinion movements for focus adjustment and positioning in both horizontal and vertical directions. The horizontal rack and pinion used as a means of fine control of the focus size adjustment can be seen on the front side of the focusing device in Figure 7.17.

The metric stage, a small X-Y moving table, was purchased from Edmund Optics. A detailed drawing of the stage is given in Appendix 7A. The movement of the metric stage allows precise positioning in both vertical and horizontal planes. For most experiments, since the focusing device was used for vertical positioning of the focal spot, only one direction movement was controlled by the metric stage.

The combining of the positioning and metric stages was intended to provide adjustable focal length, as well as micro-positioning that can be fine-tuned during the

alignment of the system. In this way, the two-dimensional X-Y axes positioning stage was provided with a third axis, Z, allowing precise positioning of the focal spot on the specimen surface. In another words, the focusing device was used as a micro-positioning lift to precisely adjust the vertical location of the specimen with respect to the last focusing optical component.

The metric stage was modified to allow free propagation of the beam through its back plate. An appropriately shaped and sized through hole was drilled on the back plate to correspond with the size of the passing through it light cone. Front and back perspective views of the metric stage, modified to prevent beam back reflection, are shown on the 3D drawing in Figure 7.18.

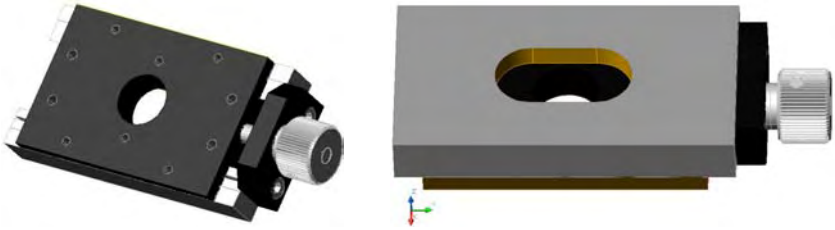

Figure 7.18: Front and back perspective views of the modified single axis metric stage

The through hole was designed with such shape and size, so it could also allow fixing of the fiber optic cable used in some of the preliminary experiments. In addition, suitable holes with metric threads were made to allow fixing of both butt and lap clamping devices, as well as the clamping fixture of the specimens and the cooling tube, used in the initial ageing experiments.

7.5.2 Clamping devices

Butt joint clamping

For proper conducting of the polymer butt joining experiments, a suitable clamping device for butt joining was designed and developed (see Figure 7.19).

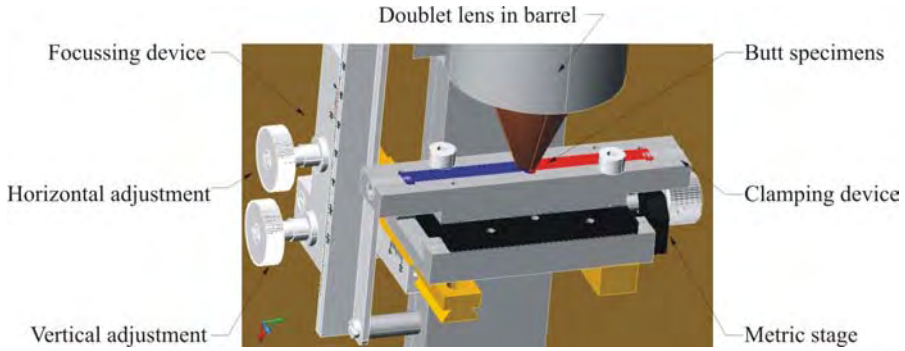

Figure 7.19: A perspective view of the butt joint clamping device

Made of aluminium, it consists of a central channel with a rectangular section and appropriate removable covering plates to hold firmly the specimens to be joined. To ensure the necessary clamping pressure at the joint interface, two identical springs are appropriately loosely accommodated into two hollow grub screws at both ends. The standard detailed design drawing is given in Appendix 7A.

The design assembly configuration of the fitting of the clamping device on the positioning and focusing device can be seen in Figure 7.17. This clamping device was initially used in the arrangement under the trunnion box, as shown in Figure 7.9c. With the later SEC modification the same clamping device together with the positioning and focusing device were fitted inside the trunnion box, as shown on the design drawing in Figure 7.10a.

Lap joint clamping

On a later stage, in order to extend the research further and study the possibility of through-transmission lap joining of transparent and differently colored polymers, another suitable clamping device was designed and developed (see Figure 7.20).

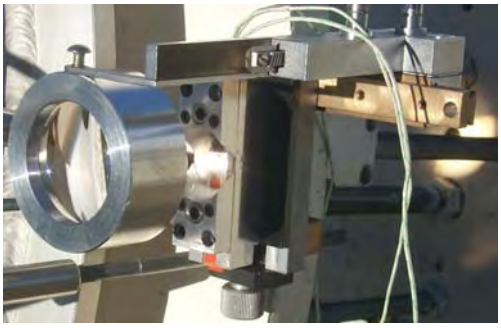

Figure 7.20: Lap joining clamping device

Similar to the butt joining clamping device, it consists of a main bottom plate with a rectangular section central channel to accommodate two specimens to be joined and two dummy specimens. The dummy specimens are used to ensure that the two specimens to be lap-joined are parallel. The thickness difference was adjusted by two identical grub screws with springs mounted on the top of each specimen.

Although the IR component propagating in the system is not significant, a transparent IR window plate (made from Barium Fluoride) was used above the top specimen to prevent the outward movement or bending of the specimens. The clamping pressure was created by a spring pushing the underside of the bottom

specimen. The standard detailed design drawing of the lap joining clamping device is given in Appendix 7A. This device was also used in the arrangements under and inside the trunnion box in the lap joining and some of the ageing experiments.

7.5.3 Experimental cooling system

Before commencement of the experiments, in particular the polymer ageing, an appropriate air-cooling system was designed and developed to avoid overheating of the specimen surface. As illustrated in the schematic diagram in Figure 7.21, the cooling system consists of a two-horse power air-compressor with standard accessories, a temperature controller having a 15 V or 240 V output power supply, and necessary automatics.

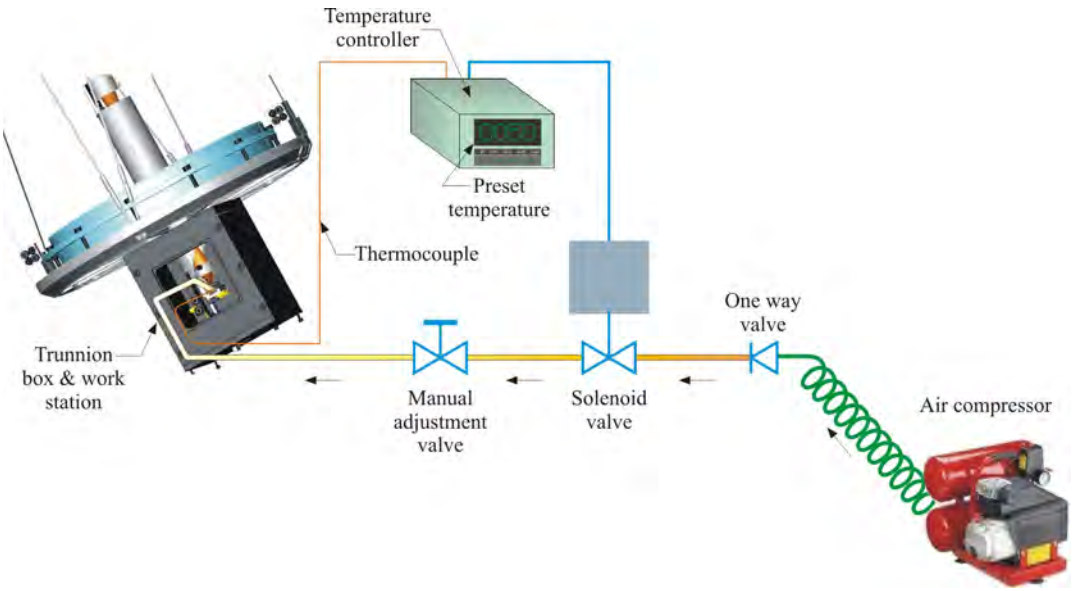

Figure 7.21: Schematic diagram of cooling system

The introduction of an appropriate temperature controller and a solenoid type valve has allowed maintaining the specimen maximum temperature at a preset value. The temperature controller uses the signal from a K-type thermocouple to switch on and off the solenoid valve. When the temperature reaches the preset value, the controller opens the airway via the solenoid valve and the released air cools down the exposed specimen surface until its temperature drops below the preset value. The air flow rate is additionally adjusted using a manually controlled valve. A photograph of the cooling system is shown in Figure 7.22.

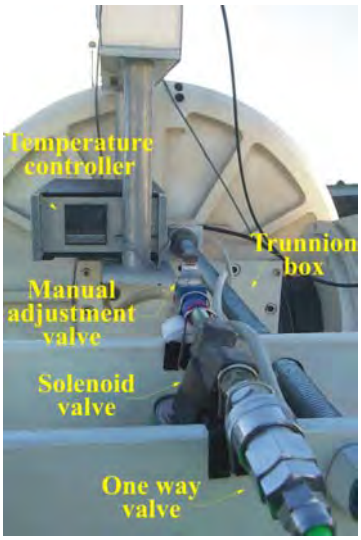

(a) Solenoid valve and temperature controller

(b) Air compressor

Figure 7.22: Cooling system

When the experiments were carried out in the trunnion box, a provisional fixture to hold the compressed air releasing pipe was used. An arrangement with the butt clamping device is shown in Figure 8.8a in Chapter 8.

Generally, the same cooling system but with extended airways through the canister, was used for the experiments carried out with the provisional third stage cone concentrator. The cooling air inlet is shown in Figure 7.23.

Figure 7.23: Cooling inlet in the provisional third stage concentrator

7.5.4 Beam control system

Attempts to control the irradiation process by mechanical obstruction of the concentrated light beam were made as an alternative to the air cooling method. Initial feasibility experiments were conducted with a hand-made light chopper and using a mini-mist/smoke maker (Figure 7.24).

Figure 7.24: Provisional light chopper and experimental mist/smoke maker

Evaluation experiments were performed to compare the insolation intensity and the temperature above and below the provisional light chopper using overshadowing strips with different sizes. The results showed that if the pulsing shadow covers the whole aperture, such a device can decrease the intensity up to 23% and the temperature up to 38%. The use of the mist/smoke maker has led to temperature decrease by 12.5% on average. However, although considered feasible, the development of a more detailed design of such a process control system has been planned for future work.

Another means of process control via selective spectral distribution has been considered. As discussed in Chapter 5, although the transparent PMMA absorbs a relatively small quantity of the incident near IR radiation, it still generates heat, making the specimen pliable which has a negative effect on the clamping pressure. To decrease this effect, a 'hot mirror' to filter out the IR component present in the incident solar spectrum and to enhance the selective heating was experimentally tested. A significant reduction of the power absorbed was achieved and as a result the temperature of the upper transparent specimen was decreased by more than 30%. In another experiment clear PMMA and PC were used instead of the 'hot mirror' and a similar effect was achieved, but the polymer optical characteristics deteriorated after prolonged use. Also, the effect of the filtering was dependent on the distance of the filter from the focal spot.

7.5.5 Experimental test rig

After completion of the development and modifications of the SEC facility systems, discussed in the previous sections, an experimental test rig was set up (Figure 7.25). It was equipped with the necessary instruments connected to a

computer (as described in Chapter 4) for measuring and recording the environmental and process parameters.

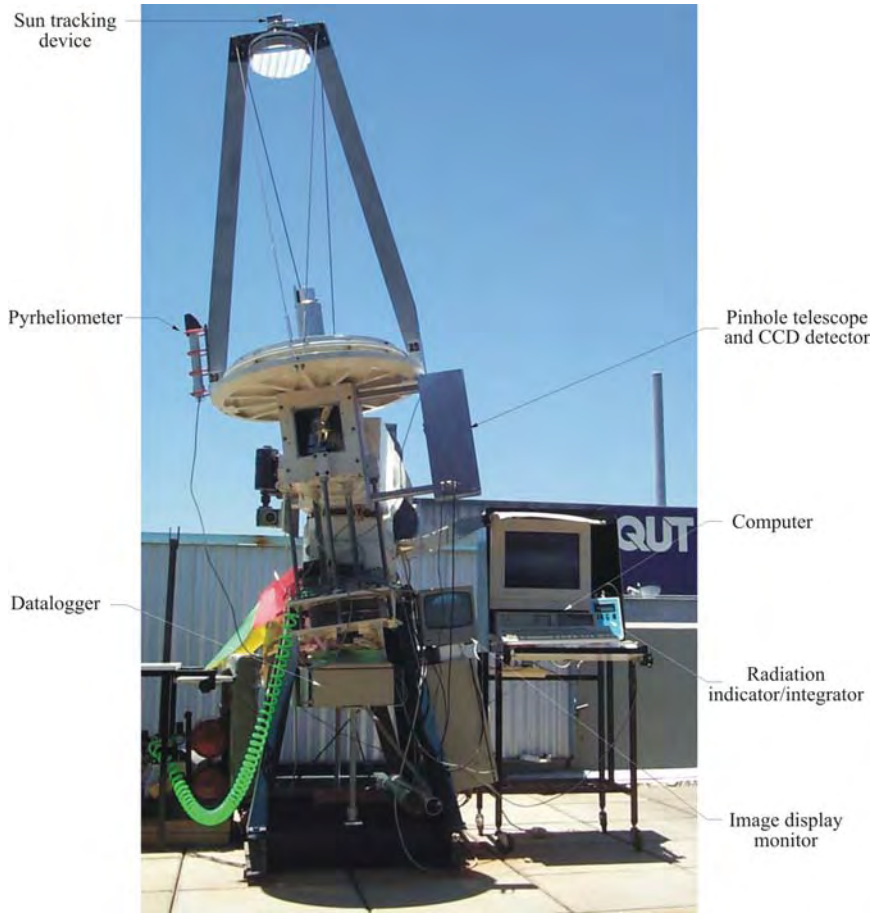

Figure 7.25: Experimental test rig

7.6 Conclusions

Through the course of the modifications of the original systems and the introduction of the especially developed auxiliary systems, it was determined that the design concepts modeled (as described in the previous chapter) were feasible. The modifications and improvement of the various SEC facility systems, discussed in this chapter, proved useful and reliable for the experimental exploration of the proposed applications.

The sun-tracking device with the especially developed for the SEC photoelectric sensor and electronics has obvious advantages compared to the initially applied methods for acquisition of the solar image. It has a two-speed automatic control, as well as a manual mode of operation, and eliminates the need for an operator and thus possible human error. It also allows additional alignment (mechanical and electronic

correction of the tracking sensor and controlling device) with the telescope principal axis. Further research towards improvement and advancement, such as process automation and reducing the number of variable parameters in the insolation utilization, is planned for future work.

The modifications described here led not only to a significant shortening of the auxiliary optical path, but also allowed integration of the beam transmitting and focusing in one compact adjustable system when conventional optics was used. Also, as expected, the significant reduction of the number of auxiliary optical components simplified the beam transmitting process and led to a decrease in power losses and spectral limitations.

The use of an optical fiber guide as an alternative means of beam transmission was considered non-feasible for applications requiring relatively high concentration and temperatures, such as polymer joining. However, with the use of a "hot mirror" it could be feasible for applications such as curing or ageing.

One novel contribution of this research is the enhancement of the image forming (Cassegrainian) concentrator with non-imaging cone-like concentrators (conical and CPC), utilizing their inherent disadvantage of excessive length. Compared to the refractive type means of transmitting the concentrated solar radiation, the truncated cone and CPC concentrators can be considered more efficient enhancing the concentration further.

Alternatively, the geometrical vector flux principle for an incoherent Lambertian source could be used to design a suitable radiation direction device. The design of a radiation direction device has been considered for future work.

The use of a light chopper and a mist/smoke maker for beam control was also considered feasible. It was found that when a light chopper was used, the intensity of beam solar radiation decreased by up to 23% and the temperature by up to 38%. A temperature drop by 12.5% on average was observed when a mist/smoke maker was used as a beam controlling device.

On the whole, the implementation of the various SEC facility systems, developed and further modified, has led to improved optical and thermal performance and the experimental study results are discussed in the following chapters.

CHAPTER 8.
EXPERIMENTAL STUDIES ON POLYMER JOINING

8.1 Introduction

In line with the research objectives, one of the first applications of the utilized concentrated solar radiation was explored for joining of clear and colored, similar and dissimilar thermoplastics. As discussed in the previous chapter, the SEC facility has been developed, modified and tested to serve as an energy source for the proposed study.

Little research on the effect of concentrated visible solar radiation on thermoplastics and no information on using solar radiation for joining thermoplastics have been found. Therefore, to study the interaction of solar radiation with the polymer, preliminary experiments were needed. The preliminary feasibility experiments involved joining transparent and white engineering thermoplastics and were performed at the beginning of the research, before the modification of the SEC systems. These initial experiments were also necessary to assess the optical and thermal characteristics and capabilities of the SEC systems and the possibility of improving them.

After the modification of the SEC facility subsequent studies with seven additional similar but differently colored and other dissimilar polymer materials were conducted. The aim was to experimentally determine the weldability of the selected thermoplastics in butt and lap joint configurations using concentrated solar radiation. Other objectives were to study the effect of color on the radiation-material interaction and to validate the relevant models discussed in Chapter 6.

The butt and lap joining experiments, reviewed in this chapter, were performed initially using the SEC facility supplemented with auxiliary imaging optics. Since no similar three-stage solar concentrator used as a radiation source for polymer processing was found, in this research a new insolation utilization system using third stage non-imaging concentrator was developed. It was explored as an alternative radiation source for polymer joining.

Advanced welding techniques particularly in IR laser welding require, as found in the literature review, a special absorbing medium and are limited by the ability of

the material to transmit IR radiation. Moreover, the range of plastics that are weldable using these techniques, are not well documented. Therefore, a new through-transmission irradiation technique utilizing concentrated solar radiation was developed and explored for polymer joining without the need for any additional absorbing substance. In most studies the tensile strength of the welded specimen pairs was determined. In some studies the joint microstructures of the fractured specimens were also analyzed.

This chapter begins with a review of the preliminary experimental study on butt joining of selected clear and white thermoplastics. Next, the experimental studies on butt joining of identically and differently colored, similar and dissimilar polymers with imaging and non-imaging auxiliary optics are described. In conclusion, the new through-transmission joining technique is presented and its application for polymer lap joining using imaging and non-imaging auxiliary optics is discussed.

8.2 Preliminary joining experiments of selected engineering thermoplastics

8.2.1 Background

In the early stages of this research the feasibility of effectively joining four types of thermoplastics such as polyvinyl chloride, high density polyethylene, high impact polystyrene and polypropylene was explored. The results from the experimental joining of the plastics appeared to be promising. The welding durations for the different thermoplastics ranged from 10 to 80 seconds. The tensile strength of the joints was found to be satisfactory and in the case of polypropylene was as high as 88% of the parent material strength. It was also found that the absorptance of the thermoplastic specimens was directly related to their opacity, and although requiring longer exposure, even translucent thermoplastics could be joined.

8.2.2 Joining of transparent and white thermoplastics

Since the provisional experiments showed that thermoplastic joining could be achieved by utilization of concentrated solar radiation, further experimental work was undertaken. To explore the feasibility of butt joining of transparent and opaque polymers with concentrated insolation, white ABS and transparent PC and PMMA were selected and 15 sets of specimens from each material were prepared. As specified in Chapter 4, the specimen shape and size were chosen to allow comparison

with similar experiments performed using microwave energy. The specimens were inserted into the slot provided by a provisional specimen holding device and exposed in the principal Cassegrainian focus using one auxiliary focusing lens, acting as a focal reducer. Also, proper compressive force was applied in order to hold the joint, preventing air to be trapped during solidification.

As discussed in Chapter 6, the heat required for the polymer joining was generated via volumetric (for transparent PC and PMMA) and surface radiation (for white ABS) effects, causing the specimens to soften and bond. After welding, the specimens were tested for strength, and the joint microstructures were also analyzed. The welded specimens are shown in Figure 8.1.

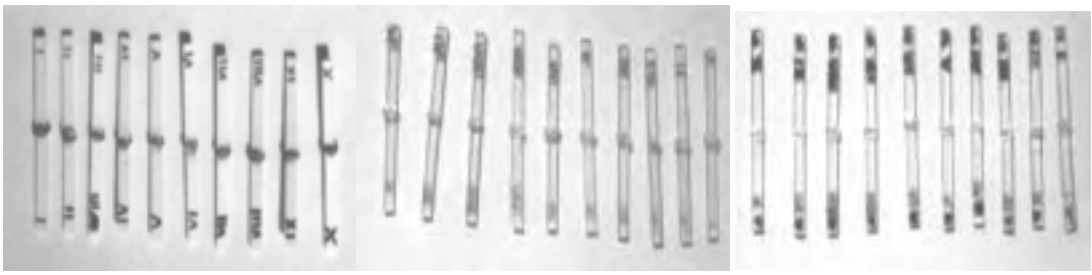

ABS PC PMMA

Figure 8.1: Welded specimens in the preliminary experiments

8.2.3 Results and discussion

8.2.3.1 Joining of thermoplastics without controlling the welding parameters

The initial experiments were performed without controlling the variation of welding parameters such as the intensity of direct insolation, the temperature at the Cassegrainian focus and the duration of the welding process.

The welding duration was controlled by visual assessment only. The temperature was measured at the exposed interface at the beginning of each experiment. Table 8.1 summarizes the results obtained during the initial experimentation.

Table 8.1: Average strength of the weld without controlling the welding parameters

Material	Welding duration [sec]	Temp. on idle running [°C]	Intensity of direct solar radiation [W/m^2]	Wind velocity [m/s]	Elongation [mm]	Average joint strength [%]
ABS	18	549	898	≤2	0.66	38.77
PC	27	565	922	≤2	0.67	27.28
PMMA	50	555	888	≤1	0.55	31.76

The temperature shown is the average maximum temperature measured on idle running before polymer exposure using one auxiliary lens.

The tensile strength of the ABS joints ranged from 9.08% to 89.83% of the parent material strength. The tensile strength of the welded PC material ranged from 18.38% to 42.11% of the parent material strength. The percentage of parent-material strength for the welded PMMA material ranged from 4.67% to 55.23%. The average weld strength of the ABS, PC and PMMA specimens compared to the parent materials was 38.77%, 27.28% and 31.76% respectively, as shown on Table 8.1.

It should be noted that this was a preliminary study and a large variation between the highest and the lowest values (especially for ABS and PMMA) was observed. This can be attributed to the fact that the quality of the weld in this study depended entirely on the manual skill of the operator. Furthermore, a number of failures falling outside the criteria for an acceptable failure, were also included in the analysis. In such instances it is preferable (AS1145.1 2001) that dumb-bell specimens are used which has been considered for future work.

8.2.3.2 Joining of thermoplastics with controlling the exposure duration

The duration, power and temperature are the important parameters that affect the quality of the weld. In order to obtain more accurate results, experiments for specific exposure duration were carried out between 9.30 am and 2.30 pm. In this period, as discussed previously, the intensity of direct solar radiation was without major fluctuations during each experiment. The specimens of each material were welded at the average duration obtained, as shown in Table 8.2.

Table 8.2: Average strength of the weld with exposure duration controlled

Material	Duration [sec]	Temp. on idle running [°C]	Intensity of direct solar radiation [W/m^2]	Joint strength [%]	Elongation [mm]	Average joint strength [%]
ABS	(1) 13	640	874	31.99%	0.56	37.87
	(2) 18	652	813	32.80%	0.63	
	(3) 23	686	935	48.83%	0.78	
PC	(1) 22	660	874	18.01%	0.47	24.64
	(2) 27	640	814	22.39%	0.49	
	(3) 32	690	941	33.52%	0.63	
PMMA	(1) 45	614	870	30.62%	0.46	33.55
	(2) 50	640	807	34.92%	0.69	
	(3) 55	710	939	35.13%	0.55	

It is obvious that with the increase of the exposure duration, the strength of the joint increases as well, probably due to an enlargement of the welding zone. Comparing the results from Tables 8.1 and 8.2, it can be seen that the obtained average joint strength for the experiments with and without controlling the exposure duration is relatively consistent.

8.2.3.3 Microscopic examinations

When a weld has been completed, as a rule the evaluation of the quality of the joint starts with an examination of the outer surface of the weld. The fusion of the welded specimens must be smooth and free of etching. In the welded specimens there must be no cracks, porous patches or notching; it must be regular and even.

In these preliminary experiments there was a significant variation in the weld strength of the tested specimens due to the manual mode of operation and varying ambient conditions. In order to investigate if sufficient beam energy had propagated into the specimens to promote fusion of the joint, microscopic examinations of sections through the fracture surfaces of the joined specimens were performed.

Figures 8.2 to 8.7 show the scanning electronic microscope images (SEM) of the welded specimens. They are based on the experiments performed without controlling the welding parameters (called experiment A for simplicity) and by controlling the exposure duration (experiment B).

Figure 8.2 shows the SEM images of the ABS specimens with the lowest tensile strength from experiments A and B. It can be seen that in experiment A a large portion of the joint interface was not bonded.

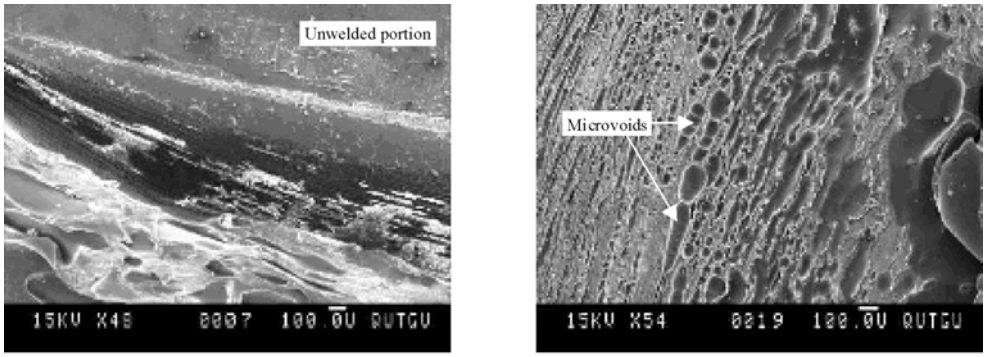

Specimen of ABS Material from Experiment A

Specimen of ABS Material from Experiment B

Figure 8.2: ABS specimens with the lowest tensile strength

Also, because the concentrated radiation beam is almost parallel to the butt joint interface and the polymer has a relatively low heat conductivity, the heat generation

at the joint interface is not very effective. This has been confirmed by the microscopic examination and observed in the SEM images shown in Figure 8.2. The fusion is evident predominantly on the surface and diminishes with depth increase. As can be seen, micro-voids were formed probably due to an evolution of gases during the welding process.

In experiment A the lowest tensile strength of weld was only 9.08% of the parent material strength. In experiment B, micro-voids were formed at the surface of the material, reducing in size towards the bottom layer. Although a large portion was not welded, the strength of the weld increased significantly to 23.79% of the parent material strength.

Figure 8.3 shows the SEM images of the ABS specimens with the highest tensile strength obtained in experiments A and B.

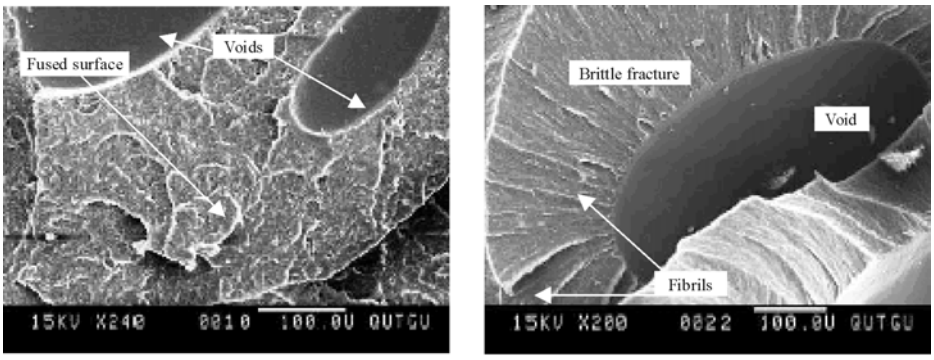

Specimen of ABS Material from Experiment A

Specimen of ABS Material from Experiment B

Figure 8.3: ABS specimens with the highest tensile strength

In experiment A, the highest tensile strength of 89.83% of the parent material strength was achieved. On the SEM image it can be seen that, compared to experiment B, a relatively larger area was bonded although voids could still be found at the surface. In experiment B, a weld strength of 66.98% of the parent material strength was obtained. During the microscopic examination irregular fibrils were observed indicating a relatively large joint area.

Figure 8.4 shows the SEM images of the PC specimens with the lowest tensile strength from experiments A and B. For experiment A, it was observed that a large portion of the joint surface was not bonded, as can be seen on the top right corner of the SEM image. When the joined specimens were subjected to a tensile load, the welded area ruptured, leaving micro-voids and cavities due to the ductile fracture. This probably was the cause for the low joint tensile strength of 18.38% of the parent material strength.

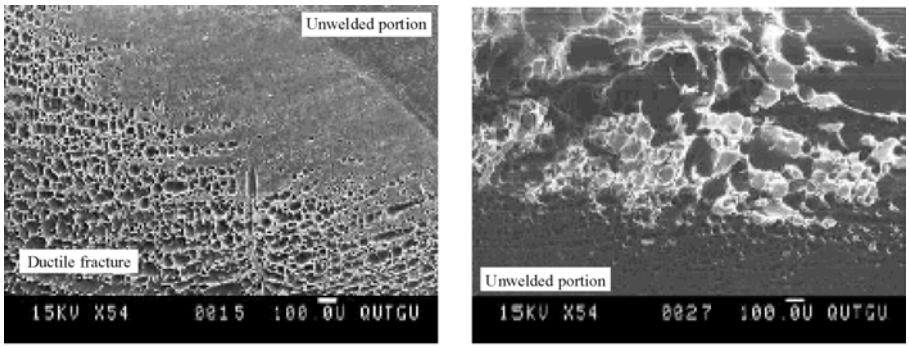

Specimen of PC Material from Experiment A

Specimen of PC Material from Experiment B

Figure 8.4: PC specimens with the lowest tensile strength

In experiment B, the fusion took place only at the top layer of the material resulting in a tensile strength of 10.36% of the parent material strength. The low tensile strength of the weld in both experiments was probably due to the relatively high processing temperature and high light transmittance of the PC material.

Figure 8.5 shows the SEM images of the PC specimens with the highest tensile strength obtained in experiments A and B.

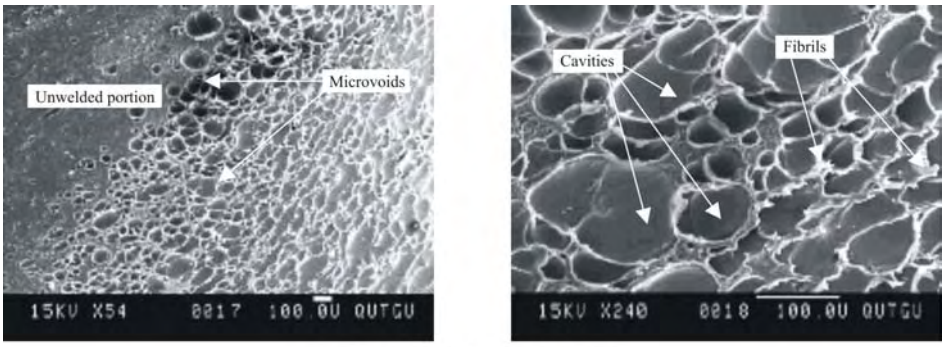

Specimen of PC Material from Experiment A

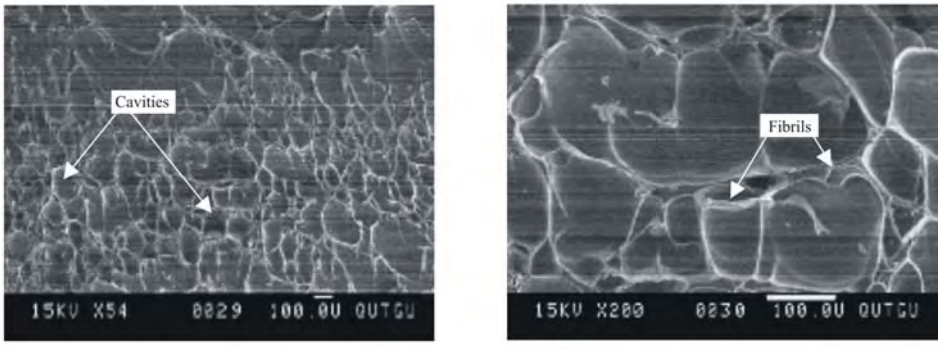

Specimen of PC Material from Experiment B

Figure 8.5: PC specimens with the highest tensile strength

It is evident from the SEM images that a relatively larger surface area was bonded in both experiments. Obviously the concentrated solar energy flux had propagated into the deeper layers of the material but still some portion of the surface

remained unwelded. The resulting tensile strength was above 40% of the parent material strength. The SEM images show a large number of micro-voids and cavities which probably affected the joint quality.

Figure 8.6 shows the SEM images of the PMMA specimens with the lowest tensile strength from experiments A and B.

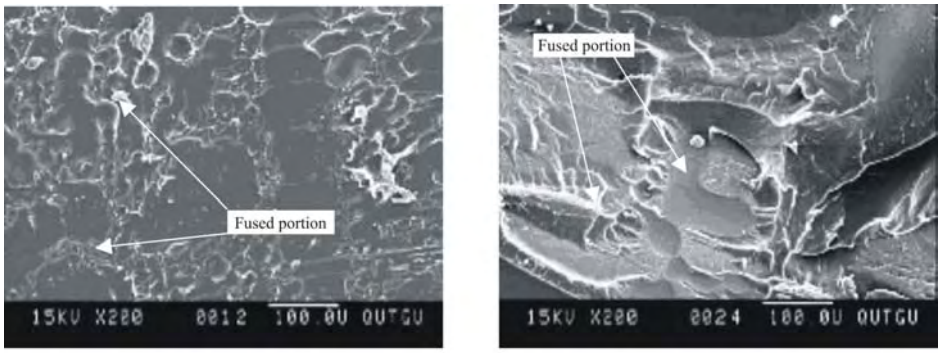

Specimen of PMMA Material from Experiment A

Specimen of PMMA Material from Experiment B

Figure 8.6: PMMA specimens with the lowest tensile strength

In experiment A, the lowest of all tested materials tensile strength of 4.67% of the parent material strength was obtained. The fusion took place only at the surface and voids were found on the joint interface, which resulted in a lower weld strength.

Similarly, in experiment B a relatively large portion of the joined interface remained unwelded. However, compared to experiment A, a higher weld strength of 19.70% of the parent material strength was achieved. Considering only the fused portion, as shown in the image on the right, the fusion took place on the surface resulting in a relatively smooth contact area with a minimal number of voids. This may be attributed to sufficient propagation of the concentrated solar beam radiation to the joint interface.

Figure 8.7 shows the SEM images of the PMMA specimens with the highest tensile strength obtained in experiments A and B. In both experiments, an weld strength of above 45% of the parent material strength was obtained, although micro-voids were present. The similar structure and void formation may have been caused by the relatively even propagation of the solar energy flux through the material. This statement was confirmed by the linear ridge pattern throughout the specimens, observed in the SEM images. The lighter contrast contours in the SEM images show the contact area of the joint. Since PMMA is brittle, not many fibrils were formed in the ruptured surface of the joint.

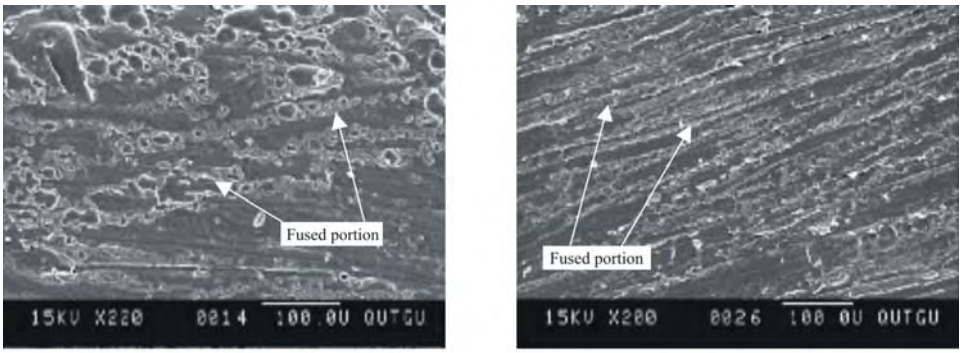

Specimen of PMMA Material from Experiment A

Specimen of PMMA Material from Experiment B

Figure 8.7: PMMA specimens with the highest tensile strength

From the preliminary experimental results the following conclusions could be drawn. Although ABS has two glass transition temperatures and a relatively high reflectance, it had the shortest welding duration. This is probably due to the fact that it has negligible transmittance of the utilized spectra and the surface radiation effect is significant.

Being transparent to the visible spectra of solar radiation, PC and PMMA absorbed less amount of direct solar radiation (3-5%), most of which was transmitted through the material and some portion reflected. As the absorptance of thermoplastics is directly related to their opacity to the concentrated solar photons from the visual range of the spectrum, longer welding duration is required for transparent plastics. Compressive force was constantly applied to the joint of the specimens during the welding process. In the case of PC, this resulted in some bubbles being trapped inside the weld. In the case of PMMA, bubbles formed in the bulk of the material, gradually emerging on the surface forced by natural convection.

On the whole, the results from this preliminary study proved that the joining of white and transparent polymers using solar energy was feasible. The data was used in the model calculations and the further modification of the SEC facility.

8.2.3.4 Comparison with thermoplastic joining using microwave energy

The results obtained in the above experiments were compared with the results from the welding of ABS and PC thermoplastics by using focused microwave energy (Table 8.3). These thermoplastics were welded at three different power inputs of 600W, 800W and 1000W (Yarlagadda and Tan 1998). The comparison between both welding processes was based on the energy consumption (kJ) required to perform the welding and the output results (strength of the welded joint). Assuming

there is no energy loss, for the microwave welding process the energy consumption was obtained by multiplying the power input in (J/s) by the welding duration (s). Considering the average reflectivity in the visible wavelength range for both primary and secondary mirrors to be not less than 80%, the solar energy consumed, E_c, is calculated by using the following equation (Stoynov et al. 2000):

$$E_c = \eta_p \eta_s \frac{\pi}{4}(D_p^2 - D_s^2) G_b \tau \qquad (8.1)$$

where η_p is the reflectivity of primary mirror, η_s is the reflectivity of secondary mirror, D_p is the diameter of primary mirror, D_s is the diameter of secondary mirror, G_b is the intensity of the direct solar radiation, and τ is the welding duration.

Table 8.3: Thermoplastic welding utilizing microwave and concentrated solar energy

Welding by means of focused microwave energy				**Welding by applying concentrated solar energy**			
Power input [W]	Welding duration [sec]	Energy consumed [kJ]	Weld strength compared with parent material [%]	Power input [J/s]	Welding duration [sec]	Energy consumed [kJ]	Weld strength compared with parent material [%]
ABS Material							
600	46	27.60	26.0	134.4	13	1.747	31.99
800	38	30.40	28.0	124.8	18	2.246	32.80
1000	34	34.00	16.4	143.4	23	3.298	48.83
PC Material							
600	140.5	84.30	11.5	134.4	22	2.957	18.01
800	66	52.80	28.2	124.8	27	3.370	22.39
1000	44.5	44.50	20.3	144.6	32	4.672	33.52

From the results shown in Table 8.3 it is evident that, in terms of energy consumption, the joining process utilizing solar energy consumed much less energy than the microwave welding process. Also, higher joint strengths were achieved when solar radiation was used, compared to the microwave energy welding process. Thus, the joining process by applying concentrated solar radiation appears to be more efficient in terms of energy consumption and output results.

8.3 Experimental butt joining of transparent and colored, similar and dissimilar polymers

8.3.1 Background

To explore the capability of the modified SEC system to serve as an energy source in the explored applications, butt joining experiments were performed with seven additional similar but differently colored and other dissimilar polymer materials. These studies were intended to experimentally determine the possibility of

utilizing concentrated solar radiation for joining of transparent thermoplastics (PC and PMMA) and opaque thermoplastics (PMMA and ABS) with different colors. The effect of polymer color on the radiation-material interaction was also explored in these studies. Performed using the SEC facility supplemented with auxiliary imaging and non-imaging optics, some of these joining experiments were used for the validation of the relevant models (discussed in Chapter 6) as well.

In general, the butt polymer joining experiments were conducted at three locations using the corresponding auxiliary imaging and non-imaging optics configurations, arranged according to the combined models described in Chapter 6.

The preliminary butt joining experiments (discussed in Section 8.2) were performed near the Cassegrainian focus with one lens and were only for the feasibility study because of the obvious practicability considerations. To explore further the possibility of using different auxiliary optics as a beam transmitting means, the butt joining experiments were performed with conventional imaging optics under and inside the trunnion box, and with non-imaging optics near the Cassegrainian focus. Accordingly, the data obtained from the experiments at each location was analyzed and the results are summarized here.

8.3.2 Experimental methodology

Test specimens with dimensions 40 x 6 mm x sheet thickness, as described in Chapter 4, were joined in a butt configuration. Both components were fixed firmly in the butt clamping device (Figure 7.17). The butt clamping device was appropriately mounted on the positioning and focusing device when conventional auxiliary optics were used (Figure 8.8a). When non-imaging optics were used, it was mounted suitably at the exit aperture of the non-imaging concentrator (Figure 8.8b).

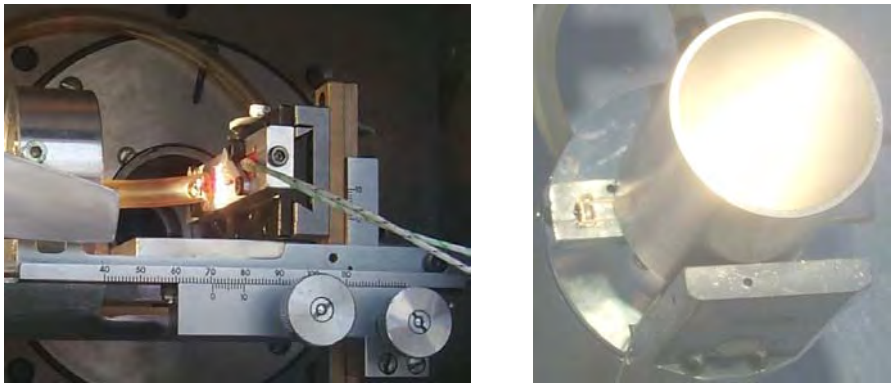

(a) imaging auxiliary optics (b) non-imaging optics

Figure 8.8: Butt joint clamping device mounting

In these experiments specimens from transparent and opaque polymers were joined and consequently subjected to tensile testing to determine the joint strength. Because the precise localization of heating is an important factor when welding thermoplastics, to ensure the bonding process, heating was limited to the immediate area around the joint interface. Two techniques were employed to prevent the polymer overheating.

In the first technique a thermocouple was embedded between the specimens at the joint interface to measure the temperature increase at the affected zone during the irradiation process. When the building of the generated heat was sufficient, it was appropriately withdrawn with the interruption of the irradiation process, before the solidification of the formed joint.

When using this technique, it was found that even with an unmasked thermocouple tip different temperature readings were obtained depending on the position of the thermocouple and polymer color. However, on the whole the thermocouple maintained higher temperature readings (3–11%) than the average temperature of the affected polymer. The temperature variations, recorded by a thermocouple embedded at the joint interface during the joining tests of one pair from each color are presented in Figures A8.1 to A8.4 in Appendix 8.

On the other hand, sufficient cooling during irradiation is considered an important factor in minimizing the thermal damage in the upper layers of the exposed to concentrated solar radiation polymer materials. Thus, in the second technique the provisional air cooling system described in Chapter 7 was used. Although designed predominantly for the ageing experiments, this system was found feasible in the joining experiments as well.

Since most of the used polymers would start decomposing above 220°C, tests were performed with the thermocouple temperature controller preset at 150°C, 180°C and 220°C. The experiments showed that presetting the temperature at 150°C slowed down the joining process significantly leading to less homogenous joints. The preset temperature of 220°C was found to be relatively high, causing yellowing and slight burning of the top layer of the ABS polymer. Therefore, 180°C was chosen to be the optimal temperature for the butt joining experiments.

The beam insolation intensity, relative humidity and wind speed, as mentioned in Chapter 5, were also measured.

8.3.3 Results and discussion

After the preliminary experiments showed that concentrated solar radiation can be utilized for butt joining of white and transparent thermoplastics, the experiments summarized here proved that all selected colored polymers can be joined as well.

8.3.3.1 Study on identically colored polymer butt joining with imaging auxiliary optics

Initially, the weldability of thermoplastics with identical colors in a butt configuration was explored using imaging auxiliary optics with five lenses. In general, in this study the joining of all colored, as well as black, white and transparent specimens, was successful. A photograph of some of the joined specimens is shown in Figure 8.9.

Figure 8.9: Identically colored specimens butt joined with imaging optics

To represent the experimental data, the results for two specimen pairs from each colored polymer were selected (shown in Table A8.1 in Appendix 8) and the average values are presented in Table 8.4.

Table 8.4: Experimental data from butt joining of polymers with identical colors using imaging optics

Specimen	Welding duration [s]	Average insolation intensity [W/m²]	Deposited solar energy [kJ]
Black + Black	22.5	938	1.492
White + White	59.5	973	4.092
Green + Green	65.5	948	4.392
Violet + Violet	71.5	928	4.693
Blue + Blue	73.5	967	5.027
Red + Red	77.5	953	5.165
Orange + Orange	94.5	959	6.405
Yellow + Yellow	98.0	965	6.688
Transparent + Transparent	189.0	957	12.789

Based on these experimental results, the deposited solar energy for each

specimen pair was calculated using Equation 6.13 and the relevant variables from the irradiated polymer model. As can be seen, the deposited solar energy required for the joining process to take place varies with the color from 4.392 to 6.688 kJ. The deposited solar energy during the joining process of each identically colored specimen pair is graphically illustrated in Figure 8.10.

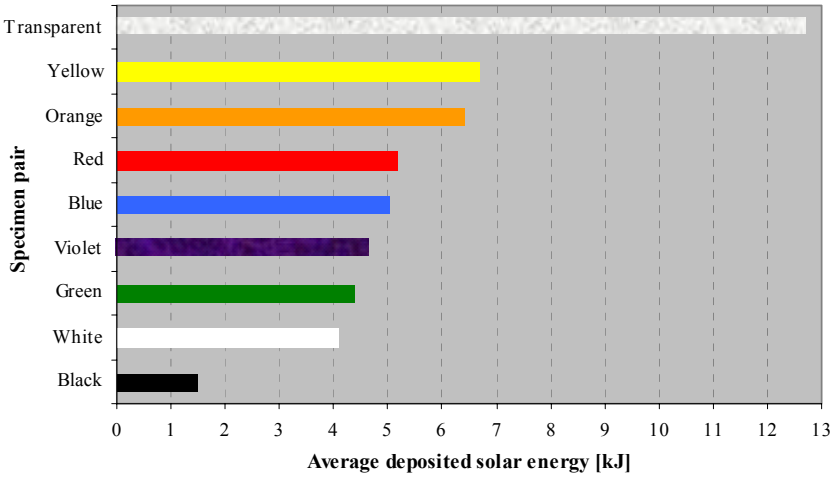

Figure 8.10: Average deposited solar energy for butt joined specimens using imaging optics

It can be seen that among the colored specimens the green required the least amount of energy/time for achieving a bond, and the yellow specimens the most (over 150% of the energy required for green).

Although relatively glossy, the black specimens absorb more than 95% of the deposited solar radiation, as determined in the spectrophotometric measurements (see Chapter 5). The gained energy, however, is absorbed on a very thin layer on the specimen surface because the black polymer, being exceptionally opaque, also has a relatively low conductivity. As a result, the temperature of the thin surface layer sharply increased, leaving that of the bulk material relatively unchanged. This led to constant liquidizing of the surface layer and therefore the joining in this clamping configuration occurred only on the top layer of the joint interface.

In contrast, the white ABS pair of specimens, although also being extremely opaque, did not exhibit such a great surface effect, most likely due to its relatively high reflectance. In addition, the ABS solution showed the lowest transmittance, probably due to scattering of the absorbed radiation by its rubber particles. In general, among the colored polymers, the least energy was required by the green and the most – by the yellow polymer. Because of the relatively low volumetric

absorption (discussed in Chapter 6), the transparent specimens exhibited the longest welding duration (up to 10 times longer than the black).

Table 8.5 lists the average results from the tensile testing of a range of butt joints made between the identically colored specimens. It can be seen that, as a percentage of the strength of the parent materials, values between 18.69% and 61.72% were obtained for the welded joints.

Table 8.5: Tensile loads of identically colored welded specimens using imaging optics

Specimen	Peak load at failure [N]	Tensile strength of joint [N/mm²]	% of parent material tensile strength
Black + Black	228.0	12.06	18.69
Green + Green	628.0	35.48	50.92
Violet + Violet	591.2	33.98	47.27
Blue + Blue	622.4	35.16	50.87
Red + Red	596.0	32.57	48.62
Orange + Orange	525.2	29.67	42.08
Yellow + Yellow	579.0	34.46	45.52
White + White	415.8	23.90	61.72
Transparent + Transparent	489.0	25.47	40.01

It should be noted that the butt clamping device used has been developed for the joining of transparent polymers. It is expected that the joint strength achieved would significantly improve if a more effective irradiation technique is used instead.

In such a technique, the irradiation of the surfaces to be joined could be more effective if the axis of the concentrated light cone is maintained normal to their plane while they are simultaneously irradiated. When the melting stage is reached, similar to the hot plate method, the joint surfaces are pressed together until the weld is formed. A schematic representation is given in Figure 8.11.

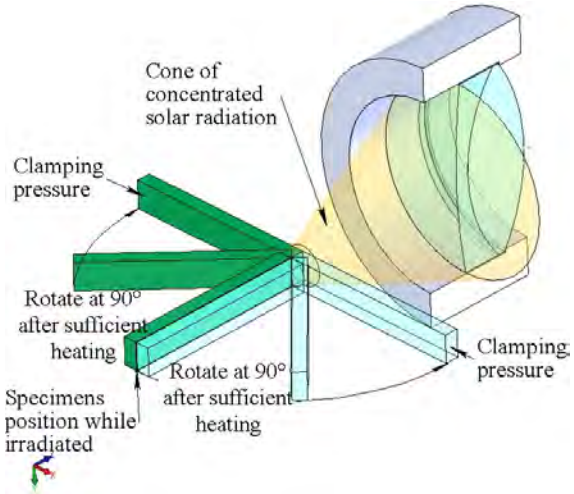

Figure 8.11: Method of clamping proposed for butt joining

With this method the possible bending of the polymer before reaching the melting point could be avoided. The application of this technique has been intended for future work. The quality of the weld could be improved if a sufficient compressive force is applied only when the entire joint interface is in its flow state while the power distribution remains uniform.

8.3.3.2 Study on identically colored polymer butt joining with non-imaging auxiliary optics

The use of an imaging solar concentrator complemented with non-imaging auxiliary optics for polymer processing could not be sourced in the literature review. Thus, the utilization of concentrated solar radiation for joining of thermoplastics with identical colors has been also studied with a SEC configuration using non-imaging auxiliary optics. As mentioned in Chapter 7, since the CNC machine arranged to manufacture the modeled CPCs was not operational at the time of these experiments, they were conducted with a simpler truncated cone concentrator (see Figure 7.16). In order to avoid the refraction losses and thus reduce the spectral and power limitations, the feasibility of a rather short light cone combined with a clamping device was explored for the butt polymer joining.

All opaque and clear samples of the studied thermoplastic materials were also successfully joined in this study. The experimental results for three specimen pairs from each colored polymer are shown in Table A8.2 in Appendix 8 and the average values are presented in Table 8.6 below. This table also contains the average results from the tensile testing of the butt joints.

Table 8.6: Experimental results from butt joining of polymers with identical colors using non-imaging optics

Specimen	Welding duration [s]	Average insolation intensity [W/m²]	Deposited solar energy [kJ]	Tensile strength of joint [N/mm²]	% of parent tensile strength
Black + Black	15	869	1.103	14.92	23.11
Green + Green	18	853	1.278	29.74	42.68
Violet + Violet	19	862	1.412	30.16	41.96
Blue + Blue	22	848	1.600	27.94	40.42
Red + Red	22	865	1.634	31.85	47.54
Orange + Orange	23	876	1.686	33.06	46.89
White + White	24	868	1.743	25.30	65.34
Yellow + Yellow	28	882	2.120	29.67	39.18
Transparent + Transparent	67	874	4.967	23.95	37.62

Although the repeatability of process variables (such as joint specimen surfaces and ambient conditions) and the visual assessment criteria of the joint cannot be ensured entirely, the results obtained for each color were relatively consistent.

Values between 23.11% and 65.34% as a percentage of the parent material strength were obtained for the welded joints. As it can also be seen, the deposited solar energy required for the joining process varies with the color from 1.103 to 2.12 kJ. The deposited solar energy during the joining process of each identically colored specimen pair is graphically illustrated in Figure 8.12. For comparison, the black, white and transparent specimen pairs are also included in graph.

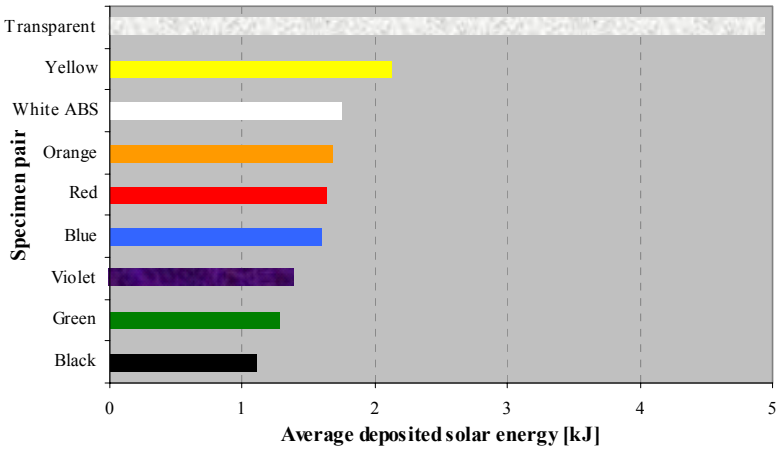

Figure 8.12: Average deposited solar energy for butt joined specimens using non-imaging optics

As in the previous study, these experiments demonstrated that, apart from the black, the green specimens required the least amount of energy/time for achieving a bond, and the yellow specimens the most. These consistent results can be rationalized on the basis that the process duration is primarily a function of the polymer absorptance and reflectance of solar radiation, if an equal amount of energy is assumed to be required. Some of the joined specimens are shown in Figure 8.13.

Figure 8.13: Identically colored specimens butt joined with non-imaging optics

Also, the process duration, or the energy in the non-imaging configuration in comparison to the configuration with five auxiliary lenses, was significantly reduced by up to four times for some of the colors. Those variations in the results, especially the inconsistent behaviour of the white ABS, are most likely due to the different optical and geometrical configurations. Furthermore, in this study the concentrated solar radiation exiting the non-imaging concentrator, incident on the specimen surface, is predominantly diffuse.

The white ABS is a terpolymer with a surface not as glossy as PMMA or PC, which experienced slight yellowing on exposure to concentrated sunlight. Also, having the highest reflectance and the lowest transmittance among all tested materials, the effective absorptance of solar radiation in the white ABS is critically dependent on the type of irradiation source.

Solar absorptance is considered one of the most important factors for effective solar energy utilization in the polymer. Therefore, the results from both experimental studies, described above, were compared to those determined for the average solar absorptance (Figure 5.23) and the results from the experimental outdoor heat generation measurements (discussed in Chapter 5 and Appendix 5F).

In general, the color absorption dependence trend, established by the spectrophotometric and outdoor heat generation measurements, was confirmed in both experimental studies. The only significant discrepancy between the joining and irradiation processes was again the behaviour of the white ABS.

The effect of different colors on the absorption behaviour of ABS during IR through-transmission has been studied by Grimm and Yeh (1998), as discussed in Chapter 3. They reported that the red polymer absorbed the most IR energy, and the blue the least, whereas in this experimental study it was found that the green polymer absorbed most of the deposited solar energy and the yellow the least. Thus, a different heating effect is achieved because of the selective absorption of the broader solar radiation (considered as a white light) by the colored polymers.

8.3.3.3 Study on butt joining of differently colored similar and dissimilar polymers with imaging auxiliary optics

The possibility of utilizing solar radiation for joining colored polymers was further explored by studying the weldability of differently colored similar and dissimilar polymers. In this study, the previously individually explored polymers

were joined in a butt configuration with all color combinations using imaging auxiliary optics. Photographs of some of the joined specimens are shown in Figure 8.14.

(a) predominant colors – red, orange and yellow

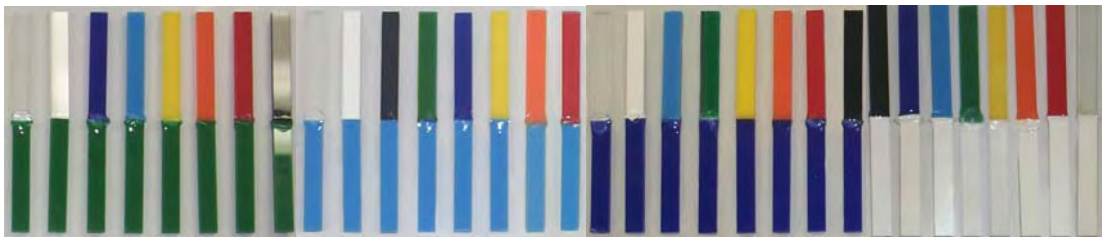

(b) predominant colors – green, blue, violet and white

Figure 8.14: Some butt joined specimens

Almost all of the pairs were successfully joined. However, during this experimental study, there were some combinations found not to be suitable, such as transparent PC and black PMMA, because of the relatively slow volumetric and fast surface phenomena taking place simultaneously.

Arranged according to the predominant color of the joined specimens, some of the experimental data obtained is given in Appendix 8 (Tables A8.3 to A8.9).

A. Tensile testing

In order to determine the achieved tensile strength of the joined test specimens, tensile tests were performed. The testing procedure is described in Chapter 4.

Tables A8.10 to A8.16 in Appendix 8 summarize the results of the tensile strength testing of the butt joints. It can be seen that the maximum tensile strength achieved is 60.99% relative to the parent material strength.

B. Microscopic examinations

In addition to the tensile tests, microscopic examinations of the fracture surfaces were performed in order to analyze the inner structural features of the tensile test specimens.

Analyses of two of the strongest and two of the weakest fractured joints are presented here. Figures 8.15 and 8.16 show the SEM images of the green and transparent PMMA specimens with the highest tensile strength of 62.28%, obtained during the experimental welding process. In Figure 8.15 fused regions are observed implying high energy absorption before fracture, thus the relatively high weld strength. However, the presence of a cavity suggests non-uniform distribution of the concentrated solar flux at the joint interface. The white patches on the image in Figure 8.16 indicate the welded regions that were fractured by the tensile test.

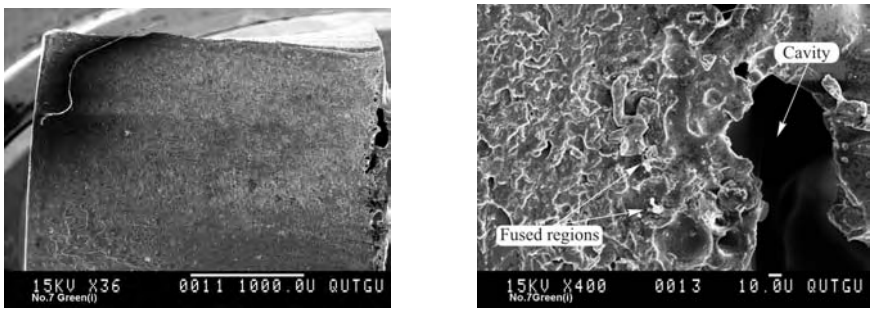

Figure 8.15: SEM images of fractured surface of green PMMA

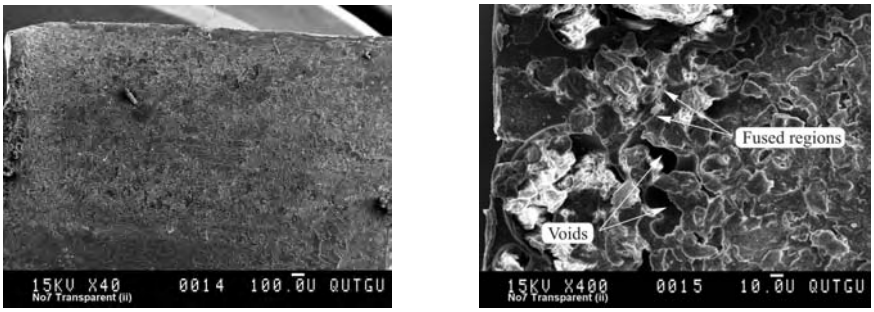

Figure 8.16: SEM images of fractured surface of transparent PMMA

The formation of voids may have been due to insufficient absorption of the concentrated solar energy and/or out-gassing of volatiles (including moisture). The void formation at the joint interface could be minimized if increased clamping pressure, where necessary, or prolonged exposure, can be ensured.

Figures 8.17 and 8.18 show the SEM images of the fractured surfaces of the yellow and green pair with the second highest relative weld strength of 60.99%. The image on the left in Figure 8.17 is a low magnification of the fractured surface of the green PMMA. Marks are present on the fracture interface indicating that possible plastic deformation has occurred during welding, thus degrading the joint strength.

Although small cavities are visible on the surface of the yellow thermoplastic, the fused regions, as can be seen on the images in Figures 8.17 and 8.18, imply that

probably a relatively larger portion of the interface surface was affected by the radiation.

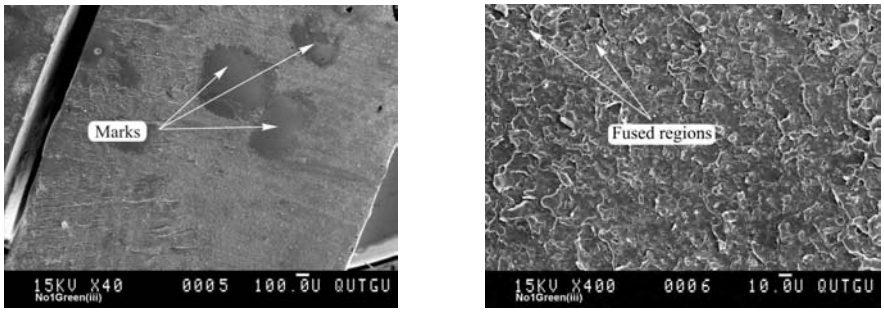

Figure 8.17: SEM images of fractured surface of green PMMA

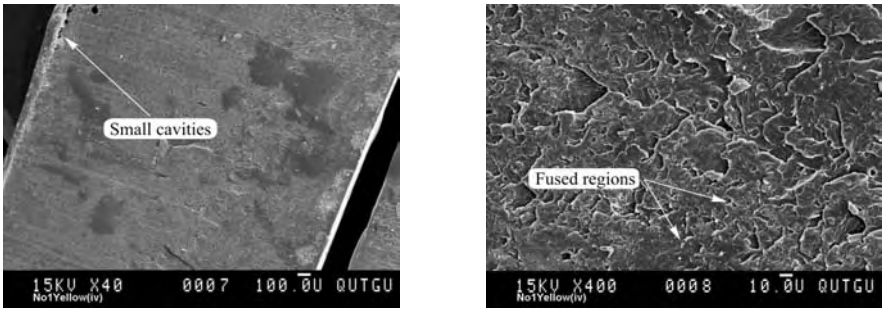

Figure 8.18: SEM images of fractured surface of yellow PMMA

Figures 8.19 and 8.20 show the SEM images of the blue and black specimens with the lowest relative tensile strength of 13.46%.

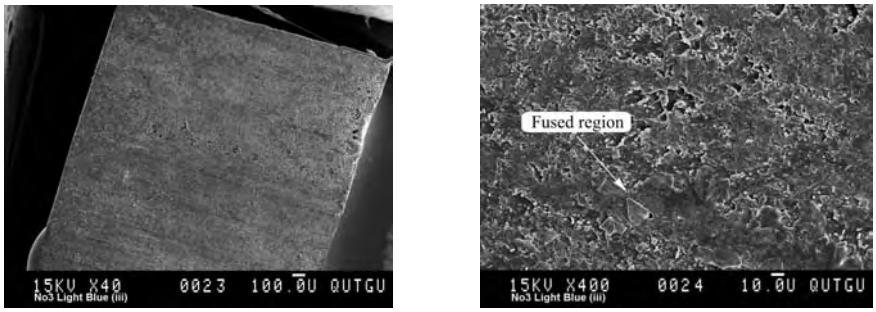

Figure 8.19: SEM images of fractured surface of blue PMMA

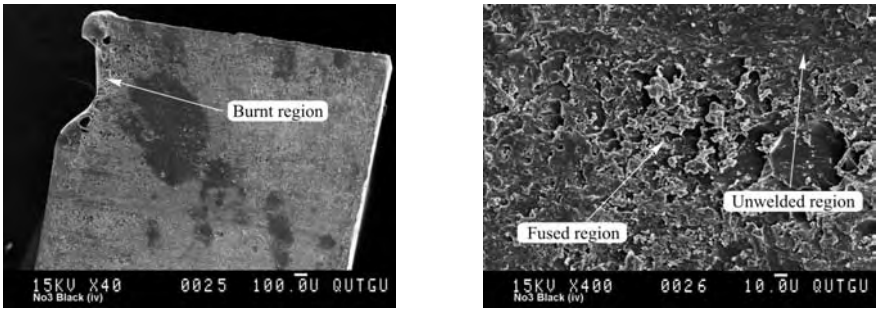

Figure 8.20: SEM images of fractured surface of black PMMA

Micro-voids and very few fused regions can be seen in the images on the right, indicating that a large portion of the joint surface was not bonded. Greater quantity

and different type of voids from the unwelded samples are observed indicating that the welding has had an effect. Because of the higher absorptance of the black component, the heat is generated by it in a relatively thin layer that could not be exchanged effectively due to the polymer low conductivity. As a result, when exposed simultaneously with another colored specimen, the black component starts to evaporate before a strong weld could be formed. This is confirmed by the left image in Figure 8.20 which shows a plastic deformation due to overheating.

Figures 8.21 and 8.22 show the SEM images of the fractured surfaces of the red and orange pair with the second lowest relative weld strength of 15.6%.

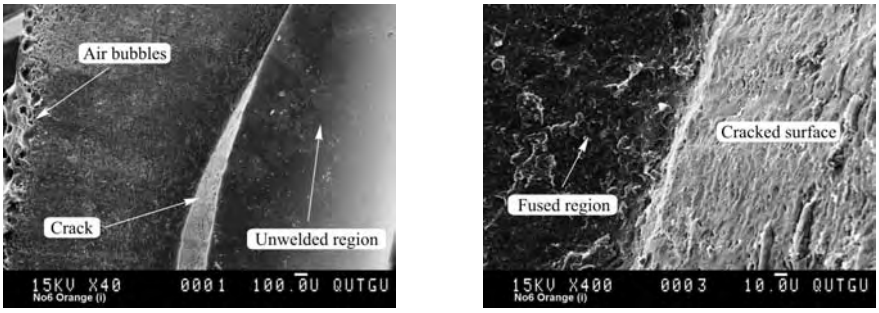

Figure 8.21: SEM images of fractured surface of orange PMMA

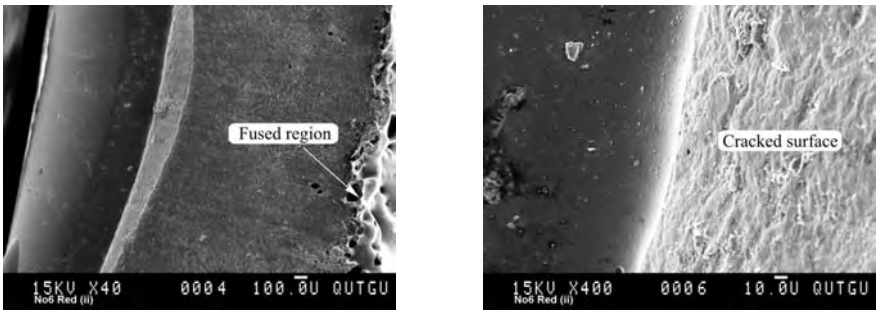

Figure 8.22: SEM images of fractured surface of red PMMA

Surface cracks in both red and orange materials can be observed. Micro-voids were formed probably due to evolution of gases during the welding process. There are also two distinct areas within both materials. The dark smooth portion in the left images indicates that no actual bonding took place at this interface. This may be due to an insufficient energy propagation into the joint interface leading to the formation of a weak weld.

8.4 Experimental lap joining of transparent and colored, similar and dissimilar polymers

As it has been found from the literature review (Chapter 3) advanced lap joining techniques such as TTIR and ClearWeld still require special dyes or pigments to

facilitate the radiation absorption process. Therefore, the study presented here was conducted to determine if concentrated solar energy can be utilized as a radiation source instead, without using any additional substance.

For this purpose, transparent thermoplastics (PC and PMMA) were joined to transparent and opaque thermoplastics (PMMA and ABS) with different colors in a lap joint configuration. Similar to the butt joining studies, the lap joining experiments were performed using the SEC facility supplemented with auxiliary imaging and non-imaging optics.

8.4.1 Through-transmission joining technique

In the through-transmission joining experiments, test specimens with the same dimensions as these used in the butt joining, were appropriately assembled in the relevant lap joining device (as described in the previous chapter), depending on the beam transmitting means used. When imaging auxiliary optics were used, the lap joint clamping device shown in Figure 7.20 was suitably mounted on the positioning and focusing mechanism system device. When using non-imaging optics, the especially designed lap joint clamping device, combined with the truncated light cone (shown in Figure 7.16), were used to form the lap joint.

In these experiments, in most specimen pairs a transparent PMMA specimen was used as the upper light transmitting component over a transparent or opaque ABS and PMMA from all available colors.

In general, a bond created by welding is a result of intermolecular diffusion at the joint interface. In the through-transmission joining process the concentrated solar radiation beam propagates through the transparent upper component and is absorbed by the bottom component, causing heating of the joint interface of both components. As a result, the adjacent surfaces of the two components are melted and joined by the clamping pressure applied. The process is illustrated in Figure 6.21 in Chapter 6.

The temperature variation during the joining process was measured by a thermocouple, placed at the joint interface and in contact with the light transmitting and absorbing components. The thermocouple was removed when a sufficient melt pool was created to form a joint. The specimens joined by this technique were consequently subjected to tensile testing to determine the joint strength.

8.4.2 Results and discussion

In the studies discussed in the previous section it has been demonstrated that concentrated solar radiation can be utilized for butt joining of various types and colors thermoplastics. The through-transmission joining experiments summarized below have shown that such thermoplastics can be joined in a lap assembly as well.

8.4.2.1 Study on lap joining using auxiliary imaging optics

The feasibility of the novel through-transmission technique for joining the selected thermoplastics was explored initially using the SEC facility with auxiliary imaging optics.

In general, all opaque colored specimens, used as a bottom substrate, were successfully joined in lap joint configurations with the transparent upper component. Furthermore, successful lap joining was achieved between two similar clear polymers (PMMA and PMMA) and two dissimilar clear polymers (PMMA and PC). Some of the joined specimens are shown in Figure 8.23.

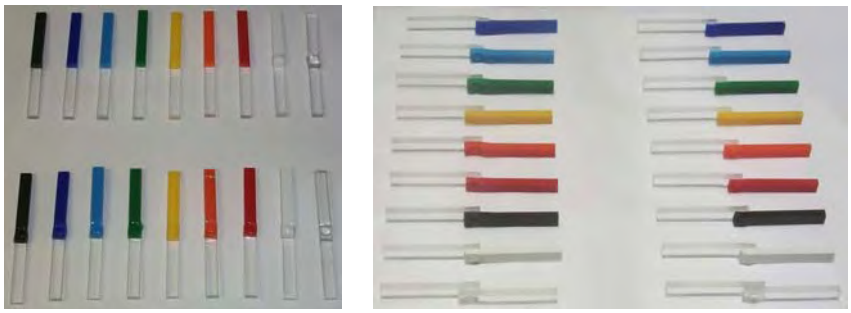

Figure 8.23: Lap joined specimens using imaging optics

The average values from the experimental results for each colored polymer are presented in Table 8.7.

Table 8.7: Experimental results from lap joining using imaging optics

Specimen	Welding duration [s]	Average insolation intensity [W/m²]	Deposited solar energy [kJ]
Transparent PMMA + Black PMMA	21	1021	1.820
Transparent PMMA + Green PMMA	26	1032	2.277
Transparent PMMA + Violet PMMA	30	1027	2.615
Transparent PMMA + Blue PMMA	32	1043	2.832
Transparent PMMA + Red PMMA	37	1026	3.222
Transparent PMMA + Orange PMMA	44	1061	3.962
Transparent PMMA + Yellow PMMA	50	1052	4.464
Transparent PMMA + White ABS	70	1060	6.297
Transparent PMMA + Transparent PMMA	100	1012	8.588
Transparent PMMA + Transparent PC	114	1010	9.771

As can be seen, the deposited solar energy required for the through-transmission joining process to take place varies with the color from 2.277 to 4.464 kJ. The average deposited solar energy during the joining process of each specimen pair is graphically illustrated in Figure 8.24.

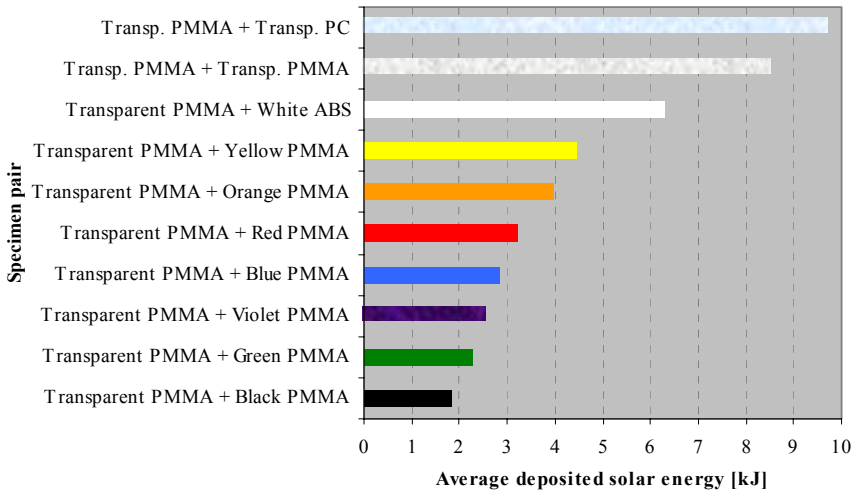

Figure 8.24: Average deposited solar energy for lap joined specimens using imaging optics

Table 8.8 lists the average results from the tensile testing of the lap joints made using imaging optics. It can be seen that, as a percentage of the strength of the parent materials, values between 25.8% and 63.79% were obtained for the welded joints in the lap configuration.

Table 8.8: Tensile loads of lap joined specimens using imaging optics

Specimen	Tensile strength of joint [N/mm²]	% of parent material tensile strength
Transparent PMMA + Black PMMA	16.66	25.80
Transparent PMMA + Green PMMA	44.45	63.79
Transparent PMMA + Violet PMMA	36.45	50.71
Transparent PMMA + Blue PMMA	28.93	41.84
Transparent PMMA + Red PMMA	29.38	43.85
Transparent PMMA + Orange PMMA	27.98	39.68
Transparent PMMA + Yellow PMMA	34.68	45.80
Transparent PMMA + White ABS	16.43	42.42
Transparent PMMA + Transparent PMMA	32.26	50.68
Transparent PMMA + Transparent PC	30.68	48.20

During this experimental study it was found that the joint strength can be improved by increasing the clamping pressure. However, because the strength of the

glass cover, used in the clamping device, limits the clamping pressure increase, moderate tensile joint strengths were achieved. Better strength could be achieved if stronger glass cover or other clamping means ensuring higher and more uniform pressure are used.

8.4.2.2 Study on lap joining with non-imaging auxiliary optics

In this study the feasibility of using the SEC facility with non-imaging auxiliary optics for joining the selected thermoplastics by employing the developed through-transmission technique was explored.

In general, the joining of all colored as well as black, white and transparent specimens was successful. A photograph of some of the joined specimens is shown in Figure 8.25.

Figure 8.25: Lap joined specimens using non-imaging optics

Average values of the experimental results obtained for the specimen pairs of transparent over each colored specimen are presented in Table 8.9.

Table 8.9: Experimental results from lap joining using non-imaging optics

Specimen	Welding duration [s]	Average insolation intensity [W/m²]	Deposited solar energy [kJ]
Transparent PC + Black PMMA	23	864	1.563
Transparent PMMA + Green PMMA	28	827	1.846
Transparent PMMA + Violet PMMA	32	791	2.166
Transparent PMMA + Blue PMMA	42	827	2.980
Transparent PMMA + Red PMMA	42	866	3.108
Transparent PMMA + Orange PMMA	43	855	3.117
Transparent PMMA + Yellow PMMA	46	827	3.250
Transparent PMMA + White ABS	173	744	10.900

As can be seen, the deposited solar energy required for the through-transmission joining process to take place varies with the color (from 1.846 to 3.25 kJ). Compared to the previous study, a lesser amount of deposited solar energy was required to achieve a bond in this study. It should be noted, however, that the affected and the joint areas were relatively small.

The temperature variations during the through-transmission joining of a pair from each color were recorded by a thermocouple embedded at the joint interface. The results are shown in Figures A8.5 to A8.8 in Appendix 8. The average deposited solar energy during the joining process of each specimen pair is graphically illustrated for comparison in Figure 8.26.

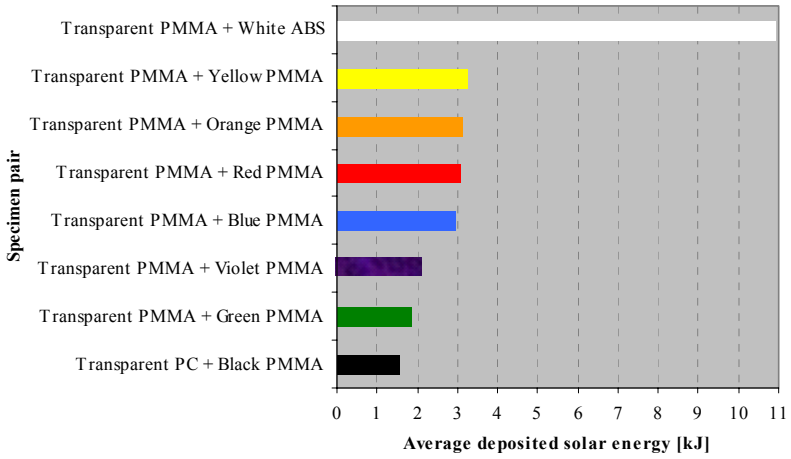

Figure 8.26: Average deposited solar energy for lap joined specimens using non-imaging optics

It should be noted that, in general, in both through-transmission joining studies the color dependence trend established in the butt joining studies was confirmed except for the white ABS. Increased welding duration and deposited energy were required to achieve the lap joints of transparent PMMA over white ABS in both studies. Compared to the butt joining studies, this exception could be contributed to the relatively low ABS transmittance and significant reflectance of the light scattered by the transparent substrate.

Table 8.10 lists the average results from the tensile testing of the lap joints made. Values between 19.26% and 49.01% as a percentage of the strength of the parent materials were obtained for the welded joints. Compared to the results obtained with the imaging optics, lower joint strengths were achieved with the non-imaging optics, probably due to the smaller size of the affected area.

Table 8.10: Tensile loads of lap joined specimens using non-imaging optics

Specimen	Peak load at failure [N]	Tensile strength of joint [N/mm²]	% of parent material tensile strength
Transparent PC + Black PMMA	235.0	12.43	19.26
Transparent PMMA + Green PMMA	604.4	34.15	49.01
Transparent PMMA + Violet PMMA	508.2	29.21	40.63
Transparent PMMA + Blue PMMA	494.0	27.91	40.37
Transparent PMMA + Red PMMA	484.6	26.48	39.53
Transparent PMMA + Orange PMMA	436.2	24.64	34.95
Transparent PMMA + Yellow PMMA	296.8	17.67	45.63
Transparent PMMA + White ABS	528.0	30.34	40.08

It should be noted that in both through-transmission joining studies, when the joints were tensile tested, the failure occurred predominantly outside the bonded area, in the bottom substrate. This indicates that the joint is relatively stronger than the material itself. On the other hand, this may be due to the slight difference in the thicknesses of both parts and also may be attributed to stresses created in the boundary between the exposed and non-exposed parts. The latter is evident from the failure of the black component which has almost the same thickness as the transparent part.

8.5 Conclusions

In general, the experimental studies discussed here, have proved that all thermoplastics used, regardless of their color, can be successfully joined using concentrated solar energy. The results from the tensile testing showed large deviations in tensile strength. These deviations could be attributed to differences in material properties between pairs from dissimilar polymers, non-repeatability of ambient conditions and the complex stresses within the joint produced by the testing equipment. Because of the relatively small size of the specimens, many of them were damaged during the tensile testing by the grip fixtures and therefore discarded. Thus, future studies will need to address the differences in loading conditions and eliminate the stresses created in the polymer materials by the grip fixtures. Because the specimens were chosen on the basis of energy considerations, they were not ideal for obtaining the highest strength possible using the joining techniques developed in this research. Since the specimens were cut from large sheet materials, the surfaces to be joined were machined incurring additional surface roughness and residual stress.

The tensile strengths of the joints achieved with the through-transmission technique utilizing solar radiation may be considered relatively low by industry standards. However, they are comparable to the results achieved for similar polymers with other advanced plastic joining methods (see Lin et al. 2000; Kagan et al. 2002; Rhew et al. 2003; Grewell et al. 2003).

The differently colored specimens, although from the same polymer, required different amount of energy to be softened, melted and joined, as expected. In some of the assigned polymers the scattering of solar radiation, particularly in the IR region, dominated the absorption. The scattering of the photons within these polymers prevented the penetration, and therefore the heating uniformity, into the deeper layers of the material. This could be avoided by varying the beam diameter to achieve an appropriate penetration depth.

Concentrated solar energy causes melting of the material which is limited by the exposed area/volume, thus joining is possible before an excessive heat affected zone is developed. Also, because the polymer has a low thermal conductivity, the joint interface layer has a relatively small volume and little heat is conducted into the adjacent area. Therefore, the possibility of polymer degradation is decreased.

Both butt and lap joining experiments have demonstrated that apart from the black, the green specimens required the least amount of energy/time for achieving a bond, and the yellow specimens – the most. The findings for the absorption dependence on a particular color, however, may not be entirely valid for materials with different grade or color specifications.

It is interesting to note that similar findings have been reported by researchers using different radiation source with longer wavelength range than the utilized in this research. The green pigment in Polyamide has been found by other researches to absorb most of the IR radiation and the yellow the least (Kagan et al. 2001; Grewell et al. 2002). The present research has extended the radiation absorption knowledge over a relatively broader wavelength range of near IR, visible and UV radiation for several similar and dissimilar, clear and colored thermoplastic materials.

Unlike most of the advanced welding techniques, the developed through-transmission technique removes the need to use a special absorbing medium of the radiant energy such as carbon black or other pigments and dyes. Furthermore, successful lap joining has been achieved between two similar clear polymers (PMMA and PMMA) and two dissimilar clear polymers (PMMA and PC).

CHAPTER 9.
STUDIES ON ACCELERATED SOLAR RADIATION EXPOSURE AND ADHESIVE CURING OF POLYMERS

9.1 Introduction

In addition to the polymer joining studies discussed in the previous chapter and in accordance with the objectives of this research, another two alternative applications of concentrated solar energy utilization were explored. The possibility of using the developed SEC facility for performing accelerated natural weathering tests and studying the polymer ageing process was investigated. The plastics technology has shown that lighter and cheaper polymer materials and composites can displace many conventional materials in harsh environmental outdoor conditions. Therefore, the proof of their satisfactory long-term performance under such conditions, including intense sunlight exposure, becomes critical.

Indoor weathering of polymers, as discussed in Chapter 3, could cause unrealistic degradation mechanisms and failure of the exposed material. Thus, for many products, in order to evaluate their durability and color change resistance, there is a requirement for natural outdoor exposure. By utilizing the actual terrestrial solar radiation spectra, an outdoor testing could provide more realistic information about the degradation behaviour of the exposed polymer materials.

The review of publications on accelerated ageing of polymers in Chapter 3 has shown that there is a need for facilities for ultra accelerated natural sunlight exposure testing of materials in order to predict their service time. For this reason and since application of a similar configuration for weathering of polymers has not been found in the literature, studies on ultra accelerated ageing of polymers were initiated.

It has been evident from the review of polymer processing technologies that electromagnetic radiation could be used not only in the processes of heat generation and accelerated ageing but in radiation curing of adhesives as well. The current radiation curing techniques utilize various spectral ranges of electromagnetic radiation including ultraviolet, infrared, microwave and radio frequencies. Very little research on the effect of visible solar radiation and no information on using concentrated natural solar radiation for adhesive curing of thermoplastic bonds have

been found. Therefore, after calculations of the energy required, experimental studies were conducted to explore the feasibility of concentrated insolation utilization for this purpose. The preliminary investigation on the possibility of adhesive curing with solar radiation has indicated that utilization of concentrated insolation for curing of advanced UV-VIS light-sensitive adhesives may be feasible.

This chapter begins with a review of the study on irradiation exposure and photoelastic stress analysis which was initiated to assess the effect of concentrated solar radiation on the properties of thermosetting and thermoplastic polymers. The results from the experiments performed without cooling to visualize the residual thermal stresses, induced by the exposure to concentrated solar radiation, are discussed. Next, the experimental methodology and results from the temperature-controlled natural ultra accelerated ageing of transparent and colored polymers are described. In conclusion, the studies on curing of adhesives for thermoplastic bonding utilizing concentrated insolation are discussed.

9.2 Irradiation exposure and photoelastic stress analysis

Photoelastic stress analysis is a widely used non-destructive technique for accurately measuring surface strains to determine the stresses in polymers (part or structure) during static or dynamic testing. The photoelastic method is based on a unique property of some transparent materials, in particular, certain plastics, to become 'birefringent' i.e. to exhibit colorful patterns when subjected to polarized light. When a photoelastic material is placed between polarizing and analyzing disks, the strain patterns (and thus the stress distributions) are revealed by interference fringes which are consequently associated with the distribution of the internal stresses.

The white diffuse light, which is generally used in photoelastic stress testing, is composed of all wavelengths in the visible spectrum. Each color in the spectrum, starting with the shortest visible wavelength, the violet, is extinguished in turn according to its wavelength and its relevant complementary color is seen. These complementary colors, in fact, make up the fringe pattern which appears as a series of successive and contiguous differently colored bands. They are called isochromatics in which the different degree of birefringence is represented by each band (Measurements Group 1994).

This study was initiated to assess the effect of concentrated solar radiation on the

properties of thermosetting and thermoplastic polymers. To better understand the concentrated light propagation in the material, a transmission polariscope (described in Chapter 4) was used to visualize the studied effect. A number of experiments were performed to visualize the residual thermal stresses induced by the exposure to concentrated solar radiation without controlled forced cooling.

Initially, the specially formulated for the polariscope photoelastic material PSM-1 was subjected to gradually increasing exposure on concentrated beam insolation. Being relatively translucent, and allowing the propagation of solar radiation throughout its bulk, this material was chosen for visualization of the caused stress concentrations. It was observed that the material already had a number of colored fringes before the exposure. They may have been caused by the machining or due to stresses originating from the process of mixture and curing. There was no significant change in the existing fringes after an exposure of more than 50 Wh with an average intensity of 804 W/m^2. During the subsequent exposure to another 50 Wh, the material became brittle at the exposed surface, probably due to overheating. A photograph of the exposed sample is given in Figure 9.1 (left).

In this experimental study it was found that the transparent materials also form colored fringes after exposure to concentrated solar radiation. The transparent PC, exposed to equivalent amount of irradiation as that of the PSM-1, is shown on the same figure (9.1) at the commencement of the glass transition and bubble forming. During this period it was observed that the gases trapped in the exposed sample moved upwards, and when the exposure continued, they were released in the atmosphere and the surface of PC ruptured. The circular blue fringe surrounded by red indicating the size of the focal spot can be seen on the right picture in Figure 9.1. This effect was found useful for determining the size and shape of the focal spot.

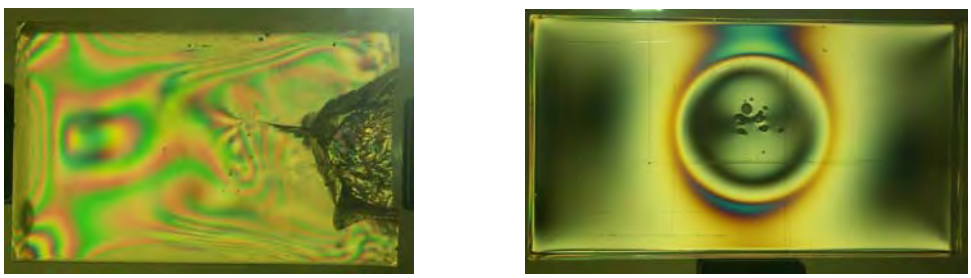

Figure 9.1: Photoelastic stress pattern for PSM-1 (left) and transparent PC (right)

Because of its 'birefringent' property, PMMA was also used for studying the stress and detrimental effect caused by concentrated solar energy. Several specimens

from transparent PMMA with different thicknesses were exposed to gradually increasing amount of concentrated solar radiation. The change of the photoelastic stress pattern was examined with a polariscope after each exposure. The specimens were exposed at the principal Cassegrainian focus as shown in Figure 9.2.

Figure 9.2: Insolation irradiation exposure location

The two PMMA samples shown in Figure 9.3 were cut from a cylinder with a diameter of 50 mm. The first sample was with height equal to its diameter and the second sample was with half of the height of the first one to ensure that it has half of the volume. Since both specimens were thick enough, when exposed to equal amount of radiated they formed bubbles that were growing closer and consequently joining together in a bigger bubble, as shown in Figure 9.3.

Figure 9.3: Photoelastic stress pattern in transparent PMMA - side and top views

As the exposure continued above a critical value (in this case around 120 Wh for the smaller sample and about 160 Wh for the larger one), eventually the bubbles burst leaving a hemispherical valley. During these processes there were no significant changes observed in the fringe patterns (probably formed by the machining). However, gradually with the exposure the fringes, becoming more stochastic, were pushed down by the incoming solar photons leaving a boundary, visible on the left picture in Figure 9.3. On the right picture in the same figure the forming of the hole in the sample can be seen. The picture in the middle shows the top view of the larger sample after the rupture.

In order to study the extent of propagation of the concentrated solar radiation in a

transparent polymer, a subsequent experiment with a relatively longer (125 mm) PMMA sample with diameter 35 mm was irradiated continuously with concentrated insolation at incremental intervals of 20 Wh. The photoelastic stress pattern was examined without an external load after each incremental step and the results compared. The sample was viewed and photographed on the polariscope after each exposure portion and most of the images are presented in Figure 9.4.

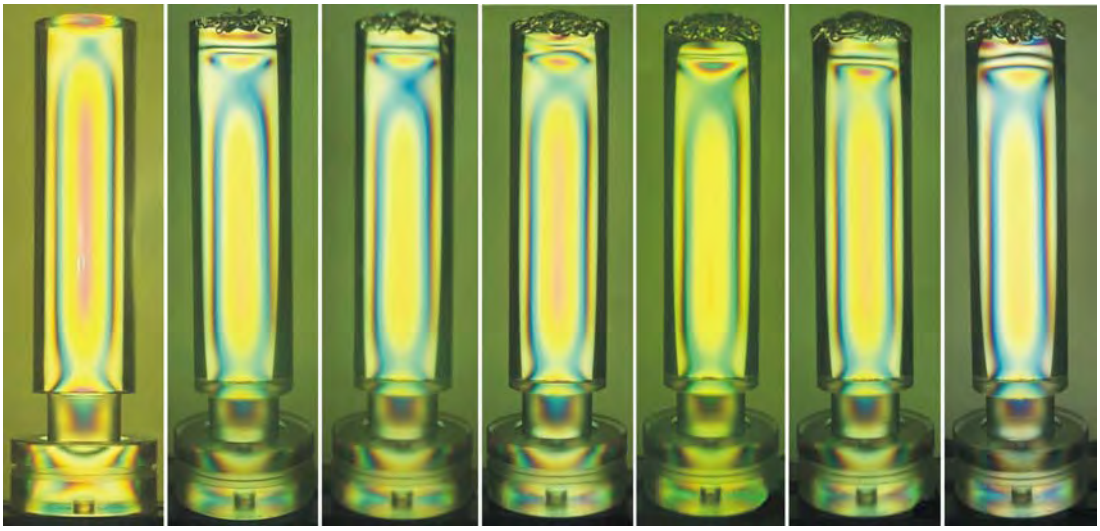

(a) before exposure (b) after 20 Wh (c) after 40 Wh (d) after 60 Wh (e) after 80 Wh (f) after 100 Wh (g) after 120 Wh

Figure 9.4: Photoelastic stress pattern change with irradiation duration build-up

If subjected to a load, specially formulated photoelastic materials viewed under polarized light typically display colorful patterns proportional to the stress in the material. Similar fringe profile as shown in Figure 9.4(a) was observed when the unexposed PMMA sample was illuminated with polarized light. This frozen residual stress visible throughout the bulk of the specimen was probably caused by its machining. The color sequence (blue-red-yellow-green-blue) that can be seen on the top surface of the unexposed material could be interpreted in photoelasticity as an existence of low stressed region.

When the PMMA cylindrical sample was irradiated from the top along its axis, it was observed that the fringe pattern of the top section was shifting down gradually. It appeared that the concentrated solar photons were forcing down the existing fringes without modifying them or creating additional stress concentrations into the bulk of the material. With further irradiation build-up, only increased bubble forming on the top layer was observed, with no significant change in the fringe patterns in the deeper layers. This was probably caused by the gradually increasing roughness of the sample front surface and obstructing the light propagation. After

irradiation exposure of about 120 Wh, the interaction of the concentrated light with the roughened surface reached its peak and a formation of a meniscus-like surface started.

Apart from the significance of this study for evaluation of the light propagation depth and residual thermal stress formation in thick transparent polymer samples, it was a valuable tool for determining the size and shape of the focal spot.

After the general evaluation of the response of the exposed materials to concentrated solar radiation, a controlled accelerated ageing of thermosetting and thermoplastic polymers was performed and is described in the following section.

9.3 Natural accelerated ageing of transparent and colored polymers

9.3.1 Background

Any polymer material exposed to outdoor environment degrades with time due to various external factors and conditions, as discussed in Chapter 3. Solar radiation typically takes a major part in this process because its broad spectral range includes also UV radiation. In general, the colors of the exposed plastics fade and the incident solar radiation can cause thermal stress in the polymer material.

Typically, when subjected to elevated temperatures, most polymers start to undergo chemical changes even without the simultaneous involvement of another compound, which is referred to as thermal degradation. However, it is often difficult to distinguish between thermal and thermo-chemical degradation because the polymer materials are only rarely chemically pure. In this study this becomes even more complicated because different colors i.e. different dyes and impurities are involved and the UV component in the radiation source is not controllable.

As discussed in the previous chapter, the effective utilization of solar radiation is greatly dependent on its absorption in the polymer. When absorbed in the polymer, solar radiation provides the driving force for various chemical and physical processes that oxidize or reduce the polymer substance. The rate of radiation absorption depends upon the spectral overlap between the light source and the polymer absorption spectrum.

In general, the absorption spectra of most plastic materials is determined by the absorption characteristics of all their functional groups. When energetic enough electromagnetic radiation is absorbed in a polymer, it could cause a scission of

chemical bonds and subsequent formation of photoproducts such as carbonyl group (C=O), carboxyl group (COOH), hydroxyl group (OH) etc. It is well-known that the carboxyl index, the relative content of carboxyl end-groups, is a valuable parameter to quantify polymer degradation, and the carboxyl end-groups act as a catalyst to promote further degradation (Fechine et al. 2002).

The studies described here were initiated to assess the feasibility of using an appropriate SEC configuration as an energy source for accelerated natural weathering of polymers under controlled weathering conditions.

9.3.2 Experimental methodology

On the basis of AS 1745, ASTM G90 and some associated patents (Caryl and Helmick 1960; AS1745.1 1989; Robbins 1989; ASTM-G90 1999), a method for ultra accelerated natural sunlight exposure of polymer materials utilizing the SEC facility was developed and used in the experimental work.

Exposure conditions

According to AS 1745.1 the exposure time varies within the four global geographical radiation zones in Australia, but the minimum duration of exposure is one year and the maximum is five years. With the experiments in these studies it was intended to accelerate the ageing of the sample materials by irradiation with higher concentrations of natural sunlight equivalent to five years outdoor exposure.

The mean annual total global radiation for Brisbane, as specified in AS1745.2, is 6600 MJ/m^2 (or 6600 J/mm^2) (AS1745.2 1989). Thus, for the used non-imaging third stage concentrator having a 6 mm exit aperture diameter, the irradiation amount required to simulate one year outdoor exposure would be 733 Wh/m^2. In order to allow variation of the parameters, a spreadsheet was formulated and the derived formulas and calculated values are given in Table 9.1.

Table 9.1: Estimation of typical accelerated annual equivalent exposure

Parameter	Symbol	Units	Value	Formula
Annual total global irradiation	H	MJ/m^2	6600	as per AS 1745.2
Annual total global irradiance	G	Wh/m^2	1833333.333	H x 10^6/3600
Exposed area	Aa	m^2	2.82743 x 10^{-5}	π x 0.006^2/4
Annual irradiation reqd for exposed area	E	Wh	51.8363	G x A
Clear aperture area primary	Ac	m^2	0.221	
Combined mirror efficiency	η_1	-	0.64	0.8 x 0.8
Third stage efficiency	η_2	-	0.5	
Integrated irradiation reqd for exposed area	Ec	Wh/m^2	732.9791	E/(Ac x η_1 x η_2)

During the exposure, convective cooling was provided by blowing pressurized dry air over the top surface of the samples. The especially developed cooling system is described in Chapter 7. The surface temperature of the exposed samples was kept relatively constant under 50°C. Since the black panel thermometer has been considered not feasible due to the size of the focal spot, in some of the experiments (e.g. with black, green specimens) the thermocouple tip was masked accordingly.

Future work has been planned to improve the temperature control process by installing two temperature sensitive components (thermistor and thermocouple) to allow simultaneous and continuous recording of the temperature while controlling it.

Test specimens

The test specimens used in the accelerated ageing experiments were of the same type and dimensions as those used in the polymer joining studies (described in the previous chapter), namely white ABS and transparent and opaque PMMA with different colors. Specimens from photoelastic material PSM-1 and non-UV stabilized Polypropylene (PP) film were also exposed.

Three control specimens of each parent material were kept in the dark at room temperature and were used for determining the initial non-exposed parent material property values and for comparison with the exposed specimens.

Specimen mounting

The specimens were mounted in the especially provided compartment at the exit aperture of the non-imaging concentrator ensuring effective cooling of the irradiated area (see Figure 9.5).

Figure 9.5: Specimen mounting – a sectional view and a photograph

Assessment

To distinguish any sign of degradation, initially a visual inspection of the exposed specimens was performed with the optical aid of a 12x hand lens and a

stereo microscope. To study the ageing effects on polymer microstructure, attenuated total reflectance (ATR) measurements were performed using Fourier Transform Infrared (FTIR) spectroscopy. This analytical technique was used to detect any changes in the chemical bonds of the material, in particular to identify carbonyl and hydroxyl absorptions due to oxidation.

In addition, the degradation and failure characteristics were analyzed using tensile fracture stress technique. The results from the visual, FTIR and tensile testing were subjected to comparison tests with those of the control samples and subsequently analyzed.

Exposure procedure

In general, the procedure for the ultra accelerated durability tests of the polymer materials comprised the following:

1. Initial appearance and physical properties of the control and test specimens were recorded.
2. One test specimen at a time was mounted and exposed under the defined above conditions.
3. After exposure, the specimen was dismounted and a visual inspection in comparison with the control specimens was performed.
4. Surface analysis by FTIR spectroscopy on both test and control specimens was performed.
5. Mechanical tests on both test and control specimens were performed.

9.3.3 Results and discussion

Initially, the specimens were exposed to irradiation equivalent to one year and subjected to FTIR spectroscopy for spectral analysis. Since no evidence of photodegradation was found, in the subsequent experiments the specimens were exposed to irradiation equivalent to five years.

Visual inspection

In general, although no chalking or discoloration, crazing, flaking or cracking were observed, the visual inspection of the exposed specimens showed fairly diverse changes in their appearance. They ranged from no visible change in the transparent and white specimens to minor surface discoloration in some colored specimens and pitting in the black specimens.

FTIR spectroscopy

Initially, a photoelastic plastic material PSM-1 was exposed to determine if any stress caused by the ageing process utilizing concentrated insolation has occurred. Since this material has been supplied with the Polariscope used and no specific chemical formulation about it has been available at the time, it was subjected to FTIR spectrometric evaluation, as shown in Figure 9A.1 in Appendix 9. The spectral characteristics have been found to be very similar to OL0840 Araldite PR 805 Epoxy Ester Emulsion. Figure 9.6 shows the FTIR spectrum of the PSM-1 sample after exposure. The circle indicates the area with some observable changes.

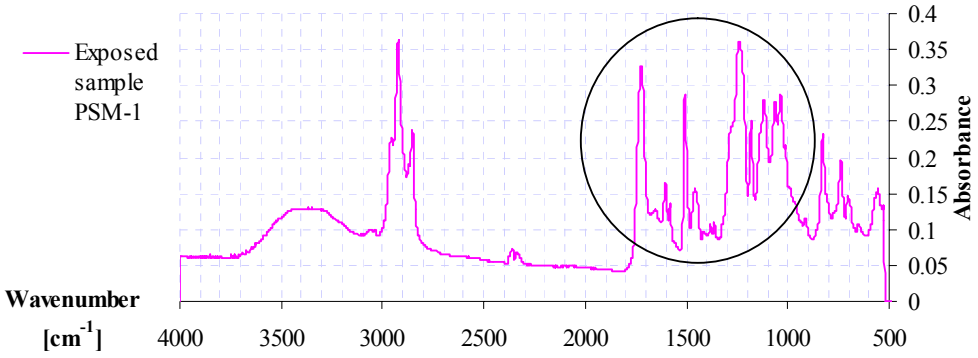

Figure 9.6: FTIR absorption spectrum of exposed PSM-1 sample

This area is shown in enlarged view in Figure 9.7. The FTIR absorption spectrum of the unexposed PSM-1 sample is shown in Figure 9A.2 in Appendix 9.

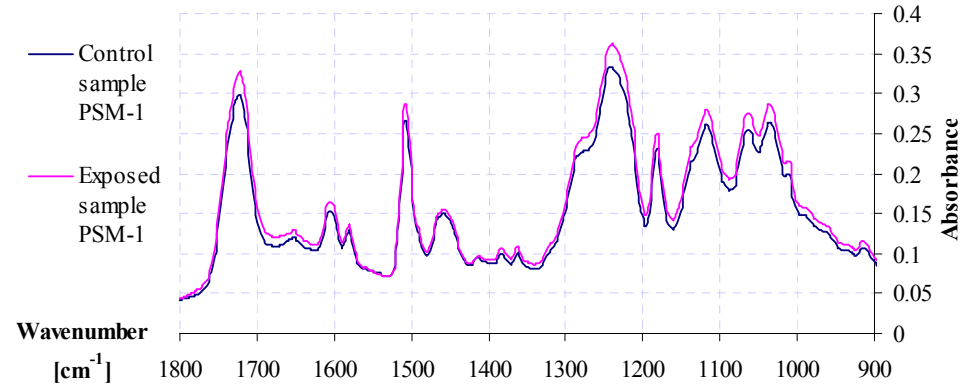

Figure 9.7: FTIR absorption spectrum of exposed PSM-1 with observable changes

In the exposed PSM-1 sample a slight increase of absorption intensities at 1735-1750 cm^{-1} was observed in the carbonyl band which could be attributed to oxidation. The increased absorption at 1243 cm^{-1} could be associated with C-O-C groups (Chiantore et al. 2000).

Another exposed material in which spectral modifications were observable, was the non-UV stabilized Polypropylene (PP). Figure 9.8 shows that the IR

transmittance of PP decreased significantly (by ~50%) after the exposure.

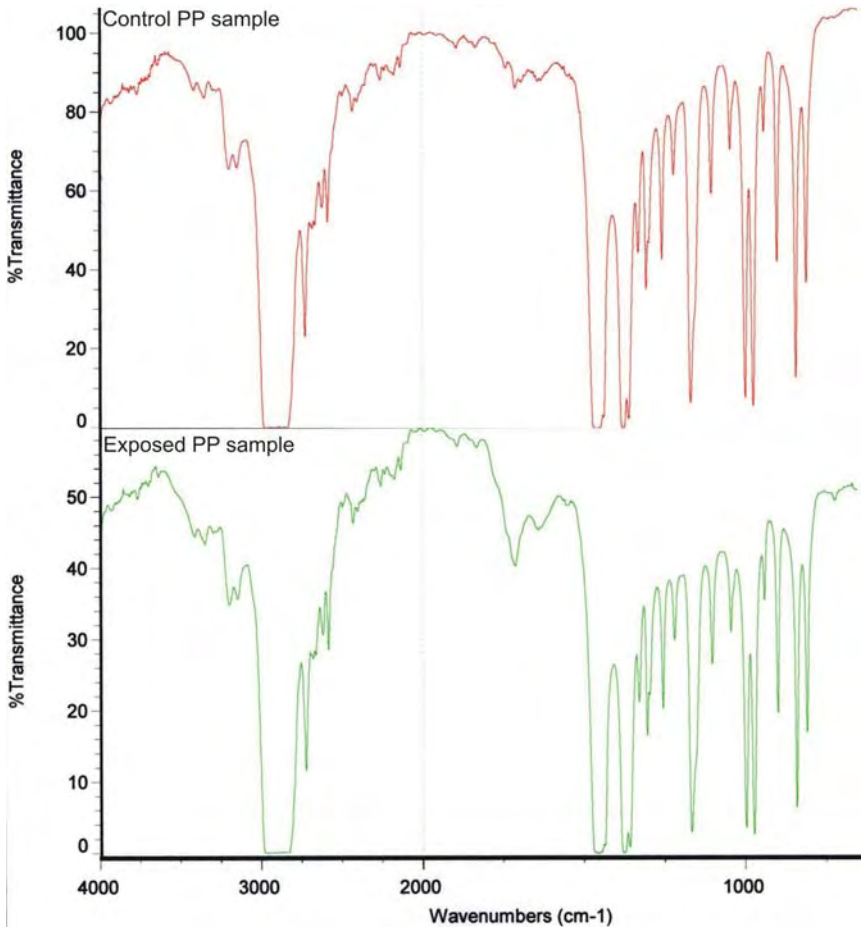

Figure 9.8: FTIR transmission spectra of control and exposed PP samples

Figure 9.9 illustrates the part of the FTIR spectrum that showed identifiable changes in the exposed PP.

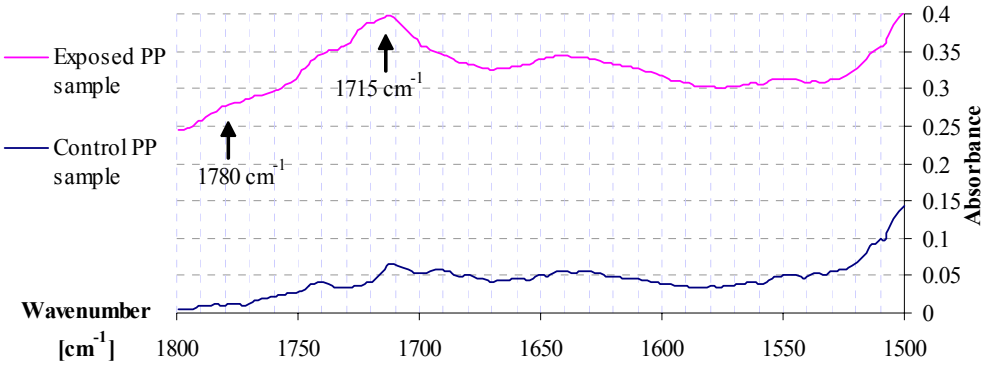

Figure 9.9: Comparison FTIR absorption spectra of PP with observable changes

The full FTIR spectra of the exposed PP sample compared to the control sample are given in Figure 9A.3 in Appendix 9. For comparison, the typical absorption spectrum of PP with added stabilizer (2-3% titanium dioxide) can be seen in Figure 3.18 in Chapter 3. In the exposed PP sample the observed growth of the main

carbonyl absorption at 1715 cm^{-1} can be attributed to the formation of ketone and aldehyde groups (Lazzari and Chiantore 2000). The increased absorption between 1800 and 1760 cm^{-1} is probably due to formation of γ-lactone structures which typically absorb at 1780 cm^{-1} and are always present in all types of aliphatic polymer photodegradation.

The surface FTIR spectrum of the aged ABS did not show any significant change in the carbonyl band. However, a broad absorption growth in the hydroxyl band was observed between 3600 and 3100 cm^{-1}, indicating a strong association of –OH groups (see Figure 9.10). The full FTIR spectra of the control and exposed samples are given in Figures 9A.4 and 9A.5 in Appendix 9. The presence of the hydroxyl group could be attributed to photodegradation on the surface. This behaviour indicates changes in the chemical structure associated with oxidation, caused by the accelerated natural exposure to concentrated solar radiation.

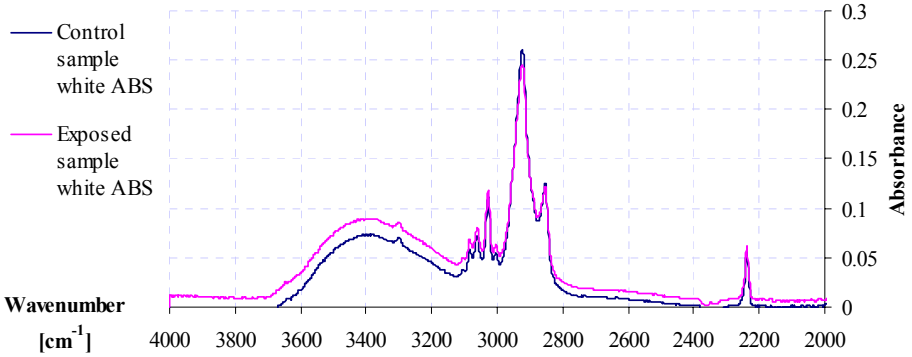

Figure 9.10: FTIR absorption spectra of white ABS with observable changes

FTIR examination of the transparent PMMA samples showed heterogeneous structure along the polymer surface. However, the observed increase in the CH_2/CH_3 absorption ratio (3000–2850 cm^{-1}) can be considered an evidence of photodegradation (see Figure 9.11). The full FTIR spectra of the control and exposed samples are given in Figures 9A.6 and 9A.7 in Appendix 9.

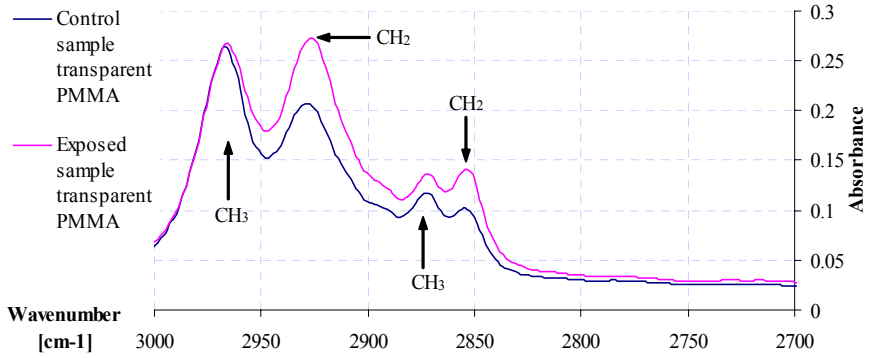

Figure 9.11: FTIR absorption spectra of transparent PMMA with observable changes

In general, the observed spectral changes for the colored PMMA specimens were insignificant. It was observed that the spectral bands of oxygen containing groups remained unchanged after exposure, thus the ageing of the opaque PMMA samples under the experimental conditions in this study did not produce an oxidative degradation. However, the observed changes were directly proportional to the absorbing capabilities of the polymer and were predominantly thermally induced.

Figure 9.12 shows the FTIR absorption spectra of the green PMMA, one of the most absorbing colored polymers. Only a small decrease of absorption in the carbonyl band is observed.

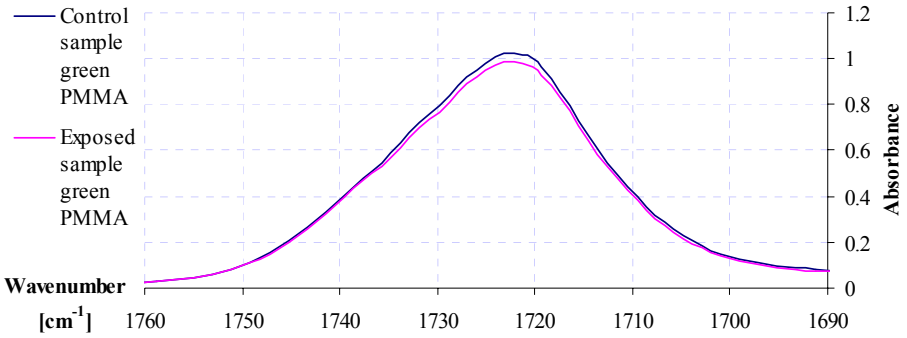

Figure 9.12: FTIR absorption spectra of green PMMA with observable changes

The full FTIR absorption spectra of the control and exposed green PMMA samples are given in Figures 9A.8 and 9A.9 in Appendix 9.

Tensile testing

The mean tensile strength of the exposed specimens from each material was determined concurrently with that of the control specimens. The results are summarized in Table 9.2.

Table 9.2: Mean tensile strength of control and exposed samples

Specimen	Tensile strength of control sample [N/mm^2]	Tensile strength of exposed sample [N/mm^2]	Tensile strength decrease [%]
Black PMMA	64.83	26.14	52.38
Green PMMA	67.61	53.37	21.06
Violet PMMA	71.97	61.77	14.17
Blue PMMA	67.66	51.86	23.35
Red PMMA	64.00	47.67	25.52
Orange PMMA	65.72	49.58	24.56
Yellow PMMA	75.23	48.15	36.00
White ABS	38.72	33.69	12.99
Transparent PMMA	73.91	47.77	35.37
PSM-1	78.79	40.51	48.58

Although sustaining insignificant photodegradation, all exposed samples experienced reduction in mechanical properties, as evident from Table 9.2. The

tensile strength of all samples decreased after the exposure. The white ABS, although showing some photodegradation, had the least reduction of tensile strength. The PSM-1 material, on the other hand, experienced significant loss of tensile strength caused probably by the oxidation. From the PMMA specimens the black was the most affected by the accelerated exposure, probably due to the relatively high additive content of the material. The rest of the PMMA samples experienced moderate reduction of tensile strength.

It should be noted that these experiments were only a part of a feasibility study and more comprehensive studies involving other materials and prolonged exposure have been planned for future work.

9.4 Curing of adhesives for thermoplastic bonding utilizing concentrated insolation

The curing mechanism of any adhesive often determines its suitability for a particular application. As discussed in the literature review on radiation curing (Chapter 3), traditional epoxy adhesives usually require relatively long curing times even under elevated temperatures. On the other hand, for some applications, the advanced UV curing method is not always suitable, and curing with visible light on its own takes longer time. Therefore, in this research studies were undertaken to assess the feasibility of utilization of concentrated solar radiation for accelerated curing of epoxy and UV/visible light adhesives for thermoplastic bonding. These studies are summarized in the following sections.

9.4.1 Feasibility study on curing of common epoxy adhesives

This study on curing of traditional epoxy adhesives was initiated to determine if the concentrated solar radiation could accelerate the curing process and also, if it would have any detrimental effect on the adhesive.

Three types of adherends, transparent PMMA, transparent PC and white ABS, were used. The test specimens were with dimensions of 50 mm x 10 mm x sheet thickness, as described in Chapter 4. The test specimens were prepared following the procedure specified in (ASTM-D2093 1997). In this study two types of adhesives, RS high strength epoxy and Rapid Araldite (RA), were used to bond the adherends. Since surface preparation of an adherend is a major factor attributing to a successful bonding, the surfaces to be bonded were wiped with a solvent-dampened cloth and

then left to dry prior to the application of the adhesive. The adherends were clamped in a fixture and bonded in a lap joint, as shown in Figure 9.13. To ensure a consistent adhesive layer thickness not less than 1 mm, glass beads with 1 mm diameter were spread on the joint interface. A clamping device was used to apply sufficient pressure on the bond interface.

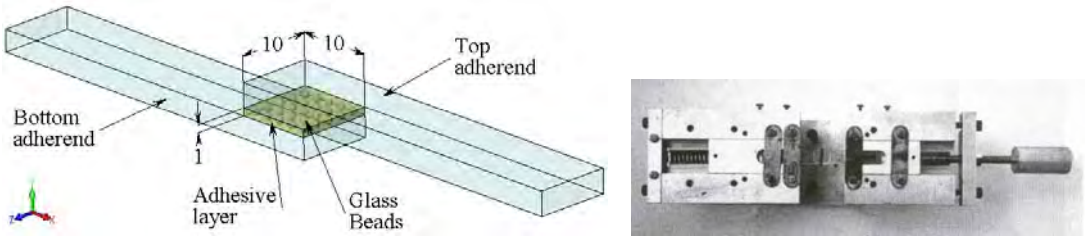

Figure 9.13: Test specimens layout and clamping device

Details of this feasibility study could be seen in Yarlagadda, Stoynov et al. 2001.

The results from this study have shown that exposure to concentrated solar radiation can reduce the curing duration of epoxy adhesives, compared to conventional methods, and thus can lead to shorter processing times. However, a difference in the solar radiation absorptance by the two components of the epoxy can affect their proportion and, depending on the thermal conductivity of the epoxy, can lead to uncontrolled uneven volumetric curing. On the other hand, although compatible with acrylic adhesives, the acrylics can be attacked by their activator before the adhesive has cured. Also, any excess uncured cyanoacrylate adhesive can cause stress-cracking in the adherend. Thus, in the following study light susceptible one-component, solvent-free adhesives were explored.

9.4.2 Curing of UV/visible light adhesives for thermoplastic bonding utilizing concentrated insolation

As discussed in Chapter 3, to take advantage of the visible light curing capability, cationic and aerobic adhesives are being increasingly used for bonding of transparent or translucent polymers. Depending on the irradiation source spectral output and the spectral susceptibility of the adhesive, it is anticipated that higher radiation intensity can lead to faster and deeper cures. Generally, the most effective curing process will occur if the spectral distribution of the source matches the spectral susceptibility of the adhesive, in particular, it would be best if the absorption maxima matches those of the light source. Such a system would eliminate the need to use complicated and expensive UV lamps to ensure the adhesive efficiency.

Some polymers are UV susceptible, others, including many grades of polycarbonate and the one used in this study, contain additives that block UV radiation, thus inhibiting the effective curing process of UV-susceptible adhesives. As can be seen from Table 9.3, PC is susceptible to wavelength bands in the UVA, as well as in the UVB regions.

Table 9.3: Susceptibility wavelengths of most polymers (Leather 1999)

Polymer	Wavelength range [nm]	UV type
Polyamide	250 – 310	UVC UVB
Polycarbonate	280 – 305 330 – 360	UVB UVA
Polyester	290 – 330	UVB UVA
Polyethylene	>300	UVA
PVC	310 – 370	UVA
Polysterene	318 – 340	UVA
Polypropylene	>370	UVA

For the above reasons, in this study the feasibility of utilizing the predominantly visible concentrated solar radiation, delivered by the SEC, was explored for curing of adhesive bonded PC adherends.

9.4.2.1 Experimental procedure

The curing behaviour of two types of light sensitive adhesives, Dymax Ultra Light-Weld and Delo-Photobond, when irradiated with concentrated solar radiation, was studied. Ultra Light-Weld is one-part solvent-free aerobic adhesive with cure catalysts responding to longwave UV, visible light or both (wavelength range of 300-500 nm). Delo-Photobond is one-part solvent-free modified acrylate that is cured with visible light in a wavelength range of 380-450 nm.

Three types of adherends, ABS, PC and PMMA with dimensions 40 mm x 6 mm x sheet thickness, were bonded using Delo-Photobond. The adherends were appropriately cleaned and the adhesive was applied to a 6 x 6 mm prepared section. Suitable springs were used in the lap joint clamping device to hold the lap joint with a relatively uniform pressure (no greater than 0.04 MPa). This fixture was suitable since it does not allow unwanted touching of the formed joint by any parts of the clamping device. In general, the test method used in this experimental study followed (ASTM-D3163 2001) and (ASTM-D1002 1999). However, it was not feasible to limit the test specimen geometry to that specified in ASTM-D1002 because of the low yield point in plastics compared to metals.

Two batches of 10 specimen pairs, each with transparent PC as a top adherend and bottom adherends from each material (transparent and opaque), were exposed

using the SEC facility. A thermocouple was embedded under the transparent adherend near the glue line and the air cooling system was used to maintain the maximum temperature below 80°C.

Delo-Photobond adhesive, according to the manufacturer's specifications, achieves full strength cure when the adherends are irradiated for minimum of 60 seconds with intensity 60 mW/cm^2 (or 600 W/m^2) by a lamp at a distance less than 70 cm. Thus, the actual minimum irradiation exposure required for each specimen pair would be equivalent to 1.296 J. Such relatively low irradiation exposure was easily obtainable only by using the sun-tracking capabilities of the SEC facility without concentration. Because of this, the first batch of 10 specimen pairs was exposed at the plane of the primary mirror for 60 seconds at 600 W/m^2 insolation intensity, or at insolation intensities and durations equivalent to 1.296 J.

The specimen pairs from the second batch were exposed on concentrated solar radiation at the Cassegrainian focus. In this case, since the minimum required energy, as calculated above on the basis of the manufacturer's recommendations, was relatively low, an additional 3 mm thick PMMA filter was used on the top of the clamping device. The specimens were exposed at approximately equal intensities for two seconds on average. After the curing process was complete, the cured samples were subjected to tensile testing and the bond strengths were assessed and compared.

9.4.2.2 Results and discussion

In general, in this feasibility study the specimen pairs from both batches exposed on non-concentrated and concentrated beam insolation were cured without discarding any specimens. A photograph of the first batch of specimens cured for 60 seconds with non-concentrated solar radiation is shown in Figure 9.14.

Figure 9.14: Specimens cured with light sensitive adhesive for 60 seconds

The second batch of specimens cured for two seconds with concentrated solar radiation is shown in Figure 9.15.

Figure 9.15: Specimens cured with light sensitive adhesive for two seconds

The bond strengths of the adhesive joints cured with non-concentrated and concentrated solar radiation are summarized in Table 9.4 and graphically illustrated in Figure 9.16.

Table 9.4: Tensile strength of cured specimens

Adherends	Load failure [N] Duration 60 sec non-concentrated	Load failure [N] Duration 2 sec concentrated
transparent PC + transparent PC	343	348
transparent PC + transparent PMMA	326	334
transparent PC + white ABS	301	336
transparent PC + yellow PMMA	289	317
transparent PC + orange PMMA	321	316
transparent PC + red PMMA	298	315
transparent PC + blue PMMA	297	292
transparent PC + violet PMMA	289	311
transparent PC + green PMMA	297	318
transparent PC + black PMMA	202	232

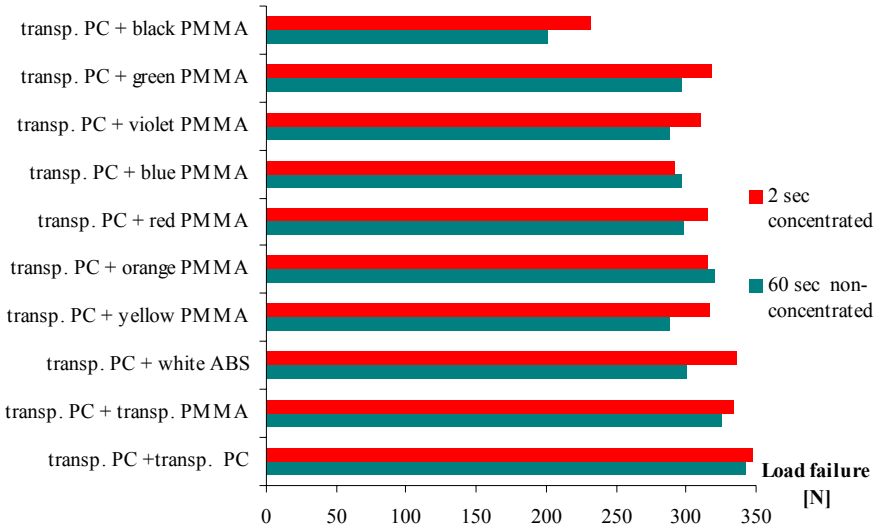

Figure 9.16: Comparison between tensile strengths of specimens cured for 60 seconds on non-concentrated light and for two seconds on concentrated light

In general, although being only a feasibility study, these experiments have shown that concentrated solar radiation could be used for significant shortening of the curing duration. It should be noted that in both experiments the air-forced cooling was negligible. The achieved tensile strengths of the specimens cured with concentrated light for two seconds are comparable, even higher than these achieved after 60 seconds exposure under non-concentrated solar radiation.

However, compared to the tensile strengths of the adherend materials, the achieved tensile strengths were relatively low in both experiments. These results may be due to the relatively low tensile strength of the adhesive itself (10 MPa) compared to that of the adherend. More comprehensive investigation into the curing behaviour of the adhesive system under solar radiation has been planned for future work.

This study was further extended to explore another two light curing adhesives, Ultra Light Weld 3094 and Ultra Light Weld 4-20418 low stress plastic and glass bonders. In this case, however, the intention was to study the feasibility of using concentrated solar energy for curing larger volumes of adhesive and test the tensile stress after cure. In particular, the possibility to use the conic third stage concentrator to achieve this, was explored.

Ultra Light Weld 4-20418 and Ultra Light Weld 3094 adhesives were cured with 14 J and 21 J respectively in appropriate cylindrical glass containers. The containers were mounted in the third stage conical concentrator along its axis. Air cooling was used to maintain the temperature below 100°C. The cured Ultra Light Weld 3094 was 10 mm in diameter and 90 mm long, whereas the cured Ultra Light Weld 4-20418 was 6 mm in diameter and 100 mm long. The cured adhesive samples are shown in Figure 9.17.

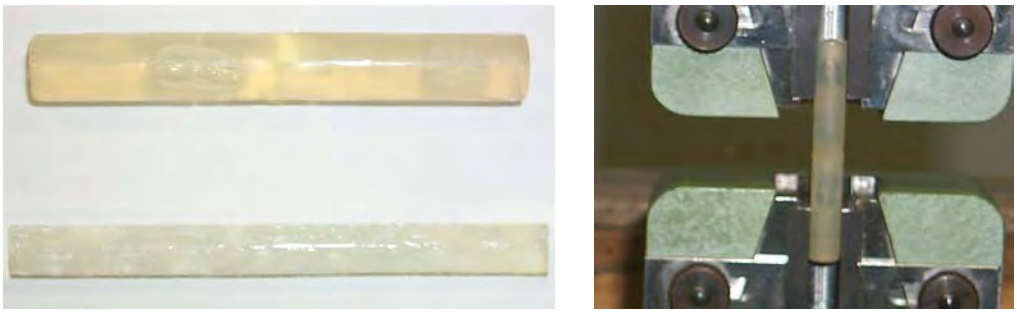

Figure 9.17: Cured Ultra Light Weld 3094 (upper left and right) and Ultra Light Weld 4-20418 (bottom left)

Although the curing of the explored Dymax light sensitive adhesives with solar radiation has been considered successful, the tensile joint strengths achieved were not significant. The tensile strengths of the cured samples were measured as 19.61 MPa for Ultra Light Weld 3094 and 9 MPa for Ultra Light Weld 4-20418.

These results are only preliminary and may have been affected by the method of curing or testing, thus more experimentation would be required for more comprehensive study. However, although the curing was successful, it is evident that the tensile strengths of these samples are significantly lower than the tensile strengths of most materials used throughout this research.

9.5 Conclusions

It has been found from the initial irradiation study that the transparent materials used in this research can form colored fringes when illuminated with polarized light after exposure to concentrated solar radiation. If in photoelasticity isochromatics are typically used for stress analysis, in this study they have been an excellent visualization tool. They have been useful for verification of important theoretically calculated optical parameters such as the shape, size and location of the focal spot, and for aligning of the optical components. Furthermore, such visualization could illustrate if welding of transparent polymers with concentrated solar radiation causes building of stresses and ageing of the exposed polymers.

The results from the polymer ageing experiments showed that ultra-accelerated exposure to concentrated sunlight can be performed with the SEC facility without introducing new (unrealistic) failure mechanisms. Prolonged outdoor exposures at lower stress levels can be substituted with significantly shortened test durations at elevated stress conditions. In this study it was demonstrated that with forced heat removal, a sufficient control of specimen temperature at very high levels of concentrated sunlight is possible without detrimental effect on the polymer. The exposure of the specimens to the entire available insolation spectrum implies that such natural accelerated tests would produce more realistic and reliable results, compared to those from the widely used laboratory weathering tests.

After accelerated natural irradiation, equivalent to five years outdoor exposure, the different polymers showed a different degree of degradation. PSM-1, PP and ABS materials experienced a formation of various functional groups associated with an oxidation, caused by the accelerated natural exposure to concentrated solar

radiation. Furthermore, the tensile strength of these materials decreased to a different extent after the exposure.

The results from the FTIR spectroscopy demonstrated a very high stability of PMMA towards photooxidation under the experimental conditions in this study. The accelerated natural exposure did not lead to a recognisable photodegradation of the PMMA polymer, except for the observed increase in the CH_2/CH_3 absorption ratio. It should be noted that since these results are strongly dependent on the utilized spectral range particularly available during the exposure, they may differ if there is a variation in the insolation spectrum or in the exposure duration. Loss of tensile strength was the most pronounced outcome of the exposure.

The experiments on curing of light sensitive adhesives showed that a higher radiation intensity would lead to faster cures. However, the speed and depth of cure are greatly affected by the irradiation source spectral output and the spectral susceptibility of the adhesive.

The experiments also demonstrated that by utilizing the concentrated solar radiation delivered by the SEC facility, it is possible to reduce the curing duration from 60 to two seconds. The tensile strengths achieved with concentrated, predominantly visible solar radiation, were comparable and even higher than those obtained when non-concentrated light was used.

It is possible, however, to increase the tensile strength of the bond by more careful specimen preparation before the curing process. The experimental curing of adhesive bonds has shown that, because the adhesive is fairly sensitive to visible light, it is very important to ensure that the adhesive is not exposed to visible sunlight before the actual curing process commences. During the experiments it has been found that polymerization may be triggered by the ambient conditions while applying the adhesive on the adherend. However, even insignificant polymerization on the exposed outer layer would prevent the efficient curing of the inner adhesive volume. It would be more appropriate, therefore, to prepare the specimen pairs in environment with sufficiently low light intensity, which was not possible in the ambient conditions near the solar concentrator. Thus, future work is necessary to address those issues.

A comprehensive chemical and physical analysis of the curing process utilizing solar energy is beyond the scope of this thesis, however, this feasibility study has provided an insight into the possibility to accelerate this process.

CHAPTER 10.
CONCLUSIONS AND SCOPE FOR FUTURE WORK

The overall aims of this research were to develop an alternative system and technique utilizing beam insolation for polymer processing, and use them to study and contribute towards better understanding of the radiation – polymer interaction. The research objectives, as specified in Chapter 1, have been fulfilled and most findings are summarized below. The major outcomes of this research are the development of a non-conventional, multi-stage solar energy concentrating system and the demonstration of its feasibility as a radiation source in various polymer processing applications.

10.1 Summary of the research outcomes

The extensive literature review (Chapters 2 and 3) confirmed that most of the advanced material processing technologies use directly or require artificial source and/or electromagnetic radiation generation mechanism. The naturally available solar electromagnetic radiation on the other hand, although utilized in several industries, has not been widely studied as a polymer processing source.

In line with the first research objective, the following conclusions have been derived. The evaluation of the typical variation of meteorological parameters and the corresponding optical and thermal characteristics of the SEC facility proved that utilizing of the available insolation as a polymer processing source is feasible (Chapter 5). The calculations of the variable SEC systems parameters and material characteristics demonstrated that the output power can be suitable for the different applications proposed.

The measured beam insolation intensity typically varies steadily by 0.83 W/m^2 (0.1%) per minute on average, and although variable throughout the year, its maximum value ranges between 800 and 1100 W/m^2. The corresponding possible net power gained by the most effective SEC arrangement was estimated to be 104 W and 143 W respectively. When successfully focused further on a 6 mm-diameter spot producing densities of 3.68 W/mm^2 and 5.06 W/mm^2 respectively, this power was found sufficient for polymer joining.

From the measurements it became evident that the temperature distribution of the irradiated polymer during polymer processing is extremely complex and has a

significant effect on the lifetime and other properties of the material. Also, the temperature distribution in the bulk of the material is usually not uniform, making the determination of the process temperature complicated. Since the temperature variation is directly dependent predominantly on the radiation source and the radiation characteristics and other material properties, spectrophotometric and thermophysical measurements were required. It was concluded that for the utilized solar spectrum by the SEC the least absorbing colored material is the yellow PMMA (69.66%), and the most absorbing is the green PMMA (94.24%).

The transparent polymers were included in this study to gain insight into the volumetric absorption affect. The results clearly showed that the transparent PMMA maintains higher transmittance (around 91%) compared to the transparent PC (around 84%), for the whole visible spectrum, despite of the thickness difference. When the transmittance of the direct solar radiation through clear PC and PMMA was studied further, lower values were obtained. It was also found that, compared to PC, clear PMMA is more transparent to UV light, especially in the black light region (approximately 370-390 nm). PC is much more absorbing, having a small peak around 315 nm, and its transmittance drops significantly at around 390 nm.

In general, the trend established from the spectrophotometric measurements was confirmed by the outdoor heat generation experiments (Chapter 5). Logically, the black PMMA recorded the fastest response (~11 seconds) in achieving the melting phase. By contrast, the transparent PMMA recorded the longest duration to reach the melting temperature (more than 60 seconds). Between the colored specimens the green PMMA had the quickest response (~17 seconds) and the yellow PMMA had the slowest (~29 seconds) (see Figure 5.34).

Based on the derived mathematical equations in Section 5.3.2, the formulated deterministic model (Appendix 5A) enabled the description of the optical path of any ray arriving at the principal Cassegrainian focus after reflection from the clear apertures of the mirrors. The operational variable parameters for such rays determined by solving the derived Equation 5.13 have been confirmed by the created SolidWorks geometrical model. An interesting result was the equation derived for the extreme angle of the cone of concentrated light beam arriving at the Cassegrainian final focus (Equation 5.16). The analysis of the developed deterministic model has led to another significant finding that when complemented with a CPC, the combined concentration of the SEC facility remains relatively

constant for any point on the rim rings, thus obliterating the shadow effect and ensuring a more homogenous irradiation output.

Most of the results obtained from the evaluation of the characteristics and capabilities of the SEC facility, as well as the relevant material properties of the thermoplastics, have been beneficial in the modeling work. The modeling (Chapter 6) has facilitated the process understanding, allowing the improvement of various aspects of the operation and performance of the SEC facility to be implemented.

The initially created optical ray tracing models of the Cassegrainian concentrator with various conventional imaging components and non-imaging concentrators have been found useful in the optimization of the initially proposed system. The modeling has shown that, depending on the application, four different principal configurations with conventional imaging refractive optics are feasible.

Using these configurations combined 3D ray tracing computer models integrated with the mechanical components were developed to address the second research objective. The 3D models simulated the entire SEC facility and predicted the image size, location and orientation in the various configurations. As a result of the evaluation and modeling, it was also concluded that non-imaging optics based on total internal reflection, such as a truncated light cone and CPC, would be more suitable for ageing and curing experiments.

While the optical and combined models enabled the design and optimization of the used optical configurations, the energy transfer modeling allowed the prediction of the heat flow and heat buildup or the temperature rise as a function of time. Better understanding of the radiation–material interaction has been gained through the modeling of the energy transfer, radiation absorption and heat generation and exchange in the irradiated polymer. The developed analytical model enabled the prediction of the temperature variation and duration for attaining the glass transition state of the irradiated polymer. The simulation results showed an almost linear temperature profile until the glass transition was reached and a non-linear profile above the glass transition. The transient model of the radiation propagation and transfer of the absorbed energy/generated heat exchange through the polymers simulated the temperature distribution during through-transmission polymer joining. The transient simulation showed a convex exponential temperature profile. The trend in the temperature variation at the selected nodal points demonstrated that, as expected, the highest temperature was achieved at the joint interface.

The experimental verification of the models showed a good correlation between the predicted and experimental results within 1.3% of the experimental values for the polymer irradiation model and 5.4% for the through-transmission model. Since most experiments were conducted outdoors in variable ambient conditions, the implementation of the models has saved a great deal of time in the system characterization. Because most radiation characteristics become variable with polymer phase change, beyond it the prediction of the entire irradiation process requires further studies which are outside the scope of this work.

A major part of this thesis was focused on the development and continuous modification of the SEC facility systems during the course of the research. Through the modifications of the original configuration and introduction of especially developed auxiliary systems, it was determined that the modeled design concepts are feasible. The modifications and improvements of the various SEC facility systems (Chapter 7) proved useful and reliable for the system operation and experimental application exploration. The modifications led not only to significant shortening of the auxiliary optical path when conventional optics was used, but also allowed the integration of the beam transmitting and focusing in a compact adjustable system. On the whole, the modeled and implemented modifications have led to considerable improvement of the optical and thermal performance of the SEC facility.

One novel contribution of this research is the enhancement of the image forming concentrator with non-imaging concentrators (conical and CPC), utilizing their inherent disadvantage of excessive length. The explored truncated cone and 3D CPC concentrators can be considered more efficient, enhancing the concentration further, compared to the refractive means of transmitting the concentrated solar radiation.

In line with the third research objective, most experimental results presented in this thesis demonstrated the ability of the SEC facility to serve as an electromagnetic radiation source for various polymer processing applications. In general, the experimental studies on polymer joining (Chapter 8) proved that all of the used identically and differently colored, similar and dissimilar thermoplastics, can be successfully joined using concentrated solar energy. The obtained tensile strengths of the joints were comparable to the results achieved for similar polymers with other advanced plastic joining methods (Section 3.3.2.7).

Both butt and lap joining experiments demonstrated that, among the colored polymer specimens, the green PMMA required the least amount of energy/time for

achieving a bond, and the yellow PMMA – the most. Reports have been published by other researchers using different materials and radiation sources with longer than the utilized in this research wavelength range (Grimm and Yeh 1998; Kagan et al. 2001; Grewell et al. 2002). The only similar trend has been reported by Kagan et al. for Polyamide in the NIR range (see Figure 3.16). However, the present research has extended the radiation absorption knowledge over a relatively broader wavelength range of visible and UV radiation (including NIR) for several similar and dissimilar, clear and colored thermoplastics.

Unlike most of the advanced polymer welding techniques, in this research the developed through-transmission technique removes the need to use a special absorbing medium of the radiant energy (e.g. carbon black or other pigments and dyes). In addition, successful lap joining was achieved between two similar clear polymers (PMMA and PMMA) and two dissimilar clear polymers (PMMA and PC). The research has shown that the concentrated solar radiation can be effectively absorbed even in highly optically transparent to the visible solar radiation polymers.

The results from the polymer ageing experiments (Chapter 9) showed that an ultra-accelerated exposure to concentrated sunlight can be performed with the SEC facility without introducing spurious failure mechanisms. It was concluded that even at very high levels of concentrated sunlight, the temperature variation could be controlled with forced heat removal preventing its detrimental effect on the polymer. At the same time, by exposure of the specimens to the entire available solar spectrum, more realistic results, compared to those from the widely used laboratory weathering tests, could be obtained.

The different polymers showed different degrees of degradation after the accelerated natural irradiation, equivalent to five years of outdoor exposure. It was observed that PSM-1, PP and ABS experienced formation of various functional groups associated with an oxidation caused by the accelerated natural exposure to concentrated solar radiation. Additionally, the tensile strength of these materials decreased to a different extent after the exposure. The FTIR spectroscopy results demonstrated a very high stability of PMMA towards photooxidation under the specific experimental conditions. The accelerated natural exposure of PMMA did not lead to a recognizable photodegradation but resulted in a loss of tensile strength.

The experiments on curing of light sensitive adhesives (Chapter 9) indicated that higher radiation intensity can lead to faster cures. It was demonstrated that by

utilizing the concentrated insolation delivered by the SEC facility, it is possible to reduce the curing duration from 60 to 2 seconds. When concentrated, predominantly visible solar radiation was used, the tensile strengths achieved were comparable and even higher than those obtained when non-concentrated light was used.

It is believed that the results obtained in this research could contribute to better understanding of radiation-induced processes using relatively broad band solar radiation which have not been a widely studied area. This work has demonstrated that the developed SEC facility can utilize the unique capabilities of solar radiation to serve as an alternative source of electromagnetic radiation for diverse applications.

10.2 Some advantages and limitations of the developed system

The system and method presented in this thesis can offer some advantages over the current polymer processing techniques that are based on electrical and electromagnetic effects or directly use different types of electromagnetic radiation. The major benefits are that it utilizes a non-artificial and clean renewable energy source, and could be used for different applications.

Compared to the current conventional joining technologies, the system and technique proposed have the advantages of being non-invasive and non-dependent on the material, and applicable for welding of similar and dissimilar, clear to clear or transparent to colored polymers.

In comparison to the IR lamps, the developed polymer joining system includes a similar, broader source of electromagnetic radiation, but relatively more energetic and far more easier to focus. Although with the recent advances in laser technology it became possible to weld even thermoplastics typically transparent to the near-IR region, the thermoplastic laser welding is still considered complicated and fairly expensive process. The Clearweld process for example, requires at least one of the welding surfaces to have a laser absorbing medium. It has to be ensured that this absorber is applied in advance at the weld interface, decomposes and the solvents evaporate prior to bringing the surfaces into contact, which is not always possible. However, if the absorber is only on the surface of the substrate, depending on the material, the melted layer may not have sufficient penetration depth. The technique developed in this research eliminates the need to use a special absorbing medium of the radiant energy by utilizing the “free” solar energy source. Moreover, it could generate heat at the joining interface independently of the wavelength and provide

more effective volumetric heating of transparent polymers since a direct energy conversion process takes place within the material being treated.

When assessing the potential applications of the developed system for utilization of solar energy, some limitations must be considered. Although solar energy is considered an inexhaustible resource, it is less intense compared to other sources, and intermittent and unreliable if used alone. Also, the process of irradiation/power dissipation in the joint interface could not be precisely controlled at this stage.

10.3 Original research contributions

During the course of this research several original theoretical and experimental contributions have been made to the field of solar energy utilization research and polymer processing. The original contributions can be summarized as follows:

- Analytical model for prediction of the temperature variation and duration for attaining the glass transition state of the irradiated polymer (Chapter 6, Section 6.6.2.2A).
- Transient heat transfer model for simulation of the temperature distribution during through-transmission polymer joining (Chapter 6, Section 6.6.2.2B).
- The geometrical modeling of the light rays and the especially derived mathematical equations (Chapter 5), including the equation allowing calculation of the extreme angle of the cone of concentrated light beam arriving at the Cassegrainian final focus (Equation 5.16).
- Development of the first multi-purpose, multi-stage solar concentrator.
- The first experimental investigation of through-transmission polymer joining without the requirement of a special absorbing medium of radiant energy.
- The formulation of the deterministic model (Appendix 5A) allowing comparison of the achievable concentration for any ray incident on the accepting clear aperture of the primary mirror.
- The finding that the combined concentration of the SEC facility when complemented with a CPC remains relatively constant for any point on the accepting clear primary aperture.
- The combining of an imaging two-stage concentrator with non-imaging third stage light cone or 3D CPC concentrators, utilizing their inherent excessive length for transmitting and further concentration of solar radiation.

- The first experimental investigation of the utilization of concentrated solar radiation for polymer processing and expanding the radiation absorption knowledge over the UV visible and NIR wavelength range for several clear and colored thermoplastic materials.
- Demonstration of the usefulness of solar radiation for joining, curing and ageing of similar and dissimilar, clear and colored thermoplastics.

10.4 Scope for future work

The following issues could be addressed in a future work in order to further improve the performance of the SEC facility and to expand its application:

1. Improving the temperature control process by:
   - installing a pair of temperature sensitive components (thermistor and thermocouple) at the exposed area to allow simultaneous continuous recording of the temperature.
   - using a remote temperature IR radiometry during irradiation.
   - further development of light chopper and mist/smoke maker control systems.
2. Further upgrading of the SEC facility including:
   - improvement of the sun-tracking with a four-quadrant sensor in an active feedback loop and using a narrow field of view (~1°) pyrheliometer.
   - using an one-way secondary mirror or behind mirror focusing.
   - development of the proposed clamping device in Chapter 8, Figure 8.11 for butt joining of colored polymers to improve the joining process.
3. Other possible application studies:
   - through-transmission welding of transparent PMMA and PC to absorbing films from different polymers and colors.
   - joining of differently colored thin polymer films and welding of fabrics.
   - more comprehensive investigation into the curing behaviour of the adhesive system under solar radiation.
   - accelerated exposure of other polymer materials (with longer exposure duration for PMMA), including distilled water spraying.
   - producing a well-adhered film by aluminium powder melting on polymers.
   - irradiation for other purposes (e.g. food, bone microbiological materials).

APPENDIX 1. OVERALL AIMS AND OBJECTIVES

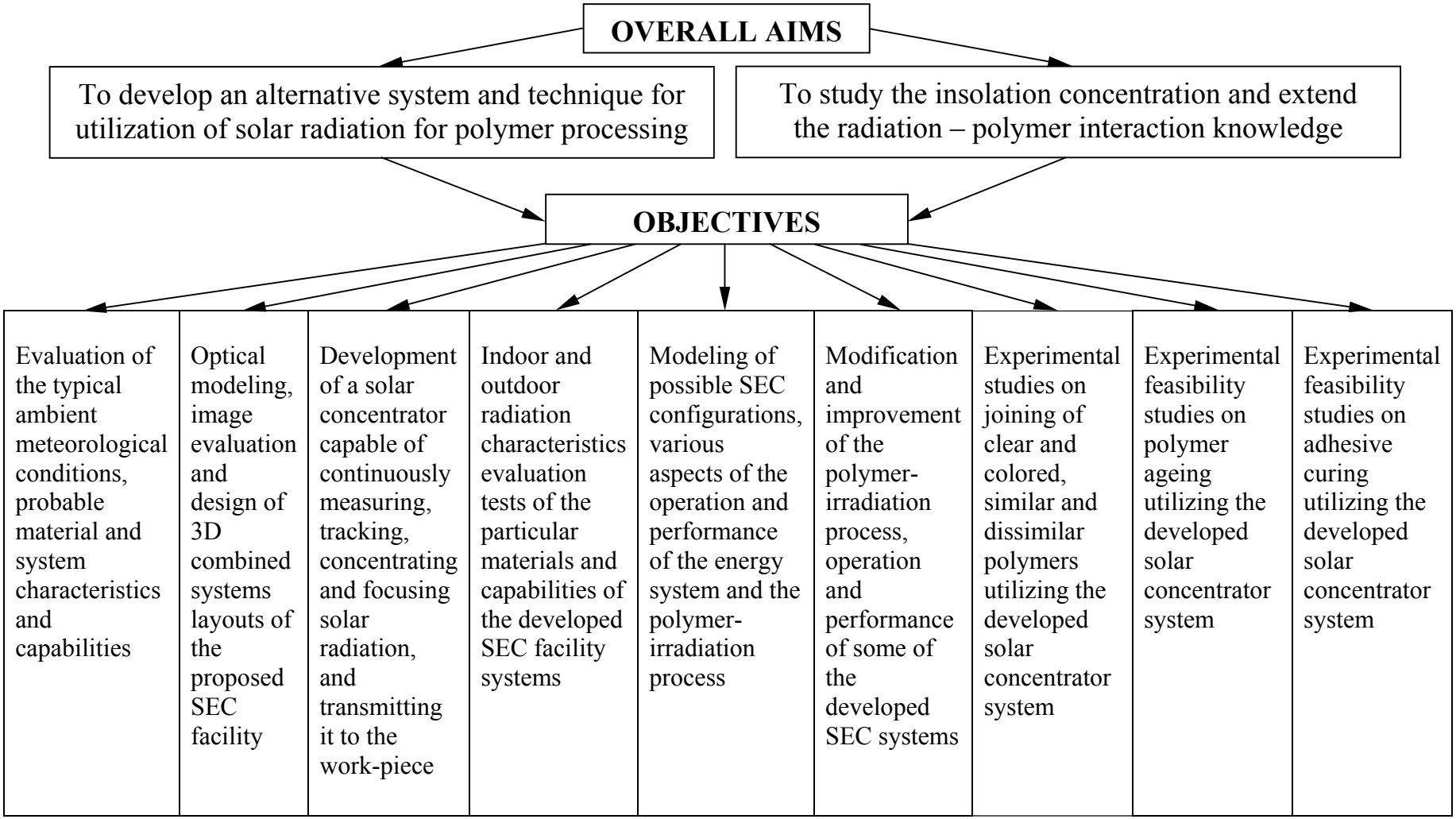

APPENDIX 2. SPECTRAL RANGES OF ELECTROMAGNETIC RADIATION

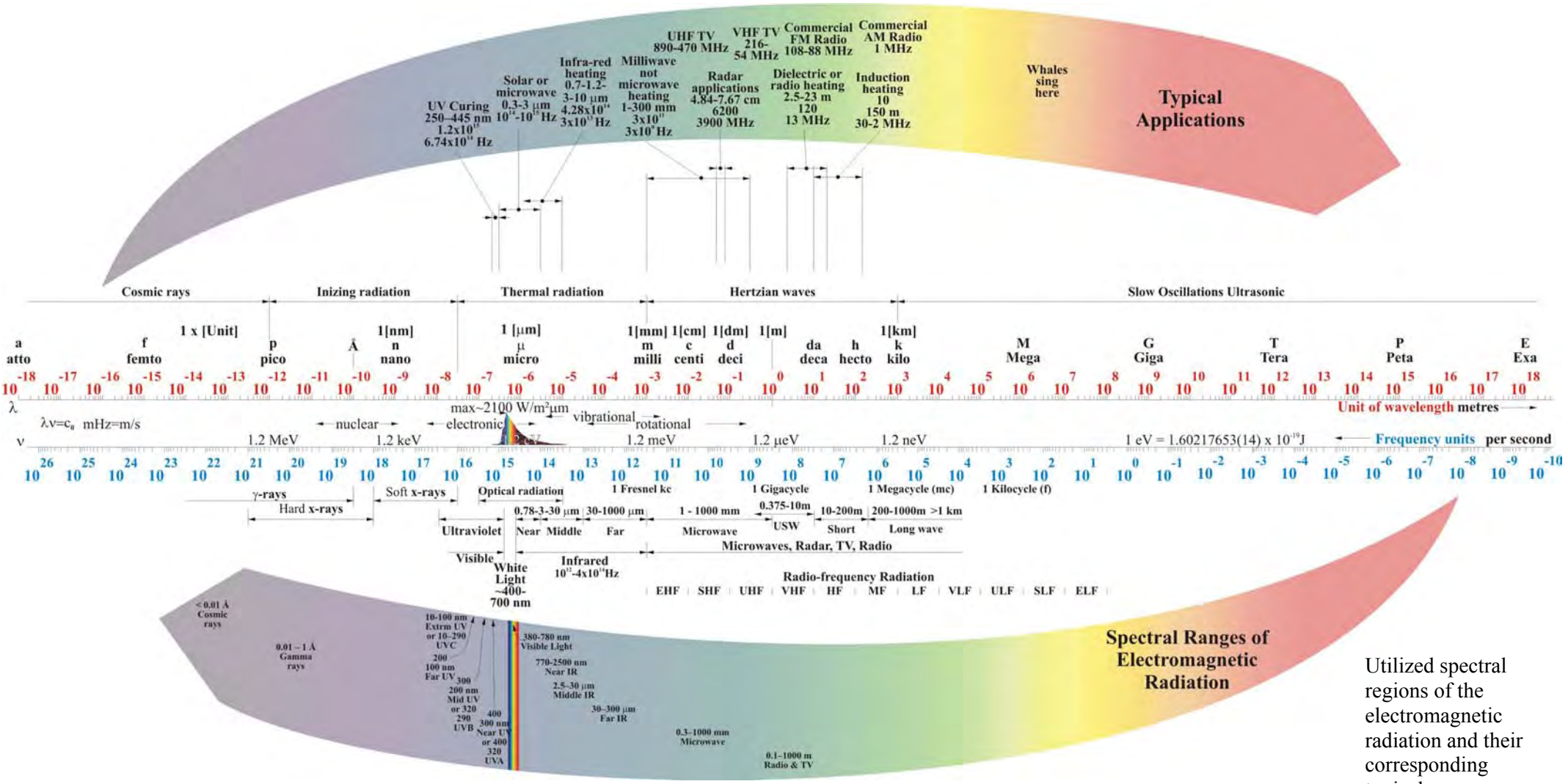

Utilized spectral regions of the electromagnetic radiation and their corresponding typical applications

APPENDIX 3. CLASSIFICATION OF POLYMERS

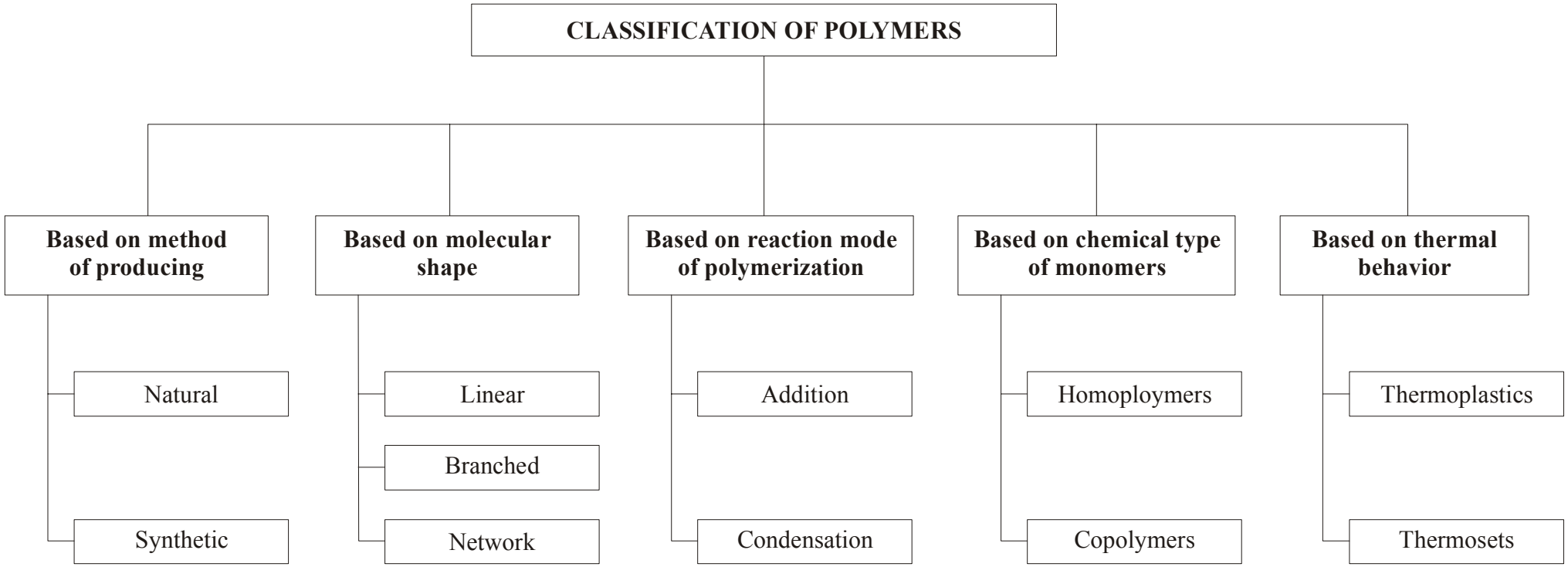

APPENDIX 4. SEC LOCATION AND PROTECTIVE SHED

APPENDIX 5A.
DETERMINISTIC MODEL FOR CALCULATION OF THE VARIABLE PARAMETERS OF SEC FACILITY

Input parameters	Symbol	Value	Unit	Approx. Value
ave sun dia	Dav	1392000.0	km	1392000.0
sun dia at perihelion	Dp	1417195.2	km	1417195.2
sun dia at aphelion	Da	1366804.8	km	1366804.8
earth-sun dist. at perihelion	Lp	143086633.0	km	147090000.0
earth-sun dist. at aphelion	La	150494225.0	km	152100000.0
sun angle at perihelion	Ap	0.283739	deg	0.276475
sun angle at aphelion	Aa	0.260181	deg	0.254540
radius primary curvature	Rp	4267.0	mm	4267.0
radius secondary curvature	Rs	7433.0	mm	7433.0
separation	s	1290.0	mm	1290.0
dia primary	dpr	590.0	mm	590.0
dia secondary	ds	240.0	mm	240.0

Yp Yp from tel axis [mm]	Xpc Xp from CC prim [mm]	Xpv Xp from prim vertex [mm]	α alpha primary [degrees]	fp f_p primary [mm]	Zp Sagitta_p primary [mm]	Cpa C_p area conc	Cpt C_p theoretic max conc.	Ys Ys (EES) calculated [mm]	Ycg Ys (SW) geom fnd [mm]	Xsc Xs from CC sec [mm]	Xsv Xs from prim vertex [mm]	Xsg Xs (SW) geom fnd [mm]	Zs sagitta secondary [mm]	β beta secondary [degrees]	ϕ ϕ=2(α-β) final angle [degrees]	v Dist_p vert to sec focus [mm]	fs f_s secondary [mm]	b B F L calculated [mm]	f E F L calculated [mm]	dmax max d_im perihelion [mm]	dmin min d_im aphelion [mm]	Csec,a C_sec Cassegrain area conc.	Csec,net C_sec_net Cassegrain	f1 f_cpc1 if d_out=6 [mm]	d1 d_in/2 cpc1 d_out=6 [mm]	L1 L_cpc1 if d_out=6 [mm]	f2 f_cpc2 if d_out=2.54 [mm]	d2 d_in/2 cpc2 d_out=2.54 [mm]	L2 L_cpc2 if d_out=2.54 [mm]	Ccpc,a C_cpc theor./geom. conc. ratio	Ccomb,a C_sec+cpc combined area conc.
300.0	**4256.441**	**-10.559**	**4.032**	**2128.207**	**10.559**	**6.397**	**233.444**	**118.612**		**7432.054**	**-1290.946**		**0.946**	**0.914**	**6.235**	**-210.594**	**1084.792**	**837.261**	**2746.113**	**27.198**	**24.940**	**578.764**	**358.165**	**3.326**	**27.625**	**280.328**	**1.408**	**11.694**	**118.672**	**84.790**	**49073.614**
299.5	**4256.476**	**-10.524**	**4.025**	**2128.225**	**10.524**	**6.397**	**232.670**	**118.414**		**7432.057**	**-1290.943**		**0.943**	**0.913**	**6.224**	**-210.555**	**1084.814**	**837.282**	**2746.159**	**27.199**	**24.941**	**576.817**	**358.153**	**3.325**	**27.671**	**281.223**	**1.408**	**11.714**	**119.051**	**85.073**	**49071.668**
299.0	**4256.511**	**-10.489**	**4.018**	**2128.243**	**10.489**	**6.397**	**231.898**	**118.217**		**7432.060**	**-1290.940**		**0.940**	**0.911**	**6.214**	**-210.516**	**1084.835**	**837.303**	**2746.205**	**27.199**	**24.941**	**574.873**	**358.141**	**3.325**	**27.717**	**282.122**	**1.407**	**11.733**	**119.432**	**85.357**	**49069.724**
298.5	**4256.546**	**-10.454**	**4.011**	**2128.260**	**10.454**	**6.397**	**231.126**	**118.019**		**7432.063**	**-1290.937**		**0.937**	**0.910**	**6.203**	**-210.477**	**1084.856**	**837.323**	**2746.251**	**27.200**	**24.941**	**572.933**	**358.129**	**3.324**	**27.763**	**283.025**	**1.407**	**11.753**	**119.814**	**85.643**	**49067.784**
298.0	**4256.581**	**-10.419**	**4.005**	**2128.278**	**10.419**	**6.397**	**230.357**	**117.821**		**7432.066**	**-1290.934**		**0.934**	**0.908**	**6.193**	**-210.438**	**1084.877**	**837.344**	**2746.296**	**27.200**	**24.942**	**570.996**	**358.117**	**3.324**	**27.810**	**283.934**	**1.407**	**11.773**	**120.199**	**85.930**	**49065.847**
297.5	**4256.616**	**-10.384**	**3.998**	**2128.296**	**10.384**	**6.397**	**229.588**	**117.623**		**7432.069**	**-1290.931**		**0.931**	**0.907**	**6.183**	**-210.399**	**1084.898**	**837.365**	**2746.342**	**27.201**	**24.942**	**569.063**	**358.105**	**3.323**	**27.856**	**284.846**	**1.407**	**11.792**	**120.585**	**86.219**	**49063.914**
297.0	**4256.651**	**-10.349**	**3.991**	**2128.313**	**10.349**	**6.397**	**228.821**	**117.426**		**7432.072**	**-1290.928**		**0.928**	**0.905**	**6.172**	**-210.361**	**1084.919**	**837.385**	**2746.388**	**27.201**	**24.943**	**567.133**	**358.093**	**3.323**	**27.903**	**285.763**	**1.407**	**11.812**	**120.973**	**86.509**	**49061.984**
296.5	**4256.686**	**-10.314**	**3.985**	**2128.331**	**10.314**	**6.397**	**228.055**	**117.228**		**7432.076**	**-1290.924**		**0.924**	**0.904**	**6.162**	**-210.322**	**1084.940**	**837.406**	**2746.433**	**27.202**	**24.943**	**565.206**	**358.081**	**3.322**	**27.950**	**286.685**	**1.406**	**11.832**	**121.363**	**86.800**	**49060.057**
296.0	**4256.721**	**-10.279**	**3.978**	**2128.348**	**10.279**	**6.397**	**227.290**	**117.030**		**7432.079**	**-1290.921**		**0.921**	**0.902**	**6.151**	**-210.283**	**1084.961**	**837.427**	**2746.478**	**27.202**	**24.944**	**563.283**	**358.069**	**3.321**	**27.997**	**287.611**	**1.406**	**11.852**	**121.755**	**87.093**	**49058.134**
295.5	**4256.756**	**-10.244**	**3.971**	**2128.366**	**10.244**	**6.397**	**226.526**	**116.833**		**7432.082**	**-1290.918**		**0.918**	**0.901**	**6.141**	**-210.244**	**1084.982**	**837.447**	**2746.524**	**27.202**	**24.944**	**561.363**	**358.058**	**3.321**	**28.044**	**288.542**	**1.406**	**11.872**	**122.150**	**87.388**	**49056.214**
295.0	**4256.790**	**-10.210**	**3.964**	**2128.383**	**10.210**	**6.397**	**225.764**	**116.635**	**116.635**	**7432.085**	**-1290.915**	**-1290.915**	**0.915**	**0.899**	**6.130**	**-210.206**	**1085.003**	**837.468**	**2746.569**	**27.203**	**24.944**	**559.447**	**358.046**	**3.320**	**28.092**	**289.478**	**1.406**	**11.892**	**122.546**	**87.684**	**49054.297**
294.5	**4256.825**	**-10.175**	**3.958**	**2128.400**	**10.175**	**6.397**	**225.003**	**116.437**		**7432.088**	**-1290.912**		**0.912**	**0.898**	**6.120**	**-210.167**	**1085.024**	**837.488**	**2746.614**	**27.203**	**24.945**	**557.533**	**358.034**	**3.320**	**28.139**	**290.418**	**1.405**	**11.912**	**122.944**	**87.981**	**49052.384**
294.0	**4256.860**	**-10.140**	**3.951**	**2128.418**	**10.140**	**6.397**	**224.243**	**116.240**		**7432.091**	**-1290.909**		**0.909**	**0.896**	**6.110**	**-210.129**	**1085.045**	**837.509**	**2746.659**	**27.204**	**24.945**	**555.624**	**358.022**	**3.319**	**28.187**	**291.363**	**1.405**	**11.933**	**123.344**	**88.280**	**49050.474**
293.5	**4256.894**	**-10.106**	**3.944**	**2128.435**	**10.106**	**6.397**	**223.485**	**116.042**		**7432.094**	**-1290.906**		**0.906**	**0.895**	**6.099**	**-210.091**	**1085.066**	**837.529**	**2746.704**	**27.204**	**24.946**	**553.717**	**358.011**	**3.319**	**28.235**	**292.313**	**1.405**	**11.953**	**123.746**	**88.581**	**49048.568**
293.0	**4256.928**	**-10.072**	**3.937**	**2128.452**	**10.072**	**6.397**	**222.728**	**115.844**		**7432.097**	**-1290.903**		**0.903**	**0.893**	**6.089**	**-210.052**	**1085.086**	**837.550**	**2746.749**	**27.205**	**24.946**	**551.814**	**357.999**	**3.318**	**28.283**	**293.267**	**1.405**	**11.973**	**124.150**	**88.883**	**49046.665**
292.5	**4256.963**	**-10.037**	**3.931**	**2128.470**	**10.037**	**6.397**	**221.972**	**115.646**		**7432.100**	**-1290.900**		**0.900**	**0.891**	**6.078**	**-210.014**	**1085.107**	**837.570**	**2746.794**	**27.205**	**24.946**	**549.914**	**357.987**	**3.318**	**28.332**	**294.227**	**1.404**	**11.994**	**124.556**	**89.186**	**49044.765**
292.0	**4256.997**	**-10.003**	**3.924**	**2128.487**	**10.003**	**6.397**	**221.217**	**115.449**		**7432.103**	**-1290.897**		**0.897**	**0.890**	**6.068**	**-209.976**	**1085.128**	**837.590**	**2746.839**	**27.206**	**24.947**	**548.018**	**357.975**	**3.317**	**28.380**	**295.191**	**1.404**	**12.014**	**124.964**	**89.491**	**49042.869**
291.5	**4257.031**	**-9.969**	**3.917**	**2128.504**	**9.969**	**6.397**	**220.464**	**115.251**		**7432.106**	**-1290.894**		**0.894**	**0.888**	**6.058**	**-209.938**	**1085.149**	**837.610**	**2746.884**	**27.206**	**24.947**	**546.125**	**357.964**	**3.317**	**28.429**	**296.160**	**1.404**	**12.035**	**125.374**	**89.798**	**49040.976**
291.0	**4257.066**	**-9.934**	**3.910**	**2128.521**	**9.934**	**6.397**	**219.712**	**115.053**		**7432.110**	**-1290.890**		**0.890**	**0.887**	**6.047**	**-209.900**	**1085.169**	**837.631**	**2746.929**	**27.206**	**24.948**	**544.236**	**357.952**	**3.316**	**28.477**	**297.134**	**1.404**	**12.055**	**125.787**	**90.106**	**49039.086**
290.5	**4257.100**	**-9.900**	**3.904**	**2128.538**	**9.900**	**6.397**	**218.961**	**114.856**		**7432.113**	**-1290.887**		**0.887**	**0.885**	**6.037**	**-209.862**	**1085.190**	**837.651**	**2746.973**	**27.207**	**24.948**	**542.349**	**357.940**	**3.315**	**28.526**	**298.113**	**1.404**	**12.076**	**126.201**	**90.416**	**49037.200**
290.0	**4257.134**	**-9.866**	**3.897**	**2128.556**	**9.866**	**6.397**	**218.211**	**114.658**		**7432.116**	**-1290.884**		**0.884**	**0.884**	**6.026**	**-209.824**	**1085.210**	**837.671**	**2747.018**	**27.207**	**24.948**	**540.466**	**357.929**	**3.315**	**28.575**	**299.097**	**1.403**	**12.097**	**126.618**	**90.728**	**49035.317**
289.5	**4257.168**	**-9.832**	**3.890**	**2128.573**	**9.832**	**6.397**	**217.463**	**114.460**		**7432.119**	**-1290.881**		**0.881**	**0.882**	**6.016**	**-209.786**	**1085.231**	**837.691**	**2747.062**	**27.208**	**24.949**	**538.587**	**357.917**	**3.314**	**28.625**	**300.086**	**1.403**	**12.118**	**127.036**	**91.041**	**49033.438**
289.0	**4257.202**	**-9.798**	**3.884**	**2128.590**	**9.798**	**6.397**	**216.716**	**114.263**		**7432.122**	**-1290.878**		**0.878**	**0.881**	**6.006**	**-209.748**	**1085.251**	**837.711**	**2747.106**	**27.208**	**24.949**	**536.711**	**357.906**	**3.314**	**28.674**	**301.079**	**1.403**	**12.139**	**127.457**	**91.356**	**49031.561**
288.5	**4257.236**	**-9.764**	**3.877**	**2128.607**	**9.764**	**6.397**	**215.970**	**114.065**		**7432.125**	**-1290.875**		**0.875**	**0.879**	**5.995**	**-209.711**	**1085.272**	**837.731**	**2747.151**	**27.209**	**24.950**	**534.838**	**357.894**	**3.313**	**28.724**	**302.079**	**1.403**	**12.160**	**127.880**	**91.672**	**49029.689**
288.0	**4257.270**	**-9.730**	**3.870**	**2128.624**	**9.730**	**6.397**	**215.225**	**113.867**		**7432.128**	**-1290.872**		**0.872**	**0.878**	**5.985**	**-209.673**	**1085.292**	**837.751**	**2747.195**	**27.209**	**24.950**	**532.969**	**357.883**	**3.313**	**28.773**	**303.083**	**1.402**	**12.181**	**128.305**	**91.990**	**49027.819**
287.5	**4257.303**	**-9.697**	**3.863**	**2128.641**	**9.697**	**6.397**	**214.482**	**113.669**		**7432.131**	**-1290.869**		**0.869**	**0.876**	**5.974**	**-209.635**	**1085.313**	**837.771**	**2747.239**	**27.210**	**24.950**	**531.103**	**357.871**	**3.312**	**28.823**	**304.092**	**1.402**	**12.202**	**128.732**	**92.310**	**49025.953**
287.0	**4257.337**	**-9.663**	**3.857**	**2128.658**	**9.663**	**6.397**	**213.740**	**113.472**		**7432.134**	**-1290.866**		**0.866**	**0.875**	**5.964**	**-209.598**	**1085.333**	**837.791**	**2747.283**	**27.210**	**24.951**	**529.240**	**357.860**	**3.312**	**28.874**	**305.107**	**1.402**	**12.223**	**129.162**	**92.631**	**49024.091**
286.5	**4257.371**	**-9.629**	**3.850**	**2128.675**	**9.629**	**6.397**	**212.999**	**113.274**		**7432.137**	**-1290.863**		**0.863**	**0.873**	**5.953**	**-209.560**	**1085.353**	**837.811**	**2747.327**	**27.210**	**24.951**	**527.381**	**357.848**	**3.311**	**28.924**	**306.126**	**1.402**	**12.244**	**129.593**	**92.954**	**49022.231**
286.0	**4257.404**	**-9.596**	**3.843**	**2128.691**	**9.596**	**6.397**	**212.260**	**113.076**		**7432.140**	**-1290.860**		**0.860**	**0.872**	**5.943**	**-209.523**	**1085.373**	**837.831**	**2747.371**	**27.211**	**24.952**	**525.525**	**357.837**	**3.311**	**28.974**	**307.151**	**1.401**	**12.266**	**130.027**	**93.279**	**49020.375**
285.5	**4257.438**	**-9.562**	**3.836**	**2128.708**	**9.562**	**6.397**	**211.522**	**112.879**		**7432.143**	**-1290.857**		**0.857**	**0.870**	**5.933**	**-209.486**	**1085.394**	**837.851**	**2747.415**	**27.211**	**24.952**	**523.672**	**357.825**	**3.310**	**29.025**	**308.182**	**1.401**	**12.287**	**130.464**	**93.605**	**49018.523**
285.0	**4257.472**	**-9.528**	**3.830**	**2128.725**	**9.528**	**6.397**	**210.785**	**112.681**		**7432.146**	**-1290.854**		**0.854**	**0.869**	**5.922**	**-209.448**	**1085.414**	**837.871**	**2747.458**	**27.212**	**24.952**	**521.823**	**357.814**	**3.310**	**29.076**	**309.217**	**1.401**	**12.309**	**130.902**	**93.934**	**49016.673**
284.5	**4257.505**	**-9.495**	**3.823**	**2128.742**	**9.495**	**6.397**	**210.049**	**112.483**		**7432.149**	**-1290.851**		**0.851**	**0.867**	**5.912**	**-209.411**	**1085.434**	**837.891**	**2747.502**	**27.212**	**24.953**	**519.977**	**357.803**	**3.309**	**29.127**	**310.258**	**1.401**	**12.330**	**131.343**	**94.263**	**49014.828**
284.0	**4257.538**	**-9.462**	**3.816**	**2128.759**	**9.462**	**6.397**	**209.315**	**112.286**		**7432.152**	**-1290.848**		**0.848**	**0.866**	**5.901**	**-209.374**	**1085.454**	**837.911**	**2747.546**	**27.213**	**24.953**	**518.134**	**357.791**	**3.308**	**29.178**	**311.305**	**1.401**	**12.352**	**131.786**	**94.595**	**49012.985**
283.5	**4257.572**	**-9.428**	**3.810**	**2128.775**	**9.428**	**6.397**	**208.582**	**112.088**		**7432.155**	**-1290.845**		**0.845**	**0.864**	**5.891**	**-209.337**	**1085.473**	**837.930**	**2747.588**	**27.213**	**24.954**	**516.296**	**357.780**	**3.308**	**29.229**	**312.356**	**1.400**	**12.374**	**132.231**	**94.928**	**49011.146**
283.0	**4257.605**	**-9.395**	**3.803**	**2128.792**	**9.395**	**6.397**	**207.850**	**111.890**		**7432.158**	**-1290.842**		**0.842**	**0.863**	**5.881**	**-209.300**	**1085.494**	**837.950**	**2747.633**	**27.213**	**24.954**	**514.460**	**357.769**	**3.307**	**29.281**	**313.414**	**1.400**	**12.396**	**132.679**	**95.264**	**49009.310**
282.5	**4257.638**	**-9.362**	**3.796**	**2128.809**	**9.362**	**6.397**	**207.119**	**111.693**		**7432.161**	**-1290.839**		**0.839**	**0.861**	**5.870**	**-209.263**	**1085.514**	**837.970**	**2747.676**	**27.214**	**24.954**	**512.627**	**357.757**	**3.307**	**29.333**	**314.477**	**1.400**	**12.417**	**133.129**	**95.601**	**49007.478**
282.0	**4257.671**	**-9.329**	**3.789**	**2128.825**	**9.329**	**6.397**	**206.390**	**111.495**		**7432.164**	**-1290.836**		**0.836**	**0.859**	**5.860**	**-209.226**	**1085.534**	**837.989**	**2747.719**	**27.214**	**24.955**	**510.798**	**357.746**	**3.306**	**29.385**	**315.545**	**1.400**	**12.439**	**133.581**	**95.939**	**49005.649**
281.5	**4257.704**	**-9.296**	**3.783**	**2128.842**	**9.296**	**6.397**	**205.662**	**111.297**		**7432.167**	**-1290.833**		**0.833**	**0.858**	**5.849**	**-209.189**	**1085.554**	**838.009**	**2747.762**	**27.215**	**24.955**	**508.972**	**357.735**	**3.306**	**29.437**	**316.619**	**1.399**	**12.462**	**134.036**	**96.280**	**49003.823**
281.0	**4257.737**	**-9.263**	**3.776**	**2128.859**	**9.263**	**6.397**	**204.935**	**111.099**		**7432.170**	**-1290.830**		**0.830**	**0.856**	**5.839**	**-209.153**	**1085.574**	**838.028**	**2747.805**	**27.215**	**24.956**	**507.150**	**357.724**	**3.305**	**29.489**	**317.699**	**1.399**	**12.484**	**134.493**	**96.622**	**49002.000**
280.5	**4257.770**	**-9.230**	**3.769**	**2128.875**	**9.230**	**6.397**	**204.210**	**110.902**		**7432.173**	**-1290.827**		**0.827**	**0.855**	**5.829**	**-209.116**	**1085.594**	**838.048**	**2747.848**	**27.216**	**24.956**	**505.331**	**357.712**	**3.305**	**29.541**	**318.784**	**1.399**	**12.506**	**134.952**	**96.967**	**49000.181**
280.0	**4257.803**	**-9.197**	**3.762**	**2128.892**	**9.197**	**6.397**	**203.486**	**110.704**		**7432.176**	**-1290.824**		**0.824**	**0.853**	**5.818**	**-209.079**	**1085.614**	**838.067**	**2747.891**	**27.216**	**24.956**	**503.515**	**357.701**	**3.304**	**29.594**	**319.876**	**1.399**	**12.528**	**135.414**	**97.313**	**48998.366**
279.5	**4257.836**	**-9.164**	**3.756**	**2128.908**	**9.164**	**6.397**	**202.763**	**110.506**		**7432.179**	**-1290.821**		**0.821**	**0.852**	**5.808**	**-209.043**	**1085.634**	**838.087**	**2747.934**	**27.216**	**24.957**	**501.703**	**357.690**	**3.304**	**29.647**	**320.972**	**1.399**	**12.551**	**135.878**	**97.661**	**48996.553**
279.0	**4257.869**	**-9.131**	**3.749**	**2128.925**	**9.131**	**6.397**	**202.041**	**110.309**		**7432.181**	**-1290.819**		**0.819**	**0.850**	**5.797**	**-209.006**	**1085.653**	**838.106**	**2747.977**	**27.217**	**24.957**	**499.894**	**357.679**	**3.303**	**29.700**	**322.075**	**1.398**	**12.573**	**136.345**	**98.010**	**48994.744**
278.5	**4257.902**	**-9.098**	**3.742**	**2128.941**	**9.098**	**6.397**	**201.320**	**110.111**		**7432.184**	**-1290.816**		**0.816**	**0.849**	**5.787**	**-208.970**	**1085.673**	**838.125**	**2748.020**	**27.217**	**24.958**	**498.088**	**357.668**	**3.302**	**29.753**	**323.184**	**1.398**	**12.596**	**136.814**	**98.362**	**48992.939**
278.0	**4257.934**	**-9.066**	**3.736**	**2128.958**	**9.066**	**6.397**	**200.601**	**109.913**		**7432.187**	**-1290.813**		**0.813**	**0.847**	**5.777**	**-208.934**	**1085.693**	**838.145**	**2748.062**	**27.218**	**24.958**	**496.286**	**357.657**	**3.302**	**29.807**	**324.298**	**1.398**	**12.618**	**137.286**	**98.716**	**48991.137**
277.5	**4257.967**	**-9.033**	**3.729**	**2128.974**	**9.033**	**6.397**	**199.883**	**109.716**	**109.716**	**7432.190**	**-1290.810**	**-1290.810**	**0.810**	**0.846**	**5.766**	**-208.897**	**1085.713**	**838.164**	**2748.105**	**27.218**	**24.958**	**494.487**	**357.646**	**3.301**	**29.860**	**325.418**	**1.398**	**12.641**	**137.760**	**99.071**	**48989.338**
277.0	**4258.000**	**-9.000**	**3.722**	**2128.990**	**9.000**	**6.397**	**199.167**	**109.518**		**7432.193**	**-1290.807**		**0.807**	**0.844**	**5.756**	**-208.861**	**1085.732**	**838.183**	**2748.148**	**27.219**	**24.959**	**492.691**	**357.635**	**3.301**	**29.914**	**326.545**	**1.397**	**12.664**	**138.237**	**99.428**	**48987.542**
276.5	**4258.032**	**-8.968**	**3.715**	**2129.007**	**8.968**	**6.397**	**198.451**	**109.320**		**7432.196**	**-1290.804**		**0.804**	**0.843**	**5.745**	**-208.825**	**1085.752**	**838.203**	**2748.190**	**27.219**	**24.959**	**490.899**	**357.624**	**3.300**	**29.968**	**327.677**	**1.397**	**12.687**	**138.717**	**99.788**	**48985.750**
276.0	**4258.064**	**-8.936**	**3.709**	**2129.023**	**8.936**	**6.397**	**197.737**	**109.122**		**7432.199**	**-1290.801**		**0.801**	**0.841**	**5.735**	**-208.789**	**1085.771**	**838.222**	**2748.232**	**27.219**	**24.959**	**489.110**	**357.613**	**3.300**	**30.022**	**328.816**	**1.397**	**12.709**	**139.199**	**100.149**	**48983.961**
275.5	**4258.097**	**-8.903**	**3.702**	**2129.039**	**8.903**	**6.397**	**197.025**	**108.925**		**7432.202**	**-1290.798**		**0.798**	**0.840**	**5.724**	**-208.753**	**1085.791**	**838.241**	**2748.275**	**27.220**	**24.960**	**487.325**	**357.602**	**3.299**	**30.077**	**329.960**	**1.397**	**12.732**	**139.683**	**100.512**	**48982.176**
275.0	**4258.129**	**-8.871**	**3.695**	**2129.055**	**8.871**	**6.397**	**196.313**	**108.727**		**7432.205**	**-1290.795**		**0.795**	**0.838**	**5.714**	**-208.717**	**1085.810**	**838.260**	**2748.317**	**27.220**	**24.960**	**485.543**	**357.591**	**3.299**	**30.131**	**331.111**	**1.396**	**12.756**	**140.170**	**100.878**	**48980.393**
274.5	**4258.161**	**-8.839**	**3.688**	**2129.072**	**8.839**	**6.397**	**195.603**	**108.529**		**7432.208**	**-1290.792**		**0.792**	**0.837**	**5.704**	**-208.681**	**1085.830**	**838.279**	**2748.359**	**27.221**	**24.961**	**483.764**	**357.580**	**3.298**	**30.186**	**332.268**	**1.396**	**12.779**	**140.660**	**101.245**	**48978.615**
274.0	**4258.194**	**-8.806**	**3.682**	**2129.088**	**8.806**	**6.397**	**194.894**	**108.332**		**7432.211**	**-1290.789**		**0.789**	**0.835**	**5.693**	**-208.645**	**1085.849**	**838.298**	**2748.401**	**27.221**	**24.961**	**481.988**	**357.569**	**3.298**	**30.241**	**333.431**	**1.396**	**12.802**	**141.152**	**101.614**	**48976.839**
273.5	**4258.226**	**-8.774**	**3.675**	**2129.104**	**8.774**	**6.397**	**194.186**	**108.134**		**7432.213**	**-1290.787**		**0.787**	**0.834**	**5.683**	**-208.610**	**1085.869**	**838.317**	**2748.443**	**27.221**	**24.961**	**480.216**	**357.558**	**3.297**	**30.296**	**334.600**	**1.396**	**12.825**	**141.647**	**101.985**	**48975.067**
273.0	**4258.258**	**-8.742**	**3.668**	**2129.120**	**8.742**	**6.397**	**193.480**	**107.936**		**7432.216**	**-1290.784**		**0.784**	**0.832**	**5.672**	**-208.574**	**1085.888**	**838.336**	**2748.485**	**27.222**	**24.962**	**478.447**	**357.547**	**3.297**	**30.352**	**335.776**	**1.396**	**12.849**	**142.145**	**102.359**	**48973.298**
272.5	**4258.290**	**-8.710**	**3.662**	**2129.136**	**8.710**	**6.397**	**192.775**	**107.739**		**7432.219**	**-1290.781**		**0.781**	**0.831**	**5.662**	**-208.538**	**1085.907**	**838.355**	**2748.527**	**27.222**	**24.962**	**476.682**	**357.536**	**3.296**	**30.407**	**336.958**	**1.395**	**12.872**	**142.645**	**102.734**	**48971.533**
272.0	**4258.322**	**-8.678**	**3.655**	**2129.152**	**8.678**	**6.397**	**192.071**	**107.541**		**7432.222**	**-1290.778**		**0.778**	**0.829**	**5.652**	**-208.503**	**1085.926**	**838.374**	**2748.568**	**27.223**	**24.963**	**474.920**	**357.525**	**3.295**	**30.463**	**338.146**	**1.395**	**12.896**	**143.149**	**103.112**	**48969.771**
271.5	**4258.354**	**-8.646**	**3.648**	**2129.168**	**8.646**	**6.397**	**191.368**	**107.343**		**7432.225**	**-1290.775**		**0.775**	**0.827**	**5.641**	**-208.467**	**1085.946**	**838.393**	**2748.610**	**27.223**	**24.963**	**473.161**	**357.514**	**3.295**	**30.519**	**339.341**	**1.395**	**12.920**	**143.654**	**103.491**	**48968.012**
271.0	**4258.386**	**-8.614**	**3.641**	**2129.184**	**8.614**	**6.397**	**190.667**	**107.146**		**7432.228**	**-1290.772**		**0.772**	**0.826**	**5.631**	**-208.432**	**1085.965**	**838.412**	**2748.651**	**27.224**	**24.963**	**471.406**	**357.503**	**3.294**	**30.575**	**340.543**	**1.395**	**12.944**	**144.163**	**103.873**	**48966.256**
270.5	**4258.417**	**-8.583**	**3.635**	**2129.200**	**8.583**	**6.397**	**189.967**	**106.948**		**7432.231**	**-1290.769**		**0.769**	**0.824**	**5.620**	**-208.397**	**1085.984**	**838.431**	**2748.693**	**27.224**	**24.964**	**469.654**	**357.493**	**3.294**	**30.632**	**341.751**	**1.394**	**12.967**	**144.675**	**104.257**	**48964.504**
270.0	**4258.449**	**-8.551**	**3.628**	**2129.216**	**8.551**	**6.397**	**189.268**	**106.750**		**7432.233**	**-1290.767**		**0.767**	**0.823**	**5.610**	**-208.361**	**1086.003**	**838.449**	**2748.734**	**27.224**	**24.964**	**467.905**	**357.482**	**3.293**	**30.688**	**342.965**	**1.394**	**12.991**	**145.189**	**104.643**	**48962.756**
269.5	**4258.481**	**-8.519**	**3.621**	**2129.232**	**8.519**	**6.397**	**188.570**	**106.552**		**7432.236**	**-1290.764**		**0.764**	**0.821**	**5.600**	**-208.326**	**1086.022**	**838.468**	**2748.776**	**27.225**	**24.964**	**466.160**	**357.471**	**3.293**	**30.745**	**344.187**	**1.394**	**13.016**	**145.706**	**105.031**	**48961.010**
269.0	**4258.512**	**-8.488**	**3.614**	**2129.248**	**8.488**	**6.397**	**187.874**	**106.355**		**7432.239**	**-1290.761**		**0.761**	**0.820**	**5.589**	**-208.291**	**1086.041**	**838.487**	**2748.817**	**27.225**	**24.965**	**464.417**	**357.460**	**3.292**	**30.802**	**345.415**	**1.394**	**13.040**	**146.226**	**105.421**	**48959.268**
268.5	**4258.544**	**-8.456**	**3.608**	**2129.264**	**8.456**	**6.397**	**187.179**	**106.157**		**7432.242**	**-1290.758**		**0.758**	**0.818**	**5.579**	**-208.256**	**1086.060**	**838.505**	**2748.858**	**27.226**	**24.965**	**462.679**	**357.450**	**3.292**	**30.860**	**346.650**	**1.393**	**13.064**	**146.748**	**105.813**	**48957.529**
268.0	**4258.575**	**-8.425**	**3.601**	**2129.279**	**8.425**	**6.397**	**186.485**	**105.959**		**7432.245**	**-1290.755**		**0.755**	**0.817**	**5.568**	**-208.221**	**1086.079**	**838.524**	**2748.899**	**27.226**	**24.966**	**460.943**	**357.439**	**3.291**	**30.917**	**347.891**	**1.393**	**13.088**	**147.274**	**106.208**	**48955.794**
267.5	**4258.607**	**-8.393**	**3.594**	**2129.295**	**8.393**	**6.397**	**185.793**	**105.762**		**7432.248**	**-1290.752**		**0.752**	**0.815**	**5.558**	**-208.186**	**1086.098**	**838.543**	**2748.940**	**27.226**	**24.966**	**459.211**	**357.428**	**3.291**	**30.975**	**349.140**	**1.393**	**13.113**	**147.802**	**106.605**	**48954.062**
267.0	**4258.638**	**-8.362**	**3.588**	**2129.311**	**8.362**	**6.397**	**185.102**	**105.564**		**7432.250**	**-1290.750**		**0.750**	**0.814**	**5.548**	**-208.151**	**1086.117**	**838.561**	**2748.981**	**27.227**	**24.966**	**457.483**	**357.418**	**3.290**	**31.033**	**350.395**	**1.393**	**13.137**	**148.334**	**107.004**	**48952.333**
266.5	**4258.670**	**-8.330**	**3.581**	**2129.327**	**8.330**	**6.397**	**184.412**	**105.366**		**7432.253**	**-1290.747**		**0.747**	**0.812**	**5.537**	**-208.116**	**1086.136**	**838.580**	**2749.022**	**27.227**	**24.967**	**455.757**	**357.407**	**3.289**	**31.091**	**351.657**	**1.393**	**13.162**	**148.868**	**107.405**	**48950.608**
266.0	**4258.701**	**-8.299**	**3.574**	**2129.342**	**8.299**	**6.397**	**183.723**	**105.169**		**7432.256**	**-1290.744**		**0.744**	**0.811**	**5.527**	**-208.081**	**1086.155**	**838.598**	**2749.063**	**27.228**	**24.967**	**454.035**	**357.396**	**3.289**	**31.149**	**352.927**	**1.392**	**13.187**	**149.406**	**107.809**	**48948.886**
265.5	**4258.732**	**-8.268**	**3.567**	**2129.358**	**8.268**	**6.277**	**183.036**	**105.971**		**7432.245**	**-1290.755**		**0.755**	**0.817**	**5.501**	**-205.026**	**1099.608**	**838.603**	**2756.857**	**27.305**	**25.038**	**449.776**	**355.379**	**3.288**	**31.295**	**356.107**	**1.392**	**13.248**	**150.752**	**108.820**	**48944.627**
265.0	**4258.763**	**-8.237**	**3.561**	**2129.374**	**8.237**	**6.397**	**182.350**	**104.773**		**7432.262**	**-1290.738**		**0.738**	**0.808**	**5.506**	**-208.012**	**1086.192**	**838.635**	**2749.144**	**27.228**	**24.968**	**450.601**	**357.375**	**3.288**	**31.267**	**355.487**	**1.392**	**13.236**	**150.489**	**108.623**	**48945.452**
264.5	**4258.794**	**-8.206**	**3.554**	**2129.389**	**8.206**	**6.397**	**181.665**	**104.576**		**7432.264**	**-1290.736**		**0.736**	**0.806**	**5.496**	**-207.977**	**1086.211**	**838.654**	**2749.185**	**27.229**	**24.968**	**448.889**	**357.365**	**3.287**	**31.326**	**356.777**	**1.392**	**13.261**	**151.036**	**109.033**	**48943.740**
264.0	**4258.825**	**-8.175**	**3.547**	**2129.405**	**8.175**	**6.397**	**180.981**	**104.378**		**7432.267**	**-1290.733**		**0.733**	**0.805**	**5.485**	**-207.943**	**1086.230**	**838.672**	**2749.225**	**27.229**	**24.969**	**447.180**	**357.354**	**3.287**	**31.385**	**358.075**	**1.391**	**13.286**	**151.585**	**109.446**	**48942.031**
263.5	**4258.856**	**-8.144**	**3.540**	**2129.420**	**8.144**	**6.397**	**180.299**	**104.180**		**7432.270**	**-1290.730**		**0.730**	**0.803**	**5.475**	**-207.909**	**1086.248**	**838.690**	**2749.266**	**27.230**	**24.969**	**445.475**	**357.344**	**3.286**	**31.444**	**359.380**	**1.391**	**13.311**	**152.138**	**109.861**	**48940.326**
263.0	**4258.887**	**-8.113**	**3.534**	**2129.436**	**8.113**	**6.397**	**179.618**	**103.982**		**7432.273**	**-1290.727**		**0.727**	**0.802**	**5.464**	**-207.874**	**1086.267**	**838.709**	**2749.306**	**27.230**	**24.969**	**443.773**	**357.333**	**3.286**	**31.504**	**360.693**	**1.391**	**13.337**	**152.693**	**110.278**	**48938.624**
262.5	**4258.918**	**-8.082**	**3.527**	**2129.451**	**8.082**	**6.397**	**178.938**	**103.785**		**7432.275**	**-1290.725**		**0.725**	**0.800**	**5.454**	**-207.840**	**1086.286**	**838.727**	**2749.346**	**27.230**	**24.970**	**442.074**	**357.323**	**3.285**	**31.564**	**362.013**	**1.391**	**13.362**	**153.252**	**110.698**	**48936.925**
262.0	**4258.949**	**-8.051**	**3.520**	**2129.467**	**8.051**	**6.397**	**178.260**	**103.587**		**7432.278**	**-1290.722**		**0.722**	**0.799**	**5.444**	**-207.806**	**1086.304**	**838.745**	**2749.387**	**27.231**	**24.970**	**440.379**	**357.312**	**3.285**	**31.624**	**363.340**	**1.390**	**13.388**	**153.814**	**111.121**	**48935.230**
261.5	**4258.980**	**-8.020**	**3.514**	**2129.482**	**8.020**	**6.397**	**177.583**	**103.389**		**7432.281**	**-1290.719**		**0.719**	**0.797**	**5.433**	**-207.771**	**1086.323**

256.5	4259.284	-7.716	3.446	2129.635	7.716	6.397	170.881	101.412		7432.308	-1290.692		0.692	0.782	5.329	-207.433	1086.506	838.943	2749.823	27.235	24.974	421.950	357.199	3.279	32.301	378.450	1.388	13.674	160.210	115.930	48916.800
256.0	4259.314	-7.686	3.440	2129.650	7.686	6.397	170.218	101.215		7432.311	-1290.689		0.689	0.780	5.319	-207.400	1086.524	838.961	2749.863	27.236	24.974	420.294	357.189	3.278	32.364	379.871	1.388	13.701	160.812	116.383	48915.145
255.5	4259.344	-7.656	3.433	2129.665	7.656	6.397	169.556	101.017		7432.314	-1290.686		0.686	0.779	5.308	-207.367	1086.542	838.979	2749.902	27.236	24.975	418.642	357.178	3.278	32.428	381.300	1.387	13.728	161.417	116.838	48913.493
255.0	4259.374	-7.626	3.426	2129.680	7.626	6.397	168.896	100.819		7432.316	-1290.684		0.684	0.777	5.298	-207.333	1086.560	838.996	2749.941	27.236	24.975	416.993	357.168	3.277	32.491	382.738	1.387	13.755	162.026	117.296	48911.844
254.5	4259.404	-7.596	3.419	2129.695	7.596	6.397	168.236	100.622		7432.319	-1290.681		0.681	0.776	5.287	-207.300	1086.578	839.014	2749.980	27.237	24.975	415.348	357.158	3.276	32.555	384.185	1.387	13.782	162.638	117.757	48910.199
254.0	4259.433	-7.567	3.413	2129.710	7.567	6.397	167.578	100.424		7432.322	-1290.678		0.678	0.774	5.277	-207.267	1086.596	839.032	2750.019	27.237	24.976	413.706	357.148	3.276	32.619	385.639	1.387	13.809	163.254	118.221	48908.557
253.5	4259.463	-7.537	3.406	2129.725	7.537	6.397	166.921	100.226		7432.324	-1290.676		0.676	0.773	5.267	-207.234	1086.614	839.049	2750.058	27.237	24.976	412.067	357.138	3.275	32.683	387.102	1.387	13.836	163.873	118.687	48906.918
253.0	4259.493	-7.507	3.399	2129.740	7.507	6.397	166.266	100.029		7432.327	-1290.673		0.673	0.771	5.256	-207.201	1086.632	839.067	2750.097	27.238	24.976	410.432	357.128	3.275	32.748	388.574	1.386	13.863	164.496	119.156	48905.282
252.5	4259.523	-7.477	3.392	2129.755	7.477	6.397	165.612	99.831		7432.330	-1290.670		0.670	0.770	5.246	-207.168	1086.650	839.084	2750.135	27.238	24.977	408.799	357.118	3.274	32.812	390.054	1.386	13.891	165.123	119.627	48903.650
252.0	4259.552	-7.448	3.386	2129.770	7.448	6.397	164.959	99.633		7432.332	-1290.668		0.668	0.768	5.235	-207.135	1086.668	839.102	2750.174	27.239	24.977	407.171	357.108	3.274	32.877	391.543	1.386	13.918	165.753	120.102	48902.021
251.5	4259.582	-7.418	3.379	2129.784	7.418	6.397	164.307	99.435		7432.335	-1290.665		0.665	0.767	5.225	-207.102	1086.686	839.119	2750.212	27.239	24.977	405.545	357.098	3.273	32.943	393.041	1.386	13.946	166.387	120.579	48900.396
251.0	4259.611	-7.389	3.372	2129.799	7.389	6.397	163.657	99.238		7432.338	-1290.662		0.662	0.765	5.215	-207.069	1086.703	839.137	2750.251	27.239	24.978	403.923	357.088	3.273	33.008	394.547	1.385	13.973	167.025	121.060	48898.773
250.5	4259.641	-7.359	3.366	2129.814	7.359	6.397	163.008	99.040		7432.340	-1290.660		0.660	0.763	5.204	-207.036	1086.721	839.154	2750.289	27.240	24.978	402.304	357.078	3.272	33.074	396.063	1.385	14.001	167.667	121.543	48897.155
250.0	4259.670	-7.330	3.359	2129.829	7.330	6.397	162.360	98.842		7432.343	-1290.657		0.657	0.762	5.194	-207.004	1086.739	839.172	2750.328	27.240	24.979	400.688	357.068	3.272	33.140	397.587	1.385	14.029	168.312	122.029	48895.539
249.5	4259.699	-7.301	3.352	2129.843	7.301	6.397	161.713	98.645		7432.345	-1290.655		0.655	0.760	5.183	-206.971	1086.756	839.189	2750.366	27.241	24.979	399.076	357.058	3.271	33.206	399.121	1.385	14.057	168.961	122.518	48893.927
249.0	4259.729	-7.271	3.345	2129.858	7.271	6.397	161.068	98.447		7432.348	-1290.652		0.652	0.759	5.173	-206.938	1086.774	839.206	2750.404	27.241	24.979	397.467	357.048	3.270	33.273	400.663	1.385	14.086	169.614	123.010	48892.318
248.5	4259.758	-7.242	3.339	2129.873	7.242	6.397	160.424	98.249		7432.351	-1290.649		0.649	0.757	5.163	-206.906	1086.792	839.223	2750.442	27.241	24.980	395.862	357.038	3.270	33.340	402.215	1.384	14.114	170.271	123.505	48890.712
248.0	4259.787	-7.213	3.332	2129.887	7.213	6.397	159.781	98.052		7432.353	-1290.647		0.647	0.756	5.152	-206.874	1086.809	839.241	2750.480	27.242	24.980	394.259	357.028	3.269	33.407	403.776	1.384	14.142	170.932	124.002	48889.110
247.5	4259.816	-7.184	3.325	2129.902	7.184	6.397	159.140	97.854		7432.356	-1290.644		0.644	0.754	5.142	-206.841	1086.827	839.258	2750.518	27.242	24.980	392.660	357.018	3.269	33.474	405.347	1.384	14.171	171.597	124.503	48887.511
247.0	4259.845	-7.155	3.318	2129.917	7.155	6.397	158.499	97.656		7432.358	-1290.642		0.642	0.753	5.131	-206.809	1086.844	839.275	2750.556	27.242	24.981	391.065	357.009	3.268	33.542	406.926	1.384	14.199	172.265	125.007	48885.915
246.5	4259.874	-7.126	3.312	2129.931	7.126	6.397	157.861	97.459		7432.361	-1290.639		0.639	0.751	5.121	-206.777	1086.862	839.292	2750.594	27.243	24.981	389.472	356.999	3.268	33.610	408.516	1.383	14.228	172.938	125.514	48884.323
246.0	4259.903	-7.097	3.305	2129.946	7.097	6.397	157.223	97.261		7432.364	-1290.636		0.636	0.750	5.111	-206.745	1086.879	839.309	2750.632	27.243	24.981	387.883	356.989	3.267	33.678	410.114	1.383	14.257	173.615	126.024	48882.734
245.5	4259.932	-7.068	3.298	2129.960	7.068	6.397	156.587	97.063		7432.366	-1290.634		0.634	0.748	5.100	-206.713	1086.896	839.326	2750.669	27.244	24.982	386.297	356.979	3.267	33.747	411.723	1.383	14.286	174.296	126.538	48881.148
245.0	4259.961	-7.039	3.292	2129.974	7.039	6.397	155.952	96.865		7432.369	-1290.631		0.631	0.747	5.090	-206.681	1086.914	839.343	2750.707	27.244	24.982	384.715	356.969	3.266	33.815	413.341	1.383	14.315	174.981	127.054	48879.566
244.5	4259.989	-7.011	3.285	2129.989	7.011	6.397	155.318	96.668		7432.371	-1290.629		0.629	0.745	5.079	-206.649	1086.931	839.360	2750.744	27.244	24.982	383.136	356.960	3.266	33.885	414.969	1.382	14.344	175.670	127.573	48877.987
244.0	4260.018	-6.982	3.278	2130.003	6.982	6.397	154.685	96.470		7432.374	-1290.626		0.626	0.744	5.069	-206.617	1086.948	839.377	2750.782	27.245	24.983	381.560	356.950	3.265	33.954	416.607	1.382	14.374	176.364	128.096	48876.411
243.5	4260.047	-6.953	3.271	2130.018	6.953	6.397	154.054	96.272		7432.377	-1290.623		0.623	0.742	5.059	-206.585	1086.966	839.394	2750.819	27.245	24.983	379.988	356.940	3.265	34.024	418.255	1.382	14.403	177.061	128.622	48874.838
243.0	4260.075	-6.925	3.265	2130.032	6.925	6.397	153.424	96.075		7432.379	-1290.621		0.621	0.741	5.048	-206.553	1086.983	839.411	2750.856	27.245	24.983	378.419	356.931	3.264	34.093	419.912	1.382	14.433	177.763	129.151	48873.269
242.5	4260.104	-6.896	3.258	2130.046	6.896	6.397	152.795	95.877	95.877	7432.382	-1290.618	-1290.618	0.618	0.739	5.038	-206.521	1087.000	839.428	2750.893	27.246	24.984	376.853	356.921	3.263	34.164	421.580	1.382	14.463	178.469	129.684	48871.703
242.0	4260.132	-6.868	3.251	2130.060	6.868	6.397	152.168	95.679		7432.384	-1290.616		0.616	0.738	5.027	-206.490	1087.017	839.445	2750.930	27.246	24.984	375.290	356.911	3.263	34.234	423.258	1.381	14.492	179.179	130.220	48870.141
241.5	4260.160	-6.840	3.245	2130.075	6.840	6.397	151.542	95.482		7432.387	-1290.613		0.613	0.736	5.017	-206.458	1087.034	839.461	2750.968	27.247	24.984	373.731	356.902	3.262	34.305	424.947	1.381	14.522	179.894	130.759	48868.581
241.0	4260.189	-6.811	3.238	2130.089	6.811	6.397	150.917	95.284		7432.389	-1290.611		0.611	0.734	5.007	-206.427	1087.051	839.478	2751.004	27.247	24.985	372.175	356.892	3.262	34.376	426.646	1.381	14.553	180.613	131.301	48867.026
240.5	4260.217	-6.783	3.231	2130.103	6.783	6.397	150.293	95.086		7432.392	-1290.608		0.608	0.733	4.996	-206.395	1087.068	839.495	2751.041	27.247	24.985	370.622	356.883	3.261	34.447	428.355	1.381	14.583	181.337	131.847	48865.473
240.0	4260.245	-6.755	3.224	2130.117	6.755	6.397	149.671	94.889		7432.394	-1290.606		0.606	0.731	4.986	-206.364	1087.085	839.512	2751.078	27.248	24.985	369.073	356.873	3.261	34.519	430.075	1.380	14.613	182.065	132.396	48863.924
239.5	4260.273	-6.727	3.218	2130.131	6.727	6.397	149.050	94.691		7432.397	-1290.603		0.603	0.730	4.975	-206.333	1087.102	839.528	2751.115	27.248	24.986	367.527	356.864	3.260	34.591	431.805	1.380	14.644	182.798	132.949	48862.378
239.0	4260.301	-6.699	3.211	2130.145	6.699	6.397	148.430	94.493		7432.399	-1290.601		0.601	0.728	4.965	-206.302	1087.119	839.545	2751.151	27.248	24.986	365.984	356.854	3.260	34.663	433.546	1.380	14.674	183.535	133.505	48860.835
238.5	4260.329	-6.671	3.204	2130.159	6.671	6.397	147.812	94.295		7432.402	-1290.598		0.598	0.727	4.955	-206.270	1087.136	839.561	2751.188	27.249	24.986	364.445	356.845	3.259	34.736	435.298	1.380	14.705	184.276	134.065	48859.295
238.0	4260.357	-6.643	3.197	2130.174	6.643	6.397	147.195	94.098		7432.404	-1290.596		0.596	0.725	4.944	-206.239	1087.153	839.578	2751.225	27.249	24.987	362.909	356.835	3.259	34.809	437.061	1.379	14.736	185.023	134.628	48857.759
237.5	4260.385	-6.615	3.191	2130.188	6.615	6.397	146.579	93.900		7432.407	-1290.593		0.593	0.724	4.934	-206.208	1087.170	839.594	2751.261	27.249	24.987	361.376	356.826	3.258	34.882	438.835	1.379	14.767	185.773	135.195	48856.227
237.0	4260.413	-6.587	3.184	2130.201	6.587	6.397	145.964	93.702		7432.409	-1290.591		0.591	0.722	4.923	-206.177	1087.186	839.611	2751.297	27.250	24.987	359.847	356.816	3.257	34.956	440.620	1.379	14.798	186.529	135.765	48854.697
236.5	4260.441	-6.559	3.177	2130.215	6.559	6.397	145.351	93.505		7432.412	-1290.588		0.588	0.721	4.913	-206.146	1087.203	839.627	2751.333	27.250	24.988	358.320	356.807	3.257	35.029	442.416	1.379	14.829	187.289	136.339	48853.171
236.0	4260.469	-6.531	3.171	2130.229	6.531	6.397	144.739	93.307		7432.414	-1290.586		0.586	0.719	4.903	-206.116	1087.220	839.644	2751.370	27.250	24.988	356.797	356.797	3.256	35.103	444.223	1.379	14.860	188.055	136.917	48851.648
235.5	4260.496	-6.504	3.164	2130.243	6.504	6.397	144.128	93.109		7432.417	-1290.583		0.583	0.718	4.892	-206.085	1087.236	839.660	2751.406	27.251	24.988	355.278	356.788	3.256	35.178	446.042	1.378	14.892	188.824	137.498	48850.129
235.0	4260.524	-6.476	3.157	2130.257	6.476	6.397	143.519	92.912		7432.419	-1290.581		0.581	0.716	4.882	-206.054	1087.253	839.676	2751.442	27.251	24.989	353.762	356.779	3.255	35.253	447.872	1.378	14.924	189.599	138.083	48848.612
234.5	4260.551	-6.449	3.150	2130.271	6.449	6.397	142.910	92.714		7432.422	-1290.578		0.578	0.715	4.871	-206.023	1087.270	839.693	2751.478	27.252	24.989	352.249	356.769	3.255	35.328	449.714	1.378	14.955	190.379	138.672	48847.099
234.0	4260.579	-6.421	3.144	2130.285	6.421	6.397	142.303	92.516		7432.424	-1290.576		0.576	0.713	4.861	-205.993	1087.286	839.709	2751.514	27.252	24.989	350.739	356.760	3.254	35.403	451.567	1.378	14.987	191.164	139.265	48845.590
233.5	4260.606	-6.394	3.137	2130.298	6.394	6.397	141.698	92.319		7432.427	-1290.573		0.573	0.712	4.851	-205.962	1087.303	839.725	2751.549	27.252	24.990	349.233	356.751	3.254	35.479	453.433	1.377	15.019	191.953	139.861	48844.083
233.0	4260.634	-6.366	3.130	2130.312	6.366	6.397	141.093	92.121		7432.429	-1290.571		0.571	0.710	4.840	-205.932	1087.319	839.741	2751.585	27.253	24.990	347.730	356.742	3.253	35.555	455.310	1.377	15.052	192.748	140.461	48842.580
232.5	4260.661	-6.339	3.123	2130.326	6.339	6.397	140.490	91.923		7432.432	-1290.568		0.568	0.709	4.830	-205.902	1087.336	839.757	2751.621	27.253	24.990	346.230	356.732	3.253	35.631	457.199	1.377	15.084	193.547	141.066	48841.080
232.0	4260.688	-6.312	3.117	2130.339	6.312	6.397	139.888	91.725		7432.434	-1290.566		0.566	0.707	4.819	-205.871	1087.352	839.774	2751.656	27.253	24.991	344.733	356.723	3.252	35.708	459.100	1.377	15.116	194.352	141.674	48839.584
231.5	4260.716	-6.284	3.110	2130.353	6.284	6.397	139.288	91.528		7432.436	-1290.564		0.564	0.706	4.809	-205.841	1087.368	839.790	2751.692	27.254	24.991	343.240	356.714	3.252	35.785	461.013	1.376	15.149	195.162	142.285	48838.091
231.0	4260.743	-6.257	3.103	2130.367	6.257	6.397	138.689	91.330		7432.439	-1290.561		0.561	0.704	4.799	-205.811	1087.385	839.806	2751.727	27.254	24.991	341.750	356.705	3.251	35.862	462.938	1.376	15.182	195.977	142.901	48836.601
230.5	4260.770	-6.230	3.097	2130.380	6.230	6.397	138.091	91.132		7432.441	-1290.559		0.559	0.702	4.788	-205.781	1087.401	839.822	2751.762	27.254	24.992	340.264	356.696	3.250	35.940	464.876	1.376	15.215	196.798	143.521	48835.114
230.0	4260.797	-6.203	3.090	2130.394	6.203	6.397	137.494	90.935		7432.444	-1290.556		0.556	0.701	4.778	-205.751	1087.417	839.838	2751.798	27.255	24.992	338.780	356.686	3.250	36.018	466.827	1.376	15.248	197.623	144.145	48833.631
229.5	4260.824	-6.176	3.083	2130.407	6.176	6.397	136.899	90.737		7432.446	-1290.554		0.554	0.699	4.767	-205.721	1087.434	839.854	2751.833	27.255	24.992	337.300	356.677	3.249	36.097	468.789	1.376	15.281	198.454	144.773	48832.151
229.0	4260.851	-6.149	3.076	2130.421	6.149	6.397	136.304	90.539		7432.449	-1290.551		0.551	0.698	4.757	-205.691	1087.450	839.869	2751.868	27.255	24.993	335.824	356.668	3.249	36.175	470.765	1.375	15.314	199.291	145.406	48830.674
228.5	4260.877	-6.123	3.070	2130.434	6.123	6.397	135.712	90.342		7432.451	-1290.549		0.549	0.696	4.747	-205.661	1087.466	839.885	2751.903	27.256	24.993	334.350	356.659	3.248	36.254	472.754	1.375	15.348	200.132	146.042	48829.201
228.0	4260.904	-6.096	3.063	2130.448	6.096	6.397	135.120	90.144		7432.453	-1290.547		0.547	0.695	4.736	-205.631	1087.482	839.901	2751.938	27.256	24.993	332.880	356.650	3.248	36.334	474.755	1.375	15.381	200.980	146.683	48827.731
227.5	4260.931	-6.069	3.056	2130.461	6.069	6.397	134.530	89.946		7432.456	-1290.544		0.544	0.693	4.726	-205.601	1087.498	839.917	2751.973	27.256	24.993	331.413	356.641	3.247	36.414	476.769	1.375	15.415	201.832	147.327	48826.264
227.0	4260.958	-6.042	3.050	2130.475	6.042	6.397	133.941	89.749		7432.458	-1290.542		0.542	0.692	4.715	-205.572	1087.514	839.933	2752.008	27.257	24.994	329.950	356.632	3.247	36.494	478.797	1.374	15.449	202.691	147.976	48824.801
226.5	4260.984	-6.016	3.043	2130.488	6.016	6.397	133.353	89.551		7432.461	-1290.539		0.539	0.690	4.705	-205.542	1087.530	839.948	2752.042	27.257	24.994	328.490	356.623	3.246	36.574	480.838	1.374	15.483	203.555	148.630	48823.340
226.0	4261.011	-5.989	3.036	2130.501	5.989	6.397	132.766	89.353		7432.463	-1290.537		0.537	0.689	4.695	-205.513	1087.546	839.964	2752.077	27.257	24.994	327.033	356.614	3.246	36.655	482.892	1.374	15.517	204.424	149.287	48821.883
225.5	4261.037	-5.963	3.029	2130.514	5.963	6.397	132.181	89.155		7432.465	-1290.535		0.535	0.687	4.684	-205.483	1087.562	839.980	2752.112	27.258	24.995	325.579	356.605	3.245	36.736	484.959	1.374	15.552	205.299	149.949	48820.430
225.0	4261.064	-5.936	3.023	2130.528	5.936	6.397	131.597	88.958	88.958	7432.468	-1290.532	-1290.532	0.532	0.686	4.674	-205.454	1087.578	839.995	2752.146	27.258	24.995	324.129	356.596	3.244	36.818	487.041	1.373	15.586	206.181	150.616	48818.979
224.5	4261.090	-5.910	3.016	2130.541	5.910	6.397	131.015	88.760		7432.470	-1290.530		0.530	0.684	4.663	-205.424	1087.594	840.011	2752.180	27.259	24.995	322.682	356.587	3.244	36.900	489.136	1.373	15.621	207.067	151.287	48817.532
224.0	4261.116	-5.884	3.009	2130.554	5.884	6.397	130.433	88.562		7432.472	-1290.528		0.528	0.683	4.653	-205.395	1087.610	840.027	2752.215	27.259	24.996	321.238	356.578	3.243	36.982	491.245	1.373	15.656	207.960	151.962	48816.089
223.5	4261.143	-5.857	3.002	2130.567	5.857	6.397	129.853	88.365		7432.475	-1290.525		0.525	0.681	4.643	-205.366	1087.626	840.042	2752.249	27.259	24.996	319.798	356.569	3.243	37.065	493.367	1.373	15.691	208.859	152.642	48814.648
223.0	4261.169	-5.831	2.996	2130.580	5.831	6.397	129.275	88.167		7432.477	-1290.523		0.523	0.680	4.632	-205.337	1087.641	840.058	2752.283	27.260	24.996	318.360	356.561	3.242	37.148	495.504	1.373	15.726	209.764	153.327	48813.211
222.5	4261.195	-5.805	2.989	2130.594	5.805	6.397	128.697	87.969		7432.479	-1290.521		0.521	0.678	4.622	-205.308	1087.657	840.073	2752.317	27.260	24.997	316.927	356.552	3.242	37.231	497.656	1.372	15.761	210.674	154.016	48811.777
222.0	4261.221	-5.779	2.982	2130.607	5.779	6.397	128.121	87.772		7432.482	-1290.518		0.518	0.677	4.611	-205.279	1087.673	840.088	2752.351	27.260	24.997	315.496	356.543	3.241	37.315	499.821	1.372	15.797	211.591	154.710	48810.347
221.5	4261.247	-5.753	2.976	2130.620	5.753	6.397	127.546	87.574		7432.484	-1290.516		0.516	0.675	4.601	-205.250	1087.688	840.104	2752.385	27.261	24.997	314.069	356.534	3.241	37.399	502.001	1.372	15.832	212.514	155.408	48808.919
221.0	4261.273	-5.727	2.969	2130.633	5.727	6.397	126.972	87.376		7432.486	-1290.514		0.514	0.674	4.591	-205.221	1087.704	840.119	2752.419	27.261	24.998	312.645	356.525	3.240	37.483	504.196	1.372	15.868	213.443	156.112	48807.495
220.5	4261.299	-5.701	2.962	2130.646	5.701	6.397	126.400	87.179		7432.489	-1290.511		0.511	0.672	4.580	-205.192	1087.720	840.134	2752.453	27.261	24.998	311.224	356.517	3.240	37.568	506.405	1.371	15.904	214.378	156.820	48806.075
220.0	4261.325	-5.675	2.955	2130.659	5.675	6.397	125.829	86.981		7432.491	-1290.509		0.509	0.670	4.570	-205.163	1087.735	840.150	2752.487	27.262	24.998	309.807	356.508	3.239	37.654	508.630	1.371	15.940	215.320	157.533	48804.657
219.5	4261.351	-5.649	2.949	2130.672	5.649	6.397	125.259	86.783		7432.493	-1290.507		0.507	0.669	4.559	-205.135	1087.751	840.165	2752.520	27.262	24.998	308.392	356.499	3.238	37.739	510.869	1.371	15.976	216.268	158.250	48803.243
219.0	4261.376	-5.624	2.942	2130.684	5.624	6.397	124.691	86.585		7432.496	-1290.504		0.504	0.667	4.549	-205.106	1087.766	840.180	2752.554	27.262	24.999	306.982	356.491	3.238	37.825	513.123	1.371	16.013	217.222	158.973	48801.832
218.5	4261.402	-5.598	2.935	2130.697	5.598	6.397	124.124	86.388		7432.498	-1290.502		0.502	0.666	4.539	-205.078	1087.782	840.195	2752.587	27.263	24.999	305.574	356.482	3.237	37.912	515.393	1.370	16.049	218.183	159.701	48800.425
218.0	4261.428	-5.572	2.929	2130.710	5.572	6.397	123.558	86.190		7432.500	-1290.500		0.500	0.664	4.528	-205.049	1087.797	840.210	2752.621	27.263	24.999	304.170	356.473	3.237	37.999	517.678	1.370	16.086	219.151	160.434	48799.020
217.5	4261.453	-5.547	2.922	2130.723	5.547	6.397	122.993	85.992		7432.503	-1290.497		0.497	0.663	4.518	-205.021	1087.812	840.226	2752.654	27.263	25.000	302.769	356.465	3.236	38.086	519.979	1.370	16.123	220.125	161.171	48797.619
217.0	4261.479	-5.521	2.915	2130.736	5.521	6.397	122.430	85.795		7432.505	-1290.495		0.495	0.661	4.507	-204.992	1087.828	840.241	2752.687	27.264	25.000	301.371	356.456	3.236	38.174	522.296	1.370	16.160	221.105	161.914	48796.222
216.5	4261.504	-5.496	2.908	2130.748	5.496	6.397	121.867	85.597		7432.507	-1290.493		0.493	0.660	4.497	-204.964	1087.843	840.256	2752.720	27.264	25.000	299.976	356.447	3.235	38.262	524.628	1.370	16.197	222.093	162.662	48794.827
216.0	4261.529	-5.471	2.902	2130.761	5.471	6.397	121.307	85.399		7432.509	-1290.491		0.491	0.658	4.487	-204.936	1087.858	840.271	2752.754	27.264	25.001	298.585	356.439	3.235	38.350	526.977	1.369	16.235	223.087	163.415	48793.436
215.5	4261.555	-5.445	2.895	2130.774	5.445	6.397	120.747	85.202		7432.512	-1290.488		0.488	0.657	4.476	-204.908	1087.874	840.286	2752.787	27.265	25.001	297.197	356.430	3.234	38.439	529.341	1.369	16.273	224.088	164.174	48792.048
215.0	4261.580	-5

210.5	4261.805	-5.195	2.828	2130.899	5.195	6.397	115.223	83.225		7432.534	-1290.466		0.466	0.642	4.372	-204.630	1088.024	840.433	2753.113	27.268	25.004	283.499	356.346	3.229	39.351	553.909	1.367	16.659	234.488	172.058	48778.350
210.0	4261.829	-5.171	2.821	2130.912	5.171	6.397	114.677	83.027		7432.536	-1290.464		0.464	0.640	4.362	-204.602	1088.039	840.448	2753.145	27.268	25.004	282.147	356.338	3.228	39.445	556.462	1.367	16.698	235.569	172.878	48776.998
209.5	4261.854	-5.146	2.814	2130.924	5.146	6.397	114.133	82.829		7432.538	-1290.462		0.462	0.638	4.351	-204.575	1088.054	840.462	2753.177	27.268	25.004	280.799	356.329	3.228	39.539	559.032	1.366	16.738	236.657	173.703	48775.650
209.0	4261.878	-5.122	2.808	2130.936	5.122	6.397	113.590	82.632		7432.541	-1290.459		0.459	0.637	4.341	-204.548	1088.068	840.477	2753.209	27.269	25.005	279.454	356.321	3.227	39.633	561.621	1.366	16.778	237.753	174.534	48774.304
208.5	4261.903	-5.097	2.801	2130.948	5.097	6.397	113.049	82.434		7432.543	-1290.457		0.457	0.635	4.331	-204.521	1088.083	840.491	2753.241	27.269	25.005	278.112	356.313	3.227	39.728	564.228	1.366	16.818	238.857	175.372	48772.962
208.0	4261.927	-5.073	2.794	2130.961	5.073	6.397	112.508	82.236		7432.545	-1290.455		0.455	0.634	4.320	-204.493	1088.098	840.506	2753.273	27.269	25.005	276.773	356.304	3.226	39.824	566.854	1.366	16.859	239.968	176.215	48771.624
207.5	4261.952	-5.048	2.787	2130.973	5.048	6.397	111.969	82.039	82.039	7432.547	-1290.453	-1290.453	0.453	0.632	4.310	-204.466	1088.113	840.520	2753.304	27.270	25.006	275.438	356.296	3.225	39.920	569.499	1.365	16.899	241.088	177.065	48770.288
207.0	4261.976	-5.024	2.781	2130.985	5.024	6.397	111.432	81.841		7432.549	-1290.451		0.451	0.631	4.299	-204.439	1088.127	840.535	2753.336	27.270	25.006	274.106	356.288	3.225	40.016	572.162	1.365	16.940	242.215	177.920	48768.956
206.5	4262.000	-5.000	2.774	2130.997	5.000	6.397	110.895	81.643		7432.552	-1290.448		0.448	0.629	4.289	-204.412	1088.142	840.549	2753.368	27.270	25.006	272.777	356.280	3.224	40.113	574.845	1.365	16.981	243.351	178.782	48767.627
206.0	4262.025	-4.975	2.767	2131.009	4.975	6.397	110.360	81.446		7432.554	-1290.446		0.446	0.628	4.279	-204.385	1088.156	840.563	2753.399	27.271	25.006	271.451	356.272	3.224	40.210	577.547	1.365	17.022	244.495	179.650	48766.302
205.5	4262.049	-4.951	2.760	2131.021	4.951	6.397	109.826	81.248		7432.556	-1290.444		0.444	0.626	4.268	-204.358	1088.171	840.577	2753.431	27.271	25.007	270.129	356.263	3.223	40.308	580.269	1.365	17.064	245.647	180.525	48764.979
205.0	4262.073	-4.927	2.754	2131.034	4.927	6.397	109.294	81.050		7432.558	-1290.442		0.442	0.625	4.258	-204.332	1088.185	840.592	2753.462	27.271	25.007	268.810	356.255	3.223	40.406	583.010	1.364	17.105	246.808	181.406	48763.660
204.5	4262.097	-4.903	2.747	2131.046	4.903	6.397	108.763	80.852		7432.560	-1290.440		0.440	0.623	4.248	-204.305	1088.200	840.606	2753.494	27.272	25.007	267.494	356.247	3.222	40.505	585.771	1.364	17.147	247.976	182.293	48762.345
204.0	4262.121	-4.879	2.740	2131.058	4.879	6.397	108.233	80.655		7432.562	-1290.438		0.438	0.622	4.237	-204.278	1088.214	840.620	2753.525	27.272	25.008	266.182	356.239	3.222	40.604	588.552	1.364	17.189	249.154	183.187	48761.032
203.5	4262.145	-4.855	2.734	2131.070	4.855	6.397	107.704	80.457		7432.565	-1290.435		0.435	0.620	4.227	-204.252	1088.229	840.634	2753.556	27.272	25.008	264.872	356.231	3.221	40.704	591.354	1.364	17.231	250.340	184.088	48759.723
203.0	4262.168	-4.832	2.727	2131.081	4.832	6.397	107.176	80.259		7432.567	-1290.433		0.433	0.619	4.216	-204.225	1088.243	840.648	2753.587	27.272	25.008	263.566	356.223	3.221	40.804	594.176	1.363	17.274	251.534	184.995	48758.417
202.5	4262.192	-4.808	2.720	2131.093	4.808	6.397	106.650	80.062		7432.569	-1290.431		0.431	0.617	4.206	-204.199	1088.257	840.662	2753.618	27.273	25.008	262.264	356.215	3.220	40.905	597.018	1.363	17.316	252.738	185.909	48757.114
202.0	4262.216	-4.784	2.713	2131.105	4.784	6.397	106.126	79.864		7432.571	-1290.429		0.429	0.616	4.196	-204.172	1088.272	840.676	2753.649	27.273	25.009	260.964	356.207	3.219	41.006	599.882	1.363	17.359	253.950	186.829	48755.815
201.5	4262.240	-4.760	2.707	2131.117	4.760	6.397	105.602	79.666		7432.573	-1290.427		0.427	0.614	4.185	-204.146	1088.286	840.690	2753.680	27.273	25.009	259.668	356.199	3.219	41.107	602.767	1.363	17.402	255.171	187.757	48754.519
201.0	4262.263	-4.737	2.700	2131.129	4.737	6.397	105.080	79.469		7432.575	-1290.425		0.425	0.613	4.175	-204.120	1088.300	840.704	2753.711	27.274	25.009	258.375	356.191	3.218	41.210	605.673	1.362	17.445	256.401	188.691	48753.226
200.5	4262.287	-4.713	2.693	2131.141	4.713	6.397	104.559	79.271		7432.577	-1290.423		0.423	0.611	4.164	-204.094	1088.314	840.718	2753.741	27.274	25.010	257.086	356.183	3.218	41.312	608.600	1.362	17.489	257.641	189.633	48751.936
200.0	4262.310	-4.690	2.687	2131.153	4.690	6.397	104.039	79.073		7432.579	-1290.421		0.421	0.610	4.154	-204.068	1088.328	840.732	2753.772	27.274	25.010	255.799	356.175	3.217	41.415	611.549	1.362	17.533	258.889	190.582	48750.650
199.5	4262.334	-4.666	2.680	2131.164	4.666	6.397	103.521	78.876		7432.581	-1290.419		0.419	0.608	4.144	-204.041	1088.342	840.746	2753.803	27.275	25.010	254.516	356.167	3.217	41.519	614.520	1.362	17.576	260.147	191.537	48749.367
199.0	4262.357	-4.643	2.673	2131.176	4.643	6.397	103.004	78.678		7432.584	-1290.416		0.416	0.606	4.133	-204.015	1088.356	840.760	2753.833	27.275	25.010	253.237	356.159	3.216	41.623	617.514	1.362	17.621	261.414	192.500	48748.087
198.5	4262.380	-4.620	2.666	2131.188	4.620	6.397	102.488	78.480		7432.586	-1290.414		0.414	0.605	4.123	-203.990	1088.371	840.773	2753.863	27.275	25.011	251.960	356.152	3.216	41.728	620.529	1.361	17.665	262.691	193.470	48746.811
198.0	4262.404	-4.596	2.660	2131.199	4.596	6.397	101.973	78.283		7432.588	-1290.412		0.412	0.603	4.112	-203.964	1088.385	840.787	2753.894	27.275	25.011	250.687	356.144	3.215	41.833	623.567	1.361	17.709	263.977	194.448	48745.538
197.5	4262.427	-4.573	2.653	2131.211	4.573	6.397	101.460	78.085		7432.590	-1290.410		0.410	0.602	4.102	-203.938	1088.398	840.801	2753.924	27.276	25.011	249.417	356.136	3.215	41.939	626.628	1.361	17.754	265.273	195.433	48744.268
197.0	4262.450	-4.550	2.646	2131.223	4.550	6.397	100.948	77.887		7432.592	-1290.408		0.408	0.600	4.092	-203.912	1088.412	840.814	2753.954	27.276	25.011	248.150	356.128	3.214	42.046	629.713	1.361	17.799	266.578	196.425	48743.001
196.5	4262.473	-4.527	2.639	2131.234	4.527	6.397	100.437	77.689		7432.594	-1290.406		0.406	0.599	4.081	-203.886	1088.426	840.828	2753.984	27.276	25.012	246.887	356.120	3.214	42.152	632.820	1.360	17.845	267.894	197.425	48741.737
196.0	4262.496	-4.504	2.633	2131.246	4.504	6.397	99.928	77.492		7432.596	-1290.404		0.404	0.597	4.071	-203.861	1088.440	840.842	2754.014	27.277	25.012	245.627	356.113	3.213	42.260	635.951	1.360	17.890	269.219	198.433	48740.477
195.5	4262.519	-4.481	2.626	2131.257	4.481	6.397	99.420	77.294		7432.598	-1290.402		0.402	0.596	4.060	-203.835	1088.454	840.855	2754.044	27.277	25.012	244.370	356.105	3.212	42.368	639.106	1.360	17.936	270.555	199.449	48739.220
195.0	4262.542	-4.458	2.619	2131.269	4.458	6.397	98.913	77.096		7432.600	-1290.400		0.400	0.594	4.050	-203.810	1088.468	840.869	2754.074	27.277	25.013	243.116	356.097	3.212	42.476	642.285	1.360	17.982	271.901	200.472	48737.967
194.5	4262.565	-4.435	2.613	2131.280	4.435	6.397	98.407	76.899		7432.602	-1290.398		0.398	0.593	4.040	-203.784	1088.481	840.882	2754.104	27.278	25.013	241.866	356.089	3.211	42.586	645.488	1.359	18.028	273.256	201.503	48736.716
194.0	4262.588	-4.412	2.606	2131.292	4.412	6.397	97.903	76.701		7432.604	-1290.396		0.396	0.591	4.029	-203.759	1088.495	840.896	2754.134	27.278	25.013	240.619	356.082	3.211	42.695	648.715	1.359	18.074	274.623	202.542	48735.469
193.5	4262.610	-4.390	2.599	2131.303	4.390	6.397	97.400	76.503		7432.606	-1290.394		0.394	0.590	4.019	-203.734	1088.509	840.909	2754.163	27.278	25.013	239.375	356.074	3.210	42.805	651.968	1.359	18.121	276.000	203.590	48734.225
193.0	4262.633	-4.367	2.592	2131.314	4.367	6.397	96.898	76.306		7432.608	-1290.392		0.392	0.588	4.008	-203.709	1088.522	840.923	2754.193	27.278	25.014	238.134	356.066	3.210	42.916	655.245	1.359	18.168	277.387	204.645	48732.985
192.5	4262.656	-4.344	2.586	2131.326	4.344	6.397	96.398	76.108		7432.610	-1290.390		0.390	0.587	3.998	-203.684	1088.536	840.936	2754.222	27.279	25.014	236.897	356.059	3.209	43.028	658.548	1.359	18.215	278.785	205.709	48731.747
192.0	4262.678	-4.322	2.579	2131.337	4.322	6.397	95.899	75.910		7432.612	-1290.388		0.388	0.585	3.988	-203.658	1088.550	840.949	2754.252	27.279	25.014	235.663	356.051	3.209	43.140	661.876	1.358	18.262	280.194	206.781	48730.513
191.5	4262.701	-4.299	2.572	2131.348	4.299	6.397	95.401	75.713		7432.614	-1290.386		0.386	0.584	3.977	-203.633	1088.563	840.963	2754.281	27.279	25.014	234.432	356.044	3.208	43.252	665.230	1.358	18.310	281.614	207.861	48729.282
191.0	4262.723	-4.277	2.566	2131.359	4.277	6.397	94.905	75.515		7432.616	-1290.384		0.384	0.582	3.967	-203.608	1088.577	840.976	2754.310	27.280	25.015	233.204	356.036	3.208	43.365	668.610	1.358	18.358	283.045	208.950	48728.055
190.5	4262.745	-4.255	2.559	2131.371	4.255	6.397	94.409	75.317		7432.618	-1290.382		0.382	0.581	3.956	-203.584	1088.590	840.989	2754.340	27.280	25.015	231.980	356.028	3.207	43.479	672.016	1.358	18.406	284.487	210.048	48726.831
190.0	4262.768	-4.232	2.552	2131.382	4.232	6.397	93.915	75.120	75.120	7432.620	-1290.380	-1290.380	0.380	0.579	3.946	-203.559	1088.604	841.002	2754.369	27.280	25.015	230.759	356.021	3.206	43.593	675.449	1.357	18.455	285.940	211.154	48725.610
189.5	4262.790	-4.210	2.545	2131.393	4.210	6.397	93.423	74.922		7432.622	-1290.378		0.378	0.578	3.936	-203.534	1088.617	841.015	2754.398	27.280	25.015	229.541	356.013	3.206	43.708	678.909	1.357	18.503	287.405	212.269	48724.392
189.0	4262.812	-4.188	2.539	2131.404	4.188	6.397	92.931	74.724		7432.624	-1290.376		0.376	0.576	3.925	-203.509	1088.630	841.028	2754.427	27.281	25.016	228.327	356.006	3.205	43.824	682.396	1.357	18.552	288.881	213.392	48723.177
188.5	4262.834	-4.166	2.532	2131.415	4.166	6.397	92.441	74.526		7432.626	-1290.374		0.374	0.574	3.915	-203.485	1088.644	841.042	2754.456	27.281	25.016	227.116	355.998	3.205	43.940	685.911	1.357	18.601	290.369	214.525	48721.966
188.0	4262.856	-4.144	2.525	2131.426	4.144	6.397	91.952	74.329		7432.628	-1290.372		0.372	0.573	3.905	-203.460	1088.657	841.055	2754.484	27.281	25.016	225.908	355.991	3.204	44.057	689.453	1.356	18.651	291.869	215.667	48720.758
187.5	4262.878	-4.122	2.518	2131.437	4.122	6.397	91.465	74.131		7432.630	-1290.370		0.370	0.571	3.894	-203.436	1088.670	841.068	2754.513	27.282	25.017	224.703	355.984	3.204	44.174	693.024	1.356	18.700	293.380	216.818	48719.553
187.0	4262.900	-4.100	2.512	2131.448	4.100	6.397	90.979	73.933		7432.632	-1290.368		0.368	0.570	3.884	-203.411	1088.683	841.081	2754.542	27.282	25.017	223.501	355.976	3.203	44.292	696.622	1.356	18.750	294.904	217.978	48718.352
186.5	4262.922	-4.078	2.505	2131.459	4.078	6.397	90.494	73.736		7432.634	-1290.366		0.366	0.568	3.873	-203.387	1088.697	841.093	2754.570	27.282	25.017	222.303	355.969	3.203	44.411	700.250	1.356	18.801	296.439	219.147	48717.154
186.0	4262.944	-4.056	2.498	2131.470	4.056	6.397	90.010	73.538		7432.636	-1290.364		0.364	0.567	3.863	-203.363	1088.710	841.106	2754.599	27.282	25.017	221.108	355.961	3.202	44.530	703.906	1.356	18.851	297.987	220.326	48715.959
185.5	4262.966	-4.034	2.492	2131.481	4.034	6.397	89.528	73.340		7432.638	-1290.362		0.362	0.565	3.853	-203.338	1088.723	841.119	2754.627	27.283	25.018	219.916	355.954	3.202	44.650	707.592	1.355	18.902	299.547	221.515	48714.767
185.0	4262.988	-4.012	2.485	2131.492	4.012	6.397	89.047	73.143		7432.640	-1290.360		0.360	0.564	3.842	-203.314	1088.736	841.132	2754.655	27.283	25.018	218.728	355.947	3.201	44.771	711.307	1.355	18.953	301.120	222.713	48713.579
184.5	4263.009	-3.991	2.478	2131.503	3.991	6.397	88.567	72.945		7432.642	-1290.358		0.358	0.562	3.832	-203.290	1088.749	841.145	2754.684	27.283	25.018	217.543	355.939	3.200	44.892	715.053	1.355	19.004	302.706	223.921	48712.394
184.0	4263.031	-3.969	2.471	2131.514	3.969	6.397	88.088	72.747		7432.644	-1290.356		0.356	0.561	3.821	-203.266	1088.762	841.158	2754.712	27.284	25.018	216.361	355.932	3.200	45.014	718.828	1.355	19.056	304.304	225.139	48711.212
183.5	4263.053	-3.947	2.465	2131.524	3.947	6.397	87.611	72.550		7432.646	-1290.354		0.354	0.559	3.811	-203.242	1088.775	841.170	2754.740	27.284	25.019	215.182	355.925	3.199	45.136	722.634	1.354	19.108	305.915	226.366	48710.033
183.0	4263.074	-3.926	2.458	2131.535	3.926	6.397	87.135	72.352		7432.648	-1290.352		0.352	0.558	3.801	-203.218	1088.788	841.183	2754.768	27.284	25.019	214.007	355.918	3.199	45.260	726.471	1.354	19.160	307.539	227.604	48708.858
182.5	4263.095	-3.905	2.451	2131.546	3.905	6.397	86.661	72.154		7432.650	-1290.350		0.350	0.556	3.790	-203.194	1088.801	841.196	2754.796	27.284	25.019	212.835	355.910	3.198	45.384	730.339	1.354	19.212	309.177	228.852	48707.685
182.0	4263.117	-3.883	2.445	2131.557	3.883	6.397	86.187	71.956		7432.652	-1290.348		0.348	0.555	3.780	-203.171	1088.814	841.208	2754.824	27.285	25.019	211.666	355.903	3.198	45.508	734.239	1.354	19.265	310.828	230.110	48706.516
181.5	4263.138	-3.862	2.438	2131.567	3.862	6.397	85.715	71.759		7432.654	-1290.346		0.346	0.553	3.769	-203.147	1088.826	841.221	2754.852	27.285	25.020	210.500	355.896	3.197	45.633	738.171	1.353	19.318	312.492	231.379	48705.351
181.0	4263.159	-3.841	2.431	2131.578	3.841	6.397	85.245	71.561		7432.656	-1290.344		0.344	0.552	3.759	-203.123	1088.839	841.233	2754.879	27.285	25.020	209.338	355.889	3.197	45.759	742.135	1.353	19.371	314.170	232.658	48704.188
180.5	4263.181	-3.819	2.424	2131.589	3.819	6.397	84.775	71.363		7432.657	-1290.343		0.343	0.550	3.749	-203.100	1088.852	841.246	2754.907	27.286	25.020	208.179	355.882	3.196	45.886	746.131	1.353	19.425	315.862	233.948	48703.029
180.0	4263.202	-3.798	2.418	2131.599	3.798	6.397	84.307	71.166		7432.659	-1290.341		0.341	0.549	3.738	-203.076	1088.865	841.258	2754.935	27.286	25.020	207.023	355.875	3.196	46.013	750.161	1.353	19.479	317.568	235.249	48701.873
179.5	4263.223	-3.777	2.411	2131.610	3.777	6.397	83.840	70.968		7432.661	-1290.339		0.339	0.547	3.728	-203.053	1088.877	841.271	2754.962	27.286	25.021	205.870	355.868	3.195	46.142	754.224	1.353	19.533	319.288	236.560	48700.721
179.0	4263.244	-3.756	2.404	2131.620	3.756	6.397	83.374	70.770		7432.663	-1290.337		0.337	0.546	3.717	-203.029	1088.890	841.283	2754.990	27.286	25.021	204.721	355.860	3.195	46.270	758.320	1.352	19.588	321.022	237.883	48699.571
178.5	4263.265	-3.735	2.398	2131.631	3.735	6.397	82.910	70.573		7432.665	-1290.335		0.335	0.544	3.707	-203.006	1088.903	841.296	2755.017	27.287	25.021	203.575	355.853	3.194	46.400	762.451	1.352	19.643	322.771	239.217	48698.425
178.0	4263.286	-3.714	2.391	2131.641	3.714	6.397	82.447	70.375		7432.667	-1290.333		0.333	0.542	3.697	-202.983	1088.915	841.308	2755.044	27.287	25.021	202.432	355.846	3.193	46.530	766.616	1.352	19.698	324.534	240.562	48697.282
177.5	4263.307	-3.693	2.384	2131.652	3.693	6.397	81.985	70.177		7432.669	-1290.331		0.331	0.541	3.686	-202.960	1088.928	841.320	2755.071	27.287	25.022	201.292	355.839	3.193	46.661	770.817	1.352	19.753	326.312	241.918	48696.143
177.0	4263.327	-3.673	2.377	2131.662	3.673	6.397	81.525	69.980		7432.671	-1290.329		0.329	0.539	3.676	-202.936	1088.940	841.333	2755.098	27.287	25.022	200.156	355.832	3.192	46.793	775.052	1.351	19.809	328.105	243.286	48695.006
176.5	4263.348	-3.652	2.371	2131.672	3.652	6.397	81.066	69.782		7432.672	-1290.328		0.328	0.538	3.665	-202.913	1088.953	841.345	2755.125	27.288	25.022	199.023	355.825	3.192	46.925	779.323	1.351	19.865	329.913	244.665	48693.873
176.0	4263.369	-3.631	2.364	2131.683	3.631	6.397	80.608	69.584		7432.674	-1290.326		0.326	0.536	3.655	-202.890	1088.965	841.357	2755.152	27.288	25.022	197.893	355.818	3.191	47.059	783.630	1.351	19.921	331.737	246.056	48692.743
175.5	4263.389	-3.611	2.357	2131.693	3.611	6.397	80.151	69.387		7432.676	-1290.324		0.324	0.535	3.645	-202.868	1088.978	841.369	2755.179	27.288	25.023	196.766	355.811	3.191	47.193	787.974	1.351	19.978	333.576	247.459	48691.617
175.0	4263.410	-3.590	2.350	2131.703	3.590	6.397	79.696	69.189		7432.678	-1290.322		0.322	0.533	3.634	-202.845	1088.990	841.381	2755.206	27.288	25.023	195.643	355.805	3.190	47.327	792.354	1.351	20.035	335.430	248.875	48690.493
174.5	4263.430	-3.570	2.344	2131.714	3.570	6.397	79.242	68.991		7432.680	-1290.320		0.320	0.532	3.624	-202.822	1089.002	841.394	2755.233	27.289	25.023	194.523	355.798	3.190	47.463	796.772	1.350	20.093	337.300	250.302	48689.373
174.0	4263.451	-3.549	2.337	2131.724	3.549	6.397	78.789	68.793		7432.682	-1290.318		0.318	0.530	3.614	-202.799	1089.014	841.406	2755.259	27.289	25.023	193.406	355.791	3.189	47.599	801.228	1.350	20.150	339.187	251.742	48688.256
173.5	4263.471	-3.529	2.330	2131.734	3.529	6.397	78.338	68.596		7432.683	-1290.317		0.317	0.529	3.603	-202.777	1089.027	841.418	2755.286	27.289	25.024	192.292	355.784	3.189	47.736	805.722	1.350	20.208	341.089	253.194	48687.143
173.0	4263.492	-3.508	2.324	2131.744	3.508	6.397	77.888	68.398		7432.685	-1290.315		0.315	0.527	3.593	-202.754	1089.039	841.430	2755.313	27.290	25.024	191.182	355.777	3.188	47.874	810.254	1.350	20.267	343.008	254.659	48686.032
172.5	4263.512	-3.488	2.317	2131.754	3.488	6.397	77.439	68.200	68.200	7432.687	-1290.313	-1290.313	0.313	0.526	3.582	-202.731	1089.051	841.442	2755.339	27.290	25.024	190.074	355.770	3.187	48.013	814.826	1.349	20.325	344.943	256.136	48684.925
172.0	4263.532	-3.468	2.310	2131.765	3.468	6.397	76.991	68.003		7432.689	-1290.311		0.311	0.524	3.572	-202.709	1089.063	841.454	2755.365	27.290	25.024	188.971	355.763	3.187	48.152	819.437	1.349	20.384	346.895	257.626	48683.821
171.5	4263.552	-3.448	2.303	2131.775	3.448	6.397	76.545	67.805		7432.691	-1290.309		0.309	0.523	3.562	-202.687	1089.075	841.465	2755.392	27.290	25.025	187.870	355.757	3.186	48.293	824.088	1.349	20.444	348.864	259.130	48682.721
171.0	4263.572	-3.428	2.297	2131.785	3.428	6.397	76.100	67.607		7432.693	-1290.307		0.307	0.521	3.551	-202.664	1089.088	841.477	2755.418	27.291	25.025	186.773	355.750	3.186	48.434	828.779	1.349	20.504	350.850	260.647	48681.623
170.5	4263.592	-3.408	2.290	2131.795	3.408	6.397	75.657	67.410		7432.694	-1290.306		0.306	0.520	3.541	-202.642	1089.100	841.489	2755.444	27.291	25.025	185.678	355.743	3.185	48.576	833.511	1.348	20.564	352.853	262.177	48680.529
170.0	4263.612	-3.388	2.283	2131.805	3.388	6.397	75.214	67.212		7432.696	-1290.304		0.304	0.518	3.530	-202.620	1089.112	841.501	2755.470	27.291	25.025	184.587	355.736	3.185	48.718	838.285	1.348	20.624	354.874	263.720	48679.438
169.5	4263.632	-3.368	2.277	2131.815	3.368	6.397	74.773	67.014		7432.698	-1290.302		0.302	0.517	3.520	-202.598	1089.124	841.513	2755.496	27.291	25.025	183.500	355.730	3.184	48.862	843.101	1.348	20.685	356.913	265.277	48678.350
169.0

164.5	4263.828	-3.172	2.209	2131.913	3.172	6.397	70.433	65.037		7432.715	-1290.285		0.285	0.501	3.416	-202.380	1089.241	841.628	2755.751	27.294	25.028	172.801	355.664	3.179	50.346	893.673	1.346	21.313	378.322	281.639	48667.652
164.0	4263.847	-3.153	2.203	2131.922	3.153	6.397	70.006	64.840		7432.717	-1290.283		0.283	0.500	3.406	-202.358	1089.253	841.640	2755.776	27.294	25.028	171.749	355.657	3.178	50.500	898.983	1.345	21.378	380.570	283.358	48666.600
163.5	4263.866	-3.134	2.196	2131.932	3.134	6.397	69.581	64.642		7432.719	-1290.281		0.281	0.498	3.395	-202.337	1089.264	841.651	2755.801	27.294	25.028	170.701	355.651	3.178	50.654	904.342	1.345	21.444	382.838	285.093	48665.551
163.0	4263.886	-3.114	2.189	2131.942	3.114	6.397	69.156	64.444		7432.721	-1290.279		0.279	0.497	3.385	-202.316	1089.276	841.662	2755.826	27.295	25.028	169.655	355.644	3.177	50.809	909.750	1.345	21.509	385.128	286.844	48664.506
162.5	4263.905	-3.095	2.183	2131.951	3.095	6.397	68.733	64.247		7432.722	-1290.278		0.278	0.495	3.375	-202.294	1089.287	841.674	2755.851	27.295	25.029	168.613	355.638	3.177	50.966	915.208	1.345	21.575	387.438	288.611	48663.464
162.0	4263.924	-3.076	2.176	2131.961	3.076	6.397	68.312	64.049		7432.724	-1290.276		0.276	0.494	3.364	-202.273	1089.299	841.685	2755.876	27.295	25.029	167.574	355.632	3.176	51.123	920.715	1.345	21.642	389.769	290.394	48662.424
161.5	4263.943	-3.057	2.169	2131.970	3.057	6.397	67.891	63.851		7432.726	-1290.274		0.274	0.492	3.354	-202.252	1089.310	841.696	2755.901	27.295	25.029	166.538	355.625	3.176	51.281	926.273	1.344	21.709	392.122	292.194	48661.389
161.0	4263.962	-3.038	2.162	2131.980	3.038	6.397	67.472	63.654		7432.727	-1290.273		0.273	0.491	3.343	-202.231	1089.322	841.707	2755.925	27.296	25.029	165.506	355.619	3.175	51.440	931.883	1.344	21.776	394.497	294.010	48660.356
160.5	4263.980	-3.020	2.156	2131.989	3.020	6.397	67.054	63.456		7432.729	-1290.271		0.271	0.489	3.333	-202.210	1089.333	841.718	2755.950	27.296	25.030	164.476	355.612	3.174	51.600	937.544	1.344	21.844	396.894	295.844	48659.327
160.0	4263.999	-3.001	2.149	2131.999	3.001	6.397	66.638	63.258		7432.731	-1290.269		0.269	0.488	3.323	-202.189	1089.344	841.729	2755.974	27.296	25.030	163.450	355.606	3.174	51.762	943.259	1.344	21.912	399.313	297.695	48658.301
159.5	4264.018	-2.982	2.142	2132.008	2.982	6.397	66.223	63.061		7432.732	-1290.268		0.268	0.486	3.312	-202.169	1089.356	841.740	2755.999	27.296	25.030	162.427	355.600	3.173	51.924	949.026	1.343	21.981	401.754	299.563	48657.278
159.0	4264.037	-2.963	2.135	2132.017	2.963	6.397	65.809	62.863		7432.734	-1290.266		0.266	0.485	3.302	-202.148	1089.367	841.751	2756.023	27.297	25.030	161.408	355.594	3.173	52.087	954.848	1.343	22.050	404.219	301.450	48656.258
158.5	4264.055	-2.945	2.129	2132.027	2.945	6.397	65.396	62.665		7432.736	-1290.264		0.264	0.483	3.291	-202.127	1089.378	841.762	2756.048	27.297	25.030	160.391	355.587	3.172	52.251	960.724	1.343	22.120	406.706	303.353	48655.242
158.0	4264.074	-2.926	2.122	2132.036	2.926	6.397	64.985	62.468		7432.738	-1290.262		0.262	0.482	3.281	-202.106	1089.389	841.773	2756.072	27.297	25.031	159.378	355.581	3.172	52.416	966.655	1.343	22.190	409.217	305.275	48654.229
157.5	4264.092	-2.908	2.115	2132.045	2.908	6.397	64.574	62.270		7432.739	-1290.261		0.261	0.480	3.271	-202.086	1089.400	841.784	2756.096	27.297	25.031	158.368	355.575	3.171	52.583	972.643	1.342	22.260	411.752	307.216	48653.219
157.0	4264.111	-2.889	2.109	2132.054	2.889	6.397	64.166	62.072		7432.741	-1290.259		0.259	0.478	3.260	-202.065	1089.411	841.795	2756.120	27.298	25.031	157.362	355.569	3.171	52.750	978.687	1.342	22.331	414.311	309.175	48652.212
156.5	4264.129	-2.871	2.102	2132.064	2.871	6.397	63.758	61.874		7432.742	-1290.258		0.258	0.477	3.250	-202.045	1089.422	841.806	2756.144	27.298	25.031	156.358	355.562	3.170	52.919	984.789	1.342	22.402	416.894	311.152	48651.209
156.0	4264.147	-2.853	2.095	2132.073	2.853	6.397	63.352	61.677		7432.744	-1290.256		0.256	0.475	3.240	-202.025	1089.433	841.817	2756.168	27.298	25.032	155.358	355.556	3.170	53.088	990.949	1.342	22.474	419.502	313.149	48650.209
155.5	4264.166	-2.834	2.088	2132.082	2.834	6.397	62.947	61.479		7432.746	-1290.254		0.254	0.474	3.229	-202.004	1089.444	841.828	2756.192	27.298	25.032	154.361	355.550	3.169	53.259	997.168	1.342	22.546	422.135	315.165	48649.212
155.0	4264.184	-2.816	2.082	2132.091	2.816	6.397	62.543	61.281	61.281	7432.747	-1290.253	-1290.253	0.253	0.472	3.219	-201.984	1089.455	841.838	2756.215	27.298	25.032	153.367	355.544	3.168	53.430	1003.447	1.341	22.619	424.793	317.201	48648.218
154.5	4264.202	-2.798	2.075	2132.100	2.798	6.397	62.141	61.084		7432.749	-1290.251		0.251	0.471	3.208	-201.964	1089.466	841.849	2756.239	27.299	25.032	152.377	355.538	3.168	53.603	1009.786	1.341	22.692	427.476	319.256	48647.227
154.0	4264.220	-2.780	2.068	2132.109	2.780	6.397	61.740	60.886		7432.751	-1290.249		0.249	0.469	3.198	-201.944	1089.477	841.860	2756.262	27.299	25.032	151.390	355.532	3.167	53.777	1016.187	1.341	22.766	430.186	321.332	48646.240
153.5	4264.238	-2.762	2.062	2132.118	2.762	6.397	61.340	60.688		7432.752	-1290.248		0.248	0.468	3.188	-201.924	1089.488	841.870	2756.286	27.299	25.033	150.406	355.526	3.167	53.952	1022.650	1.341	22.840	432.922	323.427	48645.256
153.0	4264.256	-2.744	2.055	2132.127	2.744	6.397	60.942	60.491		7432.754	-1290.246		0.246	0.466	3.177	-201.904	1089.499	841.881	2756.309	27.299	25.033	149.425	355.520	3.166	54.128	1029.175	1.340	22.914	435.684	325.544	48644.275
152.5	4264.274	-2.726	2.048	2132.136	2.726	6.397	60.545	60.293		7432.755	-1290.245		0.245	0.465	3.167	-201.884	1089.510	841.892	2756.333	27.300	25.033	148.447	355.514	3.166	54.306	1035.764	1.340	22.989	438.474	327.681	48643.298
152.0	4264.292	-2.708	2.041	2132.145	2.708	6.397	60.149	60.095		7432.757	-1290.243		0.243	0.463	3.156	-201.864	1089.520	841.902	2756.356	27.300	25.033	147.473	355.508	3.165	54.484	1042.418	1.340	23.065	441.290	329.839	48642.324
151.5	4264.310	-2.690	2.035	2132.154	2.690	6.397	59.754	59.898		7432.759	-1290.241		0.241	0.462	3.146	-201.844	1089.531	841.913	2756.379	27.300	25.033	146.502	355.502	3.165	54.664	1049.137	1.340	23.141	444.135	332.019	48641.352
151.0	4264.327	-2.673	2.028	2132.163	2.673	6.397	59.361	59.700		7432.760	-1290.240		0.240	0.460	3.136	-201.824	1089.542	841.923	2756.402	27.300	25.034	145.534	355.496	3.164	54.845	1055.922	1.339	23.218	447.007	334.220	48640.385
150.5	4264.345	-2.655	2.021	2132.172	2.655	6.397	58.969	59.502		7432.762	-1290.238		0.238	0.459	3.125	-201.805	1089.552	841.934	2756.425	27.301	25.034	144.569	355.490	3.164	55.027	1062.775	1.339	23.295	449.908	336.444	48639.420
150.0	4264.363	-2.637	2.015	2132.181	2.637	6.397	58.578	59.305		7432.763	-1290.237		0.237	0.457	3.115	-201.785	1089.563	841.944	2756.448	27.301	25.034	143.608	355.484	3.163	55.211	1069.696	1.339	23.372	452.838	338.689	48638.459
149.5	4264.380	-2.620	2.008	2132.189	2.620	6.397	58.189	59.107		7432.765	-1290.235		0.235	0.456	3.104	-201.766	1089.573	841.954	2756.471	27.301	25.034	142.650	355.478	3.162	55.395	1076.685	1.339	23.451	455.797	340.957	48637.500
149.0	4264.398	-2.602	2.001	2132.198	2.602	6.397	57.801	58.909		7432.767	-1290.233		0.233	0.454	3.094	-201.746	1089.584	841.965	2756.494	27.301	25.035	141.695	355.472	3.162	55.581	1083.744	1.339	23.529	458.785	343.249	48636.545
148.5	4264.415	-2.585	1.994	2132.207	2.585	6.397	57.414	58.711		7432.768	-1290.232		0.232	0.453	3.084	-201.727	1089.594	841.975	2756.517	27.301	25.035	140.743	355.466	3.161	55.768	1090.875	1.338	23.608	461.804	345.563	48635.594
148.0	4264.433	-2.567	1.988	2132.216	2.567	6.397	57.029	58.514		7432.770	-1290.230		0.230	0.451	3.073	-201.707	1089.605	841.985	2756.539	27.302	25.035	139.795	355.460	3.161	55.956	1098.076	1.338	23.688	464.852	347.901	48634.645
147.5	4264.450	-2.550	1.981	2132.224	2.550	6.397	56.644	58.316		7432.771	-1290.229		0.229	0.450	3.063	-201.688	1089.615	841.995	2756.562	27.302	25.035	138.849	355.455	3.160	56.146	1105.351	1.338	23.768	467.932	350.262	48633.700
147.0	4264.467	-2.533	1.974	2132.233	2.533	6.397	56.261	58.118		7432.773	-1290.227		0.227	0.448	3.053	-201.669	1089.626	842.006	2756.585	27.302	25.035	137.907	355.449	3.160	56.337	1112.699	1.338	23.849	471.043	352.648	48632.758
146.5	4264.484	-2.516	1.968	2132.241	2.516	6.397	55.880	57.921		7432.774	-1290.226		0.226	0.446	3.042	-201.650	1089.636	842.016	2756.607	27.302	25.036	136.969	355.443	3.159	56.529	1120.122	1.337	23.931	474.185	355.058	48631.819
146.0	4264.501	-2.499	1.961	2132.250	2.499	6.397	55.499	57.723		7432.776	-1290.224		0.224	0.445	3.032	-201.631	1089.646	842.026	2756.629	27.303	25.036	136.033	355.437	3.159	56.722	1127.621	1.337	24.013	477.360	357.493	48630.884
145.5	4264.519	-2.481	1.954	2132.259	2.481	6.397	55.120	57.525		7432.777	-1290.223		0.223	0.443	3.021	-201.612	1089.657	842.036	2756.652	27.303	25.036	135.101	355.431	3.158	56.917	1135.197	1.337	24.095	480.567	359.953	48629.951
145.0	4264.536	-2.464	1.947	2132.267	2.464	6.397	54.743	57.328		7432.779	-1290.221		0.221	0.442	3.011	-201.593	1089.667	842.046	2756.674	27.303	25.036	134.172	355.426	3.158	57.113	1142.850	1.337	24.178	483.806	362.439	48629.022
144.5	4264.553	-2.447	1.941	2132.276	2.447	6.397	54.366	57.130		7432.780	-1290.220		0.220	0.440	3.001	-201.574	1089.677	842.056	2756.696	27.303	25.036	133.246	355.420	3.157	57.311	1150.582	1.336	24.262	487.080	364.950	48628.096
144.0	4264.569	-2.431	1.934	2132.284	2.431	6.397	53.991	56.932		7432.782	-1290.218		0.218	0.439	2.990	-201.555	1089.687	842.066	2756.718	27.303	25.037	132.323	355.414	3.156	57.510	1158.394	1.336	24.346	490.387	367.488	48627.174
143.5	4264.586	-2.414	1.927	2132.292	2.414	6.397	53.617	56.735		7432.783	-1290.217		0.217	0.437	2.980	-201.536	1089.697	842.076	2756.740	27.304	25.037	131.404	355.409	3.156	57.710	1166.288	1.336	24.431	493.729	370.052	48626.254
143.0	4264.603	-2.397	1.921	2132.301	2.397	6.397	53.245	56.537		7432.785	-1290.215		0.215	0.436	2.969	-201.518	1089.707	842.086	2756.762	27.304	25.037	130.488	355.403	3.155	57.912	1174.263	1.336	24.516	497.105	372.643	48625.338
142.5	4264.620	-2.380	1.914	2132.309	2.380	6.397	52.873	56.339		7432.786	-1290.214		0.214	0.434	2.959	-201.499	1089.718	842.096	2756.784	27.304	25.037	129.575	355.397	3.155	58.115	1182.322	1.336	24.602	500.516	375.262	48624.425
142.0	4264.637	-2.363	1.907	2132.318	2.363	6.397	52.503	56.142		7432.788	-1290.212		0.212	0.433	2.949	-201.481	1089.728	842.106	2756.805	27.304	25.037	128.665	355.392	3.154	58.320	1190.466	1.335	24.689	503.964	377.908	48623.516
141.5	4264.653	-2.347	1.900	2132.326	2.347	6.397	52.135	55.944		7432.789	-1290.211		0.211	0.431	2.938	-201.462	1089.738	842.115	2756.827	27.305	25.038	127.758	355.386	3.154	58.526	1198.695	1.335	24.776	507.448	380.583	48622.609
141.0	4264.670	-2.330	1.894	2132.334	2.330	6.397	51.767	55.746		7432.791	-1290.209		0.209	0.430	2.928	-201.444	1089.747	842.125	2756.849	27.305	25.038	126.855	355.381	3.153	58.733	1207.011	1.335	24.864	510.968	383.285	48621.706
140.5	4264.686	-2.314	1.887	2132.342	2.314	6.397	51.401	55.549		7432.792	-1290.208		0.208	0.428	2.917	-201.425	1089.757	842.135	2756.870	27.305	25.038	125.955	355.375	3.153	58.942	1215.416	1.335	24.952	514.526	386.017	48620.806
140.0	4264.703	-2.297	1.880	2132.351	2.297	6.397	51.036	55.351		7432.794	-1290.206		0.206	0.427	2.907	-201.407	1089.767	842.145	2756.892	27.305	25.038	125.058	355.370	3.152	59.152	1223.910	1.334	25.041	518.122	388.778	48619.909
139.5	4264.719	-2.281	1.873	2132.359	2.281	6.397	50.673	55.153		7432.795	-1290.205		0.205	0.425	2.897	-201.389	1089.777	842.154	2756.913	27.305	25.038	124.165	355.364	3.152	59.364	1232.494	1.334	25.131	521.756	391.569	48619.015
139.0	4264.735	-2.265	1.867	2132.367	2.265	6.397	50.311	54.955		7432.797	-1290.203		0.203	0.424	2.886	-201.371	1089.787	842.164	2756.934	27.306	25.039	123.274	355.359	3.151	59.578	1241.171	1.334	25.221	525.429	394.390	48618.125
138.5	4264.752	-2.248	1.860	2132.375	2.248	6.397	49.950	54.758		7432.798	-1290.202		0.202	0.422	2.876	-201.353	1089.797	842.174	2756.956	27.306	25.039	122.387	355.353	3.151	59.793	1249.941	1.334	25.312	529.142	397.242	48617.238
138.0	4264.768	-2.232	1.853	2132.383	2.232	6.397	49.590	54.560		7432.800	-1290.200		0.200	0.421	2.866	-201.335	1089.806	842.183	2756.977	27.306	25.039	121.503	355.348	3.150	60.009	1258.806	1.333	25.404	532.894	400.124	48616.354
137.5	4264.784	-2.216	1.847	2132.391	2.216	6.397	49.232	54.362	54.362	7432.801	-1290.199	-1290.253	0.199	0.419	2.855	-201.317	1089.816	842.193	2756.998	27.306	25.039	120.622	355.342	3.149	60.227	1267.767	1.333	25.496	536.688	403.038	48615.473
137.0	4264.800	-2.200	1.840	2132.399	2.200	6.397	48.875	54.165		7432.803	-1290.197		0.197	0.418	2.845	-201.299	1089.826	842.202	2757.019	27.306	25.039	119.745	355.337	3.149	60.447	1276.825	1.333	25.589	540.523	405.984	48614.596
136.5	4264.816	-2.184	1.833	2132.408	2.184	6.397	48.519	53.967		7432.804	-1290.196		0.196	0.416	2.834	-201.281	1089.836	842.212	2757.040	27.307	25.039	118.871	355.331	3.148	60.668	1285.982	1.333	25.683	544.399	408.963	48613.721
136.0	4264.832	-2.168	1.826	2132.416	2.168	6.397	48.165	53.769		7432.806	-1290.194		0.194	0.414	2.824	-201.263	1089.845	842.221	2757.060	27.307	25.040	118.000	355.326	3.148	60.891	1295.240	1.333	25.777	548.318	411.974	48612.850
135.5	4264.848	-2.152	1.820	2132.423	2.152	6.397	47.811	53.572		7432.807	-1290.193		0.193	0.413	2.814	-201.245	1089.855	842.230	2757.081	27.307	25.040	117.132	355.321	3.147	61.116	1304.599	1.332	25.872	552.280	415.019	48611.983
135.0	4264.864	-2.136	1.813	2132.431	2.136	6.397	47.460	53.374		7432.808	-1290.192		0.192	0.411	2.803	-201.228	1089.864	842.240	2757.102	27.307	25.040	116.267	355.315	3.147	61.342	1314.062	1.332	25.968	556.286	418.098	48611.118
134.5	4264.880	-2.120	1.806	2132.439	2.120	6.397	47.109	53.176		7432.810	-1290.190		0.190	0.410	2.793	-201.210	1089.874	842.249	2757.122	27.307	25.040	115.406	355.310	3.146	61.570	1323.630	1.332	26.065	560.337	421.211	48610.257
134.0	4264.895	-2.105	1.800	2132.447	2.105	6.397	46.760	52.979		7432.811	-1290.189		0.189	0.408	2.782	-201.193	1089.883	842.258	2757.143	27.308	25.040	114.548	355.305	3.146	61.800	1333.304	1.332	26.162	564.432	424.359	48609.398
133.5	4264.911	-2.089	1.793	2132.455	2.089	6.397	46.412	52.781		7432.813	-1290.187		0.187	0.407	2.772	-201.175	1089.893	842.268	2757.163	27.308	25.041	113.693	355.300	3.145	62.031	1343.086	1.331	26.260	568.573	427.543	48608.543
133.0	4264.927	-2.073	1.786	2132.463	2.073	6.397	46.065	52.583		7432.814	-1290.186		0.186	0.405	2.762	-201.158	1089.902	842.277	2757.184	27.308	25.041	112.841	355.294	3.145	62.264	1352.978	1.331	26.359	572.761	430.762	48607.692
132.5	4264.942	-2.058	1.779	2132.471	2.058	6.397	45.720	52.386		7432.815	-1290.185		0.185	0.404	2.751	-201.141	1089.911	842.286	2757.204	27.308	25.041	111.993	355.289	3.144	62.499	1362.981	1.331	26.458	576.995	434.018	48606.843
132.0	4264.958	-2.042	1.773	2132.478	2.042	6.397	45.376	52.188		7432.817	-1290.183		0.183	0.402	2.741	-201.123	1089.921	842.295	2757.224	27.308	25.041	111.147	355.284	3.143	62.736	1373.097	1.331	26.558	581.278	437.311	48605.998
131.5	4264.973	-2.027	1.766	2132.486	2.027	6.397	45.033	51.990		7432.818	-1290.182		0.182	0.401	2.731	-201.106	1089.930	842.304	2757.244	27.309	25.041	110.305	355.279	3.143	62.974	1383.328	1.331	26.659	585.609	440.642	48605.156
131.0	4264.989	-2.011	1.759	2132.494	2.011	6.397	44.691	51.793		7432.820	-1290.180		0.180	0.399	2.720	-201.089	1089.939	842.313	2757.264	27.309	25.042	109.467	355.273	3.142	63.215	1393.675	1.330	26.761	589.989	444.011	48604.317
130.5	4265.004	-1.996	1.753	2132.502	1.996	6.397	44.351	51.595		7432.821	-1290.179		0.179	0.398	2.710	-201.072	1089.948	842.322	2757.284	27.309	25.042	108.631	355.268	3.142	63.457	1404.140	1.330	26.863	594.419	447.418	48603.482
130.0	4265.019	-1.981	1.746	2132.509	1.981	6.397	44.012	51.397		7432.822	-1290.178		0.178	0.396	2.699	-201.055	1089.958	842.331	2757.304	27.309	25.042	107.799	355.263	3.141	63.701	1414.726	1.330	26.967	598.901	450.866	48602.649
129.5	4265.034	-1.966	1.739	2132.517	1.966	6.397	43.675	51.199		7432.824	-1290.176		0.176	0.395	2.689	-201.038	1089.967	842.340	2757.324	27.309	25.042	106.969	355.258	3.141	63.947	1425.433	1.330	27.071	603.433	454.353	48601.820
129.0	4265.050	-1.950	1.732	2132.524	1.950	6.397	43.338	51.002		7432.825	-1290.175		0.175	0.393	2.679	-201.021	1089.976	842.349	2757.344	27.310	25.042	106.143	355.253	3.140	64.194	1436.264	1.329	27.176	608.019	457.880	48600.994
128.5	4265.065	-1.935	1.726	2132.532	1.935	6.397	43.003	50.804		7432.826	-1290.174		0.174	0.392	2.668	-201.004	1089.985	842.358	2757.364	27.310	25.042	105.321	355.248	3.140	64.444	1447.221	1.329	27.281	612.657	461.449	48600.171
128.0	4265.080	-1.920	1.719	2132.539	1.920	6.397	42.670	50.606		7432.828	-1290.172		0.172	0.390	2.658	-200.988	1089.994	842.367	2757.383	27.310	25.043	104.501	355.243	3.139	64.696	1458.306	1.329	27.388	617.350	465.060	48599.352
127.5	4265.095	-1.905	1.712	2132.547	1.905	6.397	42.337	50.409		7432.829	-1290.171		0.171	0.389	2.647	-200.971	1090.003	842.376	2757.403	27.310	25.043	103.685	355.238	3.139	64.949	1469.520	1.329	27.495	622.097	468.714	48598.536
127.0	4265.110	-1.890	1.706	2132.554	1.890	6.397	42.006	50.211		7432.830	-1290.170		0.170	0.387	2.637	-200.954	1090.012	842.385	2757.422	27.310	25.043	102.872	355.233	3.138	65.205	1480.866	1.328	27.603	626.900	472.410	48597.722
126.5	4265.124	-1.876	1.699	2132.562	1.876	6.397	41.676	50.013		7432.832	-1290.168		0.168	0.386	2.627	-200.938	1090.021	842.394	2757.442	27.311	25.043	102.062	355.228	3.137	65.463	1492.346	1.328	27.713	631.760	476.151	48596.913
126.0	4265.139	-1.861	1.692	2132.569	1.861	6.397	41.348	49.816		7432.833	-1290.167		0.167	0.384	2.616	-200.921	1090.030	842.402	2757.461	27.311	25.043	101.255	355.223	3.137	65.722	1503.961	1.328	27.822	636.677	479.936	48596.106
125.5	4265.154	-1.846	1.685	2132.577	1.846	6.397	41.021	49.618		7432.834	-1290.166		0.166	0.382	2.606	-200.905	1090.039	842.411	2757.480	27.311	25.043	100.452	355.218	3.136	65.984	1515.715	1.328	27.933	641.653	483.767	48595.303
125.0	4265.169	-1.831	1.679	2132.584	1.831	6.397	40.695	49.420		7432.836	-1290.164		0.164	0.381	2.595	-200.889	1090.047	842.420	2757.499	27.311	25.044	99.652	355.213	3.136	66.248	1527.609	1.328	28.045	646.688	487.643	48594.502
124.5	4265.183	-1.817	1.672	2132.591	1.817	6.397	40.370	49.223		7432.837	-1290.163		0.163	0.379	2.585	-200.872	1090.056	842.428	2757.518	27.311	25.044	98.855	355.208	3.135	66.514	1539.646	1.327	28.158	651.783	491.567	48593.705
124.0	4265.198	-1.802	1.665	2132.599	1.802	6.397	40.047	49.025		7432.838	-1290.162		0.162	0.378	2.575	-200.856	1090.065	842.437	2757.537	27.312	25.044	98.061	355.203	3.135	66.782	1551.827	1.327	28.271	656.940	495.538	48592.912
123.5	4265.212	-1.788	1.659	2132.606	1.788	6.397	39.725	48.827		7432.840	-1290.160		0.160	0.376	2.564	-200.840	1090.074	842.445	2757.556	27.312	25.044	97.270	355.198	3.

APPENDIX 5B.
UV MEASUREMENT RESULTS

Table 5B.1: Typical diurnal total beam and UV intensity of solar radiation on a clear day

Time	CH 1 [W/m^2]	IL1400 [W/m^2]	UV [%]	Time	CH 1 [W/m^2]	IL1400 [W/m^2]	UV [%]	Time	CH 1 [W/m^2]	IL1400 [W/m^2]	UV [%]
10:00	940	48.0	5.11	12:09	953	55.5	5.82	14:18	894	44.1	4.93
10:03	940	48.1	5.12	12:12	955	55.6	5.82	14:21	891	42.5	4.77
10:06	941	48.2	5.12	12:15	955	55.6	5.82	14:24	893	42.1	4.71
10:09	942	48.3	5.13	12:18	955	55.5	5.81	14:27	887	41.1	4.63
10:12	943	48.4	5.13	12:21	954	55.5	5.81	14:30	883	40.6	4.60
10:15	943	48.5	5.14	12:24	953	55.3	5.80	14:33	880	39.9	4.53
10:18	944	48.6	5.15	12:27	953	55.0	5.77	14:36	875	39.1	4.47
10:21	945	48.7	5.15	12:30	951	55.1	5.79	14:39	873	38.6	4.42
10:24	946	48.8	5.16	12:33	952	54.9	5.77	14:42	871	38.2	4.39
10:27	947	48.9	5.16	12:36	951	54.7	5.75	14:45	864	37.0	4.28
10:30	948	49.0	5.17	12:39	949	54.6	5.75	14:48	860	36.5	4.24
10:33	948	49.1	5.18	12:42	948	54.3	5.73	14:51	858	35.9	4.18
10:36	949	49.2	5.18	12:45	946	54.2	5.73	14:54	853	35.0	4.10
10:39	949	49.3	5.19	12:48	945	54.0	5.71	14:57	850	34.2	4.02
10:42	950	49.4	5.20	12:51	944	54.0	5.72	15:00	845	33.6	3.98
10:45	950	49.5	5.21	12:54	944	53.8	5.70	15:03	838	32.6	3.89
10:48	950	49.6	5.22	12:57	940	53.5	5.69	15:06	832	31.5	3.79
10:51	951	49.7	5.23	13:00	939	53.1	5.65	15:09	829	30.6	3.69
10:54	951	49.8	5.24	13:03	940	53.0	5.64	15:12	827	30.2	3.65
10:57	951	49.9	5.25	13:06	937	52.7	5.62	15:15	819	29.2	3.57
11:00	951	50.0	5.26	13:09	934	52.4	5.61	15:18	816	28.4	3.48
11:03	952	50.1	5.26	13:12	933	52.0	5.57	15:21	807	27.3	3.38
11:06	952	50.2	5.27	13:15	936	52.1	5.57	15:24	801	26.4	3.30
11:09	952	52.0	5.46	13:18	934	51.8	5.55	15:27	793	25.4	3.20
11:12	952	55.1	5.79	13:21	933	51.6	5.53	15:30	783	24.4	3.12
11:15	952	55.2	5.80	13:24	931	51.4	5.52	15:35	771	24.0	3.11
11:18	953	55.3	5.80	13:27	932	51.1	5.48			**Ave**	**5.15**
11:21	953	55.4	5.81	13:30	928	50.6	5.45				
11:24	953	55.5	5.82	13:33	925	50.1	5.42				
11:27	954	55.5	5.82	13:36	926	49.8	5.38				
11:30	954	55.6	5.83	13:39	925	49.6	5.36				
11:33	954	55.4	5.81	13:42	923	49.0	5.31				
11:36	954	55.5	5.82	13:45	920	48.5	5.27				
11:39	953	55.4	5.81	13:48	918	48.1	5.24				
11:42	953	55.5	5.82	13:51	916	47.6	5.20				
11:45	954	55.6	5.83	13:54	914	47.1	5.15				
11:48	955	55.7	5.83	13:57	910	46.7	5.13				
11:51	955	55.7	5.83	14:00	907	46.2	5.09				
11:54	956	55.8	5.84	14:03	905	45.8	5.06				
11:57	955	55.7	5.83	14:06	904	45.3	5.01				
12:00	955	55.6	5.82	14:09	901	44.7	4.96				
12:03	955	55.6	5.82	14:12	900	44.3	4.92				
12:06	954	55.5	5.82	14:15	896	43.6	4.87				

Table 5B.2: UVA and UVR comparison

Time	UVR	UVA	Time	UVR	UVA
12:04	55.4	51	13:54	45.2	42
12:07	54.8	50	13:57	44.2	43
12:10	55.5	51	14:00	43.9	41
12:12	55.1	51	14:03	43.4	40
12:15	55.2	51	14:06	42.9	39
12:17	55.2	51	14:09	42.2	39
12:18	55.2	52	14:12	41.6	39
12:19	55.1	52	14:15	41.0	38
12:22	54.9	52	14:18	40.3	37
12:24	54.3	50	14:21	39.8	37
12:25	54.1	50	14:24	39.4	36
12:27	54.0	50	14:27	38.9	36
12:30	54.2	50	14:30	38.4	35
12:33	54.2	50	14:33	38.1	35
12:34	54.1	50	14:36	37.1	34
12:36	53.9	50	14:39	36.6	33
12:37	54.0	50	14:42	35.7	33
12:38	53.9	50	14:45	35.1	33
12:40	53.7	50	14:48	34.3	31
12:43	53.4	49	14:51	33.5	30
12:47	52.9	49	14:54	32.4	29
12:49	52.6	48	14:57	31.8	29
12:51	52.5	48	15:00	31.1	28
12:53	52.4	49	15:03	30.3	28
12:57	52.4	48	15:06	29.5	27
13:00	52.1	48	15:09	28.8	26
13:03	51.8	47	15:12	28.0	25
13:06	51.7	47	15:15	27.1	24
13:09	51.3	47	15:18	26.3	23
13:12	51.2	47	15:21	25.1	22
13:15	50.5	46	15:24	24.5	22
13:18	50.3	47	15:27	23.4	21
13:21	49.9	46	15:30	22.9	21
13:24	49.4	45	15:33	22.0	20
13:27	49.3	45	15:36	20.7	19
13:30	48.7	45	15:39	20.3	18
13:33	48.5	45	15:42	19.2	17
13:36	48.1	45	15:45	18.2	16
13:39	47.7	44	15:48	17.2	15
13:42	47.1	44	15:51	16.3	13
13:45	46.8	43	15:54	15.7	12
13:48	46.2	42	15:57	14.5	12
13:51	45.8	41	16:00	13.5	11

APPENDIX 5C.
OTHER SPECTRAL MEASUREMENT RESULTS

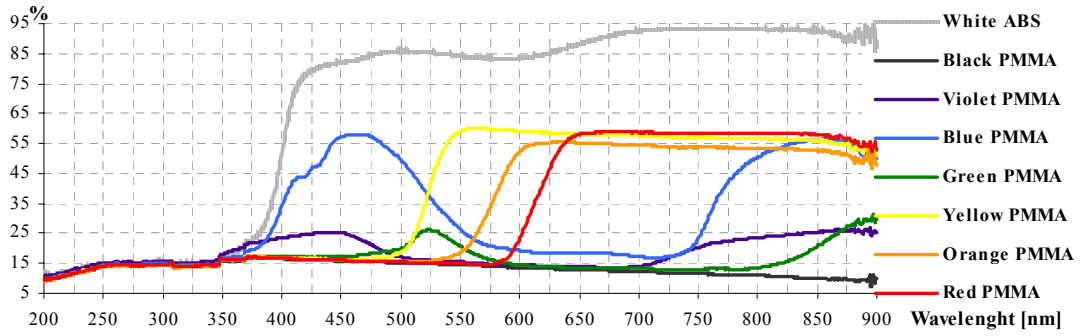

Figure 5C.1: Angular-hemispherical reflectance spectra of all samples

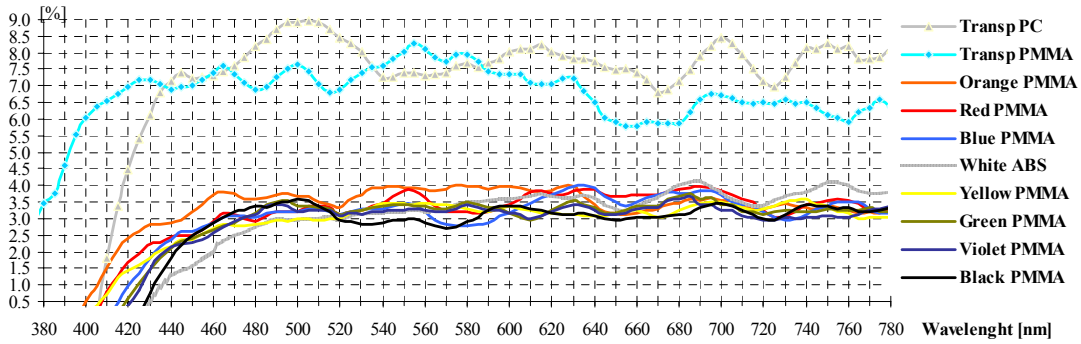

Figure 5C.2: Visible specular reflectances of all samples

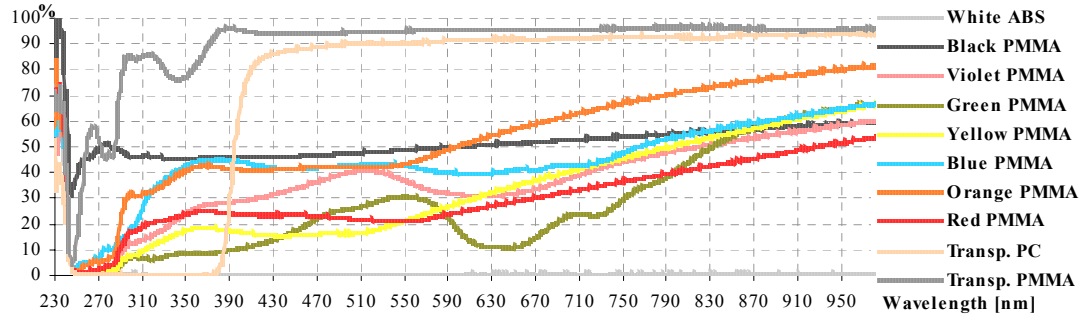

Figure 5C.3: Transmittance through chloroform solutions of all samples

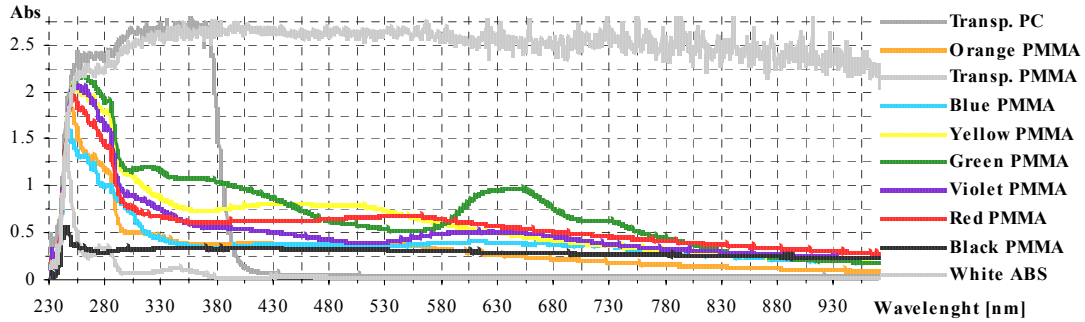

Figure 5C.4: Absorbance spectra of solutions of all samples in chloroform

Note: The chloroform spectral distribution is subtracted from the combined spectra. Furthermore, the chloroform absorption bands are typically above 3300 nm.

APPENDIX 5D.
CALCULATION OF AVERAGE UTILIZED SOLAR ABSORPTANCE

Computed average solar absorptance of green PMMA in 400-900 nm
(only the first 2 pages of the spreadsheet are shown)

Material	Green PMMA R is for 3 mm	T is for 0.17 mm	Ts is for chloroform	**Average R**	**Average T**	**Average Ts**	**Interval** lambda	
							<353.17	
Absorptance % (calculated) if Transmittance % (assumed)	**94.24459614** 0			3.794534493	1.946803067	8.916401227	lambda >353.17	lambda <395.53
SOLAR	**5.755403857**	**3.615148667**	**17.68919175**	3.985042563	2.414210662	11.05341094	lambda >395.53	lambda <418.91
lambda	**R**	**T**	**Ts**	4.0988528	2.809103465	13.51063833	lambda >418.91	lambda <438.99
900	14.34354782	12.4181118	60.45249557					
899	11.4432354	12.28888321	60.35460281					
898	19.35638046	12.21772957	60.161026	4.338808132	3.270632071	16.59440596	lambda	lambda
897	12.06323719	12.25546265	60.10693359				>438.99	<455.21
896	12.54622364	12.17399597	60.08181					
895	11.57035065	12.19877625	59.97473145	4.868145479	3.746140242	20.07019656	lambda	lambda
894	14.92672729	12.10253143	59.77703476				>455.21	<469.78
893	10.39248848	12.09557915	59.72220993					
892	13.08417511	12.04418278	59.53014374	5.620151473	4.2347735	23.08980601	lambda	lambda
891	12.02186966	12.00052261	59.37483215				>469.78	<483.82
890	10.04772472	12.03882122	59.4268074					
889	12.07865334	11.96458721	59.11688232	6.42012313	4.633978707	24.99695383	lambda	lambda
888	12.969841	11.89077377	59.03264236				>483.82	<497.93
887	12.98494148	11.91338921	59.33636856					
886	12.18891335	11.8025322	59.03728485	8.47571016	4.904571343	26.16672249	lambda	lambda
885	12.30598354	11.78687477	58.93277359				>497.93	<512.02
884	11.59261894	11.78112888	58.9068222					
883	12.027668	11.71079254	58.68418121	12.72215788	5.177890131	27.8294987	lambda	lambda
882	11.6172123	11.6959877	58.68243408				>512.02	<526.31
881	12.40348721	11.59329033	58.35528564					
880	12.40572071	11.6182518	58.29644012	12.30170028	5.429002353	29.56231199	lambda	lambda
879	11.60474396	11.58208275	58.10522461				>526.31	<540.49
878	12.11157322	11.52709579	58.13912201					
877	12.34271336	11.4543829	58.03178406	9.039484122	5.586505032	30.46399676	lambda	lambda
876	11.97230339	11.42958832	57.51593018				>540.49	<555.04
875	12.70128441	11.42742634	57.62178802					
874	12.35292149	11.37951279	57.70542145	6.459839774	5.558537313	29.88471413	lambda	lambda
873	12.75989437	11.32430267	57.33987045				>555.04	<569.73
872	12.38471413	11.30676556	57.32831192					
871	12.47867107	11.25691795	56.97838211	4.966789069	5.250349331	27.22052676	lambda	lambda
870	12.38602257	11.21774864	56.79036331				>569.73	<584.16
869	12.27625275	11.18247128	56.66334152					
868	12.49754143	11.15738106	56.77612305	4.098379339	4.606014967	21.45533603	lambda	lambda
867	12.16383839	11.12403584	56.56455231				>584.16	<598.47
866	12.34394455	11.09830284	56.45178986					
865	12.25503922	11.08186722	56.10691452	3.680460768	3.815558688	14.718901	lambda	lambda
864	12.10584927	11.02325439	55.95509338				>598.47	<613.01
863	12.3561821	11.01342201	55.75344467					
862	12.14342976	10.98610783	55.62101746	3.53034018	3.482084172	11.61874117	lambda	lambda
861	12.24983215	10.9382534	55.78516769				>613.01	<627.59
860	12.42358685	10.93151665	55.36595535					
859	12.37565613	10.88767815	55.38459015	3.488319067	3.430936066	10.97825762	lambda	lambda
858	12.33597946	10.84739685	55.00057983				>627.59	<642.22
857	12.26371574	10.82811546	55.01002502					
856	12.2452879	10.80925083	54.94547653	3.476690429	3.42664017	10.85874108	lambda	lambda
855	12.25781727	10.76761246	54.57037735				>642.22	<656.89
854	12.3459177	10.75369263	54.45085907					
853	12.3234129	10.71809864	54.21492004	3.523268319	3.677199507	12.91297499	lambda	lambda
852	12.23300362	10.68061256	53.7515564				>656.89	<671.65
851	12.32223701	10.67018986	53.83959579					
850	12.21418476	10.6357193	53.82881927	3.627161261	4.308577569	17.21970641	lambda	lambda
849	12.30654907	10.60231495	53.55804443				>671.65	<686.53
848	12.2225008	10.55888271	53.69953918					
847	12.31816196	10.54602337	53.16959	3.715719297	4.968161202	21.47962074	lambda	lambda
846	12.23036671	10.49284649	52.98977661				>686.53	<701.78
845	12.15075874	10.46451759	52.62843323					

844	12.11734962	10.42645741	52.30696869	3.693017362	5.475195199	23.65117848	lambda	lambda
843	12.23225498	10.37911892	52.39551544				>701.78	<717.44
842	12.21167183	10.32603455	52.23815918					
841	12.18000984	10.32032108	51.98293304	3.618570739	5.553392887	23.51509126	lambda	lambda
840	12.17783833	10.27858162	51.78111649				>717.44	<735.14
839	12.17705917	10.23298168	51.45669556					
838	12.20207024	10.1791954	51.4513092	3.79448703	6.020850241	26.96374226	lambda	lambda
837	12.12633228	10.14687538	51.20849609				>735.14	<751.42
836	12.1565485	10.0959177	50.84850311					
835	12.20557404	10.0538559	50.82933426	4.045220775	6.963161718	32.66897946	lambda	lambda
834	12.18198586	10.01856136	50.4172554				>751.42	<772.12
833	12.11438942	9.97901535	50.25826263					
832	12.12590408	9.925537109	50.02038956	4.068767352	7.586915942	36.23895107	lambda	lambda
831	12.13786697	9.887254715	49.52241898				>772.12	<789.10
830	12.12282562	9.846226692	49.34777451					
829	12.14321899	9.786601067	49.21731949	4.36157208	8.219999706	40.20101525	lambda	lambda
828	12.09632015	9.742137909	48.95442581				>789.10	<806.76
827	12.12402248	9.695624352	48.57083511					
826	12.09743881	9.671710014	48.34263992	5.442764737	9.184681034	45.76433449	lambda	lambda
825	12.07189083	9.614900589	48.12189102				>806.76	<826.89
824	12.07597733	9.570260048	47.95101166					
823	12.08877087	9.514468193	47.78992081	7.827239505	10.11388311	50.92129612	lambda	lambda
822	12.04371548	9.467391968	47.47906876				>826.89	<846.79
821	12.03365898	9.41037941	47.01849365					
820	12.03788853	9.359670639	46.88088989	11.83404197	10.81891561	54.8231678	lambda	lambda
819	12.04034519	9.3054533	46.54178619				>846.79	<866.15
818	12.03516006	9.249938965	45.98907852					
817	12.02841473	9.197475433	45.73130035	16.70835034	11.46792851	57.82277183	lambda	lambda
816	11.99928951	9.15196228	45.60568237				>866.15	<886.26
815	12.01769924	9.094535828	45.36531448					
814	11.98480797	9.070432663	45.02553177	20.08249033	12.11452477	59.7463229	lambda	lambda
813	11.98112011	9.013399124	44.90287399				>886.26	<909.52
812	12.00837612	8.967277527	44.72176361					
811	11.98871231	8.913419724	44.11087036					
810	11.97451115	8.865282059	43.83422852					
809	11.94835854	8.803825378	43.44575119					
808	12.00376797	8.749802589	43.37146759					
807	11.92928982	8.70203495	43.05712509					
806	12.04204082	8.644415855	42.58075333					
805	11.95561695	8.584644318	42.39593124					
804	11.98940659	8.523416519	41.74260712					
803	11.9455595	8.467494965	41.58971024					
802	11.94231606	8.403668404	41.46158981					
801	11.9111805	8.352303505	41.25188446					
800	11.95676804	8.297139168	40.84055328					
799	11.92134476	8.247952461	40.45067215					
798	11.91464138	8.19480896	40.31063461					
797	11.92932415	8.160843849	39.68091965					
796	11.90547085	8.106320381	39.71237946					
795	11.87468338	8.070459366	39.30823898					
794	11.90003967	8.016653061	38.89921188					
793	11.88245583	7.977412701	38.65460205					
792	11.92272091	7.93357563	38.43544388					
791	11.8724823	7.904782772	38.12528992					
790	11.89153004	7.854103088	37.97683716					
789	11.84432602	7.815595627	37.43225861					
788	11.86648846	7.785562515	37.48528671					
787	11.83089447	7.74922514	37.57211304					
786	11.82871437	7.721324444	37.09393692					
785	11.80392647	7.686338425	36.9742012					
784	11.81462955	7.66088295	36.66324234					
783	11.80496979	7.634692669	36.42361069					
782	11.7897377	7.607861519	36.46050262					
781	11.75917435	7.576136112	36.17526627					
780	11.75247002	7.547561169	36.15945435					
779	11.70547962	7.522686481	35.94989014					
778	11.70909214	7.49694252	35.72531891					
777	11.71328926	7.475953579	35.51937485					
776	11.7020874	7.454492092	35.3049736					
775	11.65812206	7.439247608	35.07442856					
774	11.64302635	7.412869453	34.99030685					
773	11.63350201	7.390198708	35.05800247					
772	11.62143612	7.363327503	34.66381836					
771	11.60932922	7.332515717	34.67753983					
770	11.5666008	7.309632778	34.49715805					
769	11.54671478	7.27155447	34.28741837					
768	11.50281239	7.238169193	34.0642395					
767	11.44794559	7.204499245	34.04072571					
766	11.41666412	7.168591022	33.72813034					
765	11.41080379	7.122886181	33.48744583					
764	11.34558868	7.083120823	33.24504089					
763	11.31911278	7.034912586	33.15143204					

APPENDIX 5E. PHOTOGRAPHS OF EXPOSED SPECIMENS AT FOCUS

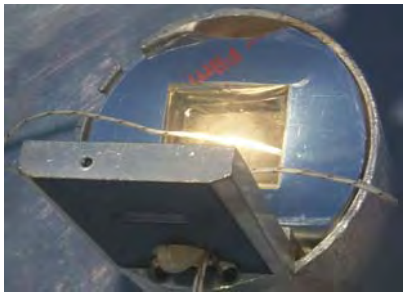

Transparent PMMA

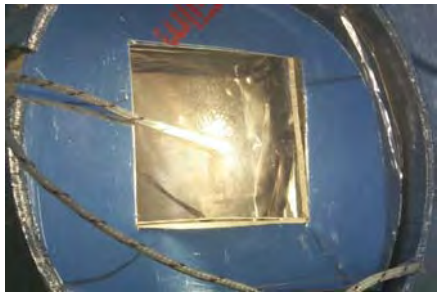

Transparent PC

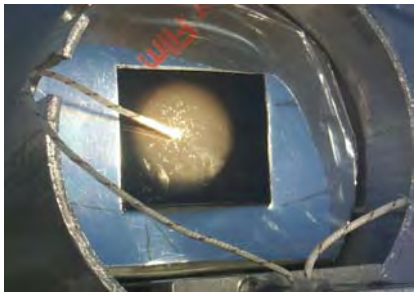

Black PMMA

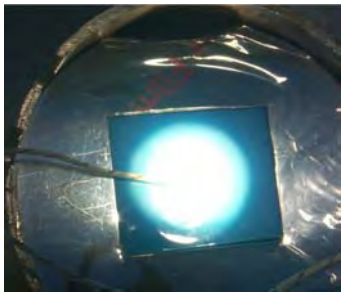

Blue PMMA

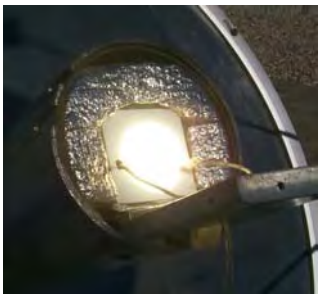

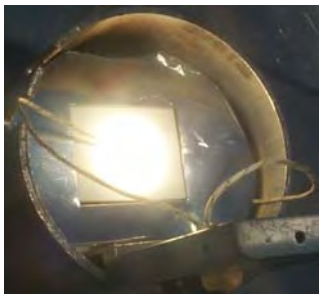

White ABS

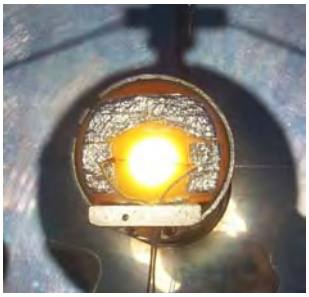

Yellow PMMA

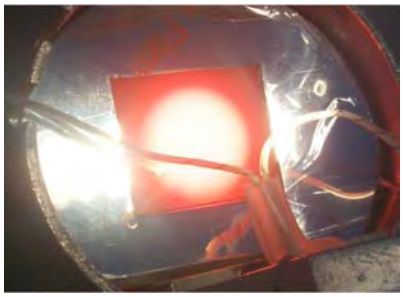

Orange PMMA

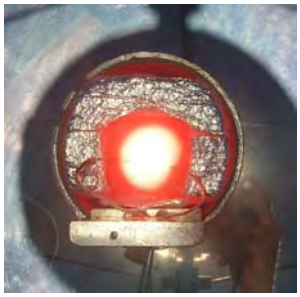

Red PMMA

APPENDIX 5F.
TEMPERATURE VARIATION DURING EXPOSURE

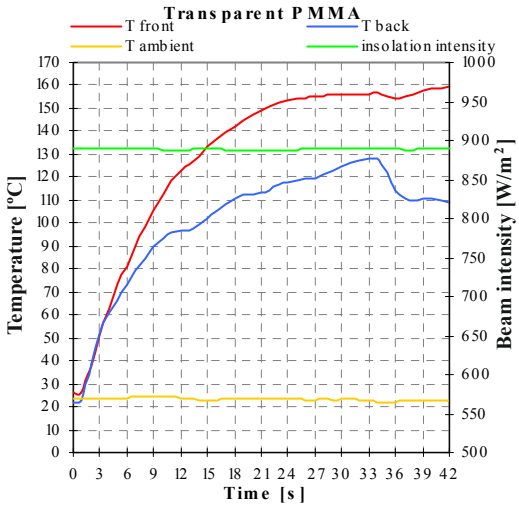

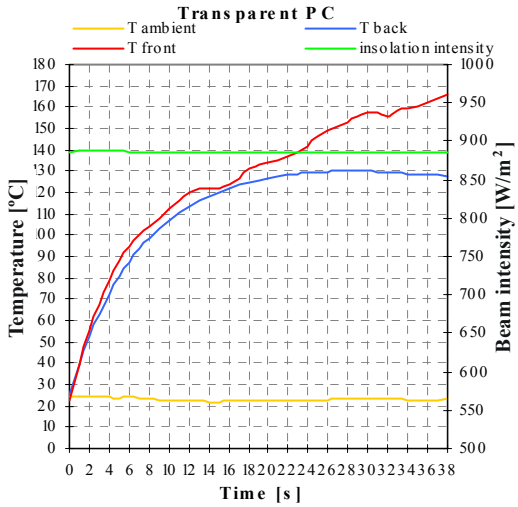

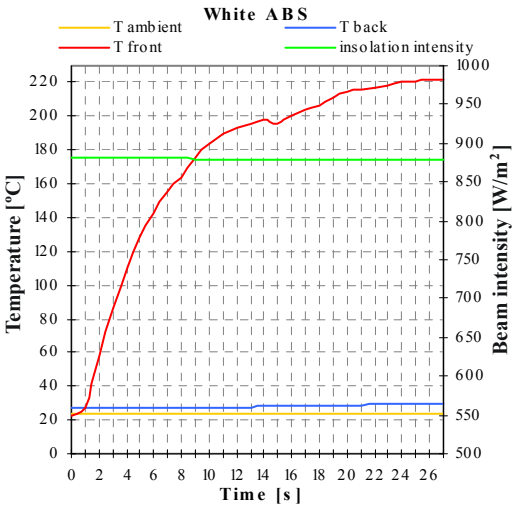

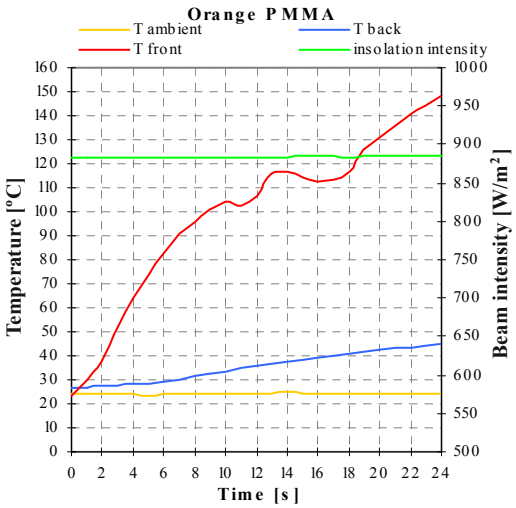

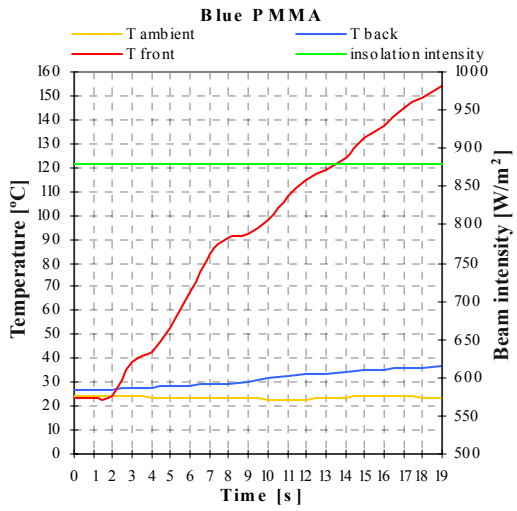
Blue PMMA
T ambient
T back
T front
insolation intensity
Temperature [ºC]
Beam intensity [W/m²]
Time [s]

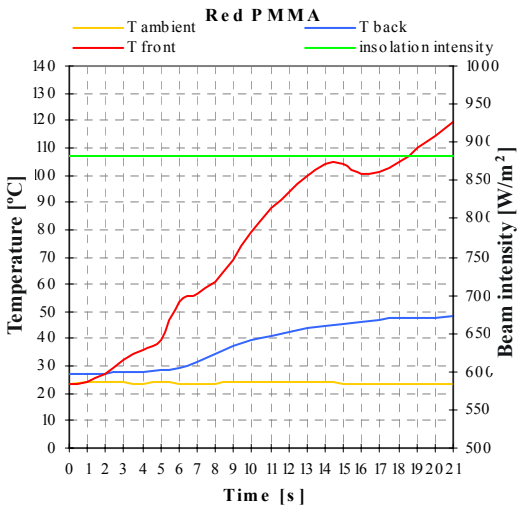
Red PMMA
T ambient
T back
T front
insolation intensity
Temperature [ºC]
Beam intensity [W/m²]
Time [s]

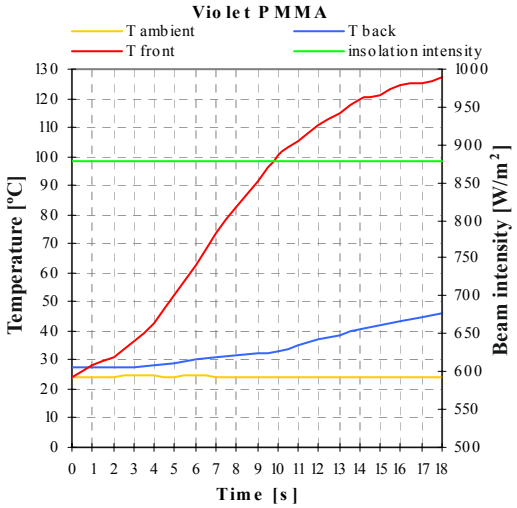
Violet PMMA
T ambient
T back
T front
insolation intensity
Temperature [ºC]
Beam intensity [W/m²]
Time [s]

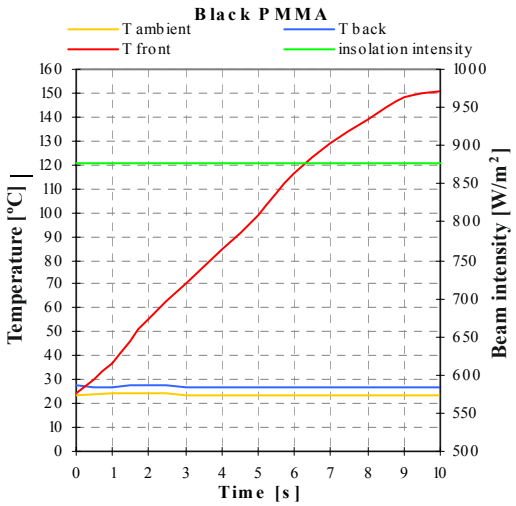
Black PMMA
T ambient
T back
T front
insolation intensity
Temperature [ºC]
Beam intensity [W/m²]
Time [s]

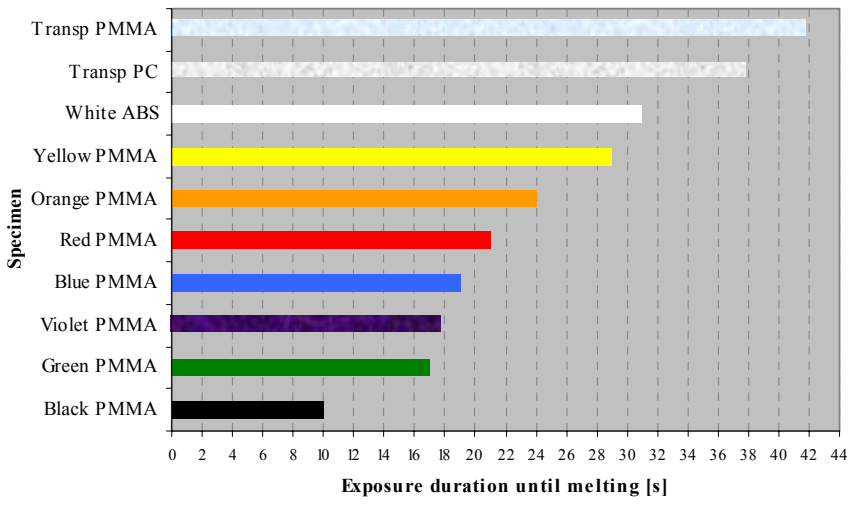
Transp PMMA
Transp PC
White ABS
Yellow PMMA
Orange PMMA
Red PMMA
Blue PMMA
Violet PMMA
Green PMMA
Black PMMA
Specimen
Exposure duration until melting [s]

APPENDIX 6A.
ALGORITHMS WRITTEN FOR THE RAY TRACING MODELS

The following algorithms have been written in Optica, a high-level component-structuring language extension of Mathematica, for modeling, ray tracing and rendering of the optical systems explored in this research.

6A.1 Ray tracing model of Cassegrainian solar energy concentrator

Using the overall dimensions and calculated parameters discussed in the previous chapters, a special function called *CassegrainConcentrator* was defined. The F/number of the system and the diameters of the primary and secondary mirrors were used as inputs to this function. The size, relative position and orientation of each component were adjustable within the model. The code written to define the *CassegrainConcentrator* is shown below.

```
Needs["Optica`Optica`"]
Clear[CassegrainConcentrator];
CassegrainConcentrator[fnumber_, bigdiameter_, smalldiameter_,
  principalfocusposition_, options___] :=
  Block[{bigmirrorthickness, smallmirrorthickness, focallength1,
     focallength2, gamma, position, holediameter},
  bigmirrorthickness = bigdiameter/10;
  smallmirrorthickness = smalldiameter/10;
  focallength1 = fnumber bigdiameter;
  position = N[smalldiameter focallength1/bigdiameter];
  gamma = N[(focallength1 - position + principalfocusposition +
  bigmirrorthickness)/position];  focallength2 = -N[position
      gamma/(gamma - 1)];  holediameter = N[.5 smalldiameter];
```

After the *CassegrainConcentrator* was defined, the relative position and orientation of the mirror components were determined in accordance with the calculations discussed in Chapter 5, as follows:

```
{Move[ParabolicMirrorWithHole[focallength1, bigdiameter,
 holediameter,bigmirrorthickness,options],{-focallength1,0,180}],
Move[ParabolicMirror[focallength2, smalldiameter,
   smallmirrorthickness, options], {-position, 0, 0}],
```

Next, the boundaries delineating the limits of the ray trace system volume were defined. The boundary components were specified to designate the three-dimensional rectangular box that would absorb the rays intercepted by its walls:

```
Boundary[{-N[1.0(focallength1 + principalfocusposition)],
      -bigdiameter/2, -bigdiameter/2},{1.4principalfocusposition,
       bigdiameter/2, bigdiameter/2}]}];
```

After defining the boundary components, ray tracing through *CassegrainConcentrator* and rendering of the system were performed. A circle of rays with a diameter of the maximum clear aperture of the primary mirror was traced through the optical components of the system:

```
DrawSystem[
  Move[{Move[CircleOfRays[590,{NumberOfRays->36}],{-853.4,0,180}],
  CassegrainConcentrator[3.56,600,240,-169.5,GraphicDesign->Wire,
        ComponentMedium -> SF11]}, {0, 0, 180}], Boxed -> False,
        Axes -> True, QuickTrace -> False];
```

Based on the computational model, the rendered image of the Cassegrainian concentrator created by the ray tracing method is illustrated below.

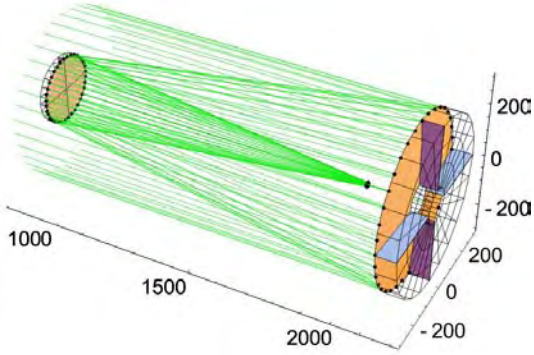

Finally, a two-dimensional image of the Cassegrainian concentrator was rendered:

```
ShowSystem[%, PlotType -> SideView, ColorView -> OpticalLength,
  ShowRange -> {0, 1, 2, 3}, QuickTrace -> False, Axes -> True,
  AxesOrigin -> {800, -320}];
            (*Press Shift+Enter to view 2D image*)
```

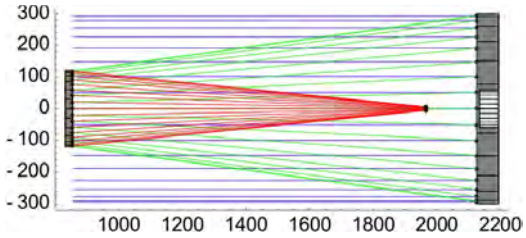

6A.2 Model with magnifying unit and three doublet lenses

To avoid all beam bending mirrors, the starting model comprised only the magnifying unit with a minimum number of auxiliary doublets as a beam transmitting means to the working site.

The model was developed with the aim of shortening the originally proposed optical path, ensuring that the final image is relocated under the trunnion box. In this model, all beam bending mirrors were removed and only three auxiliary doublets that follow the magnifying unit were used to align the light beam. The position of the final focus depends on the principal Cassegrainian focus location, as well as the adjustable magnifying unit and the doublets following it.

Firstly, the magnifying unit and three doublet lenses were positioned in the three-dimensional space as shown below.

```
firstlenspos = -1864;
Move[BiConcaveLens[78.2, 50.8, 10.4], {firstlenspos, 0, 0}],
Move[BiConvexLens[138, 50.8, 10.17], {firstlenspos - 12, 0, 0}],
Move[LensDoublet[90, -66.217, -219.8, 45, 12.5, 3, 1.516,
  1.643], {(firstlenspos - 12) - 251, 0, 180}],
Move[LensDoublet[90, -66.217, -219.8, 45, 12.5, 3, 1.516,
  1.643], {((firstlenspos - 12) - 251) - 287, 0, 180}],
Move[LensDoublet[37.33, -31.54, -124.5, 40, 15, 3, 1.620,
  1.3], {(((firstlenspos - 12) - 251) - 287) - 211, 0, 0}],
```

After setting up the boundary components settings, ray tracing through the system including the previously modeled Cassegrainian concentrator was performed.

```
Boundary[{-N[1.34(focallength1 + principalfocusposition)], -
bigdiameter/2, -bigdiameter/2}, {1.34principalfocusposition,
bigdiameter/2, bigdiameter/2}]}];
DrawSystem[
  Move[{Move[CircleOfRays[590,{NumberOfRays->36}],{-853.4,0,180}],
```

```
    CassegrainConcentrator[3.56, 600,240,-170, GraphicDesign->Wire,
ComponentMedium -> SF11]}, {0, 0, 180}], Boxed -> True,
  BoxStyle -> Dashing[{0.01, 0.01}], Axes -> True, FaceGrids->All];
```

The result is a three-dimensional rendered image of the concentrator and the modeled optical components which is shown below.

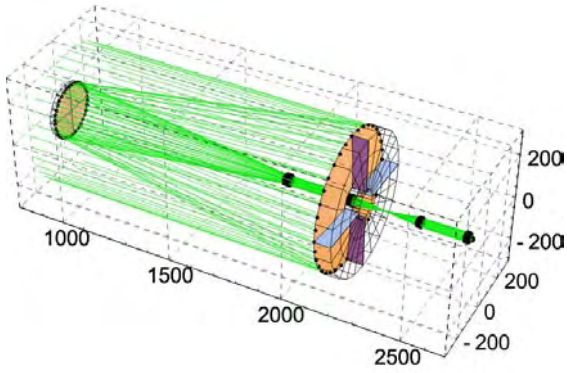

Finally, a two-dimensional image rendering of the whole system was performed. The two-dimensional projection of the rendered graphical output is presented below.

```
ShowSystem[%, PlotType -> SideView, ColorView -> OpticalLength,
    ShowRange -> {0, 1, 2, 3, 4, 5, 6, 7, 8}];
```

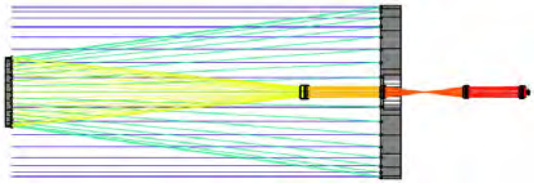

A magnified view of the lens optical components, shown below, allows to examine how the local rays and components are interacting.

6A.3 Model with magnifying unit and two doublet lenses

Further shortening of the optical path was modeled in the next arrangement of only two doublets after the magnifying unit, ensuring that the final image is relocated inside the trunnion box. Similarly to the previous model, the magnifying unit and two doublet lenses were positioned relative to each other in the three-dimensional

space, as shown below.

```
  firstlenspos = - 1851;
  Move[BiConcaveLens[78.2, 50.8, 10.4], {firstlenspos, 0, 0}],
  Move[BiConvexLens[138, 50.8, 10.17], {firstlenspos - 15, 0, 0}],
  Move[LensDoublet[90, -66.217, -219.8, 45, 12.5, 3, 1.516,
    1.6425], {(firstlenspos - 15) - 246, 0, 180}],
  Move[LensDoublet[37.33, -31.54, -124.5, 40, 15, 3, 1.620,
    1.3], {((firstlenspos - 15) - 246) - 307, 0, 0}],
```

After the system was defined, ray tracing through the system was performed using the boundary limits established.

```
  Boundary[{-N[1.24(focallength1 + principalfocusposition)], -
bigdiameter/2, -bigdiameter/2}, {1.24principalfocusposition,
bigdiameter/2, bigdiameter/2}]}];
  DrawSystem[
    Move[{Move[CircleOfRays[590,{NumberOfRays->36}],{-851,0,180}],
    CassegrainConcentrator[3.56,600,240,-169.5,GraphicDesign->Wire,
          ComponentMedium -> SF11]}, {0, 0, 180}], Boxed -> False];
```

The three-dimensional rendered image of the concentrator with the modeled optical components is shown below.

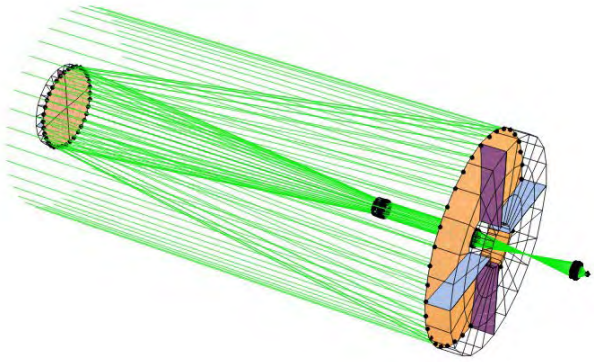

Next, rendering of a two-dimensional image of the lens optical components was performed. The two-dimensional projection of the resulting rendered graphical output is illustrated below.

```
ShowSystem[%, PlotType -> SideView, ColorView -> OpticalLength,
    ShowRange -> {3, 4, 5, 6, 7}];
```

6A.4 Model with three doublet lenses without magnifying unit

To decrease the optical losses and spectral limitations further, in the next model the magnifying unit was avoided and the optical path was aligned with three doublet lenses only. The relative position and orientation of the optical components were arranged within the horizontal plane, as shown below.

```
firstlenspos = -1802
Move[LensDoublet[96.85, -73.74, -307.76, 45, 13.15, 3, 1.716,
  1.28], {firstlenspos, 0, 180}],
Move[LensDoublet[96.85, -73.74, -307.76, 45, 13.15, 3, 1.716,
  1.28], {firstlenspos - 597, 0, 180}],
Move[LensDoublet[37.33, -31.54, -124.5, 40, 15, 3, 1.620,
  1.3], {(firstlenspos - 597) - 335, 0, 0}],
```

After defining the boundary limits, ray tracing through the whole system was performed.

```
Boundary[{-N[1.4(focallength1 + principalfocusposition)],
   -bigdiameter/2, -bigdiameter/2}, {1.4principalfocusposition,
   bigdiameter/2, bigdiameter/2}]}];
DrawSystem[Move[{Move[CircleOfRays[590, {NumberOfRays -> 36}],
   {-853.4, 0, 180}],
 CassegrainConcentrator[3.56, 600, 240, -170,GraphicDesign->Wire,
       ComponentMedium -> SF11]}, {0, 0, 180}], Boxed -> True,
  BoxStyle -> Dashing[{0.01, 0.01}], Axes->True,FaceGrids->All];
```

The three-dimensional rendered image of the concentrator with the modeled optical components is given below.

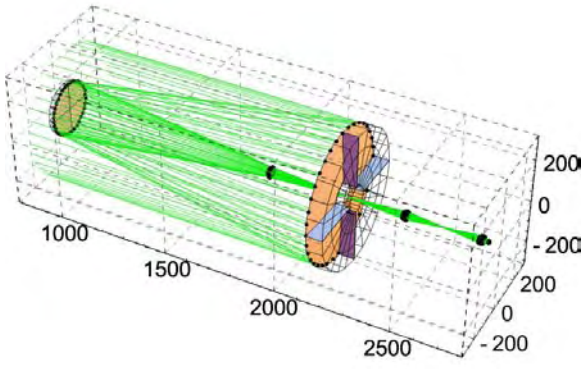

Next, rendering of a two-dimensional image of the lens components was performed. The two-dimensional projection of the rendered graphical output is shown below.

```
ShowSystem[%, PlotType -> SideView, ColorView -> OpticalLength,
    ShowRange -> {3, 4, 5}];
```

6A.5 Model with one doublet lens without magnifying unit

One doublet lens at the principal Cassegrainian focus was modeled in order to minimize the optical losses and spectral limitations in the optical components. The doublet lens, similarly to the previous models, was placed relative to the mirrors as shown below.

```
firstlenspos = -1886;
Move[LensDoublet[37.33, -31.54, -124.5, 40, 15, 3, 1.620, 1.3],
   {firstlenspos, 0, 0}],
```

After the system was defined and the boundaries established, ray tracing through the system was performed.

```
Boundary[{-N[0.965(focallength1 + principalfocusposition)],
   -bigdiameter/2, -bigdiameter/2}, {1.25principalfocusposition,
   bigdiameter/2, bigdiameter/2}]}];
DrawSystem[
```

```
Move[{Move[CircleOfRays[590, {NumberOfRays->36}],{-853.4,0,180}],
  CassegrainConcentrator[3.56,600,240,-169.5,GraphicDesign->Wire,
       ComponentMedium -> SF11]}, {0, 0, 180}], Boxed -> False,
 Axes -> True];
```

The three-dimensional rendered image of the concentrator with the modeled optical component is given below.

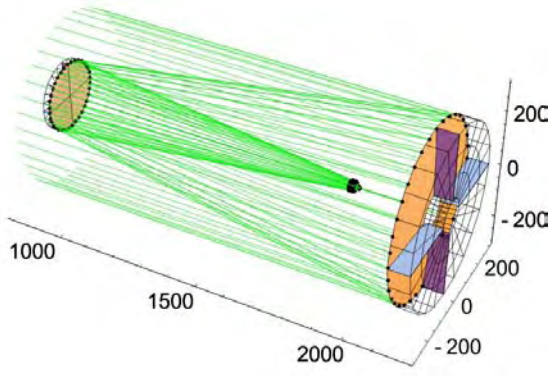

Next, rendering of a two-dimensional image of the whole system was performed. The two-dimensional projection of the rendered graphical output is demonstrated below.

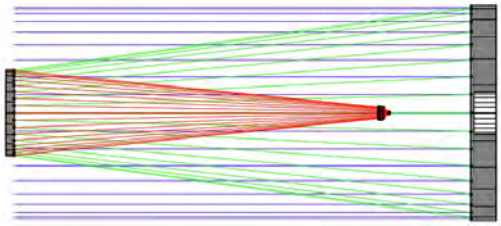

6A.6 Model with third stage concentrator

The third stage non-imaging concentrator at the principal Cassegrainian focus was modeled in order to minimize the optical losses and spectral limitations in the optical components. The third stage concentrator, similarly to the previous models, was positioned relative to the mirrors.

```
Move[ParabolicMirrorWithHole[4, 55, 6, 0], {-1815.15, 0, 180}],
```

After the system was defined and boundaries established, ray tracing through the system was performed.

```
    Boundary[{-N[
      0.926(focallength1 + principalfocusposition)],
      -bigdiameter/2, -bigdiameter/2}, {1.4principalfocusposition,
      bigdiameter/2, bigdiameter/2}]}];
DrawSystem[
  Move[{Move[CircleOfRays[590,{NumberOfRays->36}],{-853.4,0,180}],
   CassegrainConcentrator[3.56,600,240,-169.5,GraphicDesign->Wire,
      ComponentMedium -> SF11]}, {0, 0, 180}], Boxed -> False,
      Axes -> True, QuickTrace -> False];
```

The three-dimensional rendered image of the concentrator with the modeled optical component is illustrated below.

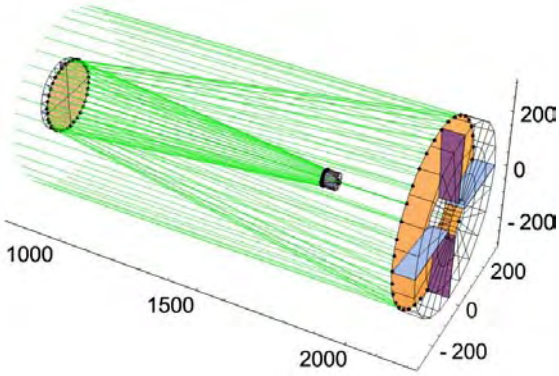

Next, rendering of a two-dimensional image of the whole system was performed. The two-dimensional projection of the rendered graphical output is demonstrated below.

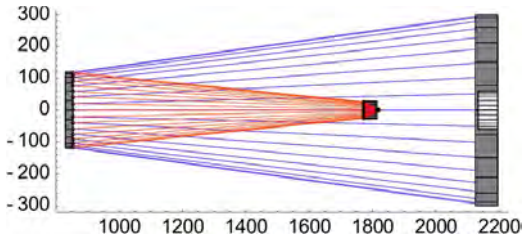

APPENDIX 6B.
RAY TRACING AND IMAGE ANALYSIS IN OSLO

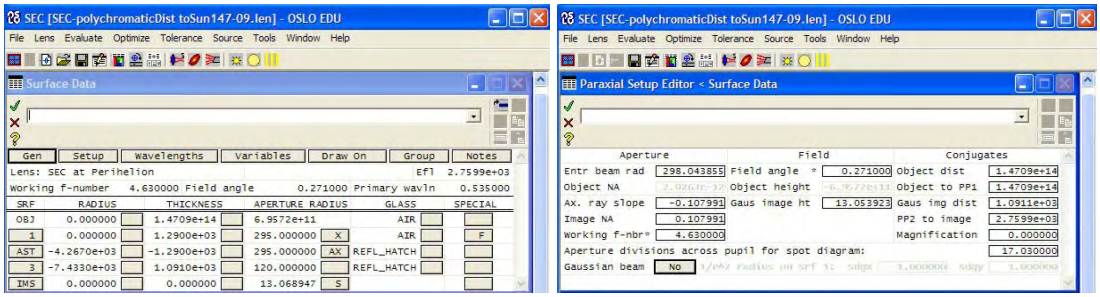

Figure 6B.1: SEC database setup - input parameters

```
*SEIDEL ABERRATIONS
 SRF      SA3            CMA3         AST3            PTZ3          DIS3
 SUM      -0.675207      0.051797     -0.003780       0.001837      8.7077e-05
*FIFTH-ORDER ABERRATIONS
SRF       SA5            CMA5         AST5            PTZ5          DIS5          SA7
SUM       -0.005484      0.000791     -4.1776e-08     2.1801e-08    8.9530e-10    -4.3643e-05
```

Figure 6B.2: Third and fifth order aberrations

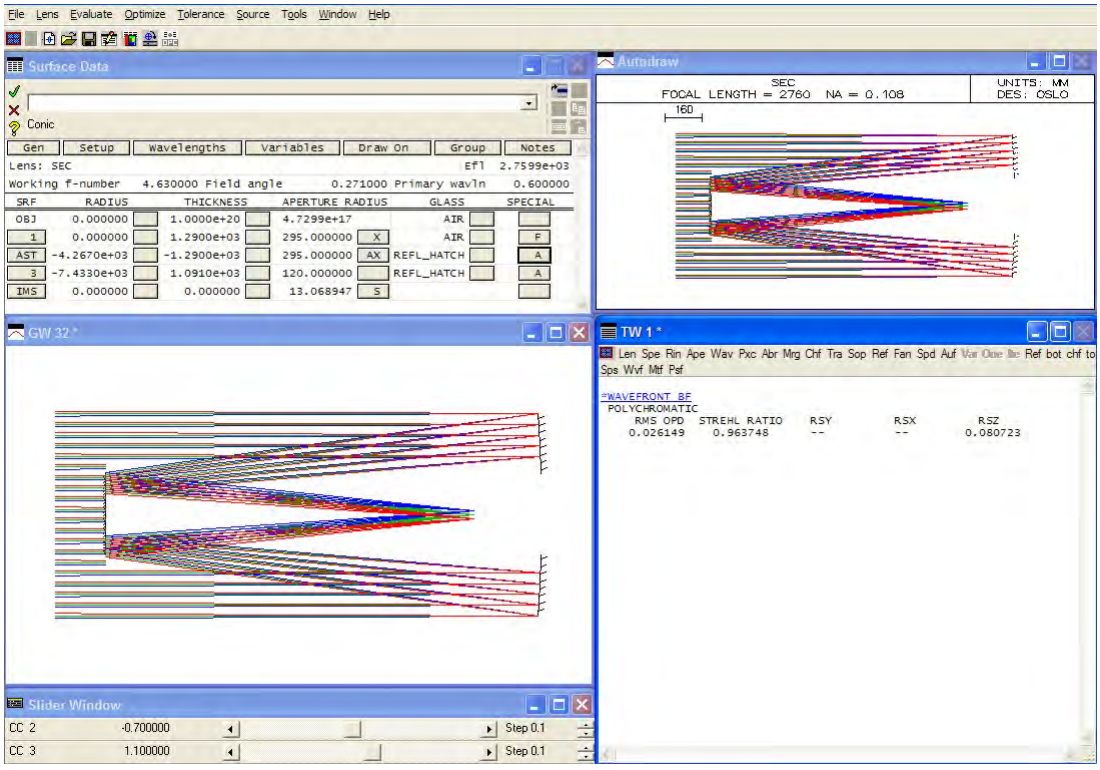

Figure 6B.3: Optimization analysis result when conic constants are variable

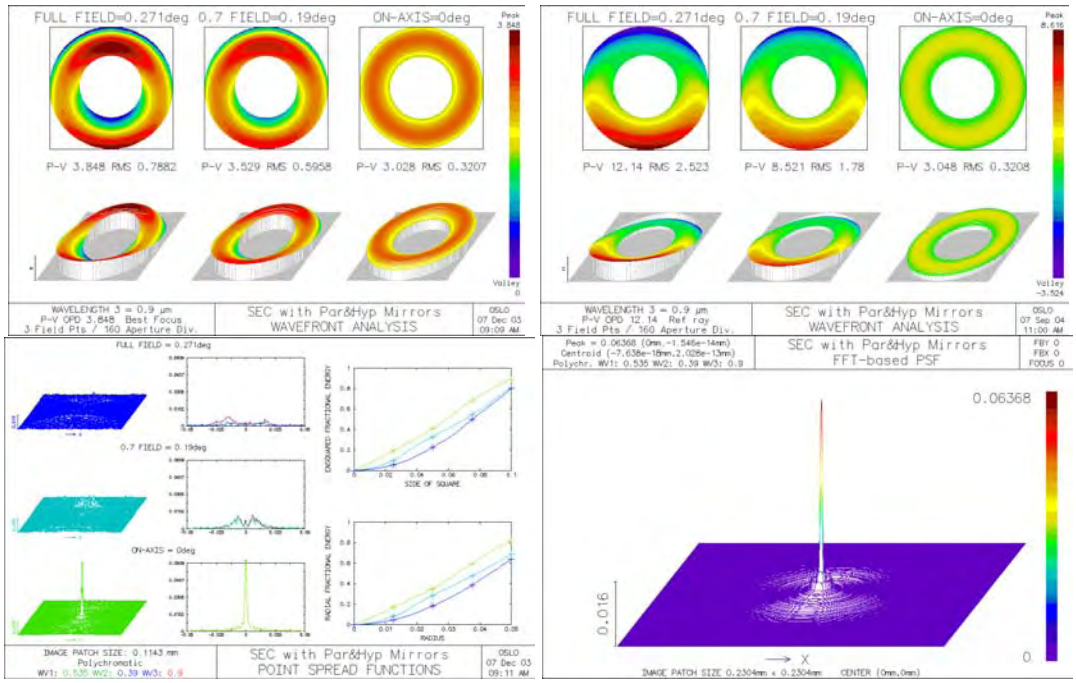

Figure 6B.4: Wavefront analysis of SEC if classical Cassegrainian configuration is used

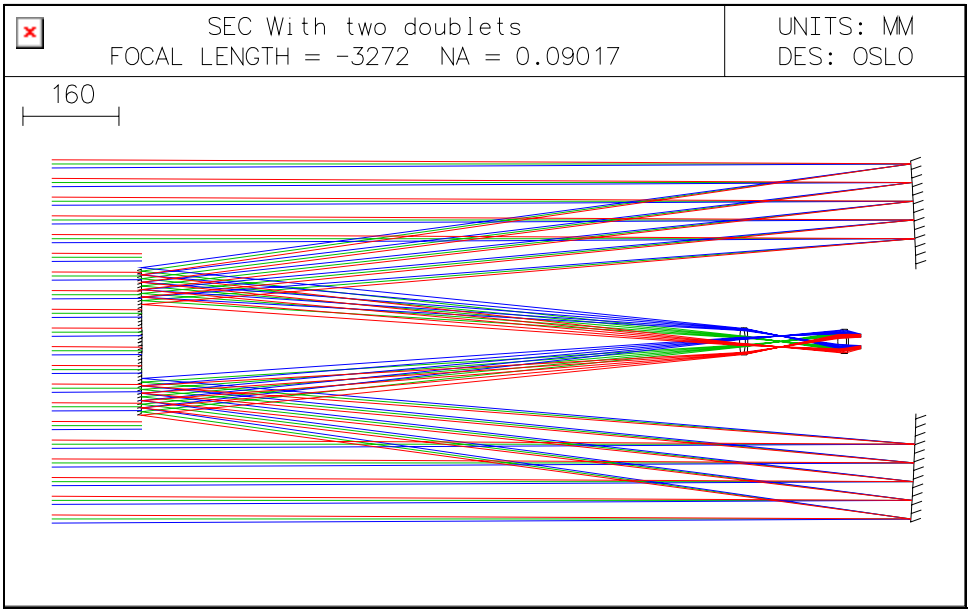

Figure 6B.5: Ray tracing model of the SEC with two doublets

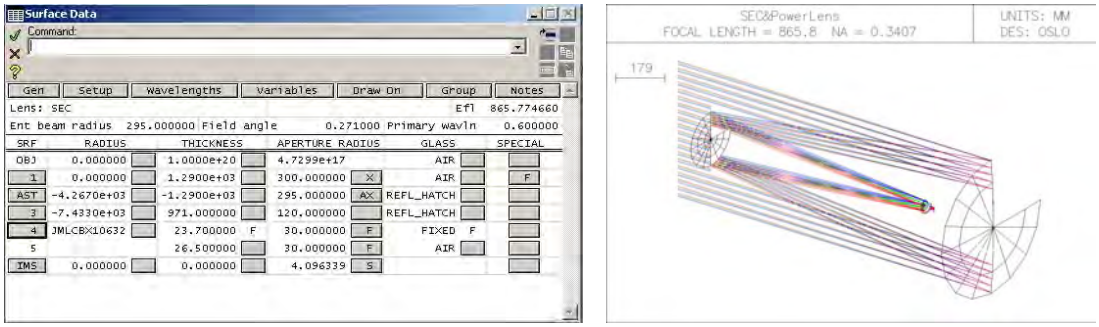

Figure 6B.6: Input parameters and ray tracing of the model with one auxiliary lens

APPENDIX 6C. CALCULATIONS OF CPC PARAMETERS

Tita_max [degrees]	d/2 out [mm]	ParabFocus [mm]	D/2 in [mm]	L-CPCheight [mm]	Exit aperture area [mm²]	Entry aperture area [mm²]	Geometric Area Concentration	Air Theoretical Concentration
2.69891070	6.00000000	6.28252476	127.42246042	2830.36002492	113.09733553	51008.41703310	451.01342834	451.28407699
3.14359290	6.00000000	6.32903114	109.41213609	2101.41449175	113.09733553	37608.05442532	332.52820899	332.72775585
4.20944210	6.00000000	6.44041530	81.74103021	1192.11580988	113.09733553	20990.85296956	185.59988943	185.71126607
5.64189584	6.00000000	6.58986362	61.03105619	678.52642754	113.09733553	11701.77233270	103.46638387	103.52847301
5.57113930	0.25000000	0.27427039	2.57515388	28.96336402	0.19634954	20.83321249	106.10267995	106.16635110
5.57113930	0.50000000	0.54854079	5.15030776	57.92672803	0.78539816	83.33284996	106.10267995	106.16635110
5.57113930	1.00000000	1.09708158	10.30061551	115.85345607	3.14159265	333.33139984	106.10267995	106.16635110
5.57113930	1.27000000	1.39329360	13.08178170	147.13388920	5.06707479	537.63021481	106.10267995	106.16635110
5.57113930	1.50000000	1.64562237	15.45092327	173.78018410	7.06858347	749.99564964	106.10267995	106.16635110
5.57113930	1.78412412	1.95732970	18.37757655	206.69694491	10.00000000	1061.02679945	106.10267995	106.16635110
5.57113930	2.00000000	2.19416315	20.60123103	231.70691213	12.56637061	1333.32559937	106.10267995	106.16635110
5.57113930	3.00000000	3.29124473	30.90184654	347.56036820	28.27433388	2999.98259858	106.10267995	106.16635110
5.57113930	4.00000000	4.38832631	41.20246205	463.41382427	50.26548246	5333.30239747	106.10267995	106.16635110
5.57113930	5.00000000	5.48540789	51.50307756	579.26728033	78.53981634	8333.28499605	106.10267995	106.16635110
5.57113930	5.50000000	6.03394867	56.65338532	637.19400837	95.03317777	10083.27484523	106.10267995	106.16635110
5.57113930	5.64189584	6.18961998	58.11499977	653.63313131	100.00000000	10610.26799453	106.10267995	106.16635110
5.57113930	6.00000000	6.58248946	61.80369308	695.12073640	113.09733553	11999.93039432	106.10267995	106.16635110
6.10000000	6.00000000	6.63758443	56.46311048	584.48203686	113.09733553	10015.65764542	88.55785681	88.61099949

APPENDIX 6D.
EXPERIMENTAL DATA USED IN EMPIRICAL MODEL

Specimen no.	Idle Temperature [°C]	Duration [sec]	Intensity of beam solar radiation [W/m^2]	Measured Tensile Strength [MPa]
1	246	35	838	35.0
2	250	34	849	36.4
3	246	35	836	36.8
4	248	34	844	37.0
5	250	34	852	37.3
6	256	34	872	37.4
7	253	34	861	37.4
8	248	34	845	37.4
9	252	34	859	37.7
10	256	34	870	37.8
11	253	34	861	37.9
12	254	34	865	38.0
13	256	34	871	38.1
14	253	34	860	38.1
15	254	34	865	38.2
16	255	34	868	38.4
17	258	34	877	38.4
18	257	34	875	38.6
19	258	34	878	38.9
20	259	34	881	39.2
21	256	34	871	39.2
22	239	35	812	39.3
23	238	35	810	39.5
24	237	35	808	39.8
25	237	35	807	40.0
26	233	35	794	40.1
27	232	36	790	39.6
28	232	36	788	41.5
29	228	36	775	41.7

APPENDIX 7A. MODIFICATION DESIGN DIAGRAMS

Schematic diagram of the electronic drive control circuit

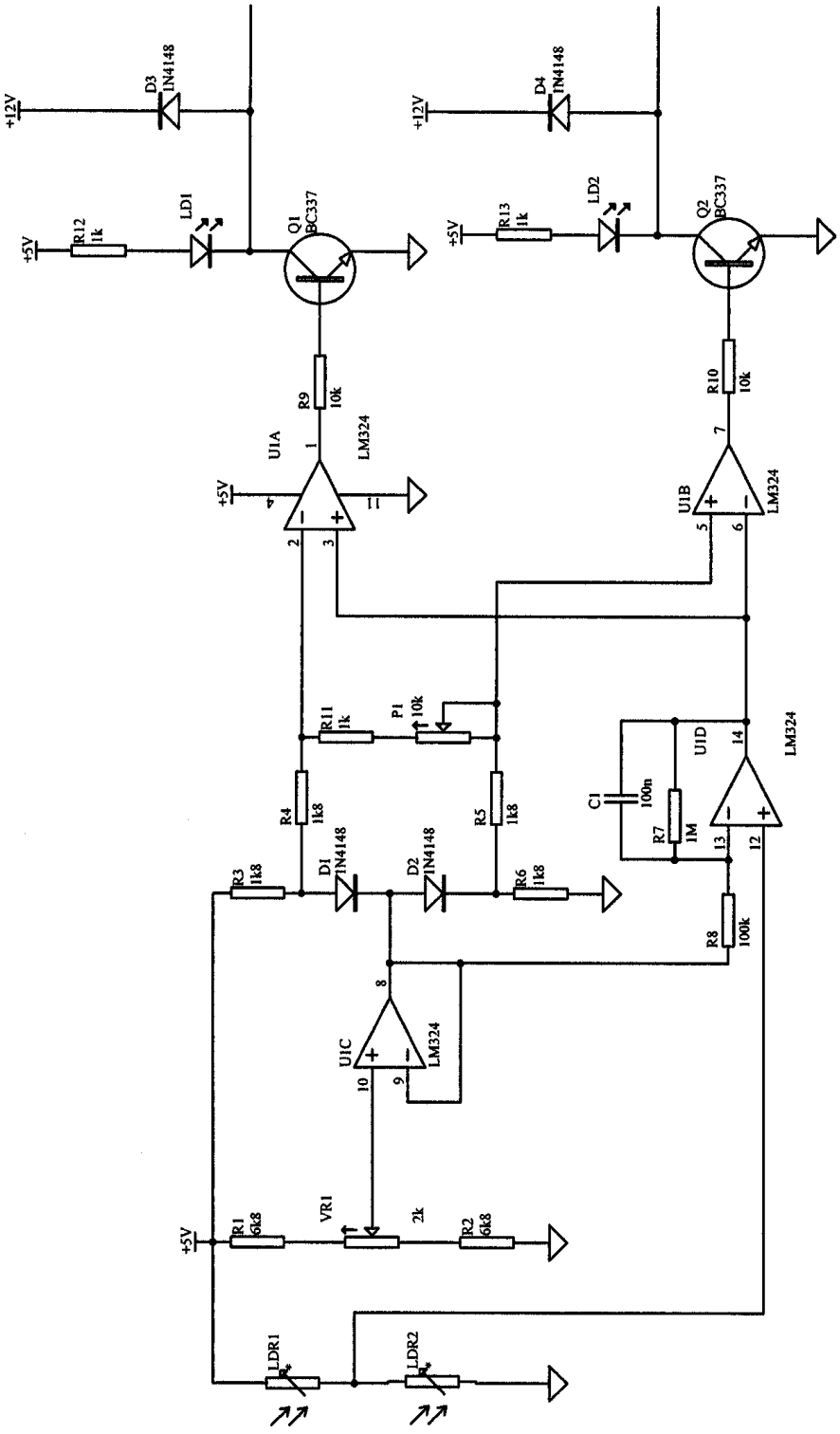

Sun tracking sensor with day-night detector and septum separation

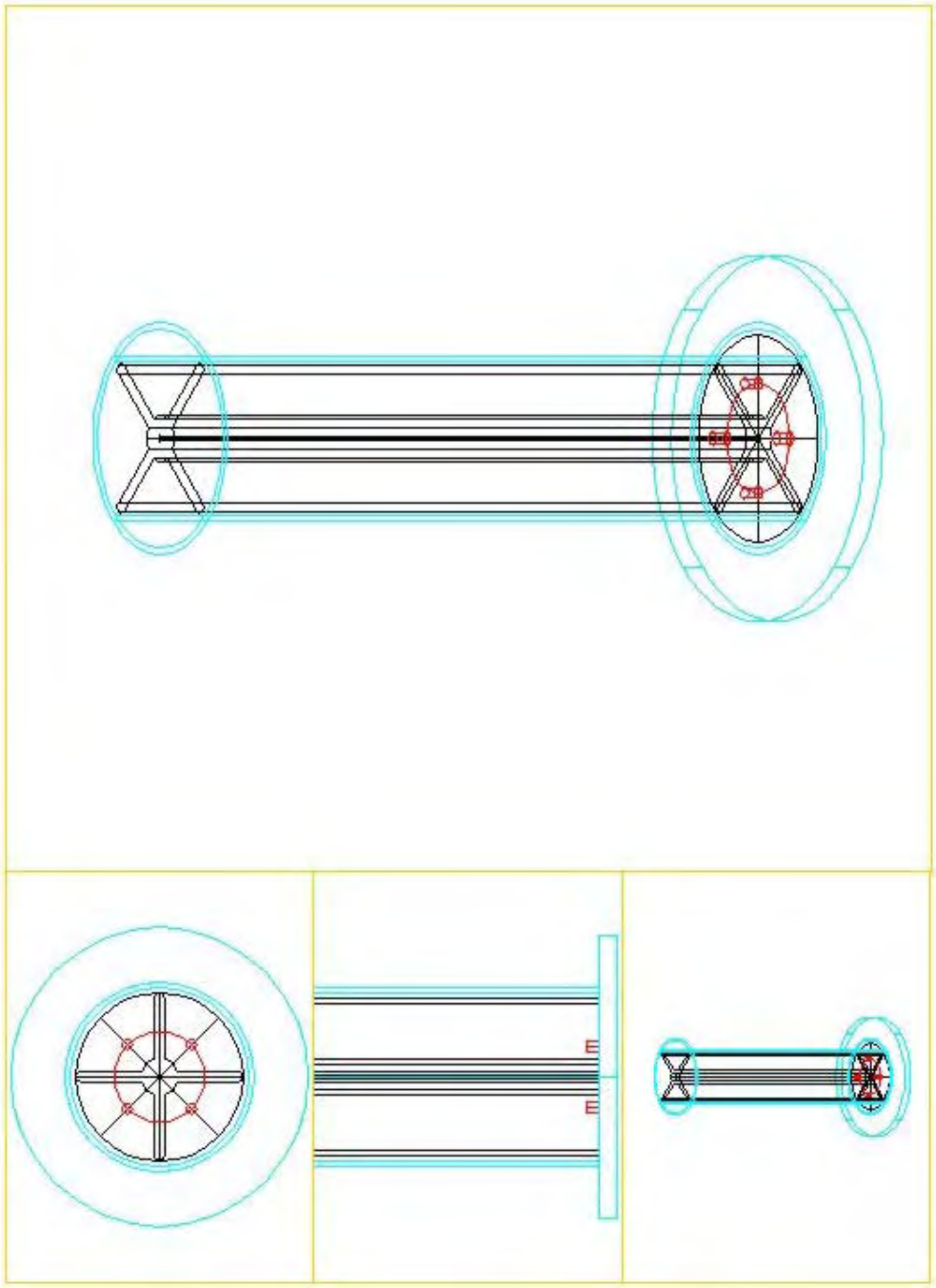

Design drawing of truncated light cone transducer

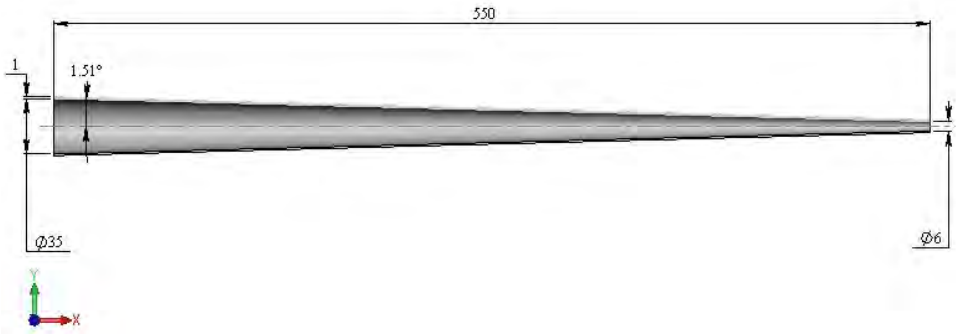

Truncated light cone with specimen holder

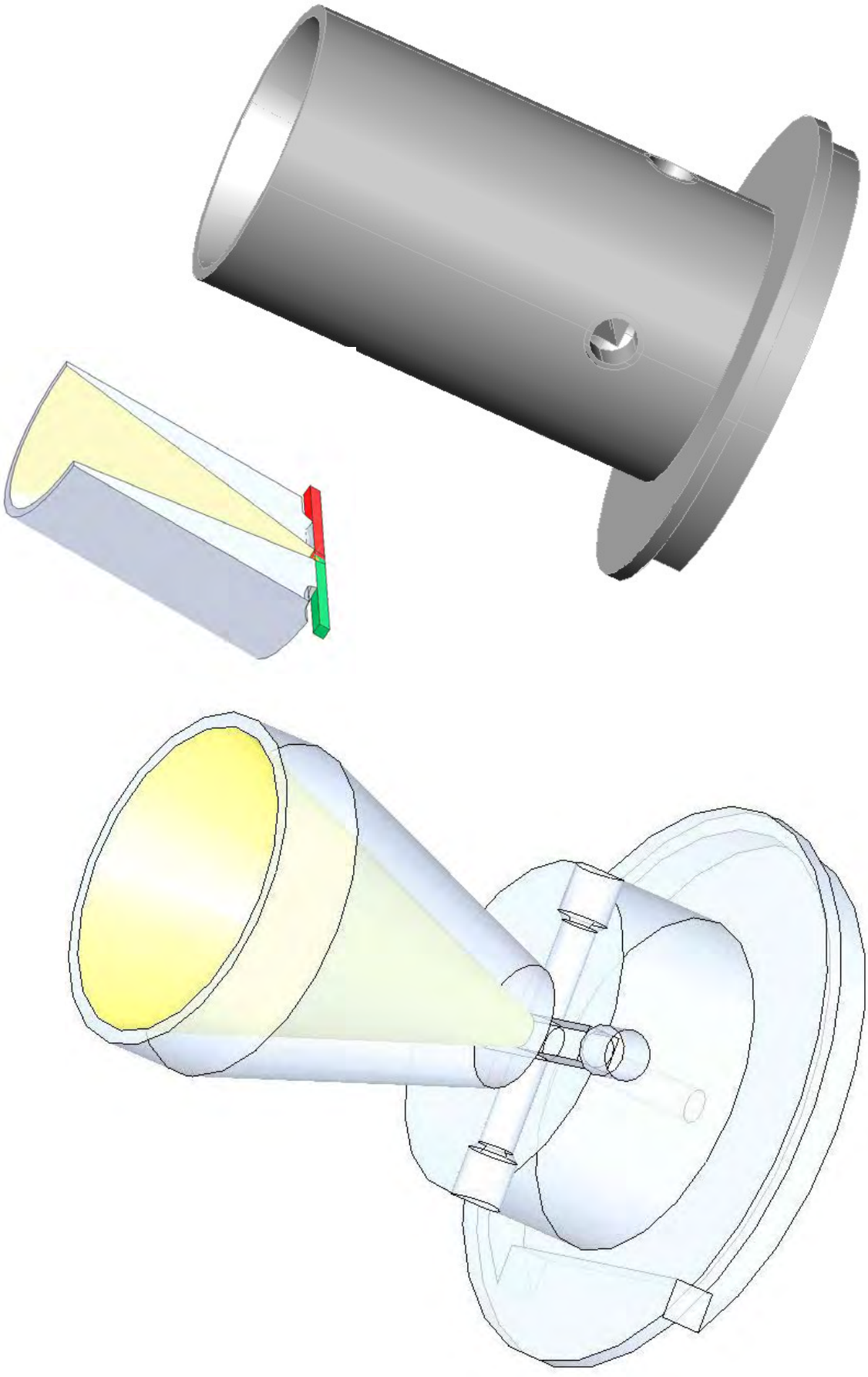

Design drawing of truncated light cone with specimen holder

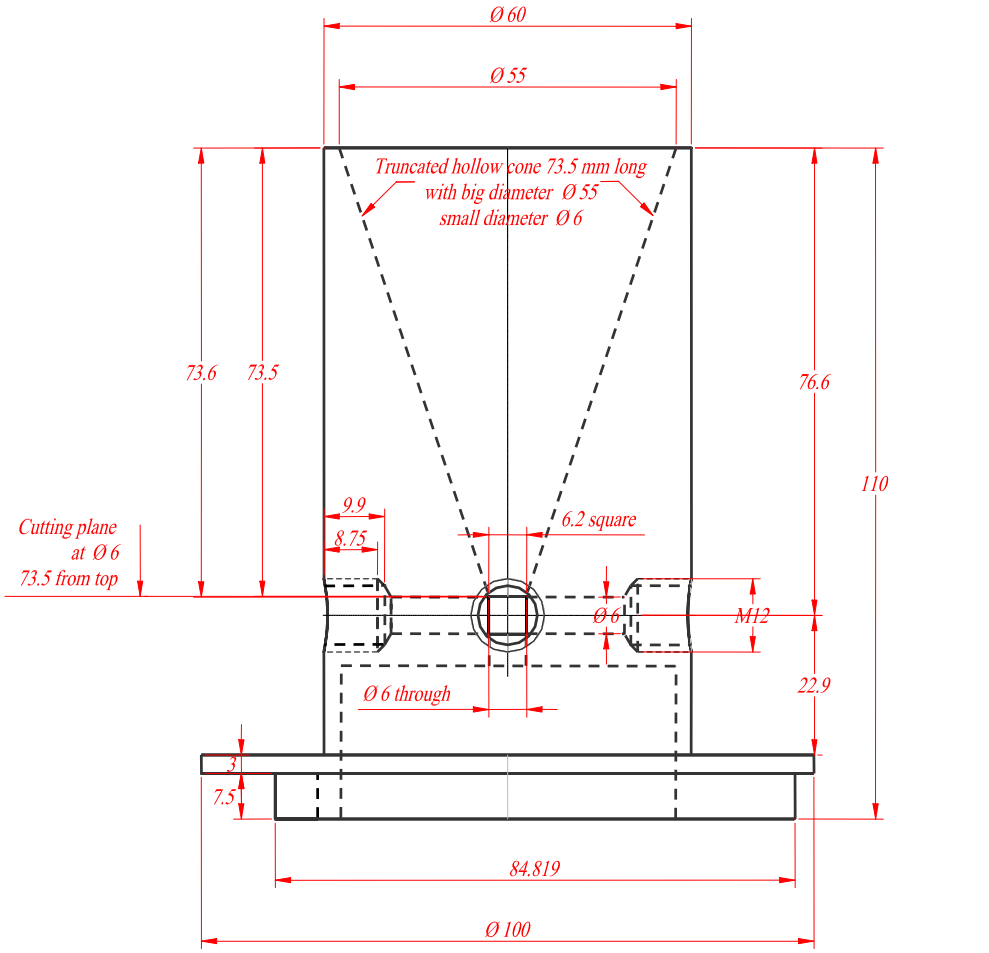

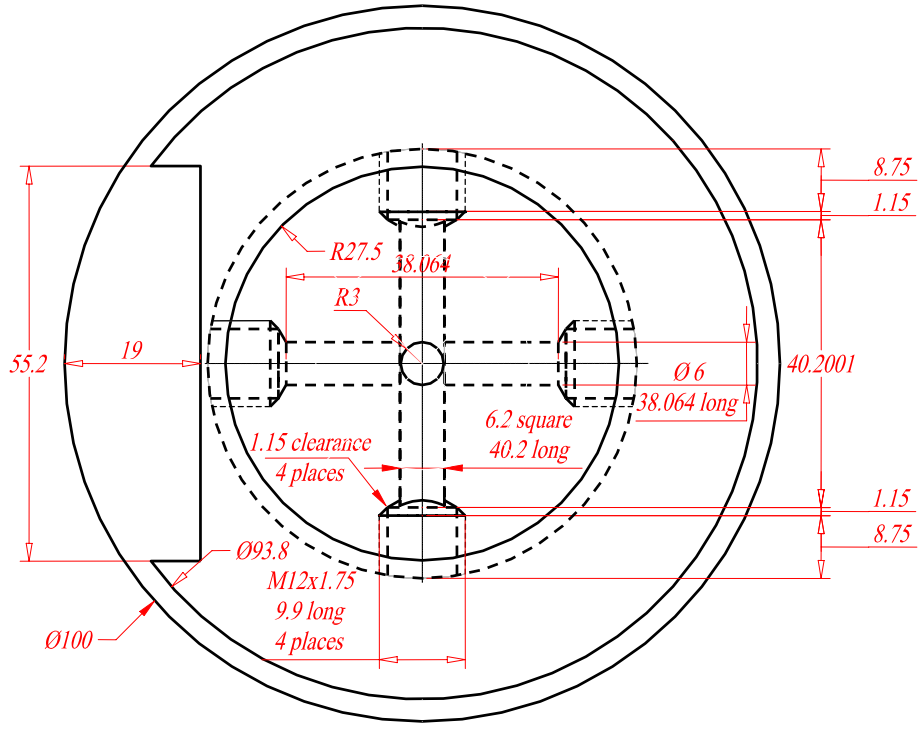

Design drawing of truncated light cone component

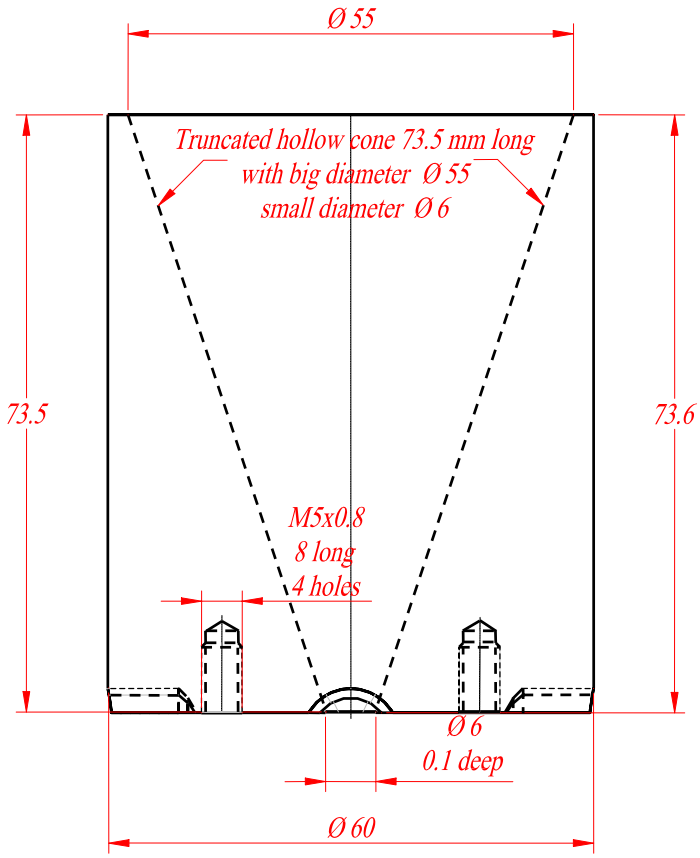

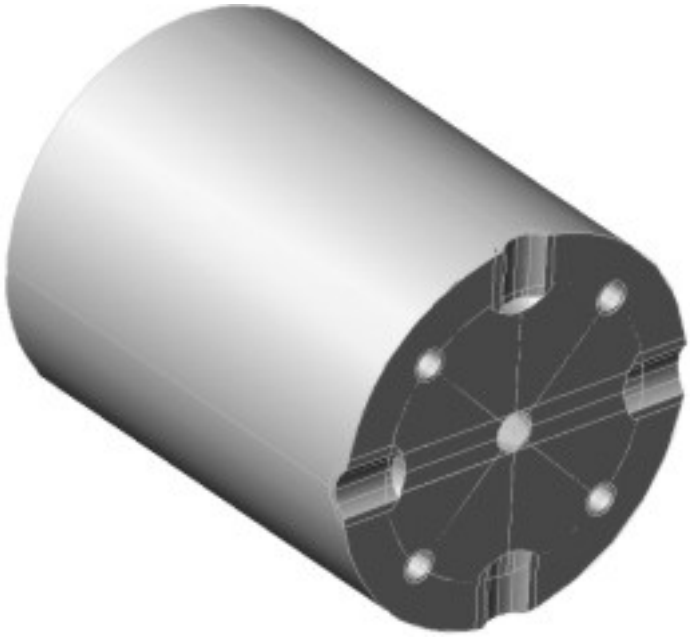

Design drawing of specimen holder component

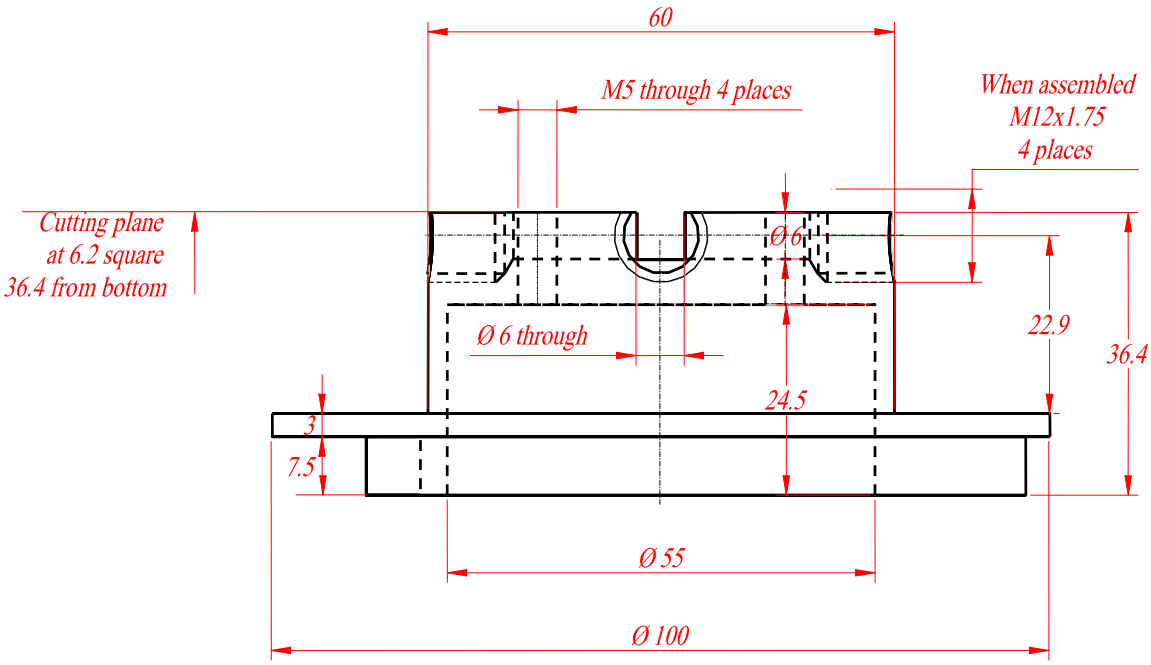

Metric stage

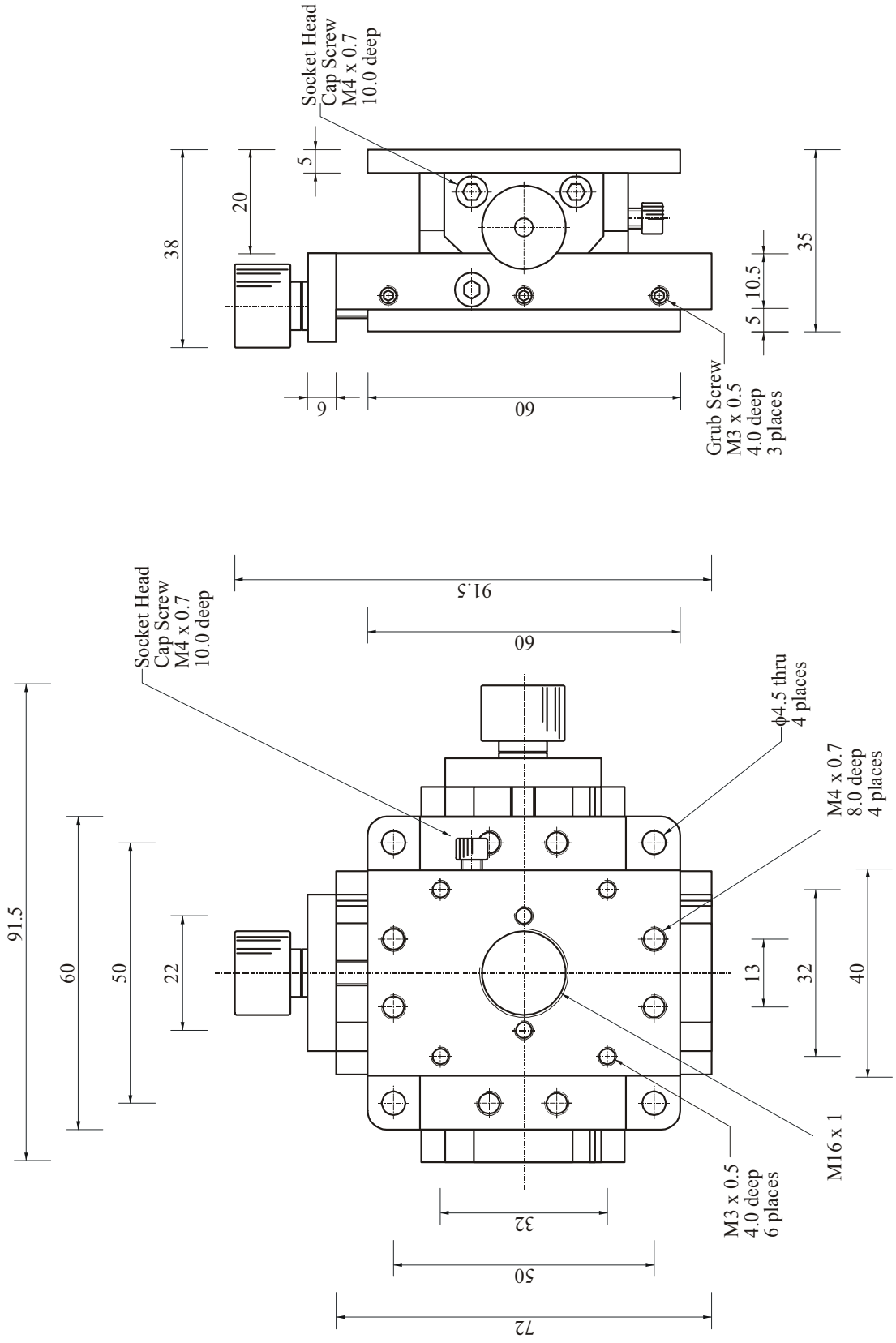

Doublet lens specification and holding barrel design drawing

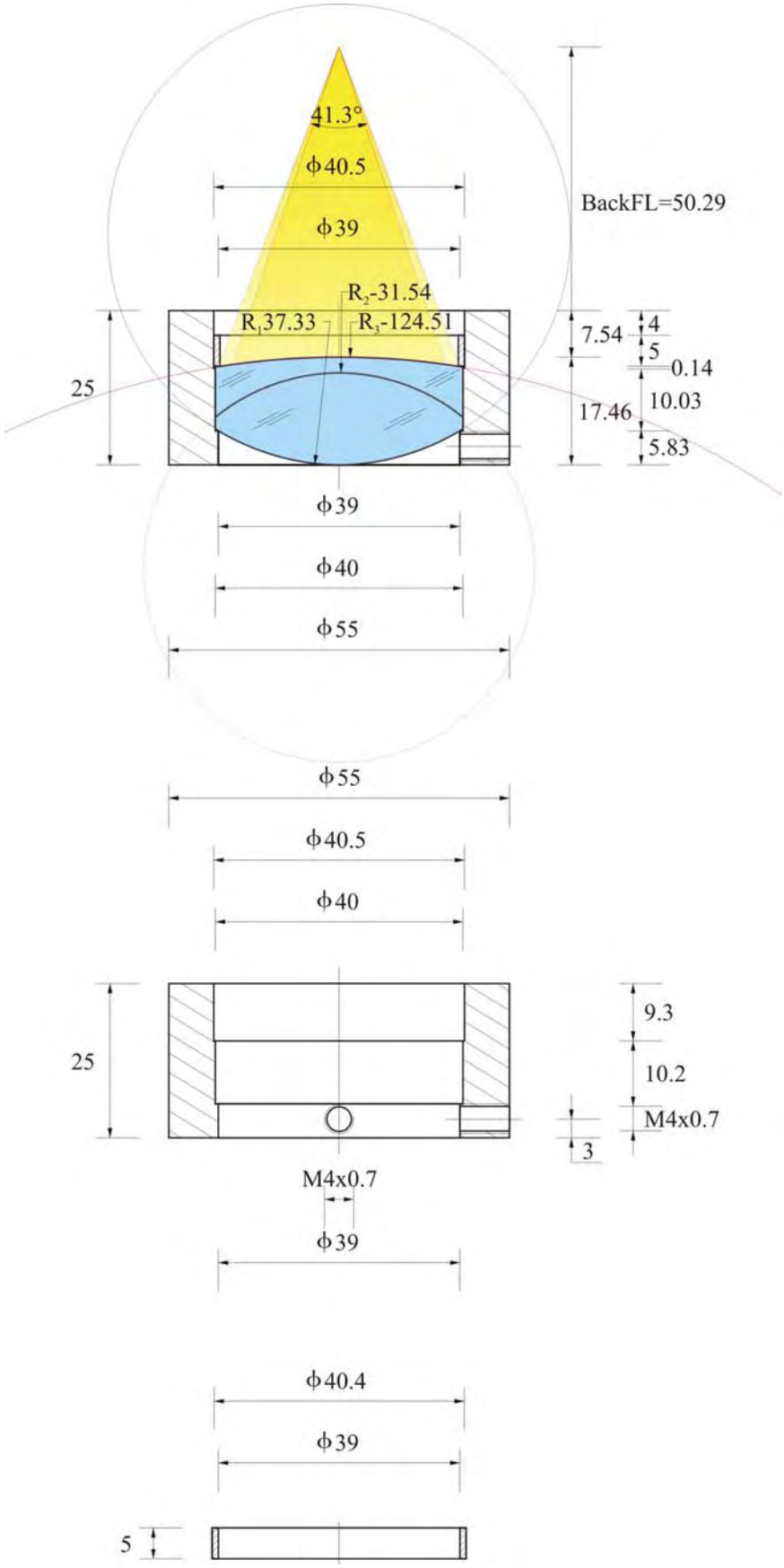

Clamping device for butt joining

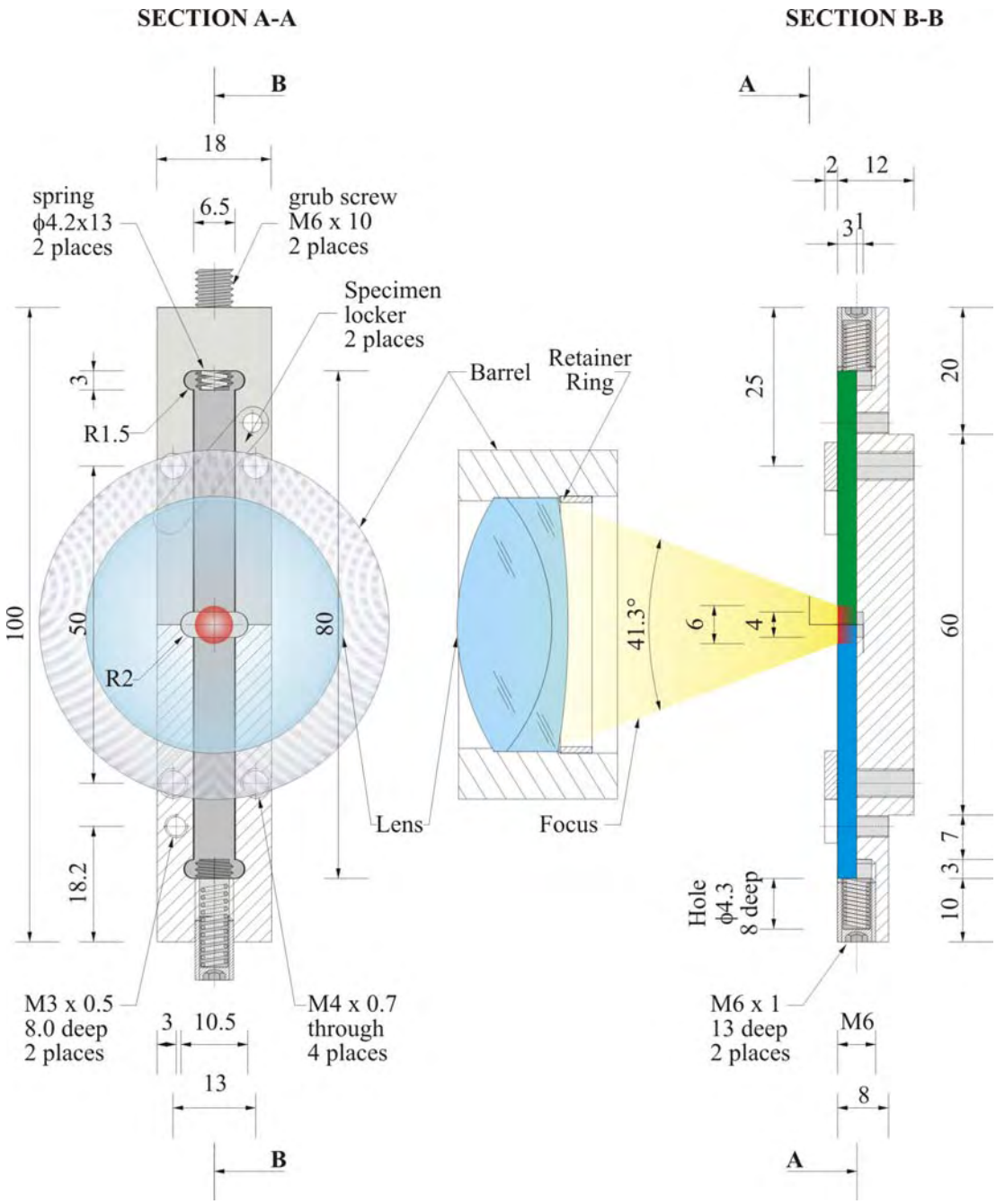

Clamping device for lap joining

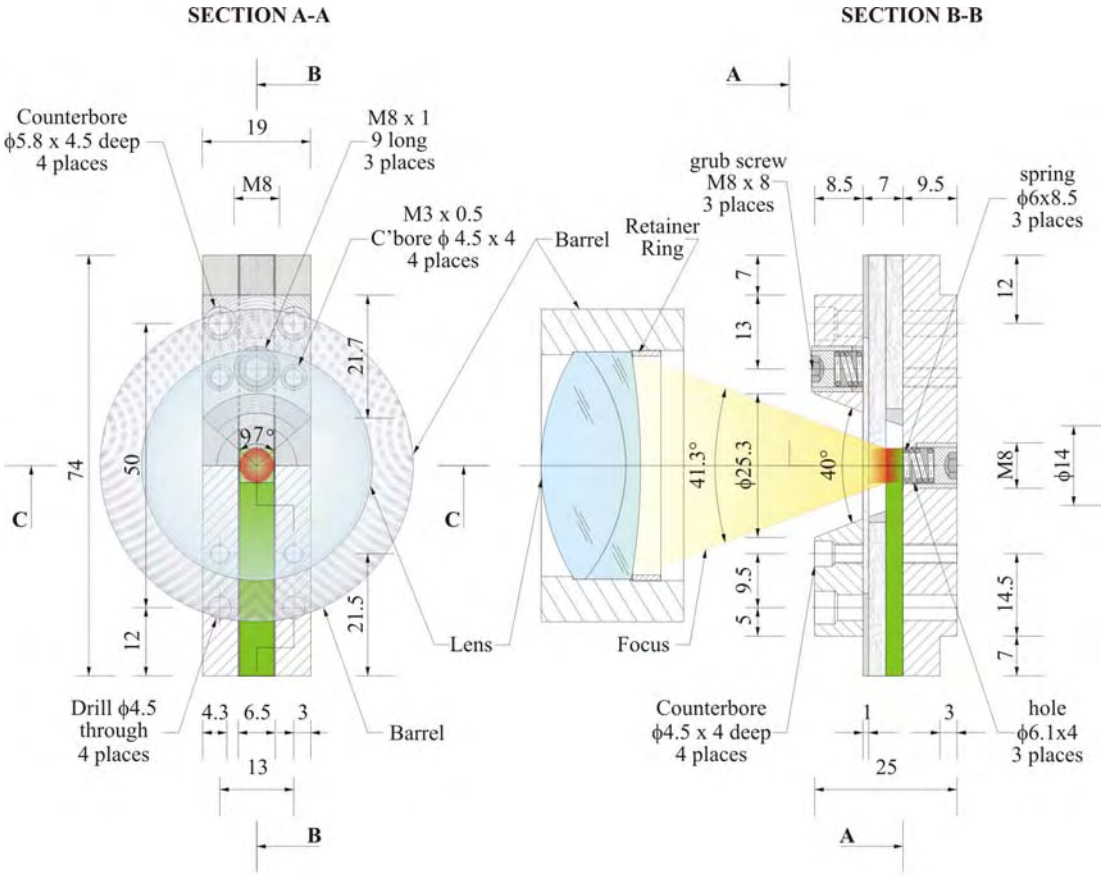

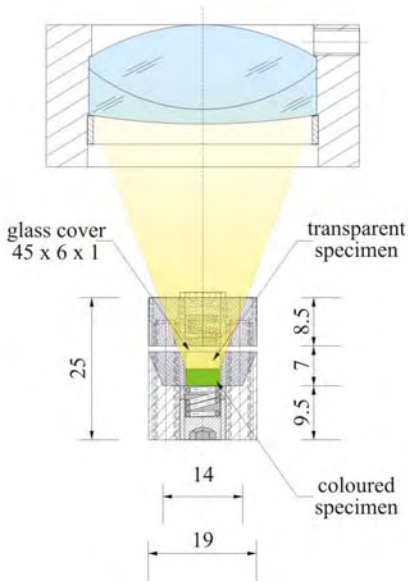

APPENDIX 7B. SOME 3D DESIGNS WITH THE SEC

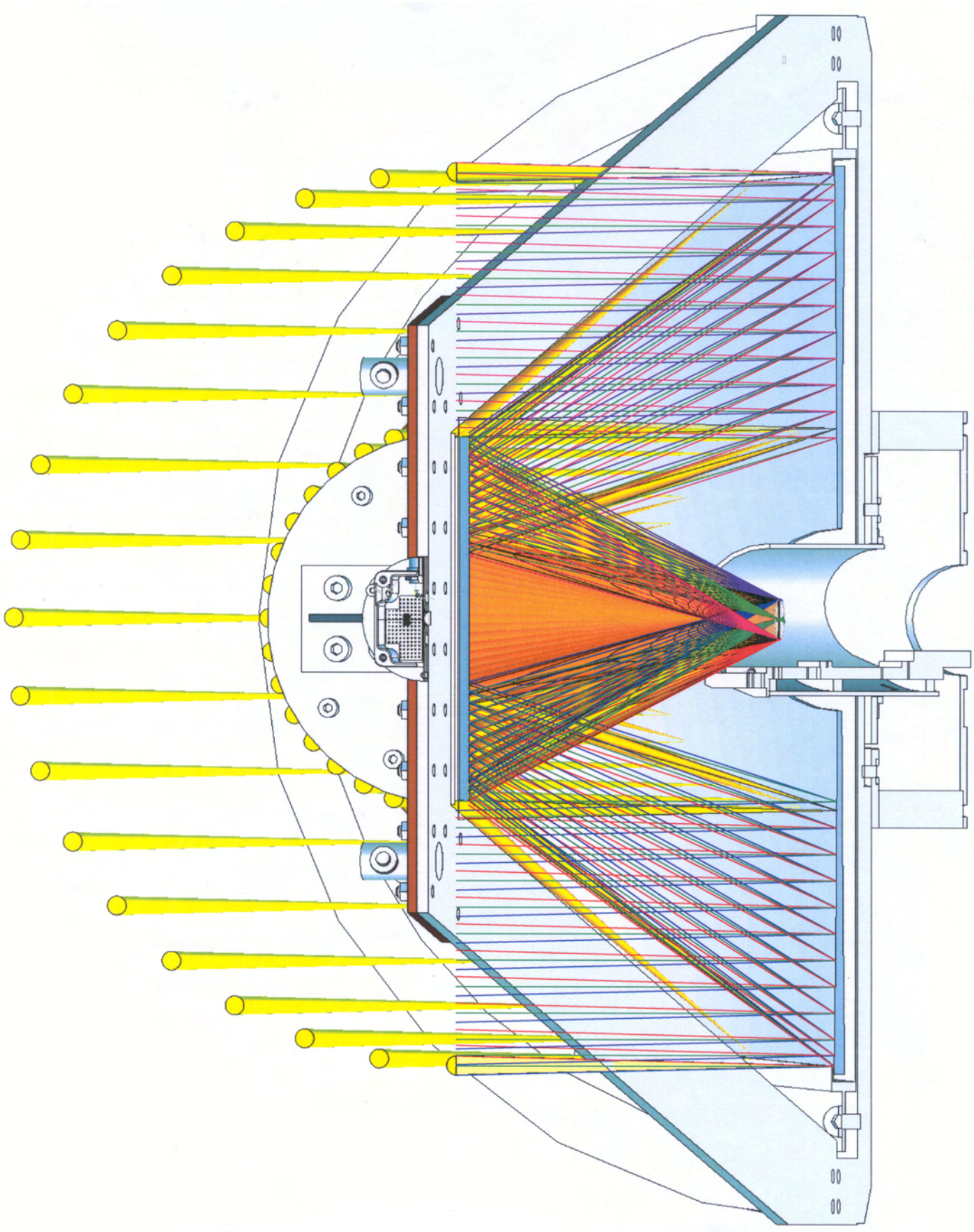

Figure 7B.1: Cassegrainian focus formation with rays and cones traced

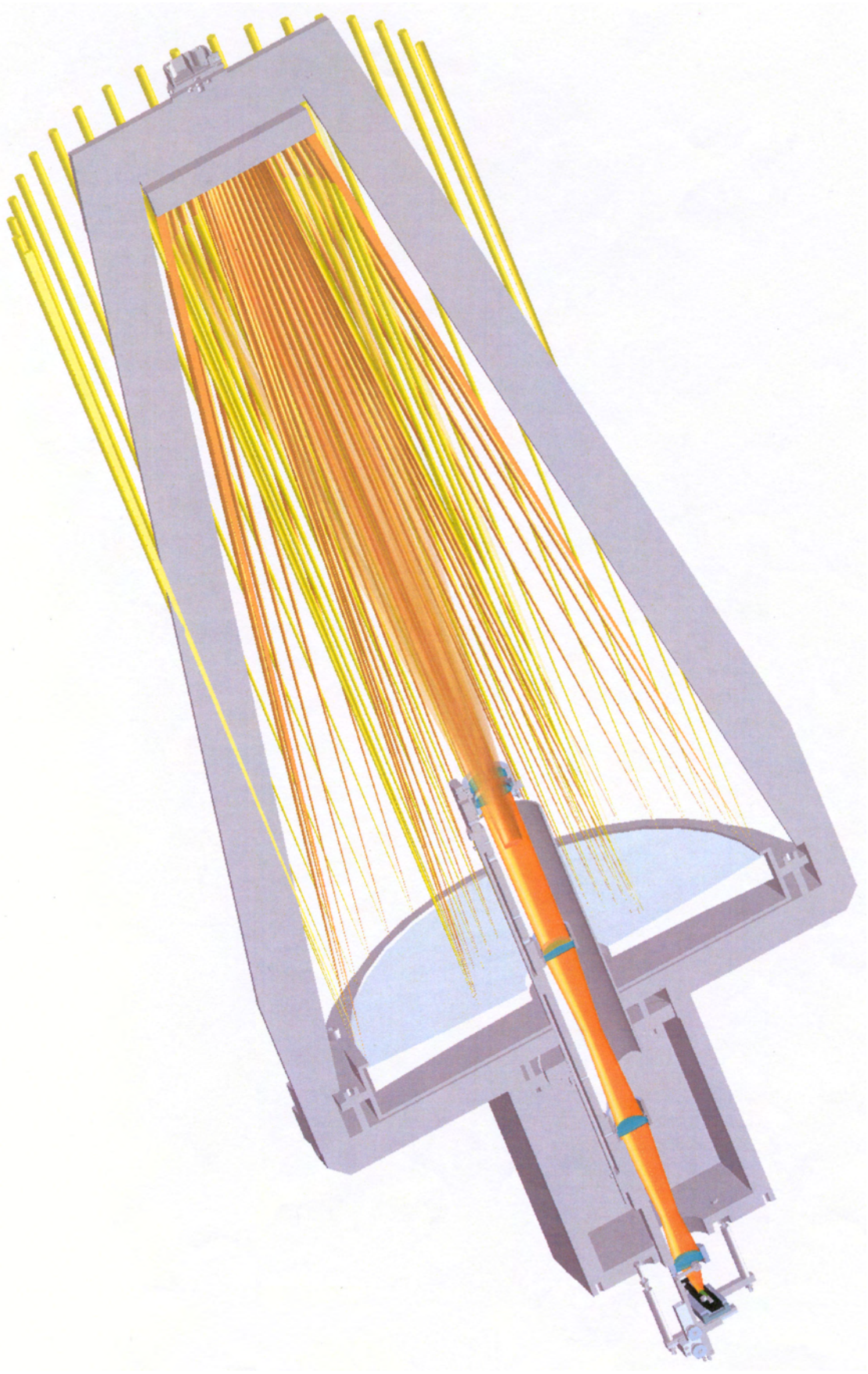

Figure 7B.2: First modification of the SEC with five conventional auxiliary lenses

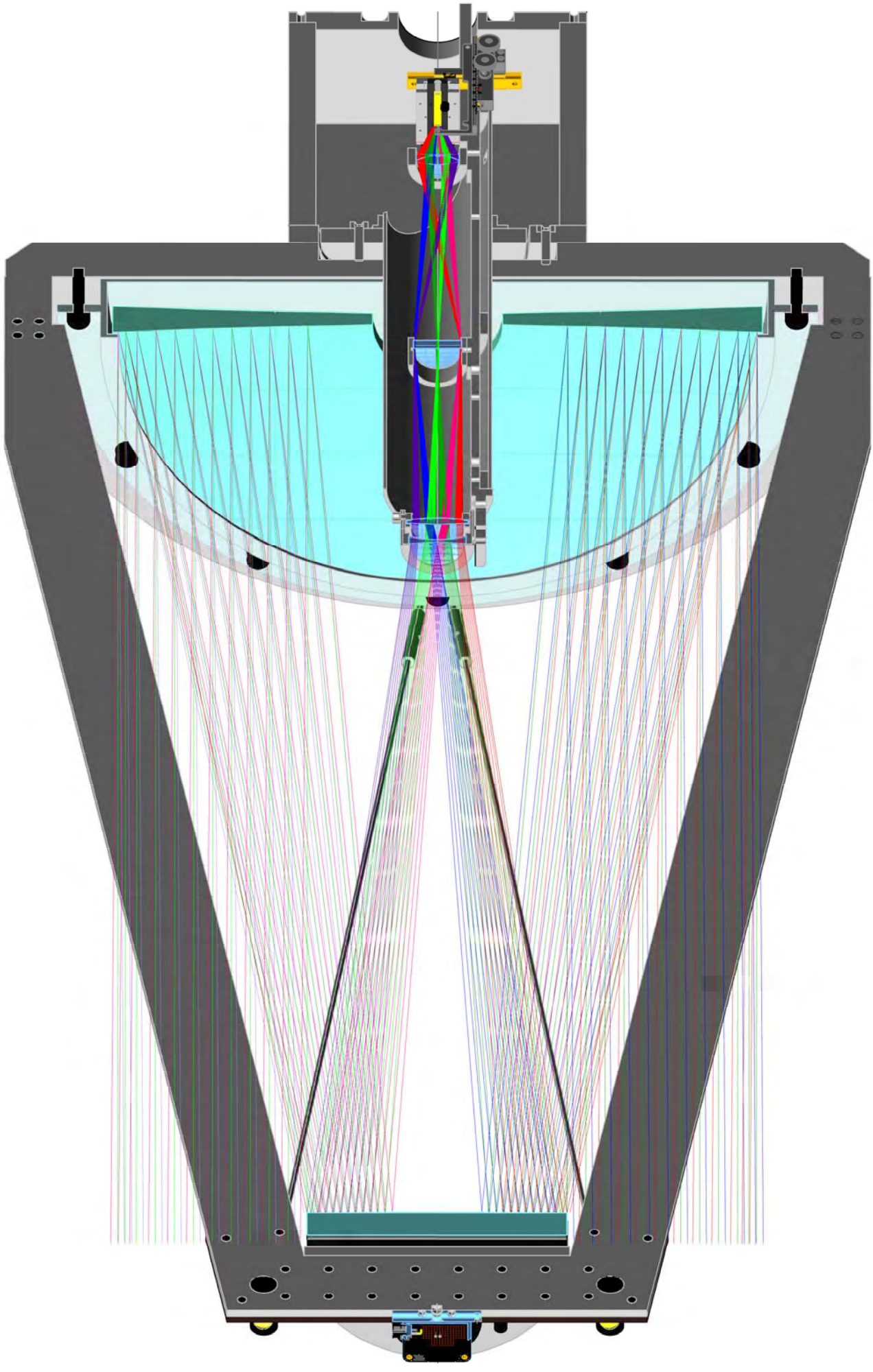

Figure 7B.3: Second modification of the SEC with four conventional auxiliary lenses

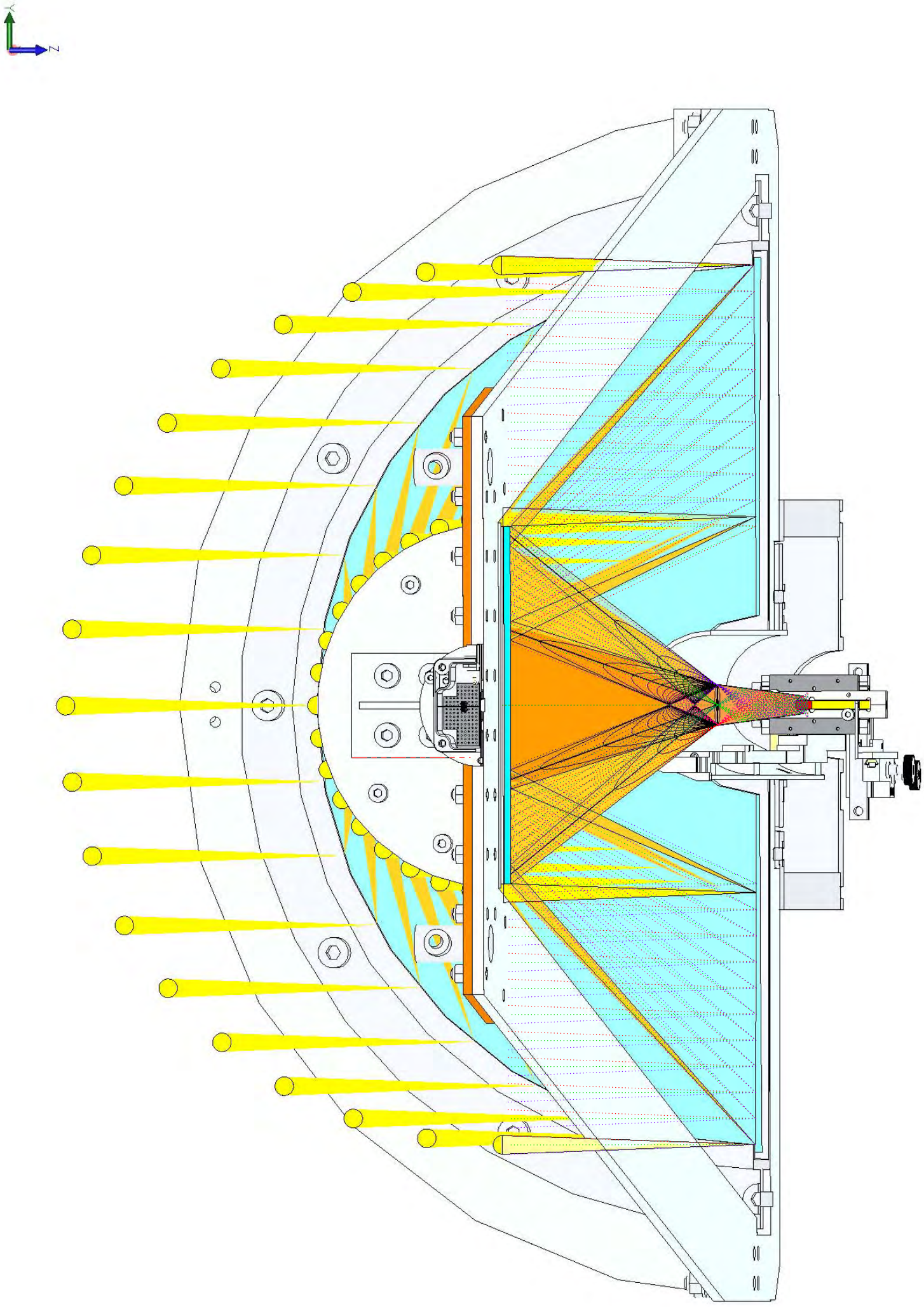

Figure 7B.4: SEC modification with an auxiliary truncated cone concentrator

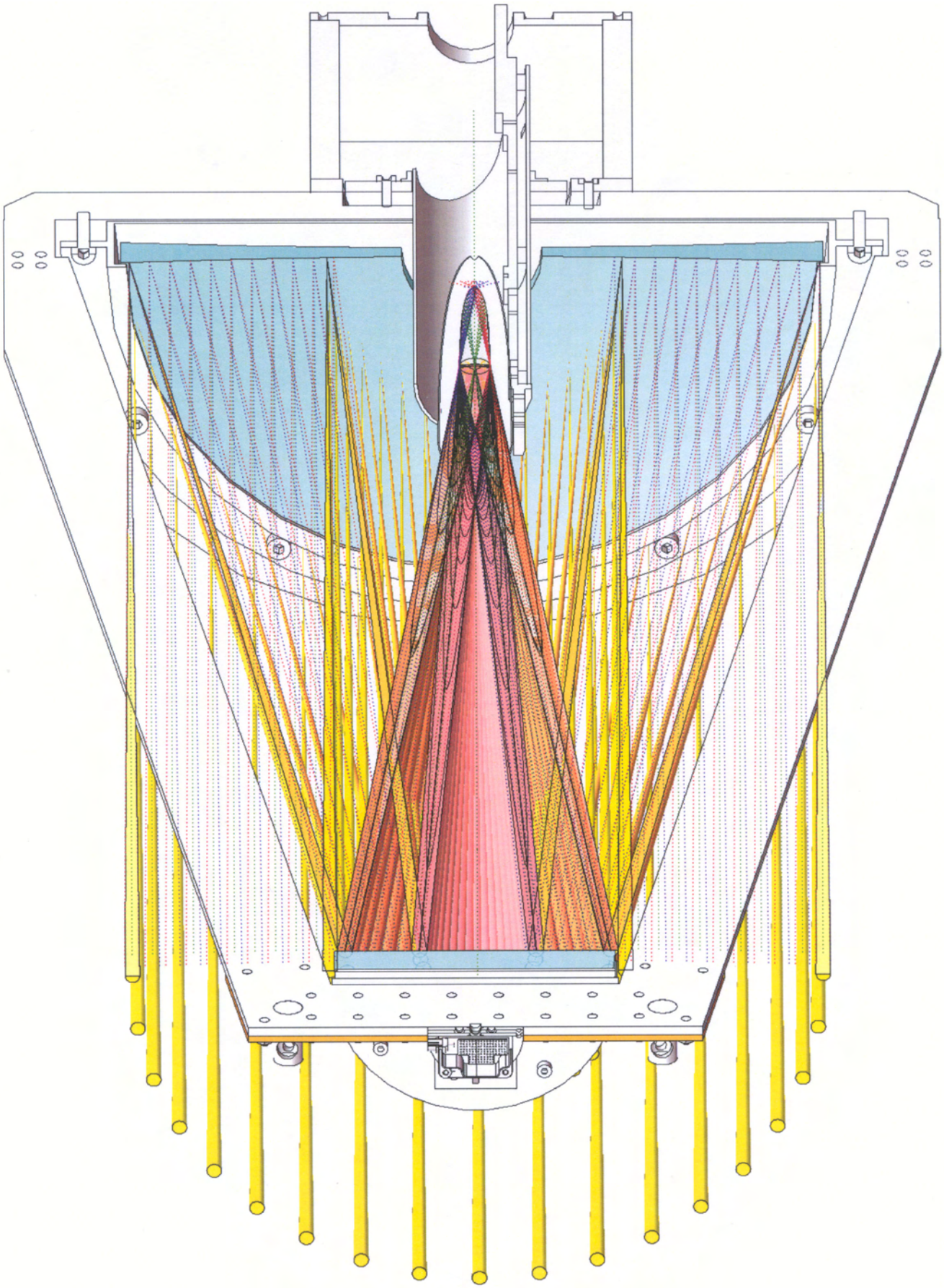

Figure 7B.5: SEC with both auxiliary CPCs and extreme cone rings and rays traced

APPENDIX 8.
EXPERIMENTAL THERMOPLASTIC JOINING RESULTS

Experimental results from butt joining of identically colored thermoplastics using imaging optics

Table A8.1: Experimental data from butt joining of polymers with identical colors using imaging optics

Specimen	Welding duration [s]	Average insolation intensity [W/m²]	Deposited solar energy [kJ]
Black + Black	23	935	1.521
	22	941	1.464
White + White	61	972	4.193
	58	973	3.991
Green + Green	70	949	4.698
	61	947	4.085
Violet + Violet	72	935	4.761
	71	921	4.624
Blue + Blue	75	969	5.140
	72	965	4.914
Red + Red	75	945	5.012
	80	940	5.318
Orange + Orange	99	957	6.700
	90	960	6.110
Yellow + Yellow	95	966	6.490
	101	964	6.886
Transparent + Transparent	181	961	12.301
	197	953	13.277

Experimental results from butt joining of identically colored thermoplastics using non-imaging optics

Table A8.2: Butt joining of polymers with identical colors using non-imaging optics

Specimen	#	Welding duration [s]	Average insolation intensity [W/m²]	Deposited solar energy [kJ]
Black + Black	1	17	871	1.257
	2	17	848	1.223
	3	11	889	0.830
White + White	1	24	866	1.764
	2	22	869	1.622
	3	25	869	1.844
Green + Green	1	19	855	1.379
	2	18	827	1.263
	3	16	877	1.191

Specimen	#	Welding duration [s]	Average insolation intensity [W/m²]	Deposited solar energy [kJ]
Violet + Violet	1	21	850	1.515
	2	20	861	1.461
	3	17	874	1.261
Blue + Blue	1	26	810	1.787
	2	24	861	1.754
	3	17	873	1.259
Red + Red	1	23	850	1.936
	2	23	897	1.615
	3	22	882	1.352
Orange + Orange	1	23	850	1.659
	2	23	897	1.751
	3	22	882	1.647
Yellow + Yellow	1	31	868	2.284
	2	30	898	2.286
	3	24	879	1.790
Transparent + Transparent	1	62	877	4.614
	2	71	869	5.236
	3	68	875	5.049

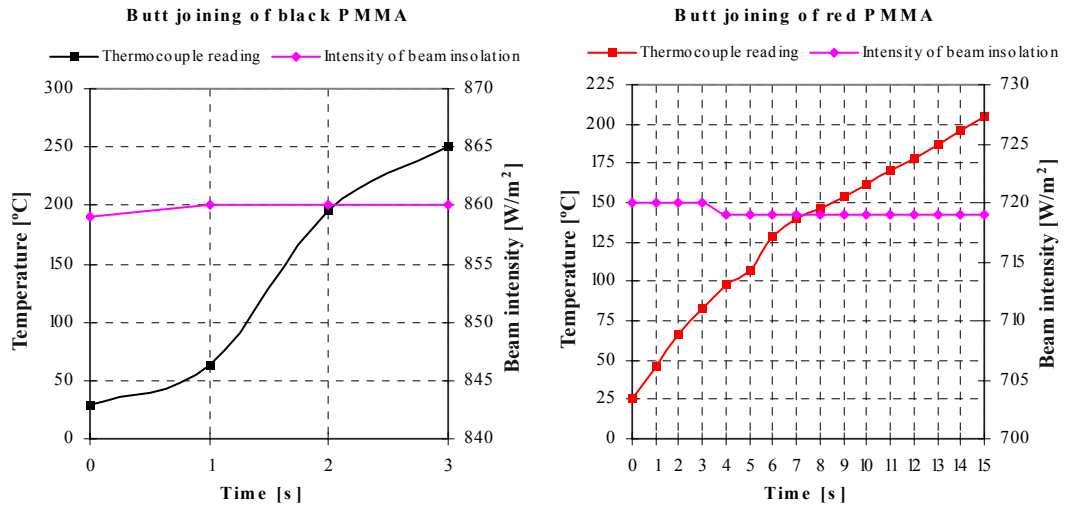

Figure A8.1: Temperature variation during butt joining of black and red PMMA

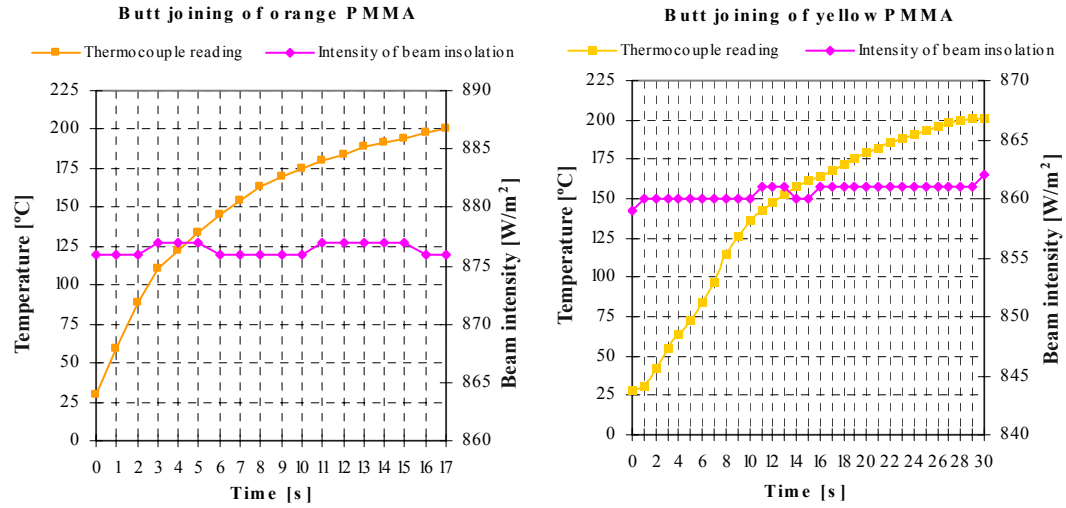

Figure A8.2: Temperature variation during butt joining of orange and yellow PMMA

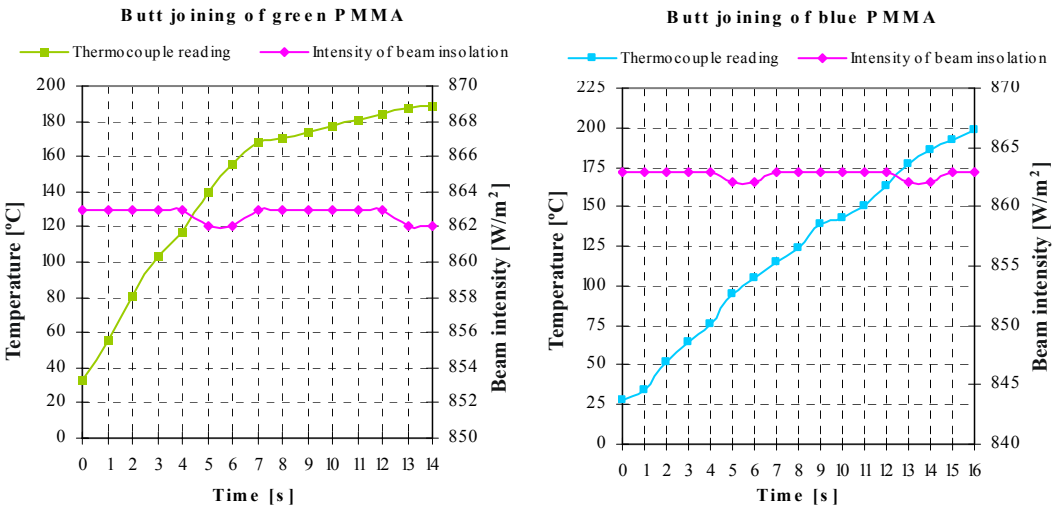

Figure A8.3: Temperature variation during butt joining of green and blue PMMA

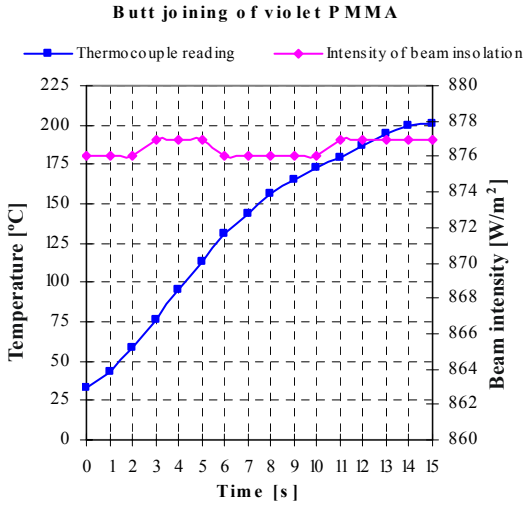

Figure A8.4: Temperature variation during butt joining of violet PMMA

Experimental results from butt joining of differently colored thermoplastics using imaging optics

Table A8.3: Welding of green PMMA as dominant color

Specimen	Welding duration [s]	Average insolation intensity [W/m²]	Deposited solar energy [kJ]
Green + Black	44	773	2.405
Green + White	63	796	3.546
Green + Violet	68	820	3.943
Green + Blue	71	781	3.921
Green + Red	72	770	3.921
Green + Orange	80	854	4.832
Green + Yellow	82	810	4.697
Green + Transparent	126	802	7.146

Table A8.4: Welding of violet PMMA as dominant color

Specimen	Welding duration [s]	Average insolation intensity [W/m²]	Deposited solar energy [kJ]
Violet + Black	45	1009	3.211
Violet + White	66	942	4.397
Violet + Green	69	1047	5.109
Violet + Red	71	935	4.695
Violet + Blue	77	950	5.173
Violet + Orange	81	958	5.488
Violet + Yellow	85	950	5.711
Violet + Transparent	131	952	8.820

Table A8.5: Welding of blue PMMA as dominant color

Specimen	Welding duration [s]	Average insolation intensity [W/m²]	Deposited solar energy [kJ]
Blue + Black	49	940	3.257
Blue + White	66	935	4.364
Blue + Green	69	957	4.670
Blue + Violet	73	948	4.894
Blue + Red	79	918	5.129
Blue + Orange	84	980	5.822
Blue + Yellow	86	955	5.808
Blue + Transparent	129	935	8.530

Table A8.6: Welding of red PMMA as dominant color

Specimen	Welding duration [s]	Average insolation intensity [W/m²]	Deposited solar energy [kJ]
Red + Black	50	854	3.020
Red + White	68	890	4.280
Red + Green	71	858	4.308
Red + Violet	73	863	4.455
Red + Blue	76	879	4.724
Red + Orange	81	878	5.029
Red + Yellow	88	884	5.501
Red + Transparent	132	895	8.355

Table A8.7: Welding of orange PMMA as dominant color

Specimen	Welding duration [s]	Average insolation intensity [W/m²]	Deposited solar energy [kJ]
Orange + Black	58	900	3.692
Orange + White	75	919	4.874
Orange + Violet	80	901	5.097
Orange + Green	83	906	5.318
Orange + Red	86	908	5.522
Orange + Blue	88	913	5.682
Orange + Yellow	90	919	5.849
Orange + Transparent	141	941	9.383

Table A8.8: Welding of yellow PMMA as dominant color

Specimen	Welding duration [s]	Average insolation intensity [W/m²]	Deposited solar energy [kJ]
Yellow + Black	60	921	3.908
Yellow + White	78	915	5.047
Yellow + Green	81	919	5.264
Yellow + Violet	83	922	5.412
Yellow + Blue	84	920	5.465
Yellow + Red	86	921	5.601
Yellow + Orange	87	919	5.654
Yellow + Transparent	143	933	9.435

Table A8.9: Welding of white ABS as dominant color

Specimen	Welding duration [s]	Average insolation intensity [W/m²]	Deposited solar energy [kJ]
White + Black	41	807	2.340
White + Green	65	899	4.133
White + Violet	66	843	3.935
White + Blue	68	867	4.169
White + Red	69	867	4.231
White + Orange	77	850	4.629
White + Yellow	80	904	5.114
White + Transparent	124	845	7.410

Tensile testing

Table 8.10: Tensile loads of differently colored specimens welded to yellow PMMA

Specimen	Peak load at failure [N]	Average peak load of control samples [N]	Tensile strength of joint [%]
Yellow + Black	264.8	1220.00	21.70
Yellow + Red	388.6	1226.00	31.70
Yellow + Orange	403.4	1248.00	32.32
Yellow + Green	752.2	1233.33	60.99
Yellow + Blue	421.0	1223.67	34.40
Yellow + Violet	408.0	1250.67	32.62
Yellow + White	380.8	673.73	56.52
Yellow + Transparent	398.2	1247.00	31.93

Table 8.11: Tensile loads of differently colored specimens welded to white ABS

Specimen	Peak load at failure [N]	Average peak load of control samples [N]	Tensile strength of joint [%]
White + Black	266.2	673.73	39.51
White + Red	403.0	673.73	59.82
White + Orange	382.0	673.73	56.70

Specimen	Peak load at failure [N]	Average peak load of control samples [N]	Tensile strength of joint [%]
White + Yellow	264.6	673.73	39.27
White + Green	368.2	673.73	54.65
White + Blue	339.4	673.73	50.38
White + Violet	325.2	673.73	48.27
White + Transparent	243.6	673.73	36.16

Table 8.12: Tensile loads of differently colored specimens welded to blue PMMA

Specimen	Peak load at failure [N]	Average peak load of control samples [N]	Tensile strength of joint [%]
Blue + Black	164.2	1220.00	13.46
Blue + Red	474.2	1226.00	38.68
Blue + Orange	416.8	1223.67	34.06
Blue + Yellow	416.8	1223.67	34.06
Blue + Green	478.4	1223.67	39.10
Blue + Violet	426.8	1250.67	34.13
Blue + White	355.8	673.73	52.81
Blue + Transparent	554.6	1222.00	45.38

Table 8.13: Tensile loads of differently colored specimens welded to violet PMMA

Specimen	Peak load at failure [N]	Average peak load of control samples [N]	Tensile strength of joint [%]
Violet + Black	245.6	1220.00	20.13
Violet + Red	486.2	1226.00	39.66
Violet + Orange	508.0	1248.00	40.71
Violet + Yellow	591.6	1250.67	47.30
Violet + Green	486.2	1233.33	39.42
Violet + Blue	445.2	1237.17	35.99
Violet + White	389.8	962.20	40.51
Violet + Transparent	398.3	1222.00	32.59

Table 8.14: Tensile loads of differently colored specimens welded to orange PMMA

Specimen	Peak load at failure [N]	Average peak load of control samples [N]	Tensile strength of joint [%]
Orange + Black	428.0	1220.00	35.08
Orange + Red	446.2	1226.00	36.39
Orange + Yellow	427.8	1248.00	34.28
Orange + Green	479.2	1233.33	38.85
Orange + Blue	494.8	1223.67	40.44
Orange + Violet	478.6	1248.00	38.35
Orange + White	330.0	673.73	48.98
Orange + Transparent	504.9	1222.00	41.32

Table 8.15: Tensile loads of differently colored specimens welded to red PMMA

Specimen	Peak load at failure [N]	Average peak load of control samples [N]	Tensile strength of joint [%]
Red + Black	385.4	1220.00	31.59
Red + Yellow	384.0	1226.00	31.32
Red + Orange	191.2	1226.00	15.60
Red + Green	499.0	1226.00	40.70
Red + Blue	479.6	1226.00	39.12
Red + Violet	392.2	1226.00	31.99
Red + White	299.4	673.73	44.44
Red + Transparent	466.9	1222.00	38.21

Table 8.16: Tensile loads of differently colored specimens welded to green PMMA

Specimen	Peak load at failure [N]	Average peak load of control samples [N]	Tensile strength of joint [%]
Green + Black	302.4	1220.00	24.79
Green + Red	428.5	1226.00	34.95
Green + Yellow	387.0	1233.33	31.38
Green + Orange	447.8	1233.33	36.31
Green + Blue	417.4	1223.67	34.11
Green + Violet	434.0	1233.33	35.19
Green + White	365.7	673.73	54.28
Green + Transparent	764.6	1227.67	62.28

Experimental results from lap joining of transparent and colored, similar and dissimilar thermoplastics using non-imaging optics

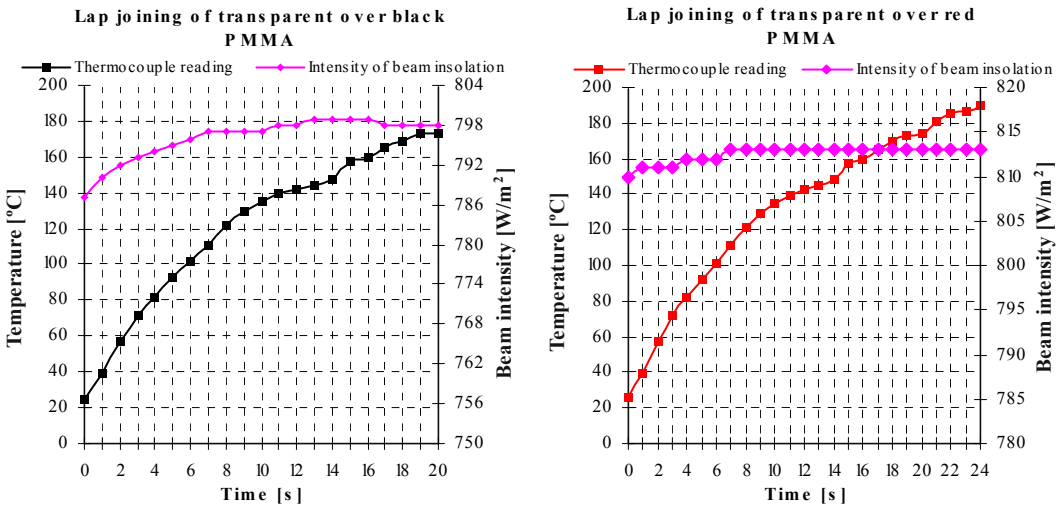

Figure A8.5: Temperature variation during lap joining of transparent PC over black PMMA and transparent PMMA over red PMMA

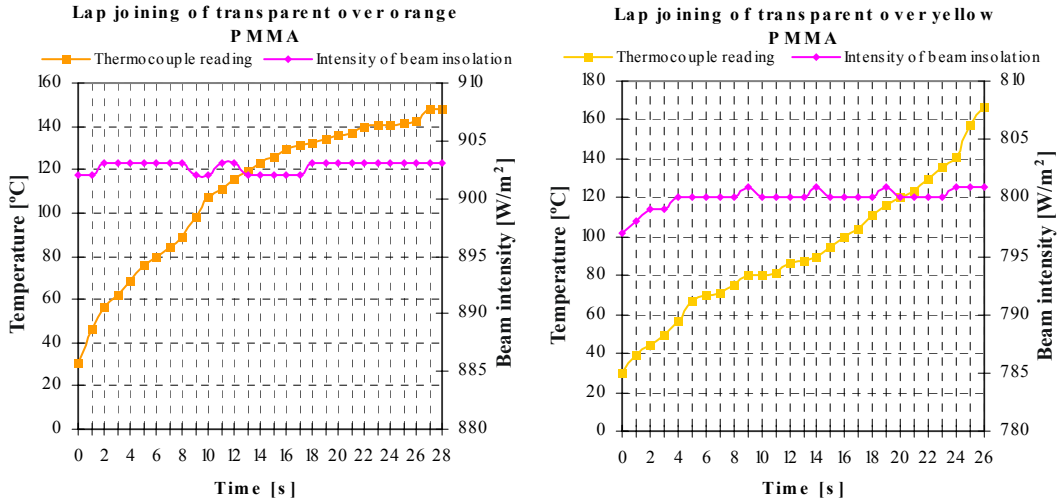

Figure A8.6: Temperature variation during lap joining of transparent over orange PMMA and transparent over yellow PMMA

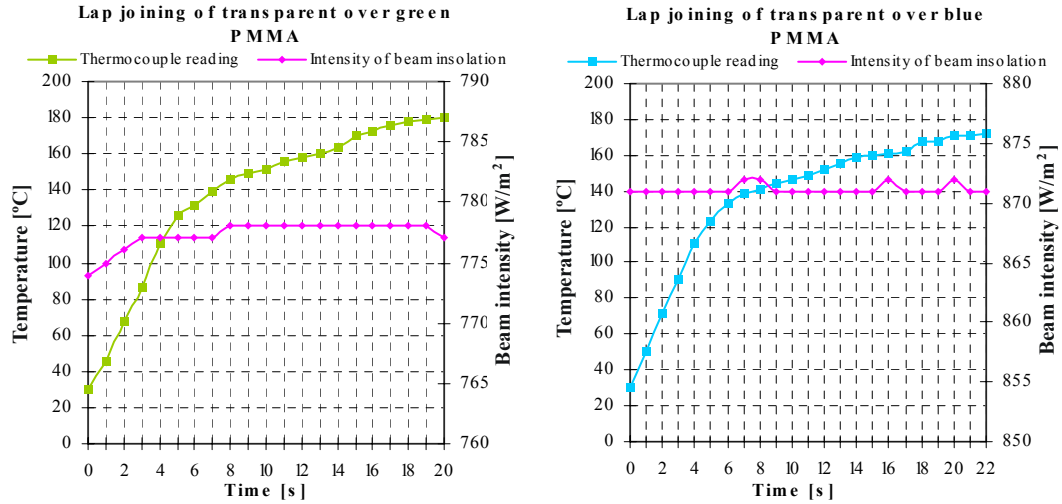

Figure A8.7: Temperature variation during lap joining of transparent over green PMMA and transparent over blue PMMA

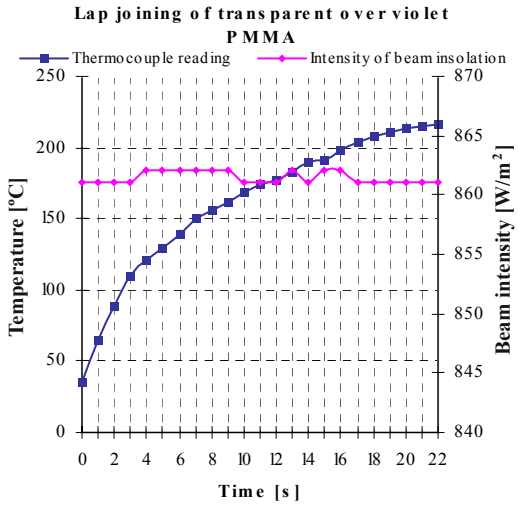

Figure A8.8: Temperature variation during lap joining of transparent over violet PMMA

APPENDIX 9.
EXPERIMENTAL RESULTS FROM STUDIES ON POLYMER AGEING

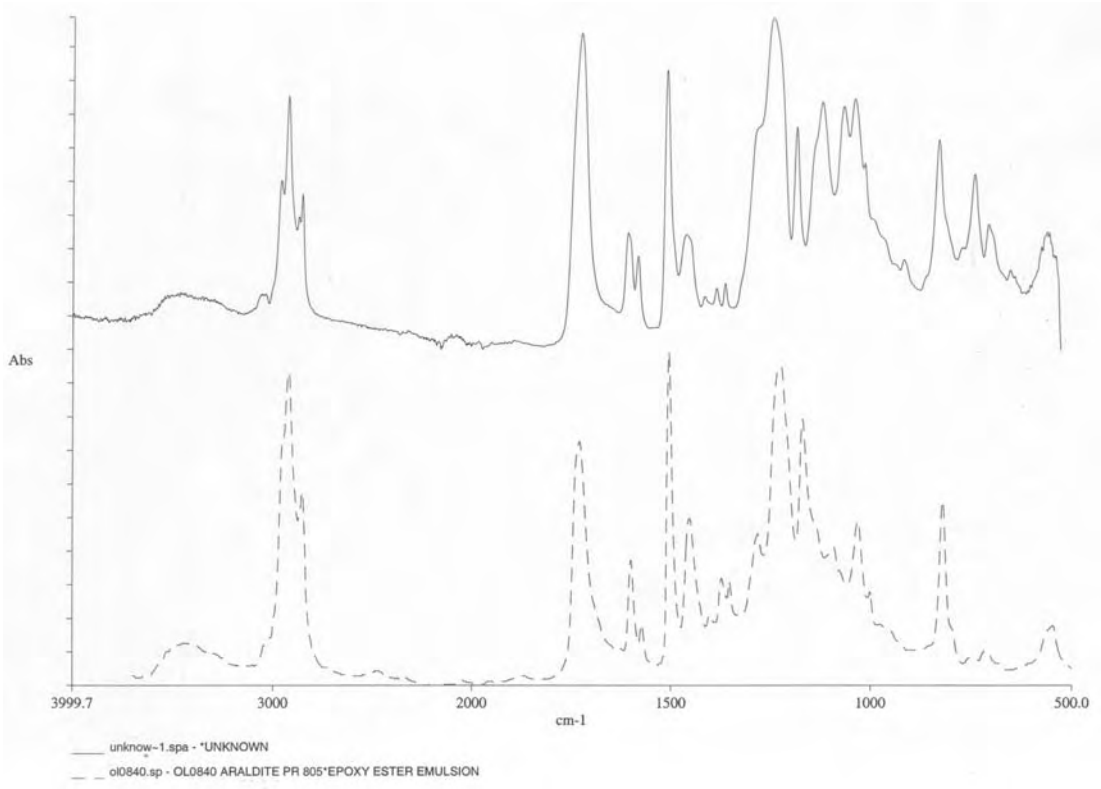

Figure 9A.1: Comparison FTIR absorption spectra of PSM-1 and Araldite PR 805 Epoxy Ester Emulsion

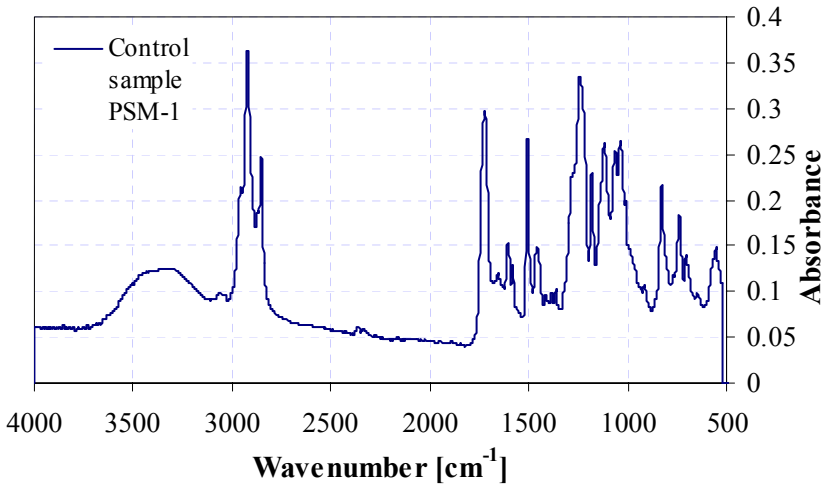

Figure 9A.2: FTIR absorption spectrum of unexposed PSM-1 sample

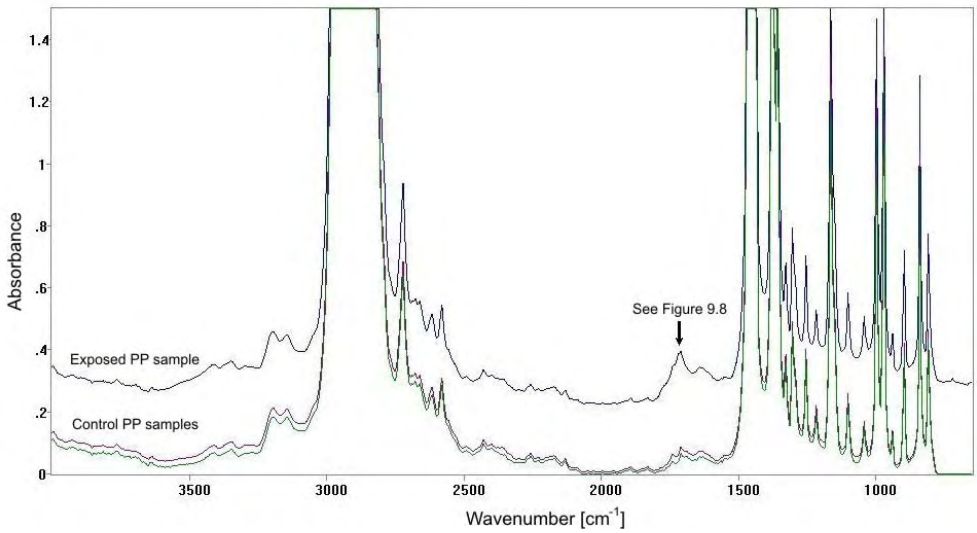

Figure 9A.3: Comparison FTIR absorption spectra of exposed and control PP samples

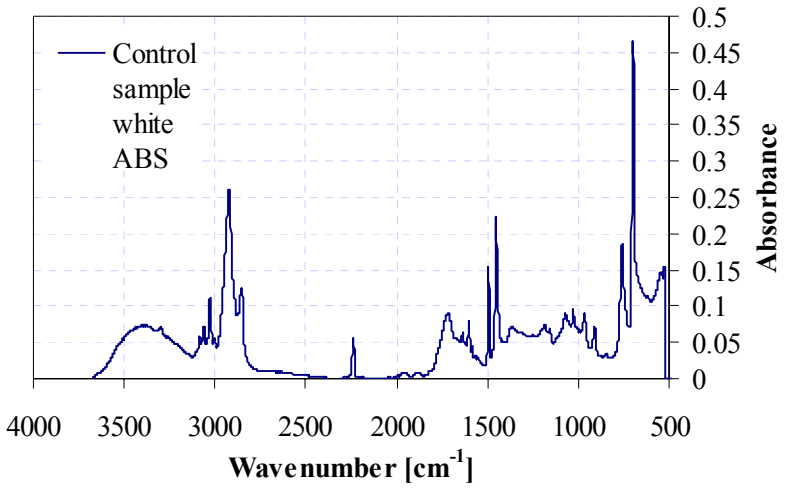

Figure 9A.4: FTIR absorption spectrum of unexposed white ABS

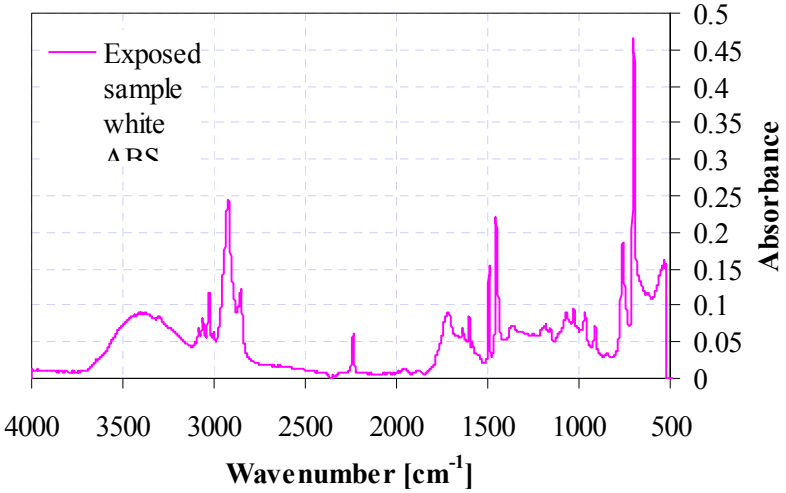

Figure 9A.5: FTIR absorption spectrum of exposed white ABS

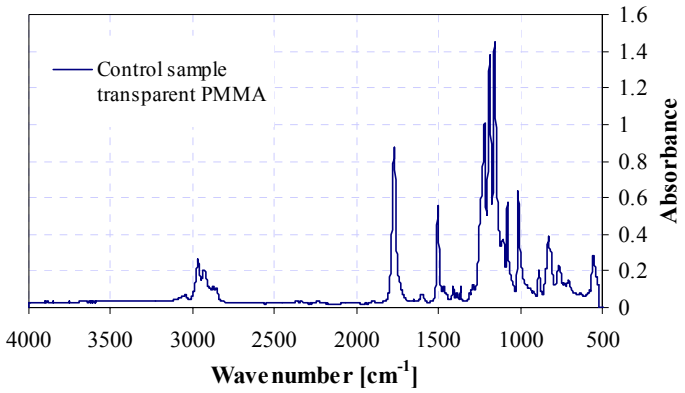

Figure 9A.6: FTIR absorption spectrum of unexposed transparent PMMA

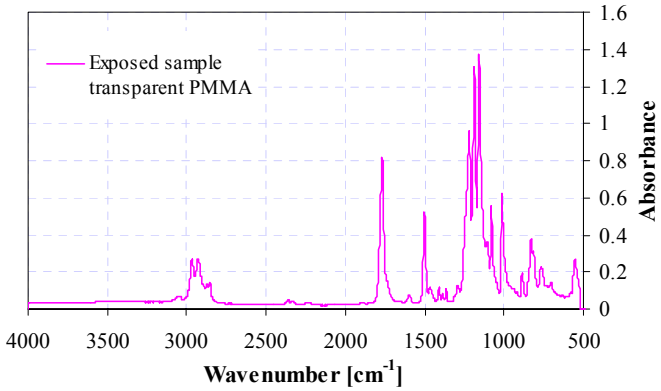

Figure 9A.7: FTIR absorption spectrum of exposed transparent PMMA

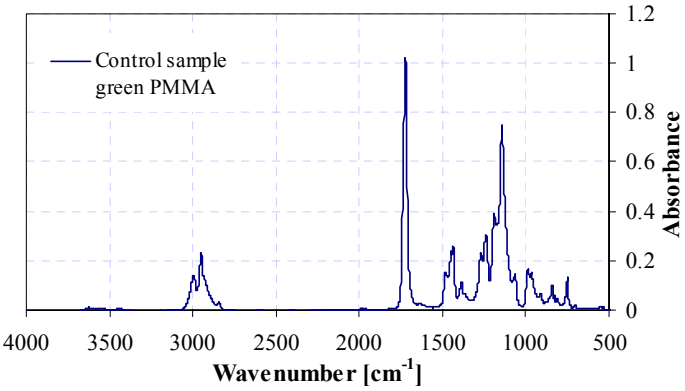

Figure 9A.8: FTIR absorption spectrum of unexposed green PMMA

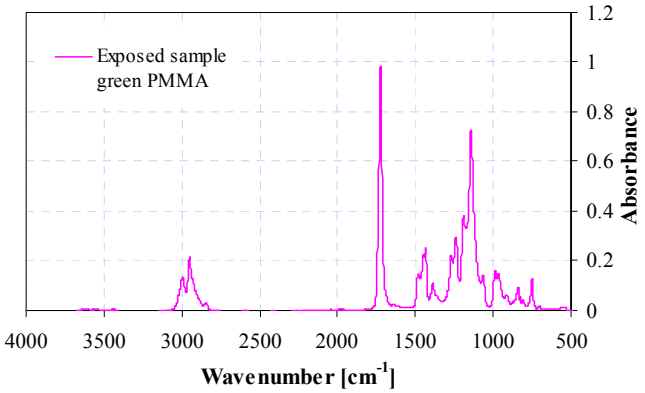

Figure 9A.9: FTIR absorption spectrum of exposed green PMMA

GLOSSARY

Absorbance, A – logarithm to the base 10 of the reciprocal of the internal transmittance T_i. $A=\log_{10}(1/T_i) = -\log_{10}T_i$ (ASTM-E284 2000).

Absorptance, α – the fraction of the incident radiant flux that is absorbed by a surface, particle or molecule etc. or the ratio of the absorbed radiant or luminous flux to the incident flux (ASTM-E284 2000).

Absorption – the transformation of radiant energy to a different form of energy by interaction with matter (ASTM-E284 2000).

Absorption coefficient, α – measure of the absorption of radiant energy from an incident beam (P_0) as it traverses an absorbing medium according to Bouguer's law , $P=P_0\, e^{-\alpha b}$, where b is the sample optical pathlength (ASTM-E131 1988).

Absorptivity, a – the absorbance divided by the product of the concentration, *c*, of the substance and the sample optical pathlength, *b*, *a=A/bc*. The units of *b* and *c* shall be specified (ASTM-E131 1988).

Achromat – a type of refractor objective made from lenses, usually two, of different materials, selected to bring two colors of light, usually blue and yellow, to the same focal point, thereby bringing the rest of the colors of visible light very near to the same focal point, thus making a decent stab at being in focus for all colors of visible light at the same time. That is, an achromat attempts to reduce longitudinal chromatic aberration. An achromat will also have spherical aberration corrected at one wavelength of light, usually green (Freeman 2002).

Aphelion – the point in its orbit where a planet is farthest from the sun.

Adherend – a body held to another body by an adhesive (ASTM-D907 2000).

Aplanatic telescope – telescope in which both primary and secondary mirrors are configured to remove spherical aberrations and coma.

Astigmatism – An aberration in optical system causing a point source to focus to a line rather than a point. In a reflecting optical system astigmatism occurs when an object point lies at some distance from the axis of the mirror. Thus, an incident ray makes an appreciable angle with the mirror axis.

Beam radiation – solar radiation from the sun that has not been scattered by dust or vapor in the atmosphere.

Chief ray – If there is no vignetting, and there are no aberrations, the chief ray is defined to be the ray that travels from a specific field point, through the center of the entrance pupil, and on to the image plane. Note that without vignetting or aberrations, any ray passing through the center of the entrance pupil will also pass through the center of the stop and the exit pupil (ZEMAX Optical Design Program User's Guide 2002).

Concentrator – an optical device (lenses or mirrors) that, as part of a solar collector, receives the unconcentrated solar irradiance and redirects (concentrates) it to a smaller area (the receiver or absorber).

Collector – see solar collector.

Concentration ratio – the ratio by which the flux density at the absorbing surface is increased.

Conjugate – Defines surface with perfect imaging at two points. The conjugate surface is defined by two user-specified points. The image surface is a reasonably good conjugate (that is, an image) of the object surface, so that rays coming from small patches of light on the object surface are imaged to patches of light on the image surface (ZEMAX Optical Design Program User's Guide 2002).

Cure – to change the physical properties of an adhesive by chemical reaction, which may be condensation, polymerization or vulcanization; usually accomplished by the action of heat and catalyst.

Dielectric – pertaining to the appearance of those materials for which the first surface reflectance is characteristic of the illuminant (ASTM-E284 2000).

Diffraction limited – The term diffraction limited implies that the performance of an optical system is limited by the physical effects of diffraction rather than imperfections in either the design or fabrication (OSLO Reference Manual 2001).

Diffuse reflectance, ρ_d – the ratio of the reflected flux to the incident flux, where the reflection is at all angles within the hemisphere bounded by the plane of measurement except in the direction of the specular reflection angle (ASTM-E284 2000).

Diffuse transmittance, T_d – the ratio of the flux transmitted by a specimen to the incident flux, the transmitted flux being measured at all forward angles except the regular transmission angle (ASTM-E284 2000).

Direct normal solar radiation – beam solar radiation measured perpendicular to the direction of the sun.

Extended source – a source of radiation with angular size exceeding the resolution achievable with the instrument used for its observation. An extended source of radiation can be resolved into a geometrical image.

F/number (F/#) – the expression denoting the ratio of the effective focal length to the aperture diameter.

Illuminance – The light density or luminous flux per unit area, incident on a surface.

Image Space F/number (IS F/#) – The infinite conjugate paraxial F/# in image space.

Index of refraction, n – the numerical expression of the ratio of the velocity of light in a vacuum to the velocity of light in a substance at a specified wavelength (ASTM-D542 2000). It depends on the frequency of the light (increasing with light frequency) because the light with different wavelength wiggles the charges with a different speed.

Insolation – the radiation from the sun received by the earth's surface, or the rate of such radiation per unit of surface. Stands for INcident (INcoming) SOLar radiATION.

Integrated irradiance – spectral irradiance integrated over a specific wavelength from λ_1 to λ_2, measured in W m^{-2}; Symbol: $G_{\lambda_1-\lambda_2} = \int_{\lambda_1}^{\lambda_2} G_\lambda d\lambda$.

Irradiation – the energy incident on a surface over some specified period of time, per unit area of surface. Occurs when a material is subjected to radiation.

Irradiance – the rate at which electromagnetic or radiant energy is incident on a surface, per unit area of surface. It has been often referred to as "flux" in the past.

Half solar rim angle, θ_{sun} – the semi-angle subtended by the sun. Also called angular half-width of the source (Rabl 1976).

Light – electromagnetic radiant power that is visually detectable by the normal human observer, radiant power having wavelengths from about 380 nm to about 780 nm (ASTM-E284 2000).

Marginal ray – the ray that travels from the center of the object, to the edge of the entrance pupil, and on to the image plane. The marginal ray defines the boundary of the cone of light diverging from an object point (ZEMAX Optical Design Program User's Guide 2002).

Meridional ray – any ray in common plane with the optical axis called meridional plane. If the system is a centered system (its axis is passing through the centers of curvature e.g. a simple lens), and if the optical axis is also contained in the plane of incidence, the ray is called a meridional ray, otherwise – a skew ray.

Numerical aperture (N.A.) – a measure of an optical device's light collecting power. $N.A. = n \sin\theta$, where n is index of refraction of the medium in which the optical device is located and θ is half of the collection angle.

Optical axis – an imaginary straight line passing through the center of curvature and the vertex of the optical surface. The optical axis is the axis of symmetry for non-spherical surfaces with rotational symmetry.

Optical efficiency – the efficiency at which a solar collector would operate if no thermal losses were considered.

Outdoor weathering – actual placement of specimens outdoors in specific locations, often those of climatic extremes. Note: This is differentiated from simulated weathering where instruments (weatherometers) are used to obtain very controlled conditions that simulate, to some degree, outdoor weathering results. Use of such instruments is described in ISO 10977.

Paraxial Working F/# – the defined conjugate paraxial F/# in image space.

Paraxial ray – a meridional or skew ray that has small angle with respect to the optical axis.

Perihelion – the point in its orbit where a planet is closest to the Sun.

Photon – a discrete quantity of electromagnetic energy or particle of light that acts as an individual unit of energy.

Phonon – a quantum of lattice vibrational energy, as a photon is quantum of electromagnetic energy (ASTM-F1389 2000).

Pinhole – a very small diameter hole in the surface of a material.

Point spread function (PSF) – the image of a point source of radiation, collected by an imaging device. A measure of the spatial fidelity of the device.

Point source – a source with small angular extent that could not be measured with currently existing equipment.

Polymerization – a chemical reaction in which the molecules of a monomer are linked together to form large molecules whose molecular weight is a multiple of that of the original substance. When two or more monomers are involved, the process is called copolymerization or heteropolymerization.

Post-cure – to cure by application of heat after the chemical exothermic reaction has subsided.

Pyrheliometer – an instrument using a collimated detector for measuring solar radiation from the sun and from a small portion of the sky around the sun at normal incidence.

Radiant flux, Φ, – the rate of flow of radiant energy, radiant power (ASTM-E284 2000).

Radiation – Electromagnetic form of energy that can be transmitted across space as well as through some materials.

Radiation flux – the energy passing through an imaginary plane per unit area per unit time and in all directions on one side of the imaginary plane. Flux differs from intensity in that the differential area for flux lies in a plane that forms the base of a hemisphere through which the radiation is passing, whereas differential area for intensity is perpendicular to the direction of propagation (adapted from Duffie and Beckman 1991).

Reciprocity law failure – non-equivalence in weathering results between a long exposure/low-intensity experiment and its counterpart with an equivalent intensity-time product where exposure time is short and intensity is high.

Reflectance, ρ – ration of the reflected radiant or luminous flux to the incident flux in the given conditions (ASTM-E284 2000).

Reflection – of radiant energy, the process by which radiant energy is returned from a material or object (ASTM-E284 2000).

Rim angle, ϕ - the semi-angle subtended by the parabola from the center of the focal plane.

Sagitta – the vertical depth of the curve of a spherical mirror, sometimes called surface sag.

Skew (oblique) ray – any non-meridional ray.

Solar collector – the total system including a receiver (which includes an absorber) and a concentrator or optical system (Duffie and Beckman 1991).

Solar irradiance, direct – solar flux coming from the solid angle of the sun's disk incident on a surface perpendicular to the axis of that solid angle. In conventional instruments the acceptance cone includes a plane angle of about 6° (ASTM-E772 1993).

Solar absorptance – the ratio of absorbed to incident solar energy (equal to unity minus the reflectance and transmittance) (ASTM-E424 1993).

Solar reflectance – the percent of solar radiation (watts/unit area) reflected by a material (ASTM-E424 1993).

Solar transmittance – the percent of solar radiation (watts/unit area) transmitted by a material (ASTM-E424 1993).

Solid angle – the three-dimensional analogue of the solar rim angle - $2\theta_{sun}$.

Spectrum – the spatial arrangement of components of radiant power in order of wavelength (ASTM-E284 2000).

Spectroscopic – derived from both Latin: spectrum meaning "an appearance or image" and Greek: skopean meaning "to view".

Specular – pertaining to flux reflected from the surface of an object, without diffusion, at the specular angle (ASTM-E284 2000). The word "specular" is derived from Latin "speculum", or mirror.

Specular reflection – reflection without diffusion in accordance with the laws of optical reflection, as in a mirror (ASTM-E284 2000).

Substrate – as related to adhesives, a material upon which the adhesive is applied (ASTM-D907 2000).

Sunlight – the portion of solar radiation which is detectable by human eye (about 44% of the total solar energy).

Sunshine duration – the sum of all time periods during the day when the direct solar irradiance equals or exceeds 120 W/m^2 (Australian Bureau of Meteorology).

Sun-tracking – term used to describe solar collectors that track the sun - for example from the East in the morning to the West in the evening - in order to maximize the amount of solar radiation intercepted.

Tensile strength, σ_t – the maximum tensile stress sustained by a test specimen during a tensile test (AS1145.1 2001).

*Terms ending in "**ivity**"* – Terms ending in "ivity" designate characteristics of materials, normally independent of size or shape, sometimes called "specific properties". Examples: conductivity and resistivity.

*Terms ending in "**ance**"* – Terms ending in "ance" designate properties of a particular object, depending not only on the material, but also upon size and shape, sometimes called "total quantities". Examples: conductance and transmittance.

*Terms ending in "**ion**"* – Terms ending in "ion" designate time rate of the process of transfer, flux, flow rate. Examples: conduction and transmission. (ASTM-C108 1998)

Thermal resistance – the ability of a material to resist the flow of heat. Degrees, per unit of heat flow rate, for a particular body or setup (where the area may not be known) (ASTM-C108 1998).

Transducer – device that converts energy from one form to another.

Transmission – of the radiant energy, the process whereby radiant energy passes through a material or object (ASTM-E284 2000).

Transmittance, τ – the ratio of transmitted flux to incident flux, under specified geometric and spectral conditions (ASTM-E284 2000).

Vertex – the local origin of coordinates to which the surface function is referred.

Vignetting - a term that refers to the reduction in aperture of a system caused by the axial separation of two apertures.

Wavefront – an imaginary surface joining all points in space that are reached at the same instant by a wave propagating through a medium. A surface connecting all field points (of electromagnetic energy) that are equidistant from the source. For parallel rays the wavefront is plane, for diverging from or converging toward a point the wavefront is considered spherical. For rays with varying divergence or convergence, the wavefront has other shapes, such as ellipsoidal and paraboloidal, depending on the nature of the source. In a light beam a wavefront is a surface in space in which all points have the same instantaneous phase ϕ (see Equation 2.2).

Wavenumber – a reciprocal value of wavelength.

Weatherometers – xenon-arc-based instruments that approximate the outdoor exposure and provide controllable temperature, relative humidity, moisture (rain) and day-night cycling. However, they do not take climatological fluctuations or environmental pollutants into account.

REFERENCES

Alimov, A. K. and Alavutdinov, D. N. (1979). Two-mirror Unit Plane and Hyperboloidal Counter-Reflectors. Applied Solar Energy **15**(3): 42-44.

Anantharaman, S. and Benatar, A. (2003). Measurement of Residual Stresses in Clearwelds using Photoelasticity. ANTEC 2003 Conference Proceedings. 1051-1055.

AS1145.1 (2001). Determination of Tensile Properties of Plastic Materials. Part 1: General Principles. Homebush, NSW, Standards Australia.

AS1745.1 (1989). Outdoor Weathering of Plastics in the Australian Environment, Part 1: Commercial Products. Homebush, NSW, Standards Australia.

AS1745.2 (1989). Outdoor Weathering of Plastics in the Australian Environment, Part 2: Guide for Design Purposes. Homebush, NSW, Standards Australia.

AS1886 (1991). Glossary of Terms Relating to Plastics. Homebush, NSW, Standards Australia.

AS2535 (1986). Solar Collectors with Liquid as the Heat Transfer Fluid Method of Testing Thermal Performance. Homebush, NSW, Standards Australia.

AS/NZS2243.5 (2004). Safety in Laboratories - Non-ionizing Radiations - Electromagnetic, Sound and Ultrasound. Homebush, NSW, Standards Australia.

ASHRAE Handbook (1977). American Society of Heating, Refrigerating and Air-Conditioning Engineers.

ASTM-C108 (1998). Standard Symbols for Heat Transmission, American Society for Testing and Materials.

ASTM-D542 (2000). Standard Test Method for Index of Refraction of Transparent Organic Plastics, American Society for Testing and Materials.

ASTM-D883 (2000). Standard Terminology Relating to Plastics, American Society for Testing and Materials.

ASTM-D907 (2000). Standard Terminology of Adhesives, American Society for Testing and Materials.

ASTM-D1002 (1999). Standard Test Method for Apparent Shear Strength of Single-Lap-Joint Adhesively Bonded Metal Specimens by Tension Loading (Metal-to-Metal), American Society for Testing and Materials.

ASTM-D1084 (1996). Standard Test Method for Solar Transmittance (Terrestrial) of Sheet Materials Using Sunlight, American Society for Testing and Materials.

ASTM-D2093 (1997). Standard Practice for Preparation of Plastics Prior to Adhesive Bonding, American Society for Testing and Materials.

ASTM-D3163 (2001). Standard Test Method for Determining Strength of Adhesively Bonded Rigid Plastic Lap-Shear Joints in Shear by Tension Loading, American Society for Testing and Materials.

ASTM-D3418 (1999). Standard Test Method for Transition Temperatures of

Polymers By Differential Scanning Calorimetry, American Society for Testing and Materials.

ASTM-E131 (1988). Standard Terminology Relating to Molecular Spectroscopy, American Society for Testing and Materials.

ASTM-E284 (2000). Standard Terminology of Appearance, American Society for Testing and Materials.

ASTM-E424 (1993). Standard Test Method for Solar Energy Transmittance and Reflectance (Terrestrial) of Sheet Materials, American Society for Testing and Materials.

ASTM-E473 (2000). Standard Terminology Relating to Thermal Analysis, American Society for Testing and Materials.

ASTM-E490 (2000a). Solar Constant and Zero Air Mass Solar Spectral Irradiance Tables, American Society for Testing and Materials.

ASTM-E772 (1993). Standard Terminology Relating to Solar Energy Conversion, American Society for Testing and Materials.

ASTM-F1389 (2000). Standard Test Methods for Photoluminescence Analysis of Single Crystal Silicon for III-V Impurities, American Society for Testing and Materials.

ASTM-G90 (1999). Standard Practice for Performing Accelerated Outdoor Weathering of Nonmetalic Materials Using Concentrated Natural Sunlight, American Society for Testing and Materials.

ASTM-G113 (1994). Standard Terminology Relating to Natural and Artificial Weathering Tests of Nonmetalic Materials, American Society for Testing and Materials.

AWSG (2003). Atlas Material Testing Technology LLC. www.atlaswsg.com.

AZTEST (2002). Arizona Desert Testing. www.aztest.com.

Bachmann, C. (1995). Expanding Capabilities with UV/Visible Light Cure Adhesives. Adhesives Age. (April): 14-20.

Baeyens, J., Smolders, K. and Vandewalle, C. (2002). Thermal Degradation of PMMA in Fluidized Beds. 2nd International Symposium on Feedstock Recycling of Plastics, Belgium.

Baranov, V. K. (1965). Opt. Mekh. Prom. **6**(1-5).

Baranov, V. K. and Melnikov, G. K. (1966). Study of the Illumination Characteristics of Hollow Focons. Soviet Journal of Optical Technology **33**: 408-411.

Beevers, A. (1991). Welding: The Way Ahead of Thermoplastics? Engineering. (231): 11-12.

Bendada, A., Cole, K., Lamontagne, M. and Simard, Y. (2003). A Hollow Waveguide Infrared Thermometer for Polymer Temperature Measurement during Injection Moulding. J. Opt. A: Pure Appl. Opt. **5**: 464-470.

Beshears, D. L., Capps, G. J., Earl, D. D., Jordan, J. K., Maxey, L. C. and Muhs, J. D. (2003). Tracking Systems Evaluation for the "Hybrid Lighting System". International Solar Energy Conference ISEC 2003, Hawaii, USA.

Birley, A. W. and Scott, M. J. (1982). Plastics Materials. Glasgow, Leonard Hill.

Blaga, A. (2002). Plastics in Glazing and Lighting Applications. CBD-213. Canadian Building Digest, National Research Council Canada.

Bliss, R. (1957). Designing Solar Furnace for Specific Performance. Solar Energy **1**(2-3): 55-62.

Bonten, C. and Tuchert, C. (2000). Welding of Plastics: Introduction into Heating by Radiation. ANTEC 2000. **1**: 1138-1142.

Born, M. and Wolf, E. (1999). Principles of Optics: Electromagnetic Theory of Propagation, Interference, and Diffraction of Light, 7th ed. Cambridge, England: Cambridge University Press.

Boxhammer, J. (1999). Surface Temperatures and Temperature Measurement Techniques on the Level of Exposed Samples During Irradiation/Weathering in Equipment. Weathering of Plastics. New York, ChemTec Publishing. pp 105-119.

Boxhammer, J. (2001). Shorter Test Times for Thermal- and Radiation-Induced Ageing of Polymer Materials, Part I: Acceleration of Increased Irradiance and Temperature in Artificial Weathering Tests. Polymer Testing **20**(7): 719-724.

Boxhammer, J., Kockott, D. and Trubiroha, P. (1993). Temperature Measurement of Polymer Surfaces During Weathering Tests. Material-Prufung **35**: 143-147.

Caldwell, S. and Grewell, D. A. (2003). Optical Correction for Heat Buildup in the Center of TTIr Plastic Welds. ANTEC 2003. 1134-1139.

Cariou, J. M., Dugas, J. and Martin, L. (1982). Transport of Solar Energy with Optical Fibers. Solar Energy **29**(5): 397-406.

Carter, J. (1992). Solar Tracking Device Having Three Sensors Separated by Four Semicircular Vanes. US Pat. No. 5148012.

Caryl, C. and Helmick, W. (1960). Apparatus and Mechanism for Concentrating Solar Rays on Objects To Be Tested. US Pat. No. 2945417.

Caykara, T. and Guven, O. (1999). UV Degradation of Poly(methyl methacrylate) and its Vinyltriethoxysilane Containing Copolymers. Polymer Degradation and Stability **65**(2): 225-229.

Cengel, Y. A. (2003). Heat Transfer: A Practical Approach. New York, McGraw-Hill.

Chen, Y. S. and Benatar, A. (1995). Infrared Welding of Polypropylene. ANTEC 1995, Society of Plastics Engineers.

Chiantore, O., Trossarelli, L. and Lazzari, M. (2000). Photoxidative Degradation of Acrylic and Metacrylic Polymers. Polymer **41**: 1657-1668.

Clemens, B. (1990). Materials Processing and Synthesis. Proceedings of a Workshop Potential Applications of Concentrated Solar Energy, Colorado, USA, National

Academy Press. 59-63.

Cobble, M. H., Hull, W. C. and Hays, R. A. (1978). Analysis of a Cassegrainian Solar Furnace. Optics Applied to Solar Energy IV **161**.

Collares-Pereira, M., Gordon, J., Rabl, A. and Winston, R. (1991). High Concentration Two Stage Optics for Parabolic Through Solar Collectors with Tubular Absorber and Large Rim Angle. Solar Energy **47**: 457-466.

Colom, X., Garcia, T., Sunol, J., Saurina, J. and Carrasco, F. (2001). Properties of PMMA Artificially Aged. Journal of Non-crystalline Solids **287**: 308-312.

Cowley, P. R. and Melville, H. W. (1952). Proceedings Royal Society, A210, p.461, London.

Crase, R. and Scott, K. (2002). Coatings That Weather the Testing Storm. www.ptbmagazine.com/Jan00/ptb.0100coat.html.

Crewdson, L. (1992). Correlation of Outdoor and Laboratory Accelerated Weathering Tests at Currently Used and Higher Irradiance Levels - Part II. Materials Life Society. First International Symposium on Weathering, Japan.

Crewdson, L. and Scott, K. (1994). A comparison of Experimental High Irradiance and Standard SAE Weathering Tests for Automotive Exterior Materials. International Congress of Society of Automotive Engineers, Detroit Michigan.

Domininghaus, H. (1988). Plastics for Engineers: Materials, Properties, Applications. Hanser, Germany.

Duffie, J. A. and Beckman, W. A. (1991). Solar Engineering of Thermal Processes, John Wiley & Sons Inc. Publication.

Dye, D., Wood, B., Fraas, L. and Muhs, J. (2003). Optical Design of an Infrared Non-imaging Device for a Full-spectrum Solar Energy System. International Solar Energy Conference ISEC 2003, Hawaii, USA.

Fechine, C. J. M., Rabello, M. S. and Souto-Mair, R. M. (2002). The Effect of UV Stabilizers on the Photodegradation of Poly(ethylene Terephthalate). Polymer Degradation and Stability **75**: 153-159.

Feuermann, D., Gordon, J. and Huleihil, M. (2002). Solar Fiber-optic Mini-dish Concentrators: First Experimental Results and Field Experience. Solar Energy **72**(6): 459-472.

Feuermann, D. and Gordon, J. M. (1998). Solar Surgery: Remote Fiber Optic Irradiation with Highly Concentrated Sunlight in lieu of Lasers. Optical Engineering **37**(10): 2760-2767.

Feuermann, D., Gordon, J. M. and Ries, H. (1999). High Flux Solar Concentration with Imaging Design. Solar Energy **65**(2): 83-89.

Fisher, R. M. (1998). Surface Temperature of Materials in Exterior Exposures and Artificial Accelerated Tests. A. S. 1202.

Frank, W. (1985). Finishings. **9**(2): 30-31.

Freeman, R. (2002). A Glossary for Telescope Buyers and Users.

http://observers.org/beginner/glossary.html.

Friedman, R. P., Gordon, J. M. and Ries, H. (1993). New Height-flux Two-stage Optical Design for Parabolic Solar Concentrator. Solar Energy **51**: 317-325.

Goldstein, J., Newbury, D., Echlin, P., Joy, D., Lyman, C., Lifshin, E., Sawyer, L. and Michael, J. (2002). Scanning Electron Microscopy and X-Ray Microanalysis, pp 1,108-109. New York, Kluwer Academic/Plenum Publishers.

Grewell, D. A. (1999). Applications with Infrared Welding of Thermoplastics. ANTEC 1999, Society of Plastic Engineers. **1**: 1411-1415.

Grewell, D. A. and Nijenhuis, W. (2000). TTIR Welding of Aliphatic Polyketone. ANTEC 2000. 1148-1152.

Grewell, D. A., Rooney, P. and Kagan, V. A. (2002). Relationship between Optical Properties and Optimized Processing Parameters for Through-Transmission Laser Welding of Thermoplastics. ANTEC 2002, Society of Plastic Engineers. **1**.

Griffiths, P. R. and de Hasseth, J. A. (1986). Fourier Transform Infrared Spectrometry. New York, John Wiley.

Grimm, R. A. (1996). Through-Transmission Infrared Welding of Polymers. ANTEC 1996, Society of Plastics Engineers. **1**: 1238-1244.

Grimm, R. A. (1998). Plastic Joining Method. US Pat. No. 5840147.

Grimm, R. A. (2002). Through-transmission Infrared Welding (TTIR) - Filter Media. ANTEC 2002. **1**.

Grimm, R. A., Christel, B. and Robinson, J. (2000). Methods for Making Nearly Invisible Welded Joints in Clear Polymers. ANTEC 2000. 1153-1158.

Grimm, R. A. and Yeh, H. (1998). Infrared Welding of Thermoplastics: Colored Pigments and Carbon Black Levels on Transmission of Infrared Radiation. Antec'98, Society of Plastic Engineers. **1**: 1026-1029.

Gruenwald, G. (1993). Plastics: How Structure Determines Properties. New York, Hanser.

Gurnee, E. F. (1977). Comparison of Elliptical and Parabolic Non-imaging Concentrators. Solar Energy **19**: 323-324.

Hammens, B. (1980). Solar Tracking Apparatus. US Pat. No. 4225781.

Handbook of Plastics Joining (1997). A Practical Guide. Norwich, NY, Plastics Design Library.

Harris, J. A. and Lenz, T. G. (1986). Thermal Performance of Solar Concentrator/Cavity Receiver Systems. Solar Energy **34**: 135-142.

Hartley, S. and Sallavanti, R. A. (2002). Clearweld^{TM} Laser Transmission Welding of Thermoplastic Polymers: Light Transmission and Color Considerations. www.clearweld.com.

Hession, P. J. and Bonwick, W. J. (1984). Experience with a Sun Tracker System. Solar Energy **32**(1): 3-11.

Hinterberger, H. and Winston, R. (1966a). Efficient Light Coupler for Treshold Cerenkov Counters. Review of Scientific Instruments **37**: 1094-1095.

Hinterberger, H. and Winston, R. (1966b). Gas Cerenkov Counter with Optimized Light-collecting Efficiency. Proc. int. Conf. Instrum. High Energy Phys. 205-206.

ICI (2003). Imperial Chemical Industries. www.fao.org/inpho/vlibrary/x0018e/X0018E0i.htm.

ICNIRP (1992). Non-Ionizing Radiation. 2nd International Non-Ionizing Radiation Workshop, Vancouver, Canada.

Imenes, A., Dey, C., Mills, D., Buie, D. and Bosi, S. (2002). A Small Paraboloidal Concentrator for Material Testing and Absorber Performance Characterisation. 11th Solar PACES International Symposium on Solar Thermal Concentrating Technologies, Zurich, Switzerland.

ISO4892 (1994). Plastics - Methods of Exposure to Laboratory Light Sources. Part 1: General Guidance. Geneva, ISO.

Jacques, L. F. E. (2000). Accelerated and Outdoor/Natural Exposure Testing of Coatings. Progress in Polymer Science **25**: 1337-1362.

Jakubowicz, I. (2001). Effects of Artificial and Natural Ageing on Impact Modified Poly(vinyl Chloride) (PVC). Polymer Testing **20**: 545-551.

Jaramillo, O. A., del Rio, J. A. and Huelsz, G. (1999). A Thermal Study of Optical Fibers Transmitting Concentrated Solar Energy. Journal of Physics D: Applied Physics **32**: 1000-1005.

Jones, I. (1998). Transmission Laser Welding of Plastics. TWI, Bulletin 75. 4 p.

Jones, I. A. and Taylor, N. S. (1994). High Speed Welding of Plastics Using Lasers. ANTEC 1994, Society of Plastics Engineers. 1360-1363.

Jones, I. A., Taylor, N. S., Sallavanti, R. A. and Griffiths, J. (2000). Use of Infrared Dyes for Transmission Laser Welding of Plastics. ANTEC 2000, Society of Plastics Engineers 58th Annual Technical Conference, Orlando, Florida. **1**: 1166-1170.

Jones, P. L. (1991). Energy World **184**: 10-13.

Jorgensen, G., Bingham, C., Goggin, R., Lewandowski, A. and Netter, J. (2000). Ultra-Accelerated Natural Sunlight Exposure Testing. US Pat. No. 6073500.

Jorgensen, G., Bingham, C., Netter, J., Goggin, R. and Lewandowski, A. (1999). A Unique Facility for Ultra-accelerated Natural Sunlight Exposure Testing of Materials. American Chemical Society.

Kagan, V. A., Bray, R. G. and Chambers, A. (2001). Forward to Better Understanding of Optical Characterization and Development of Colored Polyamides for the Infra-red/Laser Welding: Part I - Efficiency of Polyamides for Infra-red Welding. ANTEC 2001, Society of Plastics Engineers. 1262-1268.

Kagan, V. A., Bray, R. G. and Kuhn, W. P. (2000). Laser Transmission Welding of Semi-crystalline Thermoplastics - Part I: Optical Characterization of Nylon-based Plastics. ANTEC 2000. **1**: 1771-1781.

Kagan, V. A., Chambers, A. and Bray, R. G. (2001a). Forward to Better Understanding of Optical Characterization and Development of Colored Polyamides for the Infra-red/Laser Welding: Part II - Family of Colored Polyamides. ANTEC 2001, Society of Plastics Engineers. 1269-1275.

Kagan, V. A. and Punho, G. P. (2000). Laser Transmission Welding of Semi-crystalline Thermoplastics - Part II: Analysis of Mechanical Performance of Welded Nylon. ANTEC 2000. **1**: 1782-1789.

Kagan, V. A. and Woosman, N. M. (2002). Efficiency of Clear-Welding Technology for Polyamides. ANTEC 2002 Plastics: Annual Technical Conference, Volume 1: Processing.

Kaplan, G. (1985). Understanding Solar Concentrators. Technical Paper #30. Virginia, USA, Volunteers in Technical Assistance.

Kaplow, R. and Frank, R. I. (1976). A Tracking, High-Concentration Electrical and Thermal Solar Energy Collector System. 12th IEEE Photovoltaic Specialists Conference. 814-819.

Kashiwagi, T., Inaba, A., Brown, J., Hatada, K., Kitayama, T. and Masuda, E. (1986). Effects of Weak Linkages on the Thermal and Oxidative Degradation of PMMA. Macromolecules **19**: 2160-2168.

Kirgizbaev, D. A. and Zakhidov, R. A. (1974). Energy Distribution in the Concentration Field of Solar Installation with a Hyperboloidal Counter Reflector. Applied Solar Energy **10**(4): 71-76.

Kockott, D. (1996). Factors Influencing the Reliability of Results in Accelerated Weathering Tests. Durability Testing of Nonmetallic Materials. ASTM STP 1294.

Kreider, J. F. and Kreith, F. (1981). Solar Energy Handbook, McGraw-Hill USA.

Kreith, F. and Kreider, J. F. (1987). Principle of Solar Engineering, McGraw-Hill.

Krevelen, D. W. V. (1976). Properties of Polymers: Their Correlation with Chemical Structure, Elselvier.

Kribus, A. (2002). Thermal Integral Micro-Generation Systems for Solar and Conventional Use. Journal of Solar Energy Engineering **124**: 189-197.

Kribus, A., Zaibel, R. and Segal, A. (1998). Extension of the Hermite Expansion Method for Cassegrainian Solar Central Receiver Systems. Solar Energy **63**(6): 337-343.

Kribus, A., Zik, O. and Karni, J. (2000). Optical Fibers and Solar Power Generation. Solar Energy **68**(5): 405-416.

Kurosaki, Y., Matayoshi, T. and Sato, K. (2003). Overlap Welding of Thermoplastic Parts Without Causing Surface Thermal Damage by Using a CO_2 Laser. ANTEC 2003. 1121-1125.

Kwan, K. M., Cheng, K. and Benatar, A. (1998). Feasibility Study for Rapid Curing of Structural Adhesives. ANTEC 1998. 1089-1094.

Kwan, K. M., Wu, C. Y. and Benatar, A. (1998a). Rapid Curing of Polyurethane

Adhesive by Ultrasonic Vibration. ANTEC 1998. 1100-1103.

Kwan, K. M., Wu, C. Y. and Benatar, A. (1999). Rapid Heating and Curing of Structural Adhesives by Infrared and Radio Frequency. ANTEC1999. **1**: 1416-1421.

Lam, J. and Li, D. H. W. (1996). Luminous Efficacy of Daylight Under Different Sky Conditions. Energy Conversion and Management **37**(12): 1703-1711.

Langley, S. P. (1883). Experimental Determination of Wave-Lengths in the Invisible Prismatic Spectrum.

Lauf, R., Ridge, O., Bible, D. and Paulauskas, F. (1998). Method for Curing Polymers Using Variable-Frequency Microwave Heating. US Pat. No. 5721286.

Lazzari, M. and Chiantore, O. (2000). Thermal Ageing of Paraloid Acrylic Protective Polymers. Polymer **41**: 6447-6455.

Leather, C. (1999). Why sunlight is bad for plastics. British Plastics & Rubber Journal **4**(3): 4-6.

Liang, D., Monteiro, L., Teixeira, M., Monteiro, M. L. and Collares-Pereira, M. (1998). Fiber-optic solar energy transmission and concentration. Solar Energy Materials and Solar Cells **54**: 323-331.

Lin, C. B. and Lee, S. (1992). Journal of Polymer Science **44**: 2213.

Liu, K. and Piggott, M. R. (1998). Fracture Failure Processes in Polymers. I: Mechanical Tests and Results. Polymer Engineering and Science **38**(1): 60-68.

Lumsdaine, E. and Cherng, J. C. (1976). On Heat Exchangers Used with Solar Concentrators. Solar Energy **18**: 157-158.

Lynch, W. A. and Salameh, Z. M. (1990). Simple Electro-Optically Controlled Dual-Axis Sun Tracker. Solar Energy **45**(2): 65-69.

Malacara, D. and Malacara, Z. (1994). Handbook of Lens Design. New York, Marcel Dekker, Inc.

Malaczynski, G. W. and Cinpinski, G. J. (1996). Polymer Engineering and Science **6**(1): 106-116.

Malifaud, P. (1971). Optical Concentrator Without Flux Loss. US Pat. No. 3624834.

Mauk, C. E., Prendle, H. W., Jr. and Chi-Hua Sun, E. (1979). Optical and Thermal Analysis of a Cassegrainian Solar Concentrator. Solar Energy **23**: 157-167.

McGrath, G., Jones, I. A., Hilton, P. A., Kellar, E. J. C., Taylor, A. and Sallavani, R. (2001). New Advances in Plastics Joining for High Speed Production. Automotive Transportation Technology Conference, Barcelona.

Measurements Group (1994). Photoelastic Stress Analysis.

Mendenhall, C. E. (1911). On the Emissive Power of Wedge Shaped Cavities and Their Use in Temperature Measurements. The Astrophysical Journal **33**(2): 91-97.

Menges, G. (1973). Attempt to Explain Crazing in Amorphous Thermoplastics and Adhesion Fractures in Semicrystalline Thermoplastics and Filled Polymers, p.212. Deformation and Fracture of High Polymers. New York, Plenum Press.

Mills, D. R. and Giutronich, J. E. (1978). Ideal Prism Solar Concentrators. Solar Energy **21**: 423-430.

Mlinac, M., Rolich, J. and Bravar, M. (1976). Photodegradation of Colored Polyethylene Films. Journal of Polymer Science Symposium No. 57: 161-169.

Muhs, J., Earl, D., Beshears, D. and Maxey, C. (2003). Initial Results from an Experimental Hybrid Solar Lighting System in a Commercial Building and Overview of Related Value Propositions. International Solar Energy Conference ISEC 2003, Hawaii, USA.

Neumann, A. and Schmitz, A. (1998). The SCATMES Device for Measurement of Concentrated Solar Radiation. Solar Engineering, ASME 1988.

Nising, P., Zeilmann, T. and Meyer, T. (2003). On the Degradation and Stabilisation of Poly(methyl Methacrylate) in a Continuous Process. Chemical Engineering Technology **26**(5): 599-604.

Nostrell, P. (2000). Preparation and Optical Characterization of Antireflection Coatings and Reflector Materials for Solar Energy Systems. Uppsala University, Sweden. PhD Thesis.

Novikov, V. V. and al., e. (1966). Cassegrain System Modified for Solar Concentrators. Applied Solar Energy **2**(5): 10.

Nunez, C., McMinn, B. and Vitas, J. (1995). Barriers to the Use of Radiation-Curable Adhesives in Manufacturing. Adhesives Age. (January): 33-39.

Nyesyn, J. (2001). Solar Tracking System. US Pat. No. 6284968.

O'Gallagher and Winston, R. (1986). Test of a 'Trumpet' Secondary Concentrator with a Paraboloidal Dish Primary. Solar Energy **36**: 37-44.

O'Gallagher, J. and Winston, R. (1988). Performance Model for Two-stage Optical Concentrators for Solar Thermal Applications. Solar Energy **41**: 319-325.

OSLO Reference Manual (2001). Lambda Research Corporation.

Ou, B. S., Benatar, A. and Albright, C. W. (1992). Laser Welding of Polyethylene and Polypropylene Plates. ANTEC 1992, Society of Plastics Engineers. **2**: 1764-1767.

Perez, R., Ineichen, P., Seals, R., Michalsky, J. and Stewart, R. (1990). Modeling Daylight Availability and Irradiance Components from Direct and Global Irradiance. Solar Energy **44**(5): 271-289.

Plastic Reference Handbook (2000). Regal Plastic Supply Co.

Potente, H., Korte, J. and Becker, F. (1998). Laser Transmission Welding of Thermoplastics: Analysis of the Heating Phase. ANTEC 1998. **1**: 1022-1025.

Potente, H., Michel, P. and Heil, M. (1991). Infrared Radiation Welding: A Method for Welding High Temperature Resistant Thermoplastics. ANTEC 1991, Society of Plastics Engineers.

Q-Lab (2002). Q-Lab Weathering Research Service. www.q-panel.com.

Rabek, J. F. (1995). Polymer Photodegradation. Mechanisms and Experimental Methods. London, Chapman and Hall.

Rabl, A. (1976). Comparison of Solar Concentrators. Solar Energy **18**: 93-111.

Rabl, A., Goodman, N. B. and Winston, R. (1979). Practical Design Considerations for CPC Solar Collectors. Solar Energy **22**: 373-381.

Rhew, M., Mokhtarzadeh, A. and Benatar, A. (2003). Through Transmission Laser Welding of Polycarbonate and High-Density Polyethylene. ANTEC 2003. 1116-1120.

Rhew, M., Mokhtarzadeh, A. and Benatar, A. (2003a). Diode Laser Characterization and Measurement of Optical Properties of Polycarbonate and High-Density Polyethylene. ANTEC 2002. 1056-1060.

Robbins, J. (1989). Temperature-Controlled Accelerated Weathering Device. US Pat. No. 4807247.

Robieux, J. (1975). Patent 75-14585 (INPI), int. classification F03g7/02; 02KX/G02b5/10. US Pat. No.

Roman, R., Peterson, J. E. and Goswami, D. Y. (1995). An Off-Axis Cassegrain Optimal Design for Short Focal Length Parabolic Solar Concentrators. Journal of Solar Energy Engineering **117**: 51-56.

Russell, G. (1981). Solar Energy Collector Sun-tracking Apparatus and Method. US Pat. No. 4290411.

SAA-HB9 (1994). Handbook - Occupational Personal Protection. Homebush, NSW, Standards Australia.

Schulz, J. and Haberstroh, E. (2000). Welding of Polymers Using a Diode Laser. ANTEC 2000, Society of Plastic Engineers. 1196-1201.

Scishido, K., Sugina, M. and Kikuchi, S. (1989). The Optics System for the Middle-Size Solar Sterling Engine. Congress of the International Solar Energy Society, Kobe-City, Japan.

Smestad, G., Ries, H., Winston, R. and Yablonovitch, E. (1990). The Thermodynamic Limits of Light Concentrators. Solar Energy Materials **21**: 99-111.

Solar'95 (1995). Solar '95 Renewable Energy: The Future Is Now Proceedings. 33rd Annual Meeting of ANZSES. 3.

Sparrow, E. M. and Cess, R. D. (1970). Radiation Heat Transfer. Belmont, CA, Brooks Cole Publ. Co.

Stokes, V. K. (1989). Joining Methods for Plastics and Plastic Composites: An Overview. Polymer Engineering and Science **29**(19): 1310-1324.

Stone, K. and Blackmon, J. (1999). Alignment System and Method for Dish Concentrators. US Pat. No. 5982481.

Stoynov, L. and Yarlagadda, P. K. (2003). Development and Modification of a Cassegrainian Solar Concentrator for Utilization of Solar Thermal Power. International Solar Energy Conference ISEC 2003, Hawaii.

Stoynov, L. A. (1994). Solar Collector Test Stand, Renewable Energy Centre, Brisbane Institute of TAFE, Ithaca Campus.

Stoynov, L. A. (1997). Concentrating of Solar Energy (The Joining Energy). Research Report No. SEC-1997-1, Queensland University of Technology.

Stoynov, L. A., Yarlagadda, P. K. and Wang, C. Y. (2000). A Feasibility Study into Joining of Engineering Thermoplastics Utilizing Concentrated Beam Solar Radiation. Journal of Renewable Energy **21**(3-4): 333-361.

Stuart, B. H. (2002). Polymer Analysis. West Sussex, England, John Wiley & Sons. Ltd.

Summers, J. and Rabinovitch, E. (1999). Weatherability of Vinyl and Other Plastics. Weathering of Plastics. New York, ChemTec Publishing. pp 61-68.

Taylor, N. S. and Watson, M. N. (1988). Welding Techniques for Plastics and Composites. Joining and Materials. 70-76.

Tekelioglu, M. and Wood, B. (2003). Thermal Management of the PMMA Core Optical Fiber for Use in Hybrid Solar Lighting. International Solar Energy Conference ISEC 2003, Hawaii, USA.

Terry, C. K., Peterson, J. E. and Goswami, D. Y. (1996). Feasibility of an Iodine Gas Laser Pumped by Concentrated Terrestrial Solar Radiation. Journal of Solar Energy Engineering **118**(2): 136-139.

Tidjani, A. (1997). Photoxidation of Polypropylene Under Natural and Accelerated Weathering Conditions. Journal of Applied Polymer Science **64**: 2497-2503.

Tiganis, B. E., Burn, L. S., Davis, P. and Hill, A. J. (2002). Thermal Degradation of Acrylonitrite-butadiene-styrene (ABS) Blends. Polymer Degradation and Stability **76**: 425-434.

Tlusty, J. (2000). Manufacturing Processes and Equipment, Prentice Hall.

Torikai, A. and Hasegawa, H. (1998). Wavelength Effect on the Accelerated Photodegradation of PMMA. Polymer Degradation and Stability **61**: 61-364.

Umarov, G., Alimov, A. K. and Alavutdinov, D. N. (1976). A Cassegrain System for Solar Radiation. Applied Solar Energy **12**(2): 68-69.

Umarov, G., Zakhidov, R. and Kirgizbaev, D. A. (1973). Determining the Geometric Parameters of a Solar Power Element Consisting of a Hyperboloid and Paraboloid of Revolution. Applied Solar Energy **9**(4): 93-96.

Vainer, A. A. (1983). Influence of Longitudinal Adjustment in the Cassegrainian System. Applied Solar Energy **19**(6): 91-92.

Vainer, A. A. and Zakhidov, R. (1981). Computational Investigation of Cassegrainian Furnace. Applied Solar Energy **17**(2): 73-74.

Vijay, K. S. (1989). Joining Methods for Plastics and Plastic Composites: An Overview. Polymer Engineering and Science **29**(19): 1310-1324.

Wagner, J. K. (1991). Introduction to the Solar System, Saunders College Publishing.

Waterworth, M. D. (1999). Manual for Solar Telescope. Eagle Optics Pty Ltd.

Welford, W. T. and Winston, R. (1989). High Collection Nonimaging Optics. San Diego, Academic Press Inc.

Wilkie, C. A. (1999). TGA/FTIR: An Extremely Useful Technique for Studying Polymer Degradation. Polymer Degradation and Stability **66**: 301-306.

Winston, R., Cooke, D., Gleckman, P. and O'Gallagher, J. (1992). Ultra-high Solar Flux and Applications to Laser Pumping. Solar'92. 277-281.

Winston, R., Gleckman, P. and O'Gallagher, J. (1991). High Flux Solar Energy Transformation. US Pat. No. 5005958.

Wise, R. J. (1999). Thermal Welding of Polymers. Cambridge, Abington Publishing.

Wood, B. (2002). Adaptive Full-Spectrum Solar Energy Systems. Semi-Annual Technical Progress Report, University of Nevada. Prepared for National Energy Technology Laboratory, US Department of Energy.

Woosman, N. M. and Sallavanti, R. A. (2003). Achievable Weld Strengths for Various Thermoplastics Using the Clearweld Process. ANTEC 2003. 2522-2526.

Wu, C. Y. and Benatar, A. (1995). Single Mode Microwave Welding of HDPE Using Conductive Polyaniline/HDPE Composites. ANTEC 1995, Society of Plastics Engineers.

Wyland, R. (1981). Solar Tracking Device. US Pat. No. 4245616.

Wypych, G. (2003). Handbook of Material Weathering. Toronto, ChemTech Publishing.

Yarlagadda, P. K. D. V. and Tan, C. C. (1998). An Investigation Into Welding of Engineering Thermoplastics Using Focused Microwave Energy. Journal of Materials Processing Technology **74**(3): 199-212.

Yeh, H. J. and Grimm, R. A. (1998). Infrared Welding of Thermoplastics: Characterization of Transmission Behavior of Eleven Thermoplastics. ANTEC 1998, Society of Plastic Engineers. **1**: 1030-1033.

Yugami, H., Yano, M., Naito, H. and Arashi, H. (1999). Concentration of Fiber Transmitted Solar Energy by CPC for Solar Thermal Utilization. J. Phys. IV France **9**: 545-549.

Zakhidov, R. A. and Vainer, A. A. (1975). Integrated Precision Parameter for a Cassegrain System. Applied Solar Energy **11**(3-4): 107-108.

ZEMAX Optical Design Program User's Guide (2002). Focus Software.

Zhang, B. and Blum, F. (2001). Thermogravimetric Studies of PMMA on Silica. Polymer **42**(2).

Zimmerly, J. (1987). Textile World **137**(3): 103-104.

Zogbi, R. and Laplaze, D. (1984). Design and Construction of a Sun Tracker. Solar Energy **33**(3-4): 369-372.